CARRIER™

DELIVERY CATHETER

Lead the Way

To a smooth delivery of large bore catheters past tortuosity, bifurcations and vessel take offs

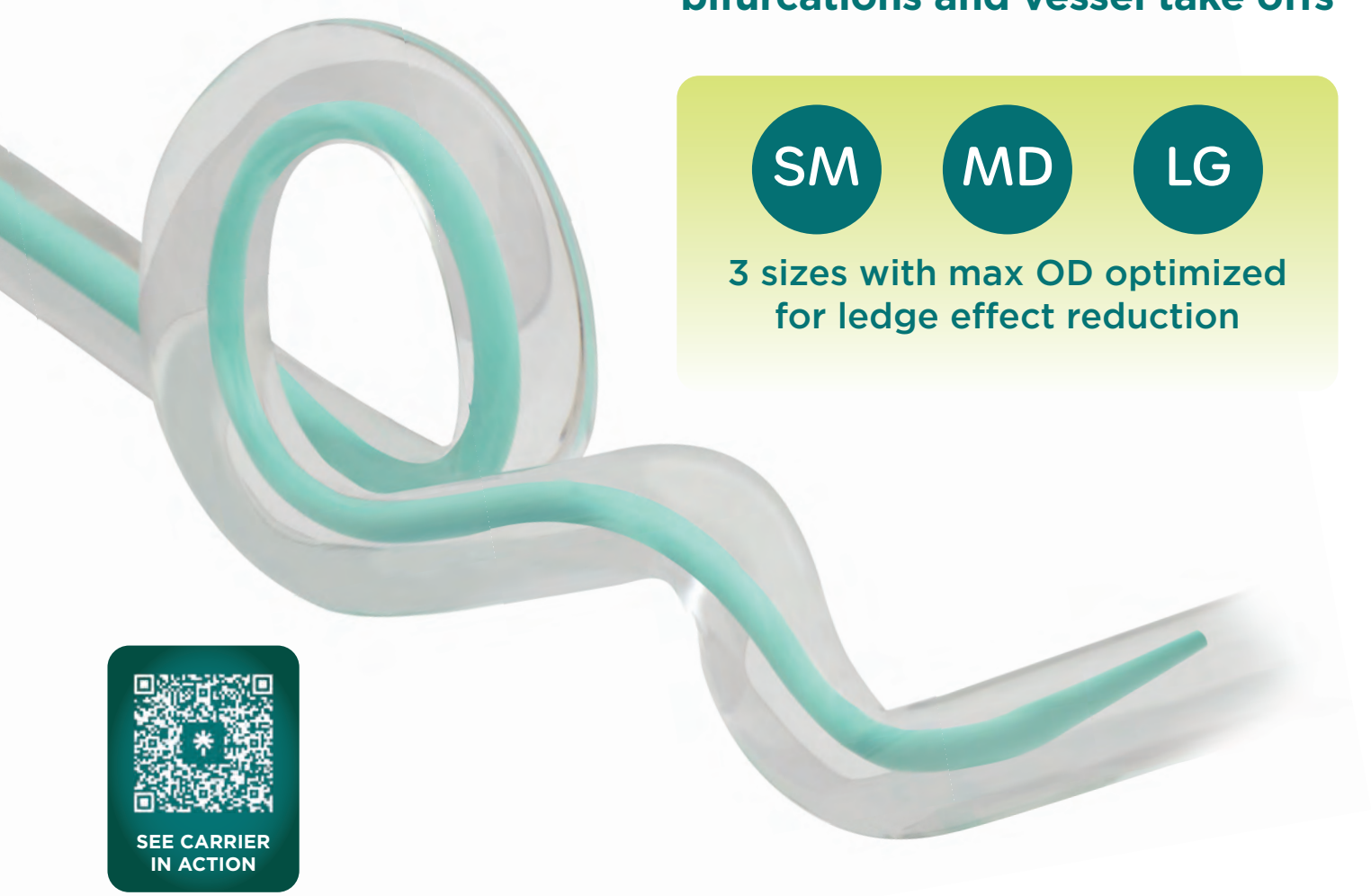

SM MD LG

3 sizes with max OD optimized for ledge effect reduction

SEE CARRIER IN ACTION

For a list of indications, warnings, precautions, and contraindications, refer to IFU-086.

Balt
29 Parker, Irvine, CA 92618 • tel 949.788.1443 • fax 949.788.1444 • **baltgroup.com**

CARRIER is a Trademark of Balt, LLC © 2024 BALT MKTG-495 Rev. A

balt
inspiring innovation

TERUMO
NEURO

Game-changing impact™

MicroVention is now Terumo Neuro

terumoneuro.com

All brand names are trademarks or registered trademarks owned by TERUMO CORPORATION, its affiliates, or unrelated third parties. MM1904 US 09/2024

Terumo Neuro Worldwide
Innovation Center
35 Enterprise
Aliso Viejo CA 92656 USA
PH +1.714.247.8000
PH +1.800.990.8368
Website: terumoneuro.com

AJNR DIGITAL TRANSITION:
Reflections from Our Readers

As a pediatric and adult neuroradiologist I prefer *AJNR* over other journals. *AJNR* has double the pediatric neuroradiology content than *AJR*, and although Pediatric Radiology has by far the most pediatric neuroradiology content, it is not concentrated in every issue. *AJNR* delivers the best bang for the buck for me.
Nadja Kadom

The *American Journal of Neuroradiology* has been instrumental to my career, not only as the platform where I published my research on spectral CT applications in head and neck imaging earlier in my career but also as a critical resource that keeps me updated on the latest advancements in neuroradiology. Serving as a senior editor in AI for *AJNR*, I am honored to contribute to the journal that has significantly shaped my professional growth and continues to influence the field.
Reza Forghani

AJNR is similar in character to many of my best neuroradiologist friends: adventurous, eager to explore new technologies, and understanding of where we are headed to improve neuroimaging care to patients.
Yvonne Lui

I have always appreciated *AJNR* as the premier international neuroimaging journal. During my career, the first-tier target for neuroimaging manuscripts for me and my team has always been *AJNR*. I know that my publications in *AJNR* will maximally reach the global neuroradiology community compared to publications in other journals and result in maximal impact on clinical practice.
Mahmud Mossa-Basha

In an era of rapid digital transformation, I hope each click will bring as much joy as opening a paper journal. While the nostalgia of printed editions is irreplaceable, I trust that digital innovation and expanded accessibility will enrich the experience of scientific journals, merging tradition with modern convenience.
Patricia Rafful

AJNR has been instrumental in my professional growth and career development. As a trainee, I turned to *AJNR* for practical and clinically relevant knowledge from trusted experts. As an academic faculty, I rely on *AJNR* to keep me abreast of the latest developments in the field. Along the way, I have been blessed with opportunities to collaborate with highly regarded colleagues on some *AJNR* articles of our own.
Paul Bunch

AJNR has educated me over the years, through my journey from residency until now in private practice.

For the last 4 decades, this journal has given me state-of-the-art insight.

Very useful for the management of patients.
Sajendra Kumar

Watch more of these reflections in a short video:

The *American Journal of Neuroradiology* has been an invaluable resource throughout my career, providing cutting-edge research and clinical insights in a trusted, print format. As the journal evolves digitally, I hope to see it continue fostering global collaboration, enhancing accessibility, and driving innovation in neuroradiology by offering seamless access to its wealth of knowledge.
Ani Hoxha

For the last 4 decades, this journal has given me state-of-the-art insight. There is no greater joy than leafing through *AJNR* and discovering the mysteries of the brain and spine. Digital publication ushers in an era of fingertip exploration of brain and spine imaging.
Gaurang Shah

AJNR

AMERICAN JOURNAL OF NEURORADIOLOGY

DECEMBER 2024
VOLUME 45
NUMBER 12
WWW.AJNR.ORG

Publication Preview at www.ajnr.org features articles released in advance of print.
Visit www.ajnrblog.org to comment on AJNR content and chat with colleagues.

EDITORIALS

1827 **Turning the Page at *AJNR*: Charting a Legacy of Excellence in the Digital Era** *Max Wintermark*

1828 ***AJNR*: A Brief History in 8 Episodes** *Mauricio Castillo, et al.*

1831 **The New *AJNR*: Personalized for YOU** *Lubdha Shah, et al.*

1832 ***AJNR Quo Vadis*? An International Perspective on the Journal's Next 10 Years** *Roland Bammer*

1834 **The Future of Academic Neuroradiology: Challenges, Opportunities, and Way Forward** *Ajay Malhotra*

1838 **The Future of Artificial Intelligence in Clinical Radiology: Savior or False Hope?** *Greg Zaharchuk, et al.*

READERS' CHOICE

1845 **Our Most Impactful Articles** *Max Wintermark*

S1 **Dural Arteriovenous Malformation of the Major Venous Sinuses: An Acquired Lesion** *Mohammad Y. Chaudhary, et al.*

S8 **Diffusion-Weighted MR Imaging of Acute Stroke: Correlation with T2-Weighted and Magnetic Susceptibility-Enhanced MR Imaging in Cats** *M.E. Moseley, et al.*

S15 **The 2021 World Health Organization Classification of Tumors of the Central Nervous System: What Neuroradiologists Need to Know** *A.G. Osborn, et al.*

S25 **MR Signal Abnormalities at 1.5 T in Alzheimer's Dementia and Normal Aging** *Franz Fazekas, et al.*

S31 **Susceptibility-Weighted Imaging: Technical Aspects and Clinical Applications, Part 1** *E.M. Haacke, et al.*

S43 **The Pipeline Embolization Device for the Intracranial Treatment of Aneurysms Trial** *P.K. Nelson, et al.*

AJNR (Am J Neuroradiol ISSN 0195–6108) is a journal published monthly, owned and published by the American Society of Neuroradiology (ASNR), 820 Jorie Boulevard, Oak Brook, IL 60523. Annual dues for the ASNR include approximately 19% for a journal subscription. The journal is printed by Intellicor Communications, 330 Eden Road, Lancaster, PA 17601; Periodicals postage paid at Oak Brook, IL and additional mailing offices. Printed in the U.S.A. POSTMASTER: Please send address changes to American Journal of Neuroradiology, P.O. Box 3000, Denville, NJ 07834, U.S.A. Subscription rates: nonmember $350 online only; institutions $425 online only (basic), $875 online only (extended). Indexed by PubMed/MEDLINE, BIOSIS Previews, Current Contents (Clinical Medicine and Life Sciences), EMBASE, Google Scholar, HighWire Press, Q-Sensei, RefSeek, Science Citation Index, SCI Expanded, ReadCube, and Semantic Scholar. Copyright © American Society of Neuroradiology.

S50 **Shift Volume Directly Impacts Neuroradiology Error Rate at a Large Academic Medical Center: The Case for Volume Limits** *Vladimir Ivanovic, et al.*

S55 **Autoimmune Encephalitis: Pathophysiology and Imaging Review of an Overlooked Diagnosis** *B.P. Kelley, et al.*

S64 **Significance of Cerebellar Tonsillar Position on MR** *A.J. Barkovich, et al.*

S69 **MR Imaging of White Matter Disease in Children** *Martha A. Nowell, et al.*

S76 **CNS Vasculitis in Autoimmune Disease: MR Imaging Findings and Correlation with Angiography** *Martin G. Pomper, et al.*

S87 **Differentiation Between Postoperative Scar and Recurrent Disk Herniation: Prospective Comparison of MR, CT, and Contrast-Enhanced CT** *Spiros Sotiropoulos, et al.*

S92 **Percutaneous Polymethylmethacrylate Vertebroplasty in the Treatment of Osteoporotic Vertebral Body Compression Fractures: Technical Aspects** *Mary E. Jensen, et al.*

S100 **Posterior Reversible Encephalopathy Syndrome, Part 1: Fundamental Imaging and Clinical Features** *W.S. Bartynski*

REVIEW ARTICLES

1846 **A Neuroradiologist's Guide to Operationalizing the Response Assessment in Neuro-Oncology (RANO) Criteria Version 2.0 for Gliomas in Adults** *Benjamin M. Ellingson, et al.* — BRAIN TUMOR IMAGING

1857 **Comprehensive Review of External and Middle Ear Anatomy on Photon-Counting CT** *Dinesh Rao, et al.* — HEAD AND NECK IMAGING

1865 **Atypical Parkinsonian Syndromes: Structural, Functional, and Molecular Imaging Features** *Graham Keir, et al.* — NEURODEGENERATIVE DISORDER IMAGING

GENERAL CONTENTS

1878 **Dural Arteriovenous Fistulas: Baseline Cognitive Changes and Changes following Treatment: A Prospective Longitudinal Study** *Zeev Itsekson-Hayosh, et al.* — NEUROINTERVENTION

1885 **Automated Segmentation of MRI White Matter Hyperintensities in 8421 Patients with Acute Ischemic Stroke** *Hosung Kim, et al.* — ARTIFICIAL INTELLIGENCE; NEUROVASCULAR/STROKE IMAGING

1895 **Clinical and Radiologic Findings in Children with Anomalous Pontine Cranial Nerves** *Karen K. Moeller, et al.* — PEDIATRIC NEUROIMAGING

1901 **Imaging Transcriptomics of Brain Functional Alterations in MS and Neuromyelitis Optica Spectrum Disorder** *Yuna Li, et al.* — NEUROIMAGING PHYSICS/FUNCTIONAL NEUROIMAGING/CT AND MRI TECHNOLOGY; ULTRA-HIGH-FIELD MRI/IMAGING OF EPILEPSY/DEMYELINATING DISEASES/INFLAMMATION/INFECTION

1910 **Macro- and Microstructural White Matter Differences in Neurologic Postacute Sequelae of SARS-CoV-2 Infection** *Erin E. O'Connor, et al.*

ULTRA-HIGH-FIELD MRI/ IMAGING OF EPILEPSY/ DEMYELINATING DISEASES/ INFLAMMATION/INFECTION

1919 ***Commentary***
Evidence for a Link of COVID-19-Associated Long-Term Neurologic Symptoms and Altered Brain Integrity?
Alexander Rau, et al.

1921 **Spontaneous Intracranial Hypotension in Children: A Multi-Institutional Review of Spinal CSF Leaks Localized on Advanced Myelography**
Ajay A. Madhavan, et al.

SPINE IMAGING AND SPINE IMAGE-GUIDED INTERVENTIONS

BOOK REVIEWS *R.M. Quencer, Section Editor*
Please visit www.ajnrblog.org to read and comment on Book Reviews.

Indicates Editor's Choices selection
Indicates Fellows' Journal Club selection
Indicates open access to non-subscribers at www.ajnr.org
Indicates article with supplemental online data
Indicates article with supplemental online video
Evidence-Based Medicine Level 1
Evidence-Based Medicine Level 2

AJNR

AMERICAN JOURNAL OF NEURORADIOLOGY

Official Journal:
American Society of Neuroradiology
American Society of Functional Neuroradiology
American Society of Head and Neck Radiology
American Society of Pediatric Neuroradiology
American Society of Spine Radiology

DECEMBER 2024 • VOLUME 45 • NUMBER 12 • WWW.AJNR.ORG

EDITOR-IN-CHIEF

Max Wintermark, MD, MAS, FASFNR, FICIS
Frank T. McGraw Memorial Chair in the Study of Cancer
Professor and Chair of Neuroradiology
The University of Texas MD Anderson Center

DEPUTY EDITOR

Lubdha M. Shah, MD, MS
Professor of Radiology and Director of Spine Imaging
Department of Radiology and Imaging Sciences
University of Utah

SPECIAL ADVISORS TO THE EDITOR-IN-CHIEF

Mauricio Castillo, MD, FACR
MA Mauro Distinguished Professor of Radiology
University of North Carolina-Chapel Hill

Robert Quencer, MD
Professor Emeritus
Department of Radiology
University of Miami

ARTIFICIAL INTELLIGENCE

Senior Editor

Reza Forghani, MD, PhD
Professor of Radiology & Artificial Intelligence
Vice Chair of AI
Director, Radiomics & Augmented Intelligence Laboratory (RAIL)
Department of Radiology
University of Florida College of Medicine

Associate Editors

Andreas Rauschecker, MD, PhD
Assistant Professor-in-Residence
Co-Executive Director and Clinical Director, Center for Intelligent Imaging (ci^2)
Department of Radiology & Biomedical Imaging
University of California, San Francisco

Sam (Seyedmehdi) Payabvash, MD
Assistant Professor of Radiology
Yale School of Medicine
Connecticut

Special Editors

Greg Zaharchuk, MD, PhD
Professor of Radiology (Neuroimaging and Neurointervention)
Stanford University
California

Spyridon Bakas, PhD
Joshua Edwards Associate Professor
Department of Pathology and Laboratory Medicine
Inaugural Director of the Division of Computational Pathology
Indiana University School of Medicine

BRAIN TUMOR IMAGING

Senior Editor

Ben Ellingson, PhD
Professor and Director of MRI Research
Director, UCLA Brain Tumor Imaging Laboratory
Department of Radiological Sciences
David Geffen School of Medicine
University of California, Los Angeles

Associate Editors

Ali Nabavizadeh, MD
Assistant Professor of Radiology
Division of Neuroradiology
University of Pennsylvania

Jana Ivanidze, MD, PhD
Assistant Professor, Department of Diagnostic Radiology
Director of Brain PET
Division of Molecular Imaging and Therapeutics
Division of Neuroradiology
Department of Radiology
Weill Cornell Medicine, New York

Special Editor

Susan Chang, MD
Professor, Neurological Surgery
University of California, San Francisco

EMERGENCY NEURORADIOLOGY

Senior Editor

Karen Buch, MD
Assistant Professor of Radiology
Massachusetts General Hospital

Associate Editors

Melissa A. Davis, MD, MBA
Vice Chair of Medical Informatics
Associate Professor
Department of Radiology and Biomedical Imaging
Yale School of Medicine
Connecticut

Jason Talbott, MD, PhD
Associate Professor, Neuroradiology Section
Department of Radiology and Biomedical Imaging
University of California, San Francisco and Zuckerberg San Francisco General Hospital

Special Editor

Brian L. Edlow, MD
Neurocritical Care Faculty, Massachusetts General Hospital
Co-Director, Mass General Neuroscience
Associate Director, Center for Neurotechnology and Neurorecovery
Affiliated Faculty, Athinoula A. Martinos Center for Biomedical Imaging
Associate Professor of Neurology, Harvard Medical School
Chen Institute MGH Research Scholar
2023-2028

HEAD AND NECK IMAGING

Senior Editor

Amy Juliano, MD
Associate Professor of Radiology
Massachusetts Eye and Ear
Harvard Medical School

Associate Editors

Burce Ozgen, MD
Clinical Professor of Radiology
University of Illinois at Chicago

David Zander, MD
Assistant Professor, Radiology
University of Colorado School of Medicine

Special Editor

Stephen Y. Lai, MD, PhD, FACS
Professor of Head and Neck Surgery
The University of Texas MD Anderson Center

HEALTH POLICIES/QUALITY IMPROVEMENT/ EVIDENCE-BASED NEUROIMAGING

Senior Editor

Nadja Kadom, MD, FACR, FAAP
Professor, Department of Radiology and Imaging Sciences
Emory University School of Medicine
Pediatric Neuroradiologist, Department of Radiology
Children's Healthcare of Atlanta

Associate Editors

Melissa M. Chen, MD
Associate Professor,
Department of Neuroradiology, Division of Diagnostic Imaging
The University of Texas MD Anderson Center

Ajay Malhotra, MBBS, MD, MMM
Professor of Radiology and Biomedical Imaging and Neurosurgery
Yale School of Medicine
Connecticut

MOLECULAR NEUROIMAGING/NUCLEAR MEDICINE

Senior Editor

Ana M. Franceschi, MD, PhD
Associate Professor of Radiology
Donald and Barbara Zucker School of Medicine at Hofstra/Northwell
The Feinstein Institutes for Medical Research
Neuro-PET Imaging
Lenox Hill Hospital
New York

Associate Editors

Nadya Pyatigorskaya, MD, PhD
Neuroradiology Department, Pitié-Salpêtrière Hospital
Researcher, Brain Institute (ICM)
France

Marc Daniel Benayoun, PhD, MD
Assistant Professor of Radiology
Co-Section Head of Nuclear Medicine
Medical Director of Nuclear Medicine and PET
Vice Chair of Radiation Drug Research Committee
Atrium Wake Forest Health
North Carolina

Special Editor

Satoshi Minoshima, MD, PhD
Anne G. Osborn Chair and Professor
Department of Radiology and Imaging Sciences
Spencer Fox Eccles School of Medicine
University of Utah

NEURODEGENERATIVE DISORDER IMAGING

Senior Editor

Gloria Chiang, MD
Associate Professor, Co-Director of the Brain Health Imaging Institute
Department of Radiology
Weill Cornell Medicine/NewYork-Presbyterian Hospital

Associate Editors

Fang Frank Yu, MD
Assistant Professor of Radiology
Division of Neuroradiology, Department of Radiology
Advanced Imaging Research Center
University of Texas Southwestern Medical Center

Priya Rajagopalan, MBBS, MPH
Assistant Professor of Radiology, Division of Neuroradiology
Associate Program Director, Neuroradiology Fellowship
Medical Director, Center for Image Acquisition
Mark and Mary Stevens Neuroimaging and Informatics Institute
Keck School of Medicine, University of Southern California

NEUROIMAGING PHYSICS/FUNCTIONAL NEUROIMAGING/CT AND MRI TECHNOLOGY

Senior Editor

Hongyu An, DSc
Professor, Mallinckrodt Institute of Radiology
Neurology, Biomedical Engineering, Electrical and Systems Engineering, Division of Biology and Biomedical Sciences
Director, Biomedical Magnetic Resonance Center
Associate Director, Center for Clinical Imaging Research
Washington University in St. Louis

Associate Editors

Timothy J. Carroll, PhD
Professor, Department of Radiology
University of Chicago

Hugo de Jong, PhD
Professor of Medical Physics Radiology and Nuclear Medicine
UMC Utrecht
the Netherlands

Special Editor

Roland Bammer, PhD, MEE, MBA, FISMRM
Head/Chair, Department of Radiology and Radiological Sciences
Professor of Radiology and Radiological Sciences, Monash University
Australia

NEUROINTERVENTION

Senior Editor

Steven Hetts, MD, FACR
Co-Chief, NeuroEndovascular Surgery Service Line
Chief of Interventional Neuroradiology, Mission Bay Hospitals
Professor of Radiology, Biomedical Imaging, and Neurological Surgery
University of California, San Francisco

Associate Editors

Kristine Blackham, MD
Associate Professor
Diagnostic and Interventional Neuroradiology
Clinic for Radiology and Nuclear Medicine
University Hospital of Basel

Maksim Shapiro, MD
Clinical Associate Professor
Departments of Radiology, Neurosurgery, and Neurology
Division of Neurointerventional Radiology
NYU Langone Health and Bellevue NYCH + Hospitals
New York

Special Editor

Giuseppe Lanzino, MD
Professor of Neurosurgery
Mayo Clinic, Minnesota

NEUROPSYCHIATRIC IMAGING

Senior Editor

Jody Tanabe, MD
Professor
Chief of Neuroradiology
University of Colorado-Anschutz Medical Campus

Associate Editors

John-Paul J. Yu, MD, PhD
Associate Professor of Radiology, Psychiatry, and Biomedical Engineering
University of Wisconsin School of Medicine and Public Health

J. Eric Schmitt, MD, PhD
Assistant Professor of Radiology and Psychiatry
Division of Neuroradiology
Perelman School of Medicine, University of Pennsylvania

Special Editor

Leanne Williams, PhD
Vincent V.C. Woo Professor of Psychiatry and Behavioral Sciences
Director of the Stanford Center for Precision Mental Health and Wellness
Stanford University
California

NEUROVASCULAR/STROKE IMAGING

Senior Editor

Mahmud Mossa-Basha, MD
Professor of Radiology, Neurology and Electrical Engineering
Vice Chair of Clinical Research and Clinical Transformation
Co-Director of the Research Vascular Imaging Lab
University of Washington School of Medicine

Associate Editors

Shalini Amukotuwa, MB BS, PhD, FRANZCR
Head of Neuroradiology and Director of MRI, Monash Health
Associate Professor of Radiology, Monash University
Australia

Myriam Edjlali, MD, PhD
Neuroradiologist, Public Assistance - Paris Hospitals (APHP)
Vice Deputy of the Imaging Lab of Paris Saclay (BioMaps), France

Special Editors

Bruce Campbell, MBBS (Hons), BMedSc, PhD, FRACP, FAHMS
Consultant Neurologist, Head of Neurology and Stroke
Department of Neurology and Melbourne Brain Centre
Royal Melbourne Hospital
Professor of Neurology, Dame Kate Campbell Fellow
University of Melbourne
Australia

David Liebeskind, MD, FAAN, FAHA, FANA, FSVIN, FWSO
Professor of Neurology
Director, Neurovascular Imaging Research Core
Director, UCLA Comprehensive Stroke Center
University of California, Los Angeles

PEDIATRIC NEUROIMAGING

Senior Editor

Caroline D. Robson, MBChB
Division Chief & Endowed Chair, Neuroradiology
Director, Head & Neck Imaging
Department of Radiology
Department of Otolaryngology
Boston Children's Hospital
Harvard Medical School

Associate Editors

Anna Trofimova, MD, PhD
Assistant Professor, Radiology and Imaging Sciences, Emory University
Pediatric Neuroradiologist, Children's Healthcare of Atlanta

Matthew Whitehead, MD
Department of Radiology, Division of Neuroradiology
Children's Hospital of Philadelphia
Associate Professor of Radiology
Perelman School of Medicine, University of Pennsylvania

Special Editor

Nomazulu Dlamini, MD, MBBS, MRCPCH, MSc (Lon), PhD
Assistant Professor, Director of Children's Stroke Program
The Hospital for Sick Children
Toronto

SPINE IMAGING AND SPINE IMAGE-GUIDED INTERVENTIONS

Senior Editor

J. Levi Chazen, MD
Associate Professor, Neuroradiology
Director, Spine Imaging
Hospital for Special Surgery
Weill Cornell Medicine
New York

Associate Editors

Jennifer McCarty, MD
UTHealth Houston

Vinil Shah, MD
Associate Professor of Radiology Neuroradiology
Division Chief
University of California, San Francisco

Special Editor

Wouter I. Schievink, MD
Professor of Neurosurgery
Director, Cerebrospinal Fluid Leak Program
Director, Vascular Neurosurgery Program
NFL Neurotrauma Consultant
Department of Neurosurgery
Cedars-Sinai Medical Center
California

ULTRA-HIGH-FIELD MRI/IMAGING OF EPILEPSY/DEMYELINATING DISEASES/ INFLAMMATION/INFECTION

Senior Editor

Erik Middlebrooks, MD
Professor of Radiology
Mayo Clinic Florida

Associate Editors

Susie Y. Huang, MD, PhD
Associate Professor of Radiology, Harvard Medical School
Associate Chair, Faculty Affairs, Department of Radiology
Director of Translational Neuro MR Imaging & Connectomics, Athinoula A. Martinos Center for Biomedical Imaging
Massachusetts General Hospital

Girish Bathla, MD, FRCR
Associate Professor, Neuroradiology
Mayo Clinic
Minnesota

Special Editor

Darin T. Okuda, MD, FAAN, FANA
Professor of Neurology
Director, Neuroinnovation Program
Director, Multiple Sclerosis & Neuroimmunology Imaging Program
Director, Radiologically Isolated Syndrome Consortium
Department of Neurology
UT Southwestern Medical Center at Dallas

OUTREACH AND EDUCATION

Senior Editor

Lea Alhilali, MD
Radiology Partners, HonorHealth Research Institute
Arizona

DIGITAL MEDIA AND ENGAGEMENT

Senior Editor

Kevin Hsu, MD
Clinical Assistant Professor
Department of Radiology
NYU Grossman School of Medicine
New York

Case Collection Editors

Matylda Machnowska, BMedSc, MD, FRCSC, ABR
Assistant Professor of Radiology, University of Toronto
Neuroradiologist, Sunnybrook Health Sciences Centre

Anvita Pauranik, MD
Clinical Assistant Professor of Radiology
BC Children's Hospital
University of British Columbia

Sandy Cheng-Yu Chen, MD
Chair, Translational Imaging Research Center
Taipei Medical University Hospital
Vice President of Taipei Medical University

Social Media Editor

Kimberly Seifert, MD, MS
Stanford University
California

Assistant Social Media Editors

Ani Hoxha, MD
Mother Theresa UHC
Albania

Maxwell Opoku, MD
Novosibirsk State Research University
Russia

Podcast Editor

Kevin Hiatt, MD
Assistant Professor, Radiology
Wake Forest University School of Medicine
North Carolina

Deputy Podcast Editor

George K. Vilanilam, MD
PGY5 Resident Physician, Department of Radiology
University of Arkansas for Medical Sciences

STATISTICS

Senior Editors

Bryan A. Comstock, MS
Senior Biostatistician, Department of Biostatistics
University of Washington

Ziyi Li, PhD
Assistant Professor, Biostatistics
The University of Texas MD Anderson Center

BOOK REVIEW EDITOR

Robert Quencer, MD
Professor Emeritus
Department of Radiology
University of Miami

JUNIOR EDITORIAL BOARD

ARTIFICIAL INTELLIGENCE

Janet Mei, MD, MPH
Johns Hopkins University School of Medicine
Maryland

BRAIN TUMOR AND NEUROPSYCHIATRIC IMAGING

Richard Dagher, MD
The University of Texas MD Anderson Center

EMERGENCY NEURORADIOLOGY AND NEUROIMAGING PHYSICS/FUNCTIONAL NEUROIMAGING/CT AND MRI TECHNOLOGY

Maryam Vejdani-Jahromi, MD, PhD
Harvard Medical School, Massachusetts General Hospital

HEAD AND NECK IMAGING

Jacqueline Junn, MD
Emory University School of Medicine
Georgia

NEURODEGENERATIVE DISORDER IMAGING

Mikail Malik, BHSc, Medical Student (MD 2T6)
University of Toronto

NEUROINTERVENTION AND HEALTH POLICIES/QUALITY IMPROVEMENT/ EVIDENCE-BASED MEDICINE

Alexandre Boutet, MD, PhD, Senior Editorial Fellow
Joint Department of Medical Imaging
University of Toronto

NEUROVASCULAR/STROKE IMAGING

Sebastiano Vacca, Medical Student
University of Cagliari Medical School

PEDIATRIC NEUROIMAGING

Matheus Dorigatti Soldatelli, MD, PhD, EDiNR/EDiPNR
Boston Children's Hospital, Harvard Medical School

SPINE IMAGING AND SPINE IMAGE-GUIDED INTERVENTIONS

Ian Mark, MD, MSM
Mayo Clinic, Minnesota

ULTRA-HIGH-FIELD MRI/IMAGING OF EPILEPSY /DEMYELINATING DISEASES/ INFLAMMATION/INFECTION

Maram Alafif, MBBS
University of California, San Diego Health

Founding Editor
Juan M. Taveras
Editors Emeriti
Mauricio Castillo, Robert I. Grossman, Michael S. Huckman, Robert M. Quencer, Jeffrey S. Ross

Managing Editor
Karen Halm
Assistant Managing Editor
Laura Wilhelm

Scientific Editor
Theresa S. Richards, PhD
Digital Publications Senior Manager
Gwen Travis
Executive Director, ASNR
Mary Beth Hepp

Turning the Page at *AJNR*: Charting a Legacy of Excellence in the Digital Era

Dear Readers, Authors, Reviewers, Sponsors, and Friends of the *American Journal of Neuroradiology (AJNR)*, It is with a mix of nostalgia and excitement that I address you today as we mark a significant milestone in the history of the *AJNR*.

Since its inception in 1980, *AJNR* has been a beacon of excellence in the field of neuroradiology, serving as a platform for the dissemination of clinical insights, groundbreaking research, and inspiring education. From our beginnings as a print-only publication to our evolution into a digital powerhouse (the *AJNR* had its first electronic publication in 2000), the *AJNR* has remained steadfast in its commitment to advancing the frontiers of neuroradiology. the *AJNR* is the official journal of the American Society of Neuroradiology (ASNR), the American Society of Functional Neuroradiology (ASFNR), the American Society of Head & Neck Radiology (ASHNR), the American Society of Pediatric Neuroradiology (ASPNR), and the American Society of Spine Radiology (ASSR).

As we gather here for the last printed issue of the *AJNR*, I am filled with gratitude for the countless authors, reviewers, and readers, as well as the editors and editorial staff who have contributed to our success over the years. Your dedication and support have been the driving force behind the *AJNR's* evolution from its inception to becoming a respected leader in the field.

While bidding farewell to our printed format may evoke a sense of nostalgia for many of us, it also marks the beginning of an exciting new chapter for the *AJNR*. Our transition to a fully digital platform opens up a world of possibilities, allowing us to deliver content in innovative ways and reach a wider audience than ever before.

In the digital age, *the AJNR* will continue to uphold the same rigorous standards of quality and integrity that have defined us for over 4 decades. Our commitment to excellence remains unwavering, and we are dedicated to providing our readers with the same unparalleled access to cutting-edge research and clinical expertise that they have come to expect from the *AJNR*.

As we embark on this new journey together, I invite you to join us in celebrating the legacy of the *AJNR* and embracing the opportunities that lie ahead. Your continued support and engagement are crucial as we navigate the evolving landscape of academic publishing and chart a course for the future of neuroradiology.

On behalf of the entire *AJNR* team, I extend my heartfelt thanks to each and every one of you for your contributions to our journal. It is an honor and a privilege to serve as your Editor-in-Chief, and I look forward to continuing this odyssey with you in the digital realm.

With warm regards,

Max Wintermark

Editor-in-Chief, *American Journal of Neuroradiology*

http://dx.doi.org/10.3174/ajnr.A8466

AJNR: A Brief History in 8 Episodes

Mauricio Castillo, and Robert Quencer

As most of our readers know, Dr Juan Taveras invited 14 American and Canadian neuroradiologists for a dinner at Keen's English Chop House (now called Keen's Steakhouse) in New York City on April 19, 1962. Although much of the discussion there concerned preparations for the Symposium Neuroradiologicum that Taveras was to host 2 years later, another important topic was the formation of a professional society comprised of North American neuroradiologists. The name the American Society of Neuroradiology (ASNR) was chosen, and the decision to host an annual meeting in conjunction with American Roentgen Ray Society (ARRS) or Radiological Society of North America (RSNA) was floated. The idea of having a dedicated journal was not considered at this time.

Episode 1: The Birth of the Journal

Today, it may seem strange that the decision to have a dedicated North American neuroradiology journal was not made by ASNR until 1978, sixteen years after its foundation.

At the end of 1977, Dr Samuel Wolpert sent a letter to the then-president of ASNR, Dr Sadek Hilal, proposing the creation of a journal, which the executive committee enthusiastically approved. Wolpert then presented his vision to the membership during the 1978 annual meeting, where it was unanimously approved. Because financial restraints would not allow the ASNR to publish its own journal, the idea of the new journal appearing under the auspices of the *Journal of Computer Assisted Tomography* (*JCAT*) (published by Lippincott) or *Neuroradiology* (published by Springer) or other publishers was suggested. Their interest was mild at best because most thought the ASNR was not large enough to fund a profitable journal (at the time it had only 500 members).

Dr Norman Leeds was then asked to serve as the first chairperson of the newly formed Publications Committee, and anticipating the creation of the journal, they offered the position of Editor-in-Chief (EIC) to Dr Hilal, who declined because he was the Editor of the already-established *JCAT*. Nevertheless, as the idea of a new journal progressed, some people started believing that it could be a threat to the coherence of radiology.

General radiologists, including those in positions of power in our different professional and scientific societies, opposed the concept of a journal dedicated to neuroradiology. In their opinion, the specialty was too small and neuroradiology articles were already being published in the *American Journal of Roentgenology* (*AJR*), *Radiology*, and *JCAT*. A new journal would deprive those important journals of material, and a relatively new subspecialty with its own publication would weaken and fragment radiology! Also, at that time, most CTs were of the head, and general radiologists feared that neuroradiologists were becoming too strong and that they would lose the revenue of head CT interpretations. The concern soon spread to the ASNR membership, and even some founding members changed sides and began opposing the idea of the journal. Other options were considered to assuage fears, and one included the publication of a single annual journal that would consist of invited and scientific presentations given at the annual meeting. Just as the idea of a proper neuroradiology journal seemed doomed, help arrived.

Dr Melvin Figley was Chair of Radiology at the newly formed department at the University of Washington School of Medicine in Seattle. Dr Figley was considered an innovator and was not a stranger to neuroradiology because he spent time in Sweden training in angiography. In 1976, he took over *AJR* (established in 1907) as its EIC and was the first to require a mandatory 2-person peer review for all manuscripts submitted. Knowing of Dr Figley's commendable traits, Norman Leeds approached him in 1978 with the notion of establishing cooperation between ASNR and the *AJR*. Dr Figley's dilemma was how to help a young subspecialty society without compromising the contents of *AJR*. He solved this issue by proposing that the new journal be published in coordination with *AJR* and that selected neuroradiology articles of interest to general radiologists would appear in *AJR* but only after having been published by the ASNR. In exchange for these articles, ARRS would publish a bimonthly dedicated neuroradiology journal at no cost to ASNR. Immediately, ASNR established a Feasibility Committee to study this proposal, and after approving the proposal, the committee also determined that the selection of the EIC would be the responsibility of the Publications Committee. The new EIC would be called Associate Editor for *AJR*, and the selection of shared articles would be his prerogative. Now ASNR was ready to start the hard work of finally establishing its journal.

Episode 2: An Editor and a Name for the New Journal

In late 1978, Dr Wolpert was chosen as Chair of the Editor Selection Committee. Of the 17 neuroradiologists contacted, 8 expressed their interest in the editorship. Interviews took place in March of 1979, and 4 of the candidates were shortlisted. Dr Taveras was at the top of the list, but he initially refused the position. Those of us who knew Taveras, know that he was a keen negotiator and that he must have had something in mind with this rejection. Later, he told the committee that he would reconsider but only if offered complete editorial freedom, the freedom to choose his Associate Editors and Editorial Board, a 5-year term, and compensation for himself and the Associate Editors. Astutely, he also required that all manuscripts related to neuroradiology, spine, and head and neck received by *AJR* be sent immediately to him, thus assuring the contents of the new journal. Once these requests were granted, he accepted the position and became the first EIC of the journal. The next big decision was choosing a name for the journal.

The newly formed Editorial Board was then consulted about a name for the new journal. To maintain a good relationship with the ARRS, the name AJR Neuroradiology was proposed but not accepted by all. A simple reshuffling of letters yielded AJNR, and

http://dx.doi.org/10.3174/ajnr.A8468

the name of the *American Journal of Neuroradiology* was then accepted by all. The first issue of *AJNR* appeared at the start of 1980 (for those of you keeping track: 18 years from the establishment of ASNR). Its cover was blue to distinguish it from the yellow cover of *AJR* and the gray one of *Radiology*. The fonts were of a yellow similar to those used in *AJR,* to honor the relationship of the 2 journals. The editorial introducing *AJNR* authored by Drs Figley and Taveras stated that "with great pride, we announce a unique concept in medical publishing—the publication of a specialty journal that will share manuscripts with a larger general readership." Instead of submitting neuroradiology-related manuscripts to Seattle, all were to be mailed to Dr Taveras in Boston. Dr Taveras was also able to make *AJNR* the official journal of the American Society of Head and Neck Radiology (established in 1976). However, in 1986, *AJR* named a new editor, Dr Robert Berk, who had difficulty accepting the previous agreement. Dr Robert Quencer, a future *AJNR* EIC, became an Associate (Deputy) Editor during these conflicts after Dr Wolpert stepped down from that position.

Due to conflicts between *AJNR* and Dr Berk (related to peer review and decisions to request revisions), in 1986 Dr Taveras negotiated for the ownership of *AJNR* to be transferred completely to ASNR (this was slated to start at the end of the decade). The journal would now proudly state on its cover, "Official Journal, American Society of Neuroradiology." Still, it was accepted that *AJR* would continue to publish some manuscripts from *AJNR* for some time. The next step would be total independence for *AJNR*.

Episode 3: AJNR *Goes to Chicago and Becomes Self-Published*

Dr Michael Huckman, from Chicago, had been the last neuroradiology fellow of Dr Taveras at Washington University in St Louis, and in 1990, he was named EIC of *AJNR*. Dr Huckman was Chief of Neuroradiology at Rush University, one of the first institutions in the United States to purchase a CT scanner. Dr Huckman was a true believer in not only in peer review but also editorial freedom. In 1991 (although some sources state that it happened in 1992), *AJNR* became independent and published by ASNR (self-published). Additionally, it went from 6 to 10 issues per year. Dr. Huckman also renegotiated the EIC's contract with a fixed first term of 4 years and a second one, if judged acceptable by the Publications Committee, for another 4 years. However, this last term could be shortened depending on the EIC's wishes. Perhaps the most important achievement during this period was the growth of international recognition of the journal as the pre-eminent one worldwide and the fact that newly formed subspecialty societies such as the American Society of Pediatric Neuroradiology (established in 1990) and the American Society of Spine Radiology (established in 1993) elected to make *AJNR* their journal. As one of the Associate Editors, Dr Ken Maravilla stepped down from his position, and Dr Mauricio Castillo was selected to fill that position. Dr Quencer continued to serve as Associate Editor under Dr Huckman, but soon things would change for him.

Episode 4: AJNR *Goes to Miami and the Electronic Era Begins*

In 1998, Dr Robert Quencer took over as EIC. He expanded the Editorial Board to include experts in physics and clinical disciplines related to neuroimaging and established periodic changes in its members to maintain *AJNR* as current and vibrant. In 2005, he presided over the 25th anniversary of *AJNR*. His tenure was not without conflicts because interventional neuroradiologists threatened to break away from the journal, but he negotiated their continued support of *AJNR*. The journal cover was freshened to include illustrations of the most important articles published, and the transition to a website and an electronic submission platform was established. Under Dr Quencer, annual submissions surpassed 1000 manuscripts for the first time. In addition, during his time, *Neurographics* was established. Its original purpose was to publish selected scientific exhibits from the annual meeting, and he and Dr Castillo served as its initial editors. One of the Associate Editors during this time was Dr Robert Grossman, then Chief of Neuroradiology at the University of Pennsylvania.

Episode 5: AJNR *Goes to New York City for a Short Time*

In 2006, the journal was lucky to have Dr Robert Grossman as its new EIC, a world-famous neuroradiologist and scientist who, by then, was Chair of Radiology at New York University. Bob's initial goals were to decrease the backlog of articles pending publication, tighten the acceptance rate, shorten the times from submission to acceptance to publication, and nearly eliminate case reports and technical notes. Publication Preview (electronic ahead of print) was started to accelerate publication. Government-funded research was given immediate open access, and the online supplemental data of articles were moved online. A monthly review article feature was also started. He also established a diverse group of Associate Editors (Dr Castillo was one of them) and a new and dynamic Editorial Board. Bob's tenure as EIC was short (1 year), and when he was named Dean of the Medical School at New York University, he decided to step down from the journal.

Episode 6: AJNR *Goes to Chapel Hill and Becomes More Interactive and Engaged*

When Dr Castillo took over as EIC, the changes made to the journal were relatively new, and it was decided to make changes around the journal rather than to it, to increase reader engagement. Associate Editors and Editorial Board members remained unchanged for 2 years. However, new activities included podcasts, Case of the Week (nearly 15,000 views monthly), Case of the Month, Classic Case, Brain Snacks, Image Quiz, *AJNR* Special and Custom Collections, Editor's Choices, Fellows' Journal Club, and the new Blog website (to which all book reviews were moved). *AJNR* started participating in social media before other journals did. The entire collection of *AJNR* since its inception was digitized and placed online. The website was remodeled several times to increase interactivity, and halfway into his tenure, it already registered over 10 million unique annual visits. A mobile device app was also developed. Priority peer review (3 days maximum) and fast-track publication were given to level 1 evidence-based manuscripts. An editorial fellowship program was launched. To honor Dr Lucien Levy, who unfortunately died during his tenure as Associate Editor, a prize for the best research publication was established. All content was released

after 12 months, and gold-level open access (free for all immediately after publication) was offered to authors for a small fee. The Impact Factor of *AJN*R nearly doubled during Dr Castillo's tenure.

Regrettably, *AJNR* lost the participation of the then-called American Society of Interventional and Therapeutic Neuroradiology (ASITN), which transformed into the Society of Neurointerventional Surgery (SNIS) and started publishing its journal. At the end of Dr Castillo's tenure, the cover of the journal was revised, the table of contents was changed to reflect the wide interests of clinical neuroradiologists, a plagiarism-detection initiative was started, and the Associate Editors and Editorial Board became diverse and international. The Associate Editor in charge of spine-related submissions during this time was Dr Jeffrey Ross.

Episode 7: AJNR *Goes West and Confronts a Pandemic*

In 2015, Dr Jeff Ross, of Phoenix, Arizona, was named EIC of *AJNR*. Dr. Ross is a world-renowned neuroradiologist specializing in spinal imaging. Jeff started his tenure by revamping the Editorial Board to include a statistician and later an artificial intelligence editor. He continued and expanded his popular "journal scan" feature, which summarized pertinent advances published in other journals. Jeff was unfortunately confronted by the Coronavirus disease 2019 (COVID-19) pandemic. During this period, the overall number of submissions increased by 40% (more than 1700 in 2020), which resulted in long work hours for him and his team, who dealt with this situation without additional resources. He prioritized the publication of COVID-related articles and was open to publishing case reports again. He later revised the website, making it more modern and easier to use. During his tenure, the Impact Factor of *AJNR* was the highest in the history of the journal.

Episode 8: AJNR *Goes to Houston: A Work in Progress*

Dr Max Wintermark, Chair of Neuroradiology at the MD Anderson Cancer Center, took over as EIC in 2023, and in this short period, he has already made considerable changes to the journal. He immediately revamped the Editorial Board and created teams in charge of specific topics. The time from manuscript submission to the first decision is now only 15 days, and the manuscript-submission process was streamlined. These initiatives have already resulted in a significant rise in the number and quality of submissions. Concerned about younger neuroradiologists who are interested in academic publication, he created an Academy of Reviewers, which intends to train new manuscript reviewers, and he established a "Junior" Editorial Board. Annual prizes for early career, women in neuroradiology, and global neuroradiology articles were created. Participation in social media has been granted priority, and a new activity, *AJNR* Scantastic, which translates recent publications into educational features, was instituted. *AJNR* will go to electronic-only publication after this last print issue in keeping with modern trends. We are sure that Dr Wintermark will continue to revolutionize *AJNR*, and we look forward to future changes.

Be sure to tune in again 6 years from now for a new episode!

Both authors have been lucky to know and work with all 7 *AJNR* EICs. Of the EICs. Drs Taveras (1962), Huckman (1987), Quencer (1994), Grossman (2006), Castillo (2013), and Wintermark (2024) have also served as Presidents of ASNR. Drs Grossman, Castillo, and Wintermark were ASNR Presidents while being EICs.

The authors acknowledge the help of Karen Halm during the preparation of this piece.

The New *AJNR*: Personalized for YOU

Lubdha Shah, MD
Deputy Editor, *American Journal of Neuroradiology*
Max Wintermark, MD
Editor-in-Chief, *American Journal of Neuroradiology*

The new digital *American Journal of Neuroradiology (AJNR)* is for YOU, our *AJNR* readers. This transition to a purely electronic format accompanies exciting enhancements to the *AJNR* Web site. We've developed many new features with a focus on making rapidly progressing scientific and educational content more accessible. The new interface will not only be more straightforward to navigate with easily searchable content, but also will be personalized to the reader's interests through our redesigned homepage. Cultivated collections of articles will be changeable depending on the reader's preferences.

Unlike the print format, which allowed only static images, the digital format will have multimedia capabilities such that authors will be able to submit stacks of medical images and video clips to better demonstrate the findings and convey critical points. The online platform will also enable high image resolution. In line with the multimedia capabilities, there will be a new type of journal article: the video article. Authors will have the opportunity to create a brief video with narration to explain procedures, innovative findings, and complicated concepts, which may be better described visually. The *AJNR* Editorial Board will continue to uphold the rigorous standards of quality and integrity to ensure *AJNR* provides the highest quality of research and innovative clinical advances.

This new digital format is in keeping with the current evolution of digital academic publishing. The advancements were developed based on the comments we received from our readers, authors, and reviewers. They represent the vision of the Editor-in-Chief and Deputy Editor with achievement as the result of considerable efforts from *AJNR* editorial staff and *AJNR* Junior Editors. With input from our stakeholders, this format will continue to improve. The new digital *AJNR* will reach a wider readership of not only radiologists of various subspecialties and levels of training but also other medical specialties from all over the world.

We are thrilled and confident that this digital evolution will reinforce *AJNR* as the premiere journal of neuroradiology as well as the official journal of the American Society of Neuroradiology (ASNR), the American Society of Functional Neuroradiology (ASFNR), the American Society of Head & Neck Radiology (ASHNR), the American Society of Pediatric Neuroradiology (ASPNR), and the American Society of Spine Radiology (ASSR).

http://dx.doi.org/10.3174/ajnr.A8467

AJNR Quo Vadis? An International Perspective on the Journal's Next 10 Years

Roland Bammer

Since the first article was penned by the inaugural Editor-in-Chief Juan Manuel Taveras (1919–2002)[1] in January 1980, *AJNR* has come a long way. *AJNR* has established itself as the premier journal for all aspects of the neuroradiology subspecialty. Despite being officially the journal of the American Society of Neuroradiology and of the American Societies of Functional Neuroradiology, Head and Neck Radiology, Pediatric Neuroradiology, and Spine Radiology, *AJNR* has attracted a large international following with numerous excellent contributions each year from across the globe.

"To move the world, we need to move ourselves" (Socrates). This quote also applies to neuroradiology and *AJNR* more specifically. The field of neuroradiology is continuously evolving. The new Editor-in-Chief of *AJNR*, Max Wintermark, with the Editorial Board's support, has already set many new transformative initiatives in motion. These will ensure that *AJNR* will remain integral to keeping those interested in this field connected and apprised of new developments. The rate at which neuroradiologic insights and innovation are introduced, however, is continuously increasing, especially in an era of broader access to information and global connectedness. Contributions from Asia and the rate of increase of journal submissions from there are just one such example. For *AJNR* to maintain its relevance, it will be crucial to keep up with this pace; ensure that information content remains timely, relevant, and correct; and is disseminated quickly. For the benefit of its readership, it will also be crucial for the journal to both identify and adapt to new trends swiftly, not only on content but also on its delivery.

In the last few years, the topics that gained the most attention in radiology have certainly been machine learning and artificial intelligence (AI), and they will most likely remain major talking points in the next few years. Neuroradiology has been an early adopter of this technology. Initially feared, AI is being increasingly embraced by institutions, mainly because of its broad range of applications and the radical impact AI may have on improving clinical workflows, increasing radiologic productivity and diagnostic confidence, speeding up image acquisition, and reducing image noise and radiation and/or contrast dose. Faced with an ever-growing workload and a shortage of radiologists and technologists, many hope that AI will be the savior.

While we are still in the process of understanding the performance of individual AI tools and currently there are many more new fields of applications just being discovered and introduced, we will eventually see this technology becoming commoditized. AI will augment radiology like so many other innovations before (eg, multidetector CT, PACS, parallel imaging, and so forth), albeit on a much broader scale and at greater dissemination speed.

Before readers become too fatigued about, for example, the next tumor classification or hemorrhage-detection algorithm, a key consideration for *AJNR* should be that authors who report on AI-tools that are not commercially available share their algorithms and corresponding data with the community so that others can build and expand on their work and/or validate the method on their own data.

The key to AI algorithms is not only the network architecture but also the training and validation data, the weights of the network, and other implementation details. In the future, *AJNR* can play an important role here to facilitate collaboration and create a living ecosystem akin to the Papers with Code initiative, which evolved in the computer science community. *AJNR* can be a curator of relevant data for use in developing and testing algorithms and can provide a framework for publishing validated studies. In the age of generative AI, *AJNR* must also be the sentinel that ensures the veracity and accuracy of published work on AI algorithms that are relevant to neuroradiology; i.e., *AJNR* must serve as a credible source of information that is valued by researchers and clinicians alike around the world.

AI aside, the last few years have also ushered in several considerable technologic breakthroughs. Among them, FDA-approved ultra-high-field ($B_0 = 7T$) and ultra-low-field ($B_0 = 64mT$) MRI, TOF-PET, and photon-counting CT. Thanks to recent developments in consumer electronics, we now have access to virtual reality goggles that boast internal displays and have better performance (i.e., pixels, refresh rate, and luminance) than diagnostic PACS monitors. Another consumer technology that benefits radiology is satellite-based Internet access. We all notice a scarcity of radiologists globally and that, especially after coronavirus disease 2019 (COVID-19), many radiologists, particularly the younger generation, value flexibility in their work environment and location; this can be enabled by such leaps in technology. The advent of satellite-based Internet access will not only have an impact on where neuroradiologists can read their studies, it will conversely have an impact on the source of the studies, be it from the Australian Outback or the middle of the Amazon. Obviously, some areas will not have high-end MRI and CT machines producing immaculate data, but it will provide opportunities for neuroradiologists to provide expert opinions on basic scans, share protocols electronically, teach local health care providers and radiologists, or contribute in any other form to a democratized access to high-level neuroradiology expertise globally.

Neuroradiologists have always been early adopters of new technology (eg, MRI, PET, photon-counting CT). At the 10th anniversary, J.M. Taveras wrote, "Try to be the expert in 1 area of radiology, but do not become a specialist in a single machine or procedure."[2] This mantra also applies to *AJNR* because, with some notable exceptions, the more generalized a journal becomes, the less interesting it becomes for its specialist readership. The journal will no doubt keep its clinical edge and core mission, but

Founder, Shareholder, Boardmember: iSchemaView, Inc. (RapidAI).
http://dx.doi.org/10.3174/ajnr.A8494

Prof. Roland Bammer

it will be also important for *AJNR* to keep up with technologic innovations and the impacts these may have on the diagnostic/interventional work-up of patients and their outcomes.

During *AJNR*'s journey to date, we have also encountered many new advances in imaging methods, such as quantitative susceptibility mapping, DTI, arterial spin-labeling and dynamic susceptibility contrast perfusion MRI, MRI fingerprinting, measurement of glymphatic flow, material decomposition CT (eg, blood versus iodine), single-energy reconstruction CT, CT perfusion, as well as practice-altering interventional methods such as mechanical thrombectomy and middle meningeal artery embolization, which have dramatically changed patient survival and quality of life. Not infrequently, *AJNR* has published seminal papers that demonstrated the diagnostic utility of these nascent technologies and procedures, thus providing much-needed empiric and methodologic evidence to support their use in clinical practice. These publications will continue to be a major pillar of the journal. Yet, despite key contributions and leadership of neuroradiologists, *AJNR* has missed out on publishing the primary results of landmark trials. To some extent, it is the limited reach of the journal; after all, it caters to a small subspecialty. However, a major aspect is the prestige and Impact Factor draw of the major clinical journals. If we (as neuroradiologists and neuroradiology researchers) want to help our community's journal become more visible, perhaps we should start publishing our trials in *AJNR* and pay less attention to publication vanity metrics. Of course, there are also the appointment and promotion committees and other bodies who still pay attention to where we publish, which adds an additional level of difficulty.

To increase its international standing, *AJNR* may need, in the future, to also reflect on regional differences in radiologic and health care provision. Countries with a greater proportion of public health funding or smaller budgets might use different guidelines or imaging tests, simply because of the lack of reimbursement or access to technology and drugs. For example, some countries in Europe or Asia reimburse only regular head CTs for acute strokes, but, to our surprise, not CTAs. Similarly, the latest Alzheimer treatment drugs are not yet approved in Australia. These practice variations should be considered in peer review and editorials.

Although some readers (including this author) prefer to read journal articles in printed form, the future lies in the electronic journal. This format is not only cheaper to produce, it also allows a greater number of articles and pages to be published and offers many other benefits ranging from provision of Online Supplemental Data, videos, data and code, author-generated pitch decks, and AV-files, as well as multilanguage translations and AI-generated (Blinkist-like) summaries. It also improves access, given the limited number of printed copies and the requirement for a subscription to access an article, it also improves access, which in turn benefits the journal as it will increase the number of citations.

Despite the current skepticism around generative AI relative to plagiarism and the proliferation of fake articles, AI-augmented writing (when in the right hands) will eventually be seen as beneficial (and perhaps more pleasing to the readership), especially for authors whose first language is not English or who are not eloquent writers like Nancy Fischbein or Pamela Schaefer. We will need to draw the line, however, when generative AI is used to create large pieces of a manuscript and "invent" content or when "publication farms" are creating "variations on a theme," just for the sake of yet another publication. Fortunately, publishers already have tools to screen for such blunt attempts at plagiarism.

The publication media and clinical/technical topics may change; however, *AJNR*'s mission will not. The key role of the journal will remain to provide an outlet for authors to share their findings with an interested audience primarily in neuroradiology and related fields, perhaps with added considerations of alternative vantage points and differences in practices on both other sides of the 2 big ponds (i.e., Europe, Africa, and Asia). Despite all the excitement around imaging technology and AI, the future demand will remain strong for empiric studies, with a focus on diagnostic or interventional neuroradiology that aid and improve the practice of neuroradiology. As wonderful as annual meetings are, not everyone can attend in person; thus, it is important that the society have a journal in which members can share their latest discoveries in neuroradiology and to which we can refer to expand our knowledge of new treatments, standards, nomenclatures, and imaging findings.

I wish *AJNR* all the best for its next chapter as an electronic-only journal.

REFERENCES

1. Taveras JM. **The development of neuroradiology in the United States.** *AJNR Am J Neuroradiol* 1980; 1:1–2
2. Taveras JM. **Editor's comments on the 10th Anniversary of AJNR.** *AJNR Am J Neuroradiol* 1989;10:1–2

The Future of Academic Neuroradiology: Challenges, Opportunities, and Way Forward

Ajay Malhotra, Associate Editor

Academic neuroradiology has a vital role in driving scientific progress, improving patient outcomes, and disseminating knowledge to the next generation of radiologists. From the early adoption of skull radiographs shortly after the discovery of X-rays, to ventriculography in 1918, pneumooencephalography in 1919, and arteriography in 1927, neuroradiology has come a long way in being a driver of development and adoption of emerging technologies to advance science in all key missions.[1] To ensure continued success, we must confront the challenges facing our field and work on potential opportunities to continue our progress.

Challenges Facing Academic Neuroradiology

Academic radiology practices have been expanding into the community by building larger networks.[2] Academic practices employ 28% of radiologists and account for 45% of very large practices.[3] As US medical schools prioritize the growth of the clinical enterprise, with a shift of focus toward clinical services, the revenue share of clinical services of US medical schools increased from 20% in 1977 to 48% in 2000, and 62% in 2022.[4,5] Between 2000 and 2023, the number of radiology faculty across US medical schools has nearly doubled, with most of the growth in the nontenured clinical educator track (includes the Clinical, Clinician-Educator, or Clinician Scholar track with primary responsibilities in teaching, teaching and patient care, or patient care).

Imaging volumes have been on an upward trajectory and are likely to continually increase. Coupled with declining reimbursements and greater emphasis on clinical productivity, this increase often comes at the expense of the academic mission.[6] There is a supply deficit of newly trained radiologists relative to the number of radiologists needed in practice at a population level, and this shortage is projected to be an ongoing long-term challenge.[7] In recent national surveys, academic practices hired the most radiologists but had higher turn-over, and academic radiologists are less likely to stay in the same practice for 5 years.[3] In an era of increasing specialization, even smaller practices are hiring fellowship-trained neuroradiologists who often cover general practice as well.[3] Historically, financial compensation in private practices has been higher than in academic practices, albeit with higher expected clinical productivity. All these factors are creating challenges for academic programs in recruiting and retaining faculty for areas that have historically been critical for academic medicine—subspecialized radiologic consulting services, academic scholarship, teaching, mentoring, and research leadership. Recent studies of academic radiologists are showing high rates of burnout with a low sense of professional fulfillment and an intention to leave, especially among female radiologists.[8]

Financial compensation in academic radiology increased in the last decade but barely kept pace with inflation.[9] This has come with increased expectations of clinical productivity, and the differential with private practices for the work relative value unit generation is narrowing. To respond to market conditions, academic programs are showing increasing staffing flexibility to provide better work-life balance.[3] The use of teleradiology in academic radiology has increased since the coronavirus 2019 (COVID) pandemic, and this trend seems to be persisting.[10] Academic practices are more likely to allow even daytime telework than private practices.[3] However, despite having certain advantages, these have potential negative effects and create challenges, including decreased integration with the clinical care teams, less opportunities for collaborative research, loss of mentoring opportunities for junior faculty and trainees, and a negative impact on education.[10]

Artificial intelligence (AI) has been one of the most heavily researched fields in radiology, including neuroradiology, and has been proposed for multiple radiology-related tasks, including image acquisition and reconstruction, image lesion detection, triage, disease classification and prognostication, and radiology report analysis, among others.[11,12] More than 40% of FDA-approved AI algorithms in radiology are for neuroimaging.[13] However, the value proposition offered by the vendors through marketing is frequently different from the reasons for approval by the FDA. Concerns about the clinical applicability of AI are multiple, including trust in AI performance and lack of generalizability, insufficient evidence on its impact on workflow, the requirement of institutional support, medicolegal implications, and lack of a clear path to reimbursement.[14] Fears of AI replacing radiology jobs have been expressed and may be dissuading US medical students from considering the specialty.[15]

The focus on clinical productivity has not, surprisingly, adversely affected academic scholarship/productivity.[16] Research funding has become increasingly challenging, with rising research costs and greater competition for federal funding sources.[16] This challenge is made worse by the National Institutes of Health (NIH) salary support cap, which particularly affects specialties like radiology in which the average salary is substantially greater than the NIH cap. Academic practices have to bridge the difference if they want to support funded research. Across time, academic radiology departments have increasingly become 2 distinct subentities: the clinical enterprise and the research wing, with the research side predominantly constituting nonclinician research scholars and nonradiologist clinicians.

Potential Opportunities and Way Forward

While challenges are many, it is imperative for the leadership in academic neuroradiology to focus on advancement and excellence in the field, requiring attention to all key missions of academic neuroradiology:

http://dx.doi.org/10.3174/ajnr.A8539

Ajay Malhotra, MBBS, MD, MMM, Associate Editor

1) Clinical practice:
   a) Prevent commoditization. Academic practices need to focus on quality and service.[17] Quality should address not just the quality of images but the accuracy and helpfulness of the radiologic consultation. Service includes pleasant patient experience, coverage not only for read-outs but also for clinician consults, and tumor boards/conferences where patient care decisions are made. Overemphasis on fast turn-around reports and lower cost per unit of service will only lead to commoditization and loss of appreciation for the expertise and value of the subspecialized academic neuroradiologist.
   b) Provide highly subspecialized tertiary care. Historically, academic practices used to be the "go-to" for the most complex, difficult cases. As practices expand into the community, there is a tendency to create a general pool of neuroradiologists providing the gamut of services. It is imperative for academic programs to create and maintain "centers of excellence" with highly subspecialized experts not just to provide the cutting-edge care but to also advance the science and train the next generation of radiologists.
   c) Faculty tracks with distinct, clear delineation of responsibilities and expectations. As academic programs expand with emphasis on clinical work, it will be critical to create a group of core academic faculty to advance collaborations and research with referring physicians, while maintaining a larger pool of clinical faculty to focus on the clinical care. However, success would depend on creating the right incentives.
   d) Transparent policies regarding promotions and advancement opportunities in academic departments. As departments expand with a larger cohort of clinical faculty, there has been a tendency to use administrative positions for career advancement, which may limit opportunities for core, academic faculty, creating disenchantment.
   e) Transparent incentives for on-site work. Differential/lower clinical productivity expectation is one way to incentivize faculty who work on-site, are available for clinical consults, work with trainees, and attend interdisciplinary conferences.
   f) Diversity. Academic radiology and neuroradiology remain under-represented by women and certain groups despite efforts at the national and institutional level to improve diversity.[18-20] Identifying the reasons and creating a welcoming environment with mentorship would help radiology attract the best talent and improve the diversity in the workforce. Fair, transparent compensation policies will also help.[9]
   g) Leveraging AI for assessing workflows and improving operating efficiencies.
2) Education and training:
   a) Curriculum for training. To create the workforce of the future, academic neuroradiology needs to train fellows for dedicated academic practice as well as a larger pool for hybrid/private practice. Fellows going into hybrid/private practices have historically opted for shorter training (1-year fellowship). It is imperative that fellows are well–trained before going into practice, and ASNR has created specific curriculum to ensure adequate didactic and practical training.[21] Useful online resources have been created, including lectures and articles to augment education.[21] It is important to keep this process iterative to keep pace with evolving needs. For candidates opting for more research-focused, rigorous academic careers in complex, tertiary care centers, a distinct curriculum for advanced clinical training, as well as resources for research are critical.
   b) Strategies for virtual education. Technology should be used to ensure synchronous virtual readouts and enable personal interaction and feedback.
   c) Mentoring programs need to be rigorous at the institutional level as well as in regional/national societies. ASNR has made tremendous effort in setting up mentorship programs for trainees and faculty, and these are helpful not just for academic/research but also for promoting well-being and participation in society.
3) Research:

Innovation and research require more than individual talent and hard work.[16]

In an era of increasing competition and limited funding from federal sources such as the NIH, it is imperative for academic programs to prioritize and provide resources for promoting research.[22] Specialty societies such as the ASNR have played a crucial role in providing funding for faculty and trainees, as well as grant-writing programs and training programs such as Comparative Effectiveness in Research Training (CERT)/Value of Imaging Through Comparative Effectiveness (VOICE). These

have also been instrumental in providing mentorship opportunities from experts in the field. However, individual academic programs need to do more. Individual academic departments have used research budgets for gap funding and bridge loans mostly for research faculty, and concerns have been expressed about the survival of "clinician-scientists" in the modern era.[16] Academic radiology departments and institutional leadership need to recognize that investments in clinical translational research create "ecosystems" not just to foster scientific enquiry and collaborations but also to increase the clinical applicability of research. However, rethinking is required for the way this has been incentivized in the past. Many academic departments give faculty protected academic time per week, often with little correlation to academic productivity.[16] Academic "bonuses" with low thresholds for academic productivity might only promote a sense of "well-being" in the short-term. Defining expectations for academic productivity, no guaranteed bonus, and tying the bonus to productivity in a transparent manner will help in promoting clinical research. Departments should also be transparent in their policies on administrative time-off/bonuses because it is increasingly coming at an opportunity cost for academic advancement.

The emergence of AI technologies is creating an unprecedented opportunity for industry partnerships not just for development/validation of new technologies but also for the clinical application and value proposition of these new technologies. Alternative sources of funding such as crowdfunding need to be explored.[23] Neuroradiology also needs to focus on patient-centered outcome research and make use of funding available through PCORI (https://www.pcori.org/). Academic neuroradiology also needs to improve health services research by sitting at the decision-making table. Declining reimbursements and exploding imaging volumes make it imperative for the field to establish the effectiveness/cost-effectiveness of what we do.[24] It is imperative for academic neuroradiology to establish the value proposition to convince patients, referring physicians, third-party payers, and policy makers of the critical role played by the field.

In conclusion, while challenges are many, academic neuroradiology would do well to focus on the opportunities and create a path to continued excellence. Providing highly complex care has been a strength for academic radiology practice and has often allowed academic practices to command high reimbursements for the care provided to patients. This care requires consistent, ongoing innovation and collaboration with clinical care teams. The incorporation of new technology leading to dramatic improvements in stroke care is one such example. The ability to collect and analyze large amounts of quantitative data brings unprecedented insights into fields such as tumor characterization, prognostication, and personalized treatment-planning. Academic radiology has a critical role to play in defining ways to diagnose and monitor conditions with substantial public health burden, such as neurodegenerative diseases. Flexible physician training and staffing with clear incentives aligned with expectations would help academic radiology avoid burnout and improve access to care. As articulated by Simone,[25] we in academic radiology have the privilege of working in a profession that helps the sick while engaging in intellectual enquiry. As practice paradigms evolve, maintaining a focus on scientific enquiry will be the key to ensuring advancement.

REFERENCES

1. Leeds NE, Kieffer SA. **Evolution of diagnostic neuroradiology from 1904 to 1999.** *Radiology* 2000;217:309–18 CrossRef Medline
2. Natesan R, Yang WT, Tannir H, et al. **Strategic expansion models in academic radiology.** *J Am Coll Radiology* 2016;13:329–34 CrossRef Medline
3. Dibble EH, Rubin E, Duszak R Jr, et al. **The 2021 ACR/RBMA Workforce Survey: practice types, employment trends, and hiring needs.** *J Am Coll Radiology* 2024;21:493–502 CrossRef Medline
4. **The Leadership Plenary Address by Association of American Medical Colleges Board of Directors Chair Lilly Marks.** In: Learn Serve Lead 2019: Navigating a New Normal. November 8-12, 2019. Phoenix, Arizona
5. Association of American Medical Colleges. **Revenue by Source, FY 1977 through FY 2022.** https://www.aamc.org/data-reports/data/iv-revenue-source-fy-1977-through-fy-2022. Accessed June 10, 2024
6. Christensen EW, Nicola GN, Rula EY, et al. **Budget neutrality and Medicare physician fee schedule reimbursement trends for radiologists, 2005 to 2021.** *J Am Coll Radiol* 2023;20:947–53 CrossRef Medline
7. Ismail M, Hanna TN, Davis MA, et al. **The remote academic radiologist: AJR Expert Panel narrative review.** *AJR Am J Roentgenol* 2024;222:e2329601 CrossRef Medline
8. Higgins M, Nguyen MT, Kosowsky T, et al. **Burnout, professional fulfillment, intention to leave, and sleep-related impairment among faculty radiologists in the United States: an epidemiologic study.** *J Am Coll Radiol* 2021;18:1359–64 CrossRef Medline
9. Malhotra A, Futela D, Joshi R, et al. **Academic radiology physician financial compensation in the United States: trends and distribution.** *Radiology* 2024;313:e241057. CrossRef Medline
10. Recht MP. **Work from home in academic radiology departments: advantages, disadvantages and strategies for the future.** *Acad Radiol* 2023;30:585–89 CrossRef Medline
11. Chae A, Yao MS, Sagreiya H, et al. **Strategies for implementing machine learning algorithms in the clinical practice of radiology.** *Radiology* 2024;310:e223170 CrossRef Medline
12. Wagner DT, Tilmans L, Peng K, et al. **Artificial intelligence in neuroradiology: a review of current topics and competition challenges.** *Diagnostics (Basel)* 2023;13:2470 CrossRef Medline
13. Bajaj S, Khunte M, Moily NS, et al. **Value proposition of FDA-approved artificial intelligence algorithms for neuroimaging.** *J Am Coll Radiol* 2023;20:1241–49 CrossRef Medline
14. Allen B, Agarwal S, Coombs L, et al. **2020 ACR Data Science Institute Artificial Intelligence Survey.** *J Am Coll Radiol* 2021;18:1153–59 CrossRef Medline
15. Reeder K, Lee H. **Impact of artificial intelligence on US medical students' choice of radiology**. *Clin Imaging* 2022;81:67–71 CrossRef Medline
16. Chu LC, Rowe SP, Fishman EK. **Clinician-scientists: can they survive in the modern era?** *J Am Coll Radiol* 2021;18:192–97 CrossRef Medline
17. Forman HP, Larson DB, Kaye AD, et al. **Masters of radiology panel discussion: the commoditization of radiology.** *AJR Am J Roentgenol* 2011;196:843–47 CrossRef Medline
18. Wu X, Bajaj S, Khunte M, et al. **Diversity in radiology: current status and trends over the past decade.** *Radiology* 2022;305:640–47 CrossRef Medline
19. Wu X, Khunte M, Bajaj S, et al. **Diversity in radiology residents relative to other specialties: trends over the past decade.** *Acad Radiol* 2023;30:2736–40 CrossRef Medline

20. Prajapati P, Wu X, Bajaj S, et al. **Trends of diversity in neuroradiology trainees in United States 2015-2022.** *AJNR Am J Neuroradiol* 2023;44:1009–11 CrossRef Medline
21. ASNR. **Fellowship Curriculum.** https://www.pathlms.com/asnr/courses/55779#. Accessed September 15, 2024
22. Chetlen AL, Degnan AJ, Guelfguat M, et al. **Radiology research funding: current state and future opportunities.** *Acad Radiol* 2018;25:26–39 CrossRef Medline
23. Khunte M, Zhong A, Lee C, et al. **Proportion of industry payment value by category in radiology relative to other specialties.** *Clin Imaging* 2024;114:110237 CrossRef Medline
24. Wu X, Hughes DR, Gandhi D, et al. **CT angiography for triage of patients with acute minor stroke: a cost-effectiveness analysis.** *Radiology* 2020;294:580–88 CrossRef Medline
25. Simone JV. **Understanding academic medical centers: Simone's maxims**. *Clin Cancer Res* 1999;5:2281–85 Medline

The Future of Artificial Intelligence in Clinical Radiology: Savior or False Hope?

Greg Zaharchuk, and Janet Mei

Making predictions is hard, especially about the future.

Yogi Berra

Artificial intelligence (AI), defined here as deep learning and transformer-based computer vision and language models, has been proposed as a revolutionary technology for radiology, possibly more impactful than past revolutions such as new imaging modalities and/or the adoption of PACS. However, some suggest that AI is overhyped and may not meaningfully address the core challenges facing radiology. Medicine is an inherently conservative field, and rapid technology adoption is the exception rather than the norm. In other specialties, changes are often triggered by landmark clinical trials or new guidelines. In radiology, in which much of our work occurs upstream of clinical decision-making, linking practice changes to improved patient outcomes is difficult. Without clear evidence of clinical impact, financial incentives will likely drive technology adoption. This is already visible, where products that have made inroads are largely those have led to improved efficiency or cost-effectiveness. Conversely, adoption has been slower for technologies promising improved diagnostic accuracy. In this editorial, what the next decade may hold for AI in radiology will be explored, drawing on current applications while also exploring the history of similar medical technologies to better understand the potential forms that AI might take and how it will be integrated into practice.

INTRODUCTION

Radiology is primed for disruption. Past models, both private and academic, are struggling to keep pace with the surge in imaging studies, particularly because there has been no commensurate increase in the number of radiologists.[1] Likewise, this increased demand is straining noninterpretive parts of our field, leading to longer service hours, without enough scanners or technologists to run them. Simultaneously, declining reimbursement rates per study and rising operational costs highlight the need for AI solutions that could help radiology departments manage higher volumes cost-effectively. Clearly, the current system is unsustainable.

Will AI be our savior? Perhaps AI will soon become good enough to autonomously read studies without human supervision, or maybe, more realistically, it could provide a "first draft" of the report much like a good trainee, complete with relevant measurements and comparisons with prior studies. Short of this, it could optimize our reading environment, making us more efficient and accurate by standardizing the readout process and reducing distractions. Finally, AI-driven image acceleration and other upstream applications could improve operational efficiency and alleviate financial pressures. The following will explore each of these areas.

AI for Interpretation

Even though only about 20% of the reimbursement for radiology departments comes from the interpretive "professional" fee, it is front and center for practicing radiologists. This 20–80 reimbursement split may understate the value of AI for interpretive work, because there is evidence that the cost (as opposed to the reimbursement) within a radiology practice is actually more equally split between professional and technical areas.[2] Assuming that the number of radiologists is largely capped in the next 10 years (though ideas such as importing foreign medical graduates and using midlevel providers might alter this calculus), how could AI reduce the time spent per study without decreasing quality? Three options are possible (Figure 1):

1) Doctor AI: Read some studies completely autonomously (normal CTA head and neck studies in patients with low-quality indications anyone?).
2) Trainee AI: Predraft reports, including measurement of lesion sizes and comparison with prior studies. A radiologist would then confirm or edit the reports similar to the traditional academic model.
3) House Elf AI: No diagnostic capabilities but AI helps streamline the process of moving from images to reports: better study organization (imagine hanging protocols that work), less need to call/interact with technologists, quality assessment and control, and maybe even executive summaries of cases with links to key images. This improvement could also include "stream of consciousness" reporting. Such AI would reduce hidden costs associated with interpretation.

Note that none of these scenarios are what is currently the rage: one-off AI detection and triage algorithms for individual diseases like intracranial hemorrhage and cervical spine fracture. There are literally hundreds of these one-off implementations, raising questions about whether this is the right approach long term. While the computer vision technology to perform these tasks is remarkable, multiple studies in real-life settings suggest that it does not reduce interpretation time or improve outcomes for neuroradiologic applications.[3-6] Thus, they will remain niche products for early adopters, though they could become building blocks of larger systems described above.

Doctor AI

The most ambitious of these scenarios is autonomous AI, capable of generating complete diagnostic reports from imaging. This possibility is only on the table due to recent explosive improvements in performances of so-called "foundational models," based on large-vision language models, many of which use self-supervised contrastive learning. Current performance for image to report based AI has mostly focused on the areas where we have the most data, such as 2D imaging like chest X-rays.[7] More

http://dx.doi.org/10.3174/ajnr.A8550

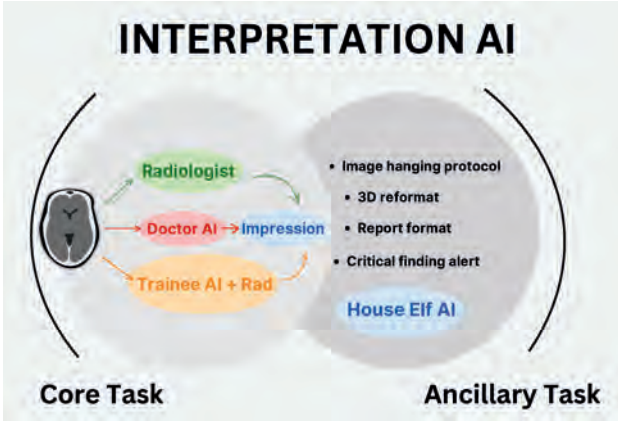

FIG 1. Varying levels of AI integration in radiologic workflows, ranging from full autonomy to efficiency optimization. In the Doctor AI model, AI autonomously generates complete reports with minimal-to-no need for physician input. The Trainee AI model involves AI-assisted prepopulation of reports but with more physician oversight, like an attending overseeing a resident or fellow. The House Elf AI model does not alter the physician's interpretation process but enhances the diagnostic environment, boosting radiologists' productivity through AI-driven efficiency improvements and removing distractions. It helps with better study organization, report structuring and formatting, less need to call/interact with technologists, quality assessment and control, and automatic critical finding alerts. Such AI would reduce hidden costs and wasted time associated with interpretation. Rad indicates radiologist.

recently, several groups have sought to extend these models to 3D imaging modalities, such as abdominal or head CT.[8,9] While impressive progress is clearly being made, the performance remains suboptimal. The examples shown in preprints demonstrate clear errors on relatively simple tasks and overall performance that is well below anything remotely useful.

However, we wouldn't bet against it improving given the rapid pace of improvement, computer vision detection of cats and dogs has quickly given way to conversational AI that can provide image captions or create movies from short text prompts. For this task, there are semi-infinite amounts of training data: all the paired imaging examinations and reports we have created during last 20 or so years. Incredible amounts of money are being spent by early-stage start-ups as well as large incumbents who believe this task is feasible. It is likely that the winners here will be institutions or companies that can combine extremely large, diverse data sets with massive compute budgets. These entities will need to incorporate radiologist domain expertise to navigate all the details that radiologists learn in residency. Another current unsolved problem is how to handle context, from comparison with priors to the integration of information from the electronic health records that is known to be essential for radiologists to provide value.

The biggest challenges here will be determining and then achieving adequate performance (what exactly is the error rate for radiologists anyway?); overcoming the (probably high) regulatory hurdles, given the potential for ultimately reducing the number of radiologists needed (expect your friendly professional association to weigh in on this); the acceptance of such technology by patients;[10] and potential medicolegal concerns (who is on the hook for mistakes?). Perhaps we can find subsets of examinations that might represent initial implementations, such as noncontrast head CTs without priors, or perhaps AI could be trained not to detect individual abnormalities but rather to detect the absence of abnormalities, a so-called "normal detector," and remove them from the worklist. This latter approach is particularly attractive because the rise in the number of imaging studies is being driven largely by low-quality indications, resulting in more studies with normal findings filling our lists.[11-13] I sometimes feel transported back to my days in residency during my screening mammography rotation when I sit down for the evening emergency department shift. Perhaps one day, we will remark on those "old days" when we had to actually read the studies with normal findings, much like some of us talk about using alternators, to be greeted by blank stares.

It may be instructive to look back on a technology that promised such automation. In the 1990s, interpretations of Pap smears by cytologists had all the elements we see in today's radiology: too many studies and too few people to read cases.[14] Computer-based algorithms had reasonable performance. However, the autonomous reading approach was ultimately not successful, given the reluctance of the FDA to approve what they considered a "high-risk" device. Thus, the first implementations were for quality control applications, looking at cases with negative findings with the hope of reducing false-negatives. The most successful paradigm turned out to be one in which cases deemed to have normal findings by the machine were flagged for the cytologist, who then had to review only the 20 "most abnormal" high-power fields flagged by the AI rather than examine the whole slide, thus resulting in time-savings. This improvement leads to our next category of interpretative AI.

Trainee AI

A recent survey showed that only 21% of patients are comfortable with AI providing radiology reports, suggesting the need for alternatives.[10] Thus, if truly autonomous AI, even if possible, is not deemed palatable by regulators, patients, and payors, this model could be scaled back to the idea of providing a draft, which would need to be checked by the radiologist before sign off. This approach is similar to that seen in academic practices, in which residents and fellows review images, interrogate the medical record, pull up relevant priors, and ultimately draft a report that is then edited in response to the attending's feedback. This approach is an attractive example of "human in the loop" AI, in which the radiologist is still liable ultimately for the read, making clear the medicolegal responsibility.[15] It may also be more palatable to regulators and professional societies, though clearly there might be worries about "mills" that just sign off on whatever these models produce. Such models might also be used to address the most common or laborious examinations; however, as for the Doctor AI implementation above, figuring out how to give AI the proper context is still likely to be a challenging undertaking. Of course, for maximal efficiency, both approaches need to be fully integrated into the radiologist's reading environment, interfacing with the electronic medical record and dictation software.

Such an approach will need to prove that its use leads to equivalent outcomes with less cost. This lower cost could be due

to faster per-study reading by the radiologist, though little data exist about AI helping speed up interpretation. Concerns exist as to whether radiologists are capable or willing to overrule AI results when they are wrong.[16] Others have suggested combining these draft reports with oversight by nonradiologist midlevel providers. While this approach is attractive because there remains a human in the loop who can step in and rectify obvious mistakes, studies suggest that this may be the worst of both worlds, because individuals with less training are less willing to contradict erroneous AI outputs. Thus, the combination of trainee AI and midlevel providers, while attractive to payors, might not benefit patients.

House Elf AI

Further down on the omniscient scale would be House Elf AI. This recognizes all the inefficiencies in the current system and uses AI to mitigate them, thereby making the radiologist's experience better and allowing faster and more accurate reads. The overall goal is to maximize image-interpretation time and minimize all the other distractors. This could be considered as a radiologist's "personal assistant" who can just fix everything so that when he or she sits down to read cases, everything is perfectly ready for efficiency. The advantages of this approach are many. As stated by the American economist W. Edwards Deming, "Uncontrolled variation is the enemy of quality." As imaging groups get larger, the amount of complexity increases exponentially, exacerbating the problems of variability. Finally, such an AI approach would not have a heavy diagnostic component, mitigating fears of radiologist de-skilling.[17] It should be straightforward to deploy and require minimal regulatory burden or societal resistance.

It is difficult to estimate how much inefficiency there is in the current system, but it is likely high. Radiologists are currently asked to do many noninterpretive tasks as part of their daily job. The first and most obvious is the time spent wrangling with report dictation software. Even under the best of circumstances, time spent in report creation takes away from time interpreting images. How much time do we waste daily looking away from images to find where to insert text and to correct misspellings and faulty capitalization? This is not a good use of a radiologist's time. Some radiologists have begun to use "scribes" who handle this aspect of report creation.[18] This use can lead to noticeable efficiencies, similar to medical scribes that have been used for clinical visits. AI has already been implemented to listen to patient-doctor conversations and transcribe first drafts of clinical notes that doctors can then lightly edit.[19] Implementation of this use in the radiology space would be a game changer for productivity.

Beyond acting as a scribe, AI could finally allow us to use hanging protocols, a dream of radiologists for decades. Hanging protocols enhance efficiency by standardizing the PACS layout of imaging series and prior comparisons and can lead to increased efficiency.[20] As everyone knows, these never seem to work, which is largely due to the variability in the naming conventions that different scanners use or that are flummoxed by simple things like series name changes or repeat studies. While PACS companies continue to promise that they will work "in the next version," we need to fix the problem of variability at the root source. AI can be used to evaluate the DICOM header with natural language processing and computer vision of the pixel data to classify sequences into standardized names, regardless of the names the technologists use at the scanner.[21] Such technology can also "grade" the quality of sequences, evaluating the presence of motion, the correct extent of organ coverage, and the SNR. One time saver here is that AI can determine the best of multiple motion-degraded studies and send only that one to the PACS for interpretation, saving PACS storage space and radiologist's interpretation time, reducing the frustration and risks associated with evaluating suboptimal motion-degraded images.

Finally, as we move to more 3D imaging, we can envision software that automatically performs reformats in standardized imaging planes (Fig 2). Once implemented, this change will result in serial imaging studies that will always be aligned, leading to simple comparisons of lesions and their sizes without the need for time-consuming reformatting by the radiologist. This improvement would also free the technologist from doing the reformats and dealing with radiologists' phone calls when the technologist makes a mistake. This time could be used for additional patient care or even improved throughput for certain imaging studies that are reformat-heavy, such as CT.

The largest challenge to introducing such AI into operations is how to estimate its value. Radiologists and technologists see the value immediately, but administrators may not be familiar with all the hidden costs that are being borne by the organization as variability increases. Studies to demonstrate improved efficiency by technologists (ie, the ability to scan more patients) by freeing them from the need for reformats and attention to potential errors could be performed. For radiologists, even more than accuracy (which should increase), demonstration that they can read more studies per unit time is essential. It is possible that AI-driven software could enable 3D labs at sites that cannot currently staff them or allow them to operate in a timely fashion with fewer full-time employees, including off-hours and holidays. Removing these easily automatable tasks from both groups will reduce the radiologist's and technologist's burnout and help with staff retention. Last, in the age of big data, removing variability should finally enable imaging data to be optimally integrated into downstream processes. These will include internal uses, subsuming the need for smart DICOM routers to send the right sequences to third-party AI applications. Benefits would accrue outside the radiology department, enabling the easier consumption of images into planning software for other departments or into aggregated data sets for research. There is specific synergy here with integrating images into vision language models. Despite imaging being 90% of data by storage volume, the extreme variability makes it difficult to integrate into predictive models due to the infeasibility of manual data organization at scale. Such AI tools might, in fact, accelerate our movement toward the more diagnostically oriented AI in the Doctor and Trainee models.

The Back Office

While all these applications described above sound great, the big question remains: How will departments afford them? While we have described how return-on-investment (ROI) could be measured for these, most of the reimbursement in our field comes from the "technical component," which is meant to support the

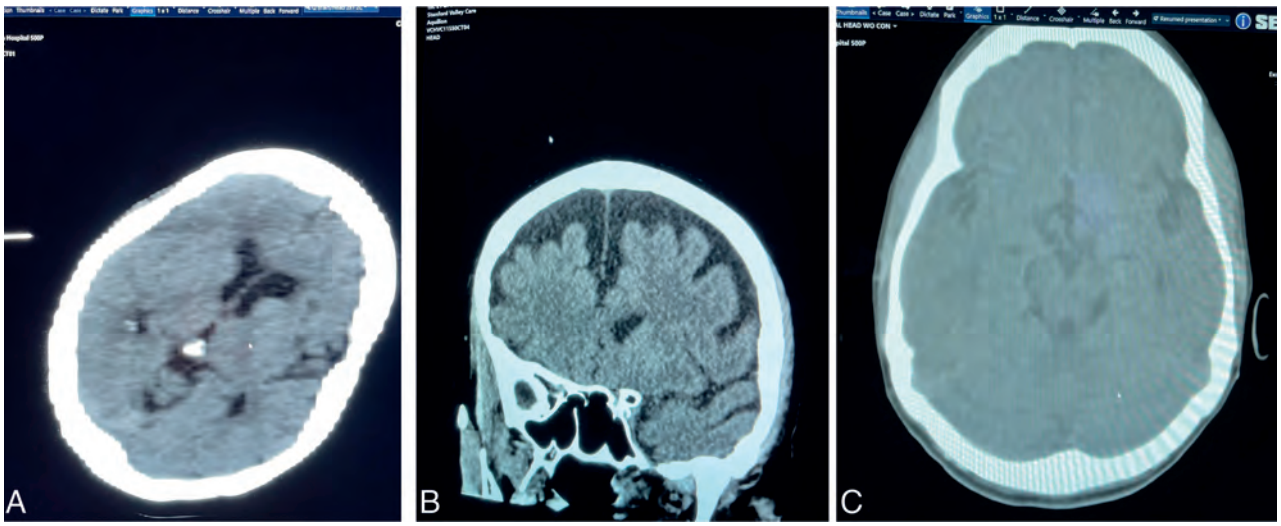

FIG 2. Variability in quality among human-generated 3D reformatted images from noncontrast head CTs, highlighting the potential benefits of automation. *A*, Stairstep artifacts caused by reformats from thicker slab imaging. *B*, Poor alignment of a reformat intended to be coronal. *C*, Inadvertent exclusion of the anterior portion of the head after reformatting.

infrastructure and costs incurred performing an imaging study, typically about 80% of total reimbursement. Thus, AI that enhances scanning efficiency without adding resources has become one of the early AI success stories in radiology—a trend expected to continue and accelerate.

Several companies have successfully introduced AI tools for accelerating image acquisition and reducing the radiation dose. These innovations were initially pioneered by independent companies and later adopted by larger scanner vendors, yielding 20%–50% reductions in scan times without compromising diagnostic quality.[22,23] To date, millions of scans have been expedited using these methods, particularly in MRI and PET, two of the most time-consuming and costly imaging modalities. However, we believe we are at the beginning of a very long road on what is possible here. The combination of low-field MRI with AI image-quality improvement is largely unexplored. A mid- or low-field MRI scanner, with improved performance around metallic implants due to reduced susceptibility artifacts, could potentially achieve image quality comparable with that of a 3T scanner with the help of AI. Who would not want such a system? In addition to reduced cost and sitting requirements, lower electricity costs also make it more environmentally friendly.[24]

AI also has the potential to significantly cut down repeat scans due to patient motion (Fig 3*B*), which currently accounts for about 15% of all MRI scans.[25] Synthetic MRI can help complete examinations for patients who cannot tolerate the full scan (Fig 3*C*), avoiding the need to reschedule or resort to sedation.[26] Most important, we will need the "House Elf AI" described above to decide when and how to apply such capabilities, because the radiologist does not have time to oversee them.

All these solutions clearly address current problems, and the ROI for potential buyers is easy to calculate. It is also attractive to patients who prefer shorter, lower-radiation-dose scans and could yield a competitive advantage in a saturated radiology market. Nevertheless, smaller groups with fewer information technology (IT) resources still struggle to implement such solutions. The other headwind here is the fear by some radiologists that these methods might "hallucinate" (add new structures or remove existing ones) otherwise not be able to provide quality care; so far, these are theoretic risks that have not been seen under typical operating conditions.[27]

AI Applications No One Really Wants but That We Will Likely Get Anyway

The overlap of what is doable and what increases revenue means that we are going to see some applications that may not be what patients or radiologists really need. One example is software that scans radiologists' reports to determine whether downstream studies recommended by radiologists are being performed, and if not, it contacts the patients and providers to follow up. This software sounds good,[28] but there have not been randomized trials to determine whether such approaches improve patient care. Instead, much of the discussion is around avoiding potential litigation. Many recommendations made by radiologists are not evidence-based and are likely to drive up costs without providing benefit. This issue has been evaluated with respect to the recent practice of reporting small thyroid nodules and recommending follow-up ultrasound, an approach no longer recommended because it could not be shown to have benefit.[29] There might be niche indications in which such recommendations are of value, such as those that incorporate well-vetted guidelines for screening. Opportunistic AI screening might fall into this category, which, if used sparingly and wisely, could allow radiology to help our referring colleagues in truly unique ways, by starting conversations about occult diseases and risk factors,[30] though evidence of this value should precede implementation.

Will hospitals view these applications as "money makers" and justify them to avoid patients "falling through the cracks" of the system? Realistically though, we question the value and ethics of alerting already alert-fatigued physicians about a 1-mm questionable aneurysm to be followed up yearly on an outpatient basis (especially if the patient has really good insurance).

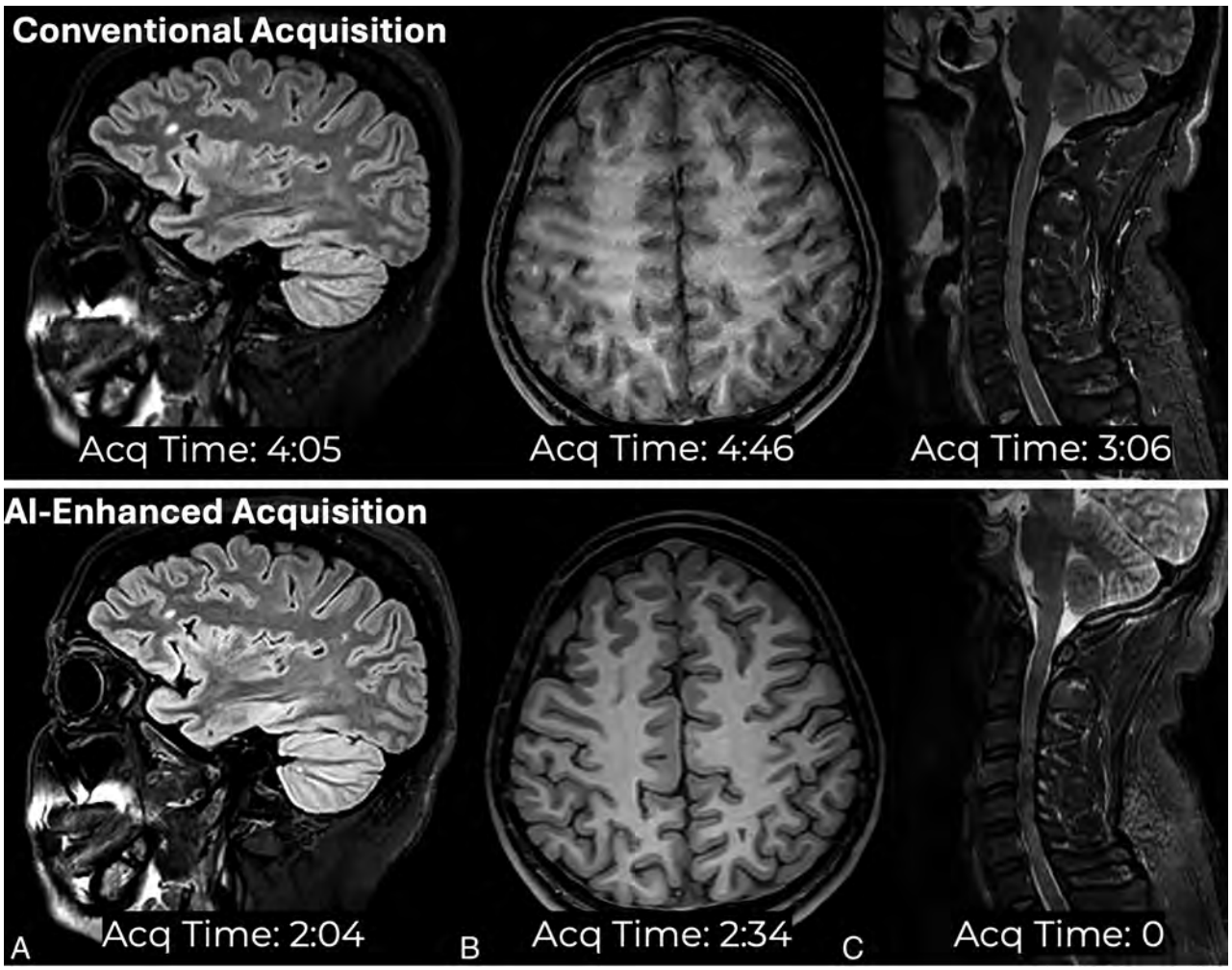

FIG 3. Examples of AI to accelerate MRI acquisition: noise reduction (*A*), super-resolution (*B*), and image synthesis (*C*). Note in *B* that the shorter scan also avoided the patient motion evident in the longer scan. Acq indicates acquisition.

While we do not totally exclude the possibility that there could be some value here, we suspect most will just increase medical costs and inconvenience the patient and their providers. But knowing how our system works, we wouldn't bet against such applications being part of our future.

Another application that has gotten some traction is the idea of creating "patient-friendly" reports with AI. This leveling of language and removal of jargon is a strong suit of current large language models, such as GPT-4 (https://openai.com/index/gpt-4/).[31] Currently, radiology reports are meant to convey information between physicians. However, some hospitals are driven by financial models that reward patient satisfaction and engagement, and providing patients with such targeted reports could improve these metrics. There is nothing inherently problematic about this practice, but we have larger problems to fix in the field, and if patients wish to understand and interact with their reports more deeply, there are many publicly available resources available. Studies demonstrating that such methods improve patient care would change my opinion, but until then, such an AI application is a distraction from more pressing problems even if it is an "easy win" for departments.

Implementation Woes: Is Radiology IT Up to the Job?

Predicting the future of AI in radiology must take into account the bandwidth and the number of clinical informatics personnel to implement and maintain these technologies. Given the need to support legacy systems, implement cybersecurity, and get all the legacy systems to work together, there is not much time for new projects in most IT departments. Adding AI software trials and long-term monitoring to their responsibilities poses a significant challenge.

If we are to make any significant progress during the next 10 years, departments and practices must invest strategically in their IT capabilities to make it happen. This problem is a chicken-and-egg one, in which the financial benefits will only accrue after significant financial resources are provided to implement AI algorithms. Otherwise, we will end up with a few choices from legacy vendors whose products may or may not satisfy radiologists' needs.

Closing Thoughts

There will be new AI applications in the next 10 years (Table 1). The sweet spot will be applications that improve patient care and radiologists' productivity with either net neutral or financially

Benefits and challenges for clinical AI integration in the next 10 years

Benefits

1) Improved radiologist efficiency: AI can automate repetitive tasks like image segmentation and preliminary reporting, allowing radiologists to focus on more complex cases. With an aging population and growing diagnostic needs, AI can help manage the rising volume of cases, ensuring timely diagnosis and care.
2) Shorter scan times and improved standardization: AI can optimize scan protocols, leading to quicker examinations with fewer artifacts and errors, reducing the need for repeat imaging. By standardizing image naming, orientation, and organization, display protocols can be used to reduce radiologists' interpretation times.
3) Cost reduction for health care payors: By automating image analysis and improving workflow efficiency, AI can reduce the overall cost of radiologic examinations and decrease the burden on health care systems.
4) Environmental impact: The use of AI to reduce scan time or create better image quality can reduce the per-person carbon footprint of imaging. AI-based augmentation of low-dose CT and MR contrast examinations can reduce downstream marine environment pollution.

Challenges

1) Demonstrating the value of interpretative AI: Clinical studies must focus on the reporting times of radiologists and demonstrate that AI applications really reduce the time per study and can increase the overall number of studies read by radiologists in a shift, without loss of quality.
2) Technical infrastructure: Skilled IT personnel are needed to deploy, test, and maintain AI systems, possibly posing a challenge, especially for smaller or underfunded institutions. These professionals are in high demand in most health care systems.
3) Regulatory issues: Navigating the evolving regulatory landscape for AI in health care (such as FDA approval) is complex and could slow down the adoption of AI tools. In-house-developed applications might not be FDA-approved but could increase medicolegal risks.
4) Integration into clinical workflow: All radiologists work differently. Incorporating AI into established workflows without disrupting the clinical routine or overburdening radiologists with additional tasks is challenging. Implementing AI so that it fits into the ecosystem of our legacy systems (scanners, routers, PACS) is not easy.
5) Clinician's trust: Radiologists may be hesitant to adopt AI, especially if they are unsure about its accuracy or reliability, making widespread adoption slower.

positive characteristics. The tsunami of imaging studies coupled with the limited number of radiologists will require some solution and where we end up on the Doctor AI/Trainee AI/House Elf AI spectrum will be determined by a range of factors including the capability of vision language models and the burden of regulations that will be imposed by external forces. if we had to bet, we suspect will land somewhere between the Doctor and Trainee AI paradigms, meanwhile taking the "easy wins" from the House Elf model. There will be much handwringing regarding the decline in radiologists' independent clinical skill levels, though this decline has been a constant part of our history as a field. There will be just too much work for us to expect an unchanging high level of individual acumen, though we will continue to value expert diagnosticians as we do now.

The ability of AI to impact and replace technologic cost with software should usher in new, cheaper devices that are easier to maintain and better for the environment, reducing technical component costs while improving the patient experience. There is no question that the task will be difficult, with plenty of issues surrounding these technologies, from data distribution drift to enshrinement of old biases. Pivotal clinical trials of new technologies will be challenging, especially given the pace of innovation. However overall, radiology has always embraced new technologies and found ways to innovate and improve patient care even with incomplete knowledge. This evolution, however, must be a 2-way street. Radiologists need to actively engage with AI developers, contributing their domain expertise and ethical judgment. Meanwhile, regulatory bodies need to trust radiologists to oversee and implement AI applications responsibly. Only then can we fully realize the potential of AI in radiology during the next decade.

ACKNOWLEDGMENT

The authors thank Laura Wilhelm for her illustrations, which enhanced this editorial.

REFERENCES

1. **Why scan-reading artificial intelligence is bad news for radiologists.** November 29, 2017. *The Economist*. https://www.economist.com/free-exchange/2017/11/29/why-scan-reading-artificial-intelligence-is-bad-news-for-radiologists.
2. Anzai Y, Heilbrun ME, Haas D, et al. **Dissecting costs of CT study: application of TDABC (time-driven activity-based costing) in a tertiary academic center.** *Acad Radiol* 2017;24:200–08 CrossRef Medline
3. Voter AF, Larson ME, Garrett JW, et al. **Diagnostic accuracy and failure mode analysis of a deep learning algorithm for the detection of cervical spine fractures.** *AJNR Am J Neuroradiol* 2021;42:1550–56 CrossRef Medline
4. Savage CH, Tanwar M, Elkassem AA, et al. **Prospective evaluation of artificial intelligence triage of intracranial hemorrhage on noncontrast head CT examinations.** *AJR Am J Roentgenol* 2024 Sep 4. [Epub ahead of print] CrossRef Medline
5. Arbabshirani MR, Fornwalt BK, Mongelluzzo GJ, et al. **Advanced machine learning in action: identification of intracranial hemorrhage on computed tomography scans of the head with clinical workflow integration.** *NPJ Digit Med* 2018;1:9 CrossRef Medline
6. Del Gaizo AJ, Osborne TF, Shahoumian T, et al. **Deep learning to detect intracranial hemorrhage in a national teleradiology program and the impact on interpretation time.** *Radiology Artif Intell* 2024;6: e240067 CrossRef Medline
7. Thawkar O, Shaker A, Mullappilly SS, et al. **XrayGPT: chest radiographs summarization using medical vision-language models.** *arXiv.org* 2023. https://arxiv.org/abs/2306.07971v1.
8. Yang L, Xu S, Sellergren A, et al. **Advancing multimodal medical capabilities of Gemini.** *arXiv.org* 2024. https://arxiv.org/abs/2405.03162v1.
9. Blankemeier L, Cohen JP, Kumar A, et al. **Merlin: a vision language foundation model for 3D computed tomography.** *arXiv.org* 2024. https://arxiv.org/abs/2406.06512v1.

10. Ney E, Berger E. **Patients are more comfortable with AI making diagnoses than answering the phone at their doctor's office, but overwhelmingly concerns persist**. *Survery Bain & Company* 2024. https://www.bain.com/about/media-center/press-releases/2024/patients-are-more-comfortable-with-ai-making-diagnoses-than-answering-the-phone-at-their-doctors-office-but-overwhelmingly-concerns-persist/.
11. Tu LH, Malhotra A, Venkatesh AK, et al. **Head and neck CTA utilization: analysis of ordering frequency and nonroutine results communication, with focus on the 50 most common emergency department clinical presentations.** *AJR Am J Roentgenol* 2022;218:544–51 CrossRef Medline
12. Tung M, Sharma R, Hinson JS, et al. **Factors associated with imaging overuse in the emergency department: a systematic review.** *Am J Emerg Med* 2018;36:301–09 CrossRef Medline
13. Mehan WA, Shin D, Buch K. **Effect of provider type on overutilization of CT angiograms of the head and neck for patients presenting to the emergency department with nonfocal neurologic symptoms.** *J Am Coll Radiol* 2024;21:890–95 CrossRef Medline
14. Lew M, Wilbur DC, Pantanowitz L. **Computational cytology: lessons learned from pap test computer-assisted screening.** *Acta Cytol* 2021;65:286–300 CrossRef Medline
15. American College of Radiology. **Thinking about AI.** 2024. https://www.acr.org/Practice-Management-Quality-Informatics/ACR-Bulletin/Articles/June-2021/Thinking-About-AI.
16. Bernstein MH, Atalay MK, Dibble EH, et al. **Can incorrect artificial intelligence (AI) results impact radiologists, and if so, what can we do about it? A multi-reader pilot study of lung cancer detection with chest radiography.** *Eur Radiol* 2023;33:8263–69 CrossRef Medline
17. Brady AP, Allen B, Chong J, et al. **Developing, Purchasing, Implementing and Monitoring AI Tools in Radiology: Practical Considerations—A Multi-Society Statement from the ACR, CAR, ESR, RANZCR and RSNA**. *Radiol Artif Intell* 2024;6:e230513 CrossRef Medline
18. Sami F. **TeleRadiology Scribing in Action.** YouTube 2020 Nov 6. https://www.youtube.com/watch?v=Uvc9opoZs7A.
19. Tierney AA, Gayre G, Hoberman B, et al. **Ambient artificial intelligence scribes to alleviate the burden of clinical documentation.** *N Engl J Med Catal* 2024;5 CrossRef
20. Geis JR. **Medical imaging informatics: how it improves radiology practice today.** *J Digit Imaging* 2007;20:99–104 CrossRef Medline
21. Arnold TC, Duffy B, Zaharchuk G, et al. **Harmonization of Longitudinal Multicenter Imaging Data Through Natural Language Processing and Brain Alignment Algorithms.** In: *Proceedings of the Annual Meeting of the American Society of Neuroradiology*. May 18–22, 2024. Las Vegas, Nevada; 466
22. Kim M, Kim HS, Kim HJ, et al. **Thin-slice pituitary MRI with deep learning-based reconstruction: diagnostic performance in a postoperative setting.** *Radiology* 2021;298:114–122 CrossRef Medline
23. Bash S, Wang L, Airriess C, et al. **Deep learning enables 60% accelerated volumetric brain MRI while preserving quantitative performance: a prospective, multicenter, multireader trial**. *AJNR Am J Neuroradiol* 2021;42:2130–37 CrossRef Medline
24. Heye T, Knoerl R, Wehrle T, et al. **The energy consumption of radiology: energy- and cost-saving opportunities for CT and MRI operation.** *Radiology* 2020;295:593–605 CrossRef Medline
25. Duffy BA, Zhao L, Sepehrband F, et al; Alzheimer's Disease Neuroimaging Initiative. **Retrospective motion artifact correction of structural MRI images using deep learning improves the quality of cortical surface reconstructions**. *Neuroimage* 2021;230:117756 CrossRef Medline
26. Tanenbaum LN, Bash SC, Zaharchuk G, et al. **Deep learning-generated synthetic MR imaging STIR spine images are superior in image quality and diagnostically equivalent to conventional STIR: a multicenter, multireader trial.** *AJNR Am J Neuroradiol* 2023;44:987–93 CrossRef Medline
27. Radmanesh A, Muckley MJ, Murrell T, et al. **Exploring the acceleration limits of deep learning variational network-based two-dimensional brain MRI.** *Radiol Artif Intell* 2022;4:e210313 CrossRef Medline
28. White T, Aronson MD, Sternberg SB, et al. **Analysis of radiology report recommendation characteristics and rate of recommended action performance.** *JAMA Netw Open* 2022;5:e2222549 CrossRef Medline
29. Hoang JK, Langer JE, Middleton WD, et al. **Managing incidental thyroid nodules detected on imaging: white paper of the ACR Incidental Thyroid Findings Committee.** *J Am Coll Radiol* 2015;12:143–50 CrossRef Medline
30. Pickhardt P, Summers R, Garrett J, et al. **Opportunistic screening: Radiology Scientific Expert Panel.** *Radiology* 2023;307:e222044 CrossRef Medline
31. Lyu Q, Tan J, Zapadka ME, et al. **Translating radiology reports into plain language using ChatGPT and GPT-4 with prompt learning: results, limitations, and potential.** *Vis Comput Ind Biomed Art* 2023;6:9 CrossRef Medline

Our Most Impactful Articles

In this last paper edition of the *American Journal of Neuroradiology* (*AJNR*), we proudly present a selection of articles that have been voted by our dedicated readers as the most impactful on the practice of neuroradiology since the inception of the journal. The chosen articles were evaluated based on their relevance, innovation, and the tangible impact they have had on clinical practice and research in neuroradiology. Each selection represents a pivotal moment in the advancement of our discipline, addressing key challenges and offering solutions that resonate with the current landscape of patient care.

Accompanying these articles are insights from the authors themselves, accessible through QR codes available in the printed copy of the journal. The authors reflect on their experiences during the writing process, sharing where they were in their careers when inspiration struck and how their ideas evolved into the impactful studies we recognize today. These narratives provide a deeper understanding of the thought processes and motivations behind each article, fostering a greater appreciation for the ongoing pursuit of knowledge in neuroradiology.

We invite you to explore these remarkable contributions, which not only represent individual achievements but also collectively advance our understanding and practice in the field. Thank you to all who participated in the voting process, and congratulations to our authors for their outstanding work!

Max Wintermark, Editor-in-Chief of the *AJNR*

http://dx.doi.org/10.3174/ajnr.A8540

Dural Arteriovenous Malformation of the Major Venous Sinuses: An Acquired Lesion

Mohammad Y. Chaudhary,[1,2]
Ved P. Sachdev[3]
Soo H. Cho[1]
Imre Weitzner, Jr.[1]
Smiljan Puljic[2]
Yun Peng Huang[1]

Arteriovenous malformations of the dura are thought to be congenital. However, arteriographic investigations of four patients who, after a head injury, developed dural arteriovenous fistulae with features of congenital malformations suggest that these abnormal communications may also be acquired. Thrombosis or thrombophlebitis in the dural sinus or vein may be the primary event in their formation. The pathogenesis is probably "growth" of the dural arteries normally present in the walls of the sinuses during the organization of an intraluminal thrombus. This may result in a direct communication between artery and vein or sinus, establishing an abnormal shunt. Ultimate fibrosis of the sinus wall and intraluminal thrombus may be the factors responsible for the spontaneous disappearance of such malformations.

Most dural arteriovenous malformations (AVMs) that involve the major venous sinuses present either spontaneously or as incidental findings during arteriography performed for other reasons. They occur predominantly in women over age 40 years [1]. The angiomatous network, multiple feeding arteries, numerous arteriovenous (AV) shunts, and occasional association with cerebral angiomas [2], as well as a few cases reported in children [3], suggest that these AVMs are congenital. Thrombosis of the draining sinus or vein is thought to be responsible for the occasional spontaneous disappearance of these lesions [4, 5].

Our experience with four patients who, after a head injury, developed dural AV fistulae with features of congenital malformations prompted a review of the literature and this report. In two of our four cases, transverse and sigmoid sinus abnormalities were demonstrated angiographically before the AV fistulae developed. In case 3, angiography 2 years earlier for unrelated reasons was normal; no AV shunt was seen. Although in case 4, there was no angiographic evidence of a dural fistula before head injury, the posttrauma onset of symptoms and the angiographic findings strongly suggested that this lesion had been acquired.

Cases 1 and 3 were studied by serial angiography with selective internal, external, and common carotid injections, while stereo magnification serial angiography with selective and superselective catheterization of the feeding arteries was performed in cases 2 and 4. The first three patients were followed by periodic angiography for up to 4 years, and the AV shunts were seen to close spontaneously.

Case Reports

Case 1

A 56-year-old woman was examined for headaches and dizzy spells. Cerebral angiography to rule out transient ischemic attacks was normal (figs 1A and 1B). Control of her mild diabetes caused her headaches and dizzy spells to disappear.

She was brought to the emergency room after a head injury 2 months later. She had a bruise over the right occipitomastoid area, was confused and disoriented, but she had no

Received May 7, 1981; accepted after revision September 9, 1981.

Presented at the annual meeting of the American Society of Neuroradiology, Chicago, April 1981.

[1]Department of Radiology, Mount Sinai Hospital, New York, NY 10029.

[2]Department of Radiology, New York Medical College, Westchester County Medical Center, Valhalla, NY 10595. Address reprint requests to M. Y. Chaudhary (present address).

[3]Department of Neurosurgery, Mount Siani Hospital, New York, NY 10029.

AJNR 3:13–19, January/February 1982
0195-6108/82/0301-0013 $00.00
© American Roentgen Ray Society

neurologic deficit. When, after 1 week, her condition had not improved, cerebral angiography was performed, which showed a normal arterial phase. In the venous phase, however, the wall of the right sigmoid sinus was irregular and the internal jugular vein (fig. 1C) was not opacified, indicating thrombosis or thrombophlebitis.

She recovered completely, but 6 months later returned to the hospital complaining of tinnitus and a buzzing noise in her right ear. Auscultation revealed an audible bruit over the right mastoid region. Cerebral angiography showed multiple dural AV fistulae supplied by the occipital and middle meningeal branches of the right external carotid artery (figs. 1D–1E).

At surgery, the meningeal branches of the occipital artery and the mastoid emissary vein were ligated extracranially. Postoperatively, her complaints of tinnitus and buzzing noise behind her right ear disappeared, but, on auscultation, bruit was still audible. A repeat angiogram showed that AV shunts were still present but flow through them had decreased (fig. 1F). Follow-up arteriography a year later (not illustrated) showed that the right middle meningeal artery was no longer supplying the fistulous communications. Instead, the arterial supply from the transosseous and other meningeal branches of the occipital and the ascending pharyngeal arteries appeared to have increased. The major venous flow at this time was noted to be via the condyloid and other emissary veins into the paravertebral venous plexus. The internal jugular vein opacification was delayed, suggesting stenosis or occlusion in the region of the jugular bulb.

She returned to the hospital again 3 years after her first admission complaining of right occipital headaches. Right common, external, and internal carotid arteriography showed that the fistulous communications had disappeared spontaneously (fig. 1G). The right sigmoid sinus was abnormal; its lumen was narrowed and its wall irregular, particularly at the site of the previous fistulous communication (fig. 1H). The patient was treated conservatively, and her headaches improved with medication.

Case 2

A 50-year-old male construction worker was admitted to the hospital after a head injury that caused him to lose consciousness for 15 min. He was confused but neurologically intact on admission. Skull films showed diastasis of the right lambdoidal suture, but a computed tomography (CT) scan was normal. After 3 weeks, he had not improved and was increasingly disoriented. CT was repeated, and compression and blunting of the frontal horn of the left lateral ventricle were evident.

These findings prompted bilateral common carotid arteriography, which revealed a left frontoparietal subdural hematoma and an AV fistula in the scalp on the right side (figs. 2A and 2B). The subdural hematoma was evacuated, and it was decided to evaluate the scalp fistula at a later date. He was readmitted 6 months later. Angiography did not show the previous scalp lesion. Instead, multiple dural AV fistulae were seen, draining into the right lateral sinus (figs. 2C–2F). The patient refused treatment but returned a month later for embolization.

A preembolization angiogram showed that the fistulae had disappeared spontaneously; the lateral sinus was not opacified but the angiomatous network was still evident (fig. 2G). Irregularity of the right lateral sinus wall and the defect in its lumen noted previously were absent, perhaps indicating organization and fibrosis of the intraluminal thrombus (fig. 2H). Follow-up on this patient continued.

Case 3

A 38-year-old man was brought to the emergency room in a coma after a head injury. He had a bruise over the left temporooccipital area and was bleeding from the left ear. Skull films revealed a left temporal fracture traversing the mastoid air cells; a CT scan showed bifrontal intracerebral hematomas. He improved gradually with conservative treatment, but after 3 weeks he had a grand mal seizure. Cerebral angiography confirmed the bifrontal intracerebral avascular masses and, in addition, showed a dural AV fistula in the wall of the right lateral sinus (figs. 3B–3D) draining into a cortical vein.

Review of the right common carotid arteriogram obtained during a workup for headaches 2 years earlier was normal (fig. 3A). In that study no AV shunt was seen. Because the patient was in poor condition, he was treated conservatively and improved gradually. A repeat CT scan 8 weeks later revealed that the hematomas had been replaced by areas of decreased attenuation. Angiography 2 years after the patient was discharged showed the fistula had closed spontaneously (fig. 3E).

Case 4

A 66-year-old man with a left acoustic neurinoma had a complete hearing loss on the left and slight facial asymmetry, with minimal left facial droop. He also had slight weakness of his right arm that he attributed to a head injury 3 years earlier, at which time he was unconscious for 3 days. CT and cerebral angiography confirmed a mass lesion in the left cerebellopontine angle.

Left external carotid arteriography also revealed a dural AV fistula in the wall of the superior sagittal sinus in the falx (figs. 4A–4F). At surgery, all of the meningeal feeders were ligated and the dura excised. Surprisingly, after surgery, strength in his right arm increased. He was readmitted to the hospital 3 months later and the mass lesion in the left cerebellopontine angle, which proved to be an acoustic neurinoma, was successfully removed. An angiogram at this time showed the dural AV shunt had not recurred.

Discussion

Normal Arterial Supply of the Dural Walls of the Venous Sinuses

In considering the pathogenesis of these malformations, a brief review of the normal arterial supply of the dura walls of the great venous sinuses may be useful. The dura mater is highly vascular, especially in the region of the great venous sinuses. The middle meningeal artery normally ends in the anterior and posterior paramedian meningeal branches, which run along the insertion of the dural wall of the superior sagittal sinus at the convexity, as far as the cribiform plate anteriorly, and to the foramen magnum posteriorly. These paramedian vessels also receive collaterals from the anterior and posterior meningeal arteries, each of which, before termination, gives off branches to the dura of the roof and lateral wall of the superior sagittal sinus [2]. A similar rich dural arterial network is created in the walls of the lateral and sigmoid sinuses by the abundant collateral and anastomotic channels between the middle meningeal artery and the meningeal branches of the occipital, ascending pharyngeal, and internal carotid arteries. Physiologic AV shunts between these meningeal arterial networks and dural venous sinuses have been described [6–8].

Previous Reports

During the past decade, over 70 cases of dural AV malformations have been reported [9]. Although found in both

genders and at all ages, their incidence is highest in women over 40 years old [1]. Recent reports have described the angiographic anatomy of the feeding arteries [10–12]. A very high incidence of abnormalities of recipient venous channels has also been reported [13]. These abnormalities are described as irregularity and rigidity of the wall, stenosis and septation with filling defects in the lumen, and retrograde flow with partial or complete occlusion of the draining venous sinus or vein. Such changes are believed to be due to venous thrombosis, which is thought to be responsible for the occasional spontaneous disappearance of these lesions [4, 5].

While these malformations are generally considered congenital [14], a few authors maintain that they are acquired [1, 2, 15]. Aminoff [15] suggested that since dural arteries and veins (unlike brain parenchymal vessels) are closely associated anatomically, trauma, especially a fracture crossing these vessels, can cause their simultaneous rupture, resulting in a fistulous communication. However, this concept holds true only for major branches of the middle meningeal arteries and their accompanying veins. It does not apply to dural AV malformations located in the walls of major venous sinuses, as venous blood from the dural walls of these sinuses appears to drain directly into the sinuses. Furthermore, middle meningeal and other posttrauma AV fistulae are usually seen in an immediate postictus period and have a classic angiographic appearance [16], with a single AV shunt between the ruptured artery and vein.

We found at least three case reports of dural AV malformations located in the walls of the venous sinus in which the onset of symptoms was preceded by head injury [4, 17, 18]. In each of these, as well as in our cases, the lesion consisted of multiple AV shunts, and the interval between trauma and the time at which symptoms appeared varied from a few weeks to 6 months. Because most reported cases did not have a history of trauma, we feel that a mechanism other than direct trauma itself is responsible for the development of these fistulae.

Pathogenesis

Thrombosis or thrombophlebitis of the draining vein or sinus appears to be a common feature of these lesions and may be related to their origin.

In a discussion of these fistulae, Djindjian and Merland [2] described in detail the venous abnormalities indicating sinus thrombosis and suggested that such venous abnormalities resulted from previous medical problems. They noted that in almost all of their patients, complaints of bruit and other symptoms had been preceded by a variety of medical illnesses, surgical and obstetric procedures, and head trauma. They postulated that thrombosis or thrombophlebitis resulting from such prior events precedes the development of fistulous communications. According to this hypothesis, the abnormal communications are merely a pathologic "opening-up" of physiologic AV shunts in the dural walls of the venous sinuses in response to phlebitis.

This hypothesis was partly confirmed by Houser et al. [1], who angiographically demonstrated that venous abnormalities preceded the formation of fistulous communications in two of their patients. They postulated that "the indigenous dysplastic dural vessels present within the sinus wall develop further, establishing a direct artery-to-sinus communication during the organization of an intravenous thrombus." No experimental work supporting either of the above hypotheses is available. However, patient histories, angiographic findings of prior venous abnormalities, the prolonged interval before fistulae develop, and the dysplastic vessels in surgical specimens and in angiograms (fig. 2G) tend to support the hypothesis of Houser et al. [1].

The cases reported in children may be explained by compression and injury of the dural sinuses from calvarial molding during birth [19], resulting in sinus thrombosis and fistulous communications during the organization and recanalization of the intraluminal thrombus. No matter what the mechanism, once the shunts are established, the rapid flow of blood through them causes the preexistent rich meningeal arterial network in the sinus wall and surrounding dura mater to dilate and hypertrophy. Abundant collateral and anastomotic channels between various meningeal arteries result in multiple feeders.

Our Experience

In our first two cases, the shunts were located in the walls of the lateral and sigmoid sinuses and drained into the lumen of the respective sinus. In contrast, in cases 3 and 4, even though the abnormal shunts were located in the walls of the lateral and the superior sagittal sinus, they drained into the cortical veins in a retrograde manner. The fistulae were located at a point where the recipient cortical veins normally entered the sinus. The retrograde flow in these veins suggested that thrombosis and occlusion had occurred at their junction with the respective sinus. Close examination of the early films of the arterial phase in each case revealed that, like congenital malformations, the abnormal shunts were multiple and confined to an abnormal segment of the dural wall of the respective sinus.

The spontaneous disappearance of these abnormal dural fistulae have been reported previously [4, 5] and it is thought to be due to thrombosis of the recipient sinus or vein. However, preexisting venous abnormalities in two of our cases, as well as in those reported by Houser et al. [1], indicate that thrombosis itself is not responsible for the spontaneous closure of these shunts. Ultimate fibrosis of the intraluminal thrombus and the inflamed sinus wall probably resulted in occlusion of the fistulous communications. Partial or complete obliteration of the dural sinus [4] may also result. If the sinus remains patent, narrowing and stenosis of its lumen and irregularity (cases 1 and 2) of its wall, particularly at the site of the shunts, may be seen. The long interval before the shunts closed spontaneously may be related to the slow organizing and fibrosing process [20]. That the angiomatous network persisted after the shunts had closed (case 2) is possibly related to alterations in the normal lamination of elastic muscle fibers in the walls of dural arteries as a result of hemodynamic changes.

The four dural AV malformations reported here appear to be acquired and this may be the mechanism in many others. Thrombosis or thrombophlebitis of the recipient venous

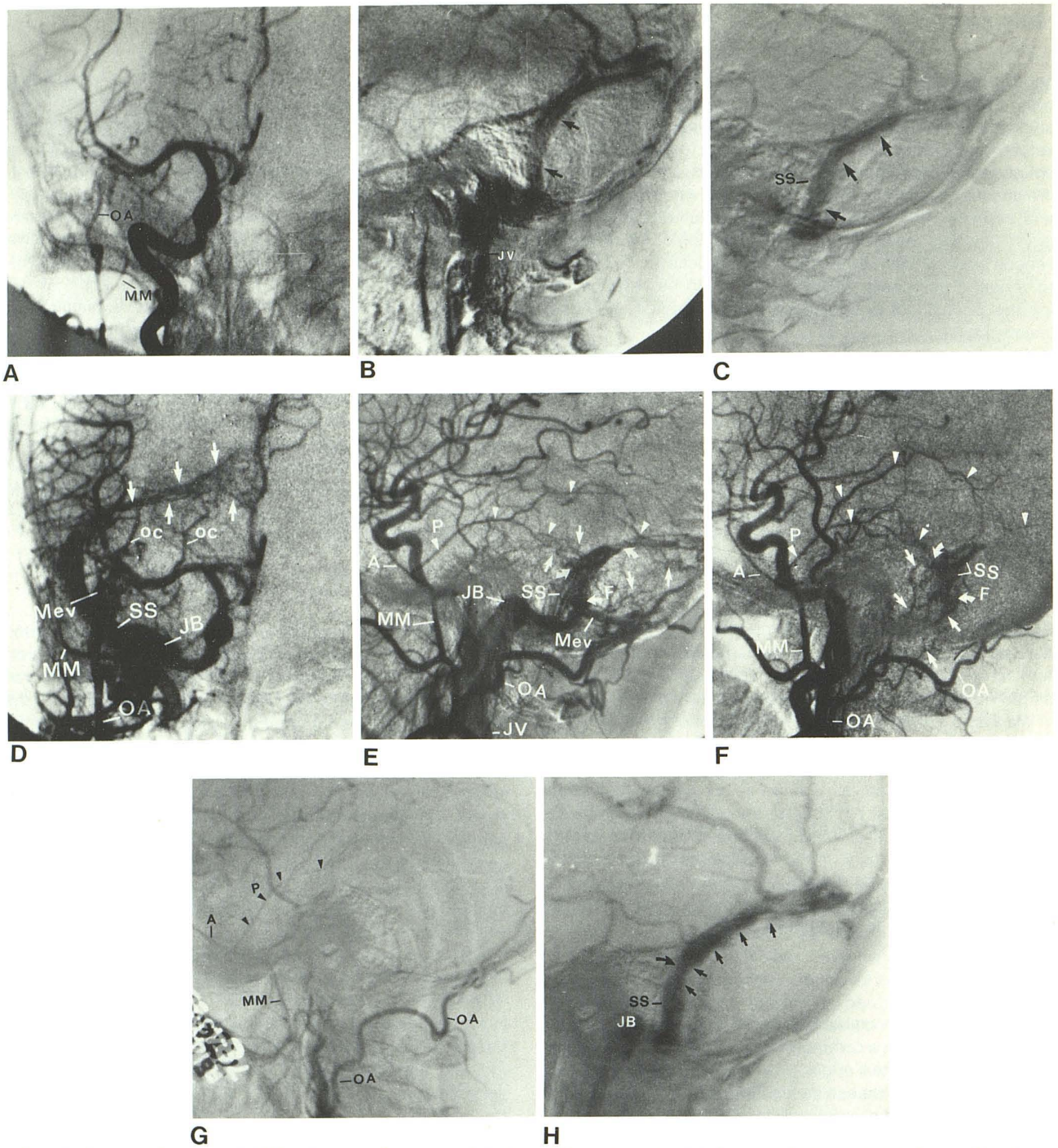

Fig. 1.—Case 1. Normal arterial (**A**) and venous (**B**) phases of right common carotid arteriogram 2 months before trauma. Occipital (OA) and middle meningeal (MM) arteries of normal size and course. Sigmoid sinus (*arrows*) and jugular vein (JV) are normally opacified. **C**, 1 week after injury. Irregular wall and lumen (*arrows*) of sigmoid sinus. Jugular vein not opacified. Arterial phase was normal. **D** and **E**, 6 months later. Hypertrophied middle meningeal (*arrowheads*) and occipital artery branches (OC) terminate directly into meningeal vascular network (*straight arrows*) in wall of lateral and sigmoid sinuses. This supplies multiple fistulous communications (F, *curved arrows*) in wall of sigmoid sinus (SS). Sigmoid sinus, mastoid emissary vein (Mev), and jugular vein (JV) are opacified early in arterial phase. JB = jugular bulb; A = anterior and P = posterior branches of middle meningeal artery. **F**, 1 week after surgery and 7 months after trauma. Meningeal branches of occipital artery ligated extracranially. However, fistulae (F, *curved arrows*) persist and are supplied by posterior branch of middle meningeal artery (*arrowheads*) and by a few transosseous meningeal branches of occipital artery (*straight arrows*). **G**, External carotid arteriogram 2½ years after trauma. Occipital and middle meningeal arteries of normal size. No AV shunt. **H**, Irregular sinus wall (*straight arrows*) and apparently stenotic lumen of sigmoid sinus (*curved arrow*) at site of previously demonstrated shunt.

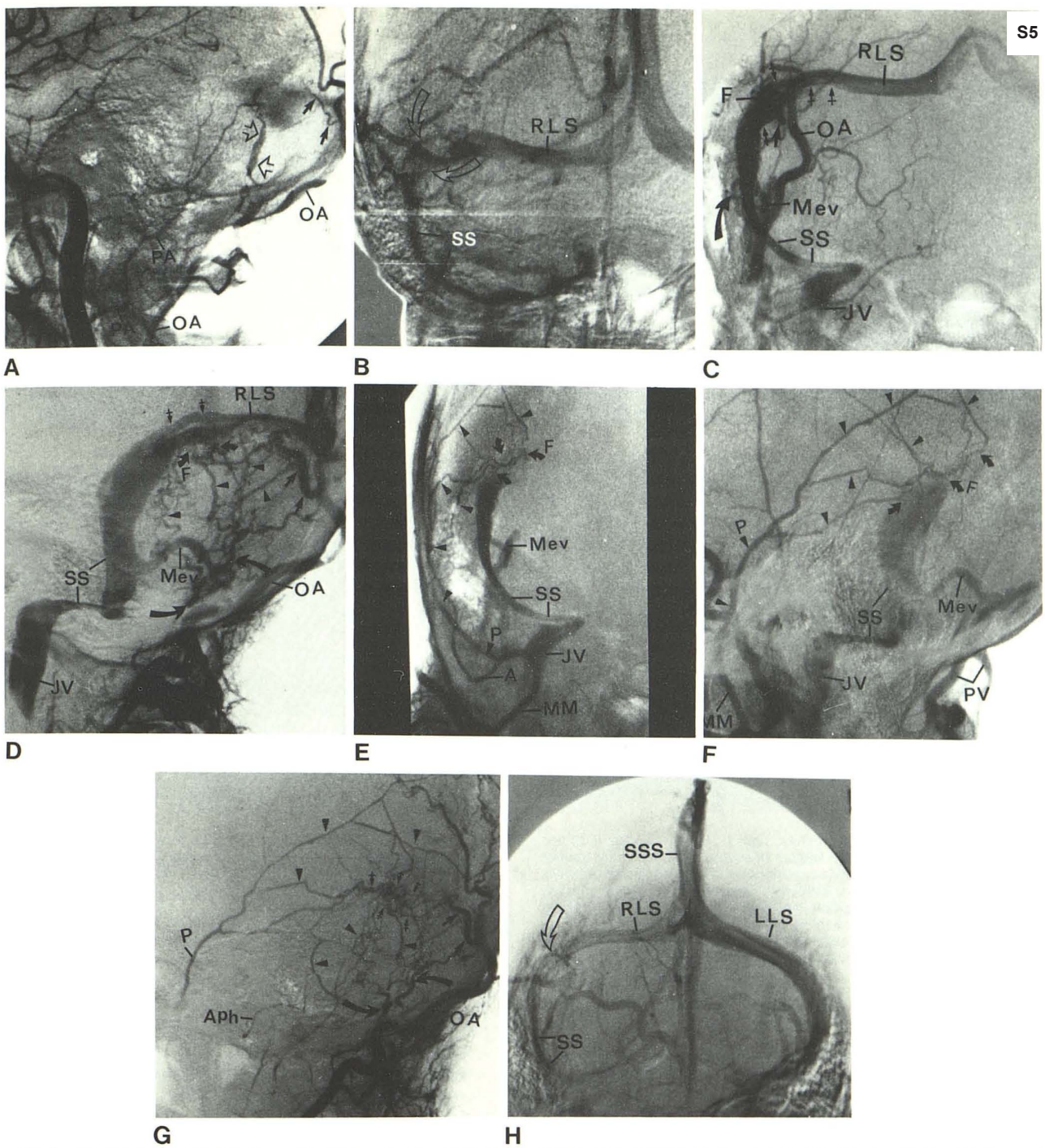

Fig. 2.—Case 2. **A**, 3 weeks after trauma. Posterior auricular artery (PA) supplies fistulous communication in scalp. Early appearing vein (*open arrows*) drains into paravertebral venous plexus. Normal occipital artery and meningeal branches (*solid arrows*). **B**, Anteroposterior view of venous phase. Right lateral sinus (RLS) is normal up to its bend. Filling defect in lumen (*arrows*) where sinus is crossed by diastatic lambdoidal suture. Sigmoid sinus markedly narrowed and stenotic. **C** and **D**, 6 months after injury. Selective arteriogram of right occipital artery. Hypertrophied occipital artery. Mastoid meningeal branches (*long curved arrows*) and transosseous meningeal branches (*straight arrows*) also enlarged and supply rich dural vascular network (*arrowheads*). Fistulae (F, *short curved arrows*) between meningeal vascular network and right lateral sinus. Lesion mimics malformation and consists of multiple AV shunts, indicated by numerous meningeal arteries terminating directly into lumen of right lateral sinus. Shunts at previously seen intraluminal defect (**B**). Sigmoid sinus (SS), mastoid emissary vein (Mev), and jugular vein (JV) opacified early in arterial phase. Wall is irregular (*crossed arrows*) with septation and narrowing of lumen of right lateral sinus. Sigmoid sinus also narrowed in transverse diameter. **E** and **F**, Right internal maxillary artery injection. Posterior (P) temporal convexity branch of middle meningeal artery (MM) is hypertrophied and supplies dural vascular network (*arrowheads*). Vascular network also supplies fistulous communications (*curved arrows*). Multiple meningeal arteries terminate directly into lumen of right lateral sinus. PV = paravertebral vein. **G**, Superselective right occipital arteriogram 1 month later (7 months after trauma). Fistulous communications have closed spontaneously. Occipital artery, its mastoid meningeal branches (*curved arrows*), and transosseous meningeal branches (*straight arrows*), although still hypertrophied, are relatively small in caliber. Meningeal vascular network still present, and there is retrograde opacification of posterior (P) temporal convexity branch of the middle meningeal artery and meningeal branch of ascending pharyngeal (Aph) artery, indicating free communication between various meningeal arteries. There is also a network of dural arteries (*crossed arrows*), perhaps representing newly formed vessels in wall of abnormal segment of lateral sinus. No opacification of the venous system. **H**, Right internal carotid injection with compression of left jugular vein. Small right lateral sinus (RLS) but previous irregularity of wall, septation, and defect in lumen (*arrow*) (**B–D**) are absent. Sigmoid sinus is still narrowed and stenotic. Despite compression of left jugular vein, major venous flow is into left lateral sinus (LLS), indicating compromise of lumen of right lateral and sigmoid sinuses.

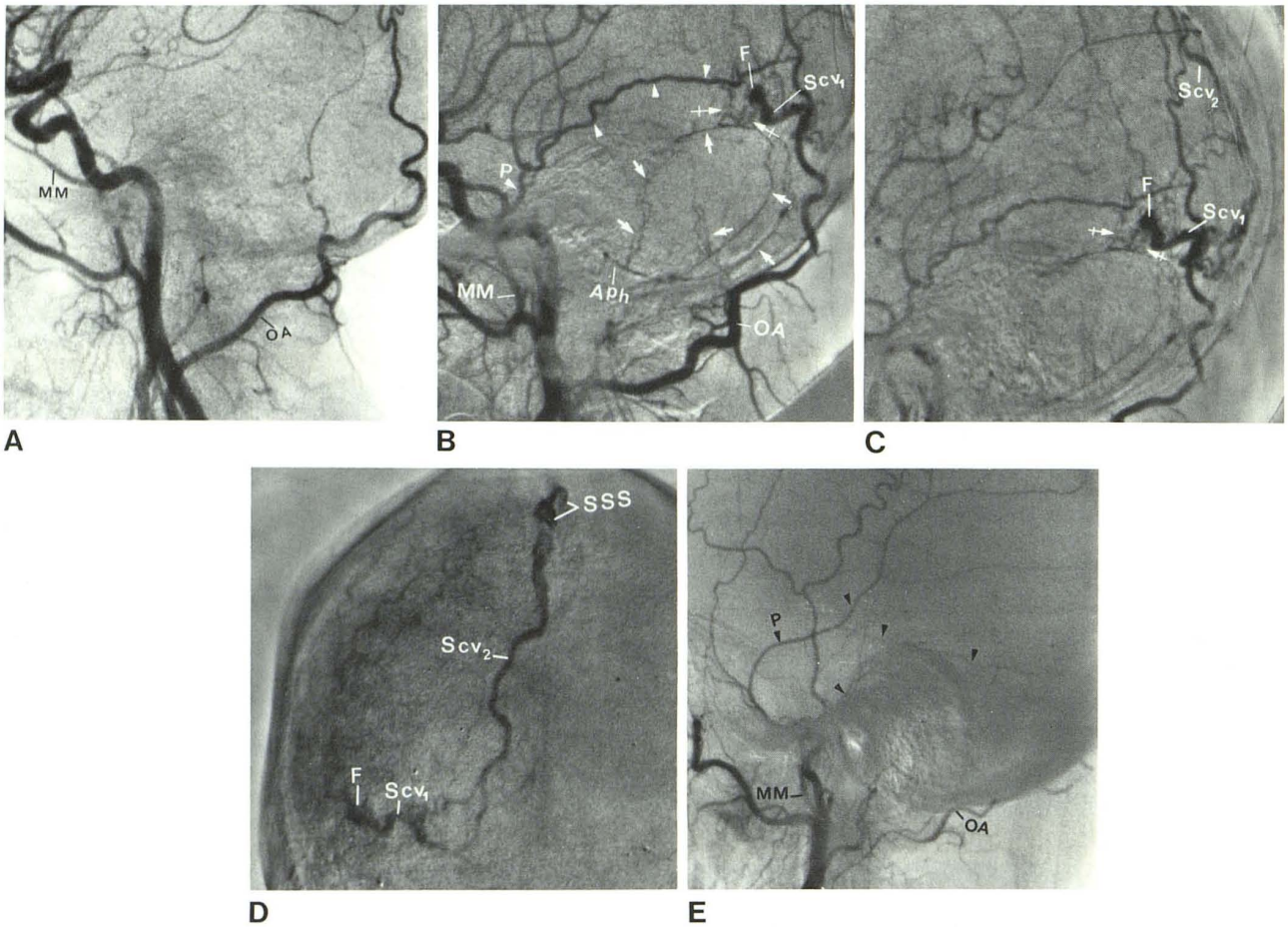

Fig. 3.—Case 3. **A**, 2 years before trauma. Normal occipital (OA) and middle meningeal (MM) arteries and no AV shunt. **B**, 3 weeks after trauma. Hypertrophied occipital and middle meningeal arteries. Meningeal branches of ascending pharyngeal artery (Aph), meningeal branches of occipital artery (*uncrossed arrows*) and of middle meningeal artery (MM) supply vascular network (*crossed arrows*) in dural wall of lateral sinus. Multiple small meningeal arteries from this network terminate into superficial cortical vein (Scv_1), which is opacified retrogradely through these shunts. Fistula (F) is where cortical vein normally enters sinus. Posterior branch of middle meningeal artery (P, *arrowheads*). **C** and **D**, Late arterial and capillary phases. Superficial cortical vein (Scv_1) drains into another cortical vein (Scv_2) through collateral veins. Cortical vein Scv_2 drains upward into superior sagittal sinus (SSS). Vascular network (*crossed arrows*). **E**, 2 years after trauma. Occipital artery and posterior temporal convexity branch (*arrowheads*) of middle meningeal artery (MM) are normal and there is no AV shunt. Selective occipital artery injection was also normal.

channel seems to precede the development of abnormal AV communications. One may speculate that similar thrombosis of developing venous channels during the embryologic period may be similarly responsible for brain parenchymal AV malformations. Selective, and, if possible, superselective, catheterization of the feeding arteries with magnification filming is the most appropriate way to study these lesions. Close scrutiny and a detailed review of the draining venous channels hold the key to understanding their topography and pathophysiology.

REFERENCES

1. Houser OW, Campbell JK, Campbell RJ, Sundt TM. Arteriovenous malformation affecting the transverse dural sinus—an acquired lesion. *Mayo Clin Proc* **1979**;54:651–661
2. Djindjian R, Merland JJ. *Superselective arteriography of the external carotid artery*. New York: Springer, **1978**:34–35, 405–412
3. Epstein B, Platt N. Visualization of an intracranial arteriovenous fistula during angiocardiography in an infant with congestive heart failure. *Radiology* **1962**;79:625–627
4. Bitoh S, Sakaki S. Spontaneous cure of dural arteriovenous malformation in the posterior fossa. *Surg Neurol* **1979**;12:111–114
5. Magidson MA, Weinberg PE. Spontaneous closure of a dural arteriovenous malformation. *Surg Neurol* **1976**;6:107–110
6. Browder J, Kaplan AH. Cerebral dural sinuses and their tributaries. Springfield, IL: Thomas, **1976**:19–20
7. Kerber CW, Newton TH. Macro and micro vasculature of the dura mater. *Neuroradiology* **1973**;6:175–179
8. Rowbotham CF, Little E. Circulation of the cerebral hemispheres. *Br J Surg* **1965**;52:8–20
9. Kuhner A, Krastel A, Stoll W. Arteriovenous malformations of

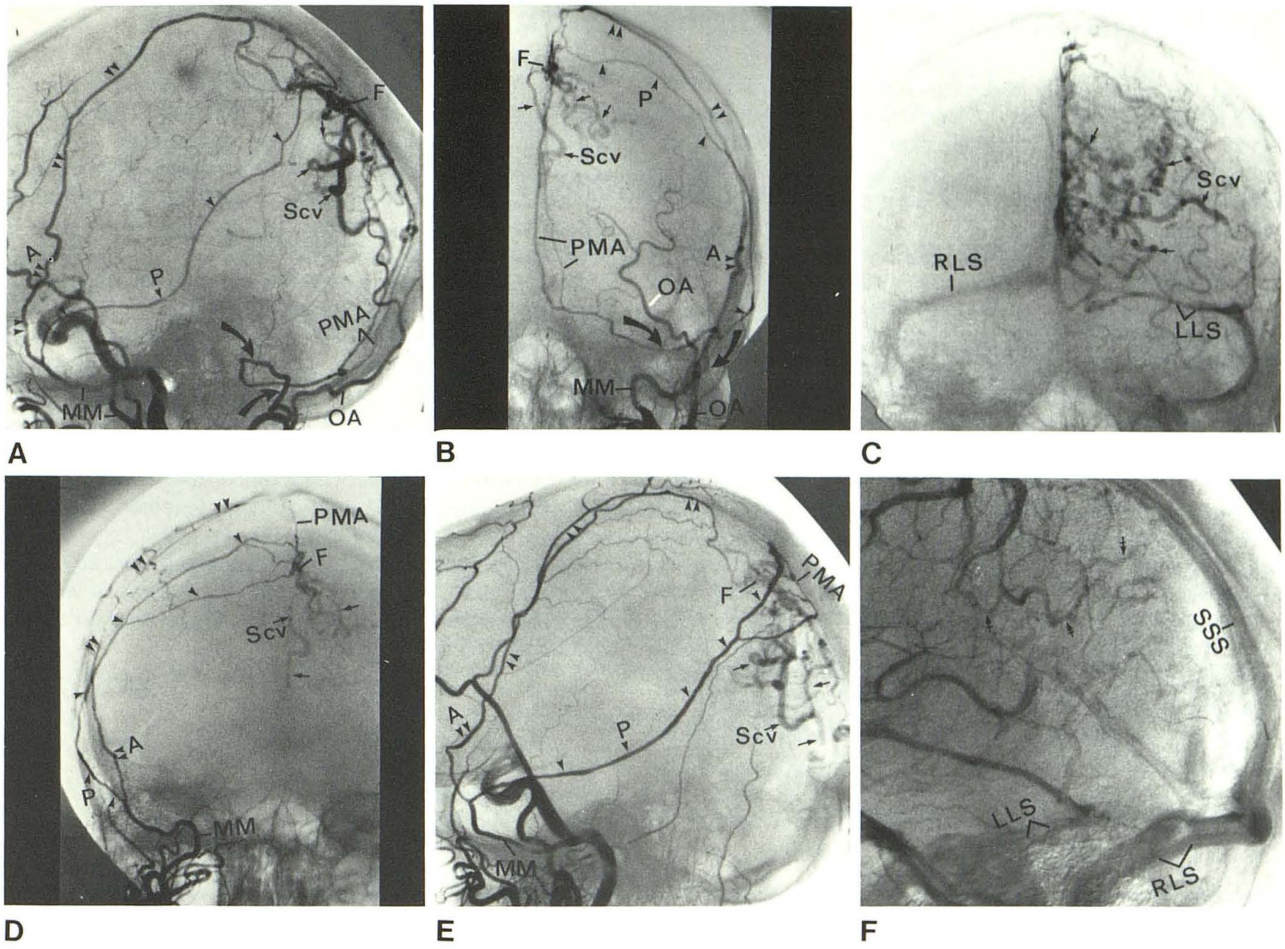

Fig. 4.—Case 4. **A** and **B**, Left external carotid arteriograms. Hypertrophied mastoid meningeal (*curved arrows*) branches of occipital artery (OA), anterior (A, *double arrowheads*), and posterior (P, *single arrowheads*) convexity branches of middle meningeal (MM) artery constitute paramedian meningeal artery (PMA), which supplies fistulous communications (F) in wall of superior sagittal sinus. Venous drainage into numerous superficial cortical (Scv, *straight arrows*) veins of left cerebral hemisphere. **C**, Same injection. Superficial cortical veins (*arrows*) of left cerebral hemisphere drain retrogradely into left lateral sinus. **D** and **E**, Right external carotid arteriograms. Anterior (*double arrowheads*) and posterior (*single arrowheads*) convexity branches of right middle meningeal artery also supply fistulous communications (F) through paramedian meningeal artery (PMA). Again, venous drainage is into superficial cortical veins of left cerebral hemisphere, which are opacified retrogradely. **F**, Venous phase of left internal carotid injection. Lack of superficial cortical veins apparent in left parietooccipital region and blood appears to drain from this area through collateral venous channels (*arrows*) into superior sagittal sinus (SSS), a clearly acquired feature.

the transverse dural sinus. *J Neurosurg* **1976**;45:12–19
10. Newton TH, Weidner W, Greitz T. Dural arteriovenous malformations in the posterior fossa. *Radiology* **1968**;90:27–35
11. Houser OW, Baker HL, Rhoton AL, Okazaki H. Intracranial dural arteriovenous malformations. *Radiology* 1972;105:55–64
12. Urdanibia JF, Silvela J, Soto M. Occipital dural arteriovenous malformations. *Neuroradiology* **1974**;7:57–64
13. Dichgans VJ, Gottschaldt M, Voigt K. Arteriovenöse Dura-Angiome am Sinus transversus. Klinische Symptome, charakteristische arterielle Versorgung und häufige venöse Abflustörungen. *Zentralb Neurochir* **1972**;33:1–18
14. Takekawa SD, Holman BC. Roentgenologic diagnosis of anomalous communications between external carotid artery and intracranial veins. *AJR* **1965**;95:822–825
15. Aminoff MJ. Vascular anomalies in the intracranial dura mater. *Brain* **1973**;96:601–612
16. Schecter MM, Zingesser LH, Rayport M. Torn meningeal vessels: an evaluation of a clinical spectrum through the use of angiography. *Radiology* **1965**;86:686–695
17. Handa J, Yoneda S, Handa H. Venous sinus occlusion with a dural arteriovenous malformation of the posterior fossa. *Surg Neurol* **1975**;4:433–437
18. Feldman AR, Hieshima G, Gianotta LS, Gade FG. Traumatic dural arteriovenous fistula supplied by scalp; meningeal, and cortical arteries. *Neurosurgery* **1980**;6:670–673
19. Newton TH, Gooding CA. Compression of superior sagittal sinus by neonatal calvarial molding. *Radiology* **1975**;115:635–640
20. Kalbag MR, Woolf LA. *Cerebral venous thrombosis with special reference to primary aseptic thrombosis*. London: Oxford, **1967**:246–247

Diffusion-Weighted MR Imaging of Acute Stroke: Correlation with T2-Weighted and Magnetic Susceptibility-Enhanced MR Imaging in Cats

M. E. Moseley[1]
J. Kucharczyk[1]
J. Mintorovitch[2]
Y. Cohen[2]
J. Kurhanewicz[1]
N. Derugin[1]
H. Asgari[1]
D. Norman[1]

We evaluated the temporal and anatomic relationships between changes in diffusion-weighted MR image signal intensity, induced by unilateral occlusion of the middle cerebral artery in cats, and tissue perfusion deficits observed in the same animals on T2-weighted MR images after administration of a nonionic intravascular T2* shortening agent. Diffusion-weighted images obtained with strong diffusion-sensitizing gradient strengths (5.6 gauss/cm, corresponding to gradient attenuation factor, b, values of 1413 sec/mm^2) displayed increased signal intensity in the ischemic middle cerebral artery territory less than 1 hr after occlusion, whereas T2-weighted images without contrast usually failed to detect injury for 2–3 hr after stroke. After contrast administration (0.5–1.0 mmol/kg Dy-DTPA-BMA, IV), however, T2-weighted images revealed perfusion deficits (relative hyperintensity) within 1 hr after middle cerebral artery occlusion that corresponded closely to the anatomic regions of ischemic injury shown on diffusion-weighted MR images. Close correlations were also found between early increases in diffusion-weighted MR image signal intensity and disrupted phosphorus-31 and proton metabolite levels evaluated with surface coil MR spectroscopy, as well as with post-mortem histopathology.

These data indicate that diffusion-weighted MR images more accurately reflect early-onset pathophysiologic changes induced by acute cerebral ischemia than do T2-weighted spin-echo images.

***AJNR* 11:423–429, May/June 1990**

In vivo diffusion-weighted MR imaging, which measures the microscopic motion of water protons, has been used recently to characterize brain tissue abnormalities caused by cerebral ischemia [1, 2]. Acute stroke, however caused, produces a rapid and progressive disruption of mitochondrial oxidative phosphorylation, with ensuing losses of high energy phosphates and increases in inorganic phosphate and lactate. These metabolic disturbances precipitate glial and neuronal transmembrane Na^+/K^+ transport failure, resulting in a shift of fluid and Na^+ from the extracellular to the intracellular compartment after a latency of only a few minutes [3].

Moseley et al. [2] evaluated the potential of diffusion-weighted MR imaging for early detection of regional cerebral-ischemia-induced edema using a cat model. Diffusion-weighted images were acquired by using very strong gradient strength factors (b values of up to 1413 sec/mm^2). Evidence of cerebral injury could be found as early as 45 min after unilateral occlusion of the middle cerebral artery (MCA) using diffusion-weighted MR imaging, whereas T2-weighted spin-echo images failed to demonstrate clear increases in signal intensity in the MCA territory even 2–3 hr after occlusion. Close correlations were also established between diffusion-weighted tissue signal intensity ratios and metabolic abnormalities measured with surface coil phosphorus-31 and proton MR spectroscopy. These data [2] provided the first evidence that diffusion-weighted MR images accurately reflect early-onset pathophysiologic changes induced by acute cerebral ischemia.

Received October 30, 1989; revision requested December 13, 1989; revision received January 8, 1990; accepted January 8, 1990.

[1] Department of Radiology, Box 0628, University of California, San Francisco, CA 94143. Address reprint requests to M. E. Moseley.

[2] Department of Pharmaceutical Chemistry, University of California, San Francisco, CA 94143.

0195–6108/90/1103–0423
© American Society of Neuroradiology

The objective of the present study was to compare the anatomic extent and severity of ischemic brain injury shown on diffusion-weighted MR imaging with tissue perfusion deficits demonstrated by the combined use of a nonionic intravascular T2* magnetic susceptibility contrast agent and conventional T2-weighted spin-echo MR imaging. Diffusion-weighted MR images were also evaluated in relation to assessments of cerebral metabolic injury obtained via surface coil phosphorus-31 and proton MR spectroscopy from the ischemic MCA territory. Finally, histochemical mapping of the viability of the electron transport chain enzymes was carried out with 2-, 3-, and 5-triphenyl tetrazolium chloride (TTC) [4] to correlate spatially the evolution of ischemic tissue injury with the MR imaging/spectroscopy results.

Materials and Methods

Thirteen young adult cats weighing 2.0 to 4.5 kg were anesthetized intravenously with 30 mg/kg Nembutal. Polyethylene catheters were placed in the temporal vein and artery for blood pressure monitoring and drug administration. The right MCA was isolated via the transorbital approach and occluded just proximal to the origin of the lateral striate arteries with bipolar electrocautery followed by complete surgical transection. The dural incision and orbit were covered with a saline-moistened gauze and an absorbable gelatin sponge. The muscles overlying the ipsilateral parietal fossa were excised unilaterally to optimize the placement of the MR-spectroscopy surface coil in a standard location over the MCA territory.

A 2-T chemical shift imager/spectrometer unit (General Electric Medical Systems, Fremont, CA), equipped with GE Acustar self-shielded gradient coils (± 20 gauss/cm, 15-cm bore size) was used. Phosphorus-31 and proton MR spectroscopy was performed with a 2 × 3 cm double-tuned surface coil positioned over the MCA territory after scalp and muscle retraction. MR imaging was performed with an 8.5-cm inner-diameter low-pass birdcage proton imaging coil. The imaging birdcage and surface coils were equipped with a detuning capacitor switch to perform sequential spectroscopy and imaging without changing the position of the animal in the magnet. Successive multislice diffusion-weighted images, MR spectra, and T2-weighted images were obtained for at least 5 hr after occlusion. T2-weighted images, 2800/80, 160 (TR/TEs), with 3-mm slices and 1-mm gap were obtained with a field of view (FOV) of 80 mm in which two scans were averaged for each one of the 128 phase-encoding steps, resulting in a total acquisition time of 12 min. Cardiac-gated and nongated single and multislice coronal and axial diffusion-weighted spin-echo images, 1000–1800/80 (TR range/TE), with 3-mm slices, 1-mm gap, and FOV = 80 mm were acquired with a diffusion-gradient pulse duration of 20 msec along the slice-selection direction, a gradient separation of 40 msec, and very large diffusion-sensitizing gradient (b) values of 1413 sec/mm^2 (gradient strength of 5.6 gauss/cm). These gradients were ramped to avoid excessive dB/dt effects. Four to eight scans were averaged for each of 128 phase-encoding steps, resulting in a total collection time of about 16 min.

Region-of-interest (ROI) image analyses were carried out in the injured middle temporal cortex, ectosylvian gyrus, and caudate nucleus, and compared with the corresponding uninjured contralateral gray matter regions. A signal intensity ratio was calculated as the ROI image intensity ratio of an abnormal, ischemic region over that of the normal, contralateral side.

Phosphorus-31 MR spectra at 34.6 MHz were acquired by single-pulse experiments from 256 signal averages with an effective TR of 2250 and a total acquisition time of 9.6 min. Proton (85.6 MHz) spin-echo spectra (tau = 128 and 192 msec) were acquired with water presaturation, TR of 1750, and 128 signal averages, resulting in a total collection time of 5 min.

MR spectra were phased and analyzed with a line-fitting computer simulation program. The beta, alpha, and gamma peaks for ATP and the peaks for phosphocreatine (PCr), phosphodiester (PD), inorganic phosphate (Pi), and injured inorganic phosphate (Pii) and phosphomonoester (PM) were resolved. The Pii:PCr ratio was calculated to quantify the bioenergetic status of the tissues. From the proton spectra, the peak areas of lactate and N-acetylaspartate (NAA) were resolved and the lactate:NAA ratios calculated. The presence of lactate was confirmed from comparison of tau = 128 msec and tau = 192 msec spin-echo experiments in which the lactate peak is inverted at tau = 192 msec. To compare the MR spectroscopy peak area ratios with the MR imaging tissue contrast values, the ROI chosen were the superior and middle frontoparietal gyri, which correspond anatomically to the cerebral tissues beneath the surface coil.

In order to compare the anatomic region of perfusion deficiency with the areas of high signal intensity on diffusion-weighted MR images, cats were also tested with a nonionic T2*-shortening contrast agent, Dy-DTPA-bis (methylamide) (Dy-DTPA-BMA). The Dy-DTPA-BMA complex was prepared by Salutar, Inc. (Sunnyvale, CA) by refluxing stoichiometric amounts of dysprosium oxide and DTPA-BMA. The contrast agent was infused intravenously over approximately 3 min at doses of 0.5 or 1.0 mmol/kg beginning at phase-encoding step 32 and finishing at step 60 of the T2-weighted image acquisition (Fig. 1). Dy-DTPA-BMA injections were given at different times following MCA occlusion in individual cats. After injection, the magnetic susceptibility effect was evaluated for 15–60 min in both ischemic and normal hemispheres by comparing ROI intensity to precontrast T2-weighted and diffusion-weighted ROI intensities.

At the conclusion of the MR protocol, 15 ml/kg of a 2% solution of TTC was infused transcardially. The brain was removed from the cranium after 10–20 min, immersed in a 2% triphenyl tetrazolium chloride (TTC) solution for another 10–20 min, and then stored overnight in 10% buffered formalin in a light-shielded container. Twenty-four to thirty-six hours later the brain was sectioned coronally at 2–3 mm and immediately examined for histologic evidence of ischemic damage. TTC stains normal brain tissues red and injured tissues pink (ischemic) to gray-white (necrotic) [5].

Results

Detection of Ischemic Injury with Diffusion-Weighted MR Imaging

Corresponding diffusion- and T2-weighted spin-echo images, taken within 1 hr after occlusion (Fig. 2, left panels) and

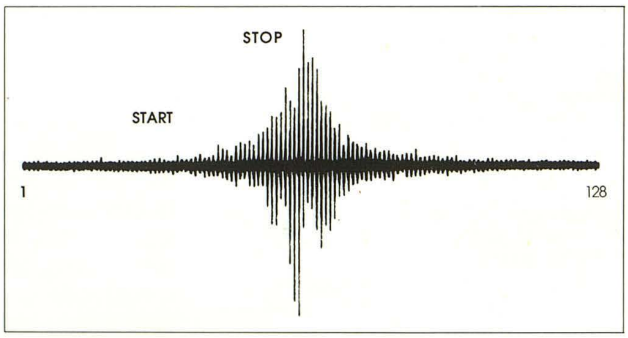

Fig. 1.—Method of collection of contrast-enhanced T2-weighted spin-echo signal (12-min acquisition) images. The time of administration of Dy-DTPA-BMA contrast during the 128 phase-encoding step sequence was between scans 32–60 in order to maximize plasma contrast concentration during the most sensitive stage of signal acquisition (scans 40–80).

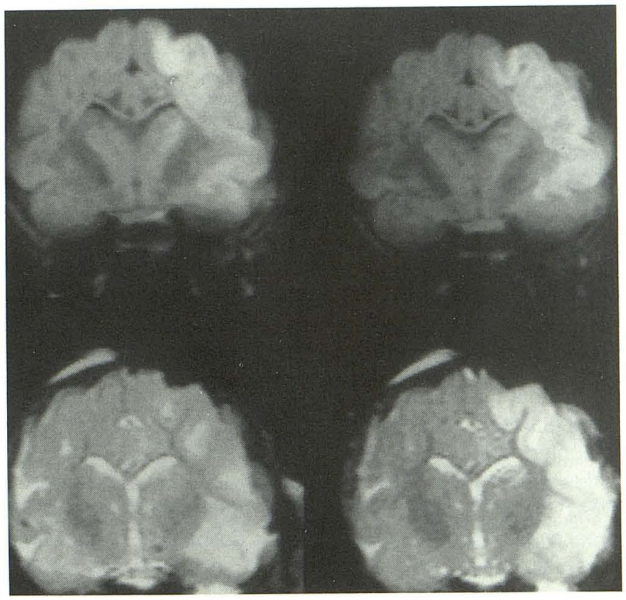

Fig. 2.—Diffusion-weighted coronal images 1800/80/4 (3-mm slice, 1-mm slice gap, FOV=80 mm, b = 1413 sec/mm^2) at level of optic chiasm 1 hr (*upper left*) and 5 hr (*upper right*) after MCA occlusion. Compared with contralateral control regions, signal intensity ratios increased by 55%, 60%, and 30%, measured in gray matter in the ectosylvian gyrus, middle temporal gyrus, and caudate nucleus, respectively, 1 hr after stroke. Corresponding T2-weighted spin-echo images 2800/160/2 (3-mm slices, 1-mm slice gap, FOV=80 mm) are shown in lower panels. 1 hr after stroke was induced, the T2-weighted image (*lower left*) shows only subtle mass effect in the temporal cortex ipsilateral to the occlusion. Measured relative signal intensity ratios increased by 16% in the gray matter of the ectosylvian gyrus, 24% in the middle temporal gyrus, and 10% in the caudate nucleus. At 5 hr after occlusion (*lower right*), hyperintensity is seen throughout MCA territory, although the signal intensity ratio of ischemic/nonischemic regions is substantially lower than the corresponding diffusion-weighted image (*upper right*).

5 hr after MCA occlusion (right panels), are shown for a single representative animal. The T2 tissue signal intensity ratio in the MCA territory ipsilateral to the occlusion was not significantly different from the contralateral normal hemisphere at 1 hr after stroke (lower left panel). By comparison, the signal intensity ratio in the corresponding diffusion-weighted image (upper left panel) was significantly elevated in the cortical and subcortical gray matter.

Five hours after MCA occlusion, T2-weighted images clearly demonstrated tissue injury, including increased mass-effect and hyperintensity (edema) throughout the MCA territory (Fig. 2, lower right panel). The anatomic distribution of increased signal intensity was similarly widespread on diffusion-weighted MR images (Fig. 2, upper right panel). Signal enhancement was observed in both parietal and temporal cortical areas inferior to the middle parietal gyrus, the medial aspect of the head of the caudate, and the lateral part of the globus pallidus. More posteriorly, there was extensive cortical and subcortical involvement of gray matter. A small region of hyperintensity was often seen in the inferior lateral sulcus, extending onto the temporal part of the occipital pole. A continuing close anatomic correspondence between diffusion-weighted and T2-weighted hyperintensity was seen 9 hr and 12 hr (Fig. 3) after occlusion. There was also close correspondence between the areas of high signal intensity on diffusion-weighted and T2-weighted MR images after MCA occlusion, and the distribution of ischemic tissue injury shown in subsequent TTC-stained coronal sections (Fig. 4).

The time course of changes in bioenergetic status induced by stroke was monitored by surface coil MR spectroscopy in all cats. Within 1 hr after occlusion, abnormal phosphorus-31 and proton metabolite ratios, determined from the Pii/PCr and lactate/NAA peak area ratios, respectively, were found (Fig. 5). Hyperintensity observed on diffusion-weighted MR images was closely associated with elevated lactate/NAA and Pii/PCr on MR spectroscopy, whereas no clear temporal relationship was found between the MR spectroscopy results and T2-weighted MR imaging at the early time points (up to about 2 hr).

Correlation of Regional Perfusion Deficits with Diffusion-Weighted MR Imaging

The purpose of the experiments with Dy-DTPA-BMA was twofold. First, we wanted to establish whether a nonionic T2*

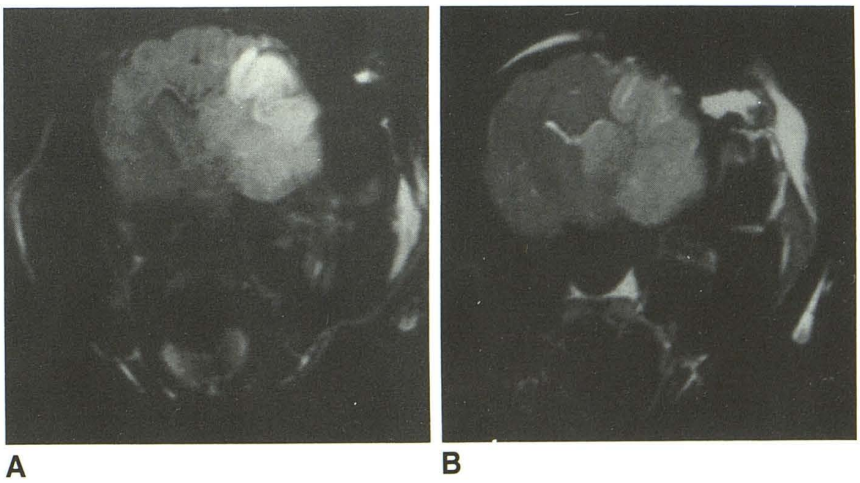

Fig. 3.—*A* and *B*, 12 hr after MCA occlusion, the diffusion-weighted (*A*) and T2-weighted (*B*) images show hyperintensity throughout ischemic MCA territory. Note, however, that the signal intensity ratio of the ischemic/nonischemic regions remains higher in the diffusion-weighted images. Same animal and MR parameters as Fig. 2.

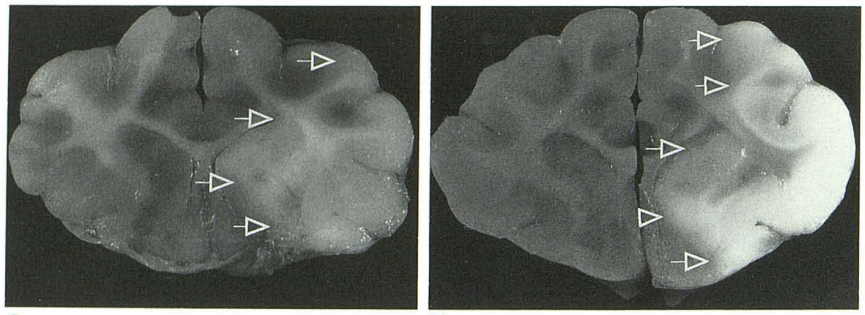

Fig. 4.—*A* and *B*, Triphenyl tetrazolium chloride (TTC)-stained coronal sections of cat brain show areas of ischemic damage at 5 hr (*A*) and 12 hr (*B*) after permanent unilateral occlusion of MCA. Ischemic or infarcted tissues (*arrows*), which lack viable electron transport chain enzymes, appear white. Note the close correspondence of the injured area with regions of hyperintensity in the diffusion-weighted and T2-weighted images (Fig. 3).

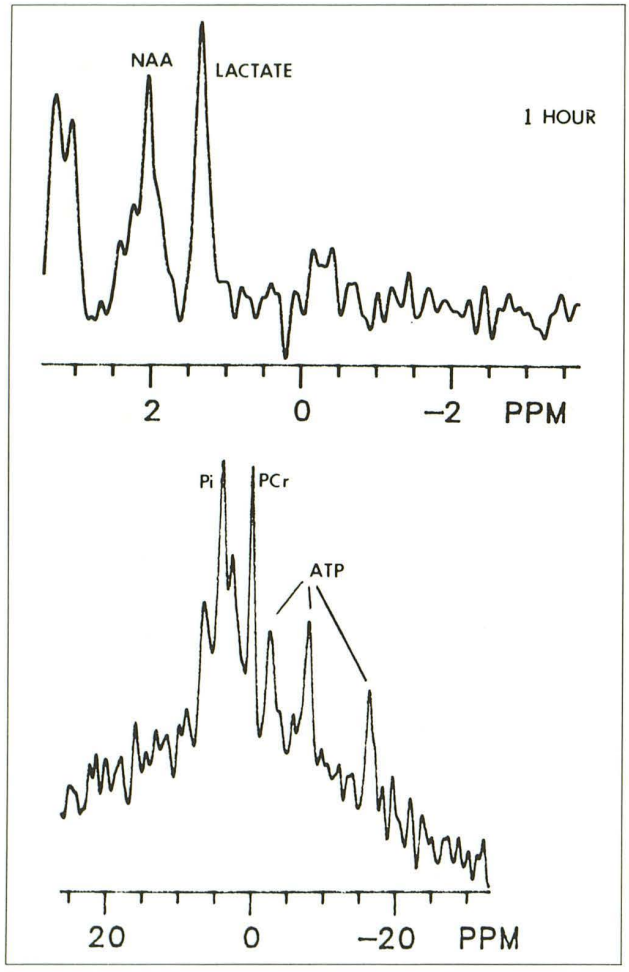

Fig. 5.—Proton (*top*) and phosphorus-31 (*bottom*) spectra obtained with a surface coil placed over the ischemic MCA territory 1 hr after unilateral arterial occlusion in same cat as Fig. 2. Evidence of metabolic injury is shown by the increased Pii/PCr and lactate/NAA ratios obtained from a surface coil placed on the skull over the ischemic parietal lobe. The abnormal phosphorus-31 and proton and metabolite ratios suggest that the hyperintensity observed on diffusion-weighted images 1 hr after occlusion is related to a disruption of normal oxidative phosphorylation in the MCA territory.

magnetic susceptibility contrast agent would allow early detection of ischemia-induced perfusion deficits using standard T2-weighted spin-echo MR imaging. Second, we wanted to compare anatomically the regions of perfusion deficits demonstrated with Dy-DTPA-BMA contrast-enhanced T2-weighted MR images with areas of high signal intensity on diffusion-weighted MR images. Using a 1 mmol/kg dosage of Dy-DTPA-BMA, we observed maximum signal intensity decreases of 35% in the gray matter of the normal, nonischemic cerebral hemisphere during the first 15 min after injection. No signal intensity changes were observed in the cortical and subcortical gray matter ipsilateral to the MCA occlusion, which consequently appeared bright on the postcontrast T2-weighted images. Signal intensity changes in the internal capsule of both the normal and ischemic hemispheres were relatively small, but the centrum semiovale was noticeably affected. At 45 min after administration of contrast material, signal intensity had recovered to over 90% of precontrast control values in all cerebral tissues (Fig. 6).

Perfusion deficits resulting from occlusion of the MCA were detected as a relative T2-weighted MR image hyperintensity of the ischemic tissues compared with the normally perfused areas in the contralateral hemisphere. Relative hyperintensity was found in the ischemic basal ganglia as early as 30 min after occlusion for both the 1 mmol/kg and 0.5 mmol/kg doses (Fig. 7). Signal differences between ischemic and contralateral control tissues were observed for gray matter and, to a lesser extent, for the white matter in the internal capsule. By comparison, T2-weighted MR images without contrast failed to demonstrate any significant signal differences prior to the detection of cerebral edema (signal hyperintensity) approximately 2–3 hr after MCA occlusion.

Regions of perfusion deficiency correlated well anatomically with areas of high signal intensity on diffusion-weighted MR images from the earliest (30 min) to the latest (12 hr) postocclusion observation periods employed in this study. An example of the close correspondence in anatomy between the region of perfusion deficit and diffusion MR image-determined area of tissue injury 5 hr after MCA occlusion is shown in Fig. 8.

Discussion

Early Detection of Ischemic Brain Injury

The results of this study confirm and extend our previous report [2] that diffusion-weighted MR imaging can significantly advance the time of detection of cerebral ischemic insults. In the present investigation evidence of stroke was seen in the

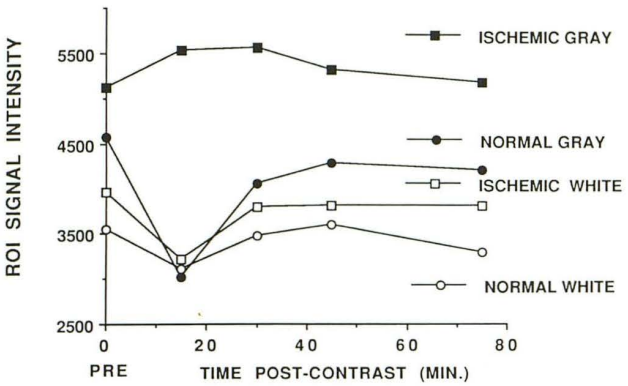

Fig. 6.—Signal intensity changes measured in normal and ischemic brain regions of one cat using a T2-weighted spin-echo pulse sequence 2800/160/2 after administration of 1 mmol/kg Dy-DTPA-BMA IV 1 hr after MCA occlusion. The susceptibility-induced signal attenuation was most prominent 15 min after contrast injection except in the nonperfused gray matter ipsilateral to the MCA occlusion. Signal attenuation washout occurred in all tissues within approximately 60 min after Dy-DTPA-BMA injection.

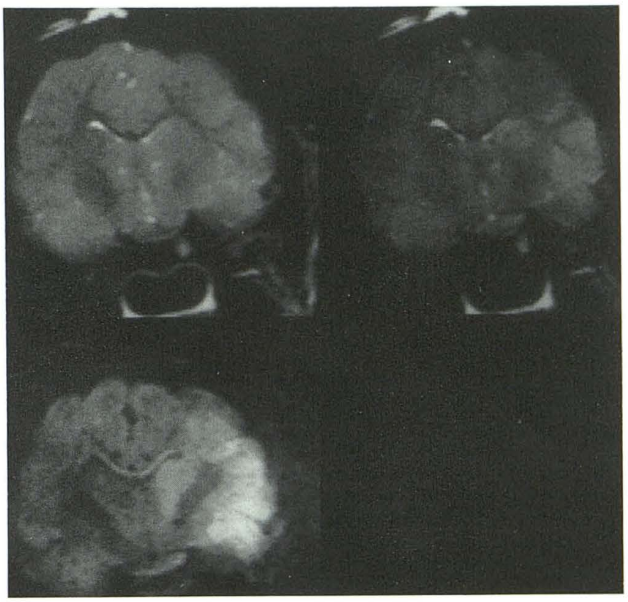

Fig. 7.—T2-weighted spin-echo images before (*upper left*) and after (*upper right*) administration of 0.5 mmol/kg Dy-DTPA-BMA approximately 1 hr after occlusion of right MCA. Corresponding diffusion-weighted image is shown at *lower left*. On the diffusion-weighted MR image, relative signal intensity ratios increased in the gray matter by 159% in the ectosylvian gyrus, 94% in the middle temporal gyrus, and 100% in the caudate nucleus. Corresponding signal intensity ratios increased in the magnetic susceptibility-enhanced MR image by 74%, 39%, and 101%, respectively. By comparison, the T2-weighted MR image without contrast did not clearly demonstrate the region of tissue injury at this early time.

MCA territory as early as 45 min following occlusion using diffusion-weighted MR images, whereas T2-weighted spin-echo images without contrast did not demonstrate increased signal intensity until 2–3 hr after occlusion. A close correlation was also found between diffusion-weighted tissue signal intensity increases and abnormal phosphorus-31 and proton metabolite ratios, which suggests that the hyperintensity seen after ischemia is likely related to a disruption of normal oxidative phosphorylation.

Correlation with Perfusion Deficits

The close spatial correlation between the regions of diffusion-weighted MR image hyperintensity and areas of high signal intensity on T2-weighted images following Dy-DTPA-BMA administration suggests that this contrast agent has significant utility in the early detection of cerebral ischemic insults. Relaxivity of paramagnetic chelates like Dy-DTPA-BMA is influenced by molecular diffusion through microscopic heterogeneous magnetic fields [6]. Chelates that have poor longitudinal relaxation but large magnetic moments produce contrast enhancement through loss of spin-echo signal intensity. Since Dy-DTPA-BMA remains in the intravascular compartment and its concentration within patent blood vessels is relatively uniform, signal intensity should be proportional to the fractional voxel volume occupied by vessels containing the agent. This magnetic susceptibility mechanism of MR contrast enhancement thus has the notable advantage of demarcating regions of deficient blood flow without crossing the blood-brain barrier. The results of the present study confirm our previous report [7] that intravenous Dy-DTPA-BMA can significantly advance the time of detection of cerebral ischemic insults caused by perfusion deficits.

Nature of Diffusion-Weighted MR Hyperintensity

The measured apparent diffusion coefficient in the hyperintense ischemic brain regions was approximately half that in the contralateral MCA territory, indicating slower microscopic proton diffusion [1, 2]. Motion artifacts, which can present severe problems for diffusion-weighted images [1, 8], were largely eliminated in the present investigation by a combination of barbiturate anesthesia, immobilization of the head in a restraint device, and the use of four or eight signal averages. The close temporal and anatomic correspondence between the appearance of hyperintensity on magnetic susceptibility-induced images and diffusion-weighted MR imaging suggests that the altered signal reflects stroke-induced perfusion deficits rather than motion artifact.

The precise origin of the hyperintense signal on diffusion-weighted MR images does, however, remain unclear. Several issues complicate the interpretation of the lower apparent diffusion coefficient in the occluded MCA territory. First, ischemic tissue injury is by its very nature multifactorial. It includes hypoxia, substrate deprivation, and toxic metabolite accumulation [9]. Second, cerebral tissues are composed of many different cell types that respond differently, and perhaps independently, to ischemia [10]. While no accurate data have been collected concerning the relative volumes occupied by neurons versus glia in cat cerebral cortex, one recent estimate is that they are about equal [11]. There is ultrastructural evidence that astrocytic glial swelling is an early event following cerebral ischemia [12, 13]. Increases in intracellular sodium, calcium, and chloride following stroke have generally been regarded as critical factors influencing astrocytic swelling [12, 14], but changes in extracellular K+ [15], lactic acid

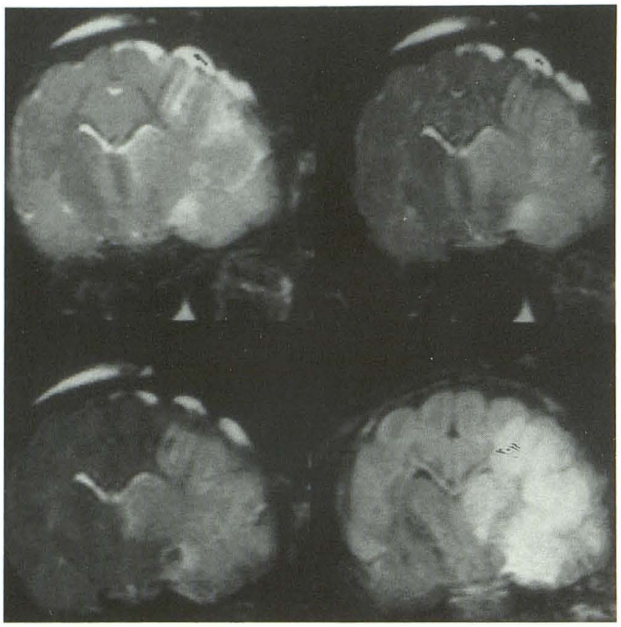

Fig. 8.—5–7 hr after MCA occlusion, hyperintensity was observed in the same anatomic regions on T2-weighted (*upper left*), diffusion-weighted (*lower right*), and magnetic susceptibility-enhanced (*upper right*) images 15 min after injection of 0.5 mmol/kg Dy-DTPA-BMA and 15 min after 1.0 mmol/kg Dy-DTPA-BMA (*lower left* image). On precontrast T2-weighted MR image, signal intensity ratios increased by 109% in the ectosylvian gyrus, 18% in the middle temporal gyrus, and 39% in the caudate nucleus. The corresponding MR signal intensity ratios increased after injection of 0.5 mmol/kg Dy-DTPA-BMA by 83%, 34%, and 118%, respectively. After 1.0 mmol/kg Dy-DTPA-BMA, signal intensity ratios increased by 168%, 51%, and 211%, respectively. Finally, on the diffusion-weighted MR image, the corresponding increases in signal intensity ratios were 66%, 113%, and 61%, respectively.

and/or pH [16, 17], and free fatty acids and oxygen radicals [18] also play a role.

It is now known that severe focal ischemia causes both extra- and intracellular lactic acidosis, and that this acidosis is associated with gray matter edema predominantly affecting the astrocyte population of cells [16]. Astrocytes appear to be less resistant than neurons to acidosis and lose their normal morphology, membrane integrity, and cytoskeletal configuration with smaller drops in pH [19]. We have shown in preliminary experiments (Kucharczyk et al., unpublished results) that administration of calcium channel blockers preserved pre-ischemia concentrations of high-energy phosphates, maintained low levels of Pi and lactate, and also significantly reduced both tissue hyperintensity on diffusion-weighted images and histologically measured infarct size. This apparent drug-induced reversibility of diffusion-weighted image hyperintensity also indicates that the diffusion-weighted MR changes observed as early as 45 min after occlusion were not due to cell death. Considered together, these data suggest the possibility that ischemia may precipitate a loss of cellular volume control resulting from increased intracellular acidification of astrocytes as the primary event. Sodium ions taken up as a result of activated Na+/H+ transmembrane exchange would then cause water to flow into the intracellular compartment to maintain osmotic balance, resulting in cytotoxic edema, slower or restricted microscopic proton diffusion, and, consequently, hyperintensity on diffusion-weighted MR images.

Tissue osmolality changes following ischemia may also be a factor in the observed diffusion MR image hyperintensity. Recent studies suggest that the osmotic pressure gradient between blood and brain may have an important influence on the development of ischemic brain edema. Hatashita and Hoff [20] demonstrated that a hydrostatic pressure gradient across the capillary develops within minutes after the onset of ischemia and represents the driving force for early accumulation of edema. The osmolality in normal brain cortical tissue is about 8 mOsm/kg higher than that of plasma [20]. Other studies have shown that a significant increase in osmolality of ischemic brain tissue occurs within 2–6 min following ischemia [21, 22]. The increased brain osmolality correlates with water content, and could therefore account, at least in part, for the early accumulation of edema and reduced apparent diffusion coefficient after ischemic injury.

Since there is a direct relationship between temperature and the diffusion coefficients that quantify thermal Brownian motion, it is also possible that the high-intensity signal observed on diffusion-weighted MR imaging may be related to temperature changes in the ischemic MCA territory. Le Bihan et al. [23] used a phantom heated inside a clinical 0.5-T whole body imaging system to demonstrate that a 1°C change in temperature corresponds to a 2.4% change in diffusion coefficient. Busto et al. [24] have demonstrated that intraischemic brain temperature may fall by up to 7°C following bilateral carotid/vertebral occlusion in the rat. Pre- or postischemia induction of brain hypothermia may actually confer a substantial cerebroprotective effect [25].

Although cerebral blood flow was not directly measured in the present study, the Dy-DTPA-BMA contrast-enhanced MR images suggest considerable regional heterogeneity in blood flow disturbances throughout the ischemic MCA territory. In nearly all cases, signal hyperintensity was observed earlier in the region of the basal ganglia than neocortex on both magnetic susceptibility-enhanced and diffusion-weighted MR images. On this basis, it would appear that nonanastomosing end-arterial tissues, such as the caudate and putamen, might undergo more rapid and greater drops in temperature, following ischemia, since no collateral circulation is available [26]. In collaterally perfused areas such as neocortex, on the other hand, reductions in tissue temperature may be offset by continued blood flow in the partially ischemic watershed regions. A reduction in brain tissue temperature could therefore theoretically account for the observed hyperintensity on diffusion-weighted MR images. Further studies are required, however, to precisely assess the relative importance of postischemic hypothermia to the increases in signal intensity observed on diffusion-weighted MR images.

Finally, another possibility is that physiological motions within the cranium related to arterial blood flow pulsations might contribute to the differences in apparent proton diffusion in normally perfused versus ischemic regions. A reduction in cerebral blood flow after MCA occlusion might attenuate

pulsatile brain motions, thereby leading to a decrease in apparent proton diffusion and an observed diffusion-weighted hyperintensity in the ischemic tissues.

In summary, in vivo diffusion-weighted MR imaging accurately characterized early-onset brain tissue abnormalities caused by cerebral ischemia. Changes in signal intensity induced by acute stroke were observed much earlier on diffusion-weighted MR images than on T2-weighted spin-echo images. Hyperintensity seen on diffusion-weighted MR images was closely associated with evidence of metabolic disruption obtained by MR spectroscopy, whereas no clear temporal relationship was found between the MR spectroscopy results and T2-weighted MR imaging. Finally, the results of studies with a T2* shortening contrast agent, Dy-DTPA-BMA, suggest that the diffusion-weighted intensity is related to cerebral perfusion deficits.

REFERENCES

1. LeBihan D, Breton E, Hallemand D, et al. Separation of diffusion and perfusion in intravoxel incoherent motion MR imaging. *Radiology* **1988**; 168:497–505
2. Moseley M, Cohen Y, Mintorovitch J, et al. Early detection of regional cerebral ischemic injury in cats: evaluation of diffusion and T2-weighted MRI and spectroscopy. *Magn Reson Med* (in press)
3. Hossmann KA, Sakaki S, Zimmerman V. Cation activities in reversible ischemia of the cat brain. *Stroke* **1977**; 8:77–81
4. Siedler E. New mitro-monotetrazolium salts and their use in histochemistry. *Histochem J* **1980**;12:519–530
5. Bose B, Osterholm JL, Berry R. A reproducible experimental model of focal cerebral ischemia in the cat. *Brain Res* **1984**;311:385–391
6. Cacheris W, Rocklage SM, Quay S, et al. *Radiology* **1988**;169:383
7. Moseley ME, Kucharczyk J, Kurhanewicz J, et al. Comparison of MR imaging after administration of dysprosium-based magnetic-susceptibility contrast media with diffusion-weighted MR imaging in evaluation of regional cerebral ischemia. *Radiology* **1989**;173(P):383 (abstr)
8. Merboldt KD, Bruhn H, Frahn J, et al. MRI of "diffusion" in the human brain: new results using a modified CE-FAST sequence. *Magn Reson Med* **1989**;7:423–429
9. Ljunggren B, Schutz H, Siesjo BK. Changes in energy state and acid-base parameters of the rat brain during complete compression ischemia. *Brain Res* **1974**;73:277–289
10. Hossman K-A. The pathophysiology of ischemic brain swelling. In: Inaba Y, Klatzo I, Spatz M, eds. *Brain edemia*. Berlin: Springer-Verlag, **1985**: 367–384
11. Dietzel I, Heinemann U, Luz HD. Relations between slow extracellular potential changes, clial potassium buffering, and electrolyte and cellular volume changes during neuronal hyperactivity in cat brain. *Glia* **1989**;2: 25–44
12. Kimelberg HK, Ransom BR. Physiological and pathological aspects of astrocytic swelling. In: Federoff S, Vernadakis A, eds. *Astrocytes*. Orlando: Academic Press, **1986**:129–166
13. Chiang J, Kowada M, Ames A, et al. Cerebral ischemia III. Vascular changes. *Am J Pathol* **1968;**52:455–476
14. Rothman SM, Olney JW. Glutamate and the pathophysiology of hypoxic-ischemic brain damage. *Ann Neurol* **1986**;19:105–111
15. Moller M, Mollgard K, Lund-Anderson H, et al. Concordance between morphological and biochemical estimate of fluid spaces in rat brain slices. *Exp Brain Res* **1974;**22:299–314
16. Siesjo BK. Membrane events leading to glial swelling and brain edema. In: Inaba Y, Klatzo I, Spatz M, eds. *Brain edema*. Berlin: Springer-Verlag, **1985**:200–209
17. Norenberg MD, Mozes LW, Gregarios JB, et al. Effects of lactic acid on astrocytes in primary culture. *J Neuropathol Exp Neurol* **1987**;46:154–166
18. Chan PH, Fishman RA. Free fatty acids, oxygen free radicals, and membrane alterations in brain ischemia and injury. In: Plum F, Pulsinelli W, eds. *Cerebrovascular diseases*. New York: Raven Press, **1985**:161–168
19. Goldman SA, Pulsinelli WA, Clarke WY, et al. The effects of extracellular acidosis on neurons and glia in vitro. *J Cereb Blood Flow Metab* **1989**; 9:471–477
20. Hatashita S, Hoff JT. Biomechanics of brain edema in acute cerebral ischemia. *Stroke* **1988**;19:91–97
21. Schuier JF, Hossmann KA. Experimental brain infarction in cats. II. Ischemic brain edema. *Stroke* **1980**;11:593–597
22. Bandaranayake MN, Nemoto ME, Stezoski W. Rat brain osmolality during barbiturate anesthesia and global brain ischemia. *Stroke* **1978**;9:249–254
23. Le Bihan D, Delannoy J, Levin RL. Temperature mapping with MR imaging of molecular diffusion: application to hyperthermia. *Radiology* **1989**; 171:853–857
24. Busto R, Dietrich WD, Globus MT, et al. Small differences in intraischemic brain temperature critically determine the extent of ischemic neuronal injury. *Cereb Blood Flow Metab* **1987**;7:729–738
25. Busto R, Dietrich WD, Globus MT, et al. The importance of brain temperature in cerebral ischemic injury. *Stroke* **1989**;20:1113–1114
26. Grand W. Microsurgical anatomy of the proximal middle cerebral artery and the internal artery bifurcation. *Neurosurgery* **1980**;7:151–159

The 2021 World Health Organization Classification of Tumors of the Central Nervous System: What Neuroradiologists Need to Know

A.G. Osborn, D.N. Louis, T.Y. Poussaint, L.L. Linscott, and K.L. Salzman

ABSTRACT

SUMMARY: Neuroradiologists play a key role in brain tumor diagnosis and management. Staying current with the latest classification systems and diagnostic markers is important to provide optimal patient care. Publication of the 2016 World Health Organization Classification of Tumors of the Central Nervous System introduced a paradigm shift in the diagnosis of CNS neoplasms. For the first time, both histologic features and genetic alterations were incorporated into the diagnostic framework, classifying and grading brain tumors. The newly published 2021 World Health Organization Classification of Tumors of the Central Nervous System, May 2021, 5th edition, has added even more molecular features and updated pathologic diagnoses. We present, summarize, and illustrate the most salient aspects of the new 5th edition. We have selected the key "must know" topics for practicing neuroradiologists.

ABBREVIATIONS: DGONC = diffuse glioneuronal tumor with oligodendroglioma-like features and nuclear clusters; EPN = ependymoma; ETMR = embryonal tumor with multilayered rosettes; FISH = fluorescence in situ hybridization; NEC = not elsewhere classified; NOS = not otherwise specified; MB = medulloblastoma; MGNT = myxoid glioneuronal tumor; MVNT = multinodular and vacuolating neuronal tumor; PF = posterior fossa; SC = spinal cord; ST = supratentorial; WHO = World Health Organization; *IDH* = *isocitrate dehydrogenase*

Publication of the 2016 World Health Organization (WHO) Classification of Tumors of the Central Nervous System introduced a paradigm shift in the diagnosis of CNS neoplasms. For the first time, both histologic features and genetic alterations were incorporated into the diagnostic framework, classifying and grading brain tumors.

The rapidly evolving molecular landscape demanded interim updates between WHO editions (typically every 7 years). In late 2016, the Consortium to Inform Molecular and Practical Approaches to CNS Tumor Taxonomy (cIMPACT-NOW) was created under the sponsorship of the International Society of Neuropathology to provide such updates.[1,2] To date, 7 updates[3-10] have been published to bridge the gap between the 4th edition and the newly published (May, 2021) 5th edition of the famed "blue book."[11]

We present, summarize, and illustrate the most salient aspects of the new 5th edition. We have selected the key "must know" topics for practicing neuroradiologists. The 2021 WHO Classification of Tumors of the Central Nervous System can be ordered in either print or digital form from the WHO website and should be part of every neuroradiologist's library.

General Features and Recommendations

Tumor Taxonomy and Nomenclature. Prior editions used the terms "entities" and "variants." The current edition uses the terms "types" and "subtypes" and keeps tumor names as simple as possible. Newly recognized or redefined types and subtypes are summarized in the Online Supplemental Data.

Tumor Grading. The 5th edition uses Arabic numerals instead of Roman numerals to conform to other WHO grading systems and decrease the likelihood of typographic errors when grading within types. Tumor grades are now designated specifically as CNS WHO grades 1–4 ("CNS" is always added to distinguish the grading system from those of systemic neoplasms because CNS grading differs conceptually, eg, grading of diffuse astrocytomas from 2 to 4, without a 1).

Not Otherwise Specified and Not Elsewhere Classified. Not otherwise specified (NOS) is used when molecular information is not available/not performed/not successful. Not elsewhere classified (NEC) is used when necessary diagnostic testing was

Received July 19, 2021; accepted after revision November 8.

From the Department of Radiology and Imaging Sciences (A.G.O., K.L.S.), University of Utah School of Medicine, Salt Lake City, Utah; Department of Pathology (D.N.L.), Massachusetts General Hospital, Harvard Medical School, Boston, Massachusetts; Department of Radiology (T.Y.P.), Boston Children's Hospital, Harvard Medical School, Boston, Massachusetts; and Intermountain Pediatric Imaging (L.L.L.), Primary Children's Hospital, University of Utah School of Medicine, Salt Lake City, Utah.

Please address correspondence to Karen L. Salzman, MD, Professor of Radiology and Imaging Sciences, Leslie W. David Endowed Chair in Neuroradiology, University of Utah School of Medicine, 30 N 1900 E SOM 1A71, Salt Lake City, UT 84132; e-mail: karen.salzman@hsc.utah.edu; @TYPoussaintMD

Indicates open access to non-subscribers at www.ajnr.org

Indicates article with online supplemental data.

http://dx.doi.org/10.3174/ajnr.A7462

Layered neuropathology diagnosis[a]

Brain (right frontal)
Integrated diagnosis: glioblastoma, IDH-wildtype[b]
Histologic diagnosis: diffuse astrocytic tumor with mitotic figures
WHO CNS grade: 4
Molecular information:
IDH: wildtype (DNA sequencing)
ATRX: retained nuclear expression, consistent with wild-type (immunohistochemistry)
p53: rare positive cells, consistent with wild-type (immunohistochemistry)
EGFR: amplified (FISH)

[a] Illustrative example of a layered neuropathology report beginning with site and identifier and with integrated diagnosis as the top line.
[b] Although this tumor lacks microvascular proliferation and necrosis, the presence of *EGFR* amplification necessitates a diagnosis of glioblastoma in an IDH-wildtype diffuse astrocytic glioma.

successfully performed but the results do not readily permit a WHO diagnosis (eg, entities that are not yet recognized as part of the WHO Classification).[3] NOS and NEC can be used for any tumor type.

"Layered" Reports and Integrated Diagnosis. A matrix approach to an integrated pathologic diagnosis is used throughout the 5th edition (Table). Features such as location (eg, cerebrum or cerebellum), histopathology, and molecular information (when available) are combined into the top layer (in reality the "bottom line") to create an integrated diagnosis. Tumor grade reflects a combination of histologic features and genetically defined mutation status. If molecular information is unavailable, tumor entities are generally designated by NOS.

General Taxonomy

The WHO 5th edition organizes CNS neoplasms into several major groups: gliomas, glioneuronal, and neuronal tumors; choroid plexus tumors; embryonal tumors; pineal tumors; cranial and paraspinal nerve tumors; meningioma; mesenchymal, nonmeningothelial tumors; melanocytic tumors; hematolymphoid tumors; germ cell tumors; tumors of the sellar region; and metastases to the CNS. In this overview, we will focus on the tumor groups with specific changes such as newly recognized tumor entities, revised nomenclature, and restructured tumor groupings.

Gliomas, Glioneuronal, and Neuronal Tumors

Gliomas, glioneuronal, and neuronal tumors, along with the embryonal tumors, have undergone the most important changes since the 2016 4th edition. There are now 14 newly recognized ("new") gliomas and glioneuronal tumors in the 5th edition of the blue book. In addition, for the first time, the WHO classification divides diffuse gliomas into adult-type and pediatric-type neoplasms.

Gliomas

Neuropathologic Essentials. Glioma characterization requires more than simply determining whether a tumor exhibits 1p/19q codeletion on fluorescence in situ hybridization (FISH) and is isocitrate dehydrogenase (IDH) mutant or IDH-wildtype on immunohistochemistry, to implement the 2021 WHO classification fully. For example, IDH-wildtype diffuse astrocytic gliomas in patients 55 years of age and younger should also be investigated for noncanonical (ie, non-R132H) *IDH1* mutations and *IDH2* mutations. In other molecular markers such as loss of ATRX expression or *TERT* promoter mutations, the presence of *TP53* or histone H3 mutations, *EGFR* amplification, or *CDKN2A/B* alterations, and so forth need to be evaluated in specific diagnostic pathways.

Some genetic changes have convenient immunohistochemistry surrogate assays (eg, *IDH1* R132H, ATRX, p53, *BRAF* V600E, H3K27M, H3 G34R/V), while others can be detected with FISH (eg, *CDKN2A/B* homozygous deletion, *EGFR* amplification, 1p/19q codeletion). Next-generation sequencing assays will detect many of these and other events such as mutations and fusions. Methylome profiling has also emerged as a powerful tool that can be used itself for classification and can also either directly or indirectly identify many of the above molecular alterations.

Four general groups of diffuse gliomas are recognized in the 2021 WHO classification: 1) adult-type diffuse gliomas, 2) pediatric-type diffuse low-grade gliomas, 3) pediatric-type diffuse high-grade gliomas, and 4) circumscribed astrocytic gliomas.

Adult-type diffuse gliomas are astrocytoma, IDH-mutant; oligodendroglioma, IDH-mutant and 1p/19q-codeleted; and glioblastoma, IDH-wildtype. IDH-mutant diffuse astrocytomas are now graded 2–4 within type; the terms IDH-mutant "anaplastic astrocytoma" and "glioblastoma" have been dropped. In addition, if an IDH-mutant diffuse astrocytoma exhibits *CDKN2A/B* homozygous deletion, it is designated as a CNS WHO grade 4 neoplasm, even if histologic features of malignancy such as necrosis and microvascular proliferation are absent.

Imaging features suggestive of an IDH-mutant diffuse astrocytoma grade 2 include a homogeneous T2-hyperintense circumscribed supratentorial mass typically in the frontal or temporal lobes without calcification or enhancement. The T2-FLAIR mismatch sign, characterized by T2 homogeneity of the mass with relatively hypointense signal throughout most of the lesion on FLAIR compared with T2 sequences except for a peripheral rim of hyperintense signal, is highly predictive of IDH-mutant diffuse astrocytoma. The T2-FLAIR mismatch sign has high specificity but low sensitivity for IDH-mutant diffuse astrocytomas.[12,13] Imaging features of IDH-mutant diffuse astrocytoma grade 3 may be indistinguishable from grade 2 IDH-mutant diffuse astrocytomas. However, grade 3 astrocytomas may have T2 heterogeneity and enhancement as well as elevated maximum relative CBV. The mean maximum relative CBV is significantly higher in WHO grade 3 astrocytomas than in WHO grade 2 astrocytomas.[14] Imaging features typical of oligodendroglioma, IDH-mutant and 1p/19q-codeleted, tumors include frontal lobe location, heterogeneity, and calcification with variable enhancement (Fig 1).[12]

The presence of any one of the following 5 criteria is sufficient to designate an IDH-wildtype diffuse astrocytic glioma as a glioblastoma. IDH-wildtype is characterized by the following: microvascular proliferation or necrosis or *TERT* promotor mutation or *EGFR* gene amplification or +7/–10 chromosome copy number changes. Such tumors are no longer called "diffuse astrocytic glioma, IDH-wildtype with molecular features of glioblastoma multiforme." If an IDH-wildtype tumor exhibits none of these histologic or molecular features (eg, appears as a lower grade than a glioblastoma, CNS WHO grade 4), it would be classified as diffuse astrocytoma, NEC (Fig 1).

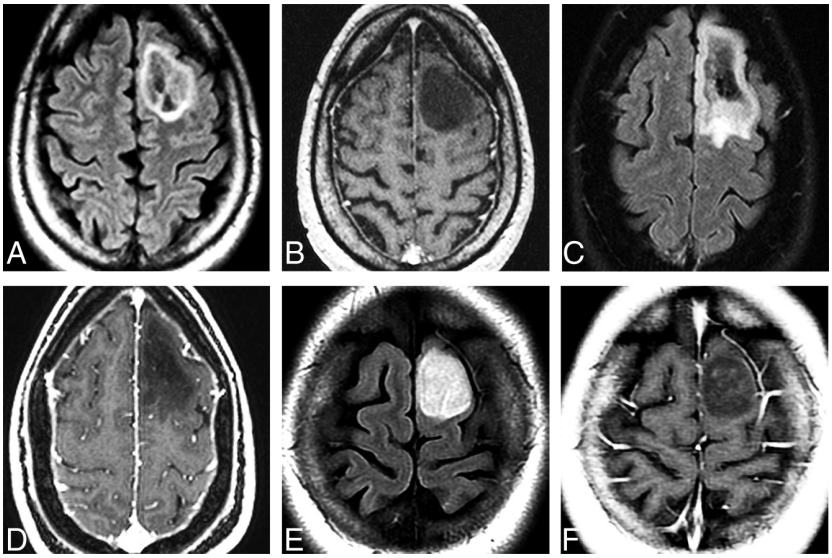

FIG 1. Adult-type diffuse gliomas. Series of 3 cases illustrates the importance of complete IDH mutation status determination and the investigation of other molecular markers in evaluation of adult-type diffuse astrocytomas. Axial FLAIR (*A*) and postcontrast TIWI (*B*) in a 54-year-old man with a first-time seizure shows a well-delineated left frontal lobe mass with a hyperintense rim surrounding a mixed signal mass. No enhancement is present. Pathology disclosed diffuse astrocytoma without necrosis or microvascular proliferation. Immunohistochemistry demonstrated that the tumor was *IDH*-mutant. Next generation sequencing disclosed *CDKN2A/B* homozygous loss, so the tumor was upgraded to WHO CNS grade 4. Axial FLAIR (*C*) and postcontrast TIWI (*D*) in a 44-year-old woman with a first-time seizure demonstrate a left frontal mass that was completely resected. Pathology findings were consistent with WHO CNS grade 3. Initial immunohistochemistry was negative for *IDH1* mutation, but further investigation disclosed the presence of an *IDH2* mutation. Final pathologic diagnosis is diffuse astrocytoma, *IDH*-mutant, grade 3. The patient is alive without evidence of disease 4 years after the initial diagnosis. Axial FLAIR (*E*) and postcontrast TIWI (*F*) in a 24-year-old woman with a first-time seizure show a well-delineated nonenhancing left frontal lobe mass that was surgically resected. Histologically, the tumor was WHO CNS grade 2 but IDH-wildtype on immunohistochemistry. No further investigation was conducted. One year later, the tumor recurred and re-resection demonstrated *EGFR* amplification and was, therefore, upgraded to glioblastoma (WHO CNS grade 4). The patient died of disseminated disease 18 months after the initial diagnosis.

Pediatric-type diffuse low-grade gliomas are diffuse astrocytomas, *MYB* or *MYBL1*-altered; angiocentric gliomas (Fig 2); polymorphous low-grade neuroepithelial tumor of the young (a newly recognized entity exhibiting oligodendroglioma-like histology with variable morphology and MAPK-pathway alterations);[15] and diffuse low-grade gliomas, MAPK pathway–altered. Angiocentric gliomas are T2-hyperintense masses typically in the temporal or frontal lobe cortex in young patients with seizures (Fig 2). Polymorphous low-grade neuroepithelial tumors of the young are typically well-circumscribed T2-hyperintense lesions on MR imaging with central calcification and peripheral cystic components (Fig 3). They are commonly supratentorial, most often within the temporal lobe.[15,16] Diffuse low-grade glioma, MAPK pathway–altered, is a group of neoplasms that are IDH- and H3-wildtype and include most tectal gliomas. Up-regulation of the *RAS/MAPK* pathway is almost universal in these lesions, with a spectrum of *FGFR1* and *BRAF* mutations. Histologic features of malignancy and molecular alterations such as *CDKN2A/B* mutations are absent.[17,18] The classic tectal gliomas are not considered a distinct WHO entity. Most fit histologically and genetically into either pilocytic astrocytoma with *BRAF* alterations and *NRAS* mutations or diffuse low-grade glioma, *MAPK* pathway–altered.

Pediatric-type diffuse high-grade gliomas are defined primarily by molecular features and include diffuse midline glioma, H3K27-altered (note that the term "mutant" has been changed) (Fig 4); diffuse hemispheric glioma, *H3 G34*-mutant (an *H3F3A*-mutant, IDH-wildtype tumor that exhibits glioblastoma-like histology, often with primitive embryonal regions) (Fig 5); diffuse pediatric-type high-grade glioma, H3-wildtype and IDH-wildtype (a group of tumors with different possible genotypes); and infant-type hemispheric glioma (Fig 6).[19,20] The classic diffuse intrinsic pontine gliomas seen on MR imaging as expansile T2-hyperintense lesions are most commonly diffuse midline gliomas, H3K27-altered pathologically, similar to the 2016 WHO description. However, other gliomas may affect the pons.[21] In addition to the more common pediatric brainstem glioma presentation, H3K27-altered high-grade gliomas occur in adults and have the same lethality as in their pediatric counterparts.[18] Unilateral thalamic or bithalamic lesions are common in H3K27-altered high-grade gliomas as is aggressive local spread and early metastatic dissemination.

Infant-type hemispheric gliomas are tumors of early childhood that exhibit high-grade astrocytic (often glioblastoma-like) histologic features with alterations in *ALK/ROS1/NTRK/MET*. A large, bulky nearly holohemispheric, heterogeneous-appearing tumor with intratumoral hemorrhage is typical.

Circumscribed astrocytic gliomas include long-recognized neoplasms (such as pilocytic and subependymal giant cell astrocytomas) and 2 new entities, high-grade astrocytomas with piloid features and astroblastoma, *MN1*-altered. While not designated as separate entities, the molecular characterization of low-grade gliomas has had a profound effect on their treatment. For instance, the identification of BRAF V600E mutations allows targeted disruption by using BRAF inhibitors, with favorable clinical results.[22]

The diagnosis of high-grade astrocytoma with piloid features recognizes unusual cases in which a relatively circumscribed tumor with distinct piloid cytology occurs in the setting of a more malignant astrocytoma (WHO grades 3 or 4).[23] These tumors usually occur in adults, exhibit *CDKN2A/B* deletions, and have a distinct DNA methylation profile that differs from the typical childhood pilocytic astrocytomas. Most of these tumors occur in

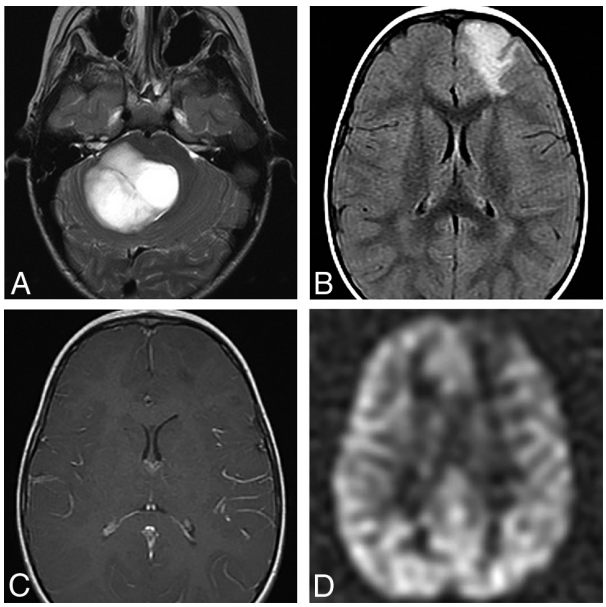

FIG 2. Pediatric-type diffuse low-grade glioma. Axial T2 (*A*) MR image in a 7-year-old boy with a diffuse astrocytoma, *MYB*-altered, shows a hyperintense mass in the pons with no significant surrounding edema. There was no enhancement and no diffusion restriction of the mass (not shown). Axial FLAIR (*B*), postcontrast T1 (*C*), and arterial spin-labeling (ASL) (*D*) in a 1-year-old child with an angiocentric glioma show a FLAIR hyperintense mass involving the cortex and subcortical white matter of the left frontal lobe. There is no enhancement (*C*) and decreased perfusion (*D*) on ASL imaging.

the posterior fossa (PF), are T2-hyperintense, and show heterogeneous enhancement.[23] The relationship with so-called "anaplastic pilocytic astrocytomas" and pre-existing pilocytic astrocytomas is currently undetermined.

Astroblastoma, *MN1*-altered, is newly classified as a circumscribed astrocytic glioma (in 2016 it was categorized with "other gliomas"). *MN-1* alterations are present in 70%.[24] If *MN-1* alteration is absent or not determined, the tumor is designated NEC or NOS, respectively. Most astroblastomas are located superficially in a cerebral hemisphere and are relatively well-circumscribed tumors that can be multicystic or "bubbly" in appearance. Edema is minimal or absent (Fig 7).[8,25,26] No formal grade for astroblastoma is assigned in the 5th edition.

Miscellaneous 5th Edition Glioma Items. In 2021, pilomyxoid astrocytoma continues to be considered a variant of pilocytic astrocytoma, not a distinct entity. The location modifier (third ventricle) has been dropped from choroid glioma. Like medulloblastoma, it only occurs in 1 location; therefore, a location modifier is not necessary.

Glioneuronal and Neuronal Tumors

Ganglioglioma, desmoplastic infantile ganglioglioma/astrocytoma, dysembryoplastic neuroepithelial tumor, and other mixed glioneuronal tumors such as rosette-forming glioneuronal tumor are unchanged. Newly clarified and added tumor entities include diffuse glioneuronal tumor with oligodendroglioma-like features and nuclear clusters (DGONC), myxoid glioneuronal tumor (MGNT), and multinodular and vacuolating neuronal tumor (MVNT).

DGONC is included in the 5th edition as a provisional entity, defined primarily by a DNA methylation profile. As the name implies, histology is oligodendroglioma-like with large cells that have clusters of nuclei. DGONCs are primarily pediatric tumors but can occur at all ages.[27]

MGNT is a CNS WHO grade 1 neoplasm that is stereotypically located in the septum pellucidum, though it can also occur in the corpus callosum and periventricular white matter. Oligodendrocyte-like tumor cells are embedded in a prominent myxoid stroma. Specific mutations in *PDGFRA* are definitional.[28,29] In addition to location, suggestive imaging findings include T2 hyperintensity, peripheral FLAIR hyperintensity, and lack of enhancement (Fig 8). MGNTs are considered CNS WHO grade 1 neoplasms, but many cases exhibit ventricular dissemination or local recurrence/progression.[8,29]

MVNT was considered a pattern of ganglion cell tumors in the 2016 WHO. Whether MVNT represented a neoplastic or malformative process was then unknown. Now MVNTs are recognized as clonal neoplasms of the MAPK pathway with mutations in *MAPK2K1* and *BRAF* (excluding V600E) as well as *FGFR2* fusions. MVNTs are nonprogressive CNS WHO grade 1 lesions. MR imaging features are virtually pathognomonic with clusters of T2-FLAIR hyperintense nodules (little bubbles) along the undersurface of the cerebral cortex and subcortical white matter.[30,31] MVNT-like lesions have also been reported in the posterior fossa.[32]

Ependymal Tumors

Ependymomas (EPNs) are the last of the glioma/glioneuronal/neuronal tumor groupings. The 2016 WHO divided ependymal tumors into 4 subgroups: subependymoma (CNS WHO grade I), myxopapillary ependymoma (CNS WHO grade I), ependymoma (CNS WHO grade II), and anaplastic ependymoma (CNS WHO grade III).

In a major departure since the 2016 WHO, ependymomas are now uniquely grouped by location.[8,9] The WHO recognized 3 distinct anatomic sites: supratentorial (ST), PF, and spinal cord (SC) EPNs. Within each specific anatomic site, molecularly defined subgroups are defined by gene and DNA methylation profiling. Each differs in location, age, prognosis, and clinicopathologic characteristics.[9]

ST-EPN. *ZFTA* fusion–positive ependymomas (formerly *RELA*-fusion ependymoma) are extraventricular hemispheric tumors that exhibit rearrangement of partners with the *ZFTA* (formerly *C11orf95*) genes (Fig 9). These tumors are the largest group of currently defined ST-EPNs. They occur in both children and adults and are designated CNS WHO grade 2 or 3 neoplasms. They appear as relatively well-defined mixed cystic-solid masses on imaging studies. *YAP1*-fusion ST-EPNs are found mostly in children younger than 3 years of age and have a better prognosis than *ZFTA* ependymomas.[33] Tumors that do not have the *ZFTA*- or *YAP1*-fusion events are termed ST-EPN are described by their histologic features.

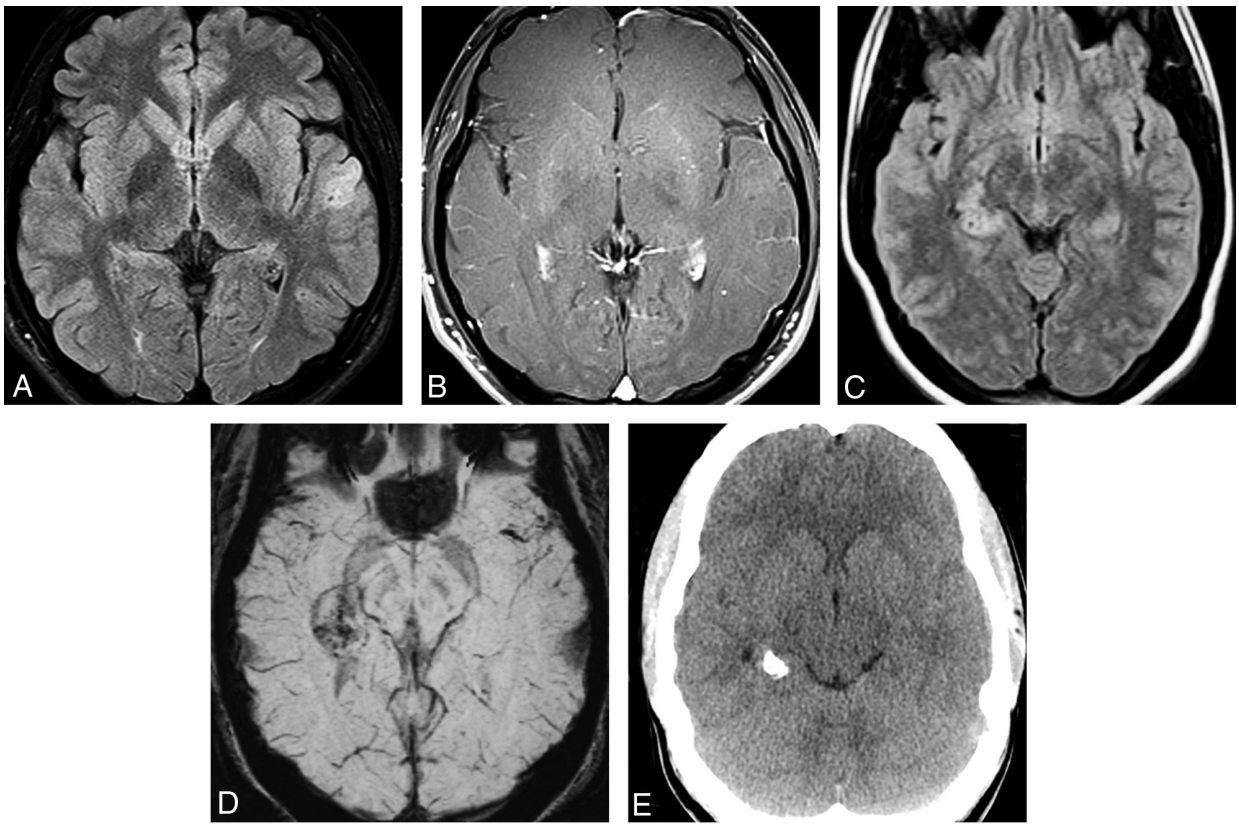

FIG 3. Two patients with the WHO 2021 new-entity polymorphous low-grade neuroepithelial tumor of the young (PLNTY). Axial FLAIR (*A*) and postcontrast T1-weighted (*B*) MR images in a 19-year-old man with refractory epilepsy show a hyperintense, nonenhancing mass in the cortex and subcortical white matter of the left temporal lobe. Axial FLAIR (*C*) and susceptibility-weighted (*D*) MR images and a noncontrast CT image (*E*) in a 19-year-old woman with progressive seizure show a FLAIR-hyperintense, SWI-hypointense mass with characteristic calcification seen on CT in the right medial temporal lobe (Case courtesy of M. Castillo, MD).

PF-EPNs can now be divided molecularly into 2 subgroups: PF-EPN A and PF-EPN-B.[34] PF-A ependymomas occur mainly in infants, exhibit loss of H3K27me3 expression on immunohistochemistry, exhibit EZHIP overexpression, and have significantly worse outcome than PF-EPN-B tumors. PF-EPN-B tumors are more common in older children and adults. Posterior fossa ependymomas are characterized on MR imaging as a lobulated, heterogeneous mass in the body or inferior fourth ventricle, which often extends through the foramen of Magendie into the cisterna magna or through the foramina of Luschka into the cerebellopontine angle cisterns. Calcification and cystic changes are often seen. Both the histology and imaging features of the 2 posterior fossa ependymoma subgroups are similar, but PF-EPN-A tumors are more likely to have a lateral location within the posterior fossa and show cerebellar invasion.[9,35] Tumors that cannot be evaluated further are termed posterior fossa ependymomas and are described by their histologic features.

Spinal Ependymomas. The 2021 WHO recognizes a new type of spinal cord ependymoma with *MYCN*–amplification. *MYCN*-amplified ependymoma is mostly found in adults and exhibits anaplastic histology. These tumors are typically located in the cervical or thoracic spinal cord and extend over many spinal segments. These spinal cord tumors are heterogeneously T2-hyperintense and enhancing and are typically extramedullary or have an exophytic portion if intramedullary and are characterized by leptomeningeal disease. Early dissemination and poor prognosis are typical.[9,36] Of note, myxopapillary ependymomas are now designated CNS WHO grade 2 neoplasms because their biologic behavior is more consistent with this designation.[9]

Choroid Plexus Tumors

The classification of choroid plexus tumors remains unchanged in 2021, though these are now listed separately from the glial and glioneuronal neoplasms.

Embryonal Tumors

The 2021 WHO classifies CNS embryonal tumors into 2 groups: medulloblastoma and other CNS embryonal tumors (the term "primitive neuroectodermal tumor" has been abandoned since 2016).

Medulloblastoma

As in 2016, medulloblastomas (MBs) can be either molecularly or histologically defined. The molecularly-defined MB subgroups are defined by DNA methylation or transcriptome profiling and remain unchanged: medulloblastoma, *WNT*-activated; medulloblastoma, *SHH*-activated and *TP53* wild-type; medulloblastoma,

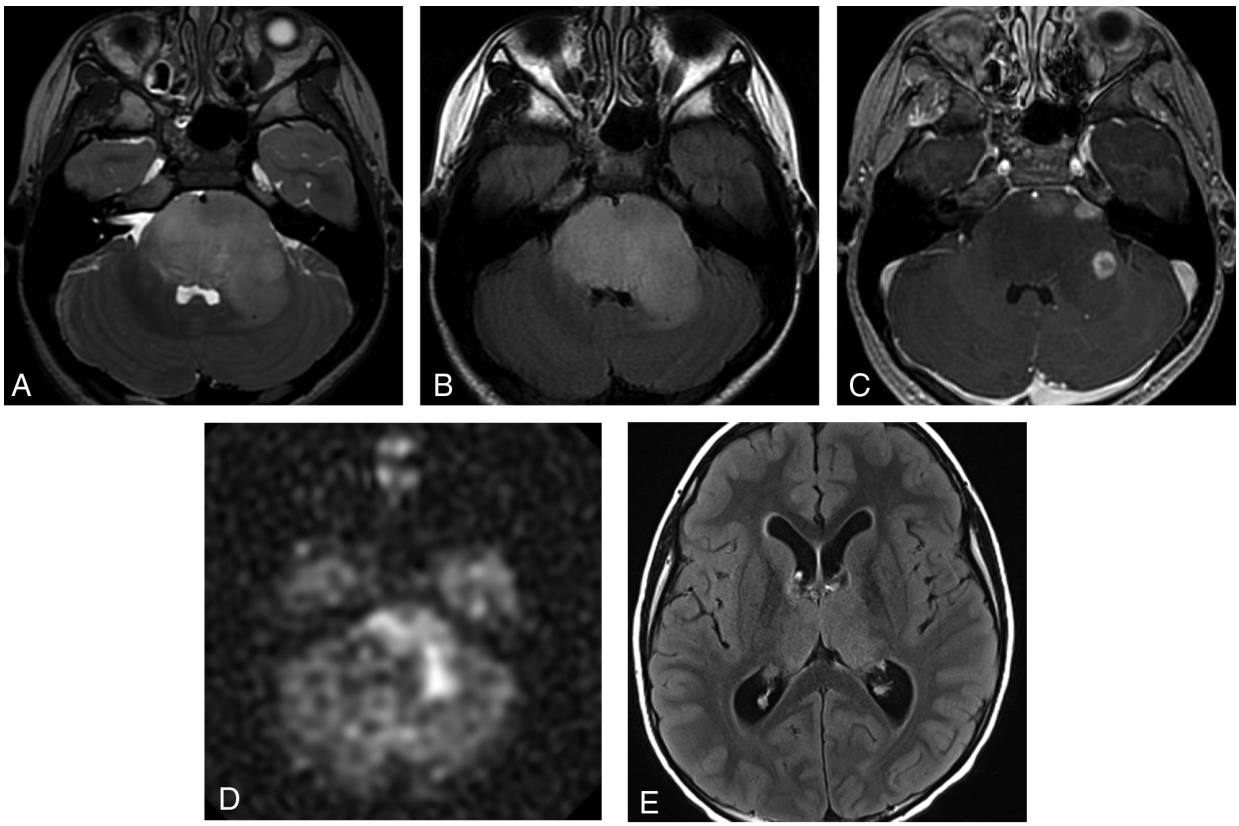

FIG 4. Pediatric-type diffuse high-grade gliomas. Diffuse midline glioma, H3K27-altered in an 8-year-old girl with cranial neuropathies. Axial T2 (*A*) and FLAIR (*B*) MR images show an expansile, hyperintense pontine mass. Axial postcontrast T1 MR image (*C*) shows heterogeneous enhancement within the mass. Arterial spin-labeling (ASL) perfusion (*D*) shows increased perfusion. *E*, Axial FLAIR MR image shows a bithalamic hyperintense mass. Postcontrast T1WI showed no significant enhancement, and ASL perfusion showed increased perfusion within the bilateral thalami (not shown). These WHO grade 4 tumors have a poor prognosis.

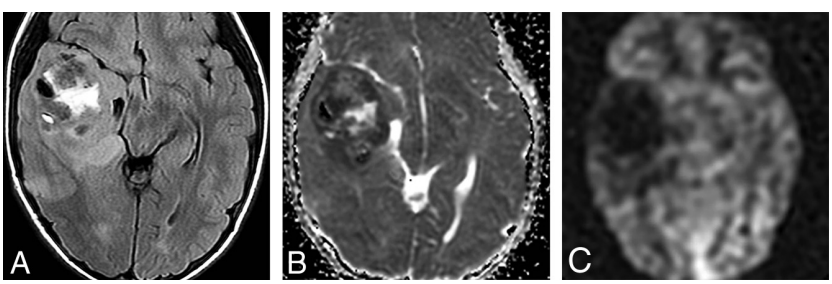

FIG 5. Diffuse hemispheric glioma, H3 G34-mutant and IDH-wildtype tumor in an 8-year-old boy. *A*, Axial FLAIR shows a large, very heterogeneous right temporal lobe mass with minimal surrounding edema. *B*, An ADC map in the same case shows restricted diffusion consistent with a high-cellularity tumor. *C*, Arterial spin-labeling perfusion shows decreased perfusion in the tumor. In pediatric tumors, perfusion is often less helpful compared with diffusion-weighted imaging in discriminating tumor grade. Histology demonstrated necrosis, hemorrhage, and neovascularity in a glioblastoma-like pattern, consistent with grade 4 tumor.

SHH-activated and *TP53*-mutant; and medulloblastoma, non-*WNT*/non-*SHH*.[11,37-39]

Medulloblastoma, *WNT*-activated, represents approximately 10% of MBs. There are 2 age-determined subtypes: children and adults. *WNT* MBs can be found in all posterior fossa locations and are thought to arise from the lower rhombic lip. Imaging studies suggest that the cerebellar peduncle and cerebellopontine angle are the most characteristic but not the only location. *WNT*-activated MBs have the best prognosis of all 4 groups. Metastases are rare at diagnosis, and the 5-year survival rate is 95%.[11,37,38]

Medulloblastoma, *SHH*-activated/*TP53* wild-type, represents approximately 30% of MBs overall but accounts for nearly two-thirds of MBs occurring between 3–16 years of age. This MB subgroup has the most striking biologic, pathologic, and clinical heterogeneity of all 4 subgroups. *SHH*-activated MBs arise from granule neuron progenitor cells in the upper rhombic lip, so a cerebellar hemispheric location is typical. These MBs have 4 provisional molecular subtypes as defined by DNA methylation or transcriptome profiling: *SHH-1* and *SHH-2* are the most common subgroups to exhibit desmoplastic or medulloblastoma with extensive nodularity histology. Desmoplastic MBs are more common in adults and have a predilection for the lateral cerebellar hemisphere.[37] *SHH-3* and *SHH-4* most commonly

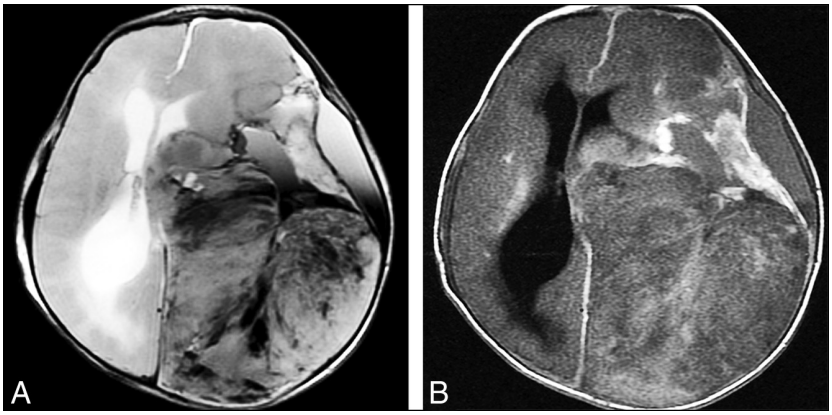

FIG 6. Infant-type hemispheric glioma, NOS. A male neonate child with macrocephaly and bulging fontanelles had a large, heterogeneous-appearing mass on an emergent CT scan (not shown). Axial T2-weighted (*A*) and postcontrast T1-weighted (*B*) MR images show a very heterogeneous mass with enhancement involving almost the entirety of the left cerebral hemisphere.

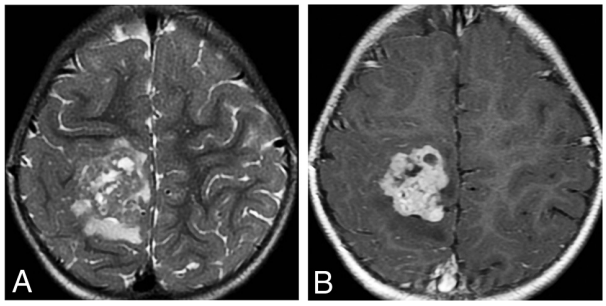

FIG 7. Axial T2WI in a 19-month-old child with astroblastoma, MN1-altered. *A*, Axial T2WI shows a bubbly-appearing mixed-signal hemispheric mass with little surrounding edema. *B*, Postcontrast T1WI shows that the mass enhances strongly but heterogeneously.

exhibit classic or large-cell anaplastic histology and can be found in all locations.[39,40]

Medulloblastoma, *SHH*-activated/*TP53*-mutant, is the rarest of the MB subtypes and has the worst overall prognosis.[11,40]

Medulloblastoma, non-*WNT*/non-*SHH*, is the most common MB subtype, representing 50%–60% of all MBs. This subtype encompasses the former group 3 (20%) and group 4 (40%–50%) MBs. This subtype has 8 molecular subgroups (Gp3/4–1 to Gp3/4–8) as determined by methylation profiling. Non-*SHH*, non-*WNT* MBs can be found in all locations and often exhibit minimal or no enhancement.[11]

Other CNS Embryonal Tumors

This group of "other" embryonal tumors includes atypical teratoid/rhabdoid tumor and the addition of several "new" tumor types: a provisional type called cribriform neuroepithelial tumor and CNS tumor with *BCOR* internal tandem duplication. One embryonal tumor with a newly identified genotype is CNS neuroblastoma, *FOXR2*-activated. This group also includes embryonal tumor with multilayered rosettes (ETMR).

Cribriform Neuroepithelial Tumor. Cribriform neuroepithelial tumor (provisional diagnosis) is a nonrhabdoid neuroectodermal tumor characterized molecularly by loss of nuclear *SMARCB1/INI1* expression and histologically by cribriform strands/ribbons. Cribriform neuroepithelial tumors occur near the ventricles in young children and have a better prognosis than atypical teratoid/rhabdoid tumors.[40]

CNS Tumor with *BCOR* Internal Tandem Duplication. CNS tumors with *BCOR* internal tandem duplication are mostly hemispheric malignant tumors of children and adolescents that are characterized by internal tandem duplication in the *BCOR* gene, similar to other systemic tumors.[41]

ETMR was included in 2016 specifically as chromosome 19 microRNA cluster–altered. An additional subtype, *DICER1*-mutated ETMR, has been recently described. ETMRs subsume many prior entities such as embryonal tumor with abundant neuropil and true rosettes, medulloepithelioma, ependymoblastoma, and many tumors formerly known as CNS primitive neuroectodermal tumors. ETMRs are tumors of infants and children younger than 4 years of age. They are seen on imaging studies as large, cellular, relatively well-demarcated-but-heterogeneous-appearing masses.[42] While they do occur in the posterior fossa, most are supratentorial hemispheric lesions (70% of cases). Necrosis and intratumoral hemorrhage are common. Solid components of the tumors typically exhibit restricted diffusion. Enhancement varies from patchy, sparse to mostly absent (Fig 10).[42]

CNS Neuroblastoma, *FOXR2*-Activated. CNS neuroblastoma is a newly recognized embryonal tumor that has a characteristic histology and *FOXR2* gene alterations.[43] These primary CNS neuroblastomas have a peak at 5 years of age and are characterized by neuronal differentiation, high vascularity, necrosis, and endothelial proliferation. Imaging shows a large, heterogeneous supratentorial mass with prominent cysts, necrosis, little surrounding edema, and variable enhancement.

Keep in mind that the imaging differential diagnosis of a large, bulky, heterogeneous hemispheric mass in an infant or young child includes ETMR, infant-type hemispheric glioma, *ZFTA* ependymoma, CNS neuroblastoma, *FOXR2*-activated and CNS embryonal tumor, NOS or NEC. The term primitive neuroectodermal tumor has been abandoned since 2016.

Pineal Tumors

With 1 exception, pineal tumors remain unchanged since 2016. A newly codified tumor, desmoplastic myxoid tumor of the pineal region, *SMARCB1*-mutant, is now recognized. This rare tumor of the pineal region (not specifically the pineal gland) has both desmoplastic and myxoid changes but no histopathologic signs of malignancy.[44] Only a limited number of cases have been reported with an age range of 15–61 years (median, 40 years).[11]

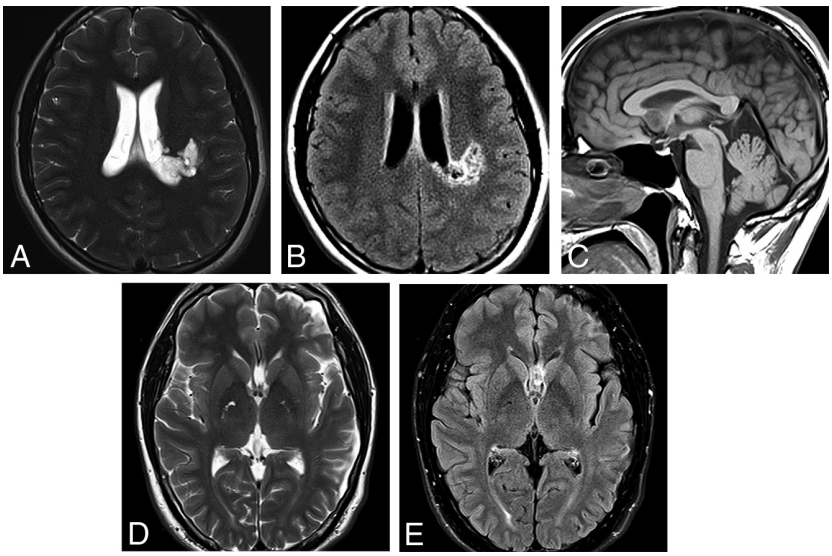

FIG 8. Two cases of MGNT are illustrated. *A*, Axial T2WI in a 14-year-old boy shows an extremely hyperintense, slightly bubbly mass in the left juxtaventricular white matter. *B*, Axial FLAIR shows a hyperintense rim surrounding a largely isointense center of the mass. Smaller-but-similar-appearing lesions are adjacent to the mass. The mass did not enhance following contrast administration. *C*, Sagittal T1WI in a 39-year-old man shows a well-demarcated mass in the corpus callosum rostrum/septum pellucidum. *D*, The mass is extremely hyperintense on T2WI. *E*, FLAIR shows that the mass has a hyperintense rim with an isointense center. The mass is thought to represent an MGNT because of its classic location and signal characteristics but is not biopsy-proven.

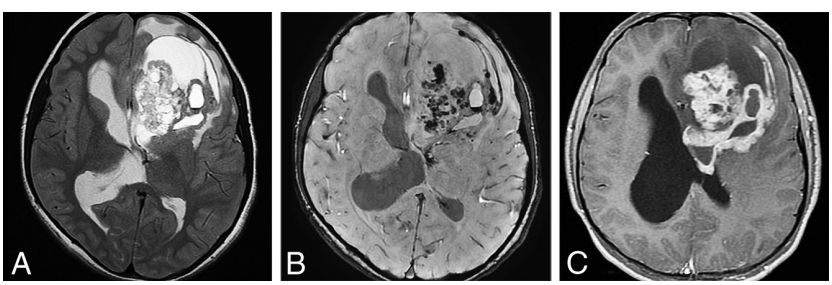

FIG 9. *ZFTA* fusion–positive ependymoma in an 11-year-old girl. *A*, Axial T2WI shows a large, bulky, heterogeneous left frontal mass. *B*, Susceptibility-weighted scan shows intratumoral hemorrhage. *C*, Strong-but-very heterogeneous enhancement is seen on postcontrast T1WI.

Cranial and Paraspinal Nerve Tumors

The term malignant melanotic nerve sheath tumor, previously called melanotic schwannoma, has been changed, in part, because it behaves more aggressively than nonmelanotic schwannomas and also to conform with soft-tissue nomenclature.

Meningiomas

In terms of the overall classification, the meningioma tumor group remains unchanged. However, there are a number of molecular alterations that are now recognized as diagnostically and prognostically useful.

Mesenchymal, Nonmeningothelial Tumors

Mesenchymal, nonmeningothelial tumors are divided into 2 groups: soft-tissue tumors and chondro-osseous tumors. The only major changes in 2021 are with soft-tissue tumors.

Soft-Tissue Tumors

Soft-tissue tumors are subcategorized into fibroblastic and myofibroblastic tumors, vascular tumors, skeletal muscle tumors, and tumors of uncertain differentiation. The term hemangiopericytoma is now considered obsolete, and the preferred term "solitary fibrous tumor" is used to correspond to extracranial solitary, fibrous tumors. Solitary, fibrous tumors are the most common nonmeningothelial mesenchymal neoplasm and share the common molecular feature of *NAB2-STAT6* gene fusions. Tumor grades vary from WHO 1–3 (WHO grade III solitary fibrous tumors were previously referred to as "anaplastic hemangiopericytomas"). Imaging features often resemble those of meningiomas.

There are 3 newly recognized intracranial soft-tissue tumors: intracranial mesenchymal tumor, *FET-creB* fusion-positive; *CIC*-rearranged sarcoma; and primary intracranial sarcoma, *DICER1*-mutant.[11,45]

Intracranial mesenchymal tumor, *FET-creB* fusion-positive, often features specific *EWSR1-creB1* fusions. These tumors can be extra-axial or intraventricular. The cerebral convexities are the most common location. They are typically T2-FLAIR hyperintense, exhibit strong enhancement, and often have a dural "tail." The major differential diagnosis is atypical or anaplastic meningioma.[11,45]

CIC-rearranged sarcoma corresponds to similar soft-tissue tumors. Multiple *CIC*-fusion partners have been identified. Round-cell sarcomas with myxoid features are typical. These tumors can occur at any age but are most common in adolescents and young adults. They are highly aggressive and are designated as WHO CNS grade 4 lesions.[11,45]

Primary intracranial sarcoma, *DICER1*-mutant, is a highly-malignant CNS sarcoma that is part of the expanding spectrum of *DICER1* and type 1 neurofibromatosis syndromes. This intracranial sarcoma primarily occurs in children and young adults, exhibiting malignant spindle cell morphology often with focal rhabdomyoblastic differentiation.[11,45]

Hematolymphoid Tumors

Other than grouping lymphomas and histiocytic tumors together as hematolymphoid tumors, no significant changes occurred in the 2021 WHO.

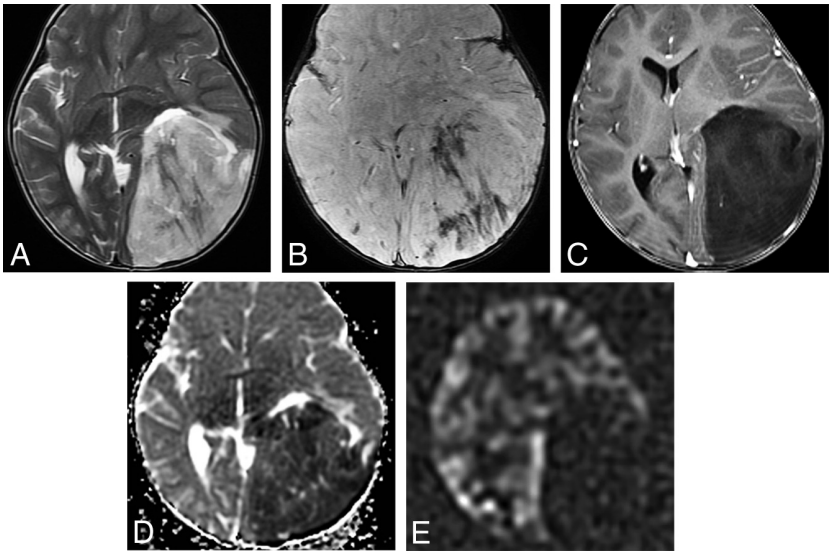

FIG 10. Embryonal tumor with multilayered rosettes in a 1-year-old girl. *A*, An axial T2-weighted scan shows a large, left parieto-occipital mass with little surrounding edema. *B*, The mass exhibits hemorrhage on susceptibility-weighted imaging and no enhancement following contrast administration (*C*). *D*, Strikingly restricted diffusion is seen on the ADC map. *E*, Arterial spin-labeling perfusion shows decreased perfusion in the tumor.

Germ Cell Tumors

No significant 2021 changes were made in germ cell neoplasms.

Tumors of the Sellar Region

Pituitary adenomas are now designated as pituitary adenoma/pituitary neuroendocrine tumors to correspond to systemic neuroendocrine tumors. Pituitary neuroendocrine tumors are now also classified according to adenohypophyseal cell lineages, rather than just by the hormone produced. Pituicytoma, granular cell tumor of the sellar region and spindle cell oncocytoma remain unchanged from WHO 2016, and though they are classified as separate tumor types, they are considered a related group of tumor types with possibly morphologic variations of the same tumor.[11,46]

One new tumor, pituitary blastoma, has been added to the 2021 WHO Classification of sellar region tumors. Pituitary blastomas are rare embryonal sellar neoplasms of infants (median age, 8 months) that are associated with somatic or germline *DICER1* mutations. Pituitary blastomas are hypophyseal tumors that resemble a 10- to 12-week embryonic-stage pituitary gland. Primitive blastemal cells similar to those in pleuropulmonary blastomas, neuroendocrine cells, and Rathke-type epithelium in rosettes/glandular structures are characteristic. Pituitary blastomas are designated WHO CNS grade 4 neoplasms.[11,45]

Summary

The 2021 5th edition WHO Classification of CNS neoplasms (the series popularly known as the Blue Books) builds on the trend of molecular tumor classification first introduced in the 2016 (4-plus) edition. Gliomas are divided into adult-type diffuse gliomas, pediatric-type diffuse low-grade gliomas, pediatric-type diffuse high-grade gliomas, and circumscribed astrocytic gliomas. WHO grades are now expressed in Arabic numbers instead of Roman numerals. The 5th edition introduces 14 new gliomas and glioneuronal tumors and 8 other new tumors into the neuropathologic lexicon.[36] The critical importance of identifying mutations other than the canonical *IDH1* R132H mutation in diffuse gliomas, especially in patients younger than 55 years of age, is emphasized. Neuroradiologists must familiarize themselves with the updated WHO Classification of CNS neoplasms to function appropriately as part of the modern neuro-oncology clinical team.

Disclosure forms provided by the authors are available with the full text and PDF of this article at www.ajnr.org.

REFERENCES

1. Louis DN, Aldape K, Brat DJ, et al. **Announcing cIMPACT-NOW: the Consortium to Inform Molecular and Practical Approaches to CNS Tumor Taxonomy.** *Acta Neuropathol* 2017;133:1–3 CrossRef Medline
2. Louis DN, Aldape K, Brat DJ, et al. **cIMPACT-NOW (the Consortium to Inform Molecular and Practical Approaches to CNS Tumor Taxonomy): a new initiative in advancing nervous system tumor classification.** *Brain Pathol* 2017;27:851–52 CrossRef Medline
3. Louis DN, Wesseling P, Paulus W, et al. **cIMPACT-NOW update 1: not otherwise specified (NOS) and not elsewhere classified (NEC).** *Acta Neuropathol* 2018;135:481–84 CrossRef Medline
4. Louis DN, Giannini C, Capper D, et al. **cIMPACT-NOW update 2: diagnostic clarifications for diffuse midline glioma, H3K27M-mutant and diffuse astrocytoma/anaplastic astrocytoma, IDH-mutant.** *Acta Neuropathol* 2018;135:639–42 CrossRef Medline
5. Brat DJ, Aldape K, Colman H, et al. **cIMPACT-NOW update 3: recommended diagnostic criteria for "diffuse astrocytic glioma, IDH-wildtype, with molecular features of glioblastoma, WHO grade IV."** *Acta Neuropathol* 2018;136:805–10 CrossRef Medline
6. Ellison DW, Hawkins C, Jones DTW, et al. **cIMPACT-NOW update 4: diffuse gliomas characterized by MYB, MYBL1, or FGFR1 alterations or BRAF V600E mutation.** *Acta Neuropathol* 2019;137:683–87 CrossRef Medline
7. Brat DJ, Aldape K, Colman H, et al. **cIMPACT-NOW update 5: recommended grading criteria and terminologies for IDH-mutant astrocytomas.** *Acta Neuropathol* 2020;139:603–08 CrossRef Medline
8. Louis DN, Wesseling P, Aldape K, et al. **cIMPACT-NOW update 6: new entity and diagnostic principle recommendations of the cIMPACT-UTRECHT meeting on future CNS tumor classification and grading.** *Brain Pathol* 2020;30:844–56 CrossRef Medline
9. Ellison DW, Aldape KD, Capper D, et al. **cIMPACT-NOW update 7: advancing the molecular classification of ependymal tumors.** *Brain Pathol* 2020;30:863–66 CrossRef Medline
10. Louis DN, Ellison DW, Brat DJ, et al. **cIMPACT-NOW: a practical summary of diagnostic points from Round 1 updates.** *Brain Pathol* 2019;29:469–72 CrossRef Medline
11. WHO Classification of Tumours Editorial Board. World Health Organization Classification of Tumours of the Central Nervous System. 5th ed: Lyon: International Agency for Research on Cancer; 2021

12. Batchala PP, Muttikkal TJ, Donahue JH, et al. **Neuroimaging-based classification algorithm for predicting 1p/19q-codeletion status in IDH-mutant lower grade gliomas.** *AJNR Am J Neuroradiol* 2019;40:426–42 CrossRef Medline
13. Patel SH, Poisson LM, Brat DJ, et al. **T2-FLAIR mismatch, an imaging biomarker for IDH and 1p/19q status in lower-grade gliomas: a TCGA/TCIA project.** *Clin Cancer Res* 2017;23:6078–85 CrossRef Medline
14. Doig D, Kachramanoglou C, Dumba M, et al. **Characterisation of isocitrate dehydrogenase gene mutant WHO grade 2 and 3 gliomas: MRI predictors of 1p/19q co-deletion and tumour grade.** *Clin Radiol* 2021;76:785 CrossRef Medline
15. Chen Y, Tian T, Guo X, et al. **Polymorphous low-grade neuroepithelial tumor of the young: case report and review focus on the radiological features and genetic alterations.** *BMC Neurol* 2020;20:123 CrossRef Medline
16. Benson JC, Summerfield D, Carr C, et al. **Polymorphous low-grade neuroepithelial tumor of the young as a partially calcified intra-axial mass in an adult.** *AJNR Am J Neuroradiol* 2020;41:573–78 CrossRef Medline
17. Ryall S, Zapotocky M, Fukuoka K, et al. **Integrated molecular and clinical analysis of 1,000 pediatric low-grade gliomas.** *Cancer Cell* 2020;37:569–83 CrossRef Medline
18. Ross JL, Velazquez Vega J, Plant A, et al. **Tumor immune landscape of paediatric high-grade gliomas.** *Brain* 2021;144:2594–2609 CrossRef Medline
19. Roux A, Pallud J, Saffroy R, et al. **High-grade gliomas in adolescents and young adults highlight histomolecular differences from their adult and pediatric counterparts.** *Neuro Oncol* 2020;22:1190–1202 CrossRef Medline
20. Yekula A, Gupta M, Coley N, et al. **Adult H3K27M-mutant diffuse midline glioma with gliomatosis cerebri growth pattern: case report and review of the literature.** *Int J Surg Case Rep* 2020;68:124–28 CrossRef Medline
21. Aboian MS, Solomon DA, Felton E, et al. **Imaging characteristics of pediatric diffuse midline gliomas with histone H3 K27M mutation.** *AJNR Am J Neuroradiol* 2017;38:795–800 CrossRef Medline
22. Muñoz Pérez JP, Muchart J, Santa-María López V, et al. **Targeted therapy for pediatric low-grade glioma.** *Childs Nerv Syst* 2021;37:2511–20 CrossRef Medline
23. Bender K, Perez E, Chirica M, et al. **High-grade astrocytoma with piloid features (HGAP): the Charite experience with a new central nervous system tumor entity.** *J Neurooncol* 2021;153:109–20 CrossRef Medline
24. Chen W, Soon YY, Pratiseyo PD, et al. **Central nervous system neuroepithelial tumors with MN1-alteration: an individual patient data meta-analysis of 73 cases.** *Brain Tumor Pathol* 2020;37:145–53 CrossRef Medline
25. Hirose T, Nobusawa S, Sugiyama K, et al. **Astroblastoma: a distinct tumor entity characterized by alterations of the X chromosome and MN1 rearrangement.** *Brain Pathol* 2018;28:684–94 CrossRef Medline
26. Mhatre R, Sugur HS, Nandeesh BN, et.al. **MN1 rearrangement in astroblastoma: study of eight cases and review of literature.** *Brain Tumor Pathol* 2019;36:112–20 CrossRef Medline
27. Deng MY, Sill M, Sturm D, et al. **Diffuse glioneuronal tumour with oligodendroglioma-like features and nuclear clusters (DGONC): a molecularly defined glioneuronal CNS tumour class displaying recurrent monosomy 14.** *Neuropathol Appl Neurobiol* 2020;46:422–30 CrossRef Medline
28. Lucas CH, Villanueva-Meyer JE, Whipple N, et al. **Myxoid glioneuronal tumor, PDGFRA p.K385-mutant: clinical, radiologic, and histopathologic features.** *Brain Pathol* 2020;30:479–94 CrossRef Medline
29. Chiang JC, Harreld JH, Tanaka R, et al. **Septal dysembryoplastic neuroepithelial tumor: a comprehensive clinical, imaging, histopathologic, and molecular analysis.** *Neuro Oncol* 2019;21:800–08 CrossRef Medline
30. Lecler A, Broquet V, Bailleux J, et al. **Advanced multiparametric magnetic resonance imaging of multinodular and vacuolating neuronal tumor.** *Eur J Neurol* 2020;27:1561–69 CrossRef Medline
31. Nunes RH, Hsu CC, da Rocha AJ, et al. **Multinodular and vacuolating neuronal tumor of the cerebrum: a new "leave me alone" lesion with a characteristic imaging pattern.** *AJNR Am J Neuroradiol* 2017;38:1899–1904 CrossRef Medline
32. Lecler A, Bailleux J, Carsin B, et al; ENIGMA Investigation Group (EuropeaN Interdisciplinary Group for MVNT Analysis). **Multinodular and vacuolating posterior fossa lesions of unknown significance.** *AJNR Am J Neuroradiol* 2019;40:1689–94 CrossRef Medline
33. Kupp R, Ruff L, Terranova S, et al. **ZFTA-translocations constitute ependymoma chromatin remodeling and transcription factors.** *Cancer Discov* 2021;11:2216–29 CrossRef Medline
34. Wang G, Jia Y, Ye Y, et al. **Identification of key methylation differentially expressed genes in posterior fossa ependymoma based on epigenomic and transcriptome analysis.** *J Transl Med* 2021;19:174 CrossRef Medline
35. Witt H, Mack SC, Ryzhova M, et al. **Delineation of two clinically and molecularly distinct subgroups of posterior fossa ependymoma.** *Cancer Cell* 2011;20:143–57 CrossRef Medline
36. Raffeld M, Abdullaev Z, Pack SD, et al. **High level MYCN amplification and distinct methylation signature define an aggressive subtype of spinal cord ependymoma.** *Acta Neuropathol Commun* 2020;8:101 CrossRef Medline
37. Reis J, Stahl R, Zimmermann H, et al. **Advanced MRI findings in medulloblastomas: relationship to genetic subtypes, histopathology, and immunohistochemistry.** *J Neuroimaging* 2021;31:306–16 CrossRef Medline
38. Coltin H, Sundaresan L, Smith KS, et al. **Subgroup and subtype-specific outcomes in adult medulloblastoma.** *Acta Neuropathol* 2021;142:859–71 CrossRef Medline
39. Skowron P, Farooq H, Cavalli FM, et al. **The transcriptional landscape of SHH medulloblastoma.** *Nat Comm* 2021;12:1749 CrossRef Medline
40. Cai C. **SWI/SNF deficient central nervous system neoplasms.** *Semin Diagn Pathol* 2021;38:167–74 CrossRef Medline
41. Tauziede-Espariat A, Pierron G, Seigfried A, et al. **The EP300:BCOR fusion extends the genetic alteration spectrum defining the new tumoral entity of "CNS tumors with BCOR internal tandem duplication."** *Acta Neuropathol Commun* 2020;8:178 CrossRef Medline
42. Shih RY, Koeller KK. **Embryonal tumors of the central nervous system: from the radiologic pathology archives.** *Radiographics* 2018;38:525–41 CrossRef Medline
43. Korshunov A, Okonechnikov K, Schmitt-Hoffner F, et al. **Molecular analysis of pediatric CNS-PNET revealed nosologic heterogeneity and potent diagnostic markers for CNS neuroblastoma with FOXR2-activation.** *Acta Neuropathol Commun* 2021;9:20 CrossRef Medline
44. Thomas C, Wefers A, Bens S, et al. **Desmoplastic myxoid tumor, SMARCB1-mutant: clinical, histopathological and molecular characterization of a pineal region tumor encountered in adolescents and adults.** *Acta Neuropathol* 2020:277–86 CrossRef Medline
45. Louis DN, Perry A, Wesseling P, et.al. **The 2021 WHO Classification of Tumors of the Central Nervous System: a summary.** *Neuro Oncol* 2021;23:1231–51 CrossRef Medline
46. Lopes MB. **The 2017 World Health Organization Classification of Tumors of the Pituitary Gland: a summary.** *Acta Neuropathol* 2017;134:521–55 CrossRef Medline

MR Signal Abnormalities at 1.5 T in Alzheimer's Dementia and Normal Aging

Franz Fazekas[1]
John B. Chawluk[2]
Abass Alavi[1]
Howard I. Hurtig[2]
Robert A. Zimmerman[1]

The type, frequency, and extent of MR signal abnormalities in Alzheimer's disease and normal aging are a subject of controversy. With a 1.5-MR unit we studied 12 Alzheimer patients, four subjects suffering from multiinfarct dementia and nine age-matched controls. Punctate or early confluent high-signal abnormalities in the deep white matter, noted in 60% of both Alzheimer patients and controls, were unrelated to the presence of hypertension or other vascular risk factors. A significant number of Alzheimer patients exhibited a more extensive smooth "halo" of periventricular hyperintensity when compared with controls (p = .024). Widespread deep white-matter hyperintensity (two patients) and extensive, irregular periventricular hyperintensity (three patients) were seen in multiinfarct dementia. Areas of high signal intensity affecting hippocampal and sylvian cortex were also present in five Alzheimer and two multiinfarct dementia patients, but absent in controls. Discrete, small foci of deep white-matter hyperintensity are not characteristic of Alzheimer's disease nor do they appear to imply a vascular cause for the dementing illness. The frequently observed "halo" of periventricular hyperintensity in Alzheimer's disease may be of diagnostic importance. High-signal abnormalities in specific cortical regions are likely to reflect disease processes localized to those structures.

Alzheimer's disease is estimated as the underlying cause in 50–60% of dementia cases [1]. Therefore, it represents a serious health problem for the elderly, with about 15% of those over 65 demonstrating some degree of dementia [2]. Although the ability to diagnose Alzheimer's disease clinically has improved [3], there is still a need to increase the accuracy of in vivo diagnosis. MR imaging has shown unprecedented sensitivity in detecting pathologic changes of the brain and has the potential to contribute to this goal.

The occurrence of white-matter signal abnormalities on MR has been noted with increasing age [4–6], and extensive white-matter damage has been demonstrated in patients suffering from presumed vascular dementia [5, 7, 8]. However, reports dealing with the MR appearance of Alzheimer's disease have been anecdotal and controversial. Whereas some investigators have found no signal abnormalities in Alzheimer's disease [9], others have reported almost as many abnormalities as are seen in multiinfarct dementia (MID) [10]. More information is needed to evaluate fully the potential of MR in the diagnosis of dementia.

This report attempts to describe the type and frequency of signal abnormalities that may be observed in patients with a clinical diagnosis of Alzheimer's disease and contrasts these with findings in healthy elderly controls and patients with MID. To our knowledge this is the first time a high-field MR system has been used to address this question.

Subjects and Methods

The 25 subjects in this study were selected from a group of elderly individuals currently under investigation at our institution for cerebral abnormalities associated with normal aging

This article appears in the May/June 1987 issue of *AJNR* and the August 1987 issue of *AJR*.

Received September 19, 1986; accepted after revision December 9, 1986.

This work was supported by NIA Teaching Nursing Home grant P01AG03934 and NIH Clinical Research Center grant 5–M01RR00040.

[1] Department of Radiology, Divisions of Nuclear Medicine and Neuroradiology, Hospital of the University of Pennsylvania, 3400 Spruce St./G1, Philadelphia, PA 19104. Address reprint requests to A. Alavi (Nuclear Medicine).

[2] Department of Neurology, Cerebrovascular Research Center, Hospital of the University of Pennsylvania, Philadelphia, PA 19104.

***AJR* 149:351–356, August 1987**
0361–803X/87/1492-0351
© American Roentgen Ray Society

and dementia. These subjects were carefully screened by a neurologist and underwent a comprehensive laboratory evaluation consisting of an automated blood chemistry battery, tests for vitamin B12 deficiency and thyroid dysfunction, as well as ECG, electroencephalogram, and chest radiograph. All subjects underwent CT, MR, and positron emmission tomography scanning. The mini-mental state examination [11] and the Blessed dementia scale [12] were included as part of the neuropsychological test battery.

In 12 subjects a diagnosis of Alzheimer's disease was established according to clinical diagnostic criteria set forth in the DSM III (*Diagnostic and Statistical Manual of Mental Disorders*) [13] and expanded on by an NINCDS–ADRDA consensus committee [14]. All Alzheimer patients scored 2 or less on a modification of Hachinski's vascular dementia scale [15] and demonstrated no other clinical cause for their dementing illness. In four other demented subjects a Rosen-Hachinski score [15] of greater than 4 suggested a multiinfarct state as the cause of dementia. Impairment was defined by mini-mental state examination scores as mild (>20), moderate (11–20), and severe (10 or less). Nine healthy elderly control subjects were also studied and were found to be free of any neurologic, psychiatric, or major systemic illnesses, although one subject had diabetes and two had a history of hypertension. The mean ages in these groups were 69 (Alzheimer), 70 (MID), and 68 (healthy controls) years old, respectively.

MR was performed on a General Electric imaging unit with a superconducting magnet to generate a field strength of 1.5 T. Image acquisition was performed with a spin-echo technique, the pulse sequences being repetition time (TR) 600–800 msec/echo time (TE) 20–25 msec for T1-weighted and TR 1500–2500 msec/TE 25–120 msec for T2-weighted images. Sagittal, axial, and coronal scans were available in every subject and interpreted by a neuroradiologist blinded to the clinical diagnosis.

A modification of suggested rating scales [5, 6] was used to describe the different types of hyperintense signal abnormalities surrounding the ventricles and in the deep white matter. Periventricular hyperintensity (PVH) was graded as 0 = absence, 1 = "caps" or pencil-thin lining, 2 = smooth "halo," 3 = irregular PVH extending into the deep white matter. Separate deep white matter hyperintense signals (DWMH) were rated as 0 = absence, 1 = punctate foci, 2 = beginning confluence of foci, 3 = large confluent areas.

The occurrence of these types of abnormality as well as the presence of other signal intensity changes were recorded for dementia patients (Alzheimer and MID) and controls, and compared among the groups. The effects of age, vascular risk factors, and dementia severity on the degree and nature of the signal abnormalities were assessed.

Results

MR revealed a variety of signal abnormalities in controls, as well as in patients with Alzheimer's disease and MID. These findings together with the subjects' clinical data are listed in Table 1 and are discussed below.

TABLE 1: Clinical Features and MR Findings in Alzheimer's Disease, Multiinfarct Dementia, and Normal Aging

Group: Case No.	Age	Duration (years)	Severity	Risk Factors	Grade		Other
					PVH	DMWH	
Probable Alzheimer's disease:							
1	70	3	Mild	H, CAD	2	0	CH
2	66	3	Mild	H	0	0	...
3	66	3	Moderate	H	2	0	...
4	77	6	Moderate	...	2	0	CH
5	80	4	Moderate	...	1	2	CH
6	61	3	Severe	...	1	1	...
7	68	10	Severe	H	1	2	...
Possible Alzheimer's disease:							
8	52	1	Mild	...	0	0	...
9	62	6	Moderate	...	2	2	CH
10	71	2	Moderate	...	2	2	CH
11	77	3	Moderate	H, D	1	1	...
12	73	5	Severe	...	2	1	...
Multiinfarct dementia:							
13	64	6	Mild	H	3	3	BGL, I
14	74	3	Moderate	H, CAD	3	3	BGL, CH
15	63	3	Moderate	H	3	2	I
16	80	1	Severe	H	1	1	BGL, CH
Control:							
17	52	...	...	D	0	1	...
18	70	...	...	...	1	1	...
19	64	...	...	...	0	0	...
20	61	...	...	H	0	0	...
21	68	...	...	...	0	2	...
22	76	...	...	...	1	0	...
23	76	...	...	...	1	2	BGL
24	83	...	...	H	3	2	...
25	65	...	...	...	0	0	...

Note.—PVH = periventricular hyperintensity; DWMH = deep white-matter hyperintensity; H = hypertension; CAD = coronary artery disease; CH = cortical hyperintensity; D = diabetes mellitus; BGL = basal ganglionic lesions; I = "classical" infarcts (infarcts confined to typical vascular territories).

Periventricular Hyperintensity

In controls, areas of abnormal high signal intensity around the ventricles were either absent or seen as caps or a pencil-thin lining of periventricular hyperintensity (PVH) (Fig. 1). The sole exception was a grade-3 PVH pattern in a healthy 83-year-old individual with a history of hypertension. PVH was noted in 10 of 12 Alzheimer subjects, with six showing a halo (Fig. 2C) of high signal intensity around the ventricles. The proportion of Alzheimer patients with a PVH score of 2 was significantly different from that in controls (Table 2). In contrast to Alzheimer patients and controls, three MID subjects (75%) showed an irregular PVH extending into the deep white matter (Fig. 3B).

Deep White-Matter Hyperintensity

The incidence and extent of deep white-matter hyperintensity (DWMH) seen in Alzheimer patients was comparable to that observed in controls. About 60% of all subjects had some foci of DWMH. However, confluent areas of DWMH (Fig. 3) were present only in MID (two patients) (Table 2).

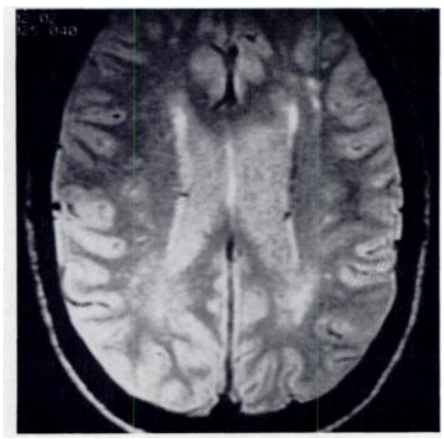

Fig. 1.—Case 18: 70-year-old male control subject with no vascular risk factors. Pencil-thin line of hyperintensity (grade 1) surrounds ventricles. Punctate foci of high signal intensity (grade 1) in deep white matter.

TABLE 2: Incident and Extent of MR Abnormalities in Alzheimer's Disease, Multiinfarct Dementia, and Normal Controls

Abnormality	No. of Patients		
	Controls	Alzheimer's disease	Multiinfarct Dementia
Periventricular hyperintensity (grade):			
0–1	8	6	1
2	0	6*	0
3	1	0	3
Deep white-matter hyperintensity (grade):			
0	4	5	0
1	2	3	1
2	3	4	1
3	0	0	2
Type of lesion:			
Cortical hyperintensity	0	5	2
Basal ganglionic foci	1	0	3
Infarct	0	0	2

* The proportion of Alzheimer patients with grade 2 periventricular hyperintensity differs significantly from that in controls ($p = .024$).

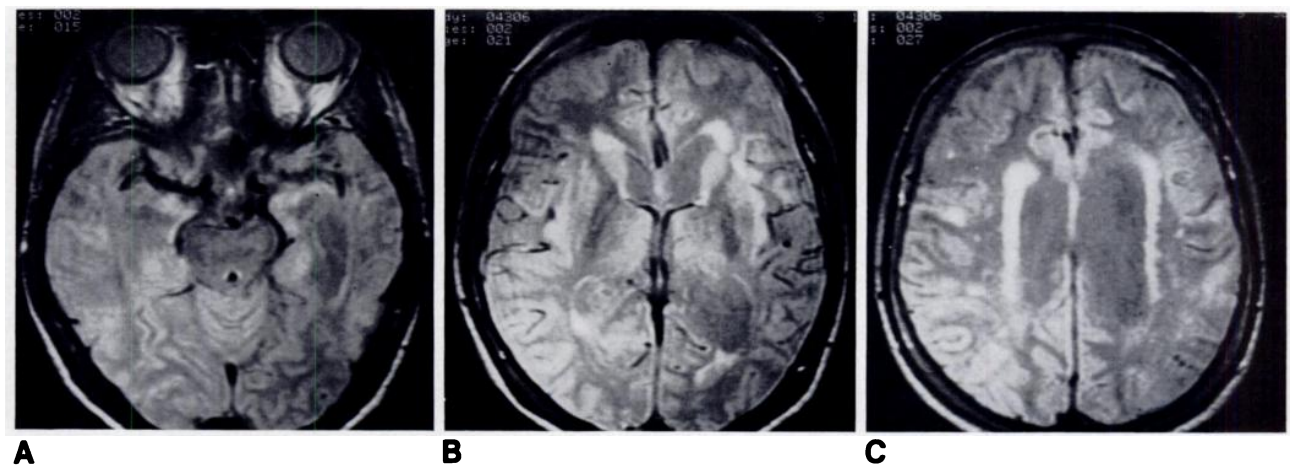

Fig. 2.—Case 9: 62-year-old woman with Alzheimer's disease and no vascular risk factors.
***A*, Signal intensity of hippocampal cortex is increased bilaterally.**
***B*, Sylvian cortex on left and right are of high signal intensity; hyperintense areas are present at tips of ventricles.**
***C*, Smooth halo of hyperintensity (grade 2) surrounds ventricles; punctate foci of high signal intensity are noted in subcortical white matter. Beginning confluence of these foci (not shown) was present on more inferior sections.**

Miscellaneous Findings

Areas of high signal intensity in cortical regions were also noted on some MR studies. In five Alzheimer patients the cortex of the sylvian and/or hippocampal-uncal regions appeared bright on T2-weighted images (Figs. 2A and 2B). Similar changes were seen in two MID subjects but were not seen in any of the controls. MR of Alzheimer subjects revealed no basal ganglionic lesions or "classical" infarcts. However, such abnormalities were common in MID (Table 2).

Correlation of MR Findings with Clinical Data

The presence of a halo of PVH in Alzheimer subjects was not correlated with the severity of dementia, nor was there a correlation of dementia severity with any other signal abnormality detected in these individuals. There was no relationship between a type 1 or 2 PVH or DWMH and vascular risk factors (see Table 1). There was a history of hypertension, however, in all subjects with an irregular PVH extending into the deep white matter or with confluent areas of DWMH (grade 3 lesions). PVH and DWMH were observed more often in the older subjects in this series, but the presence or type of white-matter signal abnormality could not be predicted on the basis of a subject's age. All subjects without any PVH abnormalities, however, were younger than 70 years.

Discussion

In recent years the routine neuroimaging study of the brain in Alzheimer's disease has been CT, the aim being to exclude possible treatable causes of the dementia. Otherwise, the capabilities of CT in supporting the diagnosis of Alzheimer's disease have been restricted to imaging diffuse cerebral atrophy considered inappropriate for the patient's age. Reports on changes in brain density with Alzheimer's disease have been controversial [16, 17].

Early experience with MR has already demonstrated its greater sensitivity in detecting cerebral abnormalities in comparison with CT [18, 19]. This is particularly true for white-matter lesions, which can be detected readily by highlighting T2 relaxation with a long spin-echo pulse-sequence method [20]. The possibility of a distinct white-matter disorder in Alzheimer's disease reported recently in a pathoanatomic study by Brun and Englund [21] supports the rationale of applying MR in the evaluation of this disease. Nevertheless, the number of white-matter signal abnormalities observed in Alzheimer's disease in this study is somewhat surprising.

Our results support the observation that foci of high signal intensity in the deep white matter are commonly seen in clinically normal elderly individuals [5, 22]. In contrast to a report by Erkinjuntti et al. [9], a similar frequency and extent of such deep white-matter lesions were seen in Alzheimer patients. The more extensive signal changes in the deep white matter seen in two of our MID patients were recently described with vascular dementia [7, 8]. In our series such widespread lesions were not present either in Alzheimer patients or in controls. Therefore, such a finding should rule against a diagnosis of pure Alzheimer's disease. The extensive deep white-matter changes observed in an 85-year-old Alzheimer patient with a gait disturbance in the series of George et al. [22] presumably reflects marked vascular damage in addition to Alzheimer's disease. Therefore, this case would be classified as a mixed type of dementia [23], a speculation supported by the neuropathologic observations

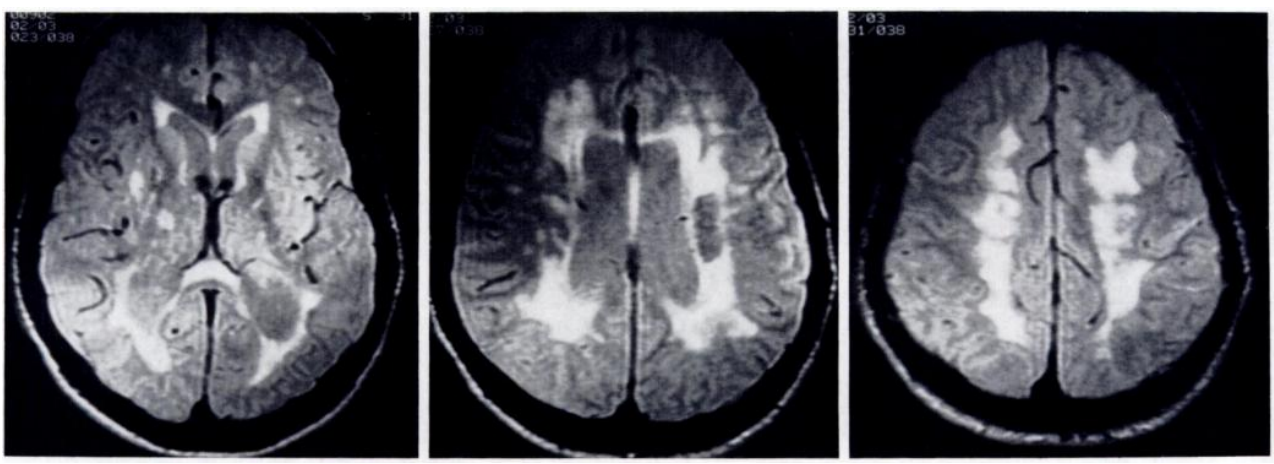

Fig. 3.—Case 13: 64-year-old man with multiinfarct dementia and history of hypertension.
***A*, Two hyperintense lesions in right putamen and thalamus; punctate foci of hyperintensity in left basal ganglia. Areas of hyperintensity surround tips of ventricles.**
***B*, Diffuse irregular hyperintensity surrounds ventricles and extends into deep white matter (grade 3).**
***C*, Confluent lesions of high signal intensity (grade 3) involve almost entire supraventricular deep white matter.**

of similar patients by the same authors [24]. In our experience the smaller white-matter lesions (punctate foci of hyperintensity or even beginning confluence of DWMH) are of no value in distinguishing Alzheimer patients from controls.

The white-matter signal abnormalities we have seen in our Alzheimer patients do not appear to be identical to the white-matter pathology described by Brun and Englund [21]. They observed large, diffuse, predominantly symmetric areas in the deep white matter with partial loss of axons, myelin sheaths, and oligodendroglial cells, accompanied by a mild reactive astrocytosis; in our series MR revealed only punctate or slightly confluent areas of high signal abnormality. Either these lesions do not produce enough change in tissue proton arrays to be fully detected by MR—their pathologic appearance being different from pronounced ischemic damage—or they have not been present in our patients. Pathologically confirmed severe ischemic changes in the deep white matter have been shown to cause extensive signal hyperintensity [7].

The similar extent, frequency, and distribution of the deep white-matter signal abnormalities seen in both healthy elderly individuals and Alzheimer patients suggest a common etiology. Possibilities include local ischemia or focal parenchymal degeneration due to aging. Whereas the presence of vascular risk factors was not correlated with the occurrence of such minor signal abnormalities, all patients (cases 13, 14, 15, and 24) with extensive deep white-matter disease or irregular PVH extending into the deep white matter (grade 3) had a history of hypertension.

The most distinctive finding in Alzheimer's disease in this study was a halo of high signal intensity surrounding the ventricles. This abnormality was detected in 50% of Alzheimer patients and was not present in controls or MID. In a review of 365 cerebral cases studied by MR, a similar pattern of PVH was invariably associated with a specific disease process, for example, hydrocephalus, supratentorial neoplasms, trauma, and rarely white-matter disease [6]. Given the smooth margin of this halolike abnormality, it seems unlikely that ischemia or demyelination would be the cause. It may rather represent an exaggeration of a similar process that has been hypothesized to cause the pencil-thin lining of PVH, more often observed in older subjects with otherwise normal MR studies [6]. This latter hypothesis is supported by our data, since all patients without PVH were younger than 70 years. It has been suggested that the periventricular subependymal lining of hyperintensity reflects an increase in interstitial water reabsorption from the white matter into the ventricles [6]. This explanation is consistent with the observation that caps of PVH seem to be present first, since the area that has to be drained of interstitial water will be greatest for the tips of the ventricles. In patients with Alzheimer's disease this bulk flow to the ventricles would therefore seem to be further enhanced. Unfortunately, no studies directly address the question of interstitial water content in Alzheimer's disease, although there is some indirect support from previous radiologic studies. Besson et al. [25], calculating the proton density of white matter on MR scans, reported a water content of white matter in Alzheimer's disease that was significantly increased over that of both controls and MID patients. Similarly, the finding of decreased white-matter density on CT [16] is consistent with increased interstitial water. White-matter changes such as those described by Brun and Englund [21] might be the underlying pathologic substrate, and MR might detect their distant effects as increased periventricular water rather than as the actual lesion.

Although its pathologic basis may not be clear, the appearance of the halo of hyperintensity in Alzheimer's disease is an important empirical observation. To date this pattern of PVH has been mostly ascribed to hydrocephalus [6] and has been claimed to be a very reliable diagnostic sign in normal-pressure hydrocephalus [26]. Since normal-pressure hydrocephalus might be considered in the differential diagnosis of Alzheimer's disease, yet requires substantially different management, the notion of a similar PVH pattern in Alzheimer's disease may be critical. Our subjects suffering from Alzheimer's disease had no clinical or radiologic signs suggestive of normal-pressure hydrocephalus.

On the basis of the above discussion, one may speculate that the rim of PVH in normal subjects widens with advancing age, making it similar to that of Alzheimer patients. Our experience with MR in normal patients over 80 years old is too limited to evaluate this possibility.

In accordance with pathologic [23] and CT data, MR detected no typical infarcts or basal ganglionic lesions in Alzheimer patients. Such abnormalities were also absent in controls, except for a tiny lenticular nucleus signal abnormality seen in one normal individual. Basal ganglionic lesions seem to be an important feature in MID, however, confirming previous CT reports [27].

Areas of cortical hyperintensity were present in five Alzheimer and two MID patients. It is likely that such abnormalities affecting the hippocampus reflect changes that have occurred in the cortical structure. A disturbed quantitative relationship of neurons to glia and associated degenerative changes (that is, a high number of senile plaques and fibrillary tangles) may be the basis for these signal-intensity changes. The topography of these histopathologic alterations seen in Alzheimer's disease corresponds well with the hippocampal hyperintensity detected on MR [28]. Congophilic angiopathy affecting cortical vessels with secondary parenchymal changes may represent another possible explanation for the observed hyperintense cortical signals. Pathologically those changes have been reported to occur less often in the hippocampus, however, than in other regions of the brain [29].

In summary, MR has demonstrated its ability to detect parenchymal changes in the brains of Alzheimer patients who have not been seen before with high-resolution CT. The implication of a signal abnormality differs with its type. Small discrete foci of DWMH are neither characteristic of Alzheimer's disease nor do they implicate a vascular cause of dementia, since they are seen to a similar extent in healthy elderly individuals. Furthermore, these punctate lesions appear to be unrelated to the presence of vascular risk factors. A smooth halo of PVH, however, is a distinctive finding in Alzheimer's disease. Areas of cortical signal hyperintensity observed in Alzheimer patients may reflect the disease process itself.

REFERENCES

1. Terry RD, Katzman R. Senile dementia of the Alzheimer type. *Ann Neurol* **1983**;14:497–506
2. Katzman R. The prevalence and malignancy of Alzheimer disease. *Arch Neurol* **1976**;33:217–218
3. Ron MA, Toone BK, Garralda ME, Lishman WA. Diagnostic accuracy in presenile dementia. *Br J Psychiatry* **1979**;134:161–168
4. Bradley WG Jr, Waluch V, Brant-Zawadzki M, Yadley RA, Wycoff RR. Patchy, periventricular white matter lesions in the elderly: a common observation during NMR imaging. *Noninvasive Med Imaging* **1984**;1:35–41
5. Brant-Zawadzki M, Fein G, Van Dyke C, Kiernan R, Davenport L, de Groot J. MR imaging of the aging brain: patchy white-matter lesions and dementia. *AJNR* **1985**;6:675–682
6. Zimmerman RD, Fleming CA, Lee BCP, Saint-Louis LA, Deck MDF. Periventricular hyperintensity as seen by magnetic resonance: prevalence and significance. *AJNR* **1986**;7:13–20, *AJR* **1986**;146:443–450
7. Kinkel WR, Jacobs L, Polachini I, Bates V, Heffner RR Jr. Subcortical arteriosclerotic encephalopathy (Binswanger's disease). Computed tomographic, nuclear magnetic resonance, and clinical correlations. *Arch Neurol* **1985**;42:951–959
8. Alavi A, Fazekas F, Chawluk J, Zimmerman R. Magnetic resonance imaging of the brain in normal aging and dementia. Presented at the Conference on Cerebrovascular Disease, Salzburg, Austria, September **1986**
9. Erkinjuntti T, Sipponen JT, Iivanainen M, Ketonen L, Sulkava R, Sepponen RE. Cerebral NMR and CT imaging in dementia. *J Comput Assist Tomogr* **1984**;8:614–618
10. Cherryman GR, Gemmell HG, Sharp PF, Besson JAO, Crawford J, Smith FW. NMR demonstration of white matter changes in the watershed area of patients with dementia. Correlation with psychiatric evaluation and J-123-isopropylamphetamine cerebral blood flow imaging. Presented at the international meeting of the Society of Magnetic Resonance in Medicine, London, August **1985**
11. Folstein MF, Folstein SE, McHugh PR. "Mini-mental state": a practical method for grading the cognitive state of patients for the clinician. *J Psychiatr Res* **1975**;12:189–198
12. Blessed G, Tomlinson BE, Roth M. The association between quantitative measures of dementia and of senile change in the cerebral gray matter of elderly subjects. *Br J Psychiatry* **1968**;114:797–811
13. American Psychiatric Association. *Diagnostic and statistical manual of mental disorders*, 3d ed. Washington, DC: American Psychiatric Association, **1980**
14. McKhann G, Drachman D, Folstein M, Katzman R, Price D, Stadlan EM. Clinical diagnosis of Alzheimer's disease. *Neurology* **1984**;34:939–944
15. Rosen WG, Terry RD, Fuld PA, Katzman R, Peck A. Pathological verification of ischemic score in differentiation of dementias. *Ann Neurol* **1980**;7:486–488
16. Naeser MA, Gebhardt C, Levine HL. Decreased computerized tomography numbers in patients with presenile dementia. *Arch Neurol* **1980**;37:401–409
17. George AE, de Leon MJ, Ferris SH, Kricheff II. Parenchymal CT correlates of senile dementia (Alzheimer disease): loss of gray-white matter discriminability. *AJNR* **1981**;2:205–213
18. Bradley WG, Waluch V, Yadley RA, Wycoff RR. Comparison of CT and MR in 400 patients with suspected disease of the brain and cervical spinal cord. *Radiology* **1984**;152:695–702
19. Baker HL, Berquist TH, Kispert DB, et al. Magnetic resonance imaging in a routine clinical setting. *Mayo Clin Proc* **1985**;60:75–90
20. Brant-Zawadzki M, Norman D, Newton TH, et al. Magnetic resonance of the brain: the optimal screening technique. *Radiology* **1984**;152:71–77
21. Brun A, Englund E. A white matter disorder in dementia of the Alzheimer type: a pathoanatomical study. *Ann Neurol* **1986**;19:253–262
22. George AE, de Leon MJ, Kalnin A, Rosner L, Goodgold A, Chase N. Leukoencephalopathy in normal and pathologic aging: 2. MRI of brain lucencies. *AJNR* **1986**;7:567–570
23. Tomlinson BE, Blessed G, Roth M. Observations on the brains of demented old people. *J Neurol Sci* **1970**;11:205–242
24. George AE, de Leon MJ, Gentes CI, et al. Leukoencephalopathy in normal and pathologic aging: 1. CT of brain lucencies. *AJNR* **1986**;7:561–566
25. Besson JAO, Corrigan FM, Foreman I, Eastwood LM, Smith FW, Ashcroft GW, Nuclear magnetic resonance (NMR): 2. Imaging in dementia. *Br J Psychiatry* **1985**;146:31–35
26. Kortman KE, Bradley WG. Magnetic resonance imaging of normal pressure hydrocephalus. Presented at the annual meeting of the American Society of Neuroradiology, New Orleans, February **1985**
27. Ladurner G, Iliff LD, Sager WD, Lechner H. A clinical approach to vascular (multiinfarct) dementia. In: Meyer JS, Lechner H, Reivich M, Ott EO, eds. *Cerebral vascular disease 4*. Amsterdam: Excerpta Medica, **1983**:236–243
28. Englund E, Brun A. Senile dementia—a structural basis for etiological and therapeutic considerations. In: Perris C, Struwe G, Jansson B, eds. *Biological psychiatry*. Amsterdam: Elsevier, **1981**:951–956
29. Vinters HV, Gilbert JJ. Cerebral amyloid angiopathy: incidence and complications in the aging brain. 2. The distribution of amyloid vascular changes. *Stroke* **1983**;14:924–928

PHYSICS REVIEW

Susceptibility-Weighted Imaging: Technical Aspects and Clinical Applications, Part 1

E.M. Haacke
S. Mittal
Z. Wu
J. Neelavalli
Y.-C.N. Cheng

SUMMARY: Susceptibility-weighted imaging (SWI) is a new neuroimaging technique, which uses tissue magnetic susceptibility differences to generate a unique contrast, different from that of spin density, T1, T2, and T2*. In this review (the first of 2 parts), we present the technical background for SWI. We discuss the concept of gradient-echo images and how we can measure local changes in susceptibility. Armed with this material, we introduce the steps required to transform the original magnitude and phase images into SWI data. The use of SWI filtered phase as a means to visualize and potentially quantify iron in the brain is presented. Advice for the correct interpretation of SWI data is discussed, and a set of recommended sequence parameters for different field strengths is given.

Susceptibility-weighted imaging (SWI) is a new means to enhance contrast in MR imaging.[1-56] Until recently, with the exception of phase being used for large-vessel flow quantification or for use in inversion recovery sequences, most diagnostic MR imaging relied only on the reading of magnitude information. The phase information was ignored and usually discarded before even reaching the viewing console. Phase images, however, contain a wealth of information about local susceptibility changes between tissues,[1,22,26,57-63] which can be useful in measuring iron content[26] and other substances that change the local field. The effects of other background magnetic fields presented a major problem by obscuring the useful phase information. Hence, for nearly 20 years, phase information in flow-compensated sequences went essentially unused as a means to measure susceptibility in clinical MR imaging.

In 1997, we developed a means to remove most of the unwanted phase artifacts and keep just the local phase of interest.[1] This set the stage for discovering other aspects of susceptibility imaging and even hinted at the future direction of susceptibility mapping.[26] We began to see different types of contrast in the SWI filtered phase images for different diseases. To make the information more accessible to radiologists, though phase and magnitude images separately are also critical pieces of information, we combined the phase and the magnitude information and thus created a new susceptibility-weighted magnitude image, which today is referred to as SWI.[22] This new pair of images (the SWI filtered phase data and the merged SWI magnitude data) is now available on at least 1 major manufacturer's systems (Siemens Medical Systems), though it took almost 10 years to see the actual implementation of this approach in a clinical setting around the world.

Many technical developments take years to leave the research environment and become part of standard radiology applications. This has been true for perfusion imaging, diffusion tensor imaging, magnetization transfer imaging, and also for SWI. The common feature of these methods is that they originated as good scientific ideas; they were simulated at first and then tested on phantoms, on volunteers, and finally on a few patients with the appropriate institutional review board approvals from the local institution where the research took place. These methods became scientifically adopted on a larger scale once they showed how clinically capable they were. If successful, the National Institutes of Health would grant funds for broader testing of these methods. Finally, with proof of the value of the method in place and with a stable software package, it would be possible for hundreds of institutions to begin using these methods for diagnostic purposes. However, even then, the final goal will not have been achieved. The method would still need to be adopted in a broad clinical environment and then executed as a standard "neuroprotocol" on a clinical platform. Once the latter step has taken place, the method should eventually be adopted by the radiology community as a whole and become part and parcel of conventional educational courses offered at radiology meetings for accreditation. Only then could we say that a method is fully incorporated into the international radiology routine.

In this review, we summarize the motivation behind SWI, the concepts that led to its discovery, the optimal parameters to use, and the interpretation of the SWI processed data and phase images; and we conclude by discussing the technology in use today, the postprocessing, and future directions of SWI research.

MR imaging has already an overabundance of different approaches for investigational anatomic, functional, and metabolic imaging. Each method focuses on a new issue, such as the delivery of blood to the tissue in perfusion-weighted imaging or molecular motion along a fiber track in diffusion tensor imaging. The susceptibility information is an adjunct to what is available with conventional spin density, T1-, and T2-weighted imaging methods. SWI offers information about any tissue that has a different susceptibility than its surrounding structures such as deoxygenated blood, hemosiderin, ferritin, and calcium. There are numerous neurologic disorders that can benefit dramatically from a very sensitive method that monitors the amount of iron in the brain, whether in the form of deoxyhemoglobin, ferritin, or hemosiderin. Such diseases and conditions include, but are not limited to, aging, multiple sclerosis (MS), stroke, trauma, vascular malformations, and tumors. There is no doubt that as SWI becomes more broadly accepted, we will see many new applications develop because of the astute observations of clinical researchers and the wide

From the Departments of Radiology (E.M.H., Y.-C.N.C.), Biomedical Engineering (E.M.H., J.N., Y.-C.N.C.), and Neurosurgery (S.M.), Wayne State University, Detroit, Mich; Karmanos Cancer Institute (S.M.), Detroit, Mich; and Department of Biomedical Engineering (Z.W.), McMaster University, Hamilton, Ontario, Canada.

This work was supported in part by the National Institutes of Health grant NIH R01 NHLBI 62983-04 and Siemens Medical Systems.

Please address correspondence to E. Mark Haacke, PhD, Wayne State University, Detroit, MI; e-mail: nmrimaging@aol.com

Indicates open access to non-subscribers at www.ajnr.org

DOI 10.3174/ajnr.A1400

availability of information for the whole spectrum of neurologic diseases seen on a daily basis in the clinical setting.

Gradient-Echo Imaging

Historically, data were first collected with a free induction decay.[64,65] The concept of a spin-echo was invented only when it was seen that local field inhomogeneities had caused dramatic signal intensity loss. For some time, the spin-echo approach was the mainstay of clinical MR imaging for resistive machines.[66] Not long after the appearance of superconducting systems on the market, gradient-echo imaging[67-69] came back to life because the field uniformity in these systems was markedly better (and has continued to improve during the last 20 years). People quickly realized that they could eliminate most artifacts in magnitude images by running the gradient-echo scans with short TEs in sequences like magnetization-preparation rapid acquisition of gradient echo.[70] This high-bandwidth sequence had little distortion and offered excellent T1 contrast (and presented a good method to collect T1-weighted data even at 3T). Longer TEs were used in 2D gradient-echo imaging but with fairly thick sections, usually 3 or 4 mm. The TEs were often chosen to be 15, 20, or rarely 25 ms because of the signal-intensity loss associated with rapid phase changes across a voxel. Imaging with longer TEs, while maintaining image quality, was only possible with 3D gradient-echo imaging. Once this was recognized and resolutions on the order of ≤ 1 mm^3 were realized with a sufficient signal intensity–to-noise ratio (SNR), the ability to look at hidden information in phase data became possible.[57,71] Thus, the stage to study susceptibility effects was set in the mid 1990s, and the first article on SWI was published in 1997.[1] To appreciate the basic elements of SWI, we must first review the basic gradient-echo sequence design on which it is based.

In MR imaging, it is necessary to create some transverse magnetization first.[72] This can be accomplished by using a transmit coil to produce a radio-frequency (rf) pulse which tips the longitudinal magnetization (M_o) partially or completely into the transverse plane. The rf pulse is applied at the Larmor frequency, $\omega = \gamma B_o$. If M_o is rotated an angle θ about the x-axis, it will create a component along y that will be picked up by a receiver coil. The data are then encoded in both the phase- and partition-encoding directions (y and z, respectively, for a transverse acquisition), while a dephasing gradient is applied in the readout direction. The read gradient is then turned on and the data are sampled. After this, the remnant signal intensity is further dephased, and rf spoiling is applied by varying the axis about which the rf is applied so that no transverse magnetization remains before the next rf pulse. All this is shown pictorially in Fig 1. The magnitude signal-intensity response for this rf-spoiled short-TR gradient-echo sequence is given by

$$1)\quad \rho_m(\theta) = \rho_o \sin\theta \exp(-TE/T2^*)\times [1 - \exp(-TR/T1)] / [1 - \cos\theta \exp(-TR/T1)]$$

where ρ_o is the tissue spin density, TR is the repeat time of each data acquisition, T1 is the tissue longitudinal relaxation time, and θ is the angle by which the magnetization is tipped (usually called the flip angle). A signal-intensity behavior example is given for white matter, gray matter, and CSF for 1.5T and 3T (Fig 2 and Table 1). The full signal-intensity response is given by (for a right-handed system)

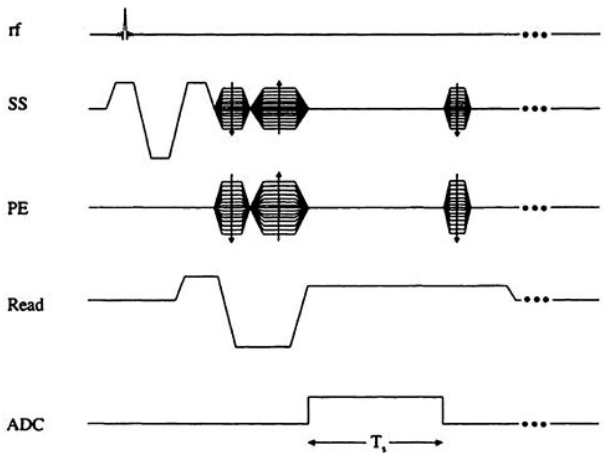

Fig 1. Gradient-echo sequence design. T_s refers to the sampling time interval. The gradient pulses are designed to give first-order flow compensation. SS indicates the slice-select gradient; PE, the phase-encoding gradient; ADC, analog-to-digital conversion.

$$2)\quad \rho(\theta) = \rho_m(\theta)\exp(-i\gamma\Delta B TE),$$

where ΔB represents the local field deviation caused by iron, for example, and γ is the gyromagnetic constant, which is equal to $2\pi \cdot 42.58$ MHz/T for protons. This can be rewritten as

$$3)\quad \rho(\theta) = \rho_m(\theta)\exp(-i\gamma g\Delta\chi B_o TE),$$

where g is a geometric factor, $\Delta\chi$ is the difference of the local magnetic susceptibility of the tissue of interest from its surroundings, and B_0 is the field strength. Starting with the Larmor equation

$$4)\quad \omega = \gamma B_o,$$

the expression for phase is

$$5)\quad \varphi = \omega t.$$

The change in phase between 2 tissues after a period of time, TE, can then be written as

$$\Delta\varphi = \Delta\omega TE,$$

where

$$\Delta\omega = \gamma\Delta B \text{ and } \Delta B = g\Delta\chi B_o$$

so that

$$6)\quad \Delta\varphi = -\gamma\Delta B TE$$

$$7)\quad \Delta\varphi = -\gamma g\Delta\chi B_o TE.$$

All of ΔB, $\Delta\chi$, and, therefore, $\Delta\varphi$ are dependent on the local tissue susceptibility.

Magnetic Susceptibility

Magnetic susceptibility is defined as the magnetic response of a substance when it is placed in an external magnetic field. When an object is placed inside a uniform magnetic field, the induced magnetization, M, is given by

$$8)\quad M = \chi H,$$

where

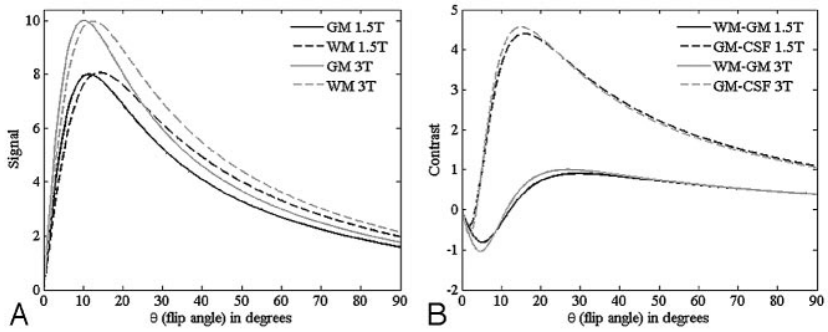

Fig 2. *A*, Plots showing the signal-intensity behavior as a function of flip angle for gray matter (GM) and white matter (WM) at field strengths 1.5T and 3T. *B*, Plots showing the corresponding contrast between GM-WM and GM-CSF. These curves are calculated taking into consideration the higher signal intensity available at 3T and assuming that bandwidth is correspondingly increased at 3T to ensure equivalent geometric distortion. Tissue parameters are given in Table 1. Note that the GM/WM contrast is highest around 20° at 3T and there is a minimum or reversal of contrast around 5° (where GM is now brighter than WM; ie, it is a high-contrast spin echo-weighted image).

Table 1: Tissue parameters used to simulate the T1-weighted images shown in Fig 2

	GM	WM	CSF
Spin density %	80	65	100
1.5T	1000 ms	650 ms	4000 ms
3T	1283 ms	838 ms	4000 ms

Note:—GM indicates gray matter; WM, white matter; CSF, cerebrospinal fluid. CSF is taken to have 100% water content.

$$H = B / \mu_o - M \quad (9)$$

and χ is the magnetic susceptibility relating M and H. We can also write

$$B = \mu H, \quad (10)$$

where $\mu = \mu_o \mu_r$ is the permeability, μ_o is the permeability in vacuum, μ_r is the relative permeability, and H the magnetic field (B is the induced magnetic field). Using the relative permeability as

$$\mu_r = 1 + \chi, \quad (11)$$

we find

$$M = \chi B/\mu_o/(1 + \chi). \quad (12)$$

For linear materials with $\chi \ll 1$, we find

$$M = \chi B/\mu_o, \quad (13)$$

and it becomes clear that the induced magnetization is directly proportional to the main field and the magnetic susceptibility. Each tissue or substance behaves somewhat differently in a magnetic field. For the purposes of this review, we shall consider only diamagnetic and paramagnetic substances. Diamagnetic substances have $\chi < 0$. For example, calcium in the body tends to be in the form of calcium phosphates such as $Ca_3(PO)_4$ and is diamagnetic. On the other hand, paramagnetic substances (ie, most iron-based materials or tissues) have $\chi > 0$. For example, deoxygenated blood has $\Delta\chi \approx 0.45$ ppm in SI units, relative to surrounding tissue. Moreover, iron-containing proteins, like ferritin and hemosiderin, tend to have varying susceptibilities depending on the amount of sequestered iron within the protein. Typically, on the basis of phase measurements from 75 subjects,[62] approximately a $\Delta\chi = 0.21$ ppm in SI units with respect to CSF, corresponds to 60 μg of iron (Fe) per gram of tissue (although this may underestimate the amount of Fe by a factor of 5). The susceptibilities of most biologic tissues[73] tend to be $<10^{-4}$. However, all forms of iron may not be visible with MR imaging if $\Delta\chi = 0$ for that substance. This can happen if the iron is shielded by other elements such as oxygen. For a more detailed description of the different forms of magnetism see Schenck[73] and Saini et al.[74]

Geometry Effects

The induced magnetization (owing to its susceptibility) in an object within a uniform external magnetic field distorts the uniform field outside the object. The spatial distribution of this deviation in the external applied field is a function of the geometry of the object.[75] The local field deviation inside and around an object is of interest because it gives rise to local phase differences in MR imaging. When discussing the effects of geometry on local field variations, we usually neglect the background field and assume that $\chi \ll 1$. For a cylinder making an angle θ to the main field, the effect on the field inside the cylinder is given by

$$\Delta B_{in} = \Delta\chi B_o(3\cos^2\theta - 1)/6 + \chi_e B_o/3, \quad (14)$$

which includes the Lorentzian sphere term. We have used $\Delta\chi = \chi_i - \chi_e$. Here, χ_i and χ_e are the susceptibilities inside and outside the cylinder, respectively. Generally, when we are looking at changes in local tissue fields, the final term $\chi_e B_o / 3$ no longer plays a role because it is a common constant both inside and outside the object. If we write

$$\Delta B_{in} = g_{in}\Delta\chi B_o, \quad (15)$$

we have

$$g_{in} = (3\cos^2\theta - 1)/6. \quad (16)$$

For blood vessels in particular, we have

$$\Delta B_{in} = \Delta\chi_{do} B_o(3\cos^2\theta - 1)/6, \quad (17)$$

where

$$\Delta\chi_{do} = 4\pi A(0.18\text{ppm})\text{Hct}(1 - Y). \quad (18)$$

Here, A is a constant to be determined by the absolute susceptibility of blood in vivo, Hct is the hematocrit, and Y is the oxygen saturation. Practically, the choice of A depends on the value of Y in vivo: with $A = 1$, then $Y = 0.55$,[1] whereas with $A = 1.5$, then $Y = 0.70$.[76,77]

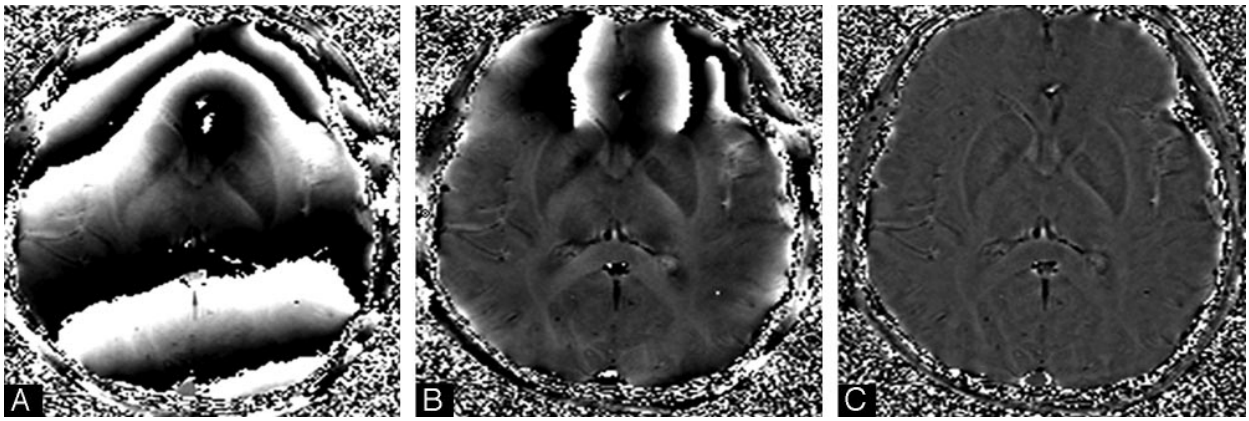

Fig 3. *A,* Raw phase image. *B,* HP-filtered phase image with a central filter size of 32 × 32; *C,* Filtered-phase image with a central filter size of 64 × 64.

The field outside is more complicated and is given by

$$\Delta B_{out} = \Delta\chi_{do} B_o \sin^2\theta \cos(2\Phi) a^2/(2r^2), \quad (19)$$

where a is the radius of the blood vessel, which is assumed as a long cylinder intercepting an angle θ with the main field, r is the distance perpendicularly from the axis of the cylinder to the position, and Φ is the angle between the vector r and the projection of the main field direction onto a plane perpendicular to the axis of the vessel. The constant term, $\chi_e B_o / 3$, has been dropped in equation 19.

For more complicated structures, the expressions for magnetic field variations around the object are not so straightforward. The key point is that susceptibility differences between 2 adjacent structures lead to a spatial field deviation within and around them, which is a function of their geometries. Following equation 6, this field deviation in turn leads to local phase changes in the MR phase images. However, phase images contain information about all magnetic fields, microscopic and macroscopic. The former may be from small amounts of local iron deposits, for example, whereas the latter consists of field changes caused by the geometry of the object, such as air/tissue interface effects, and by inhomogeneities in the main magnetic field. With all these properties brought together, the phase should be written as

$$\varphi = -\gamma(\Delta B_{local\ geometry} + \Delta B_{cs} + \Delta B_{global\ geometry} + \Delta B_{main\ field})TE. \quad (20)$$

All these terms are a function of the spatial location. The first term contains the local field changes of interest. The second term represents a chemical shift effect and causes changes of the form

$$\Delta B_{cs} = -\sigma B_0, \quad (21)$$

where σ represents the chemical shift. The difference between chemical shift and the first term in equation 20 is that chemical shift has no geometry dependence but is more of a point field change.[75] The last 2 terms create artifacts and are not our interest. They tend to have a low spatial-frequency dependence (the phase varies slowly over the image) and, for this reason, can be removed with a high-pass (HP) filter.[60]

Creating Susceptibility-Weighted Filtered-Phase Images

First, an HP filter is applied to remove the low-spatial frequency components of the background field. This is usually done by using a 64 × 64 low-pass filter divided into the original phase image (eg, an image with a matrix size of 512 × 512) to create an HP-filter effect. The end result is the HP filter. Specifically, the HP-filtered image is obtained by taking the original image $\rho(r)$, truncating it to the central $n \times n$ complex image $\rho_n(r)$, creating an image by zero-filling the elements outside the central $n \times n$ elements, and then complex dividing $\rho(r)$ by $\rho_n(r)$ to obtain a new image,[60]

$$\rho'(r) = \rho(r)/\rho_n(r), \quad (22)$$

which has most of the bothersome parts of the terms $\Delta B_{global\ geometry} + \Delta B_{main\ field}$ removed (Fig 3).

Once we have a pristine phase image with the background field changes removed, the door is open to differentiate one type of tissue from another, depending on their susceptibilities. This may be particularly useful at high field because the T1 difference between tissues begins to decrease, but any changes in susceptibility remain the same. Figure 4 shows an example of a T1-weighted image compared with the gradient-echo magnitude and phase data. Here we see that the gray matter, especially in the motor cortex area—the central sulcus—is clearly delineated in the phase image because of its iron content. Figure 5 shows an example of a phase image in the midbrain.

Marrying Magnitude and Phase Images to Create Magnitude SWI Data

Although HP-filtered phase images themselves are quite illustrative of the susceptibility contrast, they are influenced by both the intratissue phase (from ΔB_{in}) and the associated extratissue phase (from ΔB_{out}), which can impair the differentiation of adjacent tissues with different susceptibilities. Hence, the "phase mask" is designed to enhance the contrast in the original magnitude image by suppressing pixels having certain phase values. Magnitude and phase data are brought together as a final magnitude SWI dataset by multiplying a phase mask image into the original magnitude image.[22]

The phase mask is designed to be a number between zero and 1. When there are no phase characteristics that we want to

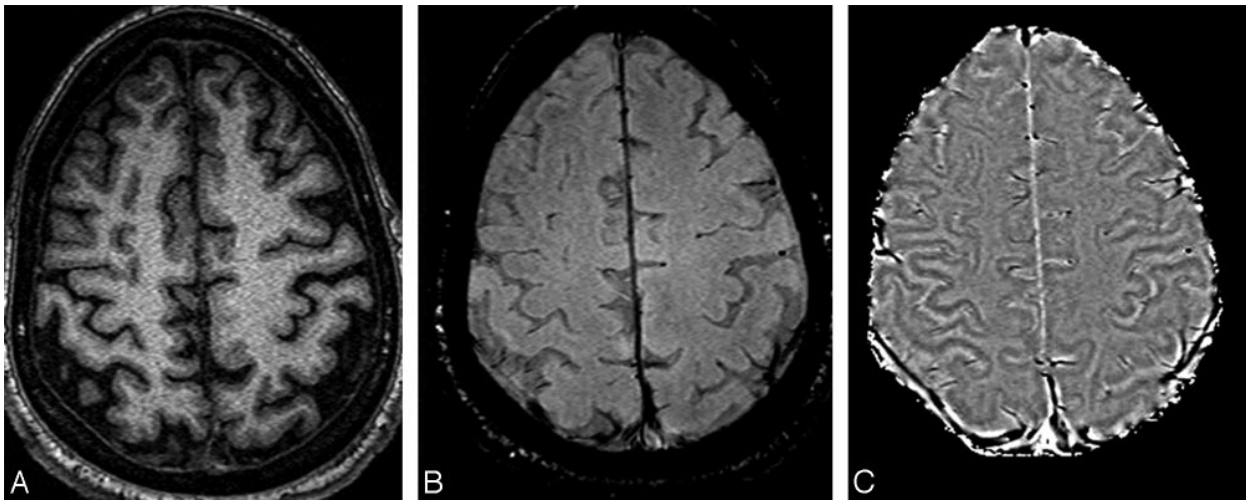

Fig 4. Short-echo T1-weighted image (*A*), compared with the SWI long-echo gradient-echo processed magnitude (*B*) and HP-filtered phase data (*C*).

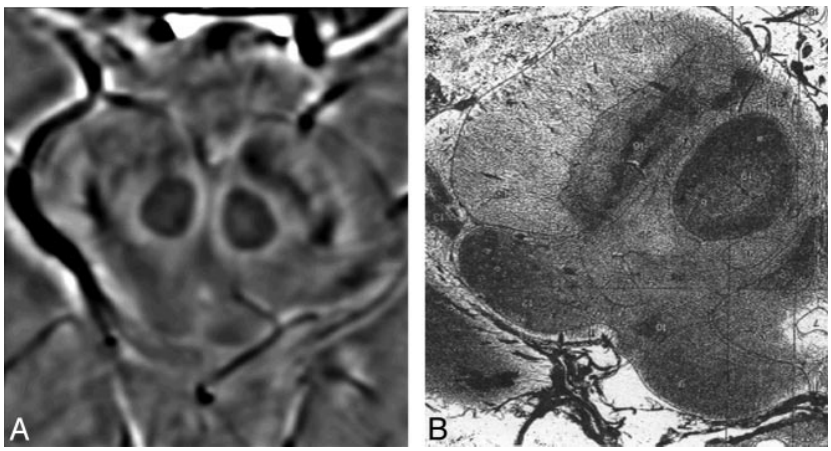

Fig 5. *A*, HP-filtered phase image in the midbrain acquired at 4T with TE = 15 ms. *B*, India ink-stained cadaver brain section showing a strong correspondence to variations in signal intensity as seen with SWI HP-filtered phase.

enhance, the phase mask is set to 1. Otherwise, the phase mask is designed to suppress the signal intensity in areas where the phase takes on certain values. For example, if the phase of interest is negative, the mask is designed as

$$f(x) = [\pi + \varphi(x)]/\pi \text{ for } -\pi < \varphi(x) < 0 \quad (23)$$

$$= 1 \text{ otherwise,}$$

where $\varphi(x)$ is the phase at location x. The phase mask can be applied any number of times to the original magnitude image $\rho(x)$ to create a new image,

$$\rho''(x) = f^m(x)\rho(x) \quad (24)$$

with a different contrast. The number of phase mask multiplications is chosen to optimize the contrast-to-noise ratio of the SWI image. This mathematical masking process is illustrated in Fig 6 and with a specific example from a 1.5T dataset shown in Fig 7.

A simple mathematical model can be built to estimate the value of m (from Equation 24).[30] The number of multiplications needed for a phase $\geq 0.3\pi$ is ≤ 4. For a phase $< 0.3\pi$, a value of $m \geq 4$ should be used. However, choosing $m = 4$ for a phase of 0.1π or π causes <25% reduction in visibility in either case, suggesting that $m = 4$ is a good compromise if one is limited to just 1 representative SWI dataset. Of course, m can be varied to produce a series of SWI data that can be used in a diagnosis. After this processing, the data are often viewed by using a minimum intensity projection (mIP) over ≥4 images. Clinically, 4 sections are the current common display, though showing a projection over 10 sections can be useful to visualize a larger coverage of the venous drainage system in a given area. Figure 8 shows projection data over the original magnitude images and the SWI processed images. One can also present the data as a sliding mIP, which means that one starts with the original series of images and mIPs over 4, moves to the next original image and mIP over 4 again so that a series of 64 images now becomes a series of 61 mIP images.

Furthermore, combining phase and magnitude information ensures the detectability of signal-intensity changes coming from both T2 and susceptibility differences between tissues. The existence of a phase difference does not necessarily lead to a T2* effect (uniform phase causes no T2′ decay), so these 2 sources of information complement each other. Also, suppressing the veins fully helps to create a clear distinction

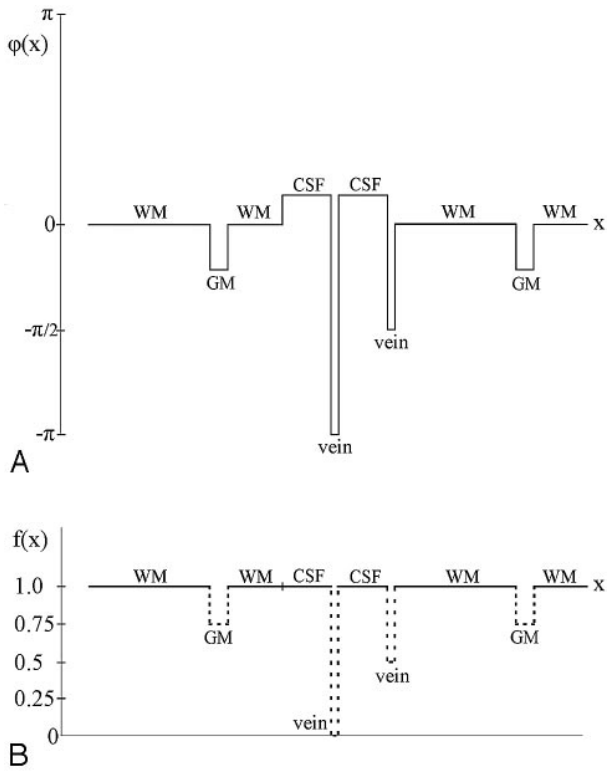

Fig 6. Pictorial depiction of the phase-masking process. *A*, Phase profile in a filtered-phase image. *B*, Corresponding profile of the mask created from *A*. Once the mask is raised to the fourth power, the vein that has a phase of $-\pi/2$ and a mask value of 0.5 will become 1-/16 and, therefore, this vein will be almost as well suppressed as the vein with a phase of $-\pi$ and f(x) = 0. GM indicates gray matter; WM, white matter.

between veins and arteries (Fig 7*D*–*F*). Therefore, we see that both magnitude and phase information are essential for proper tissue characterization, hence their marriage to create an SWI processed image.

Advanced Phase Processing

The HP-filtering method described earlier is quite successful in removing the spatially slowly varying phase effects that obscure the local intertissue phase differences of interest. However, apart from removing the spatially slowly varying background field effects, the HP filter (depending on filter size) also removes some of the physiologically or pathophysiologically relevant phase information from larger anatomic structures. For this reason, it is rare to use a central filter larger than 64 × 64 if one is interested in measuring iron content. If the main goal is just to create better MR venograms, then it is reasonable to use a central filter of 96 × 96 or 128 × 128 without much adverse effect on the small vessels.

The larger the filter size, the more background field effects can be removed, but also the concomitant loss of phase information from larger tissue structures is more probable. Ideally, background field effects could be removed by predicting the phase expected for a given individual's global head geometry. This would leave only small low-spatial-frequency phase errors, allowing a smaller filter size to be used to create the final HP result.[78] An example of this novel approach is shown in Fig 9. Although this currently is a time-consuming process, it would not be surprising to see this method implemented in a practical fashion in the coming years, making SWI more robust to air/tissue interface field effects. In that case, it may be possible to tackle problems such as subarachnoid hemorrhages, subdural hemorrhages, and possibly spine imaging.

Another important consideration is measuring iron. Currently, phase, measured from filtered MR images, is found to be the most sensitive tool for measuring relative changes in iron content in the subcortical structures of the brain.[62] Measuring iron content depends on the assignment of a given phase change in a tissue to a known amount of iron in that tissue. In Haacke et al,[62] this was done by associating the phase change in the motor cortex with 60 μg of nonheme Fe/g tissue. This ignores the fact that some of the phase shift, if not most of it, may come from heme iron and not ferritin. If this is indeed the case, the same phase shift seen in globus pallidus minus any heme iron effect may have a slope 5 times smaller. In any case, the reader needs to be aware that the absolute relationship between changes in phase and iron has not yet been established and that the relative contributions between heme and nonheme iron have not been sorted out yet. On the other hand, if blood levels remain constant and ferritin concentration does change, then any relative values of iron change in percentages would still be accurate, independent of whether this scale factor of 5 is present or not.

One problem in trying to compare phase information from 1 person to another is the geometry dependence of the phase coming from the shape of local objects of interest. If one assumes that the geometries of the structures of interest are roughly the same from person to person, then this might not be a major concern, but it is a potential problem when trying to measure absolute iron content. (It is less likely to be a problem when measuring relative changes in iron or calcium content.) The susceptibility of a structure is independent of the orientation, size, and shape of the structure; hence, a means to quantify tissue susceptibility would be of utmost importance because it will be a reliable measure of iron content. Tissue susceptibility will be an important means to quantify iron and is a topic of considerable interest in the field today.[26,27]

Recommended Imaging Parameters at Different Field Strengths

SWI can be used best at higher field strengths for a number of reasons. First, at low fields, TEs need to be much longer. For example, to obtain optimum contrast for veins at 1.5T, one needs a TE of between 40 and 80 ms. If we try to keep the product $\Delta\chi B_o TE$ constant so that the phase effect remains the same from 1 field strength to another, then the minimum TE at 3T becomes only 20 ms. This can be expressed mathematically as

$$\varphi(B_0) = -\gamma g \Delta\chi B_0 TE = \text{constant}, \quad (25)$$

which is tantamount to forcing

$$B_0 TE = B_0' TE', \quad (26)$$

where $B_0 TE$ and $B_0' TE'$ refer to the products of field strength and TE at 1.5T and 3T, respectively. This shorter TE has several advantages. First, the scanning at 3T can be run twice as fast compared with 1.5T such that in the same period of time, twice the number of sections can be obtained at 3T or an isotropic in-plane resolution can be obtained. Second, at high fields, the

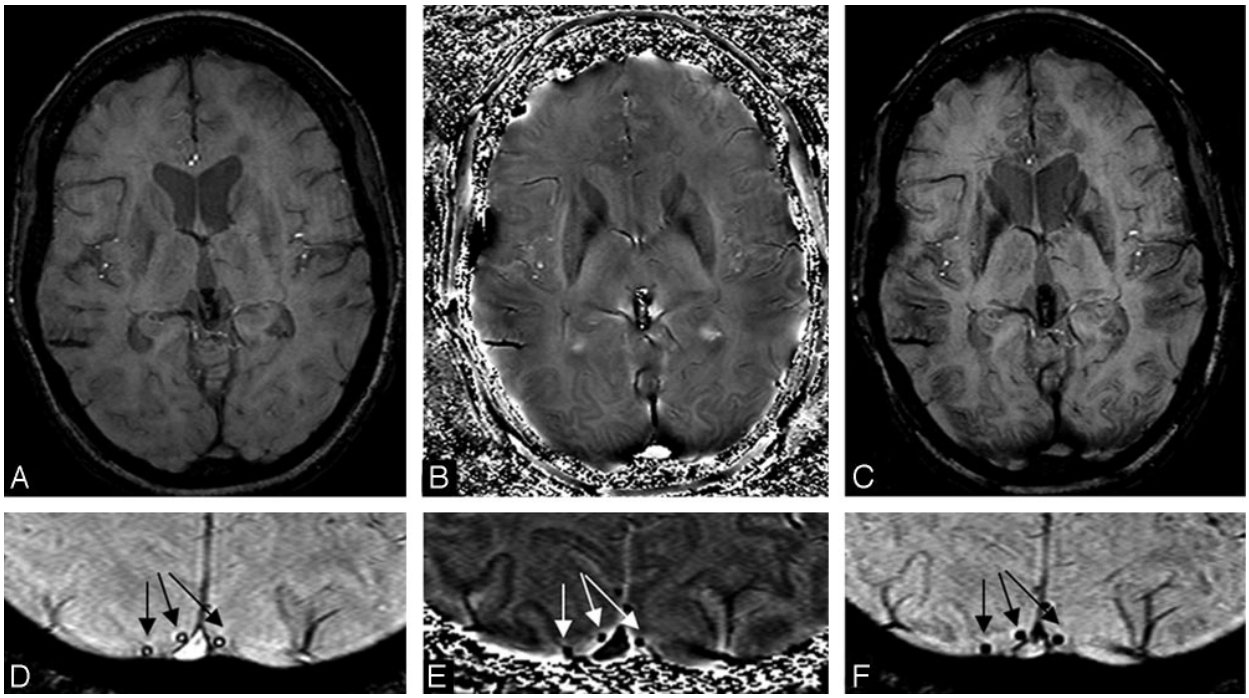

Fig 7. *A*, Unprocessed original SWI magnitude image. *B*, HP-filtered phase image. *C*, Processed SWI magnitude image (ie, after phase-mask multiplication with m = 4). *D*, Unprocessed original SWI magnitude image showing the dark hypointense ring around vein cross-sections (*arrows*). *E*, HP-filtered phase image showing the veins have low signal-intensity (*arrows*). *F*, Processed SWI magnitude image showing that the veins now appear with uniform low signal intensity (*arrows*).

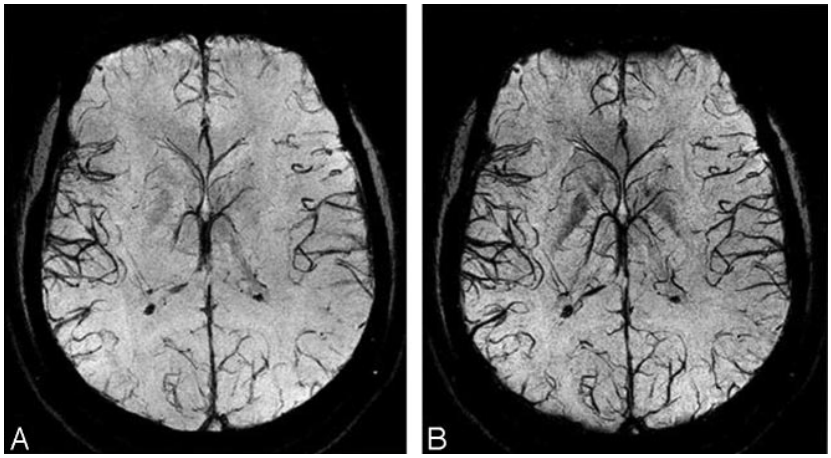

Fig 8. mIP data over the original magnitude images (*A*) and over the processed SWI images (*B*). The mIP is carried out over 7 sections (representing a 14-mm slab thickness). The images were collected at 3T. There is a dropout of signal intensity in the frontal part of the brain, but otherwise the vessel visibility is much improved in *B*. In the future, this frontal dropout should not be a problem when the air/tissue geometries are corrected (Fig 9).

SNR increases, so a sacrifice of some SNR (because the image quality at 1.5T is already good enough clinically) to obtain not only faster coverage but also higher resolution of the whole brain coverage at 3T can be easily tolerated. With parallel imaging at 3T, whole-brain coverage by using SWI can be obtained in as short as 4 minutes. Figure 10 shows the phase behavior as a function of field strength, given that equation 25 is obeyed. As expected, it is difficult to differentiate field strengths except for the fact that the SNR is higher for the 3T image than the 1.5T image. Otherwise, the phase images should have the same contrast.

The advent of very high fields such as 7T and above offers unprecedented resolution and SNR in imaging the brain. However, there are concerns about field homogeneity and high specific absorption rates (SAR). Gradient-echo imaging is one of the most robust sequences in MR imaging and continues to show its advantages at high field where images appear much more uniform than spin-echo images. SWI, for example, uses flip angles much smaller than 90°, and because the SAR varies as the square of the flip angles, SWI has a much smaller power deposition than spin-echo sequences. As discussed previously, phase can be kept invariant as a function of field strength by appropriately adjusting the TE. On the other hand, phase information from local structures does not strongly depend on local rf inhomogeneities. These 2 properties suggest that the SWI filtered-phase images can play a role in comparing subject data across field strengths. High-field images are shown in Figs 11 and 12 (for recommended imaging parameters at different field strengths, see Table 2). From

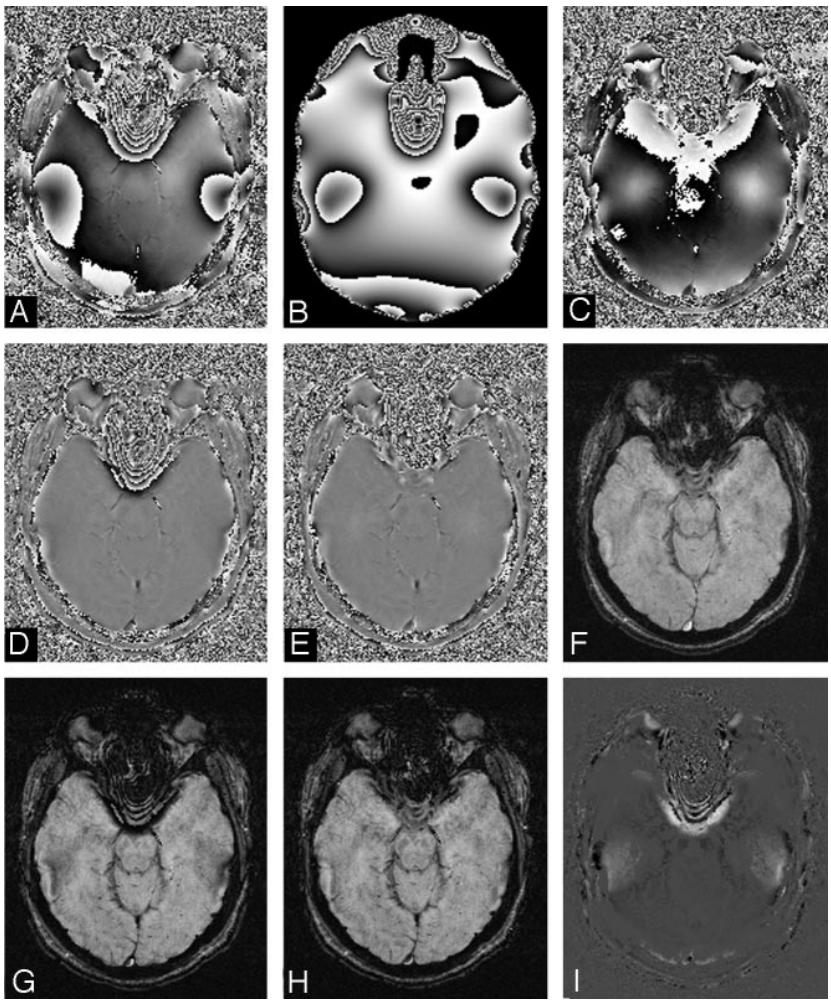

Fig 9. Results of the improved processing methodology. *A*, Original SWI phase image. *B*, Simulated phase due to air/tissue geometry at 40 ms. *C*, Result of subtracting *A* from *B* through the complex division. *D*, Result of HP filtering of *A*. *E*, Result of HP filtering of *C*. *F*, Corresponding unprocessed magnitude SWI image. *G*, Processed SWI magnitude image by using a phase mask from *D*. *H*, Processed SWI magnitude by using a phase mask from *E*. *I*, Result of subtracting *G* from *H*. Corresponding magnitude and phase images have been adjusted to the same, but appropriate, contrast levels. The size of the central filter in the HP process is 64 × 64.

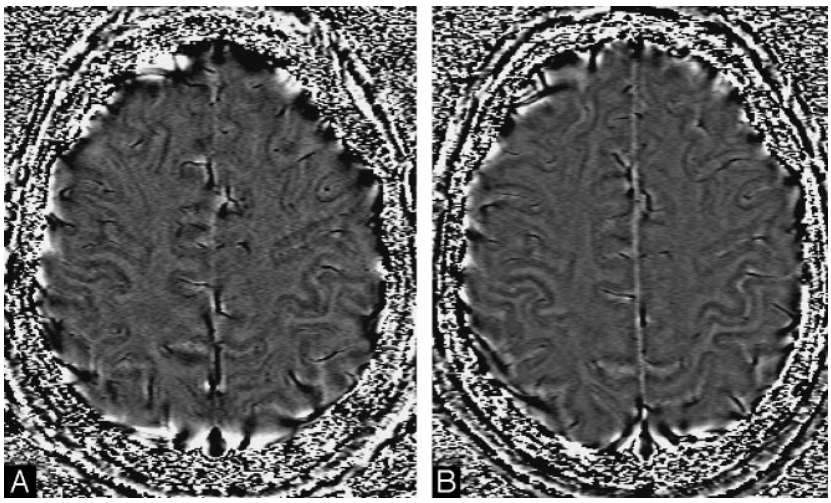

Fig 10. *A* and *B*, Phase images, keeping the product B_0TE constant. A phase image acquired at 1.5T (*A*) and the same subject at 3T (*B*) show the same overall contrast but with a better SNR. The gray/white matter contrast in these images comes from the increased MR-visible iron content in the gray matter, giving it an appearance similar to a T1-weighted scan.

Fig 11. A sample mIP from 7T data, with a resolution of 215 × 215 × 1000 μ, TE = 16 ms, TR = 45 ms, FA = 25°, and mIP over 8 sections. Image courtesy of Ge Y and Barnes S.

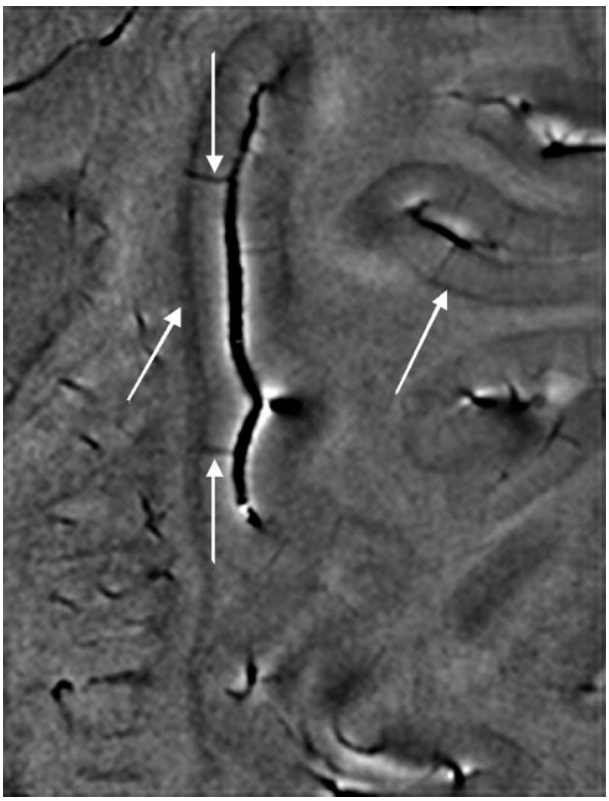

Fig 12. A zoomed image from the same dataset shown in Fig 11 reveals a dark band between the gray matter and white matter, which we assume represents the white matter arcuate fibers (*diagonal arrows*). The small vessels joining the pial veins are the venules (*vertical arrows*). Image courtesy of Ge Y and Barnes S.

the perspective of higher SNR, smaller changes in phase now become visible, and we are beginning to discover new phase variations that reveal venules and arcuate fibers similar to what one sees in stained cadaver brain studies.

Interpreting SWI Data

There are 3 components to interpret in the SWI data to make a clinical diagnosis. The first relates to the original magnitude image from, for example, a TE = 40 ms scan at 1.5T. This image usually will have a resolution of no less than 0.5 (read) × 1.0 (phase) × 2.0 mm (section). Despite the fact that the TE is so long, the image quality will be quite good apart from dephasing around the sinuses and in the air/tissue interface regions such as the pituitary gland. When compared with conventional gradient-echo scans with a TE of 25 ms (where the effects of veins are much less), SWI will tend to highlight small changes in susceptibility across a voxel as signal-intensity losses.

There are 2 key points to keep in mind when interpreting the magnitude data. First, there is no large blooming effect because the resolution is so high. The higher the resolution, the less the blooming artifacts. Second, the parameters of the sequence are chosen so that the contrast is fairly flat between normal gray matter, white matter, and CSF, though a low-enough flip angle can keep the CSF brighter than the surrounding gray and white matter. Consequently, the magnitude image clearly reveals areas with either short T2* or an oscillatory signal intensity in the magnitude image caused by the presence of deoxyhemoglobin in the major veins. This latter effect will cause a much larger signal-intensity loss than the actual T2* of the tissue because the signal intensity from the vein can cancel the signal intensity from the gray matter or white matter and, like water/fat cancellation, will cause a complete loss of signal intensity at the appropriate TE (this is why the TE in SWI was chosen to be 40 ms in the first place). For a vein of subvoxel size, this cancellation leads to a hypointense voxel with respect to its surroundings. However, for a vein covering more than a few voxels, only in those voxels in which both vein and surrounding tissue are partial-volumed do we see these signal-intensity cancellations and hypointense voxels. A voxel containing only the intravenous signal intensity does not show this signal-intensity cancellation effect. Hence, the vein appears to have a bright signal intensity inside with a hypointense ring around it (Fig 7*D*). Nevertheless, following phase-mask multiplication, the whole vein appears as a hypointense region in the processed SWI image (Fig 7*F*).

The second component to interpret in SWI data is the phase image. For a right-handed system, veins will look dark on the phase image (because the deoxygenated blood is paramagnetic relative to its surrounding tissue) and calcium will look bright (because calcium is diamagnetic relative to the brain tissue). Remnant phase artifacts may also appear by the air/tissue interfaces and above the sinuses, necessitating a careful recognition of the dark shadows in the phase images in these areas as artifacts. Newer methods are making this less of a problem.[53,78,79] Interpreting a darkening in local areas in phase images is important for MS, where iron can be associated with gray matter and white matter lesions. These iron-laden lesions will often correlate with the MS lesions seen on T2 or fluid-attenuated inversion recovery (FLAIR), but sometimes they will not, presumably depending on the stage and type of lesion.[80] The phase difference can also be used to quan-

Table 2: Range of experimental parameters advised for SWI data collection at different field strengths*				
FS	FA (degrees)	TR (ms)	TE (ms)	BW/pixel (Hz/pixel)
1.5T	18–25 (20)	50–60 (60)	40	70–100
3T	12–17 (12)	25–35 (30)	20	80–100
4T	8–15 (12)	25–35 (28)	15	80–120
7T	11–17 (14)	25–35 (30)	10–16	100–150

Note:—FS indicates field strength; FA, flip angle; BW, bandwidth.
* The values given in parentheses for FA and TR are the ones generally used by the authors. TEs given here are optimized for maximum signal cancellation from venous vasculature. Slightly shorter or longer TEs can be used for appropriate applications. However, note that for implementing shorter TEs, higher BW would be required, which would adversely affect the SNR of the image. One way to avoid this is to reduce the TR appropriately and cover more sections of the brain, which can recover some of the lost SNR.

tify iron or follow changes in iron deposition with time, to follow the resolution of cerebral hemorrhages in patients with trauma, or to monitor the development of microbleeds in patients with dementia. In the future, phase will likely also be used to quantify oxygen saturation in major veins. Because the original phase data have been filtered, we often refer to the new phase images as the SWI-filtered phase images.

The third component used in interpreting SWI is the final processed SWI. These data have taken full advantage of T2* signal-intensity losses in the magnitude image and iron increases in the phase images to highlight both types of contrast in a single image. At this point, these images show many "black holes," most often representing the cross-sections of small veins. How can we discriminate between these cross-sections and microbleeds? The best way to check for vessel connectivity is to take an mIP over a number of sections (most often 4). This is similar to using a maximum intensity projection (MIP) to see arteries in MR angiography (MRA). A point of interest here is that the MIP of SWI data can be taken as well. The resulting image, which is simply an SWI version of an MRA, is not so impressive at 1.5T; but at 3T, this MRA begins to approach the quality of a conventional MRA.[53]

A key point of practical interest is the orientation used for SWI. This is invariably transverse for a number of reasons. The foremost reason is that the phase of veins perpendicular to the main field is, in theory, opposite to that of those parallel to the main field, with the latter showing a negative phase and the former, a positive phase (equation 17). However, with an in-plane resolution to section-thickness aspect ratio of 2:4, the phase outside the small veins contributes more than the phase inside, reversing the phase behavior so that all veins show a negative phase.[30] This reversal of phase behavior makes the processing much easier because only a single negative phase mask needs to be used in the transverse orientation and this makes the visualization of the veins in the SWI-processed images much sharper.

Finally, we consider the contrast in the SWI data. Generally, the low flip angles and intermediate TEs give SWI an odd mixture of contrast. The gray matter/white matter contrast is almost nonexistent. Choosing the flip angle can play a role in getting the CSF signal intensity close to the gray matter/white matter signal intensity. This concept makes the magnitude images of little utility except as markers for microhemorrhages or other susceptibility effects. We often choose a slightly higher flip angle that suppresses partially the CSF, making it slightly darker than gray matter or white matter and (similar to FLAIR) slightly T1-weighted. In that case, edema appears bright, whereas the CSF remains suppressed. For patients with tumor, this has the effect of showing both the peritumoral edema as well as the bleeding inside the tumor.

Conversely, choosing a lower flip angle tends to highlight the spin attenuation and makes CSF a bit brighter than gray matter or white matter to regain some contrast. The former choice of, for example, 20° at 1.5T is the most popular. After processing, the SWI takes advantage of the high iron content in gray matter and begins to recreate gray matter/white matter contrast. The phase image has a lot of resemblance to a T1-weighted image. This gets carried over to the SWI. At the end, to better delineate the nature of the vascular content, we perform an MIP of the SWIs, usually over 4 adjacent images, to create an effective 8-mm-thick section. These mIP images present a great tool for visualizing vessel connectivity and microbleed locations with respect to the vasculature and other structures in the brain.

Future Directions

To date, SWI has had most of its clinical applications in the neuroimaging arena (this will be covered in Part 2 to be published in a later issue).[81] Many of the ideas relating to iron quantification remain to be validated in animal models and further tested longitudinally in patients. Technical developments such as creating susceptibility maps that remove all phase artifacts are a particularly exciting direction.[78,82] This would open the door to being able to use SWI in the spine, for example. Other developing applications include imaging cartilage, imaging calcium in atherosclerosis, imaging breast, and liver hemochromatosis.

Acknowledgments

The authors would like to thank Charbel Habib for management of all images and Alexander Boikov for reviewing the manuscript.

References

1. Reichenbach JR, Venkatesan R, Schillinger DJ, et al. **Small vessels in the human brain: MR venography with deoxyhemoglobin as an intrinsic contrast agent.** *Radiology* 1997;204:272–77
2. Baudendistel KT, Reichenbach JR, Metzner R, et al. **Comparison of functional MR-venography and EPI-BOLD fMRI at 1.5 T.** *Magn Reson Imaging* 1998;16:989–91
3. Reichenbach JR, Essig M, Haacke EM, et al. **High-resolution venography of the brain using magnetic resonance imaging.** *MAGMA* 1998;6:62–69
4. Essig M, Reichenbach JR, Schad LR, et al. **High-resolution MR venography of cerebral arteriovenous malformations.** *Magn Reson Imaging* 1999;17:1417–25
5. Lee BC, Kuppusamy K, Grueneich R, et al. **Hemispheric language dominance in children demonstrated by functional magnetic resonance imaging.** *J Child Neurol* 1999;14:78–82
6. Lin W, Mukherjee P, An H, et al. **Improving high-resolution MR bold venographic imaging using a T1 reducing contrast agent.** *J Magn Reson Imaging* 1999;10:118–23
7. Tan IL, van Schijndel RA, Pouwels PJ, et al. **MR venography of multiple sclerosis.** *AJNR Am J Neuroradiol* 2000;21:1039–42
8. Reichenbach JR, Barth M, Haacke EM, et al. **High-resolution MR venography at 3.0 Tesla.** *J Comput Assist Tomogr* 2000;24:949–57

9. Cheng YC, Haacke EM. **Predicting BOLD signal changes as a function of blood volume fraction and resolution.** *NMR Biomed* 2001;14:468–77
10. Cheng YC, Haacke EM, Yu YJ. **An exact form for the magnetic field density of states for a dipole.** *Magn Reson Imaging* 2001;19:1017–23
11. Schad LR. **Improved target volume characterization in stereotactic treatment planning of brain lesions by using high-resolution BOLD MR-venography.** *NMR Biomed* 2001;14:478–83
12. Reichenbach JR, Haacke EM. **High-resolution BOLD venographic imaging; a window into brain function.** *NMR Biomed* 2001;14:453–67
13. Reichenbach JR, Jonetz-Mentzel L, Fitzek C, et al. **High-resolution blood oxygen-level dependent MR venography (HRBV): a new technique.** *Neuroradiology* 2001;43:364–69
14. Essig M, Reichenbach JR, Schad L, et al. **High resolution MR-venography of cerebral arteriovenous malformations** [in German]. *Radiologe* 2001; 41:288–95
15. Haacke EM, Herigault G, Yu Y, et al. **Observing tumor vascularity noninvasively using magnetic resonance imaging.** *Image Analysis and Stereology* 2002;21:107–13
16. Tong KA, Ashwal S, Holshouser BA, et al. **Hemorrhagic shearing lesions in children and adolescents with posttraumatic diffuse axonal injury: improved detection and initial results.** *Radiology* 2003;227:332–39
17. Essig M, Waschkies M, Wenz F, et al. **Assessment of brain metastases with dynamic susceptibility-weighted contrast-enhanced MR imaging: initial results.** *Radiology* 2003;228:193–99
18. Abduljalil AM, Schmalbrock P, Novak V, et al. **Enhanced gray and white matter contrast of phase susceptibility-weighted images in ultra-high-field magnetic resonance imaging.** *J Magn Reson Imaging* 2003;18:284–90
19. Hermier M, Nighoghossian N. **Contribution of susceptibility-weighted imaging to acute stroke assessment.** *Stroke* 2004;35:1989–94
20. Wycliffe ND, Choe J, Holshouser B, et al. **Reliability in detection of hemorrhage in acute stroke by a new three-dimensional gradient recalled echo susceptibility-weighted imaging technique compared to computed tomography: a retrospective study.** *J Magn Reson Imaging* 2004;20:372–77
21. Tong KA, Ashwal S, Holshouser BA, et al. **Diffuse axonal injury in children: clinical correlation with hemorrhagic lesions.** *Ann Neurol* 2004;56:36–50
22. Haacke EM, Xu Y, Cheng YC, et al. **Susceptibility weighted imaging (SWI).** *Magn Reson Med* 2004;52:612–18
23. Haddar D, Haacke E, Sehgal V, et al. **Susceptibility weighted imaging: theory and applications.** *J Radiol* 2004;85:1901–08
24. Rauscher A, Sedlacik J, Barth M, et al. **Noninvasive assessment of vascular architecture and function during modulated blood oxygenation using susceptibility weighted magnetic resonance imaging.** *Magn Reson Med* 2005;54:87–95
25. Sehgal V, Delproposto Z, Haacke EM, et al. **Clinical applications of neuroimaging with susceptibility-weighted imaging.** *J Magn Reson Imaging* 2005;22:439–50
26. Haacke EM, Cheng NY, House MJ, et al. **Imaging iron stores in the brain using magnetic resonance imaging.** *Magn Reson Imaging* 2005;23:1–25
27. Mentzel HJ, Dieckmann A, Fitzek C, et al. **Early diagnosis of cerebral involvement in Sturge-Weber syndrome using high-resolution BOLD MR venography.** *Pediatr Radiol* 2005;35:85–90
28. Babikian T, Freier MC, Tong KA, et al. **Susceptibility weighted imaging: neuropsychologic outcome and pediatric head injury.** *Pediatr Neurol* 2005;33:184–94
29. Rauscher A, Sedlacik J, Barth M, et al. **Magnetic susceptibility-weighted MR phase imaging of the human brain.** *AJNR Am J Neuroradiol* 2005;26:736–42
30. Xu Y, Haacke EM. **The role of voxel aspect ratio in determining apparent vascular phase behavior in susceptibility weighted imaging.** *Magn Reson Imaging* 2006;24:155–60
31. Hamans BC, Barth M, Leenders WP, et al. **Contrast enhanced susceptibility weighted imaging (CE-SWI) of the mouse brain using ultrasmall superparamagnetic iron oxide particles (USPIO).** *Z Med Phys* 2006;16:269–74
32. Sehgal V, Delproposto Z, Haddar D, et al. **Susceptibility-weighted imaging to visualize blood products and improve tumor contrast in the study of brain masses.** *J Magn Reson Imaging* 2006;24:41–51
33. Haacke EM. **Susceptibility weighted imaging (SWI).** *Z Med Phys* 2006;16:237
34. Ashwal S, Babikian T, Gardner-Nichols J, et al. **Susceptibility-weighted imaging and proton magnetic resonance spectroscopy in assessment of outcome after pediatric traumatic brain injury.** *Arch Phys Med Rehabil* 2006;87:S50–58
35. Yoshida Y, Terae S, Kudo K, et al. **Capillary telangiectasia of the brain stem diagnosed by susceptibility-weighted imaging.** *J Comput Assist Tomogr* 2006;30:980–82
36. Noebauer-Huhmann IM, Pinker K, Barth M, et al. **Contrast-enhanced, high-resolution, susceptibility-weighted magnetic resonance imaging of the brain: dose-dependent optimization at 3 Tesla and 1.5 Tesla in healthy volunteers.** *Invest Radiol* 2006;41:249–55
37. Haacke EM, DelProposto ZS, Chaturvedi S, et al. **Imaging cerebral amyloid angiopathy with susceptibility-weighted imaging.** *AJNR Am J Neuroradiol* 2007;28:316–17
38. Vinod Desai S, Bindu PS, Ravishankar S, et al. **Relaxation and susceptibility MRI characteristics in Hallervorden-Spatz syndrome.** *J Magn Reson Imaging* 2007;25:715–20
39. Akter M, Hirai T, Hiai Y, et al. **Detection of hemorrhagic hypointense foci in the brain on susceptibility-weighted imaging clinical and phantom studies.** *Acad Radiol* 2007;14:1011–19
40. Larsen JP, Britt WI, Kido D, et al. **Susceptibility weighted magnetic resonance imaging in the evaluation of dementia.** *Radiology Case Reports* 2007;2:102
41. Sedlacik J, Rauscher A, Reichenbach JR. **Obtaining blood oxygenation levels from MR signal behavior in the presence of single venous vessels.** *Magn Reson Med* 2007;58:1035–44
42. Pinker K, Noebauer-Huhmann IM, Stavrou I, et al. **High-resolution contrast-enhanced, susceptibility-weighted MR imaging at 3T in patients with brain tumors: correlation with positron-emission tomography and histopathologic findings.** *AJNR Am J Neuroradiol* 2007;28:1280–86
43. Shen Y, Kou Z, Kreipke CW, et al. **In vivo measurement of tissue damage, oxygen saturation changes and blood flow changes after experimental traumatic brain injury in rats using susceptibility weighted imaging.** *Magn Reson Imaging* 2007;25:219–27
44. Ohta A, Naito K, Ohkubo M, et al. **Study of susceptibility-weighted imaging (SWI) using a simple MR phantom** [in Japanese]. *Nippon Hoshasen Gijutsu Gakkai Zasshi* 2007;63:1093–98
45. Thomas B, Somasundaram S, Thamburaj K, et al. **Clinical applications of susceptibility weighted MR imaging of the brain: a pictorial review.** *Neuroradiology* 2008;50:105–16
46. de Souza JM, Domingues RC, Cruz LC, et al. **Susceptibility-weighted imaging for the evaluation of patients with familial cerebral cavernous malformations; a comparison with T2-weighted fast spin-echo and gradient-echo sequences.** *AJNR Am J Neuroradiol* 2008;29:154–58
47. Harder SL, Hopp KM, Ward H, et al. **Mineralization of the deep gray matter with age: a retrospective review with susceptibility-weighted MR imaging.** *AJNR Am J Neuroradiol* 2008;29:176–83
48. Sedlacik J, Helm K, Rauscher A, et al. **Investigations on the effect of caffeine on cerebral venous vessel contrast by using susceptibility-weighted imaging (SWI) at 1.5, 3 and 7 T.** *Neuroimage* 2008;40:11–18
49. Somasundaram S, Kesavadas C, Thomas B. **Susceptibility weighted imaging in holohemispheric venous angioma with cerebral hemiatrophy.** *Neurol India* 2008;56:104–05
50. Liu HL, Wai YY, Chen WS, et al. **Hemorrhage detection during focused-ultrasound induced blood-brain-barrier opening by using susceptibility-weighted magnetic resonance imaging.** *Ultrasound Med Biol* 2008;34:598–606
51. Koopmans PJ, Manniesing R, Niessen WJ, et al. **MR venography of the human brain using susceptibility weighted imaging at very high field strength.** *MAGMA* 2008;21:149–58. Epub 2008 Jan 11
52. Fushimi Y, Miki Y, Togashi K, et al. **A developmental venous anomaly presenting atypical findings on susceptibility-weighted imaging.** *AJNR Am J Neuroradiol* 2008;29:E56
53. Du YP, Jin Z. **Simultaneous acquisition of MR angiography and venography (MRAV).** *Magn Reson Med* 2008;59:954–58
54. Hammond KE, Lupo JM, Xu D, et al. **Development of a robust method for generating 7.0 T multichannel phase images of the brain with application to normal volunteers and patients with neurological diseases.** *Neuroimage* 2008;39:1682–92
55. Zhong K, Leupold J, von Elverfeldt D, et al. **The molecular basis for gray and white matter contrast in phase imaging.** *Neuroimage* 2008;40:1561–66
56. Hu J, Yu Y, Juhasz C, et al. **MR susceptibility weighted imaging (SWI) complements conventional contrast enhanced T1 weighted MRI in characterizing brain abnormalities of Sturge-Weber syndrome.** *J Magn Reson Imaging* 2008;28:300–07
57. Haacke EM, Lai S, Yablonskiy DA, et al. **In-vivo validation of the BOLD mechanism: a review of signal changes in gradient-echo functional MRI in the presence of flow.** *International Journal of Imaging Systems and Technology* 1995;6:153–63
58. Haacke EM, Lai S, Reichenbach JR, et al. **In vivo measurement of blood oxygen saturation using magnetic resonance imaging: a direct validation of the blood oxygen level-dependent concept in functional brain imaging.** *Human Brain Mapp* 1997;5:341–46
59. Akbudak E, Norberg RE, Conturo TE. **Contrast-agent phase effects: an experimental system for analysis of susceptibility, concentration, and bolus input function kinetics.** *Magn Reson Med* 1997;38:990–1002
60. Wang Y, Yu Y, Li D, et al. **Artery and vein separation using susceptibility-dependent phase in contrast-enhanced MRA.** *J Magn Reson Imaging* 2000;12:661–70
61. Fernandez-Seara MA, Techawiboonwong A, Detre JA, et al. **MR susceptometry for measuring global brain oxygen extraction.** *Magn Reson Med* 2006;55:967–73
62. Haacke EM, Ayaz M, Khan A, et al. **Establishing a baseline phase behavior in magnetic resonance imaging to determine normal vs. abnormal iron content in the brain.** *J Magn Reson Imaging* 2007;26:256–64
63. Duyn JH, van Gelderen P, Li TQ, et al. **High-field MRI of brain cortical substructure based on signal phase.** *Proc Natl Acad Sci U S A* 2007;104:11796–801
64. Young IR, Bailes DR, Burl M, et al. **Initial clinical evaluation of a whole body**

nuclear magnetic resonance (NMR) tomograph. *J Comput Assist Tomogr* 1982;6:1–18
65. Bydder GM, Steiner RE. **NMR imaging of the brain**. *Neuroradiology* 1982;23:231–40
66. Bailes DR, Young IR, Thomas DJ, et al. **NMR imaging of the brain using spin-echo sequences.** *Clin Radiol* 1982;33:395–414
67. Edelstein WA, Hutchison JM, Johnson G, et al. **Spin warp NMR imaging and applications to human whole-body imaging.** *Phys Med Biol* 1980;25:751–56
68. Haase A, Frahm J, Matthaei D, et al. **Flash imaging: rapid NMR imaging using low flip-angle pulses.** *J Magn Reson* 1986;67:258–66
69. Frahm J, Haase A, Matthaei D. **Rapid 3-dimensional MR imaging using the flash technique.** *J Comput Assist Tomogr* 1986;10:363–68
70. Mugler JP 3rd, Brookeman JR. **Three-dimensional magnetization-prepared rapid gradient-echo imaging (3D MP RAGE).** *Magn Reson Med* 1990;15:152–57
71. Reichenbach JR, Venkatesan R, Yablonskiy DA, et al. **Theory and application of static field inhomogeneity effects in gradient-echo imaging.** *J Magn Reson Imaging* 1997;7:266–79
72. Haacke EM, Brown R, Thompson M, et al. *Magnetic Resonance Imaging: Physical Principles and Sequence Design.* New York: Wiley; 1999:5
73. Schenck JF. **The role of magnetic susceptibility in magnetic resonance imaging: MRI magnetic compatibility of the first and second kinds.** *Med Phys* 1996;23:815–50
74. Saini S, Frankel RB, Stark DD, et al. **Magnetism: a primer and review.** *AJR Am J Roentgenol* 1988;150:735–43
75. Chu SC, Xu Y, Balschi JA, et al. **Bulk magnetic susceptibility shifts in NMR studies of compartmentalized samples: use of paramagnetic reagents.** *Magn Reson Med* 1990;13:239–62
76. Weisskoff RM, Kiihne S. **MRI susceptometry: image-based measurement of absolute susceptibility of MR contrast agents and human blood.** *Magn Reson Med* 1992;24:375–83
77. Spees WM, Yablonskiy DA, Oswood MC, et al. **Water proton MR properties of human blood at 1.5 Tesla: magnetic susceptibility, T(1), T(2), T*(2), and non-Lorentzian signal behavior.** *Magn Reson Med* 2001;45:533–42
78. Neelavalli J, Cheng YC, Haacke EM. **Removal of Air/Tissue Interface Field Effects in Susceptibility Weighted Imaging. Proceedings of International Society of Magnetic Resonance in Medicine.** Toronto, Ontario, Canada; 3–9 May 2008. Abstract 3499
79. Rauscher A, Barth M, Reichenbach JR, et al. **Automated unwrapping of MR phase images applied to BOLD MR-venography at 3 Tesla.** *J Magn Reson Imaging* 2003;18:175–80
80. Haacke EM, Makki M, Ge Y, et al. **Characterizing iron deposition in multiple sclerosis lesions using susceptibility weighted imaging.** *J Magn Reson Imaging* 2009 (In press).
81. Tong KA, Ashwal S, Obenaus A, et al. **Susceptibility-weighted MR imaging: a review of clinical applications in children.** *AJNR Am J Neuroradiol* 2008;29:9–17
82. de Rochefort L, Brown R, Prince MR, Wang Y. **Quantitative MR susceptibility mapping using piece-wise constant regularized inversion of the magnetic field.** *Magn Reson Med* 2008;60:1003–09

ORIGINAL RESEARCH

P.K. Nelson
P. Lylyk
I. Szikora
S.G. Wetzel
I. Wanke
D. Fiorella

The Pipeline Embolization Device for the Intracranial Treatment of Aneurysms Trial

BACKGROUND AND PURPOSE: Endoluminal reconstruction with flow diverting devices represents a novel constructive technique for the treatment of cerebral aneurysms. We present the results of the first prospective multicenter trial of a flow-diverting construct for the treatment of intracranial aneurysms.

MATERIALS AND METHODS: Patients with unruptured aneurysms that were wide-necked (>4 mm), had unfavorable dome/neck ratios (<1.5), or had failed previous therapy were enrolled in the PITA trial between January and May 2007 at 4 (3 European and 1 South American) centers. Aneurysms were treated with the PED with or without adjunctive coil embolization. All patients underwent clinical evaluation at 30 and 180 days and conventional angiography 180 days after treatment. Angiographic results were adjudicated by an experienced neuroradiologist at a nonparticipating site.

RESULTS: Thirty-one patients with 31 intracranial aneurysms (6 men; 42–76 years of age; average age, 54.6 years) were treated during the study period. Twenty-eight aneurysms arose from the ICA (5 cavernous, 15 parophthalmic, 4 superior hypophyseal, and 4 posterior communicating segments), 1 from the MCA, 1 from the vertebral artery, and 1 from the vertebrobasilar junction. Mean aneurysm size was 11.5 mm, and mean neck size was 5.8 mm. Twelve (38.7%) aneurysms had failed (or recurred after) a previous endovascular treatment. PED placement was technically successful in 30 of 31 patients (96.8%). Most aneurysms were treated with either 1 ($n = 18$) or 2 ($n = 11$) PEDs. Fifteen aneurysms (48.4%) were treated with a PED alone, while 16 were treated with both PED and embolization coils. Two patients experienced major periprocedural stroke. Follow-up angiography demonstrated complete aneurysm occlusion in 28 (93.3%) of the 30 patients who underwent angiographic follow-up. No significant in-construct stenosis (≥50%) was identified at follow-up angiography.

CONCLUSIONS: Intracranial aneurysm treatment with the PED is technically feasible and can be achieved with a safety profile analogous to that reported for stent-supported coil embolization. PED treatment elicited a very high rate (93%) of complete angiographic occlusion at 6 months in a population of the most challenging anatomic subtypes of cerebral aneurysms.

ABBREVIATIONS: IA= intracranial aneurysm; ICA = internal carotid artery; ID = internal diameter; LICA = left ICA; MCA = middle cerebral artery; PED = Pipeline Embolization Device; PICA = posterior inferior cerebellar artery; PITA = Pipeline for the Intracranial Treatment of Aneurysms; SES = self-expanding stent

A new generation of flexible self-expanding, microcatheter-delivered, high-metal-surface-area coverage, stentlike devices has emerged, which represent a fundamentally different approach to the endovascular treatment of IAs.[1,2] These flow-diverting devices are designed to achieve aneurysm occlusion through the endoluminal reconstruction of the diseased segment of the parent artery that gives rise to the aneurysm. This approach potentially represents a more physiologic, definitive, and durable treatment of IAs in comparison with endosaccular coil embolization.[1-3] We present the results of the PITA trial, the first multicenter prospective study of intracranial aneurysms treated with a flow-diverting construct (PED; ev3/Chestnut Medical, Menlo Park, California).

Received September 20, 2010; accepted after revision October 12.

From the Neurointerventional Service (P.K.N.), Departments of Radiology and Neurosurgery, NYU Langone Medical Center, New York, New York; Department of Neurosurgery (P.L.), Eneri Instituto Medico, Buenos Aires, Argentina; Department of Neuroradiology (I.S.), National Institute of Neurosurgery, Budapest, Hungary; Department of Neuroradiology (S.G.W.), Institute of Radiology, University Hospital Basel, Basel, Switzerland; Department of Neuroradiology (I.W.), University Hospital of Essen, Essen, Germany; and Department of Neurosurgery (D.F.), Stony Brook University Medical Center, Stony Brook, New York.

The PITA trial was sponsored, funded, and conducted by Chestnut Medical Technologies. Dr Peter Kim Nelson is a stockholder and paid consultant for Chestnut Medical/ev3. Drs Szikora, Wetzel, and Lylyk are paid consultants and proctors for Chestnut Medical/ev3. Dr Fiorella is an unpaid consultant and proctor for Chestnut Medical/ev3.

Paper previously presented in part at: International Stroke Conference, February 20–22, 2008; New Orleans, Louisiana.

Please address correspondence to: David Fiorella, MD, PhD, Department of Neurosurgery, Cerebrovascular Center, State University of New York at Stony Brook, Stony Brook University Hospital, Health Sciences Center 080, Stony Brook, NY, e-mail: dfiorella@notes.cc.sunysb.edu

Indicates open access to non-subscribers at www.ajnr.org

DOI 10.3174/ajnr.A2421

Materials and Methods

Enrollment

PITA was a multicenter single-arm clinical trial of the PED conducted at 3 medical centers in Europe (Universitätsklinikum Essen, Essen, Germany, 4 patients; Medical University, Graz, Graz, Austria, 12 patients; National Institute of Neurosciences, Budapest, Hungary, 9 patients), and 1 in Argentina (Eneri Instituto Medico, Buenos Aires, Argentina, 6 patients). Subjects were included if they had wide-neck IAs (neck of >4 mm or dome/neck ratio of <1.5) or IAs that had failed previous endovascular treatment attempts. Patients were excluded if they had subarachnoid hemorrhage within 60 days, an unstable neurologic deficit, or >50% stenosis of the parent artery. Both ethics committee and local regulatory approval were obtained before patient enrollment. PITA was run in compliance with ISO14155, an international clinical trial standard. All patients provided written in-

formed consent to participate in the study. Some of the patients in the present prospective PITA dataset were included in previously published single-center case series.[1,4]

Device

The PED is a flexible microcatheter-delivered self-expanding cylindric construct composed of 48 braided strands of cobalt chromium and platinum. The individual strands measure between 28 and 33 μm in diameter (0.0011–0.0013 inches). When fully expanded to nominal diameter, the construct provides approximately 30%–35% metal surface area coverage. The construct is packaged collapsed on a delivery wire and contained within a delivery sheath. When collapsed, the construct is elongated approximately 2.5 times its nominal length (which is achieved when the construct is fully expanded).

Technique

All patients were pretreated with aspirin and clopidogrel and were treated under general anesthesia. Procedures were performed through a 6F-8F femoral artery access. Following arterial access, patients were typically administered intravenous heparin to achieve an activated clotting time of >250 seconds. A 6F guiding-catheter system was placed into the distal cervical segment of the vessel leading to the intracranial vessel targeted for treatment. A standard 0.027-inch ID microcatheter (Renegade Hi-Flo; Boston Scientific, Fremont, California) or Masstransit (Cordis Neurovascular, Warren, New Jersey) was then manipulated over a 0.014- to 0.018-inch outer diameter microwire (Synchro-14 or Transend-14 or Transend-18, Boston Scientific) into position across the aneurysm neck. When coiling was performed in conjunction with PED treatment, a standard microcatheter was navigated into the aneurysm alongside the 0.027-inch microcatheter within the parent artery.

Once the microcatheter was in position, the PED was loaded via a rotating hemostatic valve into the hub of the 0.027-inch ID delivery microcatheter and advanced with the delivery wire. The device was then deployed across the targeted landing zone through a process of microcatheter unsheathing and delivery-wire stabilization/advancement. Once deployed, the delivery microcatheter was advanced over the delivery microwire to recapture the microwire and re-establish its position across the construct. Additional PEDs were then deployed (if needed) through the delivery microcatheter by using the same technique.

Once the PED construct was in place, if coil embolization was to be performed, coils were deployed within the aneurysm through the jailed microcatheter via a parallel technique. Following coil embolization, the coiling microcatheter could be gently removed from the aneurysm without displacing the construct. Completion angiography was performed in the working angles for PED reconstruction as well as in the standard branch vessel projections.

Neurologic status was assessed before treatment, immediately after treatment, and at discharge. Subjects underwent mandatory clinical follow-up at 30 days and 180 days with repeat angiography at the 180-day follow-up to assess IA occlusion and PED status. Patients continued clopidogrel therapy (75 mg by mouth daily) for a minimum of 30 days after treatment and aspirin therapy (100 mg by mouth daily) for a minimum of 180 days after treatment.

Study End Points

The primary end points of the study were device-placement success (defined as the successful placement of at least 1 PED at the targeted landing zone) and the incidence of 30-day death or ipsilateral stroke. Secondary end points were clinical procedure success (device-placement success in the absence of periprocedural stroke/death), complete aneurysm occlusion at 180-day angiographic follow-up, incidence of new neurologic deficits after treatment, change in the Barthel Index, and rate of distal device migration.

Data Collection

Site investigators entered data on preprinted case report forms and all case-report-form data were monitored by an external contract research organization (Clin-Assist, Pacifica, California). Data were entered into a data base, and all queries were resolved. Data were analyzed by using SAS software (SAS Institute, Cary, North Carolina). Confidence intervals for continuous outcomes were calculated by using standard methods.

Angiographic Adjudication

All angiograms were reviewed by a single experienced neuroradiologist (S.G.W.) who did not participate in any of the procedures. Aneurysm occlusion grade, in-construct stenosis, and device migration were assessed. Aneurysm occlusion was graded by using a 3-point modified Raymond scale.[5] In-construct stenosis was calculated on the basis of the minimal luminal diameter and graded as none (0 to <25%), mild (>25 to <50%), moderate (>50 to <75%), or severe (>75 to 100%). Device migration was defined as the movement of the device ≥5 mm from its originally deployed location.

Results

Patient and Aneurysm Characteristics

Thirty-one patients with 31 aneurysms were enrolled between January and May 2007. Twenty-five patients were women. Average age was 54.6 years (range, 35–76 years). Twelve (38.7%) patients had undergone prior treatments of the target IA: 8 with coils only, 2 with stents only, and 2 with both coils and stents (Fig 1). Twenty-two (71%) of the aneurysms were wide-neck, 9 (29%) were large (>10 mm), and 2 were giant (>25 mm). Mean aneurysm size was 11.5 mm, and mean neck width was 5.8 mm (Table 1 and Fig 2).

Treatment: Device Placement

In total, 47 devices were placed (1.52 devices per aneurysm). In 18 cases, a single PED was used (Table 1). Adjunctive coils were placed in 16 aneurysms (51.6%), and 15 aneurysms were treated with PED reconstruction alone. A Neuroform stent (Boston Scientific) was used in 1 case to anchor the proximal end of 2 telescoping PEDs implanted within the left M1 segment of the MCA. Forty-six of 47 PEDs were implanted successfully (97.9% device-placement success). In the 1 unsuccessful PED placement, there was diminished flow in the parent ICA following deployment of the PED and coiling of the remnant aneurysm sac. During angioplasty performed to correct the attenuated flow, the ICA beyond the implant was ruptured. The indwelling PED and aneurysm coils were removed during an attempted surgical repair of the ruptured artery, and the carotid artery was ultimately ligated. In the remaining 30 patients, the entire neck of the target IA was successfully covered by the PED construct. Device-deployment success (passage of the PED through the microcatheter and release at the target site) occurred in 47 of 54 attempted PED deployments (87%). In 6 cases, a PED was introduced

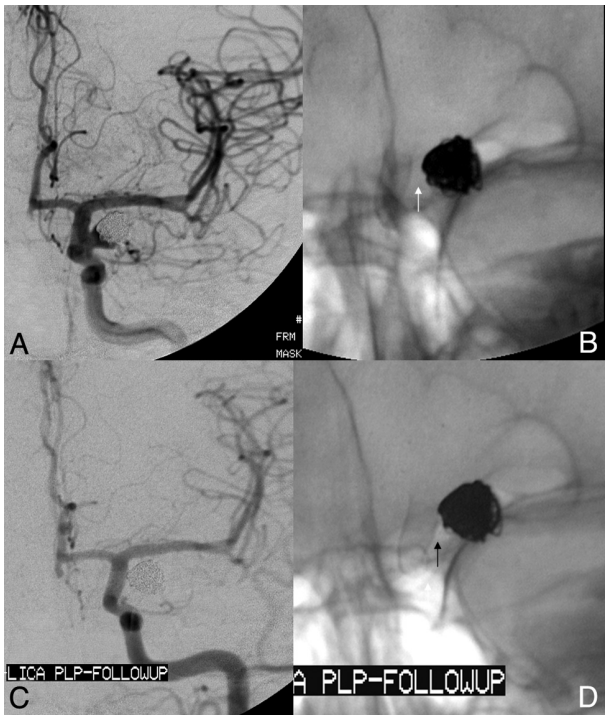

Fig 1. Laterally projecting left carotid aneurysm with residual filling after prior coiling. *A*, Subtracted carotid angiography in the frontal-projection working angle demonstrates residual filling of the aneurysm neck extending into the proximal fundus. *B*, Unsubtracted frontal projection in the working angle demonstrates a PED in position across the aneurysm neck. No additional embolization coils were added. The gap between the coil mass and PED construct (*arrow*) indicates the region of residual aneurysm filling. *C*, Follow-up angiogram in the frontal projection 6 months after treatment shows complete occlusion of the aneurysm. *D*, A native image in the frontal projection shows that the gap between the coil mass and PED construct has resolved (*arrow*). This finding indicates that the aneurysm has not only undergone complete thrombosis, but that the thrombus mass has been resorbed in the interim with contraction of the intra-aneurysmal thrombus-coil mass complex around the outside of the construct.

Table 1: Characteristics of study aneurysms and treatment

Characteristic	No. (%) or Mean (Range)
Target IA location	
Anterior	
Cavernous	5 (16.1)
Paraophthalmic	15 (48.4)
Superior hypophyseal	4 (12.9)
Posterior communicating	4 (12.9)
M1 segment	1 (3.2)
Posterior	
Distal pre-PICA vertebral	1 (3.2)
PICA vertebral	1 (3.2)
Neck ≥4 mm	22 (71.0)
Maximum aneurysm dimension (mm)	11.5 (2.5–26.6)
<10 mm	20 (64.5)
10–25 mm	9 (29.0)
≥25 mm	2 (6.5)
Number of PEDs implanted	
1	18 (58.1)
2	11 (35.5)
3	1 (3.2)
4	1 (3.2)
Adjunctive coils placed	16 (51.6)

into the microcatheter but the physician could not deliver the device to the targeted landing zone, typically due to excessive friction within the delivery microcatheter. In 1 additional case, a partially deployed PED was judged to be in a suboptimal position and was removed before full deployment. In all cases, successful device deployments were achieved on reattempted delivery during the same procedure. Deployment failures did not result in any adverse events.

Treatment: Periprocedural Outcomes

Clinical procedure success (device-placement success without in-hospital neurologic death or ipsilateral stroke) was achieved in 29/31 (93.5%) patients. Two patients had major stroke. The patient with iatrogenic rupture of the distal ICA had a large left-hemisphere stroke. A second patient experienced a periprocedural stroke manifest as right-sided hemiparesis and motor aphasia following reconstruction of the M1 segment of the left MCA with 2 overlapping PEDs and a Neuroform stent followed by coil embolization of a giant M1 aneurysm. CT imaging 2 days after the procedure showed a left deep gray matter infarction. Speech function improved significantly during the periprocedural hospitalization with marked additional improvement observed at the 30-day postprocedural visit. This event may be attributable to the coverage of regional lenticulostriate branches with multiple PEDs as well as technical complexities encountered during the placement of telescoping PEDs and an anchoring Neuroform stent as well as the subsequent coiling of the giant (25 mm) aneurysm. No subject experienced clinically significant bleeding with the use of aspirin and clopidogrel. Apart from the 2 patients with periprocedural stroke, no neurologic deterioration was observed in any of the patients at discharge.

Follow-Up: Angiographic Results at 180 Days

Diagnostic angiography at 180 days was performed in 30 of 31 patients and was assessed by an independent neuroradiologist (Table 2). Follow-up angiography was not performed for the patient in whom the PED had been surgically removed and the parent vessel ligated. Complete aneurysm occlusion was observed in 28 of 30 (93.3%) patients (Fig 3). Residual aneurysm filling was noted in 2 (6.7%). One of aneurysms not completely occluded at 180-day follow-up angiography had been treated with a conventional stent before PED treatment. One of the patients with an incompletely occluded aneurysm at 180-day angiography (the patient without an indwelling conventional stent) underwent an additional poststudy angiographic follow-up at 1 year, which demonstrated progression to complete aneurysm occlusion. Twenty-eight of 30 patients had no stenosis (0% to <25% stenosis) of the parent artery where the PED was placed. One patient showed mild (>25%-50%) stenosis but had no symptoms. In 1 patient, stenosis could not be evaluated because a large coil mass obscured visualization of a portion of the PED construct. Distal PED migration did not occur in any case.

Follow-Up: Clinical Results at 180 Days

No delayed neurologic events occurred between discharge and 180-day follow-up. No delayed hemorrhagic complications related to aspirin and clopidogrel therapy were encountered.

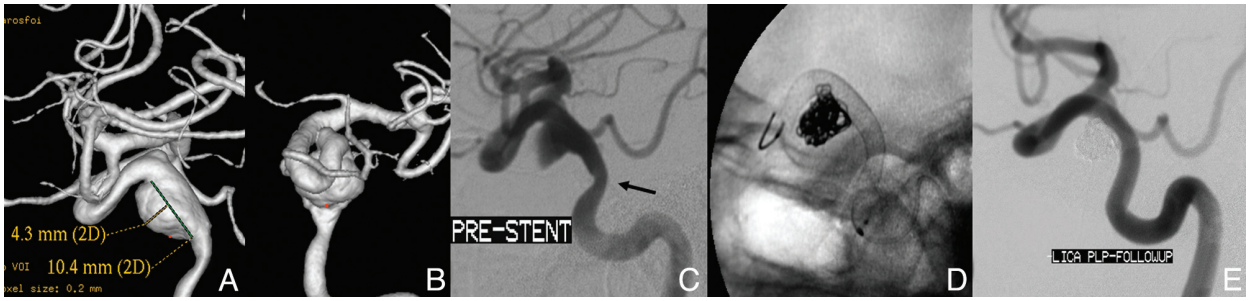

Fig 2. Dysplastic wide-neck partially thrombosed aneurysm arising from the proximal cavernous segment of the internal carotid artery. *A* and *B*, 3D images reconstructed from rotational angiographic source data demonstrate that the neck of the aneurysm incorporates >180° of the vessel circumference over a 10-mm segment of the carotid artery. *C*, Conventional angiography in the lateral working projection depicts the partially thrombosed wide-neck aneurysm arising from the circumferentially diseased segment. Just proximal to the aneurysmal segment is a mild focal stenosis (*arrow*). *D*, Native image in the lateral working-angle projection after treatment demonstrates the Pipeline construct in place across the aneurysm neck, with a loose packing of the aneurysm with embolization coils. *E*, Follow-up angiography at 180 days in the lateral working projection shows total occlusion of the aneurysm as well as complete anatomic remodeling of the diseased parent artery. The dysplastic aneurysmal vascular segment now has a smooth tubular configuration. The proximal stenosis has also completely remodeled and now is normal in caliber.

Table 2: Angiography findings at 180 days (n = 30)

Category	No. (%)
Target IA occlusion	
Complete	28 (93.3)
Residual neck	0 (0.0)
Residual filling	2 (6.7)
Device migration	
No	29 (96.7)
Yes	0 (0.0)
Unable to determine	1 (3.3)
Stenosis	
0%–25%	28 (93.3)
>25%–50%	1 (3.3)
>50%–75%	0
>75%–100%	0
Not judged	1 (3.3)

Discussion

The most important observations of the PITA trial are the following: 1) The treatment of intracranial aneurysms with PED (alone or adjunctively in support of aneurysm coiling) was feasible with a high rate of technical success. 2) Definitive endoluminal reconstruction of the parent artery with PED was achieved with a level of procedural safety analogous to that reported for the conventional coil-based endosaccular treatment of complex intracranial aneurysms. 3) Parent artery reconstruction with PED yielded a rate of complete aneurysm occlusion at 180 days that approached 100% and exceeded that traditionally reported after conventional endosaccular aneurysm treatment. 4) PED implantation was not associated with a high prevalence of delayed in-construct stenosis or thrombosis during the study interval. 5) PED was not associated with delayed clinical neurologic events following treatment.

Traditional Endosaccular Treatment of Cerebral Aneurysms

Endovascular therapy (eg, coil embolization) has been subject to criticism for a consistent failure to achieve the same level of durable and complete aneurysm exclusion that surgical aneurysm clipping typically provides. This is particularly true for large (> 10 mm) and wide-neck aneurysms, which have low rates of complete occlusion both initially and at angiographic follow-up as well as relatively high rates of recurrence with traditional endovascular endosaccular occlusion strategies.[5,6] In particular, very large and giant aneurysms are almost never completely "cured" with reconstructive endosaccular approaches and usually require numerous retreatments and lifelong imaging surveillance.[7] Numerous iterations of endovascular coils, such as complex-shaped, 3D framing, and very soft packing coils, as well as bioactive and hydrogel-coated coils have been developed in an attempt to address these limitations. However, the results of many single-center series and industry-sponsored multicenter trials have failed to demonstrate that any of these technologies have produced a marked incremental improvement in either the safety of the procedure, rate of complete aneurysm occlusion, or likelihood of aneurysm recurrence after treatment.[8,9]

The failure of endosaccular techniques to achieve a complete and durable occlusion of aneurysms has been attributed to several factors, including limitations with respect to the volumetric packing of the aneurysm sac with coils, inherent difficulties associated with achieving a continuous reconstruction of large complex aneurysm neck defects with coils, and finally a fundamental failure of the endosaccular strategy to address the underlying diseased parent vessel (Fig 1).[2]

Endoluminal Reconstruction of Cerebral Aneurysms with Flow Diverters: Putative Mechanism of Action

Endoluminal reconstruction with the PED represents a completely different approach to the endovascular treatment of intracranial aneurysms in that the parent artery defect is actually repaired by the device and the biologic response it elicits from the adjacent parent artery. The feasibility of the concept of primary endoluminal reconstruction (rather than endosaccular filling) to achieve aneurysm occlusion was demonstrated in the 1990s by the seminal work of several investigators who implanted stents, with and without endosaccular embolization coils or liquid polymers, across the necks of experimental aneurysms.[10-14] With the development of low-profile microcatheter-delivered self-expanding (eg, Neuroform, Boston Scientific; Enterprise, Cordis, Miami Lakes, Florida) and balloon-expandable intracranial stents, the concept of intracranial parent artery reconstruction became clinically feasible.[14-16] These initial self-expanding neurostents were engineered primarily for adjunctive use to support the coil

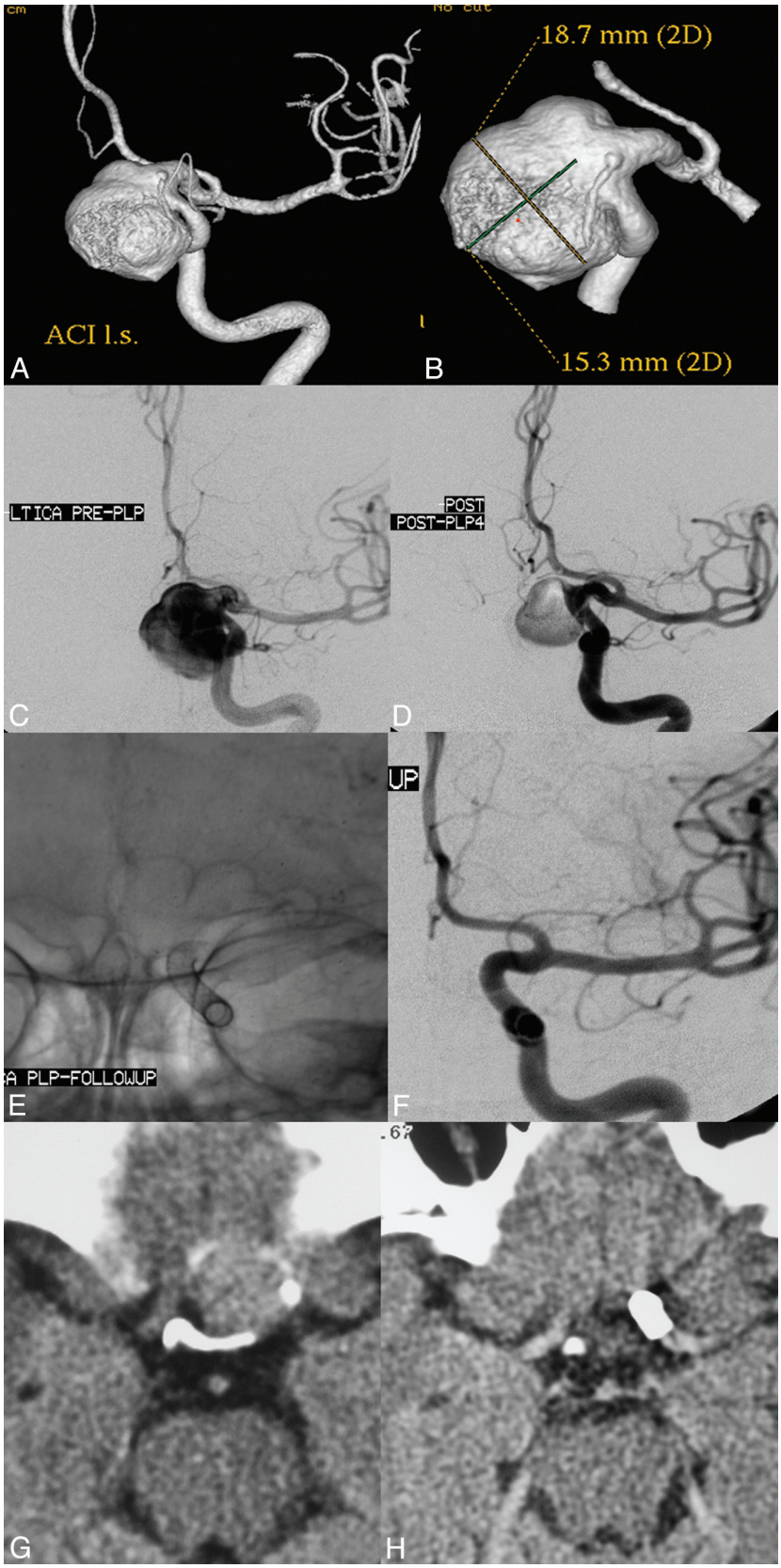

Fig 3. Left ICA parophthamalic-segment aneurysm in a patient with progressive ipsilateral vision loss. *A* and *B*, 3D reconstructed images from rotational source data show a very large wide-neck aneurysm arising from the parophthalmic segment of the left ICA. *C*, Initial angiogram in the frontal working projection demonstrates a very large aneurysm arising from the left ICA. *D*, Following reconstruction with a PED, filling of the aneurysm with contrast is diminished because flow has been redirected along the normal course of the ICA and into the left anterior circulation. The patient emerged from general anesthesia with an improvement in left-eye vision. *E*, A native image depicts the PED construct in position across the aneurysmal segment. *F*, Subtracted image from the 6-month follow-up angiogram shows anatomic reconstruction of the parent artery with complete aneurysm occlusion. *G*, Axial CT image at the level of the optic chiasm before treatment demonstrates the peripherally calcified fundus of the very large left ICA aneurysm projecting into the suprasellar cistern. *H*, Six-month follow-up axial CT image depicts a PED in place within the parent ICA with complete resolution of the aneurysm-thrombus mass. The suprasellar cistern, which was formerly effaced by the aneurysm, now appears normally filled with CSF. These serial images depict the physiologic progression that is possible in some cases after PED reconstruction—starting with mechanical flow diversion, progressing to physiologic aneurysm thrombosis and complete occlusion, followed by endoluminal parent artery reconstruction and, ultimately, anatomical restoration with resolution of the aneurysm-thrombus mass and dissipation of the regional mass effect.

embolization of cerebral aneurysms and, as such, had very low metal surface-area coverage and large cell sizes to permit traversal with a microcatheter. As such, the hemodynamic impact achieved with solitary use of these devices in most cases was minimal.[17,18]

In contradistinction to the coil-assist stents, the low-poros-

ity flow diverting constructs were designed specifically to redirect blood flow along the normal course of the parent artery, markedly altering dynamic fluid exchange across the aneurysm/parent vessel interface, thereby creating an intra-aneurysmal environment that is conducive to thrombosis. As important, however, following successful aneurysm thrombosis, the construct becomes progressively incorporated into the parent artery through a process of neointimal overgrowth. Once this has occurred, a continuous, homogeneous layer of tissue unites the normal parent artery segments proximal and distal to the aneurysm neck defect, completing the process of endoluminal reconstruction. The construct-induced neointimal overgrowth of the aneurysm neck ultimately results in the anatomic exclusion of the aneurysm from the circulation and promotes final involution of the aneurysmal mass as the intrasaccular thrombus is resorbed. Optimally, this anatomic restoration of the perivascular anatomy may lead to a resolution of any clinical sequelae related aneurysmal to mass effect and restoration of normal extravascular anatomy (Figs 1 and 3). This sequence of events has been observed clinically in individual human patients and has also been validated in a series of experimental aneurysms.[19-21]

Parent Artery Reconstruction with the Pipeline Is Technically Feasible

Ultimately, successful placement of the desired number of PEDs across the aneurysm neck was achieved 98% of the time. During the PITA trial, the PED was deployed through approved microcatheters (Renegade Hi-Flo; Masstransit) that were not specifically designed for PED implantation. These microcatheters frequently "ovalized" or kinked around vascular turns and sometimes stretched during device delivery, making PED deployment challenging, particularly in tortuous segments of the cerebral vasculature. Since the completion of PITA, a microcatheter (Marksman, ev3/Chestnut Medical) has been specifically engineered for the delivery and deployment of the Pipeline. The availability of an optimized PED delivery catheter may significantly improve the ease of device placement and reduce the frequency of delivery-deployment failures.

Parent Artery Reconstruction with the Pipeline Was Achieved with an Acceptable Procedural-Risk Profile

Two periprocedural neurologic complications were noted in the present series, both of which were major strokes. This rate of periprocedural complications (6.5%) is analogous to that reported for the endovascular treatment of aneurysms using other approved self-expanding intracranial microstents.[22-24] One of the complications related to the placement of multiple PEDs within the M1 segment of the MCA to support endosaccular coiling of a giant aneurysm was an infarction in the territory of a lateral lenticulostriate branch. This complication, to some degree, reflects an earlier stage of understanding of the device, its optimal application, and its limitations. Currently, we do not recommend overlapping multiple constructs in regions giving rise to eloquent perforators.

Pipeline Treatment Elicited a Very High Rate of Complete Aneurysm Occlusion

The rates of complete aneurysm occlusion achieved with the Pipeline surpass those reported in the literature for conventional endovascular endosaccular aneurysm treatments. In the present study, 93% of the aneurysms treated were occluded at 6-month follow-up. Moreover, 1 of the aneurysms that was incompletely occluded at 6 months progressed to complete occlusion by 12 months. These complete occlusion rates are even more impressive when considering that the types of aneurysms included in the present study—large, giant, wide-neck, and failed/recurrent—are those that are typically the most challenging for conventional coil-based endosaccular treatments. Because the efficacy of Pipeline reconstruction is not at all dependent upon the dense packing of the aneurysm fundus with embolic materials, the ability to achieve a complete and durable occlusion with the Pipeline is not dependent on the size or configuration of the aneurysm sac, the presence of intra-aneurysmal thrombus, or the width of the aneurysm neck. As such, wide-neck, fusiform, partially thrombosed, and very large-giant aneurysms may be particularly well-suited for endoluminal reconstruction.

One of the 2 aneurysms not initially occluded with the Pipeline had been previously treated with another intracranial stent. Indwelling SESs not only have the potential to complicate the delivery and deployment of flow diverters, but we hypothesize that these SESs impair effective apposition of lower porosity constructs (like the PED) to the parent artery, thus slowing or preventing the overgrowth of a contiguous and homogeneous neointimal and endothelial coverage of the aneurysm neck and potentially inhibiting complete aneurysm occlusion.[1]

Delayed In-Construct Stenosis Was Not Observed in the Present Series

In the current series, 1 asymptomatic moderate-grade (25%–50%) stenosis was observed in the 30 patients presenting for angiographic follow-up. There were no cases of high-grade (>50%) or symptomatic stenosis observed during the 180-day follow-up after PED implantation. Because the Pipeline is a bare metal device, it would be expected that most in-construct stenoses would be observed within 3–6 months of implantation.[25] As such, the present series suggests that in-construct stenosis observed after PED placement is likely to occur at a relatively low rate.

Delayed Neurologic Events Were Not Observed in the Present Series

The absence of delayed neurologic events following treatment suggests that, as with conventional endovascular aneurysm therapies, most complications with endoluminal reconstruction should be expected to occur during the early periprocedural period. Given that PED reconstruction results in a very high rate of complete aneurysm occlusion (approaching 100% in the present series) and conceivably will be associated with minimal or no recurrences after treatment, the requirement for multiple retreatments (and perhaps at some point continual angiographic or cross-sectional imaging surveillance) is likely to be substantially reduced if not eliminated altogether in most cases. This possibility is particularly important for large, giant wide-neck aneurysms and those that have failed prior treatment, because these lesions are notorious for recurrence following endovascular treatment and require long-term follow-up.[5] This potential reduction in the rate of fol-

low-up angiography and re-intervention could conceivably translate directly to lower cumulative risks for patients, fewer procedures, lower levels of radiation exposure, fewer hospital admissions, fewer imaging studies, and lower overall health care costs.

Conclusions

The PITA trial demonstrates that the reconstruction of complex aneurysms with endoluminal devices is technically feasible and can be achieved with an acceptable level of periprocedural risk. Complete angiographic occlusion of the target aneurysm was observed in a majority of cases (>90%), exceeding the occlusion rates reported after conventional coil-based endosaccular treatment strategies. It is likely that PED and similar endoluminal devices will play an important role in the future of endovascular aneurysm treatment. The optimal application of these devices will continue to be defined as clinical experience evolves.

Acknowledgement

The authors wish to acknowledge the work of Prof. Guenther Klein, who functioned as the site PI for Medical University of Graz, Graz, Austria during the PITA study.

References

1. Lylyk P, Miranda C, Ceratto R, et al. **Curative endovascular reconstruction of cerebral aneurysms with the Pipeline embolization device: the Buenos Aires experience**. *Neurosurgery* 2009;64:632–42, discussion 642–43, quiz N636
2. Fiorella D, Lylyk P, Szikora I, et al. **Curative cerebrovascular reconstruction with the Pipeline embolization device: the emergence of definitive endovascular therapy for intracranial aneurysms.** *J Neurointerv Surg* 2009;1:56–65
3. Fiorella D, Kelly ME, Albuquerque FC, et al. **Curative reconstruction of a giant midbasilar trunk aneurysm with the Pipeline embolization device**. *Neurosurgery* 2009;64:212–17, discussion 217
4. Szikora I, Berentei Z, Kulcsar Z, et al. **Treatment of intracranial aneurysms by functional reconstruction of the parent artery: the Budapest experience with the Pipeline embolization device.** *AJNR Am J Neuroradiol* 2010;31:1139–47. Epub 2010 Feb 11
5. Raymond J, Guilbert F, Weill A, et al. **Long-term angiographic recurrences after selective endovascular treatment of aneurysms with detachable coils.** *Stroke* 2003;34:1398–403
6. Ferns SP, Sprengers ME, van Rooij WJ, et al. **Coiling of intracranial aneurysms: a systematic review on initial occlusion and reopening and retreatment rates.** *Stroke* 2009;40:e523–29
7. van Rooij WJ, Sluzewski M. **Endovascular treatment of large and giant aneurysms.** *AJNR Am J Neuroradiol* 2009;30:12–18
8. Fiorella D, Albuquerque FC, McDougall CG. **Durability of aneurysm embolization with Matrix detachable coils**. *Neurosurgery* 2006;58:51–59
9. D'Agostino SJ, Harrigan MR, Chalela JA, et al. **Clinical experience with Matrix2 360 degrees coils in the treatment of 100 intracranial aneurysms.** *Surg Neurol* 2009;72:41–47
10. Szikora I, Guterman LR, Standard SC, et al. **Endovascular treatment of experimental aneurysms with liquid polymers: the protective potential of stents.** *Neurosurgery* 1996;38:339–47
11. Wakhloo AK SF, de Vries J, et al. **Coated and non-coated stents for vessel reconstruction and treatment of aneurysms and AV-fistulas: an experimental study**. *XVIIIth Congress of the European Society of Neuroradiology*, Stockholm, Sweden, September 8–11, 1992:S24
12. Turjman F, Acevedo G, Moll T, et al. **Treatment of experimental carotid aneurysms by endoprosthesis implantation: preliminary report.** *Neurol Res* 1993;15:181–84
13. Geremia G, Haklin M, Brennecke L. **Embolization of experimentally created aneurysms with intravascular stent devices.** *AJNR Am J Neuroradiol* 1994;15:1223–31
14. Wakhloo AK, Mandell J, Gounis MJ, et al. **Stent-assisted reconstructive endovascular repair of cranial fusiform atherosclerotic and dissecting aneurysms: long-term clinical and angiographic follow-up.** *Stroke* 2008;39:3288–96
15. Fiorella D, Albuquerque FC, Deshmukh VR, et al. **Endovascular reconstruction with the Neuroform stent as monotherapy for the treatment of uncoilable intradural pseudoaneurysms**. *Neurosurgery* 2006;59:291–300
16. Lylyk P, Cohen JE, Ceratto R, et al. **Endovascular reconstruction of intracranial arteries by stent placement and combined techniques.** *J Neurosurg* 2002;97:1306–13
17. Canton G, Levy DI, Lasheras JC, et al. **Flow changes caused by the sequential placement of stents across the neck of sidewall cerebral aneurysms.** *J Neurosurg* 2005;103:891–902
18. Canton G, Levy DI, Lasheras JC. **Hemodynamic changes due to stent placement in bifurcating intracranial aneurysms.** *J Neurosurg* 2005;103:146–55
19. Kallmes DF, Ding YH, Dai D, et al. **A second-generation, endoluminal, flow-disrupting device for treatment of saccular aneurysms.** *AJNR Am J Neuroradiol* 2009;30:1153–58
20. Kallmes DF, Ding YH, Dai D, et al. **A new endoluminal, flow-disrupting device for treatment of saccular aneurysms.** *Stroke* 2007;38:2346–52
21. Sadasivan C, Cesar L, Seong J, et al. **Treatment of rabbit elastase-induced aneurysm models by flow diverters: development of quantifiable indexes of device performance using digital subtraction angiography.** *IEEE Trans Med Imaging* 2009;28:1117–25
22. Benitez RP, Silva MT, Klem J, et al. **Endovascular occlusion of wide-necked aneurysms with a new intracranial microstent (Neuroform) and detachable coils**. *Neurosurgery* 2004;54:1359–67, discussion 1368
23. Biondi A, Janardhan V, Katz JM, et al. **Neuroform stent-assisted coil embolization of wide-neck intracranial aneurysms: strategies in stent deployment and midterm follow-up**. *Neurosurgery* 2007;61:460–68, discussion 468–69
24. Fiorella D, Albuquerque FC, Han P, et al. **Preliminary experience using the Neuroform stent for the treatment of cerebral aneurysms**. *Neurosurgery* 2004; 54:6–16, discussion 16–17
25. Kimura T, Yokoi H, Nakagawa Y, et al. **Three-year follow-up after implantation of metallic coronary-artery stents.** *N Engl J Med* 1996;334:561–66

ORIGINAL RESEARCH
HEALTH POLICIES/QUALITY IMPROVEMENT/EVIDENCE-BASED NEUROIMAGING

Shift Volume Directly Impacts Neuroradiology Error Rate at a Large Academic Medical Center: The Case for Volume Limits

Vladimir Ivanovic, Kenneth Broadhead, Yu-Ming Chang, John F Hamer, Ryan Beck, Lotfi Hacein-Bey, and Lihong Qi

ABSTRACT

BACKGROUND AND PURPOSE: Unlike in Europe and Japan, guidelines or recommendations from specialized radiological societies on workflow management and adaptive intervention to reduce error rates are currently lacking in the United States. This study of neuroradiologic reads at a large US academic medical center, which may hopefully contribute to this discussion, found a direct relationship between error rate and shift volume.

MATERIALS AND METHODS: CT and MR imaging reports from our institution's Neuroradiology Quality Assurance database (years 2014–2020) were searched for attending physician errors. Data were collected on shift volume specific error rates per 1000 interpreted studies and RADPEER scores. Optimal cutoff points for 2, 3 and 4 groups of shift volumes were computed along with subgroups' error rates.

RESULTS: A total of 643 errors were found, 91.7% of which were clinically significant (RADPEER 2b, 3b). The overall error rate (errors/1000 examinations) was 2.36. The best single shift volume cutoff point generated 2 groups: ≤ 26 studies (error rate 1.59) and > 26 studies (2.58; OR: 1.63, $P < .001$). The best 2 shift volume cutoff points generated 3 shift volume groups: ≤ 19 (1.34), 20–28 (1.88; OR: 1.4, $P = .1$) and ≥ 29 (2.6; OR: 1.94, $P < .001$). The best 3 shift volume cutoff points generated 4 groups: ≤ 24 (1.59), 25–66 (2.44; OR: 1.54, $P < .001$), 67–90 (3.03; OR: 1.91, $P < .001$), and ≥ 91 (2.07; OR: 1.30, $P = .25$). The group with shift volume ≥ 91 had a limited sample size.

CONCLUSIONS: Lower shift volumes yielded significantly lower error rates. The lowest error rates were observed with shift volumes that were limited to 19–26 studies. Error rates at shift volumes between 67–90 studies were 226% higher, compared with the error rate at shift volumes of ≤ 19 studies.

ABBREVIATIONS: ICC = intraclass correlation coefficient; QA = quality assurance; VIF = variance inflation factor

Medical errors are the third leading cause of death in the United States.[1] Many industries have implemented system-wide measures and technological advancements to decrease errors and fatalities. Between 1973 and 2020, the number of commercial aviation fatalities has decreased by 97%.[2] Anesthesia-related mortality in the United States has decreased by 97% from 1952 to 2005.[3] Reported rates of major errors in radiology range between 2%–6%.[4-7] Error rates in diagnostic radiology have remained relatively constant since the time they were first studied in 1949.[8-14]

Studies of both general radiology[15,16] and neuroradiology[17] have found higher shift volumes to be associated with diagnostic errors. Larger scale studies evaluating radiology error rates as a function of specific shift volume are lacking. The identification of specific shift volume ranges that minimize error rates could lead to corrective interventions. Our aims were to extend the knowledge gained from our prior work by using the same data set[17-22] to evaluate shift volume specific error rates by neuroradiologists at a large academic medical center and to identify the shift volume ranges with the lowest error rates.

MATERIALS AND METHODS

Study Setting

Institutional review board approval with a waiver of informed consent was obtained for this retrospective study. Our department's neuroradiology quality assurance (QA) database was searched for attending neuroradiologist errors between 2014–2020, which includes cases collected during the review of all addended reports and a review of computer selected studies during a clinical service, as previously described.[20] Whenever assigned to a

Received October 6, 2023; accepted after revision December 18.

From the Department of Radiology, Section of Neuroradiology (V.I., J.F.H., R.B.), Medical College of Wisconsin, Milwaukee, Wisconsin; Department of Statistics (K.B.), Colorado State University, Fort Collins, Colorado; Department of Radiology, Section of Neuroradiology (Y.-M.C.), Beth Israel Deaconess Medical Center, Boston, Massachusetts; Department of Radiology, Section of Neuroradiology (L.H.-B.), University of California Davis Medical Center, Sacramento, California; and Department of Public Health Sciences (L.Q.), School of Medicine, University of California Davis, Davis, California.

Please address correspondence to Vladimir Ivanovic, MD, Medical College of Wisconsin, Department of Radiology, 8701 Watertown Plank Rd, Milwaukee, WI 53226; e-mail: Vladimir.ivanovic@yahoo.com

Indicates article with online supplemental data.

http://dx.doi.org/10.3174/ajnr.A8119

clinical service (all shifts, all radiologists), the neuroradiologist is presented with 3 randomly computer selected CT or MR imaging examinations, and the neuroradiologist is instructed to review and assign a score (1, 2a, 2b, 3a, 3b) to each by using the American College of Radiology RADPEER system.[23] All RADPEER scores of 2 and 3 are further reviewed by either 2 additional attending neuroradiologists or the entire neuroradiology division during a quarterly QA conference to reach a consensus RADPEER score. Each reviewed examination is entered into the QA database along with its associated RADPEER score. Diagnostic error rates are expressed as the number of errors per 1000 interpreted examinations that are shift volume specific.

All 16 current or former members of the neuroradiology division are full-time employees who have completed neuroradiology fellowships. Division members have similar yearly productivity, read similar neuroimaging case mixes and rotate with similar frequency among general neuroradiology nonsubspecialized clinical services: emergency/inpatient (9-hour day shift), spine (9-hour day shift), outpatient (9-hour day shift), evening weekday call (6-hour evening shift), and weekend call (9–12-hour day shift). Attendings read a similar mix of adult and pediatric CT and MR imaging neuroradiology studies, which are read in chronological order on either a single common outpatient study worklist or a dedicated emergency/inpatient worklist. Broadly speaking, approximately 40% of the studies were dictated by trainees.

Data Collection

Data on shift volumes on the days an error was documented, the number of errors per shift volume, the total number of studies interpreted for each shift volume and demographic information were extracted from the radiology departmental database. Diagnostic error rates are expressed as the number of errors per 1000 interpreted examinations for each specific shift volume (for example, if there were 10 errors detected on all shifts of 40 studies, and there were 1000 shifts during which 40 studies were interpreted, then the error rate for a shift volume of 40 would be 10 / [40 × 1000]). The shift volume was defined as the total number of CT and MR imaging examinations that the neuroradiologist interpreted during the shift (eg, if 6 radiologists are working on a given day, this would constitute 6 total shifts for that day). We excluded shifts with 10 or fewer interpreted studies per day as outliers; many of these likely represent reports generated on administrative or off days, possibly to catch up with overflow work from the day before. For examinations comprising multiple unique accession numbers (eg, head MR imaging-MRA), each accession number was considered to be a single examination for purposes of determining shift volume.

Statistical Methods

Descriptive statistics (mean and SD for age; count and percentages for age) were obtained for the error group.

Optimal cutoff points categorizing examinations into one of several risk groups, using shift volume level as the diagnostic variable, were computed by using ordinary logistic regression.[24] Given the wide range of daily shift volume productivity within our practice, we wanted to determine more than one possible cutoff point and error rate differences for the resultant groups. Each possible combination of cutoff points, categorizing examinations into 2, 3 or 4 separate risk groups, were computed. The optimal cutoff values are defined as the ones with the most significant overall likelihood ratio test statistics, giving the most significant overall set of risk groups for a specified number of cutoff points. Individual odds ratios and *P* values comparing each group with the group with the lowest shift volume (group 1) within each split are also computed, but these were not used to determine optimality. The error rate per 1000 studies was computed for each group within a split.

To assess the impact of potential correlation among examinations read by the same radiologist, the intraclass correlation, measured by the intraclass correlation coefficient (ICC), and the resulting variance inflation factor (VIF) were examined. In the presence of high intraclass correlation or VIFs, the use of ordinary logistic regression is inappropriate. As covariate information on the attending radiologist was unavailable for all examinations, the ICC and VIF were computed by using a subset of the data analyzed in a previous study.[25] ICC values near 1 indicate high correlation, whereas values near 0 indicate low correlation. High VIFs indicate that variances of estimated parameters are higher than they would be in the absence of intraclass correlation, whereas values near 1 indicate little inflation. The ICC, its 95% confidence interval, and the VIFs were computed by using resampling techniques.[26] All statistical analyses were performed in R, version 4.1.1.

RESULTS

There were 643 patients within the error group; 349 were men (54.3%), 293 were women (45.6%), and 1 (0.2%) patient's sex was not recorded. The mean patient age was 49.8 years (SD, 25).

The estimated ICC among attending radiologists was low (0.001; 95% CI, 0–0.079), as was the estimated VIF (1.099), suggesting minimal correlation between examinations and minimal variance inflation. Six attending radiologists had small cluster sizes (having read fewer than 10 examinations). A sensitivity analysis of the ICC and VIF estimates was performed by rerunning the analysis without the small clusters. Similar estimates of the ICC (0.0005; 95% CI, 0–0.0796) and VIF (1.073) were obtained. Because of the low correlation and VIF, the method for determining optimal risk groups by using ordinary logistic regression was deemed acceptable.

A total of 643 errors were detected during the study period; 590 (91.7%) were clinically significant (RADPEER 2b, 3b). The overall error rate (per 1000 interpreted examinations) was found to be 2.36. Figure 1 presents a detailed view of the trend in error rate as a function of shift volume compared with the overall error rate. The Table presents the risk groups by shift volume for 1, 2 and 3 cutoff points. All group splits were found to be highly significant by using the likelihood ratio test ($P < .001$).

For a single cutoff point (search done for each shift volume level), group 1 consists of examinations read during shift volumes of ≤26 (error rate 1.59), whereas group 2 consists of examinations read during shift volumes of ≥27 (error rate 2.58). The odds of an examination in group 2 containing an error were found to be 63% higher than examinations in group 1 (OR: 1.63, $P < .001$).

For 2 cutoff points (search done by fours), group 1 consists of examinations read during shift volumes of ≤19 (error rate 1.34), group 2 consists of examinations read during shift volumes

between 20 and 28 (error rate 1.88), and group 3 consists of examinations read during shift volumes of ≥29 (error rate 2.6). The odds of an examination in group 2 containing an error were found to be 40% higher than examinations in group 1 (OR: 1.4, $P = .1$), whereas the odds of examinations in group 3 were found to be 94% higher than examinations in group 1 (OR 1.94, $P < .001$).

For 3 cutoff points (search done by tens), group 1 consists of examinations read during shift volumes of ≤24 (error rate 1.59), group 2 consists of examinations read during shift volumes between 25 and 66 (error rate 2.44), group 3 consists of examinations read during shift volumes between 67 and 90 (error rate 3.03), and group 4 consists of examinations read during shift volumes of ≥91 (error rate 2.07). The odds of an examination in group 2 containing an error were found to be 54% higher than examinations in group 1 (OR: 1.54, $P < .001$), the odds of an examination in group 3 containing an error were found to be 91% higher than examinations in group 1 (OR: 1.91, $P < .001$), and the odds of an examination in group 4 containing an error were found to be 30% higher than examinations in group 1 (OR 1.30, $P = .25$).

DISCUSSION

In this study, we have found that neuroradiology errors are significantly lower on low shift volumes compared with high shift volumes. Based on our data, the best outcomes are seen when shift volumes are ≤19–26 studies. Our data are in line with the findings of a recent nationwide survey of 42 academic neuroradiology division chiefs that suggested a mean optimal shift volume of between 25–33 studies.[27] Our group error rate was 2.36; if our shift volume could be limited to 19 studies, error rates could potentially decrease by 57%. The highest error rates were observed at shift volumes of between 67–90 studies, which was 226% higher than the lowest error rate, which was observed at shift volumes of ≤19 studies. Error rates at high shift volumes might be difficult to justify, given this degree of difference. Approximately 74 million CT and 39 million MR imaging studies are performed in the United States per year,[28] and decreasing the mean error rates might have a significant impact from a public health perspective.[1] Medicolegal outcomes of errors are not insignificant. An analysis of 2019 malpractice claims in diagnostic and interventional neuroradiology found a median plaintiff award of $2,877,847 and a median settlement amount of $1,950,000.[29] Missing aneurysms on CT or MR imaging may lead to plaintiff awards of $4–43 million.[30]

For 3 cutoff points, the odds ratio for the group 4 risk group decreases, seemingly suggesting that it is safer than groups 2 and 3. However, this is most likely due to comparatively limited sample sizes for the shift volume levels comprising that group. Figure 2 presents a plot of the sample size for each shift volume; shift volumes of 91 and greater can be seen to have markedly lower sample sizes than those of the lower shift volumes. Furthermore, many shift volumes after this threshold are so small that no error has yet been observed at these volume levels. Together with the overall trends seen in Fig 1, we do not have any reason to suspect that risk group 4 is any safer than groups 2 and 3. We conclude the decreased odds ratio for group 4 is the result of sample size limitations.

Prior literature has highlighted a broad range of potential strategies for reducing diagnostic errors within general and specialized practices, including interpretation

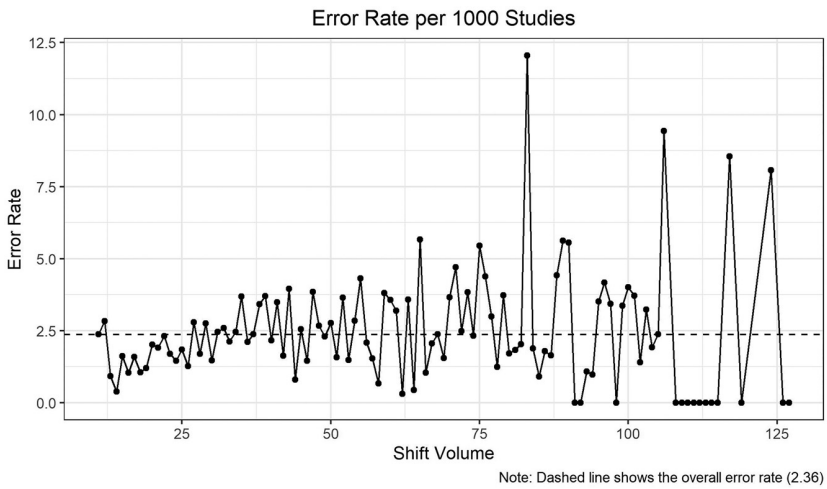

FIG 1. Detailed view of the trends in error rate as a function of shift volume level against the overall error rate.

Optimal risk groups

	Group 1 (Error Rate)[g]	Group 2 (Error Rate)	Group 3 (Error Rate)	Group 4 (Error Rate)	Odds Ratio 1 (*P* Value)	Odds Ratio 2 (*P* Value)	Odds Ratio 3 (*P* Value)	LRT *P* Value[h]
1 cut point[a]	26 and below (1.59)	27+ (2.58)	–	–	1.63 (<.001)[d]	–	–	<.001
2 cut points[b]	19 and below (1.34)	20–28 (1.88)	29+ (2.6)	–	1.40 (.10)[e]	1.94 (<.001)[e]	–	<.001
3 cut points[c]	24 and below (1.59)	25–66 (2.44)	67–90 (3.03)	91+ (2.07)	1.54 (<.001)[f]	1.91 (<.001)[f]	1.30 (.25)[f,i]	<.001

Note:—LRT indicates likelihood ratio test.
[a] Search done for each shift volume level.
[b] Search done by fours.
[c] Search done by tens.
[d] Interpretation: The odds of containing an error are 63% higher for studies in group 2, compared with studies in group 1.
[e] Interpretation: The odds of containing an error are 40% higher for studies in group 2, compared with studies in group 1; the odds of containing an error are 94% higher for studies in group 3, compared with studies in group 1.
[f] Interpretation: The odds of containing an error are 54% higher for studies in group 2, compared studies in group 1; the odds of containing an error are 91% higher for studies in group 3, compared with studies in group 1; the odds of containing an error are 30% higher for studies in group 4, compared with studies in group 1.
[g] Error rate per 1000 exams.
[h] Optimal cutoff points are defined as the ones with the most significant (likelihood ratio test) split.
[i] Odds ratio 3 decreases, seemingly suggesting that group 4 is safer (than 2); however, this is due to sample size limitations in group 4.

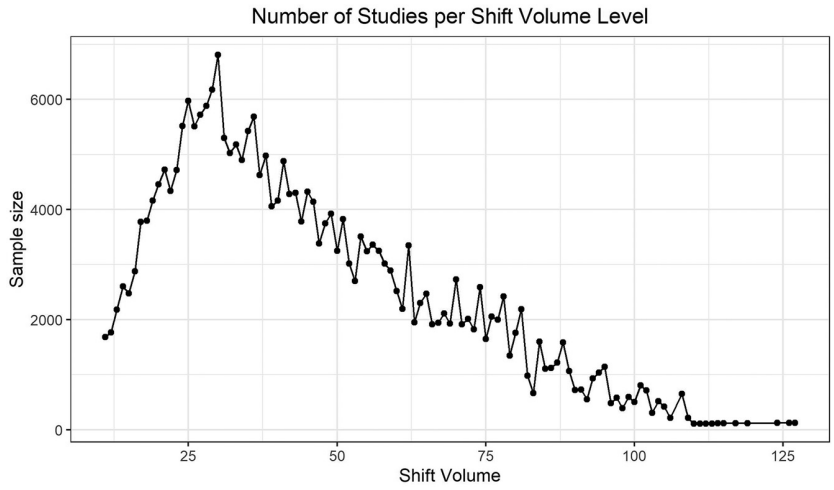

FIG 2. Sample size for each shift volume level.

by specialty and subspecialty radiologists,[9,10,31,32] lower shift volumes,[15] limits on shift lengths to less than 10 hours,[15,33] reductions in noninterpretive tasks during clinical shifts,[34] radiologist participation at multispecialty tumor boards,[20] awareness of most common types of misses,[18,19,21] and reduced interpretation speed.[35] Subspecialty interpretations of neuroradiologic studies can change clinical care up to 41% of the time when compared with those of general radiologists or nonsubspecialized neuroradiologist interpretations.[9,32] Radiologist workloads have been steadily increasing over recent decades.[36,37] If we can develop more uniform policies and hospital business models in which shift volume limits and subspecialized interpretations are incentivized to act synergistically, as has been successfully done at many institutions across the country, the error reduction rates might approximate those of the airline industry or anesthesia departments. In 2012, the Royal College of Radiologists issued a national guideline recommending that radiologists interpret up to 2 complex CT or MR imaging examinations and up to 6 CT or MR imaging examinations, overall, per hour.[38] In 2022, the Japanese College of Radiology issued a national guideline recommending that radiologists interpret up to 4 examinations per hour.[39] The American College of Radiology has not issued official guidelines aimed at reducing error rates in the United States.

The results of this study can be used to guide future strategies. In our institution, the initial step has been to reduce the effect of extreme shift volumes by adjusting workflow without increasing shift frequency. Flexibility toward a labor division based on seniority level and experience with certain studies is encouraged as part of the process. Promoting educational and research efforts, multidisciplinary consultations, and peer-review discussions allows us to maintain our focus on quality and deepening our expertise. Mid- and long-term goals of limiting shift volume within the 19–26 range should then facilitate adjustments to the traditional business models and should thereby result in increased job attractiveness and more effective support to cohesive and motivated teams while maintaining profitability.

The limitations of our study include its single-center retrospective design. Second, though our study contains a large number of detected errors compared with other publications, only a fraction of potential errors was detected, given our methods of data collection. Third, all radiologists were fellowship-trained neuroradiologists at an academic medical center. Thus, our findings may not apply for general radiology practice, for neuroradiologists at community practices, or for academic neuroradiologists who have significantly different workflows than ours. Ideally, each institution should conduct an analysis of its own data. Fourth, we did not include confounders in our analysis. Based on prior work, neuroradiologists' years of experience, trainee participation, and emergency interpretation setting did not have an impact on diagnostic errors, and shift volume was shown to be the dominant variable that influences outcomes.[25] Shift length was not evaluated as a risk factor for diagnostic error, and the same volume threshold for a 6-hour shift should be different in comparison with that of a 9-hour or 12-hour shift; our shifts were generally shorter than 9 hours, whereas prior literature suggests a significant increase in errors beyond a threshold of 10 hours.[15,33] Fifth, the analysis did not account for examination complexity (number of findings or diagnoses per study), which would be virtually impossible to evaluate, given the >250,000 studies performed during the study period. It might be reasonable to assume that higher volume shifts could have a higher proportion of negative or simple studies (negative CT head) and a lower proportion of complex MR imaging studies. Sixth, sub-analyses were not performed with respect to specific RADPEER scores (2a, 2b, 3a, or 3b). Further, prospective research is needed to determine shift volume safety cutoff points at the group and individual levels, using shift volume as the only variable and holding all possible confounders constant. Seventh, the lack of full covariate information on attending radiologists limited the analytic approaches that could be employed to handle potential intraclass correlation. Future studies should give thought to handling potential correlation though direct modeling.

CONCLUSIONS

Limiting the number of studies per shift to a low range, as opposed to high, unregulated volumes, should allow for the prevention of a significant number of diagnostic neuroradiology errors. Our study of shift volumes at a busy multispecialty, tertiary, large referral academic medical center suggests that neuroradiologic shift volumes should be limited to a 19–26 range per shift.

Disclosure forms provided by the authors are available with the full text and PDF of this article at www.ajnr.org.

REFERENCES

1. Makary MA, Daniel M. **Medical error-the third leading cause of death in the US.** *BMJ* 2016;353:i2139 CrossRef Medline
2. The flight safety foundation's aviation safety network. Fatalities per million passengers. https://aviation-safety.net/statistics/. Accessed September 23, 2023

3. Li G, Warner M, Lang BH, et al. **Epidemiology of anesthesia-related mortality in the United States, 1999–2005**. *Anesthesiology* 2009;110:759–65 CrossRef Medline
4. Wu MZ, McInnes MDF, Macdonald DB, et al. **CT in adults: Systematic review and meta-analysis of interpretation discrepancy rates.** *Radiology* 2014;270:717–35 CrossRef Medline
5. Babiarz LS, Yousem DM. **Quality control in neuroradiology: discrepancies in image interpretation among academic neuroradiologists.** *AJNR Am J Neuroradiol* 2012;33:37–42 CrossRef Medline
6. Borgstede JP, Lewis RS, Bhargavan M, et al. **RADPEER quality assurance program: a multifacility study of interpretive disagreement rates.** *J Am Coll Radiol* 2004;1:59–65 CrossRef
7. Kim YW, Mansfield LT. **Fool me twice: delayed diagnoses in radiology with emphasis on perpetuated errors.** *AJR Am J Roentgenol* 2014;202:465–70 CrossRef Medline
8. Garland LH. **On the scientific evaluation of diagnostic procedures.** *Radiology* 1949;52:309–28 CrossRef Medline
9. Loevner LA, Sonners AI, Schulman BJ, et al. **Reinterpretation of cross-sectional images in patients with head and neck cancer in the setting of a multidisciplinary cancer center.** *AJNR Am J Neuroradiol* 2002;23:1622–26 Medline
10. Rosenkrantz AB, Duszak R, Babb JS, et al. **Discrepancy rates and clinical impact of imaging secondary interpretations: a systematic review and meta-analysis.** *J Am Coll Radiology* 2018;15:1222–31 CrossRef Medline
11. Kabadi SJ, Krishnaraj A. **Strategies for improving the value of the radiology report: a retrospective analysis of errors in formally over-read studies.** *J Am Coll Radiol* 2017;14:459–66 CrossRef Medline
12. Revesz G, Kundel HL. **Psychophysical studies of detection errors in chest radiology.** *Radiology* 1977;123:559–62 CrossRef Medline
13. Quekel LGBA, Kessels AGH, Goei R, et al. **Miss rate of lung cancer on the chest radiograph in clinical practice.** *Chest* 1999;115:720–24 CrossRef Medline
14. Abujudeh HH, Boland GW, Kaewlai R, et al. **Abdominal and pelvic computed tomography (CT) interpretation: discrepancy rates among experienced radiologists.** *Eur Radiology* 2010;20:1952–57 CrossRef Medline
15. Hanna TN, Lamoureux C, Krupinski EA, et al. **Effect of shift, schedule, and volume on interpretive accuracy: a retrospective analysis of 2.9 million radiologic examinations.** *Radiology* 2018;287:205–12 CrossRef Medline
16. Kasalak Ö, Alnahwi H, Toxopeus R, et al. **Work overload and diagnostic errors in radiology**. *Eur J Radiology* 2023;167:111032 CrossRef Medline
17. Ivanovic V, Paydar A, Chang Y-M, et al. **Impact of shift volume on neuroradiology diagnostic errors at a large tertiary academic center.** *Acad Radiology* 2023;30:1584–88 CrossRef Medline
18. Vong S, Chang J, Assadsangabi R, et al. **Analysis of perceptual errors in skull-base pathology.** *Neuroradiol J* 2023;36:515–23 CrossRef Medline
19. Biddle G, Assadsangabi R, Broadhead K, et al. **Diagnostic errors in cerebrovascular pathology: retrospective analysis of a neuroradiology database at a large tertiary academic medical center.** *AJNR Am J Neuroradiol* 2022;43:1271–78 CrossRef Medline
20. Ivanovic V, Assadsangabi R, Hacein-Bey L, et al. **Neuroradiology diagnostic errors at a tertiary academic centre: effect of participation in tumour boards and physician experience.** *Clin Radiology* 2022;77:607–12 CrossRef Medline
21. Ferguson A, Assadsangabi R, Chang J, et al. **Analysis of misses in imaging of head and neck pathology by attending neuroradiologists at a single tertiary academic medical centre.** *Clin Radiology* 2021;76:786.e9–e13 CrossRef Medline
22. Ivanovic V, Broadhead K, Beck R, et al. **Factors associated with neuroradiologic diagnostic errors at a large tertiary-care academic medical center: a case-control study.** *AJR Am J Roentgenol* 2023;221:355–62 CrossRef Medline
23. Goldberg-Stein S, Frigini LA, Long S, et al. **ACR RADPEER committee white paper with 2016 updates: Revised scoring system, new classifications, self-review, and subspecialized reports.** *J Am Coll Radiology* 2017;14:1080–86 CrossRef Medline
24. Chang C, Hsieh MK, Chang WY, et al. **Determining the optimal number and location of cutoff points with application to data of cervical cancer.** *PLoS One* 2017;12:e0176231 CrossRef Medline
25. Ivanovic V, Broadhead K, Beck R, et al. **Factors associated with neuroradiology diagnostic errors at a large tertiary-care academic medical center: a case-control study.** *AJR Am J Roentgenol* 2023;221:355–62 CrossRef
26. Chakraborty H, Sen PK. **Resampling method to estimate intra-cluster correlation for clustered binary data.** *Commun Stat Theory Methods* 2016;45:2368–77 CrossRef
27. Wintermark M, Gupta V, Hess C, et al. **Realistic productivity in academic neuroradiology: a national survey of neuroradiology division chiefs.** *AJNR Am J Neuroradiol* 2023;44:759–61 CrossRef Medline
28. Mahesh M, Ansari AJ, Mettle FA. **Patient exposure from radiologic and nuclear medicine procedures in the United States and worldwide: 2009-2018.** *Radiology* 2023;307:e239013 CrossRef Medline
29. Deckey DG, Eltorai AEM, Jindal G, et al. **Analysis of malpractice claims involving diagnostic and interventional neuroradiology.** *J Am Coll Radiology* 2019;16:764–69 CrossRef Medline
30. Khan A, Khunte M, Wu X, et al. **Malpractice litigation related to diagnosis and treatment of intracranial aneurysms.** *AJNR Am J Neuroradiol* 2023;44:460–66 CrossRef Medline
31. Hatzoglou V, Omuro AM, Haque S, et al. **Second-opinion interpretations of neuroimaging studies by oncologic neuroradiologists can help reduce errors in cancer care.** *Cancer* 2016;122:2708–14 CrossRef Medline
32. Lysack JT, Hoy M, Hudon ME, et al. **Impact of neuroradiologist second opinion on staging and management of head and neck cancer.** *J Otolaryngol Head Neck Surg* 2013;42:39 CrossRef Medline
33. Ruutiainen AT, Durand DJ, Scanlon MH, et al. **Increased error rates in preliminary reports issued by radiology residents working more than 10 consecutive hours overnight.** *Acad Radiology* 2013;20:305–11 CrossRef Medline
34. Lee MH, Schemmel AJ, Pooler BD, et al. **Workflow dynamics and the imaging value chain: quantifying the effect of designating a nonimage-interpretive task workflow.** *Curr Probl Diagn Radiology* 2017;46:275–81 CrossRef Medline
35. Sokolovskaya E, Shinde T, Ruchman RB, et al. **The effect of faster reporting speed for imaging studies on the number of misses and interpretation errors: a pilot study.** *J Am Coll Radiology* 2015;12:683–88 CrossRef Medline
36. Lu Y, Arenson RL. **The academic radiologist's clinical productivity: an update**. *Acad Radiology* 2005;12:1211–23 CrossRef Medline
37. McDonald RJ, Schwartz KM, Eckel LJ, et al. **The effects of changes in utilization and technological advancements of cross-sectional imaging on radiologist workload.** *Acad Radiology* 2015;22:1191–98 CrossRef Medline
38. The Royal College of Radiologists website. Clinical radiology workload: guidance on radiologists' reporting figures. www.rcr.ac.uk. Accessed September 28, 2023
39. Japanese College of Radiology webpage. JCR statement on appropriate workload of radiologists. jcr.or.jp/english-page. Accessed September 28, 2023

AJNR

Autoimmune Encephalitis: Pathophysiology and Imaging Review of an Overlooked Diagnosis

B.P. Kelley, S.C. Patel, H.L. Marin, J.J. Corrigan, P.D. Mitsias, and B. Griffith

ABSTRACT

SUMMARY: Autoimmune encephalitis is a relatively new category of immune-mediated disease involving the central nervous system that demonstrates a widely variable spectrum of clinical presentations, ranging from the relatively mild or insidious onset of cognitive impairment to more complex forms of encephalopathy with refractory seizure. Due to its diverse clinical features, which can mimic a variety of other pathologic processes, autoimmune encephalitis presents a diagnostic challenge to clinicians. Imaging findings in patients with these disorders can also be quite variable, but recognizing characteristic findings within limbic structures suggestive of autoimmune encephalitis can be a key step in alerting clinicians to the potential diagnosis and ensuring a prompt and appropriate clinical work-up. In this article, we review antibody-mediated encephalitis and its various subtypes with a specific emphasis on the role of neuroimaging in the diagnostic work-up.

ABBREVIATIONS: NMDA = *N*-methyl D-aspartate; NMDAr = *N*-methyl D-aspartate receptor; VGKC = voltage-gated potassium channel

Autoimmune encephalitis is an important cause of new-onset altered mental status, the scope of which has only recently begun to be recognized in the medical literature.[1-3] Despite this increased recognition, it has yet to become an established diagnostic consideration outside of large tertiary referral centers.[1-5] The term "autoimmune encephalitis" generally refers to a family of closely related disease processes that share overlapping clinical features and neuroimaging findings but are ultimately differentiated by the specific antibody subtypes driving the underlying immune-mediated attack on different CNS structures.[6-8] This antibody-mediated attack on neuronal structures results in a localized inflammatory response. Thus, the clinical and imaging manifestations are dictated by the specific location of the underlying immune response within the nervous system, which leads to substantial variability. While limbic dysfunction is the single most consistent finding in autoimmune encephalitis, varying degrees of involvement are seen within the neocortex, striatum, hindbrain, spine, and peripheral nervous system based on the unique antibody profile.[3,9-12] In addition, certain antibody subtypes consistently lack imaging manifestations, while others characteristically demonstrate prominent "extralimbic" involvement.[3,7,13-15]

Although it was initially thought to be relatively rare, there is growing consensus that autoimmune encephalitis is responsible for a subset of altered mental status previously considered idiopathic.[3-5] Despite its growing recognition as a rare cause of altered mental status, autoimmune encephalitis remains a diagnosis of exclusion with more common causes often identified during the standard diagnostic evaluation.[16,17] However, more complex presentations of altered mental status may display atypical features without a clear etiology identified after routine testing.[16,17] In these situations, recognition of potential cases of autoimmune encephalitis by the radiologist can be the first step to optimizing clinical outcomes through ensuring that a prompt and appropriate clinical work-up is performed, including the use of specialized serum/CSF antibody panels, with the ultimate goal of establishing an effective treatment regimen before the onset of devastating complications.[3,5,8,18]

The purpose of this article is to discuss the subset of immune-mediated CNS conditions with features of autoimmune encephalitis (ie, antibody-mediated inflammation of the brain), provide a framework for radiologists to understand the relevant neuroimmunology, review the major antibody subtypes, and describe the constellation of clinical and imaging features that are most suggestive of this diagnosis.

From the Departments of Neuroradiology (B.P.K., S.C.P., H.L.M., J.J.C., B.G.), and Neurology (P.D.M.), Henry Ford Hospital, Detroit, Michigan.

Paper previously presented, in part, at: Annual Meeting of the American Society of Neuroradiology and the Foundation of the ASNR Symposium, May 23–26, 2016; Washington, DC.

Please address correspondence to Brendan P. Kelley, MD, MSc, Department of Radiology, Henry Ford Hospital, 2799 W Grand Blvd, Detroit, MI 48202; e-mail: brendank@rad.hfh.edu; @brendanpkelley

Indicates open access to non-subscribers at www.ajnr.org

Indicates article with supplemental on-line table.

http://dx.doi.org/10.3174/ajnr.A5086

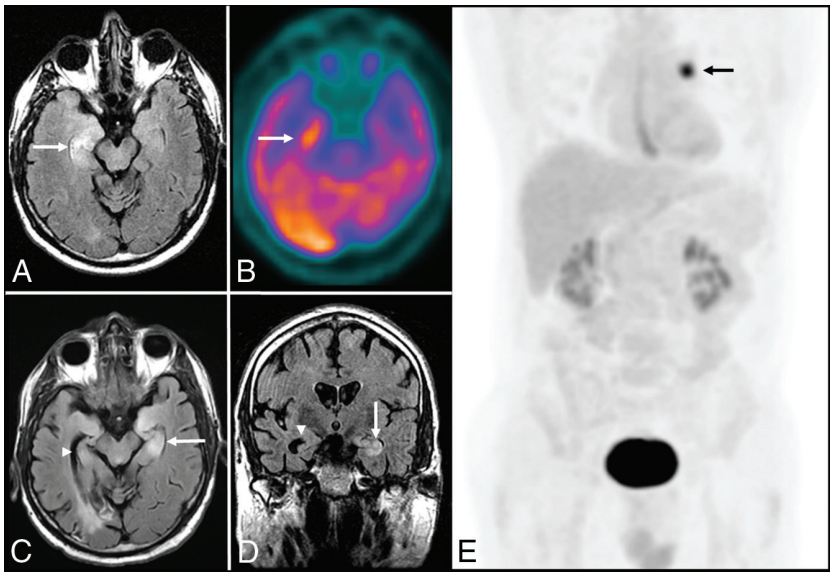

FIG 1. Anti-Hu encephalitis. A 68-year-old man with chronic obstructive pulmonary disease presented with gradually worsening memory deficits and confusion, with subclinical seizures. MR imaging of the brain demonstrates T2-FLAIR hyperintensity and mild expansion in the right medial temporal lobe (*A*), right insular cortex (not shown), and left dorsal thalamus (not shown), without restricted diffusion (not shown) or postcontrast enhancement (not shown). FDG-PET of the brain demonstrates a hypermetabolic focus within the right medial temporal lobe lesion (*B*). PET of the body demonstrates a hypermetabolic focus in the left lung (*E*), consistent with biopsy-proved small-cell lung cancer. The patient was in remission following treatment with intravenous immunoglobulin infusions, oral steroids, and chemotherapy, but he presented approximately 2.5 years later with worsening memory decline. MR imaging at that time (*C* and *D*) shows new T2-FLAIR hyperintensity in the left medial temporal lobe (*white arrow*) with volume loss within the right medial temporal lobe (*white arrowhead*). An old right occipital lobe infarct is also incidentally noted.

Pathophysiology: Models for Disease Classification

Antibody-mediated CNS disorders can be classified into 2 broad categories, paraneoplastic or nonparaneoplastic, based on the presence or absence of an underlying malignancy, respectively.[18-20] Paraneoplastic syndromes affecting the CNS are generally thought to develop in cancer when antigens shared by tumor cells and native nonneoplastic neuronal cells result in an antibody-mediated attack on previously immune-privileged neuronal structures.[2,6-8,19] Initially thought to occur in <1% of patients with cancer, more recent data suggest that the true incidence is likely much higher.[3-6] Paraneoplastic syndromes are most often seen in small-cell lung cancer but can also be seen in a variety of other cancers as well, such as neuroblastoma, germ cell tumor of the testis, breast cancer, Hodgkin lymphoma, thymoma, and immature ovarian teratomas.[19-22]

Regardless of the etiology and antibody profile, there is a clear predilection in autoimmune encephalitis for antigens within the limbic system (Figs 1 and 2).[3,10,23,24] Paraneoplastic limbic encephalitis, a specific paraneoplastic syndrome affecting the temporal lobe and limbic structures, was first described by the British neuropathologists Corsellis et al[25] in 1968 after identifying postinflammatory changes in the mesial temporal lobes of patients with progressive memory loss after being diagnosed with lung cancer. Kohler et al[26] later correlated these inflammatory changes with T2-weighted hyperintense signal changes on MR imaging of the brain. These characteristic neuroimaging findings were later validated by a larger study of 50 patients with paraneoplastic limbic encephalitis across different antibody profiles that found that 39 of 50 patients (79%) had similar T2-FLAIR hyperintense signal changes in their temporal lobes and limbic structures.[19] This study, conducted by Gultekin et al[19] in 2000, proposed the first diagnostic criteria for paraneoplastic limbic encephalitis, which included the following: 1) short-term memory loss, seizures, or psychiatric symptoms; 2) <4 years between symptom onset and cancer diagnosis; 3) exclusion of metastases, infection, metabolic, or other causes; and 4) one of the following: inflammatory CSF findings, temporal lobe T2 or FLAIR hyperintensity on MR imaging, or electroencephalogram abnormality in the temporal lobes.[19] Tüzün and Dalmau[27] subsequently modified these criteria in 2007 to account for the growing subset of nonparaneoplastic forms of autoimmune encephalitis, which also demonstrated prominent limbic involvement.

In addition to the "paraneoplastic-versus-nonparaneoplastic" categorization, antibody-mediated encephalitides can also be characterized as either group I or group II according to the location of their neuronal antigens (On-line Table), with group I antibodies targeting intracellular antigens and group II antibodies targeting antigens on the cell surface.[1,2,6,7,9,27] This distinction is clinically relevant because it has implications for treatment response, association with an underlying malignancy, and overall long-term prognosis.[9,20,22,28]

Group I Antibodies: Autoimmune Encephalitis with Intracellular Antigens

Group I antibodies target intracellular neuronal antigens, are more closely associated with an underlying malignancy, and use the same cytotoxic T-cell mechanisms when targeting the intracellular neuronal antigens and onconeuronal antigens as part of the immune response to cancer.[1,7,9,29] Group I antibodies are also associated with poor clinical outcomes, characterized by a decreased response to immunomodulatory therapy and an increased prevalence of "irreversible" neuronal damage, and often have the additional burden of an underlying malignancy.[9,19,21] Compared with group II antibodies, group I antibodies are less specific clinical markers of disease for autoimmune encephalitis and can also be seen in patients with cancer without paraneoplastic syndromes.[29,30]

Anti-Hu

Anti-Hu (anti-neuronal nuclear antibody 1) encephalitis is the most common paraneoplastic form of autoimmune encephalitis, has a relatively poor prognosis compared with other subtypes, and is associated with small-cell lung cancer in most cases (75%).[19,31] Anti-Hu syndrome is a distinct clinical phenotype described in

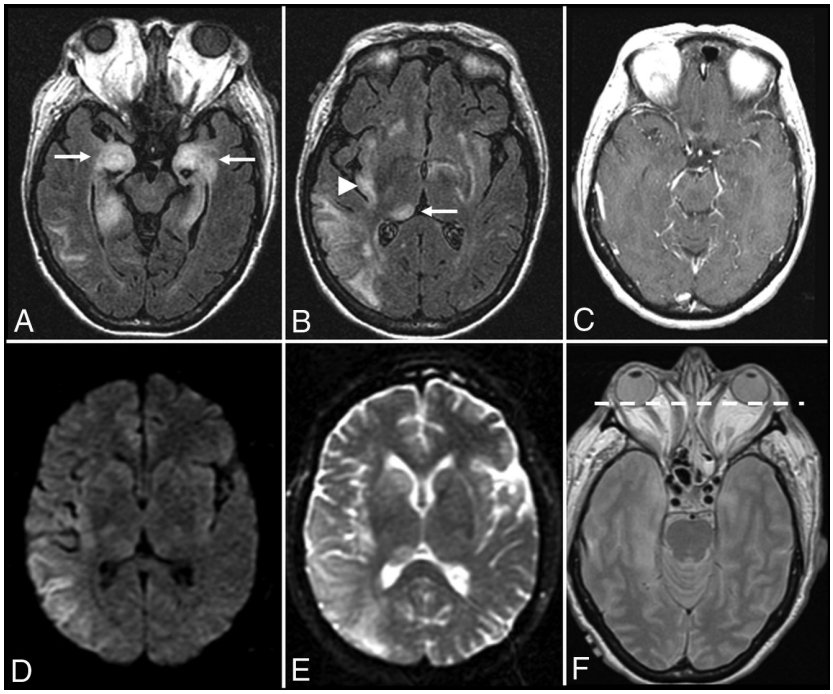

FIG 2. Graves ophthalmopathy with anti-Hu encephalitis. A 63-year-old woman with severe encephalopathy and diffuse enlargement of the extraocular muscles developed fatal autonomic dysfunction. MR imaging of the brain demonstrates prominent T2-FLAIR abnormalities in the mesial temporal lobes (*A*), right thalamus (*B*), right > left insular cortex (*B*), and posterior right temporal lobe (*B*), without enhancement (*C*) and with T2 shinethrough but no restricted diffusion on DWI (*D*) and the corresponding ADC map (*E*). There is also diffuse symmetric enlargement of the extraocular muscles, resulting in exophthalmos (*F*).

patients with cancer expressing anti-Hu antibodies and has features of paraneoplastic encephalomyelitis, paraneoplastic subacute sensory neuropathy, and paraneoplastic cerebellar degeneration.[19,31,32] While anti-Hu encephalitis is not as closely associated with seizures as some of the other major subtypes of autoimmune encephalitis, a subset of patients with anti-Hu encephalitis can present with epilepsia partialis continua, a specific seizure disorder characterized by extended focal motor epileptic seizures prominently involving the face and distal extremities that recur every few seconds/minutes.[32,33] MR imaging findings correlate with clinical features and typically include T2-FLAIR hyperintense lesions in the medial temporal lobes with variable involvement of the cerebellum and brain stem (Figs 1 and 2).[3,19,21,23]

Anti-Ma/Ta

Anti-Ma (Ma1/Ma2/Ma3) encephalitis has a better prognosis than anti-Hu and is strongly associated with testicular tumors in young men and small-cell lung cancer or breast cancer in older patients.[7,9,34,35] The association with testicular tumors in young men is so strong that some authors have advocated empiric orchiectomy in refractory cases of severe anti-Ma encephalitis for presumed microscopic neoplastic testicular tumors if certain diagnostic criteria are met and no other etiology is found.[36] According to a review of 38 patients with anti-Ma encephalitis, most patients (62%) presented with neurologic symptoms before the identification of their malignancy, which included any combination of limbic, diencephalic, or brain stem dysfunction.[13] Notably, only a minority of patients (26%) had classic symptoms of limbic encephalitis, and most patients with brain stem involvement had ophthalmoplegia (92%).[13] Abnormal findings on brain MR imaging were common (74%) and often involved classic T2-FLAIR hyperintense lesions in the medial temporal lobes with variable involvement of the thalamus and brain stem.[13] Although not classic, nodular postcontrast enhancement that can mimic tumor or infection has also been described.[13,35,36]

Anti-CV2

Anti-CV2 (collapsin response mediator protein 5) encephalitis is a unique subtype associated with small-cell lung cancer and malignant thymoma that has prominent T2-FLAIR hyperintense lesions in the striatum and clinically resembles choreiform movement disorders.[3,37] MR imaging features are also atypical compared with other types of autoimmune encephalitis in that there is less prominent involvement of the medial temporal lobe.[3,37] Most important, there is typically no restricted diffusion or T2-FLAIR hyperintense lesions in the striatum, which can help differentiate this condition from prion diseases like Creutzfeldt-Jakob disease.[3,16] When one considers this relatively rare diagnosis, it is important to first rule out more common toxometabolic disorders such as hyperammonemia, carbon monoxide poisoning, and hypoglycemia.

Anti-Glutamic Acid Decarboxylase

Glutamic acid decarboxylase (GAD) is an intracellular enzyme that catalyzes the synthesis of γ-aminobutyric acid, the major inhibitory neurotransmitter in the CNS. Anti-glutamic acid decarboxylase antibodies are unique because they are a group I antibody not typically associated with malignancy and are also associated with other nonneoplastic autoimmune conditions such as type 1 diabetes mellitus.[9,38] The anti-glutamic acid decarboxylase antibody subtype can cause a form of autoimmune encephalitis with classic temporal lobe lesions on MR imaging with the expected clinical findings of limbic encephalitis plus additional features of stiff person syndrome with early and prominent development of seizures (Fig 3).[9,38]

Additional Type I Antibody Subtypes

Amphiphysin antibodies are most often seen in breast cancer and small-cell lung cancer with associated clinical features of stiff person syndrome, myelopathy, myoclonus, and encephalomyelitis.[7,39] Ri (anti-neuronal nuclear antibody 2) antibodies are also most often seen in breast cancer and small-cell lung cancer, with features of brain stem encephalitis and opsoclonus-myoclonus syndrome.[7,39] Yo (pa-

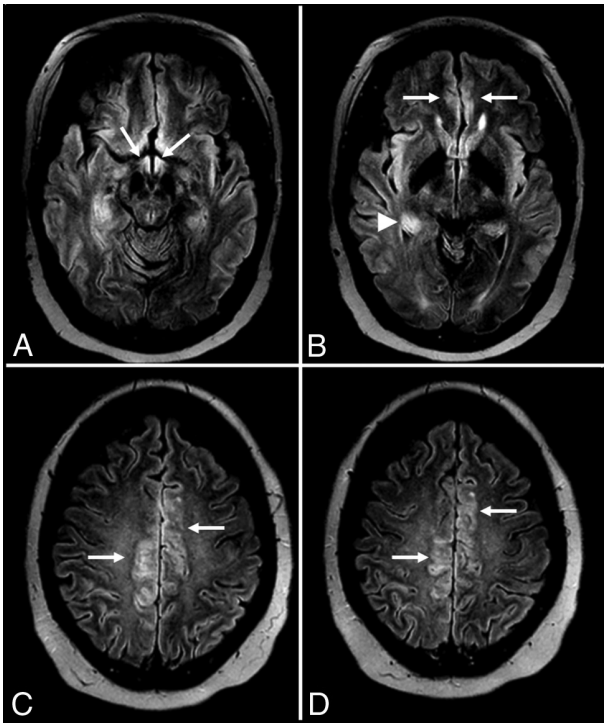

FIG 3. Anti-glutamic acid decarboxylase encephalitis. A 61-year-old woman presented with headaches, mild confusion, and nystagmus without development of psychosis, severe encephalopathy, or seizures. MR imaging of the brain demonstrates T2-FLAIR hyperintensity in the right > left hippocampus (*A* and *B*), right > left insular cortex (*B*), and bilateral cingulate gyrus (*C* and *D*) without restricted diffusion (not shown), hemorrhage (not shown), or postcontrast enhancement (not shown).

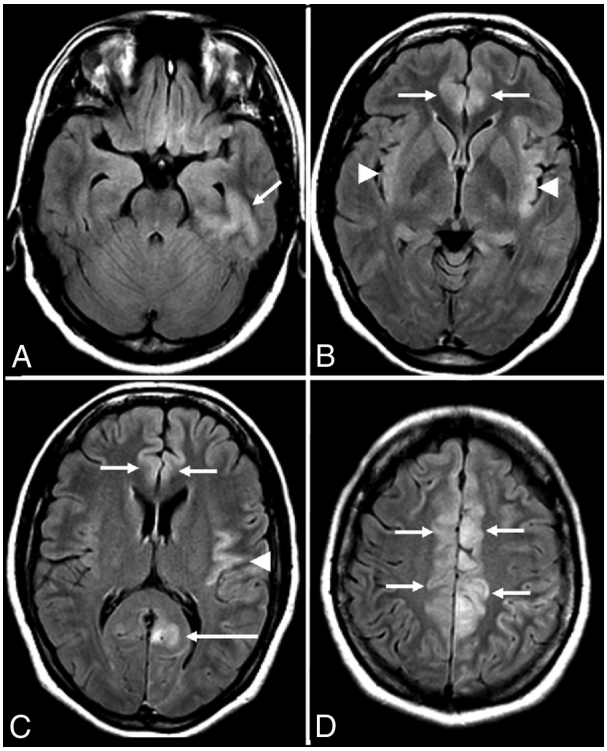

FIG 4. Anti-*N*-methyl D-aspartate receptor encephalitis. A 32-year-old woman presented with headaches, vertigo, and psychosis with subsequent development of encephalopathy and seizures. MR imaging of the brain performed after the onset of seizures 2 weeks after initial presentation demonstrates T2-FLAIR hyperintensity in the left inferior temporal lobe (*A*), left > right insular cortex (*B* and *C*), and left > right cingulate gyrus (*B–D*), without restricted diffusion (not shown), hemorrhage (not shown), or postcontrast enhancement (not shown).

rietal cell autoantibodies 1) antibodies are most often seen in ovarian cancer and breast cancer, with characteristic features of paraneoplastic cerebellar degeneration, but they can also demonstrate features of autoimmune encephalitis.[7,39,40]

Group II Antibodies: Autoimmune Encephalitis with Cell-Surface Antigens

Group II antibodies target cell-surface neuronal antigens, are less likely to be associated with an underlying malignancy, and use more "restricted" humoral immune mechanisms of neurotoxicity that typically respond better to early immunomodulatory therapy.[9,20,41] Group II antibodies also represent a more specific clinical marker of disease for antibody-mediated encephalitis, with reduction in serum antibody titers following treatment directly associated with improved neurologic outcomes.[41,42] Group II antibodies often target synaptic proteins and can result in the downregulation of receptors that leads to altered synaptic transmission associated with epileptiform activity.[9,11,15] Patients with nonneoplastic forms of autoimmune encephalitis associated with group II antibodies may have an underlying systemic autoimmune disorder or can develop symptoms following a viral infection or vaccination, but in many cases, no clear etiology is identified.[1,4,11,43] The current list of group II antibodies will likely continue to grow on the basis of the number of case reports in the medical literature of "suspected autoimmune encephalitis" or "steroid-responsive limbic encephalitis," in which a specific antibody or malignancy is not identified but the diagnosis is strongly suggested by a combination of characteristic clinical features, typical neuroimaging findings, good empiric treatment response, and no convincing alternative diagnosis.[43-45]

N-*Methyl D-Aspartate Receptor*

N-methyl D-aspartate receptor (NMDAr) encephalitis is one of the most common and best characterized subtypes of autoimmune encephalitis classically seen in young women and children with autoimmunity not associated with cancer (Fig 4).[20,28,46] This subtype is mediated by immunoglobulin G antibodies against the GluN1 subunit of the neuronal NMDAr, with inflammatory neuronal dysfunction that is thought to be initially reversible but potentially progresses to permanent neuronal destruction if untreated, due to prolonged inflammation and *N*-methyl D-aspartate (NMDA)-mediated glutamate excitotoxicity.[9,47,48] NMDAr encephalitis has a well-characterized progression of features characterized by an initial viral-like prodrome (fever, malaise, headaches, and anorexia), followed by psychiatric symptoms (anxiety, depression, schizophrenia, and psychosis), which progress to include temporal lobe dysfunction (amnesia and seizures) and ultimately culminate in severe neurologic deficits, including autonomic dysfunction, dystonia/dyskinesia, and profound encephalopathy.[3,20,49,50] There are many cautionary reports in the medical literature of young women with NMDAr encephalitis and

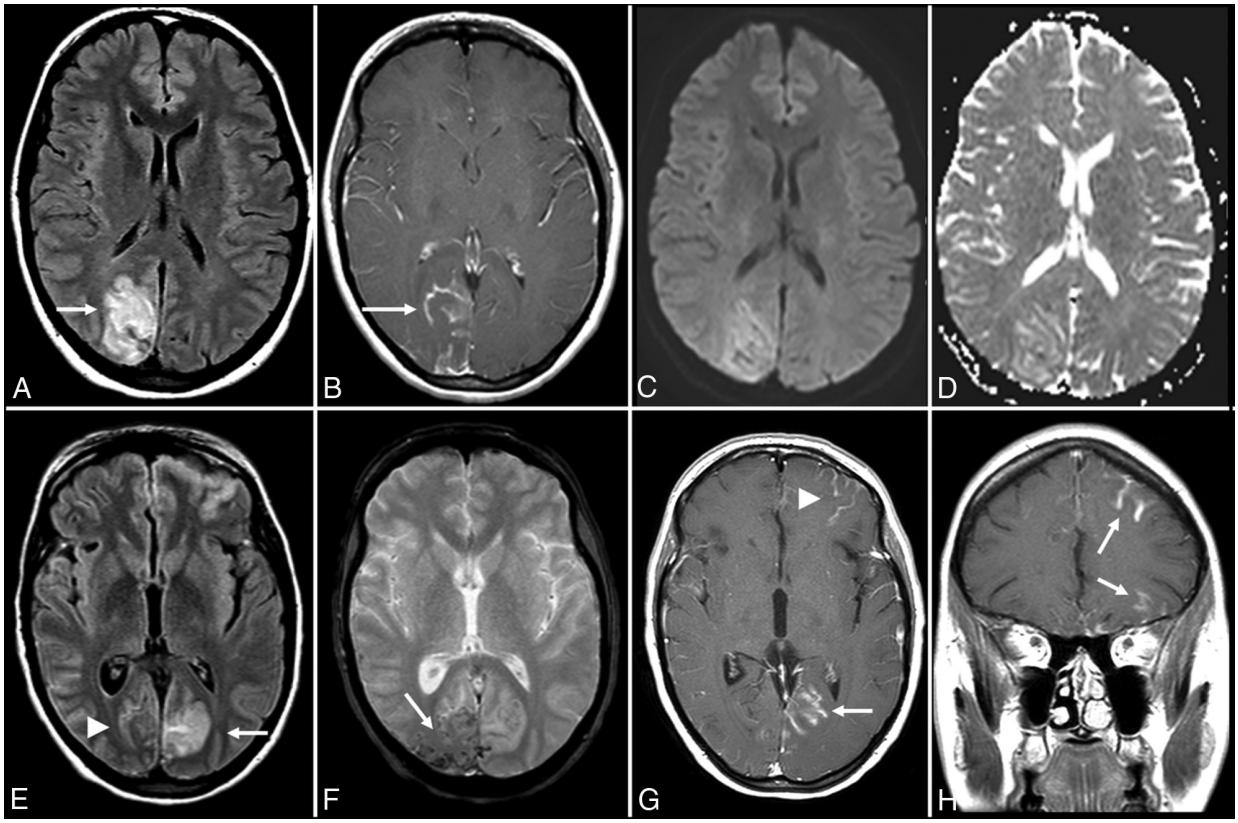

FIG 5. Anti-voltage-gated calcium channel encephalitis. A 39-year-old woman presented with left-sided weakness and left visual field deficits with subsequent development of encephalopathy and seizures. Initial MR imaging of the brain (*A–D*) demonstrates multifocal T2-FLAIR hyperintense lesions in the right parieto-occipital region (*A*), with associated pial/sulcal enhancement (*B*) and mild cortical restricted diffusion and T2 shinethrough within the subcortical white matter on DWI (*C*) and the corresponding ADC map (*D*). Follow-up MR imaging of the brain performed 34 days later (*E–H*) demonstrates decreased T2-FLAIR hyperintensity (*E*) with cortical laminar necrosis and petechial hemorrhage (*F*) at the original lesion, with progressive development on subsequent examinations of similar cortical lesions in the contralateral frontal, parietal, and occipital lobes (*E–H*).

no significant medical history who present with initial psychiatric symptoms that prompt admission to a psychiatric facility but later require transfer to the intensive care unit after development of the more severe neurologic deficits associated with this condition.[18,20,48,51]

With early diagnosis and treatment, patients with NMDAr encephalitis have a relatively good prognosis and can experience a return to their baseline functional status with complete resolution of neuroimaging abnormalities on follow-up examinations.[20,41,49] Relapsing forms of nonparaneoplastic NMDAr encephalitis have been reported, and long-term prophylaxis with steroid-sparing agents like rituximab may be required in a subset of cases.[42,48,50] A minority of cases of NMDAr encephalitis can be associated with an underlying malignancy, especially in older patients.[20,52,53] According to 1 study, 45% of adult women with NMDAr encephalitis had an underlying ovarian teratoma but only 9% of young girls had this finding.[53] In women older than 45 years of age, this same study found that 23% of women had an ovarian carcinoma instead of a teratoma.[53] This finding highlights the need to screen all patients with autoimmune encephalitis for an underlying malignancy, regardless of the antibody profile, and even to consider the possibility of a contralateral or concurrent tumor with a poor response to treatment despite removal of a tumor.[27,49] NMDAr encephalitis is an especially important diagnosis to consider in young patients with limbic encephalitis because the California Encephalitis Project found that the number of young patients in the study with NMDAr encephalitis was greater than those with any single viral etiology.[54] Anti-NMDAr antibodies have even been found in patients with herpes simplex virus encephalitis[55] and Rasmussen encephalitis,[56] which can further complicate the diagnostic work-up.

One unique feature of the NMDAr encephalitis subtype is that it is unlikely to have associated neuroimaging abnormalities on initial presentation (89%) or follow-up MR imaging of the brain (79%).[14] The lack of neuroimaging findings in NMDAr encephalitis is consistent across the medical literature, with another study reporting that most patients with NMDAr encephalitis (66%) had normal brain MR imaging findings, and the remaining 44% had wide variation in the distribution and degree of T2-FLAIR hyperintense signal changes throughout the brain.[53] Recognizing this established progression of specific symptoms and a lack of neuroimaging findings is essential to prospectively consider the diagnosis in the appropriate clinical setting, particularly when patients demonstrate characteristic electroencephalogram findings.[57] When brain MR imaging abnormalities are present, these T2-FLAIR hyperintense lesions can typically demonstrate mild transient cortical enhancement without restricted diffusion or hemorrhage (Fig 4).[3,14,53] When brain MR imaging findings are absent but the clinical findings suggest the possibility of an auto-

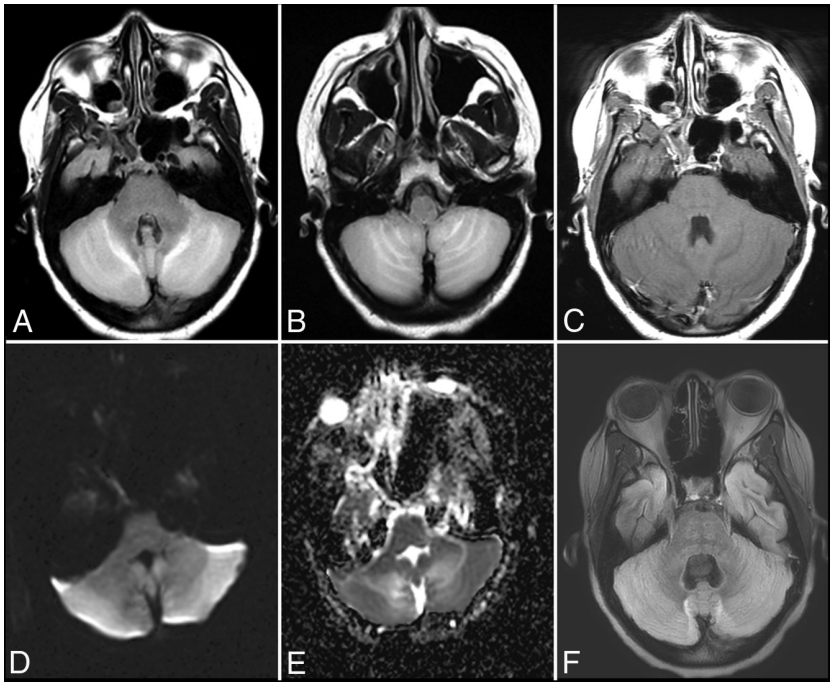

FIG 6. Anti-voltage-gated calcium channel cerebellitis. A 23-year-old woman with a history of autoimmune hepatitis presented with altered mental status. Initial brain MR imaging (*A*–*E*) demonstrates T2-FLAIR hyperintensity within the bilateral cerebellar hemispheres with mass effect on the fourth ventricle (*A* and *B*), without evidence of postcontrast enhancement (*C*) and with mild restricted diffusion on DWI (*D*) and the corresponding ADC map (*E*). A follow-up scan 1 month later (*F*) demonstrates resolution of the T2-FLAIR hyperintensity and associated mass effect on the fourth ventricle following a steroid taper.

immune encephalitis, brain FDG-PET imaging may be indicated, especially early in the disease process if clinical suspicion for autoimmune encephalitis is high, because it appears to be a more sensitive imaging technique for detecting temporal lobe abnormalities with normal brain MR imaging findings.[29,40,44,58]

Voltage-Gated Potassium Channel

Voltage-gated potassium channel (VGKC) encephalitis is one of the most common group 2 subtypes of autoimmune encephalitis, which can demonstrate classic features of limbic encephalitis but is primarily defined by the early and prominent development of medically intractable epilepsy.[24] The near-universal development of seizures in patients with VGKC encephalitis is partially explained by the high concentration of potassium channels in the limbic structures, and the epileptogenic potential of these antibodies is further supported by the observation that up to 6% of patients with a long-standing history of epilepsy were found to have circulating VGKC autoantibodies.[59] It remains unclear whether VGKC antibodies directly contribute to neuronal dysfunction independent of seizure activity, but there is growing consensus that a genetic predisposition to VGKC autoimmunity is probably an independent risk factor for the development of temporal lobe epilepsy.[9,59]

According to a recent review of 42 patients with VGKC encephalitis, most (69%) demonstrated MR imaging findings classic for autoimmune encephalitis in the acute setting (T2-FLAIR hyperintense lesions in 1 or both medial temporal lobes) and had an increased propensity to develop chronic findings of mesial temporal sclerosis on follow-up imaging (48%).[24] A subset of patients with medial temporal lobe lesions demonstrated additional findings of restricted diffusion and postcontrast enhancement (21%) that was highly associated with the development of mesial temporal sclerosis (66%).[24] Another important finding was that "extralimbic" involvement in VGKC encephalitis was exceedingly rare (5%).[24] The number of specific antibodies within the spectrum of VGKC encephalitis continues to grow, with distinction now being made for antibodies to particular antigens like leucine-rich glioma-inactivated 1, contactin-associated protein-like 2, and dipeptidyl-peptidase-like protein-6, which represent distinct subtypes of autoimmune encephalitis because these antibodies bind not to the Kv1 neuronal antigens of the VGKC but to other juxtaparanodal proteins with a different clinical profile.[6,60-63]

Voltage-Gated Calcium Channel

Voltage-gated calcium channel (VGCC) encephalitis is a relatively rare subtype described in women and young children, which is associated with the classic clinical progression of symptoms described in group II antibodies (viral prodrome → neuropsychiatric symptoms → limbic dysfunction → seizures) and can have prominent "migratory" extralimbic involvement with gyriform postcontrast enhancement and cortical laminar necrosis (Figs 5 and 6).[64,65]

γ-Aminobutyric Acid Receptor

γ-aminobutyric acid encephalitis (GABAr) has 2 subtypes that both have clinical features similar to those of VGKC encephalitis but are less common and have a better overall prognosis.[3,15,43,66] The 2 γ-aminobutyric acid receptor subtypes have different clinical profiles and are characterized by antibodies to either the γ-aminobutyric acid A-receptor or B-receptor subunits.[3,15,43,66] Patients with antibodies to the γ-aminobutyric acid B-receptor present with classic features of limbic encephalitis defined by early and frequent seizures with the development of T2-FLAIR hyperintense signal changes in 1 or both temporal lobes.[3,43,66] Patients with γ-aminobutyric acid B-receptor antibodies have a higher association with cancer than most other group II antibodies and are more often seen with small-cell lung cancer or pulmonary neuroendocrine tumors.[3,43,66] The development of autoimmune encephalitis in these patients usually precedes the diagnosis of cancer but responds well to immunosuppression and removal of the underlying tumor.[66] Patients with γ-aminobutyric acid A-receptors also have a good prognosis with adequate treatment, are not associated with cancer, and are unique because in addition to classic MR imaging findings, these patients often demonstrate

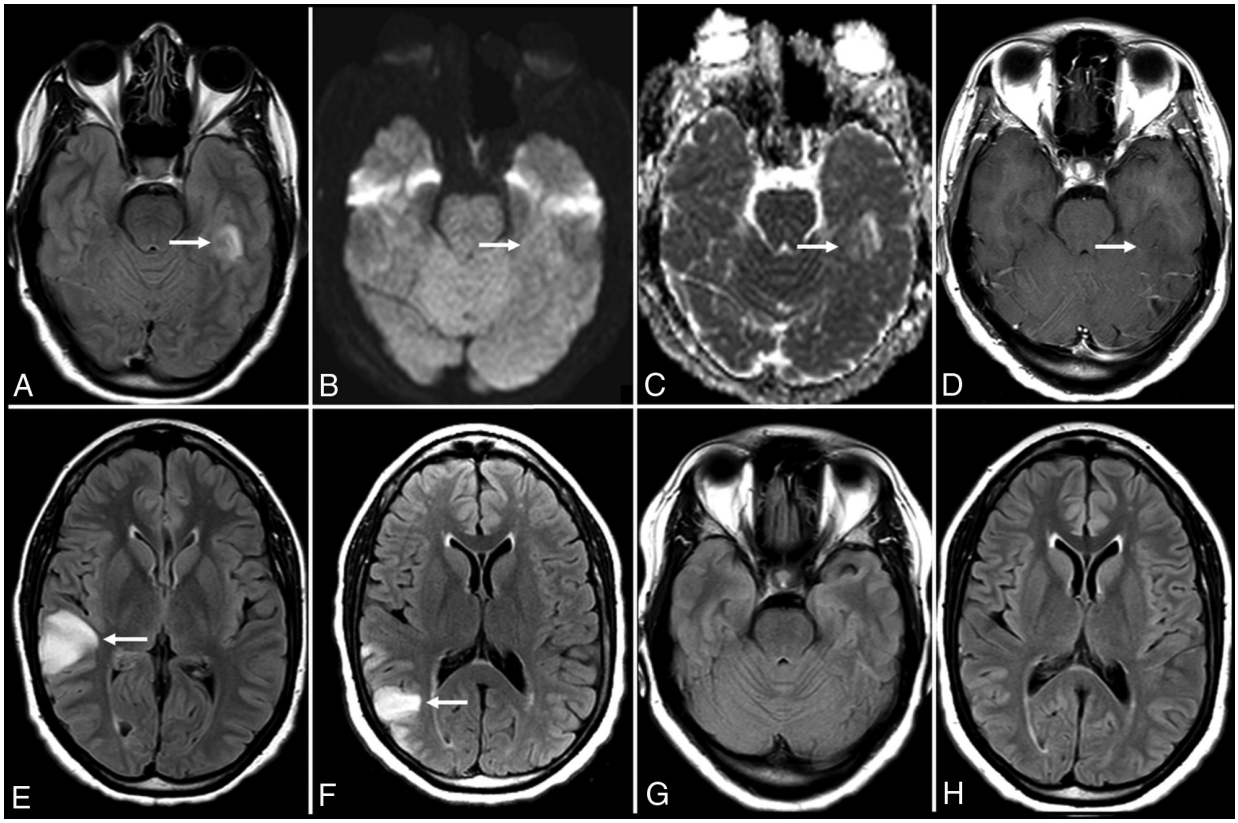

FIG 7. Hashimoto encephalitis. A 41-year-old woman presented with gradually worsening headaches and memory impairment without the development of psychosis or seizures. MR imaging of the brain (time, 0) demonstrates T2-FLAIR hyperintensity in the inferior left temporal lobe (*A*) without evidence of restricted diffusion (*B* and *C*). MR imaging of the brain (time, 21 days) demonstrates enlargement of the lesion on T2-FLAIR (not shown) without postcontrast enhancement (*D*). MR imaging of the brain (time, 3 months) demonstrates resolution of the prior lesion (not shown) but development of similar T2-FLAIR hyperintensity in the right frontoparietal junction (*E*). A subsequent scan at approximately 5 months shows near-complete resolution of that lesion with a new T2-FLAIR hyperintense lesion more posteriorly (*F*). A follow-up scan (*G* and *H*) nearly 1 year from onset shows complete resolution of the imaging abnormalities.

extensive T2-FLAIR hyperintense lesions outside of the limbic system.[3,15]

Alpha-Amino-3-Hydroxy-5-Methyl-4-Isoxazolepropionic Acid Receptor

Alpha-amino-3-hydroxy-5-methyl-4-isoxazolepropionic acid receptor (AMPAr) encephalitis is an uncommon subtype characterized by the subacute onset of purely psychiatric symptoms with T2-FLAIR hyperintensities isolated to the hippocampus. This subtype has a higher association with cancer than other cell-surface antibody subtypes and is most often seen in women with lung, breast, or thymic tumors.[3,67]

Additional Type II Antibody Subtypes

Anti-glutamate receptor 3 (GluR3) antibodies have been associated with Rasmussen encephalitis.[7] Anti-metabotropic glutamate receptor 1 (mGluR1) antibodies have been described in patients with lymphoma with cerebellar ataxia.[7] Anti-metabotropic glutamate receptor 5 (mGluR5) antibodies have been linked to limbic encephalitis associated with Hodgkin lymphoma (Ophelia syndrome).[7] Anti-D2 dopamine receptor antibodies represent a rare subtype associated with basal ganglia encephalitis.[8] Anti-glyoxylate reductase 1 (GlyR1) antibodies can be seen in 3 related groups distinguished by having dominant clinical features of stiff leg syndrome, stiff person syndrome, or progressive encephalomyelitis with rigidity and myoclonus.[6]

Systemic Autoimmunity with Encephalopathy

Neuropsychiatric manifestations of systemic autoimmune conditions such as systemic lupus erythematosus can occur and may be mediated by an antibody profile that includes antiphospholipid antibodies and anti-glutamate receptor antibodies.[68] Catastrophic antiphospholipid antibody syndrome is a condition that can present with strokelike symptoms and multifocal petechial hemorrhages throughout the brain, which are best seen on susceptibility-weighted MR imaging sequences.[68] Patients with thyroid dysfunction and antithyroid antibodies in conditions like Graves disease or Hashimoto thyroiditis can develop encephalopathy associated with their autoimmune thyroid disease that has a characteristic "migratory pattern" of neuroimaging findings with cortical T2-FLAIR lesions in different regions of the brain on sequential MR imaging examinations (Fig 7).[11,69] Hashimoto encephalopathy, in particular, is closely associated with autoimmune encephalitis, given its propensity for the combination of encephalopathy, psychiatric symptoms, and seizures.[69,70] MR imaging findings in Hashimoto encephalopathy often have more prominent fea-

tures of leukoencephalopathy (patchy and confluent T2-FLAIR hyperintense lesions in the subcortical, periventricular, and deep white matter).[2,43,70]

CONCLUSIONS

Autoimmune encephalitis is an important diagnostic consideration in patients presenting with new onset of altered mental status of unclear etiology. It includes a myriad of clinical conditions that have a common pathophysiology (ie, antibodies directed against CNS structures). The 2 distinct groups (group I, intracellular directed antibodies, and group II, cell-surface directed antibodies) have overlapping clinical and imaging features. Neuroimaging findings will most often involve the limbic structures, but involvement of the striatum, diencephalon, or rhombencephalon can be seen. A subset of patients with autoimmune encephalitis will have no neuroimaging findings despite profound neuropsychiatric dysfunction, but serum antibody testing can still ultimately lead to the diagnosis of autoimmune encephalitis. While there is no single diagnostic feature that can make this diagnosis in isolation, recognizing a certain constellation of findings during the work-up of complex and atypical cases of new-onset altered mental status is crucial to confirm the diagnosis with serologic testing and initiate treatment in a timely fashion.

ACKNOWLEDGMENTS

We are grateful to our clinical colleagues in the Department of Neurology within the Henry Ford Health System for their role in diagnosing and treating patients with autoimmune encephalitis at our institution. We would specifically like to acknowledge Dr Daniel Newman, Director of the Henry Ford Hoenselaar ALS Clinic, for his enthusiastic clinical support and expertise. We would also like to thank Dr Chunhai Hao, Chief of Neuropathology in the Department of Pathology and Laboratory Medicine at Henry Ford Hospital, for his work characterizing the histopathology of brain biopsy specimens in cases of suspected autoimmune encephalitis at our institution.

REFERENCES

1. Dalmau J, Rosenfeld MR. **Autoimmune encephalitis update.** *Neuro Oncol* 2014;16:771–78 CrossRef Medline
2. Caselli RJ, Drazkowski JF, Wingerchuk DM. **Autoimmune encephalopathy.** *Mayo Clin Proc* 2010;85:878–80 CrossRef Medline
3. da Rocha AJ, Nunes RH, Maia AC Jr, et al. **Recognizing autoimmune-mediated encephalitis in the differential diagnosis of limbic disorders.** *AJNR Am J Neuroradiol* 2015;36:2196–205 CrossRef Medline
4. Glaser CA, Gilliam S, Schnurr D, et al; California Encephalitis Project, 1998–2000. **In search of encephalitis etiologies: diagnostic challenges in the California Encephalitis Project, 1998–2000.** *Clin Infect Dis* 2003;36:731–42 CrossRef Medline
5. Armangue T, Leypoldt F, Dalmau J. **Autoimmune encephalitis as differential diagnosis of infectious encephalitis.** *Curr Opin Neurol* 2014;27:361–68 CrossRef Medline
6. Vincent A. **Autoimmune channelopathies: new antibody-mediated disorders of the central nervous system.** *F1000 Biol Rep* 2009;1:61 CrossRef Medline
7. Graus F, Saiz A, Dalmau J. **Antibodies and neuronal autoimmune disorders of the CNS.** *J Neurol* 2010;257:509–17 CrossRef Medline
8. Ramanathan S, Mohammad SS, Brilot F, et al. **Autoimmune encephalitis: recent updates and emerging challenges.** *J Clin Neurosci* 2014;21:722–30 CrossRef Medline
9. Bien CG, Vincent A, Barnett MH, et al. **Immunopathology of autoantibody-associated encephalitides: clues for pathogenesis.** *Brain* 2012;135:1622–38 CrossRef Medline
10. Demaerel P, Van Dessel W, Van Paesschen W, et al. **Autoimmune-mediated encephalitis.** *Neuroradiology* 2011;53:837–51 CrossRef Medline
11. Moscato EH, Jain A, Peng X, et al. **Mechanisms underlying autoimmune synaptic encephalitis leading to disorders of memory, behavior and cognition: insights from molecular, cellular and synaptic studies.** *Eur J Neurosci* 2010;32:298–309 CrossRef Medline
12. Oyanguren B, Sánchez V, González FJ, et al. **Limbic encephalitis: a clinical-radiological comparison between herpetic and autoimmune etiologies.** *Eur J Neurol* 2013;20:1566–70 CrossRef Medline
13. Dalmau J, Graus F, Villarejo A, et al. **Clinical analysis of anti-Ma2-associated encephalitis.** *Brain* 2004;127:1831–44 CrossRef Medline
14. Irani SR, Bera K, Waters P, et al. **N-methyl-D-aspartate antibody encephalitis: temporal progression of clinical and paraclinical observations in a predominantly non-paraneoplastic disorder of both sexes.** *Brain* 2010;133:1655–67 CrossRef Medline
15. Petit-Pedrol M, Armangue T, Peng X, et al. **Encephalitis with refractory seizures, status epilepticus, and antibodies to the GABAA receptor: a case series, characterisation of the antigen, and analysis of the effects of antibodies.** *Lancet Neurol* 2014;13:276–86 CrossRef Medline
16. Degnan AJ, Levy LM. **Neuroimaging of rapidly progressive dementias, part 1: neurodegenerative etiologies.** *AJNR Am J Neuroradiol* 2014;35:418–23 CrossRef Medline
17. Degnan AJ, Levy LM. **Neuroimaging of rapidly progressive dementias, part 2: prion, inflammatory, neoplastic, and other etiologies.** *AJNR Am J Neuroradiol* 2014;35:424–31 CrossRef Medline
18. Mittal MK, Rabinstein AA, Hocker SE, et al. **Autoimmune encephalitis in the ICU: analysis of phenotypes, serologic findings, and outcomes.** *Neurocrit Care* 2016;24:240–50 CrossRef Medline
19. Gultekin SH, Rosenfeld MR, Voltz R, et al. **Paraneoplastic limbic encephalitis: neurological symptoms, immunological findings and tumour association in 50 patients.** *Brain* 2000;123(pt 7):1481–94 CrossRef Medline
20. Dalmau J, Lancaster E, Martinez-Hernandez E, et al. **Clinical experience and laboratory investigations in patients with anti-NMDAR encephalitis.** *Lancet Neurol* 2011;10:63–74 CrossRef Medline
21. Rees JH. **Paraneoplastic syndromes: when to suspect, how to confirm, and how to manage.** *J Neurol Neurosurg Psychiatry* 2004; 75(suppl 2):ii43–50 Medline
22. de Beukelaar JW, Sillevis Smitt PA. **Managing paraneoplastic neurological disorders.** *Oncologist* 2006;11:292–305 CrossRef Medline
23. Urbach H, Soeder BM, Jeub M, et al. **Serial MRI of limbic encephalitis.** *Neuroradiology* 2006;48:380–86 CrossRef Medline
24. Kotsenas AL, Watson RE, Pittock SJ, et al. **MRI findings in autoimmune voltage-gated potassium channel complex encephalitis with seizures: one potential etiology for mesial temporal sclerosis.** *AJNR Am J Neuroradiol* 2014;35:84–89 CrossRef Medline
25. Corsellis JA, Goldberg GJ, Norton AR. **"Limbic encephalitis" and its association with carcinoma.** *Brain* 1968;91:481–96 CrossRef Medline
26. Kohler J, Hufschmidt A, Hermle L, et al. **Limbic encephalitis: two cases.** *J Neuroimmunol* 1988;20:177–78 CrossRef Medline
27. Tüzün E, Dalmau J. **Limbic encephalitis and variants: classification, diagnosis and treatment.** *Neurologist* 2007;13:261–71 CrossRef Medline
28. Suleiman J, Brilot F, Lang B, et al. **Autoimmune epilepsy in children: case series and proposed guidelines for identification.** *Epilepsia* 2013;54:1036–45 CrossRef Medline
29. Dalmau J, Bataller L. **Clinical and immunological diversity of limbic encephalitis: a model for paraneoplastic neurologic disorders.** *Hematol Oncol Clin North Am* 2006;20:1319–35 CrossRef Medline
30. Pittock SJ, Kryzer TJ, Lennon VA. **Paraneoplastic antibodies coexist and predict cancer, not neurological syndrome.** *Ann Neurol* 2004; 56:715–19 CrossRef Medline
31. Graus F, Keime-Guibert F, Reñe R, et al. **Anti-Hu-associated para-**

neoplastic encephalomyelitis: analysis of 200 patients. *Brain* 2001; 124:1138–48 CrossRef Medline
32. Rudzinski LA, Pittock SJ, McKeon A, et al. **Extratemporal EEG and MRI findings in ANNA-1 (anti-Hu) encephalitis.** *Epilepsy Res* 2011; 95:255–62 CrossRef Medline
33. Jacobs DA, Fung KM, Cook NM, et al. **Complex partial status epilepticus associated with anti-Hu paraneoplastic syndrome.** *J Neurol Sci* 2003;213:77–82 CrossRef Medline
34. Rosenfeld MR, Eichen JG, Wade DF, et al. **Molecular and clinical diversity in paraneoplastic immunity to Ma proteins.** *Ann Neurol* 2001;50:339–48 CrossRef Medline
35. Hoffmann LA, Jarius S, Pellkofer HL, et al. **Anti-Ma and anti-Ta associated paraneoplastic neurological syndromes: 22 newly diagnosed patients and review of previous cases.** *J Neurol Neurosurg Psychiatry* 2008;79:767–73 CrossRef Medline
36. Mathew RM, Vandenberghe R, Garcia-Merino A, et al. **Orchiectomy for suspected microscopic tumor in patients with anti-Ma2-associated encephalitis.** *Neurology* 2007;68:900–05 CrossRef Medline
37. Crespo-Burillo JA, Hernando-Quintana N, Ruiz-Palomino P, et al. **Chorea secondary to striatal encephalitis due to anti-CV2/CRMP5 antibodies: case description and review of the literature.** *Neurologia (Barcelona, Spain)* 2015;30:451–53 CrossRef Medline
38. Malter MP, Helmstaedter C, Urbach H, et al. **Antibodies to glutamic acid decarboxylase define a form of limbic encephalitis.** *Ann Neurol* 2010;67:470–78 CrossRef Medline
39. Ko MW, Dalmau J, Galetta SL. **Neuro-ophthalmologic manifestations of paraneoplastic syndromes.** *J Neuroophthalmol* 2008;28: 58–68 CrossRef Medline
40. Younes-Mhenni S, Janier MF, Cinotti L, et al. **FDG-PET improves tumour detection in patients with paraneoplastic neurological syndromes.** *Brain* 2004;127:2331–38 CrossRef Medline
41. Nunez-Enamorado N, Camacho-Salas A, Belda-Hofheinz S, et al. **Fast and spectacular clinical response to plasmapheresis in a paediatric case of anti-NMDA encephalitis** [in Spanish]. *Rev Neurol* 2012; 54:420–24 Medline
42. Gresa-Arribas N, Titulaer MJ, Torrents A, et al. **Antibody titres at diagnosis and during follow-up of anti-NMDA receptor encephalitis: a retrospective study.** *Lancet Neurol* 2014;13:167–77 CrossRef Medline
43. Saraya A, Mahavihakanont A, Shuangshoti S, et al. **Autoimmune causes of encephalitis syndrome in Thailand: prospective study of 103 patients.** *BMC Neurol* 2013;13:150 CrossRef Medline
44. Ances BM, Vitaliani R, Taylor RA, et al. **Treatment-responsive limbic encephalitis identified by neuropil antibodies: MRI and PET correlates.** *Brain* 2005;128:1764–77 CrossRef Medline
45. von Rhein B, Wagner J, Widman G, et al. **Suspected antibody negative autoimmune limbic encephalitis: outcome of immunotherapy.** *Acta Neurol Scand* 2017;135:134–41 Medline
46. Matoq AA, Rappoport AS, Yang Y, et al. **Anti-NMDA-receptor antibody encephalitis in infants.** *Epilepsy Behav Case Rep* 2015;4:99–101 CrossRef Medline
47. Bravo-Oro A, Acosta-Yebra D, Grimaldo-Zapata IP, et al. **Reversible cortical atrophy secondary to anti-NMDA receptor antibody encephalitis** [in Spanish]. *Rev Neurol* 2015;60:447–52 Medline
48. Kayser MS, Titulaer MJ, Gresa-Arribas N, et al. **Frequency and characteristics of isolated psychiatric episodes in anti-N-methyl-d-aspartate receptor encephalitis.** *JAMA Neurol* 2013;70:1133–39 CrossRef Medline
49. Irani SR, Vincent A. **NMDA receptor antibody encephalitis.** *Curr Neurol Neurosci Rep* 2011;11:298–304 CrossRef Medline
50. Gabilondo I, Saiz A, Galán L, et al. **Analysis of relapses in anti-NMDAR encephalitis.** *Neurology* 2011;77:996–99 CrossRef Medline
51. Titulaer MJ, McCracken L, Gabilondo I, et al. **Treatment and prognostic factors for long-term outcome in patients with anti-NMDA receptor encephalitis: an observational cohort study.** *Lancet Neurol* 2013;12:157–65 CrossRef Medline
52. Tüzün E, Zhou L, Baehring JM, et al. **Evidence for antibody-mediated pathogenesis in anti-NMDAR encephalitis associated with ovarian teratoma.** *Acta Neuropathol* 2009;118:737–43 CrossRef Medline
53. Florance NR, Davis RL, Lam C, et al. **Anti-N-methyl-D-aspartate receptor (NMDAR) encephalitis in children and adolescents.** *Ann Neurol* 2009;66:11–18 CrossRef Medline
54. Gable MS, Sheriff H, Dalmau J, et al. **The frequency of autoimmune N-methyl-D-aspartate receptor encephalitis surpasses that of individual viral etiologies in young individuals enrolled in the California Encephalitis Project.** *Clin Infect Dis* 2012;54:899–904 CrossRef Medline
55. Prüss H, Finke C, Höltje M, et al. **N-methyl-D-aspartate receptor antibodies in herpes simplex encephalitis.** *Ann Neurol* 2012;72: 902–11 CrossRef Medline
56. Takahashi Y, Mori H, Mishina M, et al. **Autoantibodies and cell-mediated autoimmunity to NMDA-type GluRepsilon2 in patients with Rasmussen's encephalitis and chronic progressive epilepsia partialis continua.** *Epilepsia* 2005;46(suppl 5):152–58 Medline
57. Gitiaux C, Simonnet H, Eisermann M, et al. **Early electro-clinical features may contribute to diagnosis of the anti-NMDA receptor encephalitis in children.** *Clin Neurophysiol* 2013;124:2354–61 CrossRef Medline
58. Baumgartner A, Rauer S, Mader I, et al. **Cerebral FDG-PET and MRI findings in autoimmune limbic encephalitis: correlation with autoantibody types.** *J Neurol* 2013;260:2744–53 CrossRef Medline
59. Majoie HJ, de Baets M, Renier W, et al. **Antibodies to voltage-gated potassium and calcium channels in epilepsy.** *Epilepsy Res* 2006;71: 135–41 Medline
60. Boronat A, Gelfand JM, Gresa-Arribas N, et al. **Encephalitis and antibodies to dipeptidyl-peptidase-like protein-6, a subunit of Kv4.2 potassium channels.** *Ann Neurol* 2013;73:120–28 CrossRef Medline
61. Lai M, Huijbers MG, Lancaster E, et al. **Investigation of LGI1 as the antigen in limbic encephalitis previously attributed to potassium channels: a case series.** *Lancet Neurol* 2010;9:776–85 CrossRef Medline
62. Irani SR, Alexander S, Waters P, et al. **Antibodies to Kv1 potassium channel-complex proteins leucine-rich, glioma inactivated 1 protein and contactin-associated protein-2 in limbic encephalitis, Morvan's syndrome and acquired neuromyotonia.** *Brain* 2010;133: 2734–48 CrossRef Medline
63. Lancaster E, Huijbers MG, Bar V, et al. **Investigations of caspr2, an autoantigen of encephalitis and neuromyotonia.** *Ann Neurol* 2011; 69:303–11 CrossRef Medline
64. Finkel L, Koh S. **N-type calcium channel antibody-mediated autoimmune encephalitis: an unlikely cause of a common presentation.** *Epilepsy Behav Case Rep* 2013;1:92–96 CrossRef Medline
65. Kaira K, Okamura T, Takahashi H, et al. **Small-cell lung cancer with voltage-gated calcium channel antibody-positive paraneoplastic limbic encephalitis: a case report.** *J Med Case Rep* 2014;8:119 CrossRef Medline
66. Lancaster E, Lai M, Peng X, et al. **Antibodies to the GABA(B) receptor in limbic encephalitis with seizures: case series and characterisation of the antigen.** *Lancet Neurol* 2010;9:67–76 CrossRef Medline
67. Joubert B, Kerschen P, Zekeridou A, et al. **Clinical spectrum of encephalitis associated with antibodies against the α-amino-3-hydroxy-5-methyl-4-isoxazolepropionic acid receptor: case series and review of the literature.** *JAMA Neurol* 2015;72:1163–69 CrossRef Medline
68. Gerosa M, Poletti B, Pregnolato F, et al. **Antiglutamate receptor antibodies and cognitive impairment in primary antiphospholipid syndrome and systemic lupus erythematosus.** *Front Immunol* 2016; 7:5 CrossRef Medline
69. Tamagno G, Celik Y, Simó R, et al. **Encephalopathy associated with autoimmune thyroid disease in patients with Graves' disease: clinical manifestations, follow-up, and outcomes.** *BMC Neurol* 2010; 10:27 CrossRef Medline
70. Rosenbloom MH, Smith S, Akdal G, et al. **Immunologically mediated dementias.** *Curr Neurol Neurosci Rep* 2009;9:359–67 CrossRef Medline

Significance of Cerebellar Tonsillar Position on MR

A. J. Barkovich[1, 3]
F. J. Wippold[2, 3]
J. L. Sherman[3, 4]
C. M. Citrin[4, 5]

It has been noted that a low degree of ectopia of the cerebellar tonsils on MR is of questionable significance. We measured the position of the cerebellar tonsils with respect to the inferior aspect of the foramen magnum in 200 normal patients and in 25 patients with a firm diagnosis of Chiari I malformation. In the normal group, the mean position of the tonsils was 1 mm above the foramen magnum with a range from 8 mm above the foramen magnum to 5 mm below. In the patients with Chiari I malformations, the mean position was 13 mm below the foramen magnum with a range from 3 mm below the foramen magnum to 29 mm below. Fourteen percent of normal patients had tonsils extending slightly below the foramen magnum. If 2 mm below the foramen magnum is taken as the lowest extent for tonsils in a normal patient, our sensitivity in predicting symptomatic patients is 100% and our specificity is 98.5% (three false positives). If 3 mm below the foramen magnum is taken as the lowest normal tonsillar position, our sensitivity is 96% and our specificity is 99.5%. MR demonstration of less than 2 mm of tonsillar ectopia is probably of no clinical significance in the absence of syringomyelia.

The Chiari I malformation is defined as displacement of the cerebellar tonsils into the cervical spinal canal [1]. Unlike many malformations of the central nervous system (CNS), this entity manifests itself in early adulthood and middle age, often with a confusing clinical picture [2–4]. Additionally, a low degree of cerebellar ectopia is often of no clinical significance [6, 7]. The advent of MRI has provided an easy and noninvasive method of imaging the cerebellar tonsils and their relationship to the foramen magnum. The purpose of this study is to establish a normal range for tonsillar position and to determine the significance of various degrees of tonsillar ectopia.

Materials and Methods

The MR studies of 200 patients with clinical signs or symptoms unrelated to the Chiari I malformation or of other cervicocranial junction abnormalities were evaluated retrospectively. The examinations of 25 additional patients with definite Chiari I malformation and associated clinical signs and symptoms were also reviewed as a separate group.

Measurements were made from the lower level of the foramen magnum to the bottom of the lowest lying tonsil. The bottom of the foramen magnum was defined as a line extending from the lowest cortical bone seen (by way of lack of signal) at the posterior lip of the foramen magnum (opisthion) to the lowest cortical bone of the clivus (basion) (Fig. 1).

Measurements were all made on T1-weighted spin-echo images with TR of 250 to 700 msec and TE of 30 to 40 msec. T2-weighted images were difficult to evaluate because of decrease in signal-to-noise ratio with long TE and, more importantly, diminished contrast resolution between CSF and tonsil from the increased relative intensity of the CSF [8]. Proton-density images were advantageous because the slight graying of the CSF creates a sharper contrast with bone while contrast between CSF and tonsils is maintained. Longer imaging times make this less practical, however. All measurements were performed on sagittal images. All the authors agreed that tonsillar position was much more difficult to evaluate on coronal

Received January 8, 1986; accepted after revision April 9, 1986.

The opinions expressed herein are those of the authors and are not to be construed as reflecting the views of the Department of the Army, the Uniformed Services University of the Health Sciences, or the Department of Defense.

[1] Department of Radiology, Letterman Army Medical Center, San Francisco, CA 94129. Address reprint requests to A. J. Barkovich.

[2] Neuroradiology Section, Department of Radiology, Walter Reed Army Medical Center, Washington, DC 20307-5001.

[3] Department of Radiology, Uniformed Services University of the Health Sciences, Bethesda, MD 20814.

[4] Magnetic Imaging of Washington, Chevy Chase, MD 20815.

[5] Department of Radiology, George Washington University School of Medicine, Washington, DC 20037.

AJNR 7:795–799, September/October 1986
0195–6108/86/0705–0795
© American Society of Neuroradiology

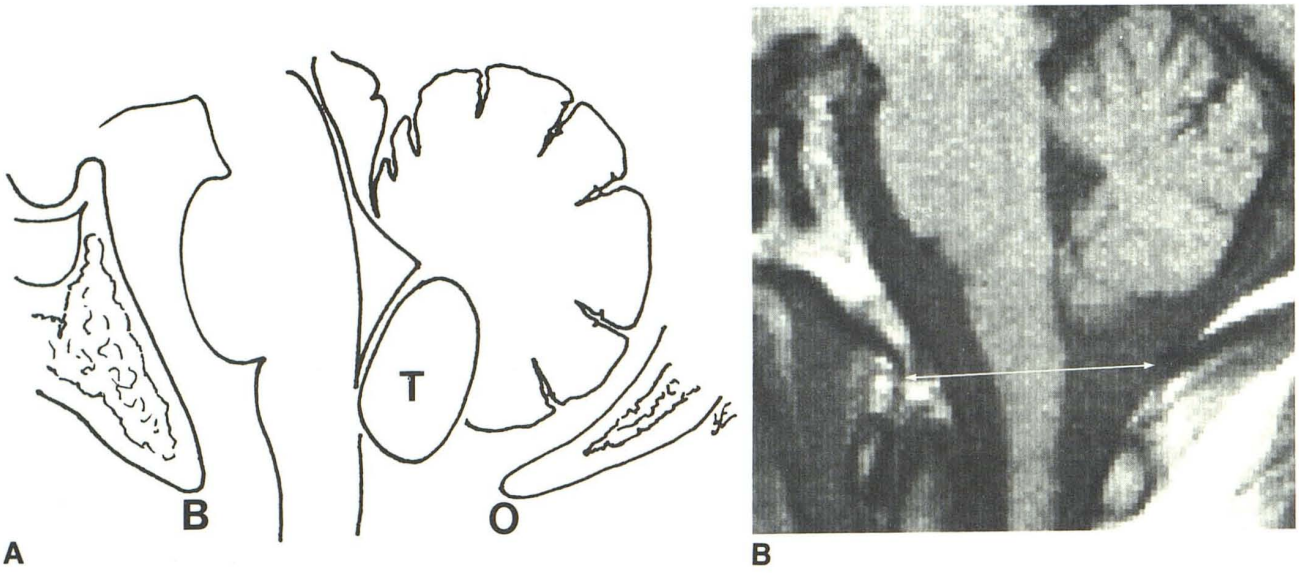

Fig. 1.—**A**, Drawing showing basion (B), opisthion (O), and cerebellar tonsil (T) in a normal patient. **B**, Midline sagittal section, SE 500/40, showing line from basion to opisthion in a nomal patient. Measurements were from this reference line. Bottoms of tonsils have a normal, rounded appearance and CSF is seen in a normal cisterna magna.

images (see discussion and Fig. 2). Distances were measured with calipers from the hard copy of the images. Measurements were to the nearest millimeter.

Patients with lesions that might affect tonsillar position were eliminated from the study. Specifically, this included any posterior fossa lesion, hydrocephalus of any origin, and supratentorial lesions causing any evidence of transtentorial herniation.

One hundred eighty-three images had a slice thickness of 1 cm and 42 images had a slice thickness of 5 mm. Ten patients had a 1-cm midline "scout" image as well as 5-mm images during a multislice sequence; measurements were identical, implying no difference in the methods.

Two scanners were used. One hundred forty-four studies were done on a 0.5-T Picker International superconducting scanner (pixel size 1.1 × 1.1 mm) and 81 were done on a 0.6-T Technicare superconducting scanner (pixel size 0.9 × 0.9 mm). Four signal acquisitions, a 256 × 256 matrix, and 2DFT reconstruction algorithms were used on all scans.

Results

Histogram results of the studies on the 200 normal and 25 Chiari I patients are given in Figure 3. The tonsillar position in the normal patients ranged from 8 mm above the foramen magnum (+8 mm) to 5 mm below the foramen magnum (−5 mm) with a mean value of +1 mm and standard deviation of 1.9 mm. In the 25 Chiari I patients, the range was from 29 mm below the foramen magnum (−29 mm) to 3 mm below the foramen magnum (−3 mm) with a mean value of −13 mm and standard deviation of 7.1 mm. As expected, the difference in means was significant ($p = 0.0001$ using the unequal variance T-test) (Table 1).

Sensitivities and specificities were calculated using 0, −1, −2, −3, −4, and −5 mm as the cutpoint (lowermost limit for normal tonsil position [See Table 2]). High sensitivities and specificities were obtained at all cutpoints from −1 to −4. The greatest overall accuracy was obtained at cutpoints of −2, −3, and −4.

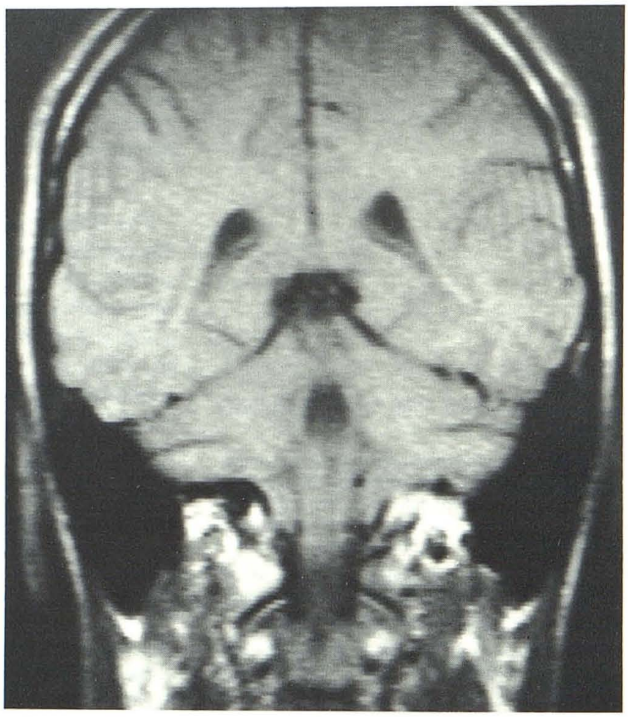

Fig. 2.—Coronal SE 700/40 through medulla and tonsils. The lower limits of foramen magnum are difficult to identify. Coronal scans were not used for this reason.

Scans were also examined for evidence of narrowing of the

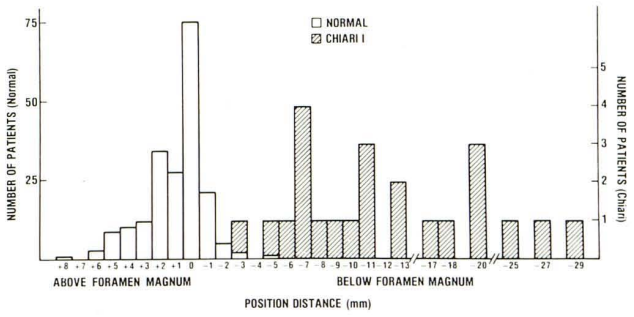

Fig. 3.—Histogram showing tonsillar positions in 200 normal and 25 Chiari I patients. Open boxes represent normal patients. Cross-hatched boxes represent patients with Chiari malformation.

TABLE 1: **Tonsil Position**

	No. of Patients (n = 225)	P (mm)	SD
Normal Pts	200	+1.0	1.90
Chiari I Pts	25	−13.12	7.08

Note.—P = average position of tip of tonsil with respect to lower border of the foramen magnum; SD = standard deviation.

TABLE 2: **Accuracy of Tonsil Position in Determination of Chiari I Malformations**

Cutpoint	Sensitivity	Specificity
0	100	85.43
−1	100	95.98
−2	100	98.49
−3	96.00	99.50
−4	96.00	99.50
−5	92.00	100

Note.—Cutpoint is the highest position considered a positive result; i.e., if zero is the cutpoint, any patient with tonsils at zero or below is considered to have Chiari I.

subarachnoid space or compression of the tonsils at the foramen magnum. All patients with ectopia of more than 1 mm showed narrowing or complete loss of the CSF spaces of the foramen magnum and cisterna magna. Pointed or "peglike" tonsils, as previously described in Chiari I malformations [8], were seen in both the symptomatic and asymptomatic patients with tonsillar ectopia. One patient had pointed tonsils prior to a suboccipital craniectomy but normally rounded tonsils on a postoperative scan (Fig. 4). Cervicomedullary kinking was present in only three of the 25 symptomatic patients (12%) and in none of the asymptomatic patients.

Discussion

In 1891, Chiari [1] published his initial paper on the hindbrain malformations that now bear his name. He divided the malformations into three types: Type I—Displacement of the cerebellar tonsils, and sometimes the lower vermis, into the cervical spinal canal. Type II—Displacement of the brainstem and lower cerebellum into the cervical spinal canal such that the elongated fourth ventricle also extends below the foramen magnum. Type III—Downward displacement of the medulla with herniation of the cerebellum first through the foramen magnum and then dorsally through a cervical spina bifida, forming a cervical encephalocele. (Only a single case of this type was described.)

The Chiari III anomalies are clinically obvious and are diagnosed at birth. Chiari II anomalies are associated with multiple other CNS malformations [9], most notably hydrocephalus and meningomyelocele, and are usually diagnosed in infancy or childhood. In Chiari I malformations, the anatomic abnormalities are less obvious, consisting of tonsillar ectopia with variable syringohydromyelia and bony craniocervical junction anomalies [2–5]. The clinical findings are diverse and inconsistent and tend to be manifested in early to middle adulthood; indeed, the patients are frequently misdiagnosed as having multiple sclerosis [2, 3]. Cranial nerve and brainstem compression can cause vertigo, facial pain, sensorineural deafness, or bulbar palsy. Cerebellar signs include ataxia, nystagmus, and oscillopsia. Also seen are spastic paraparesis secondary to compression of the pyramidal tracts, impaired proprioception, and vibratory sense from dorsal column involvement and muscle wasting with pain in the upper extremities secondary to syringomyelia [3].

Compounding the difficulty in clinical diagnosis is the question of the significance of a low degree of tonsillar ectopia. In 1963, Baker [6] noted 14 cases in which all myelographic findings were normal except that the tips of the tonsils extended 2 to 5 mm below the foramen magnum. Significantly, there was no obstruction to the free flow of contrast through the foramen magnum, implying no compression at that site. In contrast, O'Connor et al. [10], in 1973, measured tonsillar position retrospectively in 100 patients without posterior fossa or foramen magnum lesions and found that the position of the tonsillar tips was above the foramen magnum in all cases. In 1974, Bloch et al. [7] measured the position of the tonsillar tips with respect to the upper lip of the foramen magnum on myelograms of 60 "normal" and 19 "pathologic" patients. Using his results, the mean position for a tonsil is 1.3 mm below the upper lip of the foramen magnum. Considering that he counted each tonsil separately and that one tonsil is commonly 2–4 mm lower than the other [7], his results compare favorably with our mean value of 1 mm above the lower foramen magnum. The depth of the foramen magnum is usually 4–10 mm. Unfortunately, Bloch did not define his "normal" or "pathologic" groups, so there may be some variation in the populations studied.

Patients who did not clearly fall into the "normal" or "Chiari I" category were eliminated from our study. By this process, some minimally symptomatic or as yet asymptomatic patients may have been excluded, possibly yielding a somewhat low mean tonsillar position for this group.

The position of the tonsils was determined from sagittal images for several reasons. First, short TR, short TE sagittal

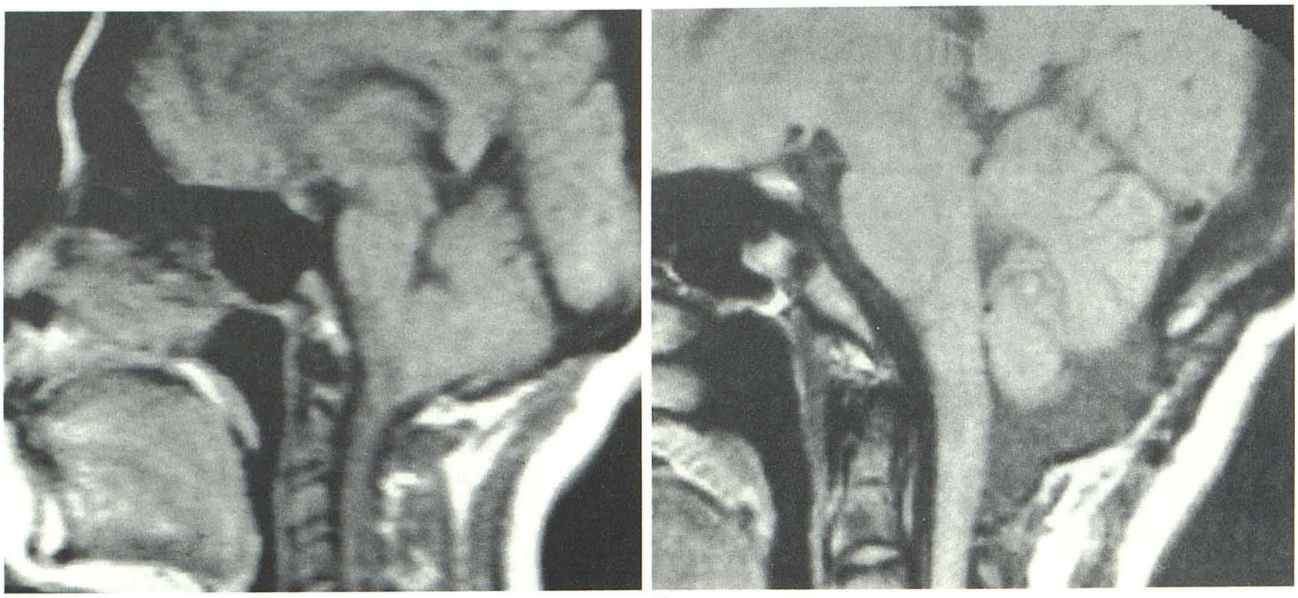

A B

Fig. 4.—**A**, Midline sagittal SE 500/40 scan in a symptomatic patient. Tonsils extend 1.1 cm below foramen magnum. Tonsils are "pointed" and cisterna magna is obliterated. The latter two findings were seen in both asymptomatic and symptomatic patients with low tonsils. **B**, Midline sagittal SE 500/40 scan after decompression via suboccipital craniectomy. Tonsils now have a normal rounded appearance.

midline spin-echo images are routinely obtained at our institution as a guide for axial and coronal slice positioning, so it was easy to obtain these images with no added examination time or discomfort for the patient. Moreover, it was more difficult to identify the foramen magnum on the coronal images (Fig. 2). The reasons for this include the lack of a high-signal-intensity diploic space to highlight the lack of signal from the cortical bone and the undulations and multiple foramina of the skull base lateral to the foramen magnum.

We could not find a significant difference in the appearance of the tonsils or basilar cisterns in the patients with asymptomatic cerebellar ectopia when compared with those with symptomatic Chiari malformations. The cisterna magna was small or nonexistent and the foramen magnum was filled with the medulla and "pointed" tonsils in both groups. The pointed appearance of the tonsils is most likely secondary to their compression within the foramen magnum. This is demonstrated by the patient illustrated in Fig. 4, in whom markedly pointed tonsils reverted to a more normally rounded appearance after decompression by a suboccipital craniectomy. The fact that compression of the tonsils is seen in asymptomatic patients would suggest that compression itself is not the primary determinant of the clinical manifestations of low-lying tonsils.

The question of why some patients with mild tonsillar ectopia are asymptomatic has been addressed by previous authors [3, 4, 11, 12]. The symptoms most likely result from the build-up of arachnoidal scarring and adhesions near the foramen magnum, possibly secondary to the repetitive rubbing of the tonsils against the bone over many years. These adhesions can cause additional or new compression of the tonsils and brainstem. They can also obstruct the flow of CSF from the basilar cisterns into the cervical subarachnoid space, which has been implicated as a possible factor in the development of syringomyelia [11].

We found cervicomedullary kinking in only three of our 25 Chiari I patients (12%). This frequency is identical to that found by Paul et al. [5] but far less than that found by Spinos et al. [8]. We did not observe such "kinking" in the normal group. This finding is, therefore, helpful when present.

A striking demarcation was noted in the degree of tonsillar ectopia between the symptomatic and asymptomatic patients. If the tonsillar tips extended 3 mm or more below the foramen magnum, all patients except one were symptomatic. No symptomatic patients had less than 3 mm of tonsillar ectopia. This was the major difference between the groups on MR.

Perhaps the greatest danger in evaluating patients for Chiari malformations is to call a positive patient's MR findings normal, and thus to end the work-up for foramen magnum lesions. It is probably better to err on the side of a false positive diagnosis, whereby further evaluation for cmpression at the foramen magnum (by myelography, for example) would reveal a lack of compression and direct the work-up elsewhere. Using this logic, a cut-off of −2 mm gives the best overall yield with no false negatives and a minimum of false positives.

In summary, there are multiple MR findings in patients with Chiari I malformations. The degree of tonsillar ectopia is the finding that most closely corresponds to the presence of clinical symptoms. Ectopia of 2 mm or less is unlikely to be of clinical significance.

REFERENCES

1. Chiari H. Uber Veranderungen des Kleinhirns infulge von Hydrocephalie des Grosshirns. *Deutsch Medizinsche Wocherschrift* **1891**;17:1172–1175
2. Appleby A, Foster JB, Handinson J, Hudgson P. The diagnosis and management of the Chiari anomalies in adult life. *Brain* **1969**;91:131–140
3. Banerji NK, Millar JHD. Chiari malformation presenting in adult life. *Brain* **1974**;97:157–168
4. Saez RJ, Onofrio BM, Yanagihara T. Experience with Arnold-Chiari malformation, 1960–1970. *J Neurosurg* **1976**;45:416–422
5. Paul KS, Lye RH, Strano FA, Dutton J. Arnold-Chiari malformation: review of 71 cases. *J Neurosurg* **1983**;58:183–187
6. Baker H. Myelographic examination of the posterior fossa with positive contrast medium. *Radiology* **1963**;81:791–801
7. Bloch S, Van Rensburg MJ, Danziger J. The Arnold-Chiari malformation. *Clin Radiol* **1974**;25:335–341
8. Spinos E, Laster DW, Moody DM, Ball MR, Witcofski RL, Kelly DL. MR evaluation of Chiari I malformations at 0.15 T. *AJNR* **1985**;6:203–208, *AJR* **1985**;144:1143–1148
9. Peach B. The Arnold-Chiari malformation: morphogenesis. *Arch Neurol* **1965**;12:527–537
10. O'Connor S, du Boulay G, Logue V. The normal position of the cerebellar tonsils as demonstrated by myelography. *J Neurosurg* **1973**;39:387–389
11. du Boulay G, Shah SH, Currie JC, Logue V. The mechanism of hydromyelia in Chiari type I malformations. *Br J Radiol* **1974**;47:579–587
12. Rhoton AL. Microsurgery of Arnold-Chiari malformations in adults with and without hydromyelia. *J Neurosurg* **1976**;45:473–483

MR Imaging of White Matter Disease in Children

Martha A. Nowell[1]
Robert I. Grossman
David B. Hackney
Robert A. Zimmerman
Herbert I. Goldberg
Larissa T. Bilaniuk

Twenty-three pediatric patients with white matter abnormalities on MR images were evaluated retrospectively to assess the contribution of MR compared with CT in diagnosing these conditions. In addition, the MR findings in major categories of white matter diseases were analyzed for sensitivity in detecting the presence of an abnormality. White matter disease categories included demyelinating disease (five cases), dysmyelinating disease (eight cases), developmental white matter abnormalities (four cases), and white matter abnormalities of unknown origin (idiopathic) (six cases), as seen on long TR images. We found that MR is not more sensitive than CT in detecting disease in the demyelinating or dysmyelinating categories, although it is more sensitive than CT in detecting the degree of disease present. In cases of developmental delay, MR is distinctly more useful than CT in demonstrating abnormalities of myelination. And in the idiopathic group, MR detected the presence of focal white matter abnormalities on long TR images in children with neurologic complaints and normal CT.

MR may serve to redefine and broaden the spectrum of reported imaging abnormalities in pediatric patients.

Although white matter diseases are uncommon in children, clinicians must be aware of their occurrence and able to recognize their MR appearances. Children can develop white matter disorders as a result of demyelination, dysmyelination, and developmental delay, as well as idiopathically. Using Poser's classification of white matter diseases, demyelinating lesions may be divided into primary disorders, such as multiple sclerosis (MS) and acute disseminated encephalomyelitis (ADEM), and secondary disorders whose origins include toxic or anoxic deficiency syndromes, viral disorders such as progressive multifocal leukoencephalopathy, and primary neuronal lesion Wallerian degeneration [1]. The more common primary dysmyelinating lesions include metachromatic leukodystrophy (MLD), Krabbe disease, Canavan disease, Alexander disease, and Pelizaeous-Merzbacher disease (PMD). The predominant secondary dysmyelinating disorders fall into the metabolic category. Poser [1] notes that adrenoleukodystrophy exhibits characteristics of both the demyelinating and dysmyelinating disorders.

We have also included in our study two other categories of disease that produce white matter abnormalities on MR: delayed myelination on a developmental basis and idiopathic pediatric white matter abnormalities. This report focuses on the MR diagnosis of pediatric white matter abnormalities.

Subjects and Methods

Twenty-three patients under 18 years old who were diagnosed as having abnormal white matter on MR were included in this study.

The study population included 11 girls and 12 boys ranging in age from 5 months to 13 years. Requirements for admission to the study were that the patient was under 18 and that a white matter abnormality was found on long TR MR images. The routine MR study performed on a GE 1.5-T Signa system included sagittal short spin-echo images 600/20/2

This article appears in the May/June 1988 issue of *AJNR* and the August 1988 issue of *AJR*.

Received June 29, 1987; accepted after revision October 15, 1987.

Presented in part at the annual meeting of the American Society of Neuroradiology, New York, May 1987, and at the annual meeting of the Society of Magnetic Resonance in Medicine, New York, August 1987.

[1]All authors: Department of Radiology, Hospital of the University of Pennsylvania, 3400 Spruce St., Philadelphia, PA 19104. Address reprint requests to R. I. Grossman.

***AJNR* 9:503–509, May/June 1988**
0195–6108/88/0903–0503
© American Society of Neuroradiology

(TR/TE/excitations) and axial and coronal long spin-echo images 2500/40, 80/2 and, if the patient was under 2 years old, 3500/40, 160/2 [2]. Eighteen patients had CT scans. One patient had both CT and cranial sonographic examinations. Two patients had no other studies, and information regarding outside examinations was unavailable in two other patients.

Results

The MR findings were categorized on the basis of clinical information. Of the 23 patients, five had demyelinating disease, eight had dysmyelinating disease, four were developmentally delayed, and six had white matter abnormalities with no known cause (Tables 1–4).

In 11 cases MR identified additional lesions not visualized on CT. These represented predominantly patchy, focal areas of increased white matter signal seen on long TR images in patients with demyelinating disease or in patients with white matter abnormalities with no known cause. In two cases the CT scans were unavailable for review. In the dysmyelinating diseases we observed that MR was equivalent to CT in identifying white matter abnormalities. Whether MR could be diagnostic early in the clinical course of the disease when CT is negative, as suggested by other authors, cannot be addressed in our group of patients because they were all studied in the subacute phases of their disease [3]. Our two cases of Alexander disease were radiologically atypical, with cerebellar and peritrigonal white matter disease as compared with frontal white matter disease, which is reported to be more common [3].

In two patients with metabolic diseases (carnitine deficiency and pyruvate dehydrogenase deficiency) CT scans with and without contrast were normal. In both cases abnormal periventricular white matter adjacent to the frontal and occipital horns was demonstrated by MR.

Only one of our four patients with perinatal asphyxia and/or developmental delay had a CT scan. This patient had a documented germinal matrix hemorrhage, and CT demonstrated periventricular low absorption in the white matter with minimal ventricular dilatation. MR also revealed a rind of hemosiderin (evidence of old hemorrhage) surrounding the lateral ventricles.

TABLE 1: Demyelinating Disorders

Clinical Diagnosis	Case No.[a]	CT	MR[b]
Acute disseminated encephalomyelitis	1	One lesion, centrum	Two white matter lesions, right and left centrum
	2	One lesion, centrum	Two centrum lesions, one medullary lesion
	3	Normal	Right parietal white matter lesion
Tick paralysis	1	One lesion, right temporal lobe	Right temporoparietal and left parietal lesions
Multiple sclerosis	1	Multiple lesions	Same number lesions

[a] Each number represents a different patient, e.g., case 1 of acute disseminated encephaloyelitis is a different patient from case 1 of tick paralysis or multiple sclerosis.

[b] All MR images are SE 2500–3500, 40/80–40/160.

TABLE 2: Dysmyelinating Disorders

Clinical Diagnosis	Case No.[a]	CT	MR[b]
Krabbe disease	1	Normal	Periventricular white matter high signal
Carnitine deficiency	1	Normal	Periventricular white matter high signal
Metachromatic leukodystrophy	1	No CT	Diffuse confluent white matter high signal
	2	No CT	Diffuse confluent white matter high signal
	3	Abnormal	Diffuse confluent white matter high signal
Alexander disease	1	Normal	Cerebellar high signal
	2	Normal	Periventricular white matter high signal
Pyruvate dehydrogenase deficiency	1	Normal	High signal in periatrial white matter

[a,b] See footnotes to Table 1.

TABLE 3: Developmental Delay

Case No.	Age	Gender	Clinical Diagnosis	CT	MR[a]
1	12 mo	M	Developmental delay, spasticity	Abnormal	Periventricular disease, ependymal hemosiderin
2	3 yr	F	Developmental delay, sensorineural hearing loss	No CT	Confluent white matter high signal
3	12 mo	F	Developmental delay, seizures, nonfocal exam	No CT	Relatively delayed myelination
4	9 yr	F	Developmental delay, esotropia	No CT	Periventricular disease

[a] All MR images are SE 2500–3500, 40/80–40/160.

TABLE 4: Unclassified White Matter Diseases

Case No.	Age	Gender	Clinical Diagnosis	CT	MR[a]
1	4 yr	M	Developmental delay, fine motor difficulties	No CT	Patchy periventricular white matter disease
2	19 mo	M	Seizures, nonfocal neurologic exam	Normal	Patchy lesions, centrum semiovale
3	6 yr	F	Hemifacial atrophy	Normal	Tiny focal lesions, ipsilateral parietal white matter
4	5 yr	M	Seizures, developmental delay, nonfocal neurologic exam	Normal	Tiny focal lesions, centrum semiovale
5	4 yr	M	Chediak-Higashi, spastic, developmental delay	Abnormal	Diffuse white matter high signal
6	5 yr	M	Ataxia, sensorineural hearing loss, developmental delay	Normal	Patchy periventricular white matter disease

[a] See footnote to Table 3.

Discussion

We have divided pediatric white matter diseases into four categories based on high-intensity abnormalities seen on long TR images and correlative clinical information: demyelinating disease, dysmyelinating disease, developmental delay (of myelination), and white matter abnormalities of unknown origin. Although there are certain trends from our data in the image patterns in these groups, MR generally lacked specificity with respect to diagnosis.

In this series CT was less sensitive to the extent of and/or number of patchy lesions in demyelinating disease. However, CT in combination with clinical history was diagnostic in all five cases. The diagnosis of a demyelinating disease in childhood is very dependent on correlation with viral titres, neurologic history, and examination. Two patients had an abnormal CT with nonenhancing hypodense focal lesions on CT, but in each case more lesions were demonstrated on MR (Fig. 1).

In one patient with ADEM, CT was normal. In one patient with tick paralysis a contrast-enhancing lesion was identified on CT, whereas two lesions were noted in the white matter on MR (Fig. 2). MR consistently depicted more lesions per patient than did CT in this category of patients. This sensitivity of long TR images is well described in the MR literature [4].

As expected, and as is also apparent from the CT and pathologic literature [1, 5–8], the dysmyelinating disorders demonstrated diffuse confluent high signal intensity in the white matter on long TR spin-echo images. We did not have any patients with a biochemically or biopsy-proved dysmyelinating disorder with patchy or focal white matter changes. We did, however, have two somewhat atypical cases of Alexander disease, both biopsy-proved (Fig. 3). One patient had diffuse cerebellar high signal intensity. The second patient had periventricular high signal, which was more prominent posteriorly. As noted in the literature [3, 9–11], Alexander disease usually manifests with abnormal white matter in the frontal region. Rarely, it involves the basal ganglia. The sensitivity of MR in these cases may result in widening the spectrum of radiologic manifestations of this disease. It is also possible that with further clinical follow-up our cases may demonstrate more typical findings and that presently we may

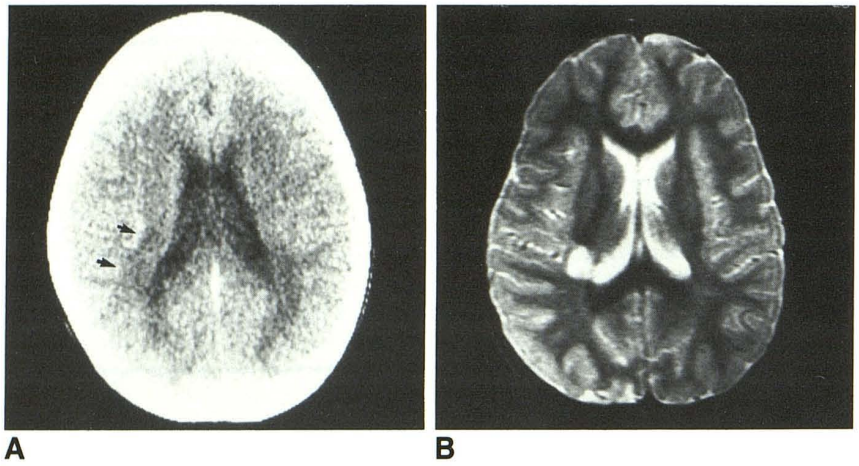

Fig. 1.—*A*, Contrast-enhanced CT scan suggests focal hypodensity in periatrial centrum semiovale on the right in 5-year-old boy who presented with a history consistent with acute disseminated encephalomyelitis (*arrows*).

***B*, Long spin-echo MR image 2500/80 at same level demonstrates unequivocal area of high signal intensity in same region as in CT scan. A second focus was seen on MR and not on CT (not shown).**

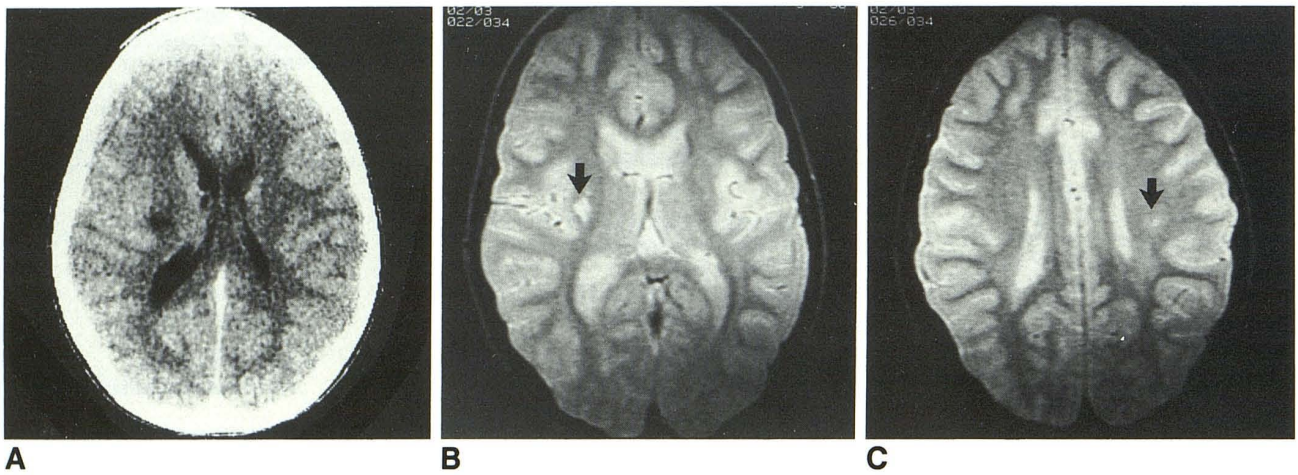

Fig. 2.—*A*, Focal hypodensity in right corona radiata on enhanced CT scan in 13-year-old boy who presented with tick paralysis is consistent with demyelination.

***B*, MR image 2500/50 shows lesion in right corona radiata (*arrow*).**

***C*, A second lesion superiorly is seen in corona radiata on left (*arrow*).**

just be imaging one point on the continuum of the disease.

In two cases with enzyme metabolic deficiencies (carnitine and pyruvate dehydrogenase), MR revealed white matter abnormalities when CT was normal (Fig. 4). One patient was scanned early in her clinical course and the second patient was scanned late in his clinical course.

Our patient with Krabbe disease (Fig. 5) demonstrated confluent periventricular high signal and the children with MLD (Fig. 6) had diffuse confluent high signal intensity in the white matter on long TR MR (long spin-echo imaging). The MLD patients were scanned several months after diagnosis. The MR findings did not appear to add any additional information to that provided by CT, which demonstrated diffuse periventricular white matter high signal in each case. The positive MR in Krabbe disease was performed early in the clinical course as was the CT, which was normal. In the literature [3, 12–14], five of eight reported cases had normal CT scans at diagnosis. If MR is performed early enough in the clinical course of the disease, the diagnosis of suspected white matter disease may be confirmed. The diagnosis of Krabbe disease is based on biochemical testing while the role of MR may be to suggest that such tests be performed at an earlier date [14].

In children with developmental delay, MR is more useful than CT, since the progression of myelination can be evaluated with greater sensitivity [15–18]. Associated findings such as old hemosiderin deposits in the germinal matrix are also made only by MR (Fig. 7). Clinical correlation and MR follow-up is necessary to fully evaluate the role of MR in this group of patients.

The last group of pediatric white matter diseases are those of unknown origin. It is in this group that perhaps MR had its

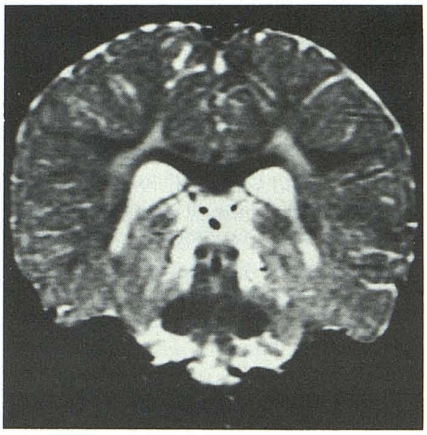

Fig. 3.—MR image 3500/16 shows patchy periventricular high signal in white matter of parietal lobes in 12-month-old boy with biopsy-proved Alexander disease. CT scan (not shown) was normal.

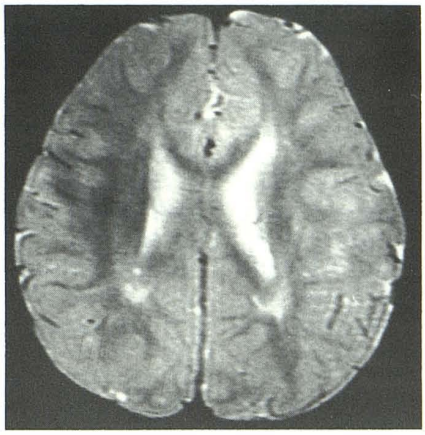

Fig. 4.—Minimal periventricular high signal is noted on long spin-echo MR image 2500/50 in patient with carnitine deficiency.

Fig. 5.—MR image 3500/20 shows confluent periventricular white matter disease in 5-month-old patient with Krabbe disease.

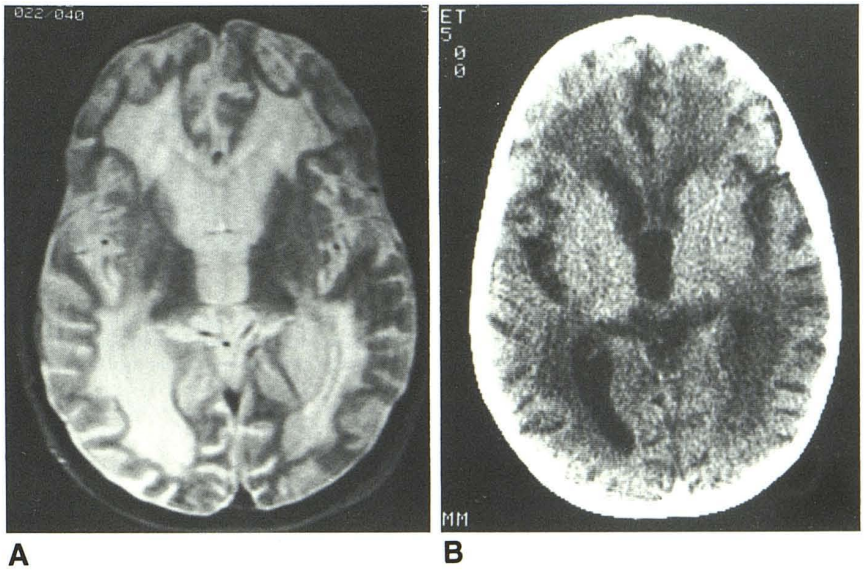

Fig. 6.—*A*, MR image 2500/80 shows diffuse confluent high signal throughout white matter in 4-year-old boy with metachromatic leukodystrophy diagnosed 3 years earlier. Moderate atrophy is present.

B, CT without contrast performed a few weeks before MR demonstrates diffuse white matter hypodensity, the extent of which is similar to that of the MR changes although somewhat less apparent.

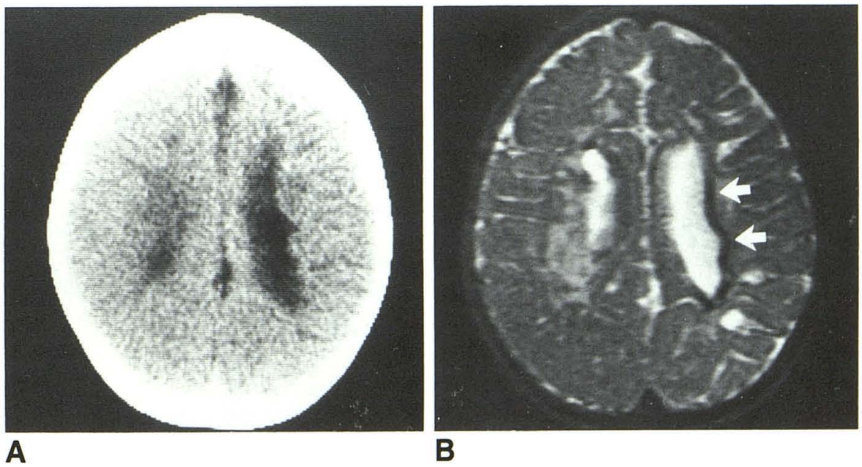

Fig. 7.—*A*, CT scan of 12-month-old infant who was premature and had a germinal matrix hemorrhage at birth shows mild ventricular dilatation and some periventricular low absorption.

B, MR image 3500/60 at same level demonstrates same degree of periventricular white matter change; in addition, some ependymal hemosiderin deposition can be seen (*arrows*).

greatest impact in lesion-detection capabilities. In our six patients there was a spectrum of clinical presentations responsible for the initial MR (Table 4). Four of these patients had normal CT, one patient had an abnormal CT, and one patient did not have CT. MR of a 3-year-old girl whose major complaint was sensorineural hearing loss and moderate developmental delay was grossly abnormal, demonstrating several patchy areas of high signal in the white matter. CT was normal. All metabolic screening tests were normal (Fig. 8). The one patient with diffuse confluent hypodensities in the white matter on CT had Chediak-Higashi disease. MR demonstrated an equivalent pattern of diffuse white matter high signal on long TR images. These images were obtained in the late stages of this patient's disease. The patient had not received prior chemotherapy or radiation, and the cause of the white matter abnormalities is unknown. There have not been prior reports in the literature of white matter disease in Chediak-Higashi disease [19] (Fig. 9). One patient with olivopontocerebellar degeneration had mild periventricular high intensity on long TR images. CT performed at the same time in his clinical course was unremarkable. To our knowledge, supratentorial white matter changes have not been described in olivopontocerebellar degeneration [20].

The remaining patients with idiopathic white matter abnor-

Fig. 8.—MR image 2500/40 of 3-year-old girl with developmental delay and sensorineural hearing loss demonstrates several areas of white matter high signal in periventricular regions. CT was normal.

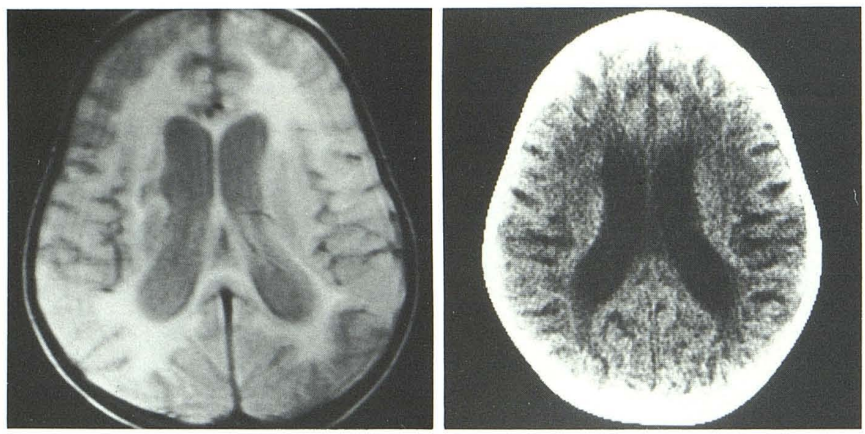

A B

Fig. 9.—*A*, Confluent white matter hyperintensity is seen on long spin-echo MR image 2500/40 in 4-year-old boy with Chediak-Higashi disease.
B, CT scan shows white matter hypodensities in same distribution.

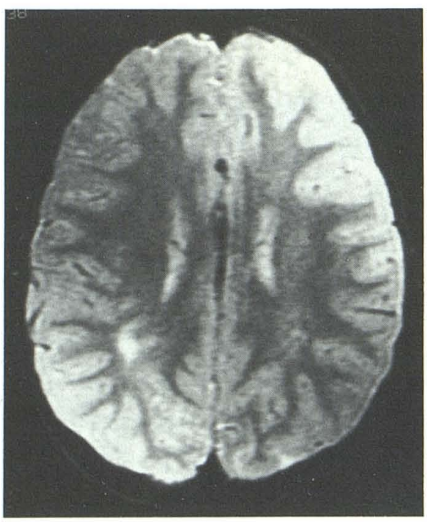

10

Fig. 10.—A few focal regions of high signal intensity are seen in this MR image 2500/80 of 4-year-old boy with developmental delay and fine motor difficulties. CT scan was negative.

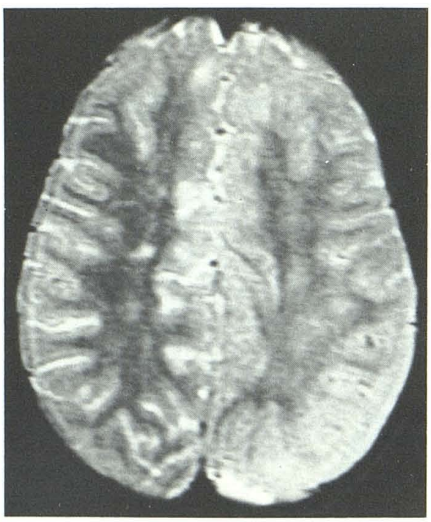

11

Fig. 11.—This 5-year-old boy presented with seizures and developmental delay with a nonfocal neurologic examination. Small focal areas of high signal intensity are seen on long spin-echo MR image 2500/40 in centrum semiovale. CT was negative.

malities had variably sized patchy focal areas of high signal intensity on long TR images in the white matter not causally related to the neurologic symptoms or examination (Figs. 10 and 11). None of these patients was premature or had a history of trauma, drug, or radiation exposure.

In summary, 23 pediatric patients with white matter disease were evaluated by MR. These patients were placed into four categories on the basis of long TR MR findings and clinical information: (1) demyelinating, (2) dysmyelinating, (3) developmental, and (4) idiopathic white matter abnormalities. MR was not more sensitive than CT or clinical evaluation in detecting white matter disease in demyelinating or dysmyelinating categories, although it certainly was more sensitive than CT in determining the extent of involvement. In the developmental group the pattern of myelination could be assessed and definitive evidence of old hemorrhage could be determined. In the idiopathic groups MR played a more useful role in identifying the existence of disease. In these cases subtle focal white matter abnormalities could be detected in children with neurologic complaints. In the latter patients a negative CT might preclude further imaging follow-up in certain clinical situations.

MR may serve to redefine and broaden the disease spectrum of reported white matter abnormalities in children.

REFERENCES

1. Poser CM. Disease of the mylen sheath. In Minckler J, ed. *Pathology of the nervous system*. New York: McGraw-Hill, **1968**:767–821
2. Nowell MA, Hackney DB, Zimmerman RA, Bilaniuk LT, Grossman RI, Goldberg HI. Immature brain: spin-echo pulse sequence parameters for high-contrast MR imaging. *Radiology* **1987**;162:272–273
3. Kingsley DP, Kendall BE. Demyelinating and neuro-degenerative disease in childhood: CT appearances and their differential diagnosis. *J Neuroradiol* **1951**;8:243–255
4. Atlas SW, Grossman RI, Goldberg HI, Hackney DB, Bilaniuk LT, Zimmerman RA. MR diagnosis of acute disseminated encephalomyelitis. *J Comput Assist Tomogr* **1986**;10:798–801
5. Heinz ER, Drayer BP, Haenggel CA, Painter MJ, Crumrine P. Computed tomography in white-matter disease. *Radiology* **1979**;130:371–378
6. Lane B, Carroll BA, Pedley TA. Computerized cranial tomography in cerebral diseases of white matter. *Neurology* **1978**;28:534–544
7. Barnes DM, Enzmann DR. The evolution of white matter disease as seen on computed tomography. *Radiology* **1981**;138:379–383
8. Robertson WC, Gomez MR, Reese DF, Okazak H. Computed tomography in demyelinating disease of the young. *Neurology* **1977**;27:838–842
9. Farrell K, Chuang S, Becker LE. Computed tomography in Alexander's disease. *Ann Neurol* **1984**;15:605–607
10. Towfighi J, Young R, Sassani J, Ramer J, Horoupian DS. Alexander's disease: further light- and electron-microscopic observations. *Acta Neuropathol (Berl)* **1983**;61:36–42
11. Holland IM, Kendall BE. Computed tomography in Alexander's disease. *Neuroradiology* **1980**;20:103–106
12. Kwan E, Drace J, Enzmann D. Specific CT findings in Krabbe disease. *AJR* **1984**;143:665–670
13. Ieshima A, Eda I, Matsui A, Yoshinok Takashima S, Takeshita K. Computed tomography in Krabbe's disease: comparison with neuropathology. *Neuroradiology* **1983**; 25:323–327
14. Baram Z, Goldman AM, Percy AK. Krabbe's disease: specific MRI and CT findings. *Neurology* **1986**; 36:111–115
15. Quencer RM. Maturation of normal primate white matter. Computed tomographic correlation. *AJNR* **1982**;3:365–372, *AJR* **1982**; 139:561–568
16. Flodmark O, Roland EH, Hill A, Whitfield MF. Periventricular leukomalacia: radiologic diagnosis. *Radiology* **1987**;162:119–124
17. Flodmark O, Becker LE, Harwood-Nash DC, Fitzhardnage PM, Fitz CR, Chuang SH. Correlation between computed tomography and autopsy in premature and full-term neonates that have suffered perinatal asphyxia. *Radiology* **1980**;137:93–103
18. Johnson MA, Pennock JM, Bydder GM, Dubowitz LMS, Thomas DJ, Young IR. Serial MR imaging in neonatal cerebral injury. *AJNR* **1987**;8:83–92
19. Sung JH, Meyers JP, Stadlan EM, Cowen D, Wolf A. Neuropathological changes in Chediak-Higashi disease. *J Neuropathol Exp Neurol* **1969**;28(1):86–118
20. Oppenheimer DR. Diseases of the basal ganglia, cerebellum and motor neurons. In Blackwood DW, Corsellis JAN, eds. *Greenfield's neuropathology*, 3rd ed. Chicago: Yearbook Medical, **1976**:623–624

AJNR: 20, January 1999

CNS Vasculitis in Autoimmune Disease: MR Imaging Findings and Correlation with Angiography

Martin G. Pomper, Timothy J. Miller, John H. Stone, William C. Tidmore, and David B. Hellmann

BACKGROUND AND PURPOSE: **MR findings in CNS vasculitis and their correlation with angiography have not been clearly defined. We therefore explored three hypotheses regarding CNS vasculitis associated with autoimmune disease: 1) MR imaging is highly sensitive; 2) a typical MR appearance exists; and, 3) MR and angiographic findings correlate well.**

METHODS: **We studied 18 patients with CNS vasculitis associated with autoimmune disease, characterized the MR lesions by type, size, number, and location, and correlated the MR findings with those of angiography.**

RESULTS: **All patients with CNS vasculitis had abnormalities on MR studies. On average, four ± two lesions per patient were detected on MR images. The lesions were located in the subcortical white matter (n = 20), cortical gray matter (n = 16), deep gray matter (n = 16), deep white matter (n = 9), and cerebellum (n = 9). Only 65% of MR lesions were evident on angiograms; 44% of the lesions revealed on angiograms were detected by MR.**

CONCLUSION: **MR imaging is sensitive for CNS vasculitis. Lesions attributable to CNS vasculitis in autoimmune disease are distributed nearly equally among cortical, subcortical, and deep gray matter structures. The modest correlation between MR imaging and angiography suggests that the two techniques provide different information about CNS vasculitis and that both types of studies are needed for the complete assessment of damage caused by vascular abnormalities.**

CNS vasculitis represents a heterogeneous group of inflammatory diseases that primarily affect the small leptomeningeal and parenchymal blood vessels of the brain (1). A variety of neurologic insults may cause CNS vasculitis, including infection, malignancy, ionizing radiation, cocaine ingestion, and autoimmune disease (1, 2). Primary angiitis of the CNS (2–4), systemic lupus erythematosus (5), polyarteritis nodosa (6), giant cell arteritis (1), and Sjögren syndrome (7) comprise the majority of autoimmune conditions associated with CNS vasculitis. In all these disorders, the precise pathogenesis remains obscure; in all, however, the immune system appears to play a central role, and immunosuppressive agents are the cornerstones of treatment. In practice, MR imaging precedes angiographic studies in the evaluation of patients. Because of the limited data available on the use of MR imaging in CNS vasculitis (4, 8–12), we reviewed our experience with this disorder. We hypothesized that MR imaging is highly sensitive, that a typical MR appearance exists, and that MR and angiographic findings correlate well.

Received June 25, 1997; accepted after revision August 26, 1998.

From the Departments of Radiology (M.G.P.) and Medicine (J.H.S., W.C.T., D.B.H.), The Johns Hopkins University School of Medicine, The Johns Hopkins Hospital, Baltimore; and the Department of Radiology (T.J.M.), Good Samaritan Hospital, Cincinnati.

Address reprint requests to David B. Hellmann, MD, The Johns Hopkins Hospital, 1830 E Monument St, Room 9030, Baltimore, MD 21205.

© American Society of Neuroradiology

Methods

The entry criteria for the study included all of the following: 1) an angiogram interpreted as positive (see definition below) for CNS vasculitis by the attending neuroradiologist at the time the angiogram was obtained; 2) a clinical history consistent with CNS vasculitis, that is, clinical findings of an acquired neurologic deficit that remained unexplained after a thorough initial evaluation (9); and 3) exclusion of nonautoimmune causes of the patient's presentation (eg, infection, malignancy, ionizing radiation, and cocaine use). Of 259 angiograms obtained at our hospital to exclude CNS vasculitis between 1986 and 1997, 30 revealed abnormalities. Of those 30 patients, 20 had autoimmune disorders. Of those 20 patients, 16 had angiograms and MR studies available for review; these 16 patients, along with two patients referred from outside institutions, were included in the study (total patients = 18).

Three rheumatologists and one medical resident reviewed the patients' medical records using a defined protocol and a data abstraction form. The information collected during the medical records review included the following: age, gender, and history of previous rheumatic diseases; risk factors for atherosclerotic vascular disease; neurologic symptoms and deficits at presentation; lumbar puncture results; original interpre-

TABLE 1: Population characteristics

Patient	Age (y)/Sex	Diagnosis
1	60/F	PACNS
2	37/F	SLE
3	33/F	PACNS
4	71/F	PACNS
5	41/F	PACNS
6	24/F	PACNS
7	59/M	PACNS
8	14/F	PACNS
9	50/F	PACNS
10	50/F	PACNS
11	19/M	PACNS
12	74/M	PACNS
13	53/F	PACNS
14	52/F	PACNS
15	51/M	PACNS
16	31/F	SLE
17	40/F	PAN
18	55/M	GCA

Note.—PACNS indicates primary angiitis of the CNS; SLE, systemic lupus erythematosus; PAN, polyarteritis nodosa; GCA, giant cell arteritis.

tations of all MR studies and angiograms; and the results of brain biopsies and postmortem studies. Brief clinical summaries were written for each patient. The presence or absence of oligoclonal bands in patients' CSF and serum antiphospholipid antibodies were also noted, but not included, in the analysis because of the small number of patients who had such tests. Patients with a history of diabetes and hypertension were excluded. No patient had multiple sclerosis or other demyelinating diseases.

MR imaging was performed on a 1.5-T imaging system. Spin-echo (SE) T1-weighted sagittal (600/20 [TR/TE]) and double-echo (T2-weighted) axial (3000/30,100) images were obtained for all patients. In one patient (patient 6), a fluid-attenuated inversion recovery (FLAIR) sequence (11004/114; TI = 2200) was also obtained. Intravenous gadopentetate dimeglumine (0.2 mL/kg) was administered to 11 patients (patients 1, 2, 4, 6–9, and 11–14), and contrast-enhanced T1-weighted images were subsequently obtained in the axial and/or coronal planes (600/20–30). MR angiography was performed in six patients (patients 4, 6, 9, 10, 13, and 14), using 3D time-of-flight imaging. Conventional biplane film screen or digital subtraction angiography was performed in all patients. Details of the angiographic procedures have been described previously (12).

Angiographic and MR findings were considered positive if interpreted by the attending neuroradiologist as being consistent with vasculitis. To evaluate the consistency of the radiologic diagnoses and to perform correlations between MR imaging and angiography, all the available radiologic studies were reviewed by two additional attending neuroradiologists who were blinded to both the clinical data and the results of other radiologic studies. Discrepancies between the reviewers were submitted to a third attending neuroradiologist for arbitration. The reviewers considered an angiogram to have positive findings if focal or diffuse areas of arterial stenosis, occlusion, dilatation, or beading were detected (1, 9); MR findings were considered positive if foci of high signal intensity were present on long-TR images. To reduce the likelihood of including in our analysis T2 bright lesions caused by small-vessel atherosclerotic disease, we excluded patients with a history of hypertension or diabetes.

We determined the type, size, and number of all lesions detected by MR imaging, and assigned each lesion to a vascular distribution using a standard atlas (13). We classified the lesions as occurring in the following brain regions: cortical gray matter, subcortical white matter, deep white matter, deep gray matter, and cerebellum. We distinguished subcortical white matter from deep white matter by defining the former as the region directly adjacent to the cortex and the latter as a region clearly separate from the cortex; for example, a periventricular or internal capsule location. To be classified as periventricular, a lesion had to be focal and adjacent to the ventricle. The volume of a lesion was estimated by tracing the lesion manually and then calculating the product of the dimensions. The reported volume for each lesion was the average of the two reviewers' estimates. When the reviewers' estimates varied more than twofold, one of the reviewers quantified the volume of the lesion in question using MedVol 1.7 (software; copyright by Bruce E. Hall, MD, The Johns Hopkins University, Baltimore, MD) and reported that measurement. We correlated the lesions detected on MR images with those found on angiograms for all patients for whom both MR images and complete (at least three-vessel) angiograms were obtained (patients 9 and 14 were excluded from the correlation studies because of incomplete angiograms). If an MR lesion fell within a vascular territory in which a clear lesion existed on the corresponding angiogram, the two lesions were judged to correlate.

We used the Scheffé test to compare the frequency of lesion occurrence in MR vascular distributions. Differences were considered significant if P values were less than .05. Statistical analysis was performed using StatView SE + Graphics 1.03 (Abacus Concepts Inc, 1988).

Results

For each patient, the demographic characteristics and diagnoses associated with CNS vasculitis are displayed in Table 1. Thirteen of the 18 patients were female (72%) and five were male (28%). The patients ranged in age from 14 to 74 years, with a mean age of 45 ± 14 years. No patient had a history of hypertension, and none had used cocaine within 3 years of disease onset.

MR Imaging

Abnormalities were revealed on the MR studies in all patients with angiographically proved CNS vasculitis. Among the 18 patients, a total of 74 vascular, parenchymal, and extraaxial lesions (each representing one row in Table 2) were detected by MR imaging, an average of four ± two lesions per patient. The number of lesions per patient ranged from as few as one to as many as nine (Figs 1 and 2). Fourteen (78%) of the 18 studies revealed bilateral disease, and 13 (72%) detected exclusively supratentorial lesions. No patient had infratentorial lesions in the absence of supratentorial findings. Some lesions extended over more than one brain region. Among the 74 lesions, 20 were located in the subcortical white matter, 16 in the deep gray matter, 16 in the cortical gray matter, nine in the deep white matter, and nine in the cerebellum. Three carotid occlusions and one subarachnoid hemorrhage (SAH) were also detected. Regarding the territories affected, the middle cerebral artery (MCA) (average, 2.3 lesions per patient) was more frequently affected than the anterior cerebral artery (ACA) (average, 0.2 lesions per patient), the pos-

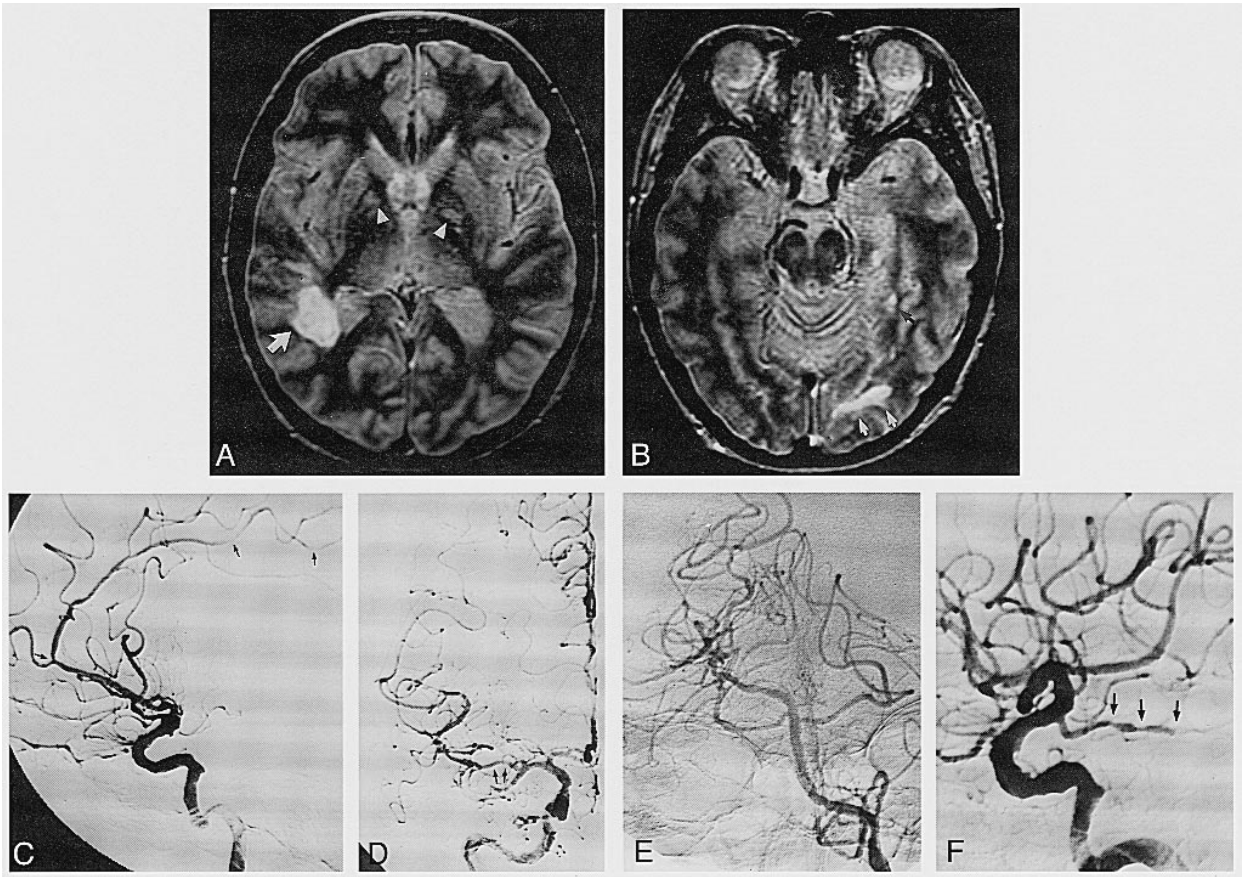

FIG 1. Patient 1: 60-year-old woman with primary angiitis of the CNS (a typical case of CNS vasculitis).

A and *B*, Axial SE MR images (3000/34). In *A*, an infarct is seen in the right subcortical white matter and the deep white matter (posterior MCA distribution) (*arrow*). Lacunar infarcts are also present in the globus pallidi (*arrowheads*). In *B*, infarcts are present in the left subcortical white matter (PCA distribution) (*white arrows*) and posterior left hippocampus (*black arrow*). Increased signal in the putamina and midbrain are artifactual.

C, Right lateral digital subtraction angiogram reveals mild narrowing of the proximal (near the A2 segment bifurcation) and several distal pericallosal artery segments (*arrows*). The MCA is poorly visible.

D, Anteroposterior digital subtraction angiogram of the right common carotid artery shows significant narrowing of the right M2 segment (*arrows*), with consequent attenuation of the more distal segments. The left MCA was normal.

E and *F*, Anteroposterior left vertebral artery (*E*) and lateral left common carotid artery (*F*) injections depict a fetal origin of the left PCA, with beading and occlusion of the PCA (*arrows* in *F*) and correlate with the MR image shown in *B*.

terior cerebral artery (PCA) (average, 0.7 lesions per patient), or the vertebral artery (average, 0.5 lesions per patient) territories ($P < .05$).

The lesions included 17 classic wedge-shaped infarctions in the cortical gray matter or cortical gray matter plus subcortical white matter (Fig 2A and B). The volume of the infarctions ranged from 0.1 to 80 cm^3, with a mean of 11.4 cm^3 (median, 2.2 cm^3). Two patients (patients 3 and 12) had parenchymal lesions associated with hemorrhage (Fig 3). Only three strictly periventricular lesions (in three different patients) were identified (Fig 4B and D). The lesion in Figure 1A was considered to reside in the subcortical white matter, because more superior images (not shown) placed the majority of this lesion in that region rather than in a periventricular location.

Correlation of MR Imaging with Angiography

Lesions involving 74 arteries were revealed by angiography. The angiographic results are presented in Table 3. A median of 6.5 days elapsed between MR imaging and angiography. We correlated the MR results with the angiographic findings on a lesion-for-lesion basis. The correlation between MR imaging and angiography is summarized in Table 4. Angiography detected 43 (65%) of the 66 lesions evident on MR images. In comparison, MR imaging detected 30 (44%) of the 68 angiographic lesions.

CNS pathologic specimens were available in four patients, one from autopsy (patient 15) and three from brain biopsies (patients 1, 2, and 4). In patients 2, 4, and 15, the clinical diagnosis of CNS vasculitis was confirmed by pathologic findings. In patient 1, the brain biopsy samples revealed no abnormalities.

Discussion

CNS vasculitis occurs frequently in the differential diagnosis of patients with neurologic signs

TABLE 2: Lesions on MR images

Patient	Location of Lesion	Lesion Size (cm^{13})	Vascular Distribution	No. of Affected Brain Regions	Time (y)
1	R CGM	15	MCA	4	1
	R SCWM	2	MCA		
	R SCWM	0.2	MCA		
	R DWM	0.2	MCA		
	R CB	0.1	SCA		
	L SCWM	1	PCA		
2	R CGM, SCWM	50	MCA	6	7
	R CGM, SCWM	50	PCA		
	R DGM	8	MCA		
	L CGM, SCWM	50	PCA		
	L DGM	3	MCA		
	L SGWM	6	MCA		
3	R CGM, DGM, SCWM	60	MCA	8	5
	R cavernous, carotid (occluded)				
	L CGM, DGM, SCWM	40	MCA		
	L cavernous, carotid (occluded)				
4	R DGM	0.4	MCA	3	11 mo
	R DGM	0.1	MCA		
	R DGM	0.1	PCA		
	R SCWM	0.3	MCA		
	L DGM	0.1	MCA		
	L DGM	0.6	MCA		
5	L parietal subarchanoid space	...	...	1	9
6	L CGM, DGM, SCWM	35	MCA	3	27
7	R CGM	15	MCA	5	10
	R DGM, DWM	15	MCA		
	R CB	0.3	AICA		
	L DGM	0.2	MCA		
8	R CGM	12	PCA	2	6
	R CGM	2.5	MCA		
	L CGM	12	PCA		
	L CGM	2	MCA		
9	R CGM, SCWM	70	MCA	5	2.5 mo
	L CGM, SCWM	80	PCA		
	L CGM, SCWM	7	MCA		
	L CB	7	PICA		
10	R DWM	0.6	PCA	3	1
	L SCWM	0.5	MCA		
	L DWM	0.6	MCA		
11	R CGM	6	PCA	4	7
	R DGM, DWM	2.5	MCA		
	R DWM	7	MCA		
	L DWM	1	BA		
12	R CGM, SCWM	10	PCA	2	1
	R SCWM	0.7	MCA		
13	R DGM	0.5	MCA	6	5
	R DGM	0.1	MCA		
	R SCWM	1.3	ACA		
	R DWM	1.4	MCA		
	R CB	8	PICA		
	R CB	8	PICA		
	L DGM	0.2	PCA		
	L DGM	0.1	MCA		
	L CB	3	PICA		
14	R DGM	1	MCA	5	3
	L CGM, SCWM	50	ACA		
	L DGM	3	MCA		
	L DWM	3	MCA		
15	R CGM, DGM, SCWM	50	MCA	4	13
	R supraclinoid carotid (occluded)				
16	R SCWM, DWM	10	MCA	4	7
	L CGM	12	ACA		
	L DWM	1	MCA		
	L DWM	1	MCA		

TABLE 2: Continued.

Patient	Location of Lesion	Lesion Size (cm^{13})	Vascular Distribution	No. of Affected Brain Regions	Time (y)
17	R SCWM	0.1	MCA	6	1
	R CB	1	SCA		
	L CGM, SCWM	60	MCA		
	L DGM	0.5	ACA		
	L CB	1	SCA		
	L CB	1	PICA		
18	R SCWM	1	MCA	3	1
	R SCWM	1	MCA		
	L SCWM	3	MCA		
	DWM*	3.5	PCA		

Note.—Each row represents one lesion. Brain regions are abbreviated as follows: R indicates right; L, left; ICA, internal carotid artery; CGM, cortical gray matter; SCWM, subcortical white matter; DWM, deep white matter; DGM, deep gray matter; CB, cerebellum; MCA, middle cerebral artery; ACA, anterior cerebral artery; PCA, posterior cerebral artery; SCA, superior cerebellar artery; AICA, anterior inferior cerebellar artery; PICA, posterior inferior cerebellar artery; BA, basilar artery. Time = days between MR imaging and angiography unless otherwise indicated.

* Lesion was in the center of the corpus callosum splenium.

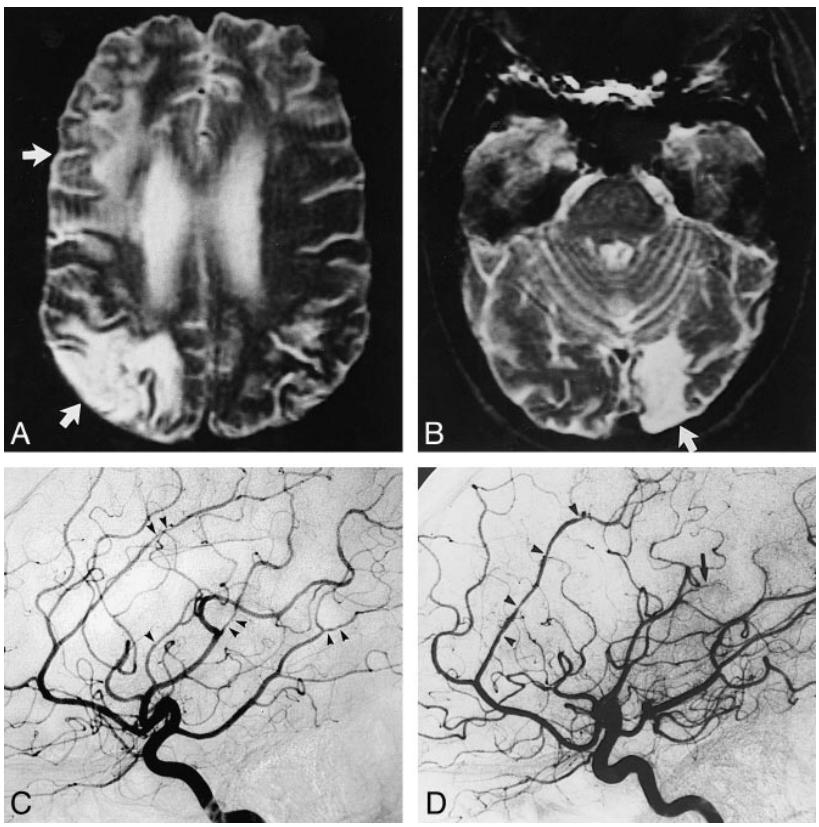

FIG 2. Patient 2: CNS vasculitis in a 37-year-old woman with systemic lupus erythematosus.

A, Axial SE MR image (3000/90) shows infarcts in the right cortical gray matter and subcortical white matter (MCA distribution, *upper arrow*; MCA/PCA watershed distribution, *lower arrow*).

B, Axial SE MR image (3000/90) shows infarcts in the left cortical gray matter and subcortical white matter (PCA distribution, *arrow*).

C, Angiogram of the left internal carotid artery shows areas of stenosis in the ACA, MCA, and PCA distributions (*arrowheads*).

D, Angiogram of the right internal carotid artery shows lesions in the ACA (pericallosal) (*arrowheads*) and severe narrowing of the distal MCA (*arrow*). Note abnormal bilateral ACAs without corresponding MR abnormality. The MR image was obtained 7 days before the angiogram.

and symptoms. In practice, however, CNS vasculitis is a rare condition. In our experience as well as that of other investigators (14), fewer than 10% of patients undergoing angiography to rule out CNS vasculitis were given that diagnosis. Enhanced understanding of the role of noninvasive testing in CNS vasculitis may facilitate these patients' evaluations. In approaching patients with possible CNS vasculitis, clinicians frequently ask neuroradiologists three questions. First, does an MR image with normal findings exclude the diagnosis of CNS vasculitis? Second, are there typical MR findings in CNS vasculitis that increase the posttest probability of CNS vasculitis and help exclude other diagnoses? Third, is the additional risk and expense of angiography justified by the information the procedure provides?

Regarding the meaning of an MR image with normal findings, our study suggests that the sensitivity of MR imaging is quite high. Indeed, among our 18 patients with CNS vasculitis, all had MR studies with abnormalities. Our findings are con-

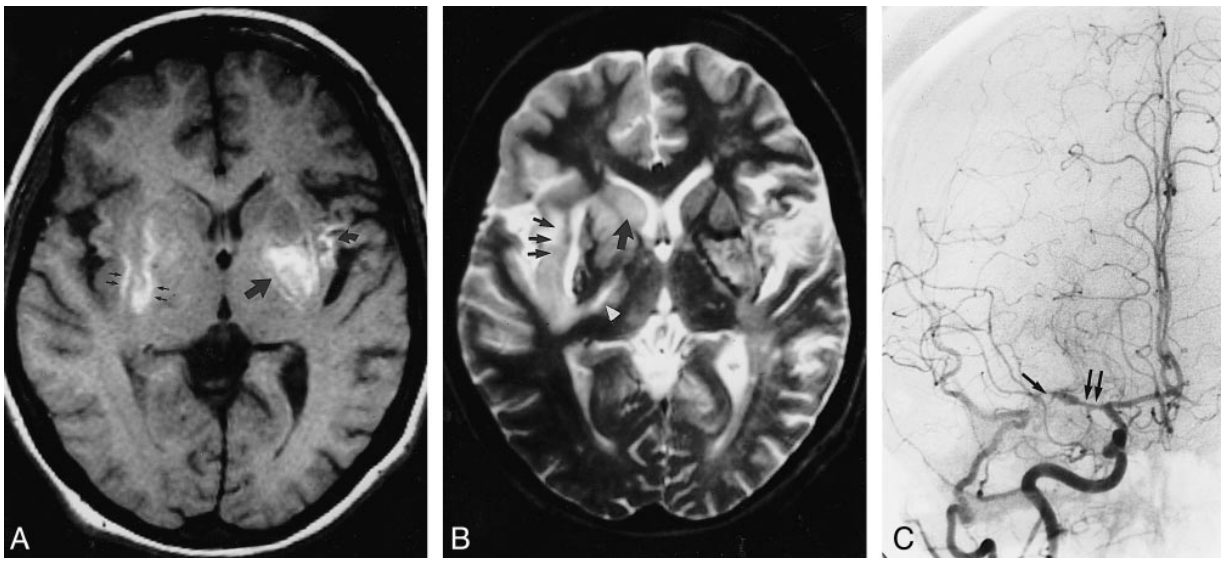

FIG 3. Patient 3: Hemorrhage in CNS vasculitis.

A, Axial SE MR image (550/25) shows T1 bright signal, consistent with hemorrhage in the left putamen (*large straight arrow*), left insular cortex (*curved arrow*), and in the region of the right external capsule (*small arrows*).

B, The corresponding T2-weighted SE image (3000/90) depicts bright signal in the basal ganglia bilaterally and particularly in the right caudate head (*large arrow*), external capsule (*small arrows*), and posterior limb, internal capsule (*arrowhead*). Abnormalities are also present in the thalami, right frontal cortex, and left periatrial white matter. The T2 bright regions are attributable to ischemia or infarction.

C, Angiogram of the right common carotid artery reveals attenuated flow in distal segments of the MCA caused by stenoses in the M1 segment (*double arrow*) and near the MCA trifurcation (*single arrow*).

sistent with the results of previous MR studies. In a review of four patients with CNS vasculitis, Vollmer et al (14) noted that MR imaging revealed substantially more lesions than CT, implying greater sensitivity. Greenan et al (15) and Harris et al (16), reporting on seven and 11 patients, respectively, with CNS vasculitis and positive angiographic findings, noted that their 18 combined patients all had abnormal MR studies. Duna and Calabrese (17) also reported a 100% sensitivity for MR imaging among seven patients with clinical diagnoses of CNS vasculitis. In contrast, Alhalabi and Moore (4), using conventional SE sequences, reported that four (24%) of 17 patients with biopsy-proved CNS vasculitis had normal MR studies. In aggregate, our results and those of others suggest that MR studies reveal abnormalities in the vast majority of patients with CNS vasculitis, and, in this sense, the sensitivity of MR imaging is quite high. However, MR imaging may not reveal all abnormal brain regions in such patients (see below).

Regarding a typical MR appearance for CNS vasculitis, the findings of our study indicate the substantial variability that may occur in CNS vasculitis. The average patient with CNS vasculitis in our study had four lesions, with a mean volume of 11.3 cm^3 per lesion; however, the range in the number of lesions per patient was wide, as was the range of infarction volumes (Figs 1 and 2). Despite this variability, the MCA distribution was affected more often than the ACA, PCA, or vertebral artery territories. Furthermore, despite the extensive collateral circulation of the subcortical white matter (18), cerebral infarctions occurred most frequently in this region. In our study, MR lesions were more evenly distributed between the gray and white matter than suggested by a previous study, which indicated a white matter predominance of lesions (4).

Although most of the lesions revealed by MR imaging were infarctions, hemorrhagic lesions also occurred. Two patients had intraparenchymal hemorrhages (patient 3, Fig 3; and patient 12) and one had SAH (patient 5, Fig 5). Thus, SAH seems to be an unusual finding in CNS vasculitis. Indeed, SAH as the sole manifestation of CNS vasculitis has been reported only once (19). In patient 6 (Fig 6), an angiogram revealed a trifurcation aneurysm of the MCA; both CT and lumbar puncture excluded SAH.

To summarize the typical appearance of CNS vasculitis on MR images, multiple subcortical infarctions are consistent with CNS vasculitis, although substantial variation in the number, size, and location of the lesions may occur in this condition. Thus, similar MR findings may occur in patients suffering from multiple sclerosis, low-grade gliomas, mitochondrial disorders, substance abuse, and other conditions (11, 14, 17, 20).

Our results indicate that in patients with CNS vasculitis, the correlation between MR imaging and angiography for individual lesions is only modest. Although each technique identified nearly the same number of lesions (66 for MR imaging and 68 for angiography; see Table 4), the correlation of specific lesions was imperfect. In our study, the majority of the MR lesions (65%) had angiographic

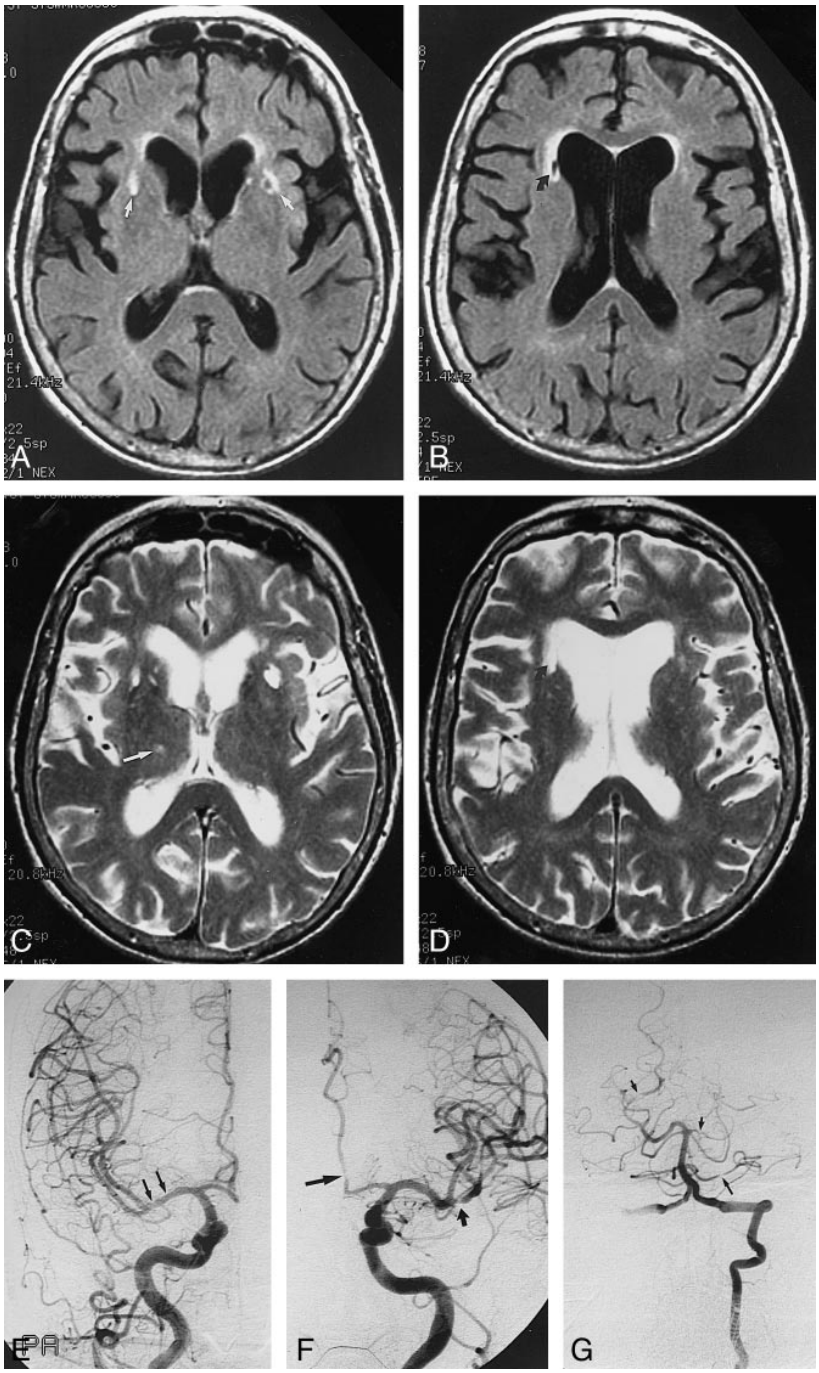

FIG 4. Patient 4: 71 year-old woman with primary angiitis of the CNS.

A and *B*, Axial FLAIR MR images (11,004/114/2200) show foci of increased signal intensity at the anterior portions of the external capsules bilaterally (*A*, *arrows*) and decreased signal adjacent to the anterior right ventricle (*B*, *curved arrow*).

C and *D*, Corresponding T2-weighted SE images (3000/91) show the lesion in the anterior right ventricle (*D, curved arrow*) and an additional lesion in the right thalamus (*C*, *arrow*).

E–G, Angiograms depict lesions in right M1 (*E, arrows*), left A2 and M2 (*F, long arrow* and *short arrow*, respectively), in both PCAs (*G, short arrows*), and in left anterior inferior cerebellar artery (*G, long arrow*).

counterparts, but some prominent MR lesions were not evident on angiograms. For example, in patient 15, the large MR infarction in the right MCA had no correlate on angiograms (Table 2). In addition, although patient 2 (Fig 2) had extensive lesions both on the MR image and the angiogram, a large right posterior cerebral infarction evident on the MR image had no corresponding lesion on the angiogram. The correlation of angiographic lesions with MR findings was worse; only a minority of angiographic lesions (44%) had correlating MR lesions (Table 4).

To our knowledge, only one other study has attempted to correlate in detail the results of MR imaging and angiography in CNS vasculitis (15). That study and ours are in agreement that only a minority (36% and 44%, respectively) of angiographic lesions correlate with MR imaging findings. Both studies also agree that the correlation of MR lesions with angiographic lesions is higher. One other

TABLE 3: Lesions detected by angiography

Patient	Diagnosis	Vessel Injected	ICA		ACA		MCA		PCA		VA		No. of Arteries Involved
			R	L	R	L	R	L	R	L	R	L	
1	PACNS	R ICA L CCA, L VA	−	−	A3	A1	M2	M1	P1, P3	Occl	SCA	PICA	8
2	SLE	R CCA, L CCA, L VA	−	−	+	−	+	+	−	+	−	−	4
3	PACNS	AA, R ICA, L ICA, L VA, R VA	−	Occl	−	−	M1, M2	−	−	−	+	−	3
4	PACNS	R CCA, L CCA, L VA	−	−	−	A2	M1	M2	+	+	−	AICA	6
5	PACNS	R CCA, L CCA, L VA	−	−	+	+	+	+	−	−	−	−	4
6	PACNA	R ICA, L CCA, L VA	−	−	+	−	−	M1, M2	−	+	−	−	3
7	PACNS	R CCA, L CCA, L VA	−	−	−	A2, A3	M3	M2	−	−	−	−	3
8	PACNS	R ICA, L ICA, L VA	−	−	A3	A3	M3	M3	+	+	−	−	6
9	PACNS	R CCA, R VA	−	NE	−	NE	M2	NE	−	−	−	−	1
10	PACNS	R CCA, L CCA, L VA	+	−	+	+	−	M3	+	+	−	PICA	8
11	PACNS	R CCA, L CCA, L VA	+	+	A1	−	M1	M1	P1, P2	P1, P2	−	−	7
12	PACNS	R CCA, L CCA, L VA	−	−	A3	−	−	−	−	P2	−	−	2
13	PACNS	R CCA, L CCA L VA	−	−	+	+	+	+	Occl	Occl	−	−	6
14	PACNS	R CCA, L CCA	+	+	A1	A3	−	M1	−	−	NE	NE	5
15	PACNS	R CCA, L ICA, L VA	−	−	A1	A1	M1	M1	−	−	−	−	4
16	SLE	R ICA, L ICA, L VA	−	−	−	+	−	−	−	−	−	−	1
17	PAN	AA, R ICA, L ICA, L VA	−	−	−	−	−	M2	−	−	−	−	1
18	GCA	AA, R CCA, L CCA	+	+	−	−	−	−	−	−	−	−	2

Note.—L indicates left; R, right; AA, aortic arch; CCA, common carotid artery; ICA, internal carotid artery; VA, vertebral artery; ACA, anterior cerebral artery; MCA, middle cerebral artery; PCA, posterior cerebral artery; SCA, superior cerebellar artery; PICA, posterior inferior cerebellar artery; AICA, anterior inferior cerebellar artery; PACNS, primary angiitis of the CNS; SLE, systemic lupus erythematosus; PAN, polyarteritis nodosa; GCA, giant cell arteritis; Occl, occluded; NE, not evaluated. Where possible, segments were assigned to appropriate segments of the corresponding vascular distribution. "+" indicates an artery affected with multiple lesions (*eg,* beading); "−" indicates an unaffected artery.

TABLE 4: MR imaging versus angiography: correlation of lesions

MR imaging		
Total MR lesions: 66	No. of MR lesions evident on angiogram: 43	Percentage of MR lesions evident on angiogram: 65%
Angiography		
Total abnormal vessels: 68	No. of angiogram lesions evident on MR: 30	Percentage of angiogram lesions evident on MR: 44%

study, which did not attempt a detailed correlation of the two imaging techniques, simply concluded that brain abnormalities identified at MR imaging were less extensive than those delineated angiographically (4).

The discrepancies between MR imaging and angiography may have several explanations. First, the differences may be attributed to the different times at which the studies were performed. This seems unlikely, since the great majority of studies were performed in close succession. Second, a patient with vascular narrowing but no tissue infarction might have an angiogram with positive results but an MR image with negative results (conversely, small-vessel abnormalities not apparent on an angiogram might lead to infarction detectable by MR imaging). Finally, subtle MR abnormalities may escape detection unless special sequences or orientations are obtained (Fig 5).

Our results emphasize that angiography often provides additional information about the extent of disease beyond that detected by MR imaging. For

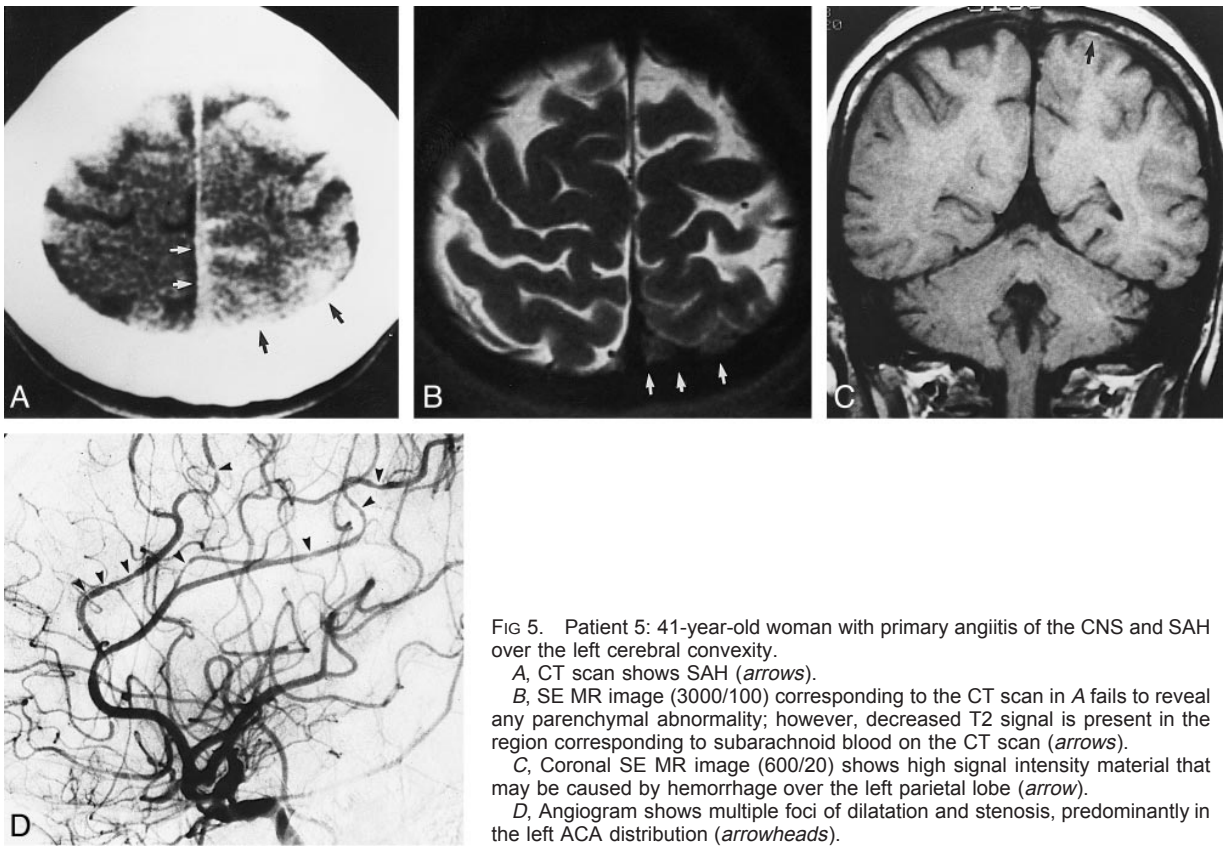

FIG 5. Patient 5: 41-year-old woman with primary angiitis of the CNS and SAH over the left cerebral convexity.

A, CT scan shows SAH (*arrows*).

B, SE MR image (3000/100) corresponding to the CT scan in *A* fails to reveal any parenchymal abnormality; however, decreased T2 signal is present in the region corresponding to subarachnoid blood on the CT scan (*arrows*).

C, Coronal SE MR image (600/20) shows high signal intensity material that may be caused by hemorrhage over the left parietal lobe (*arrow*).

D, Angiogram shows multiple foci of dilatation and stenosis, predominantly in the left ACA distribution (*arrowheads*).

example, the angiographic findings may offer an explanation for a patient's signs and symptoms that cannot be attributed to the abnormalities seen on MR images. Moreover, findings of serial studies of patients with CNS vasculitis have shown that response to treatment is more likely to be evident on angiograms than on MR images (4).

Our study has several limitations. First, CNS vasculitis is a difficult entity to define, because the diagnosis can rarely be established by a single test (2, 8, 9, 11). All imaging techniques, including MR imaging and angiography, have imperfect specificity; even brain biopsies yield high false-negative rates (4, 11, 15). In the absence of pathologic confirmation, the diagnosis of CNS vasculitis needs to be based on careful evaluation of clinical signs and symptoms, correlation with radiologic findings, and exclusion of other causes (8, 16, 21). Because this approach is not infallible, some of our patients may have been misdiagnosed. Our thorough clinical and radiologic review of these patients reduces that possibility but can never eliminate it entirely.

Because many of our patients were studied between 1986 and 1990, only six had MR angiographic studies. Despite the value of MR angiography in patients with medium- and large-vessel disease (22), the resolution of MR angiography remains insufficient for the fine vascular abnormalities that frequently accompany CNS vasculitis (22–24).

Use of a FLAIR sequence in conjunction with our routine SE sequences would probably have increased the sensitivity of MR imaging (25, 26). FLAIR imaging is particularly sensitive for periventricular and superficial cortical infarctions (27); however, FLAIR may be inferior to conventional long-TR imaging in detecting posterior fossa lesions (28, 29). Furthermore, criteria for normal FLAIR images are still being formulated (30). Because the technique has been available only routinely at our institution since 1995, only one patient underwent FLAIR imaging. In that patient (patient 4, Fig 4), the deep gray matter lesions were equally evident on the T2-weighted and FLAIR sequences, and one right-sided thalamic lesion would have been missed had FLAIR imaging been used alone. Although FLAIR imaging should be performed in all patients with possible CNS vasculitis, it should be used in conjunction with, rather than in lieu of, conventional SE sequences.

Finally, failure to use contrast medium in all the MR studies was another potential limitation. Administration of contrast material increases the detection of small infarctions on MR images (31) and may also be useful in estimating the age of a lesion. However, because of the retrospective nature of the study design, this limitation could not be remedied.

Other imaging techniques with the potential to enhance lesion detection and define brain regions

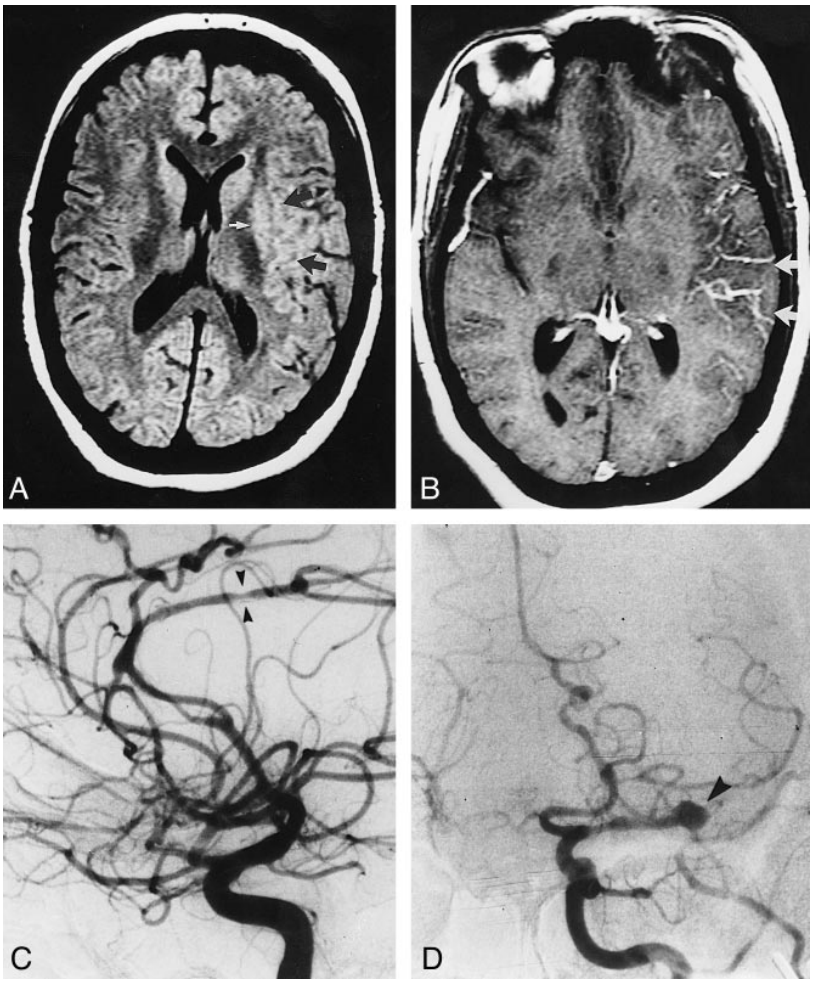

FIG 6. Patient 6: 24-year-old woman with primary angiitis of the CNS.

A, Axial SE MR image (1500/30) shows high signal intensity in the left parietal cortex, subcortical white matter (*black arrows*), and in the left putamen (*white arrow*).

B, Contrast-enhanced axial SE MR image (550/25) shows vascular and mild parenchymal enhancement (*arrows*). The vascular stasis is indicative of acute cerebral ischemia.

C, Right internal carotid artery angiogram shows narrowing in the right pericallosal artery (*arrowheads*). Superimposition of vessels immediately distal to that lesion gives the appearance of an aneurysm.

D, Left common carotid artery angiogram reveals attenuated MCA branches distal to a trifurcation aneurysm (*arrowhead*).

at risk in CNS vasculitis include perfusion- and diffusion-weighted imaging, MR spectroscopy, and positron emission tomography. These techniques may become increasingly important as more effective therapies for CNS vasculitis become available. Perfusion- and diffusion-weighted imaging may be superior to FLAIR imaging in the detection and characterization of early lesions (32).

Conclusion

MR imaging is very sensitive for CNS vasculitis and typically shows supratentorial infarctions in the cortical and subcortical regions; however, the MR appearance is not specific for CNS vasculitis. Furthermore, the correlation between MR imaging and angiography on specific lesions is only moderate. Our results suggest that these two imaging techniques provide different information about the extent of CNS vasculitis. For a complete assessment of the vascular damage resulting from CNS vasculitis, both imaging techniques should be used.

Acknowledgments

We thank Edward Herskovits for serving as arbitrator for the MR and angiographic studies and Tammy Noethen for word processing the manuscript.

References

1. Ferris EJ, Levine HL. **Cerebral arteritis: classification.** *Radiology* 1973;109:327–341
2. Calabrese LH, Fulan AJ, Gragg LA, Trumane J. **Primary angiitis of the central nervous system: diagnostic criteria and clinical approach.** *Cleve Clin J Med* 1992;59:293–306
3. Cupps TR, Moore PM, Fauci AS. **Isolated angiitis of the central nervous system: prospective diagnostic and therapeutic experience.** *Am J Med* 1983;74:97–105
4. Alhalabi M, Moore PM. **Serial angiography in isolated angiitis of the central nervous system.** *Neurology* 1994;44:1221–1226
5. Mitsias P, Levine SR. **Large cerebral vessel occlusive disease in systemic lupus erythematosus.** *Neurology* 1994;44:385–393
6. Kissel JT. **Neurologic manifestations of vasculitis.** *Neurol Clin* 1989;7:655–673
7. Wynne PJ, Younger DS, Khandji A, Silver AJ. **Radiographic features of central nervous system vasculitis.** *Neurol Clin* 1997;15:779–804
8. Moore PM. **Vasculitis of the central nervous system.** *Semin Neurol* 1994;14:307–312
9. Calabrese LH, Mallek JA. **Primary angiitis of the central nervous system: report of 8 new cases, review of the literature, and proposal for diagnostic criteria.** *Medicine* 1987;67:20–39

10. Stone JH, Pomper MG, Roubenoff R, Miller TJ, Hellmann DB. **Sensitivities of noninvasive tests for central nervous system vasculitis: a comparison of lumbar puncture, computed tomography and magnetic resonance imaging.** *J Rheumatol* 1994; 21:1277–1282
11. Duna GF, Calabrese LH. **Limitations of invasive modalities in the diagnosis of primary angiitis of the central nervous system.** *J Rheumatol* 1995;22:662–667
12. Hellmann DB, Roubenoff R, Healy R, Wang H. **Central nervous system angiography: safety and predictors of a positive result in 125 consecutive patients evaluated for possible vasculitis.** *J Rheumatol* 1992;19:568–572
13. Kretschmann HG, Weinrich W. **Cranial Neuroimaging and Clinical Neuroanatomy.** New York: Thieme; 1992
14. Vollmer TL, Guamaccia J, Harrington W, Pacia SV, Petroff OAC. **Idiopathic granulomatous angiitis of the central nervous system: diagnostic challenges.** *Arch Neurol* 1993;50:925–930
15. Greenan TJ, Grossman RI, Goldberg HI. **Cerebral vasculitis: MR imaging and angiographic correlation.** *Radiology* 1992;182:65–72
16. Harris KG, Tran DD, Sickels WJ, Cornell SH, Yuh WTC. **Diagnosing intracranial vasculitis: the roles of MR and angiography.** *AJNR Am J Neuroradiol* 1994;15:317–330
17. Duna GF, Calabrese LH. **Limitations of invasive modalities in the diagnosis of primary angiitis of the central nervous system.** *J Rheumatol* 1995;22:662–667
18. Osborn AG. **Diagnostic Neuroradiology.** St Louis: Mosby; 1994; 330–398
19. Biller J, Loftus CM, Moore SA, et al. **Isolated central nervous system angiitis first presenting as spontaneous intracranial hemorrhage.** *Neurosurgery* 1987;20:310–315
20. Calabrese LH. **Vasculitis of the central nervous system.** *Rheum Dis Clin North Am* 1995;21:1059–1076
21. Miller DH, Ormerod IEC, Gibson A, de Boulay EDGH, Rudge P, McDonald WI. **MR brain scanning in patients with vasculitis: differentiation from multiple sclerosis.** *Neuroradiology* 1987;29: 226–231
22. Dagirmanjian A, Ross JS, Obuchowski N, et al. **High resolution, magnetization transfer saturation, variable flip angle, time-of-flight MRA in the detection of intracranial vascular stenoses.** *J Comput Assist Tomogr* 1995;19:700–706
23. Stellar RJ. **Imaging blood vessels of the head and neck.** *J Neurol Neurosurg Psychiatry* 1995;59:225–237
24. Stock KW, Radue EW, Jacob AL, Bao XS, Steinbrich W. **Intracranial arteries: prospective blinded comparative study of MR angiography and DSA in 50 patients.** *Radiology* 1995;195:451–456
25. Kates R, Atkinson D, Brant-Zawadski M. **Fluid-attenuated inversion recovery (FLAIR): clinical prospectus of current and future applications.** *Top Magn Reson Imaging* 1996;8:389–396
26. Tourbah A, Deschamps R, Stievenart JL, et al. **Magnetic resonance imaging using FLAIR pulse sequence in white matter diseases.** *J Neuroradiol* 1996;23:217–222
27. Thurnher MM, Thurnher SA, Fleischmann D, et al. **Comparison of T2-weighted and fluid-attenuated inversion-recovery fast spin-echo MR sequences in intracerebral AIDS-associated disease.** *AJNR Am J Neuroradiol* 1997;18:1601–1609
28. Gawne-Cain ML, O'Riordan JI, Coles A, Newell B, Thompson AJ, Miller DH. **MRI lesion volume measurement in multiple sclerosis and its correlation with disability: a comparison of fast fluid attenuated inversion recovery (fFLAIR) and spin echo sequences.** *J Neurol Neurosurg Psychiatry* 1998;64:197–203
29. Gawne-Cain ML, O'Riordan JI, Thompson AJ, Moseley IF, Miller DH. **Multiple sclerosis lesion detection in the brain: a comparison of fast fluid-attenuated inversion recovery and conventional T2-weighted dual spin echo.** *Neurology* 1997;49:364–370
30. Gawne-Cain ML, Silver NC, Moseley IF, Miller DH. **Fast FLAIR of the brain: the range of appearances in normal subjects and its application to quantification of white-matter disease.** *Neuroradiology* 1997;39:243–249
31. Miyashita K, Naritomi H, Sawada T, et al. **Identification of recent lacunar lesions in cases of multiple small infarctions by magnetic resonance imaging.** *Stroke* 1988;19:834–839
32. Flacke S, Keller E, Hartmann A, et al. **Improved diagnosis of early cerebral infarct by the combined use of diffusion and perfusion imaging.** *Rofo Fortschr Geb Rontgenstr Neuen Bildgeb Verfahr* 1998;168:493–501

Differentiation Between Postoperative Scar and Recurrent Disk Herniation: Prospective Comparison of MR, CT, and Contrast-Enhanced CT

Spiros Sotiropoulos[1]
Neil I. Chafetz[1]
Philipp Lang[1,2,3]
Mark Winkler[1]
James M. Morris[2]
Philip R. Weinstein[4]
Harry K. Genant[1,2,5]

Twenty-five symptomatic postlumbar surgery patients had findings on lumbar spinal noncontrast CT that were equivocal for distinguishing recurrent disk herniation from postoperative epidural fibrosis (scar). Contrast-enhanced CT and lumbar MR imaging were performed to differentiate these two conditions.

Of the 14 levels, surgically explored, the diagnosis of scar or recurrent disk herniation was correct with contrast-enhanced CT at 10 levels and with MR imaging at 11 levels. At the levels operated on less than 2 years prior to MR imaging, scar more frequently demonstrated intermediate than low signal intensity. Scar older than 2 years most often showed low signal intensity.

These preliminary findings suggest that MR may be useful in differentiating postoperative fibrosis from recurrent disk herniation in a significant proportion of patients whose unenhanced CT scans are equivocal.

The diagnostic evaluation of patients presenting with failed back surgery syndrome is a challenge to both radiologists and surgeons. Although the cause of this syndrome is complex and often multifactorial, recurrent disk herniation and postoperative epidural fibrosis (scar) at the previously explored level(s) are frequent sources of symptoms [1]. While recurrent disk herniations are surgically manageable, many surgeons are reluctant to repeat surgery with reliable evidence of only postoperative fibrosis. Even though excessive intraspinal perineural scar formation with or without associated arachnoiditis can be responsible for failed back surgery syndrome, it is unlikely that a new operation will help this group of patients, since additional scarring will often result [2, 3].

Myelography and CT have not proved very reliable in differentiating between recurrent disk herniation and postoperative fibrosis [4–7]. However, it has been shown that lumbar spinal CT after administration of IV contrast medium can improve the CT differentiation between recurrent disk herniation and scar [8, 9]. Moreover, MR imaging has been demonstrated to compare favorably with myelography and CT in the evaluation of low back pain [10–16]. In fact, MR imaging, with its superior soft-tissue characterization and multiplanar imaging capability, may provide a more reliable means of distinguishing between the two tissues in question [17].

The aim of this prospective study was to assess the relative value of contrast-enhanced CT and MR imaging in distinguishing between recurrent disk herniation and scar. For this purpose, we compared the results of each imaging method with the clinical findings from 12 patients, who underwent repeat surgery.

Subjects and Methods

The recent unenhanced lumbar CT scans of 78 consecutive postoperative back patients were reviewed by two radiologists experienced in interpretating spinal CT exams. Thirty-three levels in 25 of these patients were selected for study. The following selection criteria were used: (1) previous lumbar surgery with recurrence of symptoms; (2) an assurance from the surgeon that reexploration at the level in question was a serious consideration; (3) an

Received December 31, 1986; accepted after revision November 25, 1988.

[1] Department of Radiology, Skeletal Section, C-309, Box 0628, University of California, San Francisco, CA 94143. Address reprint requests to H. K. Genant.

[2] Department of Orthopaedic Surgery, University of California, San Francisco, CA 94143.

[3] Radiologishe Klinic, Universitatsklinikum Rudolf Virchow, Standort Charlottenburg, Freie Universitat Berlin, Berlin, FRG.

[4] Department of Neurosurgery, University of California, San Francisco, CA 94143.

[5] Department of Medicine, University of California, San Francisco, CA 94143.

AJNR **10:639–643, May/June 1989**
0195–6108/89/1003–0639
© American Society of Neuroradiology

initial CT at the previously explored level(s) judged indeterminate in differentiating between recurrent disk herniation and scar; (4) absence of bony spinal canal stenosis; and (5) absence of medical contraindications to IV contrast agents.

The 25 patients fulfilling these criteria (33 levels) were studied by contrast-enhanced CT and MR imaging. Contiguous, 3-mm-thick axial CT scans were generated on a GE 9800 CT scanner. CT was performed only at the previously explored levels both before and after IV administration of contrast medium. Contrast-enhanced CT was obtained after a bolus injection of 100 ml of Conray-60 and during drip infusion of 150 ml of Conray-30.

The MR examinations were performed on three different imagers: two 0.35-T Diasonics MT/S superconductive scanners (20 patients) and one 1.5-T GE superconductive scanner (five patients).

On the mid-field system, sagittal images were obtained by using a spin-echo technique with a TR of 1000 or 1500 and TEs of 30 and 60 for 1-cm contiguous slices, and TEs of 40 and 80 for 5-mm contiguous slices. Axial images with a slice thickness of 5 mm were obtained with a TR of either 1500 or 2000 and TEs of 40 and 80. The image matrix consisted of 256 × 256 elements; the field of view was 24 cm for axial and coronal scanning.

On the high-field system, axial and sagittal images were obtained with a 25-cm prototype surface coil and a spin-echo technique with TRs ranging from 1000 to 2000 and TEs of 25 and 50, 25 and 70, or 40 and 80. Axial and sagittal images were 5-mm thick with an interslice gap of 1 mm. The image matrix consisted of 256 × 256 elements, the field of view was 20 cm for axial scanning and 24 cm for sagittal scanning.

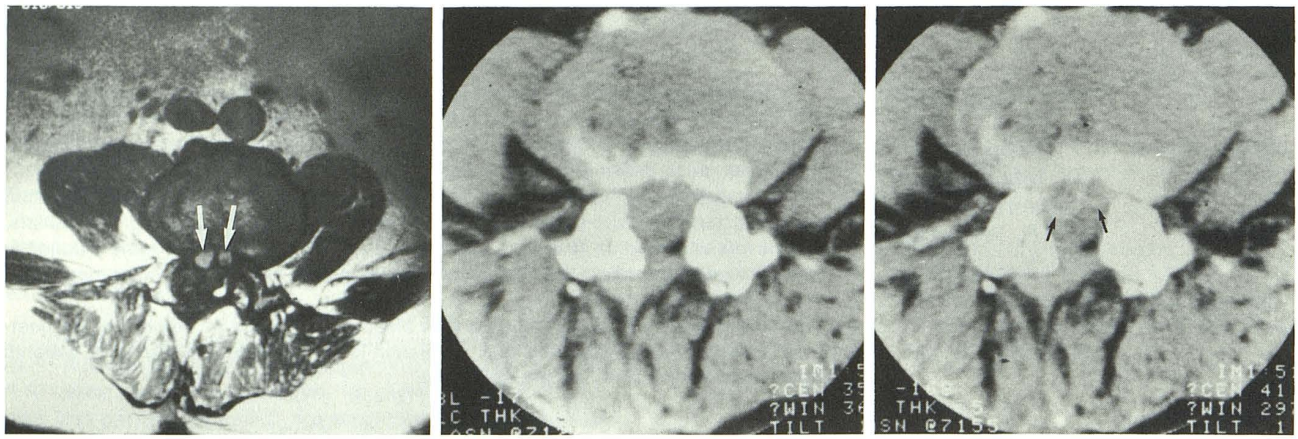

Fig. 1.—*A*, Axial MR image (1000/25) at 1.5 T shows bilobed disk herniation anterior to thecal sac (*arrows*).
***B*, Axial CT scan shows soft-tissue density replacing epidural fat on right and anterior aspects of thecal sac—findings are equivocal for scar vs recurrent disk herniation.**
***C*, Axial CT scan obtained after IV contrast administration shows enhancement of border between anterior tissue abnormality and thecal sac in a pattern that is typical of disk herniation (*arrows*).**

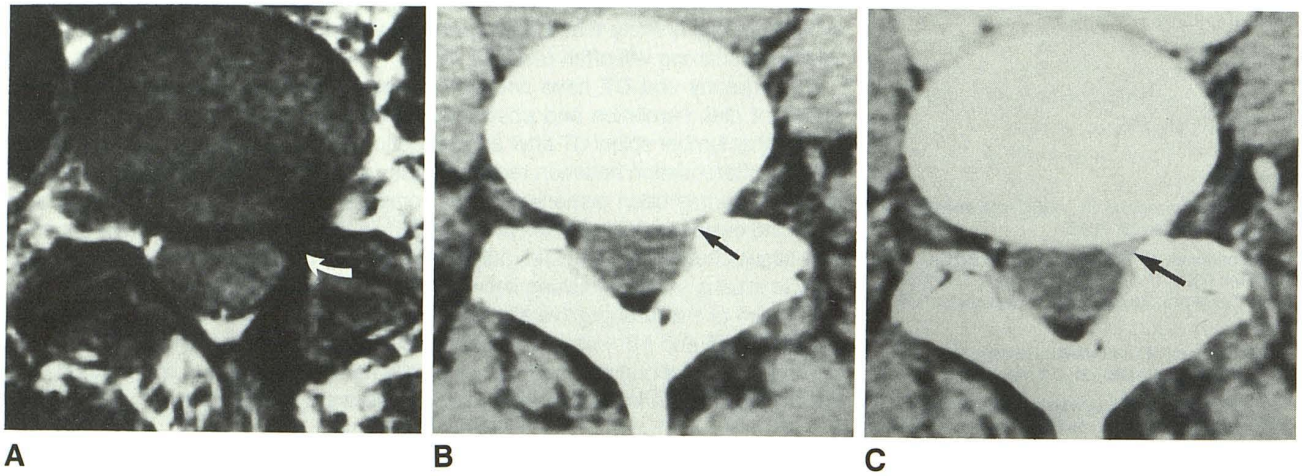

Fig. 2.—*A*, Axial MR image (1500/40) at 0.35 T shows low signal intensity region in left anterolateral epidural space (*arrow*). No clear distinction between scar or recurrent disk herniation is possible.
***B*, Axial CT scan shows soft-tissue density (*arrow*) in left lateral aspect of epidural space in this patient 7 years after lumbar surgery.**
***C*, Axial CT scan obtained after IV contrast administration shows opacification of soft-tissue density in question (*arrow*), indicating that it is postoperative fibrosis rather than recurrent disk herniation fragment.**

The imaging studies were evaluated blindly by three radiologists. Twelve patients (14 levels) subsequently underwent surgery on the basis of the clinical findings and imaging studies. The findings from imaging studies and surgical reexploration were compared at each level. The signal intensity of scar was correlated with the time interval between the last operation and MR imaging in the initial 25 patients studied by both contrast-enhanced CT and MR imaging.

Results

Comparison of Imaging Studies and Operative Findings in 12 Patients

In the 12 patients (14 levels) who underwent subsequent surgery, recurrent disk herniations were found intraoperatively at eight levels and scar at five levels. One patient (one level) had neither recurrent disk herniation nor scar; exploration was negative. At the explored levels, there were 10 correct diagnoses on contrast-enhanced CT and 11 on MR imaging. There were four incorrect diagnoses on contrast-enhanced CT and three on MR imaging.

Of the eight surgically proved cases of recurrent disk herniation, seven were correctly identified by contrast-enhanced CT and all eight by MR (Fig. 1). In one case of proved recurrent disk herniation, diagnosis by contrast-enhanced CT was that of scar.

Of the five surgically proved scar cases, three were correctly identified by contrast-enhanced CT and two by MR imaging; in one case of proved scar, the diagnosis by contrast-enhanced CT was recurrent disk herniation, while in another the result was indeterminate. Conversely, in one case of proved scar, the diagnosis by MR imaging was recurrent disk herniation, while in two others the results were indeterminate (Fig. 2). At one level, where exploration was negative, contrast-enhanced CT was indeterminate, while MR at the same level provided the correct diagnosis of normal.

Scar was typically identified as a mass, band, or strandlike structure of intermediate to low MR signal intensity that often replaced or was surrounded by epidural fat (Fig. 3A). In a few of the levels studied, ovoid fat collections were demonstrated within scar tissue. Recurrent disk herniation, on the other hand, was frequently smooth and globular in shape.

In 10 of the 12 patients who had repeat surgery the scar assumed a band or strandlike form. In the other two patients, the configuration of the scar was masslike (Fig. 3), with a bulky mass at the laminectomy site compressing the thecal sac as a form of soft-tissue-related spinal canal stenosis (Fig. 4). This finding was clearly depicted preoperatively by MR. Contrast-enhanced CT in one of these two cases also showed the abnormality, but the level of confidence in making this diagnosis was not as high as with MR imaging.

MR Signal Characteristics of Postoperative Scar

In the 33 initially examined levels (25 patients, 12 of whom were reexplored), the MR signal intensity of scar on the first echo of the long TR sequences was lower than that of thecal sac in 16 levels (Fig. 2A), approximately equal to that of thecal sac in 13 levels, and higher than that of thecal sac in four levels (Fig. 4A).

In all instances, the thecal sac demonstrated a significant increase in signal intensity from first to second echo because of the CSF, making a distinction between scar and thecal sac quite easy; on the second-echo images, scar was isointense with the thecal sac in only four levels, whereas scar demonstrated a lower signal intensity than thecal sac in 27 levels. In two levels, scar remained higher in signal intensity than the thecal sac on second-echo images. Scar signal intensity was lower than adjacent intraspinal or paraspinal fat at all levels.

Of 33 levels examined, 21 had been operated on more than 2 years prior to MR and CT; 12 levels had undergone surgery within 2 years of MR and CT examination. Of the 21 levels, 15 were noted to contain scar of low MR signal intensity (Fig. 2A); five levels had intermediate intensity; and one level had high intensity. Of the 12 levels that had been operated on within 2 years of MR and CT, MR signal intensity of scar was high in two, intermediate in eight (Fig. 3A), and low in two.

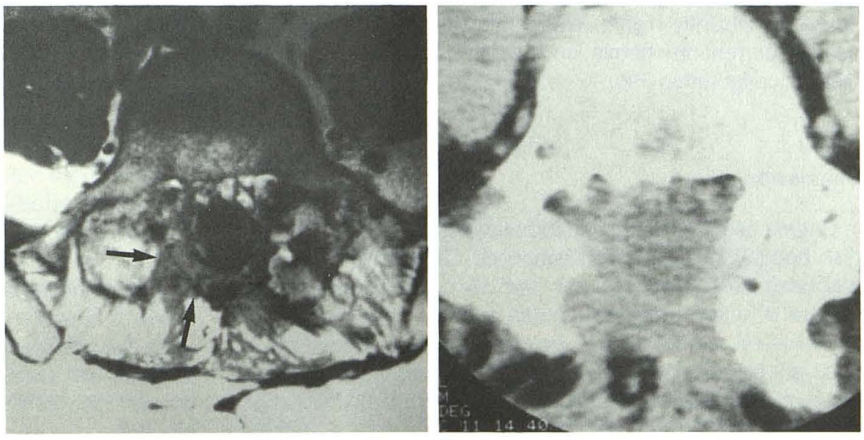

Fig. 3.—*A*, Axial MR image (1000/25) at 1.5 T shows superior soft-tissue delineation afforded by MR. High signal intensity of fat can be separated from intermediate signal intensity of scar (*arrows*), which in turn is distinct from lower signal intensity of thecal sac and nerve roots.

***B*, Axial CT scan at a level close to that of MR image shows soft-tissue density surrounding thecal sac. Note that contrast between neural and scar tissue is less than that demonstrated on MR.**

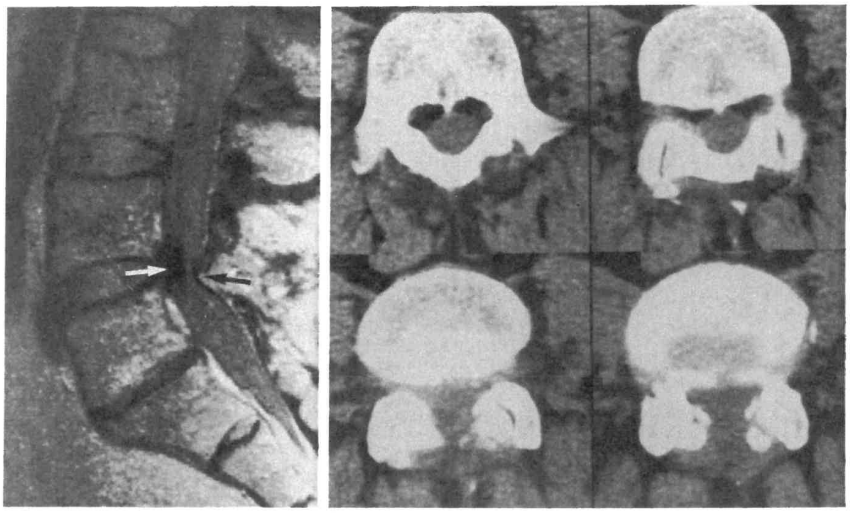

Fig. 4.—*A*, Sagittal MR image (1500/40) at 0.35 T shows compression of thecal sac at L4–L5 level by low signal intensity herniated disk anteriorly (*white arrow*) and by intermediate signal intensity postoperative fibrosis posteriorly (*black arrow*).

***B*, Four axial CT scans at L4–L5 level. Lower two scans demonstrate a laminectomy defect and replacement of normal epidural fat by soft-tissue density of indeterminate origin.**

MR Appearance of Postoperative Intervertebral Disks

In the majority of postoperative levels, the sagittal MR images demonstrated a loss of disk height as well as various degrees of anterior and/or posterior bulging of the disk; in most instances the bulge was broad-based.

Of the 33 disk levels initially examined by both contrast-enhanced CT and MR, the overall MR signal intensity of the operated disk as demonstrated on the sagittal images was considerably lower than that of both the thecal sac and the adjacent disk in 19 levels. In 12 of the 33 levels, the signal intensity of the intervertebral disk was intermediate. In two of the 33 levels, the intervertebral disk demonstrated normal signal intensity.

In many levels, no clear differentiation could be made between the posterior aspect of the intervertebral disk and adjacent scar if criteria based solely on signal intensity differences were employed. In 18 of the 33 levels, scar tissue was only slightly higher in signal intensity than the disk on the first echo, whereas in 14 of 33 levels the two structures were of approximately equal signal intensity. At only one level did a postoperative disk (proved recurrent disk herniation) demonstrate significantly higher signal intensity than the adjacent scar. Recurrent disk herniation, however, was frequently globular in configuration (Fig. 1).

Discussion

Criteria used for differentiating between scar and recurrent disk herniation on contrast-enhanced CT scans have been well described. Recurrent disk herniation is diagnosed when a mass of unenhanced soft tissue is seen in the anterior or anterolateral epidural space. Scar is diagnosed when there is relatively uniform enhancement of the extradural soft tissue in question. Secondary effects of recurrent disk herniation (i.e., mass effects on neural structures) and scar (i.e., retraction of neural structures toward scar) can be of help in distinguishing the structure in question. Scar in the anterior and anterolateral epidural space, however, may be similar in both configuration and density to a recurrent disk herniation. Although both IV and intrathecal contrast agents have been described as helpful in increasing the specificity of CT, the distinction between scar and recurrent disk herniation remains difficult. A prospective study demonstrating that contrast-enhanced CT reduced the number of incorrect diagnoses of 23 conventional CT examinations from 13 to six indicates that IV contrast enhancement is helpful but still inconclusive in approximately 25% of cases [9].

MR imaging is routinely used in the evaluation of patients with low back pain. The appearance of scar after surgery in regions of the body other than the spine as well as after myocardial infarction suggests that such tissue has a low signal intensity on MR. Furthermore, the fibrous tissue of tendons and ligaments demonstrates low signal intensity. The signal intensity of scar, however, is affected by various factors such as scar morphology and fat content, age of scar and vascularity, inflammatory changes, and technical factors.

Low-intensity strands of scar could be visually separated from adjacent fat. However, mass- or bandlike scars more often demonstrated intermediate MR signal intensity. Among the levels that were operated on less than 2 years before MR, scar more frequently demonstrated intermediate than low signal intensity (Fig. 3A), whereas older scar most often showed low signal intensity (Fig. 2A). In those instances in which regions of low signal intensity taking the form of strands or bands were noted to be coursing through fat, little difficulty was encountered in recognizing such structures as fibrotic in nature on MR. CT, however, frequently demonstrated a mixed pattern of a masslike structure, which was irregular and patchy in these patients. In these cases, the location of the tissue in question and its effect on adjacent neural structures were the only bases for the CT diagnosis. In four unoperated patients with such findings, the decision to reexplore (based on contrast-enhanced CT) was abandoned when the MR diagnosis of scar rather than disk became known.

Since there was no histologic examination of the scar tissue removed at the time of surgery, correlation between signal

intensity and degree of vascularity and extent of granulation tissue was not possible. We can only speculate that granulation tissue and vascularity might have been responsible for the higher signal intensity of immature scar. The low MR signal intensity as demonstrated in some postoperative patients may reflect the more tightly knit cohesive structure of fibrous tissue than is present in scar, which has a higher MR signal intensity.

The location and configuration of the strands of low MR signal intensity suggested scar rather than vascular structures at these locations. Intraoperative findings also failed to demonstrate vascular structures at these locations.

The MR signal intensity of the postoperative disk was most frequently lower than that of thecal sac or adjacent disks. Removal of nuclear material, which has high proton density, at the time of previous surgery, and progressive desiccation of the usually already preoperatively degenerated disk probably account for the low disk signal at the postoperative levels.

Several reports have indicated that herniated disk material in the previously unoperated patient may demonstrate quite variable signal intensities on MR [10, 11]. One of the patients studied demonstrated a recurrent disk herniation with high MR signal intensity. Intraoperatively, the reherniated tissue in this patient was found to consist primarily of nuclear material. In general, however, it appears that the postoperative disk has less variable signal intensity characteristics than the nonoperated disk.

MR and contrast-enhanced CT correlated with surgical results in 79% and 71% of the levels, respectively. MR correctly identified all eight surgically proved recurrent disk herniations whereas contrast-enhanced CT did almost as well detecting seven of eight recurrent disk herniations. When scar was the main surgical diagnosis, both methods performed poorly (only two correct MR diagnoses as compared with three by contrast-enhanced CT). Although the images acquired on the mid-field system were diagnostic in most of the patients, it appeared that the high-field system provided a clearer delineation of spinal structures and the tissues in question at the reexplored levels.

In conclusion, we believe that when nonenhanced CT of the postoperative lumbar spine is indeterminate, it is highly likely that contrast-enhanced CT or MR imaging will provide a more confident and definitive diagnosis.

REFERENCES

1. Burton CV, Kirkaldy-Willis WH, Yong-Hing K, Heithoff KB. Causes of failure of surgery on the lumbar spine. *Clin Orthop* **1981**;157:191–199
2. Langenskiold A, Kiviluoto O. Prevention of epidural scar formation after operations on the lumbar spine by means of free fat transplants. *Clin Orthop* **1976**;115:92–95
3. Yong-Hing K, Reilly J, de Korompay V, Kirkaldy-Willis WH. Prevention of nerve root adhesions after laminectomy. *Spine* **1980**;5:59–64
4. Teplick JG, Haskin ME. Computed tomography of the postoperative lumbar spine. *AJR* **1983**;141:865–884.
5. Mall JC, Kaiser JA. Computed tomography of the postoperative spine. In: Genant HK, Chafetz NI, Helms CA, eds. *CT of the lumbar spine*. Radiology Research and Education Foundation, **1982**
6. Mall JC, Kaiser JA, Heithoff KB. Postoperative spine. In: Newton TH, Potts DG, eds. *Computed tomography of the spine and spinal cord: modern neuroradiology*. San Anselmo, CA: Clavdel Press, **1983**:187–204
7. Jacobs RR, McClain O, Neff J. Control of post-laminectomy scar formation: an experimental and clinical study. *Spine* **1980**;5:223–229
8. Braun IF, Hoffman JC Jr, David PC, Landman JA, Tindel GT. Contrast enhancement in CT differentiation between recurrent disk herniation and postoperative scar: prospective study. *AJNR* **1985**;6:607–612, *AJR* **1985**;145:785–790
9. Schubiger O, Valvanis A. CT differentiation between recurrent disc herniation and postoperative scar formation: the value of contrast enhancement. *Neuroradiology* **1982**;22:251–254
10. Chafetz NI, Genant HK, Moon KL, Helms CA, Morris JM. Recognition of lumbar disk herniation with NMR. *AJR* **1983**;141:1153–1156
11. Han JS, Kaufman B, El Yousef SJ, et al. NMR imaging of the spine. *AJR* **1983**;141:1137–1145
12. Berquish TH. Magnetic resonance imaging: preliminary experience in orthopaedic radiology. *Magn Reson Imaging* **1984**;2:41–52
13. Edelman PR, Shoukimas GM, Stark DD, et al. High-resolution surface-coil imaging of lumbar disk disease. *AJR* **1985**;144:1123–1129
14. Modic MT, Feiglin DH, Piraino DW, et al. Vertebral osteomyelitis: assessment using MR. *Radiology* **1985**;157:157–166
15. Modic MT, Pavlicek W, Weinstein MA, et al. Magnetic resonance imaging of intervertebral disk disease: clinical and pulse sequence considerations. *Radiology* **1984**;152:103–111
16. Smith FW, Runge V, Permezel M, Smith CC. Nuclear magnetic resonance (NMR) imaging in the diagnosis of spinal osteomyelitis. *Magn Reson Imaging* **1984**;2:53–56
17. Sotiropoulos S, Chafetz NI, Genant HK, Winkler M. Assessment of the postoperative lumbar spine: distinction between postoperative fibrosis and recurrent disk herniation. IV contrast enhanced CT vs MRI (abstr). Presented at the Association of University Radiologists, Hartford, CT, May **1986**

Percutaneous Polymethylmethacrylate Vertebroplasty in the Treatment of Osteoporotic Vertebral Body Compression Fractures: Technical Aspects

Mary E. Jensen, Avery J. Evans, John M. Mathis, David F. Kallmes, Harry J. Cloft, and Jacques E. Dion

PURPOSE: To describe a technique for percutaneous vertebroplasty of osteoporotic vertebral body compression fractures and to report early results of its use. **METHODS:** The technique was used over a 3-year period in 29 patients with 47 painful vertebral fractures. The technique involves percutaneous puncture of the involved vertebra(e) via a transpedicular approach followed by injection of polymethylmethacrylate (PMMA) into the vertebral body. **RESULTS:** The procedure was technically successful in all patients, with an average injection amount of 7.1 mL PMMA per vertebral body. Two patients sustained single, nondisplaced rib fractures during the procedure; otherwise, no clinically significant complications were noted. Twenty-six patients (90%) reported significant pain relief immediately after treatment. **CONCLUSION:** Vertebroplasty is a valuable tool in the treatment of painful osteoporotic vertebral fractures, providing acute pain relief and early mobilization in appropriate patients.

Index terms: Interventional materials; Spine, fractures

AJNR Am J Neuroradiol 18:1897–1904, November 1997

With the aging of the American population, increasing numbers of elderly persons are sustaining vertebral compression fractures due to osteopenia. Other individuals, such as transplant recipients, suffer fractures as a result of chronic steroid use. These vertebral fractures frequently cause persistent, often excruciating pain, which significantly impairs mobility and quality of life. External bracing, analgesics, and observation may be all that is necessary for pain control in some patients, but in others, a constant requirement for narcotics can be as life-altering as the fracture itself.

Neoplastic vertebral compression fractures (1–3), giant cell tumors of the long bones (4, 5), and vertebral hemangiomas (6) have been treated in the past by surgical decompression and instillation of polymethylmethacrylate (PMMA) cement. Recently, percutaneous puncture of vertebral compression fractures, by the transpedicular or paravertebral approach under computed tomography (CT) and/or fluoroscopic guidance, has been described (7–10) (H. Deramond, R. Galibert, C. Debussche-Depriester, "Percutaneous Vertebroplasty with Methylmethacrylate: Technique, Method, Results" [abstract], *Radiology* 1990;117[suppl]:352).

Over the past 3 years, we have treated 29 patients with 47 age-related or steroid-induced osteoporotic compression fractures of the lumbar or thoracic vertebrae via percutaneous puncture and injection of PMMA. We describe the process for patient selection, the therapeutic technique, complications, pitfalls, technical results, and immediate clinical results. Long-term clinical outcomes will be described in a separate publication.

Materials and Methods

Twenty-nine patients (19 women and 10 men) with 47 compression fractures (17 thoracic, 30 lumbar) who were suffering from disabling back pain refractory to analgesic therapy were treated. Referral sources included orthope-

Received February 10, 1997; accepted after revision May 2.

From the Interventional Neuroradiology Section, Department of Radiology, University of Virginia Health Sciences Center, Charlottesville, VA 22908. Address reprint requests to Mary E. Jensen, MD.

AJNR 18:1897–1904, Nov 1997 0195-6108/97/1810–1897
© American Society of Neuroradiology

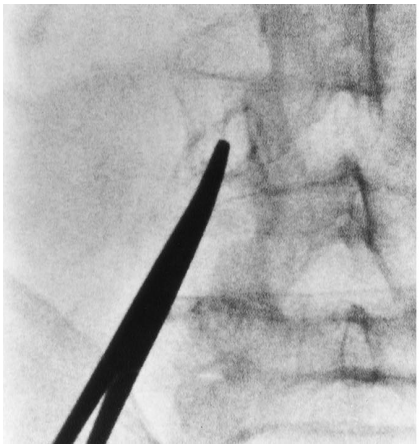

Fig 1. The pedicle to be punctured is isolated and marked with the tip of a surgical clamp. The skin, subcutaneous tissues, and periosteum are anesthetized with 0.25% bupivacaine.

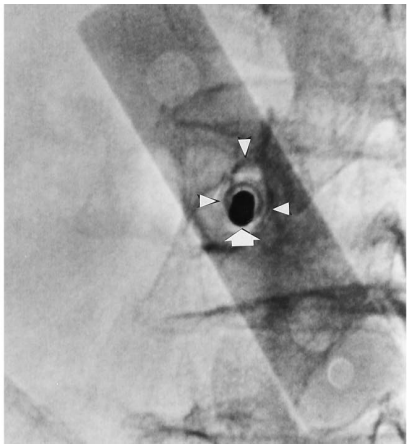

Fig 2. After a small skin incision is made, the Jamshidi needle is advanced into the pedicle. Notice that the shaft of the needle (*arrow*) maintains a bulls-eye appearance in relation to the pedicular edges (*arrowheads*) in the anteroposterior plane.

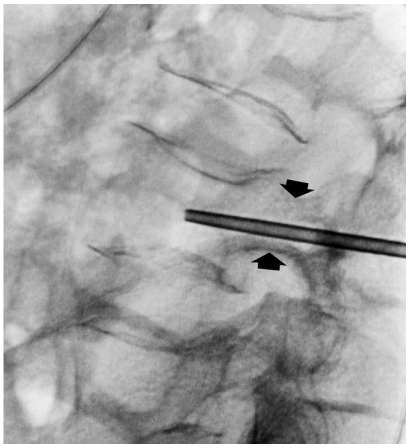

Fig 3. In the lateral plane, the shaft of the needle runs parallel to the superior and inferior cortices of the pedicle (*arrows*). After the stylet has been withdrawn, the needle tip is positioned in the middle of the vertebral body.

dics, neurosurgery, rheumatology, organ transplant service, family practice, and the pain management clinic. All patients had plain film evidence of progressive or new vertebral body compression fractures that corresponded to the level of the pain. Seventeen patients had fractures associated with age-related osteopenia and 12 patients were receiving oral steroids as part of an immunosuppressive regimen after cardiac or lung transplantation, or for chronic conditions. All patients had severe pain that limited their mobility; nine (31%) required assistance to ambulate, 10 (34%) were wheelchair bound, and 10 (34%) were limited to sitting in a chair or remaining in bed. Pain medication use varied, with eight patients (27%) using oral narcotics on an as-needed basis, 16 (55%) using oral narcotics on a 4- to 6-hour schedule, and five (17%) requiring parenteral narcotics.

Patient Selection and Preparation

Patient selection was limited to persons with focal, intense, deep pain associated with plain film evidence of a new or progressive vertebral compression fracture. Often the pain radiated along the ribs to the chest or abdomen, but lower extremity radicular pain was not reported.

Physical examination determined the patients' general health and their ability to tolerate lying prone for 1 to 2 hours. Neurologic examination was performed to evaluate possible radicular symptoms. Once the patient was accepted for treatment, an unenhanced CT scan was obtained to assess continuity of the posterior vertebral wall and to exclude other causes of pain, such as a herniated nucleus pulposus or an adjacent tumoral mass.

The procedure was discussed with the patient, and the potential benefits and risks were outlined. The potential complications specified were bleeding at the puncture site, bone infection or fracture, damage to the nerve roots or cord, extravasation of material into the surrounding epidural or paravertebral spaces, and passage of material into the venous system with embolization to the pulmonary vasculature or compression of neural tissue.

Vertebroplasty Technique

The technique described below is that which we currently use, and is the result of the experience we have gained over 3 years.

Upon completing the informed consent process, the patient is placed in the prone position on the angiography table. Monitoring of blood pressure, heart rate, and pulse oximetry is done continuously throughout the procedure. Oxygen supplied via a nasal cannula is used when necessary. Neuroleptic analgesics in the form of fentanyl (Sublimaze, Abbott Labs, North Chicago, Ill) and midazolam (Versed, Roche Pharma, Manati, Puerto Rico) are administered by the angiography nurse under the direction of the operating physician. The procedure is performed under strict sterile conditions. All personnel wear surgical masks and caps in addition to gowns and gloves for the operators, to minimize the risk of infection. The vertebral body to be treated is localized under fluoroscopic control and the skin overlying this area is prepped and draped. Biplane fluoroscopy is recommended, as it allows near simultaneous imaging of the stylet tip position in two planes, thus decreasing the overall procedure time. The anteroposterior tube is angled in such a way as to maximize the oval appearance of the pedicle ("looking down the barrel") (Fig 1). The skin over the center of the pedicle oval is anesthetized with bupivacaine hydrochloride (0.25%) (Abbott Labs) followed by deep injection of bupivacaine to and including the periosteum. A small skin incision is made with a #11 scalpel blade. A disposable 11-gauge Jamshidi needle (Manan Medical, Northbrook, Ill) is positioned with

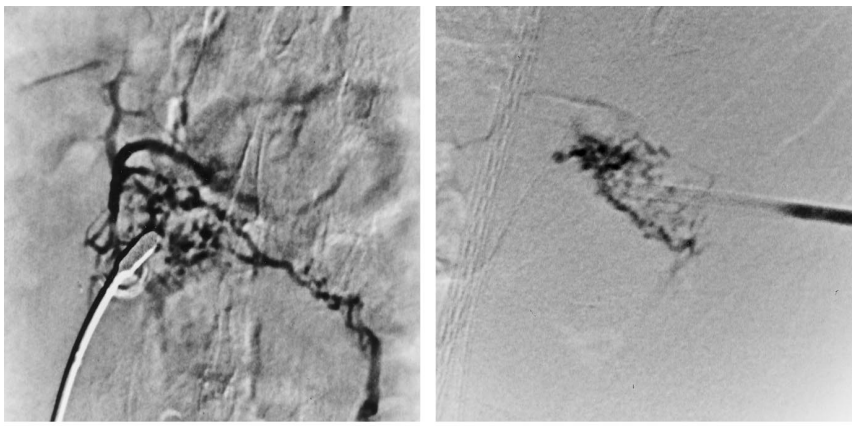

A B

Fig 4. Injection of contrast material in the anteroposterior (*A*) and lateral (*B*) planes shows filling of the bony trabeculae before opacification of the paravertebral veins. This appearance is important to recognize, since rapid filling of the venous system without intervening marrow indicates a needle position directly within the basivertebral plexus.

its tip in the center of the oval and advanced until the stylet tip abuts the bone. Lateral fluoroscopy shows the tip at the level of the upper to midpoint of the pedicle such that advancement of the needle is within the midportion of the pedicle. A slight twisting motion is used to advance the tip through the cortex, and frequent checking of needle placement in both planes is required. The anteroposterior view shows the needle shaft end-on as a circle within the center of the pedicle oval to indicate that the needle is proceeding parallel to the X-ray beam (Fig 2). The lateral view shows the needle moving roughly parallel to the superior and inferior edges of the pedicle (Fig 3) or in a slightly descending course through the pedicle. Minor adjustments in either plane may be required during needle advancement.

Once the needle tip has traversed the cortex and the pedicle and is located within soft bone marrow, less pressure may be required to advance the needle into the vertebral body. Care must be taken not to abrogate the anterior vertebral wall or the endplates. The stylet tip is placed at or near the junction of the anterior and middle third of the vertebral body line. Because the stylet tip projects beyond the end of the needle shaft, removal of the stylet will position the needle end in the middle or anterior half of the vertebral body (Fig 3).

Before injecting the PMMA, venography is done to exclude needle placement directly within the basivertebral venous complex and to ensure continuity of the posterior vertebral wall as evidenced by containment of the contrast material within the bony trabeculae (Fig 4). We use a hand injection of 5 mL of iohexol (Omnipaque 300, Nycomed, Princeton, NJ) and film in both planes at a rate of two frames per second. Rapid flow of contrast material into the vena cava and/or perivertebral veins without visibility of intervening bone marrow indicates direct communication of the needle tip with a major venous outlet and requires needle advancement. Once correct placement of the needle is confirmed, treatment is begun. If a bone biopsy is warranted, a variety of standard, commercially available biopsy needles can be passed through the Jamshidi shaft to obtain tissue samples before vertebroplasty.

In our experience, the Codman Cranioplastic, Type 1 (slow setting) material (CMW Laboratories, Blackpool, England) is the most suitable for vertebroplasty. The contents consist of a powder PMMA component (methylmethacrylate polymer with or without styrene copolymer and benzoyl peroxide) and a liquid PMMA component (methylmethacrylate monomer, ethylene dimethacrylate monomer, dimethyl p-toluidine and hydroquinone).

The powder is placed into a disposable plastic bowl and mixed with 1 g sterile tungsten powder (Nycomed) and 1.5 teaspoons (5 to 6 g) of sterile barium sulfate powder (E-Z-EM, Westbury, NY). The barium powder usually needs to be pulverized more completely before mixing, as it has a tendency to clump. The tungsten and barium are ground together with a pestle. The opacification agents are mixed thoroughly with the powdered PMMA and, for patients who are immunocompromised, 1.2 g of tobramycin (Nebcin, Eli Lilly, Indianapolis, Ind) is added to the powder mixture. A single dose of PMMA powder is divided into two equal parts to curb waste. The total powder volume (about 48 cm^3 without tobramycin, 55 cm^3 with) is measured in a 60-mL syringe and equal amounts are placed into two separate plastic bowls. Once the powder is divided, an additional 5 to 7 cm^3 are removed from each half and set aside. One half of the liquid agent (8.5 mL) is aspirated into a plastic syringe, and the unused portion is left in the glass bottle, since prolonged contact with the syringe wall will create a residue. The liquid agent is added to the powder and the slurry is mixed using a tongue blade until a thin "toothpaste" or "cake-glaze" consistency is achieved. If the material appears too thin after adding the liquid, the powder that was set aside is used to thicken the mixture. Once the desired consistency is reached, the material is poured into the back end of a 10-mL syringe, the plunger is replaced, and the material is advanced to the Luer-Lok end.

One-milliliter Luer-Lok syringes are filled from the end of the barrel. The plunger is removed and the syringe tip is held upright while 0.5 to 0.7 mL PMMA is injected into the 1-mL syringe from the 10-mL syringe. With the 1-mL

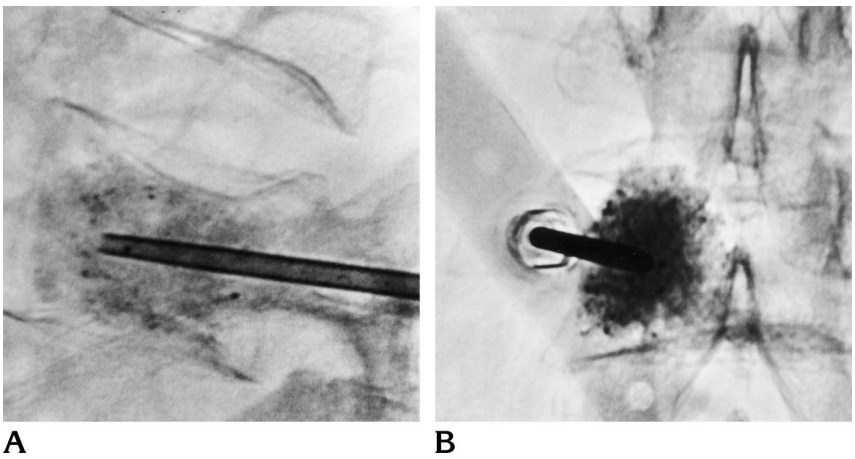

Fig 5. Injection of the hemivertebra is best seen on the lateral view (*A*) as the radiopaque material passes down the needle and disperses throughout the vertebral body. In most patients, the PMMA respects the midline (*B*), although in severely osteoporotic vertebrae, material may pass to the opposite side.

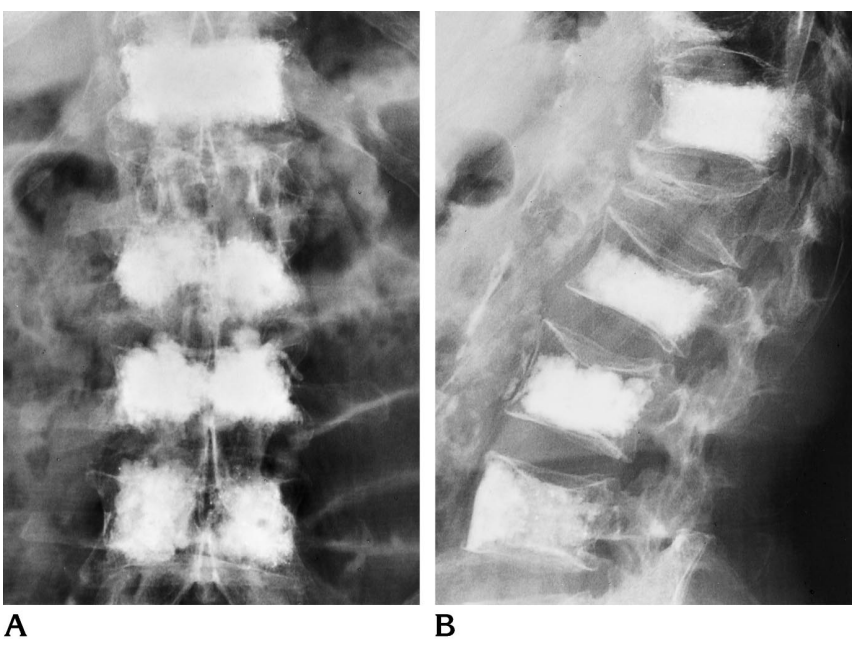

Fig 6. Anteroposterior (*A*) and lateral (*B*) views in a 69-year-old man with progressive osteoporotic compression fractures requiring hospitalization and intravenous narcotics. Four levels were treated on three occasions. The patient experienced 3 months of pain relief after injection of the L-2 and L-4 vertebral bodies. Plain film evaluation after sudden onset of new pain showed an acute fracture at L-3, which was treated. Eight months later, T-12 collapsed and was subsequently treated. The T-11 and L-1 compression fractures remained unchanged throughout this period.

syringe upright, the plunger is returned and the column of material is advanced to the tip. By using this closed system, any air present is purged, and the end of the 1-mL syringe is kept clean for easy attachment to the Jamshidi hub.

One operator injects the material as the second loads the syringes. The stylet is removed and, unless blood fills the dead space in a retrograde manner, the dead space is injected with PMMA using a long 18-gauge spinal needle. The 1-mL syringe is attached tightly to the shaft port of the Jamshidi needle and injection begins. The injection pressure required to push the material will increase over time as the vertebral body fills and the PMMA polymerizes. Injection is performed under lateral or anteroposterior oblique fluoroscopy (Fig 5) and particular attention must be paid to the region of the vena cava and the epidural space as seen on the venogram. If passage of material into the venous system is noted, the injection is slowed or halted while the material attains a thicker consistency. Injection is continued until hemivertebral or holovertebral filling is achieved, no more material can be pushed into the body, or extravasation into veins or the disk space is noted. Repositioning of the needle is not recommended, as the location of the tip will be unknown, and unwanted vascular embolization may occur. Upon completing the injection, the needle is removed and hemostasis at the puncture site is achieved by gentle pressure. The contralateral hemivertebra is then treated in the same fashion. More than one vertebra can be treated at the same time, depending on the patient's tolerance (Fig 6).

After the procedure, the patient is placed supine and asked to remain flat for 3 hours to allow complete curing of the PMMA prior to axial loading. Although patients usually remain overnight, those from our local area have been allowed to return home the same day, when appropriate.

Procedural Pitfalls and Helpful Hints

Several pitfalls and caveats have been discovered throughout our experience. It is helpful to have the patient attempt the prone position on a firm table before beginning the procedure to check for tolerance. Because most patients are receiving high doses of narcotics, the usual amount of neuroleptics needed to achieve adequate sedation may be insufficient. A dedicated nurse or other qualified person must be responsible for monitoring the patient, as respiratory distress or depression may occur quickly. Patients who experience difficulty with ventilation or who are unable to tolerate the prone position may require general anesthesia or deep sedation.

A recent CT scan to detect extension of the fracture into the posterior wall and to assess pedicle size is preferred whenever possible, particularly if the plain films show progressive collapse. In patients with questionable histories, the CT scan may also uncover other causes of pain, such as a herniated disk or a neoplastic lesion. Often, scans are obtained the same day as the initial consultation or just before treatment. Recently, we have found magnetic resonance (MR) imaging to be helpful in determining the site of an acute fracture in patients with multiple compression fractures, particularly when serial plain films are not available. The involved vertebra(e) have typically shown edema within the bone at the fracture site.

A variable degree of kyphosis may be associated with the fracture, and craniocaudad angulation may be required in addition to obliquity to attain the optimal pedicular appearance. In some instances, a significant amount of downward force may be required to advance the needle, and patients with diffuse osteopenia are at risk for rib fracture, especially with thoracic vertebral procedures. Often, the most force is needed to penetrate the pedicular cortex; thereafter, the tip usually advances easily, particularly in patients with severe osteoporosis. The needle position should be checked frequently in both planes to avoid exiting through the endplate. Once endplate penetration occurs, the needle may have to be removed and repositioned.

If the venogram shows rapid, direct filling of the basivertebral complex, the tip should be advanced into the bone instead of withdrawn. Once a track has been made, the contrast material will continue to enter the same venous system even when positioned more posteriorly. However, with severe osteopenia, there may be rapid flow of contrast material through the bone into the veins, which is misinterpreted as positioning within the vein. As long as the trabecular appearance of the bone marrow is present at the needle tip prior to venous filling, injection can be made safely. The PMMA used in this situation should be of a slightly thicker consistency than usual and the injection needs to be slower. Before PMMA injection, the dead space of the needle should be flushed with saline to remove any residual contrast material that may be confused with the embolic agent.

When adding opacification powders to the PMMA, using more than 1.5 teaspoons of barium sulfate results in a stiffer, faster-curing material that is difficult to inject. Barium powder alone does not provide as good visibility as the barium/tungsten combination. The powdered material should be mixed thoroughly to avoid clumping of the tungsten or barium. Powdered barium preparations designed for gastrointestinal work contain gums and flavors that may act as nutrients for bacteria, and should not be used. Pure barium sulfate powder is available, but needs to be sterilized by using dry heat.

The liquid agent is extremely volatile and should be opened only when needed. Inhalation of the fumes should be avoided, as the odor has occasionally induced headache and eye irritation in the operators. The package insert recommends double gloving, as there is inadequate information to determine if the PMMA resin might affect fertility in humans or have a teratogenic potential or other adverse effects on fetuses.

After mixing for approximately 1 minute, the material is relatively thin. At this point it is loaded into the 10-mL syringe. Further mixing seems to speed the polymerization and if one waits until the material appears to be of correct consistency in the bowl, it will be too thick to inject by the time the syringe is loaded. Filling the 1-mL syringes from the bowl by aspiration clogs the Luer-Lok threads, and adequate attachment to the Jamshidi stylet port may not be obtained. The dead space of the Jamshidi needle must be filled from the tip to the hub with a long 18-gauge needle, as the material does not readily drip into the hub. Injection of the air within the dead space may cause a venous air embolus.

Owing to the viscosity of the material, injection may be difficult, and the best results are obtained by using small amounts (0.5 to 0.7 mL) with the force of the injection applied parallel to the syringe cylinder. Excessive force may result in bending of the plunger. Injection through 3-mL syringes is difficult, and maximal vertebral body filling has been obtained consistently using 1-mL syringes. Non–Luer-Lok syringes do not give an adequate seal with the Jamshidi port. Care must be taken not to bear down on the Jamshidi handle, as the tip may advance further into the vertebral body.

Injection is performed under fluoroscopic control, paying particular attention to the epidural space, the spinal canal, and the perivertebral veins visible on the venogram. The lateral projection is best but may be useful for only the initial vertebral hemisphere, since the opaque cement from the first hemivertebral injection obscures the entire vertebral body in the lateral view. The anteroposterior oblique view for the contralateral hemisphere is recommended; however, the lateral plane should be checked frequently to ensure no epidural leakage. Occasionally, in severely osteoporotic vertebrae, it is possible to attain adequate filling of both sides from a single transpedicular injection (Fig 7). We consider an injection that fills the majority of the hemivertebra to be adequate. We continue the injection as long as the material remains within the vertebral body and there is no continuous leakage into paravertebral veins or into the disk space. Once adequate

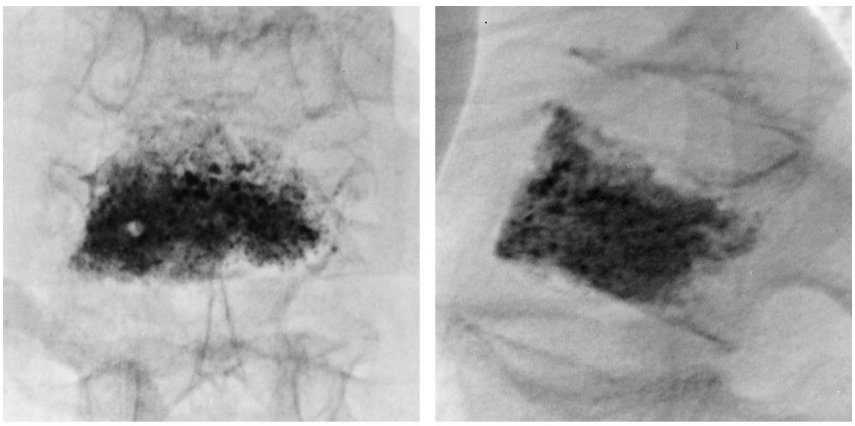

A B

Fig 7. This L-1 vertebral body was filled with 10 mL of PMMA delivered through a single pedicle. Note cross-filling of material to the contralateral hemivertebra and almost complete filling of the body from front to back.

filling is obtained, the needle is removed without replacing the stylet to prevent injection of the dead-space material.

In some patients, PMMA will traverse endplate fractures and enter the disk space, which, in our experience, is of no clinical significance. When leakage occurs, delaying further injection for a minute allows the material to thicken and form a plug before proceeding. This technique is also useful when material enters the paravertebral veins. If continued injection shows filling only of the disk space or veins, the procedure is terminated in that hemisphere.

Results

The procedures were technically successful in all patients, as defined by effective transpedicular puncture of the vertebral body with instillation of PMMA. The amount of PMMA injected per vertebral body varied from 2.5 mL to 11 mL, with an average injection amount of 7.1 mL. Four vertebral bodies were treated from a single, unipedicular approach as the PMMA flowed across the midline to adequately fill both vertebral hemispheres. All remaining patients were treated via bipedicular punctures.

Two patients undergoing thoracic vertebral punctures sustained a nondisplaced rib fracture, which caused limited chest pain that subsequently resolved. No other clinical complications were noted. In two patients, a small amount of PMMA escaped to the inferior vena cava with presumed embolization to the lungs, but no respiratory changes were seen. In nine patients, radiographs showed evidence of PMMA leakage through the endplate fracture into the disk space, with no discernible clinical effect. A follow-up CT scan in one patient with pain associated with a new fracture showed PMMA in the anterior internal venous plexus at L-4, causing flattening of the thecal sac. There was no history of radicular pain and no radicular findings on neurologic examination.

Immediate clinical response to the procedure was assessed by monitoring patients' verbal expression of perceived pain, amount and/or type of pain medication given, and changes in activity level. Two patients reported resolution of back pain immediately after vertebroplasty. Twenty-six patients (90%) described pain relief and improved mobility within 24 hours after treatment. All patients who had required parenteral narcotics were changed to oral medications on an as-needed basis. Three patients had no significant relief of pain and were continued on their pretreatment medical regimen. No worsening of pain was reported.

Discussion

PMMA has been used in anterior and posterior stabilization of the spine for metastatic disease in multiple surgical series (1–3), for bone packing after curettage of giant cell tumors of the long bones (4, 5), and in the surgical treatment of vertebral hemangiomas (6). Recently, percutaneous injection of PMMA into vertebral compression fractures via the transpedicular or paravertebral approach under CT and/or fluoroscopic guidance has been described (7–10) (Deramond et al, "Percutaneous..."). In patients being treated for chronic pain, the initial results of these small series were good, with relatively low complication rates. We believe our experience in performing vertebroplasty safely in 29 patients with 47 osteoporotic compression fractures with no significant clinical complications further validates these earlier studies. As noted above, the majority of our patients reported ini-

tial improvement in their quality of life as determined by decreased pain, increased mobility, and decreased reliance on analgesics immediately after the procedure.

Our technique is somewhat different from that used by European investigators (7–10) (Deramond et al, "Percutaneous..."). The materials we used are approved by the Food and Drug Administration; however, our use of them for percutaneous vertebroplasty would qualify as an "off-label" application. Instead of using the CT/fluoroscopic technique described by Gangi et al (9), we found the fluoroscopically guided transpedicular approach to be the easiest, safest, and least time-consuming procedure. Stringham et al (11) demonstrated that half the vertebral body can be reached via the transpedicular approach in bone biopsy specimens without compromising the anatomic structure of the pedicle. We noted that injection of PMMA spreads through the ipsilateral hemivertebra first, followed by progression across the midline in some patients.

Other authors (7–10) (Deramond et al, "Percutaneous...") did not perform venography before injecting the PMMA. We found venography to be of great use, as it confirmed needle placement within the bony trabeculae, outlined the venous drainage pattern, and delineated fractures in the bony cortex. Knowledge of the venous anatomy allowed the operator to pay particular attention to those areas during dynamic injection of the PMMA.

In our initial experience, we terminated the injection whenever filling of a paravertebral vein or extravasation through an endplate fracture was noted. However, we encountered no clinical complications from PMMA situated in either location. We terminated the injection if filling of the anterior internal venous plexus was seen, as these veins abut the dura along its anterior surface and could compress the spinal cord or nerve roots. We also terminated the injection if the PMMA continued to seek the intervertebral space or progressed through paravertebral veins.

The complication rate for this procedure has been very low in other series (7–10) (Deramond et al, "Percutaneous..."), ranging from 0% to 10%. Complications have included transient dysphagia or radiculopathy, presumably due to extravasation of PMMA with nerve root or esophageal compression (10). We know of no reports of infection in any series, including our own. We decided to add tobramycin to the PMMA when treating immunocompromised patients after reviewing several reports that described the addition of antibiotics to PMMA in an attempt to decrease surgical infection rates (12–14). One series reported a decrease in infection from 5% to 1% when tobramycin-impregnated PMMA was used for cranioplasty, vertebral body replacement, or spinal fusion (12). Although regional tissue concentrations of the drug were noted, no incidents of renal toxicity were reported nor were significant systemic levels of tobramycin detected. Aminoglycosides should not be used in any patient with a known sensitivity.

Potential toxicities of PMMA have been described. McLaughlin et al (15) found decreased pulmonary function in dogs only when the dosage of PMMA monomer was more than 35 times the amount liberated in humans during total hip replacement. Phillips et al (16) described a fall in systemic arterial blood pressure after implantation of acrylic cement into the femoral shaft, but not the acetabulum, during hip arthroplasty. These authors speculated that the hypotension may have been due to absorption of monomer or additives into the circulation. We have not seen this phenomenon during injection of vertebral bodies. Convery et al (17) studied the safety of PMMA during total hip replacement, and, like Phillips et al, noted a fall in systemic pressure that was temporally related to the implantation of the acrylic in the femoral canal. There was no evidence of pulmonary function alteration or change in liver enzyme levels that could be related to the PMMA, indicating that liver toxicity is probably not an issue.

Another potential mechanism for injury is from the thermal reaction that occurs during polymerization. A significant amount of heat is generated, which potentially could be damaging to adjacent neurologic structures. In an in vivo experiment, Wang et al (18) found no spinal cord injury occurring in dogs undergoing cervical fusion with PMMA, even when gelatin sponge was not used as an insulator. The presence of intervening ligaments and vascular-rich dura along with cerebrospinal fluid flow may act as natural insulators to dissipate any heat that is created.

This technique has possible use as a means of delivering different substances to the bone. We have done some preliminary work with naturally occurring bone materials, such as hy-

droxyapatite, for use as a bone cement and think it is conceivable that bone growth hormones or other biologically active substances could be injected percutaneously into vertebral bodies to induce new bone growth.

Conclusion

We performed percutaneous vertebroplasty in 29 patients with 47 thoracic or lumbar compression fractures that were the cause of significant pain and/or immobilization. The procedure resulted in immediate subjective improvement in pain and in increased mobility for the majority (n = 26) of the patients. The long-term outcome in this patient population is currently being analyzed and will be the subject of a future publication. Complications appear to be rare. Vertebroplasty is a valuable new tool in the treatment of osteoporotic vertebral compression fractures, providing pain relief and early mobility in appropriate patients.

References

1. Sundaresan N, Galicich JH, Lane JM, Bains MS, McCormack P. Treatment of neoplastic epidural cord compression by vertebral body resection and stabilization. *J Neurosurg* 1985;63:676–684
2. Harrington K. Anterior decompression and stabilization of the spine as a treatment for vertebral collapse and spinal cord compression from metastatic malignancy. *Clin Orthop Rel Res* 1988; 233:177–197
3. Cybulski GM. Methods of surgical stabilization for metastatic disease of the spine. *Neurosurgery* 1989;25:240–252
4. Persson BM, Ekelund L, Lovdahl, et al. Favourable results of acrylic cementation for giant cell tumors. *Acta Orthop Scand* 1984:55;209–214
5. O'Donnell RJ, Springfield DS, Motwani HK, et al. Recurrence of giant-cell tumors of the long bones after curettage and packing with cement. *J Bone Joint Surg* 1994;76A:1827–1833
6. Nicola N, Lins E. Vertebral hemangioma: retrograde embolization-stabilization with methyl methacrylate. *Surg Neurol* 1987;27:481–486
7. Galibert P, Deramond H, Rosat P, Le Gars D. Note préliminaire sur le traitement des angiomes vertébraux par vertebroplastie percutanée. *Neurochirurgie* 1987;33:166–168
8. Kaemmerlen P, Thiesse P, Bouvard H, Biron P, Mornex F. Jonas P. Vertébroplastie percutanée dans le traitement des métastases: technique et résultats. *J Radiol* 1989;70:557–562
9. Gangi A, Kastler BA, Dietemann JL. Percutaneous vertebroplasty guided by a combination of CT and fluoroscopy. *AJNR Am J Neuroradiol* 1994;15:83–86
10. Weill A, Chiras J, Simon J, et al. Spinal metastases: indications for and results of percutaneous injection of acrylic surgical cement. *Radiology* 1996;199:241–247
11. Stringham D, Hadjipavlou A, Dzioba RB, et al. Percutaneous transpedicular biopsy of the spine. *Spine* 1994;19:1985–1991
12. Shapiro S. Cranioplasty, vertebral body replacement, and spinal fusion with tobramycin-impregnated methylmethacrylate. *Neurosurgery* 1991;28:789–791
13. Goode RL, Reynolds BN. Tobramycin-impregnated methylmethacrylate for mandible reconstruction. *Arch Otolaryngol Head Neck Surg* 1992;118:201–204
14. Dierks EJ, Potter BE. Treatment of an infected mandibular graft using tobramycin-impregnated methylmethacrylate beads: report of a case. *Oral Maxillofac Surg* 1992;50:1243–1245
15. McLaughlin RE, DiFazio CA, Hakala M, et al. Blood clearance and acute pulmonary toxicity of methylmethacrylate in dogs after simulated arthroplasty and intravenous injection. *J Bone Joint Surg* 1973;55A:1621–1628
16. Phillips H, Cole PV, Letton AW. Cardiovascular effects of implanted acrylic bone cement. *Br Med J* 1971;3:460–461
17. Convery FR, Gunn DR, Hughes JD, et al. The relative safety of polymethylmethacrylate. *J Bone Joint Surg* 1975;57A:57–64
18. Wang GW, Wilson CS, Hubbard SL, et al. Safety of anterior cement fixation in the cervical spine: in vivo study of dog spine. *South Med J* 1984;77:178–179

AJNR

REVIEW ARTICLE

Posterior Reversible Encephalopathy Syndrome, Part 1: Fundamental Imaging and Clinical Features

W.S. Bartynski

SUMMARY: Posterior reversible encephalopathy syndrome (PRES) is a neurotoxic state coupled with a unique CT or MR imaging appearance. Recognized in the setting of a number of complex conditions (preeclampsia/eclampsia, allogeneic bone marrow transplantation, organ transplantation, autoimmune disease and high dose chemotherapy) the imaging, clinical and laboratory features of this toxic state are becoming better elucidated. This review summarizes the basic and advanced imaging features of PRES, along with pertinent features of the clinical and laboratory presentation and available histopathology. Many common imaging/clinical/laboratory observations are present among these patients, despite the perception of widely different associated clinical conditions.

Initially recognized in association with eclampsia, cyclosporine after transplantation, and in the setting of severe hypertension, posterior reversible encephalopathy syndrome (PRES) has become synonymous with a unique pattern of brain vasogenic edema seen in the setting of neurotoxicity.[1-14] On CT or MR imaging studies, the edema is often widespread but predominates in the parietal and occipital regions, likely leading Hinchey et al[15] to suggest the "posterior" description.

A substantial experience with PRES has evolved; and though more widely recognized, controversy still exists as to the mechanism responsible for the brain edema. Specifically, what is the role of hypertension and is the edema related to hyperperfusion or hypoperfusion? In this review, the fundamental clinical and imaging features of PRES will be emphasized with controversial issues to follow.

Imaging Patterns in PRES

At CT/MR imaging, the brain typically demonstrates focal regions of symmetric hemispheric edema (Fig 1*A*, -*B*). The parietal and occipital lobes are most commonly affected, followed by the frontal lobes, the inferior temporal-occipital junction, and the cerebellum.[16-18] Lesion confluence may develop as the extent of edema increases. MR diffusion-weighted imaging (DWI) was instrumental in establishing and consistently demonstrating that the areas of abnormality represent vasogenic edema.[19-24] The edema usually completely reverses.

The basic PRES pattern resembles the brain watershed zones, with the cortex and subcortical and deep white matter involved to varying degrees.[12,14,16,25,26] Three hemispheric pattern variants may be encountered with similar frequency (holohemispheric [Fig 1], superior frontal sulcal, and primary parietal-occipital).[27] These demarcate lateral hemispheric blood supply (middle cerebral artery [MCA]) and medial hemispheric supply (anterior cerebral artery [ACA], posterior cerebral artery [PCA]) and further reflect the junctional/watershed nature of PRES.

Characteristic lesion locations such as the inferior temporal-occipital junction, superior frontal sulcus, and parietal/occipital region likely represent junctional expression between second-order branches or distal hemispheric branches.[16] Linearly oriented focal deep white matter involvement may represent expression of PRES in the deep (intrahemispheric) watershed.[27] A continuum is noted between diminutive and extensive expression of PRES; and partial, asymmetric, or mixed forms of these patterns may be encountered.

Focal/patchy areas of PRES vasogenic edema may also be seen in the basal ganglia, brain stem, and deep white matter (external/internal capsule).[20,27-31] When they accompany hemispheric or cerebellar PRES, it is easy to recognize these areas as companion lesions. Present in isolation or when the hemispheric pattern is incompletely expressed (partial/asymmetric), the diagnosis of PRES can be challenging.[27,32] If cerebellar or brain stem involvement are extensive, hydrocephalus and brain stem compression may occur.[33-35]

Focal areas of restricted diffusion (likely representing infarction or tissue injury with cytotoxic edema) are uncommon (11%–26%) and may be associated with an adverse outcome.[20,21] Hemorrhage (focal hematoma, isolated sulcal/subarachnoid blood, or protein) is seen in approximately 15% of patients.[16,27,32]

Basic Clinical Features of Neurotoxicity with PRES

Patients at risk for PRES are summarized in the Table. Neurotoxicity with characteristic watershed CT/MR imaging features was initially noted in eclampsia, allogeneic bone marrow transplantation (allo-BMT), solid organ transplantation (SOT), and in association with severe hypertension. With similar clinical/imaging presentation recognized the mid 1990s, additional associations were noted (autoimmune conditions, thrombotic thrombocytopenic purpura, and medical renal disease), and the term "PRES" was introduced.[15,20,22] PRES is seen with unique or high-dose cancer chemotherapy (Table) and has recently been associated with infection, sepsis, and shock.[36] Additional considerations have been suggested in numerous case reports as reviewed in the Table.

Clinical/Laboratory Characteristics in PRES

Clinical symptoms at toxicity are broad but include headache, vision change, paresis, hemianopsia, nausea, and altered mentation.[37,38] Symptoms may develop over several days or may be recognized only in the acute setting. Generalized seizures

Received and accepted November 5, 2007.

From the Department of Radiology, Division of Neuroradiology, University of Pittsburgh, Presbyterian University Hospital, Pittsburgh, Pa.

Please address correspondence to Walter S. Bartynski, MD, Department of Radiology, Division of Neuroradiology, University of Pittsburgh, Presbyterian University Hospital, 200 Lothrop St, D 132, Pittsburgh PA 15213; e-mail: bartynskiws@upmc.edu

DOI 10.3174/ajnr.A0928

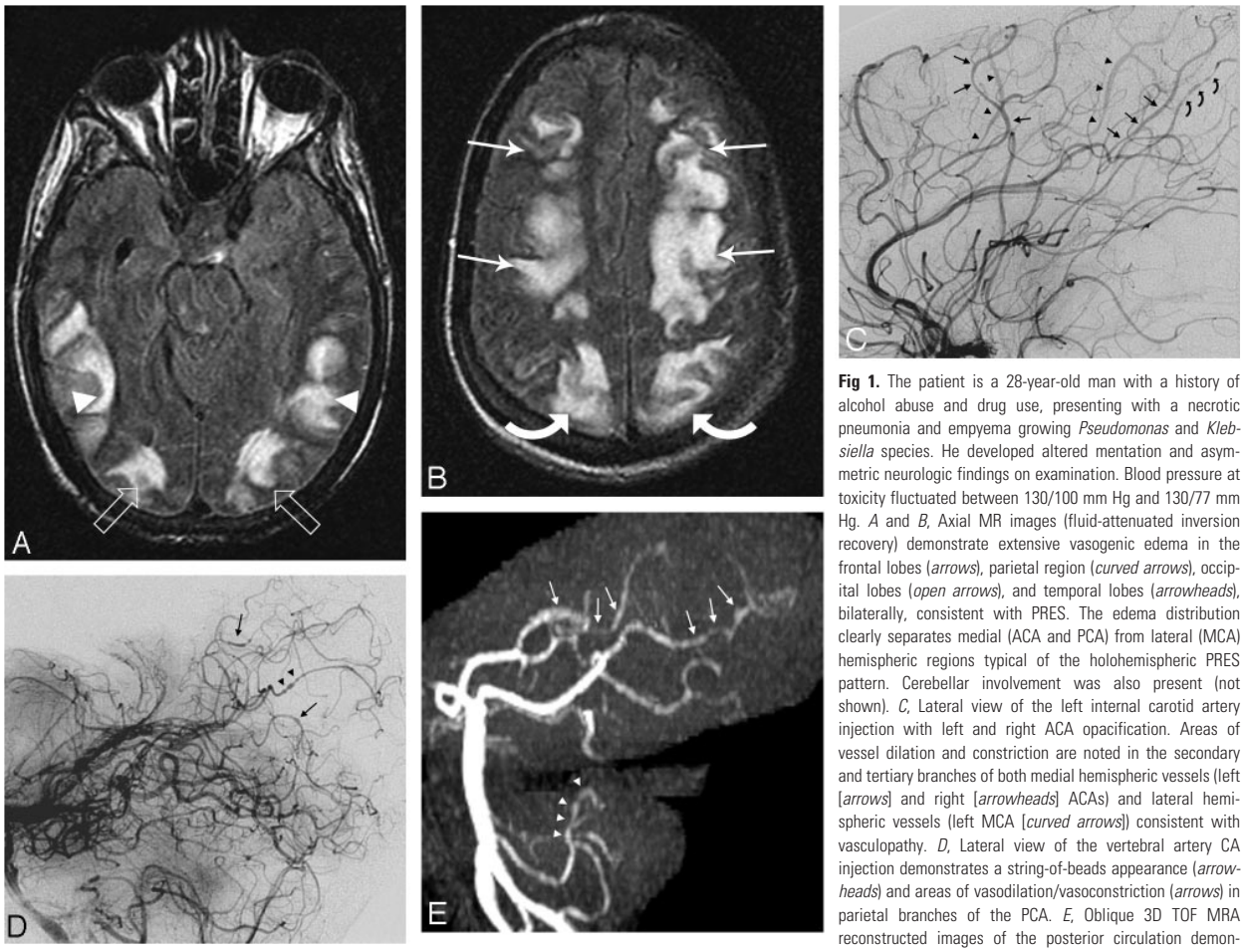

Fig 1. The patient is a 28-year-old man with a history of alcohol abuse and drug use, presenting with a necrotic pneumonia and empyema growing *Pseudomonas* and *Klebsiella* species. He developed altered mentation and asymmetric neurologic findings on examination. Blood pressure at toxicity fluctuated between 130/100 mm Hg and 130/77 mm Hg. *A* and *B*, Axial MR images (fluid-attenuated inversion recovery) demonstrate extensive vasogenic edema in the frontal lobes (*arrows*), parietal region (*curved arrows*), occipital lobes (*open arrows*), and temporal lobes (*arrowheads*), bilaterally, consistent with PRES. The edema distribution clearly separates medial (ACA and PCA) from lateral (MCA) hemispheric regions typical of the holohemispheric PRES pattern. Cerebellar involvement was also present (not shown). *C*, Lateral view of the left internal carotid artery injection with left and right ACA opacification. Areas of vessel dilation and constriction are noted in the secondary and tertiary branches of both medial hemispheric vessels (left [*arrows*] and right [*arrowheads*] ACAs) and lateral hemispheric vessels (left MCA [*curved arrows*]) consistent with vasculopathy. *D*, Lateral view of the vertebral artery CA injection demonstrates a string-of-beads appearance (*arrowheads*) and areas of vasodilation/vasoconstriction (*arrows*) in parietal branches of the PCA. *E*, Oblique 3D TOF MRA reconstructed images of the posterior circulation demonstrate areas of focal vasodilation and vasoconstriction in the PCAs bilaterally (*arrows*), consistent with vasculopathy, similar to the vertebral artery CA appearance. Posterior inferior cerebellar artery (*arrowheads*) irregularity is also present.

are common and coma may develop. In approximately 70%–80% of patients, moderate-to-severe hypertension is observed. Toxicity blood pressure is normal or only minimally elevated in 20%–30% of patients in eclampsia, allo-BMT, and most large reported PRES series.[11,15,17,22,27,39-42]

Best studied in preeclampsia/eclampsia, laboratory evidence of endothelial injury is often present with platelet consumption (thrombocytopenia) and evidence of red cell fragmentation (schistocyte formation, increase in lactate dehydrogenase [LDH]).[43,44] Developing hypertension in preeclampsia is related to systemic vasoconstriction with accompanying reduced intravascular volume and hemoconcentration. Renal dysfunction with proteinuria and hypomagnesemia occur; systemic edema develops due to a combination of altered endothelial function and reduced oncotic pressure. Hepatic ischemia may lead to liver dysfunction and, when severe, hemolysis, elevated liver enzymes, and low platelets (HELLP) syndrome.

In infection/sepsis/shock–associated PRES, a clinical pattern consistent with systemic inflammatory response syndrome develops with evidence of multiple organ dysfunction syndrome (MODS), including alteration of coagulation (thrombocytopenia), liver function (increased bilirubin), renal function (increased creatinine), pulmonary function, and cardiovascular instability.[36]

Similar features may develop in patients after allo-BMT. The effects of graft-versus-host disease (GVHD) are managed by immune suppression with cyclosporine or tacrolimus (FK-506). Cyclosporine can injure the endothelium.[45,46] At toxicity, diffuse endothelial dysfunction is often present, termed "bone marrow transplant thrombotic microangiopathy," with development of significant schistocyte counts (exceeding 10% when severe) and marked elevation of LDH.[16,17,47] A MODS pattern can develop with systemic or pulmonary edema and ischemic hepatic dysfunction, similar to preeclampsia.[48]

Major PRES-Associated Clinical "Conditions"

Preeclampsia/Eclampsia. The association of PRES with toxemia of pregnancy is well established.[1-3,5,21,24,26,49,50] Preeclampsia develops in approximately 5% of pregnancies and eclampsia, in approximately 1 in 3000 births with current management.[43,44] Eclampsia develops before gestation in 50% of patients, interpartum in 25%, and within 48 hours of delivery in 25%. Although most women are hypertensive at toxicity, blood pressure is reported as normal or only minimally elevated in 23% of patients.[39] The placenta is thought to be the primary cause of toxemia, with placenta removal and fetal delivery considered curative.[43,44]

"Delayed Eclampsia" (PRES within several weeks after delivery) can occur, and the clinical presentation is often confus-

Conditions at risk for PRES

Conditions
Toxemia of pregnancy (preeclampsia/eclampsia)
Posttransplantation:
allo-BMT
SOT
Immune suppression:
Cyclosporine
Tacrolimus (FK-506)
Infection/sepsis/shock:
Systemic inflammatory response syndrome
Multiorgan dysfunction syndrome
Autoimmune diseases:
Systemic lupus erythematosus
Systemic sclerosis (scleroderma)
Wegener's
Polyarteritis nodosa
Status-post cancer chemotherapy:
Combination high-dose chemotherapy
Reported miscellaneous drugs
Cytarabine[a,b]
Cisplatin[c]
Gemcitabine[d]
Tiazofurin[e]
Bevacizumab (Avastin)[f,g]
Kinase inhibitor BAY 34–9006[h]
Miscellaneous reported associations
Hypomagnesemia[i,j]
Hypercalcemia[k,l]
Hypocholesterolemia[m]
Intravenous immunoglobulin[n]
Guillain-Barré syndrome[o]
Ephedra overdose[p]
Dislysis/erythropoietin[q]
Triple-H therapy[r,s]
Tumor lysis syndrome[t,u]
Hydrogen peroxide[v]
Dimethyl sulfoxide stem cells[w]

[a,b] Patel AG. *J Comput Assist Tomogr* 1996;20:161–62; Vaughn DJ. *AJNR Am J Neuroradiol* 1993;14:1014–16
[c] Ito Y. *AJNR Am J Neuroradiol* 1998;19:415–17
[d] Russell MT. *Magn Reson Imaging* 2001;19:129–32
[e] Rippe DJ. *J Comput Assist Tomogr* 1988;12:1078–81
[f,g] Glusker P. *N Engl J Med* 2006;354:980–82, discussion 980–82; Ozcan C. *N Engl J Med* 2006;354:980–82, discussion 980–82
[h] Govindarajan R. *J Clin Oncol* 2006;24:e48
[i,j] Thompson CB. *Lancet* 1984;2:1116–20; Al-Rasheed AK. *Pediatr Neurol* 2000;23:353–56
[k,l] Choudhary M. *Scand J Infect Dis* 2005;37:524–26; Kim JH. *Eur Neurol* 2005;53:160–62
[m] de Groen PC. *N Engl J Med* 1987;317:861–66
[n] Voltz R. *Neurology* 1996;46:250–51
[o] Elahi A. *Neurocrit Care* 2004;1:465–68
[p] Moawad FJ. *South Med J* 2006;99:511–14
[q] Delanty N. *Neurology* 1997;49:686–89
[r,s] Sanelli PC. *Neurocrit Care* 2005;3:46–50; Wartenberg KE. *J Neuroimaging* 2006;16:170–75
[t,u] Kaito E. *Pediatr Radiol* 2005;35:722–27; Greenwood MJ. *Leuk Lymphoma* 2003;44:719–21
[v] Cannon G. *J Child Neurol* 2003;18:805–08
[w] Higman MA. *Bone Marrow Transplant* 2000;26:797–00

ing.[4,51] Blood pressure may be normal or mildly elevated, severe headache is common, and conventional angiography is often performed to exclude intracranial aneurysm. In a recently reported case, delayed eclampsia appeared to have been associated with retained placental fragments.[52] PRES has also been reported 3 weeks following resection and chemotherapy for hydatidiform mole.[53]

Infection/Sepsis/Shock. In infection, sepsis, and shock–associated PRES, gram-positive organisms predominate, and in 40% of patients, toxicity blood pressure is normal or only minimally increased.[36] At imaging, vasogenic edema is greater in normotensive patients and lower in severely hypertensive patients; and at MR angiography (MRA), reversible "vasculopathy" (diffuse/focal vasoconstriction) or vessel pruning is noted.[36] Recent reports note PRES in the setting of post-streptococcal glomerulonephritis, Henoch-Schonlein purpura, and infection-induced hypercoagulable state.[54-56]

Autoimmune Disease. PRES has been identified in patients with systemic lupus erythematosus, Wegener's granulomatosis, systemic sclerosis (scleroderma, Fig 2), and polyarteritis nodosa.[15,20,22,27,57-60] Detailed accounts of the clinical circumstances surrounding PRES in association with autoimmune disease are infrequent.[57-60] Patients are commonly managed with intermittent doses of immunosuppression (cyclophosphamide, cyclosporine) for disease control.

Cancer Chemotherapy. PRES is usually encountered after high-dose multidrug cancer therapy, typically in hematopoietic malignancies.[61-64] A variety of cancer chemotherapeutic drugs have also been noted in association with PRES (Table).

Transplantation. PRES is well recognized in the setting of bone marrow or stem cell transplantation.[11,17,18,65-68] The incidence of PRES after allo-BMT using myeloablative marrow preconditioning and cyclosporine immune suppression is approximately 7%–9% and appears to vary with a preconditioning regimen.[11,67,69] A greater frequency (16%) is reported with higher dose myeloablative regimens, and a lower frequency (3%) is noted with nonmyeloablative preconditioning.[65,69] PRES occurs most commonly in the first month after allo-BMT, with the remainder during the subsequent year after transplantation.[11,40,67,69] Reported incidence of PRES with tacrolimus immune suppression appears variable.[66,68] A high incidence of GVHD is also noted in patients with allo-BMT PRES, and a GVHD effect has been suggested.[68,70-72] Variation in cyclosporine toxicity with human leukocyte antigen match has been noted, and the rate of tacrolimus-associated PRES appears to increase with the degree of graft mismatch.[66,67]

PRES is also noted after SOT.[9,12,13,34,40,73-80] The reported incidence of PRES after SOT varies between 0.4% and 6%.[78,81] The onset of PRES varies among subtypes but tends to occur earlier after liver transplantation.[81] Systemic hypertension was found to be common in patients who develop PRES after renal transplantation but uncommon after heart, lung, or liver transplantation.[77,81,82] In our experience, transplant rejection and infection often accompany PRES in SOT.[83] After liver transplantation, PRES typically occurs early (within 2 months after transplantation), blood pressure tends to be normal, and the extent of brain edema is significant. In contrast, patients with kidney transplantation appear to develop PRES late after transplantation, are severely hypertensive, and have significantly less brain edema.[83]

After transplantation, several PRES-related risks coexist. The immune-suppressive drugs cyclosporine/tacrolimus (FK-506) inhibit T-cell activation, proliferation, and interleukin-2 production through inhibition of the calcineurin pathway.[84,85] These drugs are associated with low-level neurotoxicity in 10%–40% of patients (tremors, anxiety, psychiatric dysfunction).[37,86] Immunosuppressant blood levels do not appear to correlate with severe neurotoxicity or PRES, but immunosuppressant discontinuation or switch usually results in clinical improvement.[11,37,67,69,77,86,87] Cyclosporine can induce endothelial injury/dysfunction leading to enhanced vasoconstrictive effects (increased endothelin and thrombox-

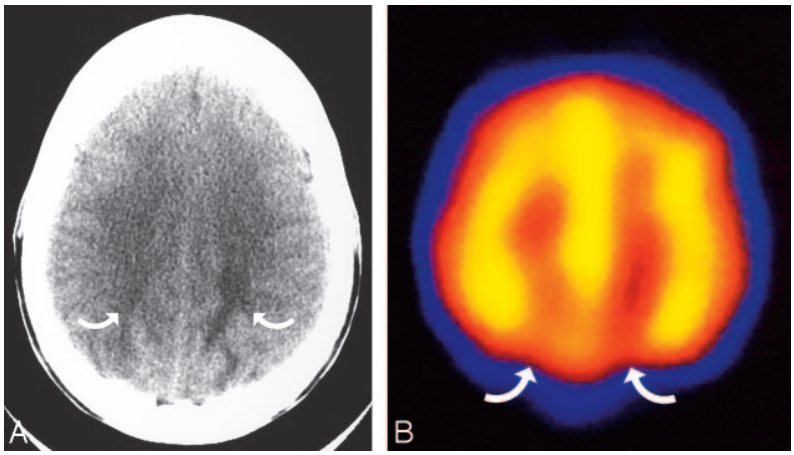

Fig 2. The patient is a 38-year-old woman with scleroderma, severe hypertension (190/110 mm Hg), and acute renal failure, with altered mental status that progressed to seizure. *A*, Axial brain CT image obtained at toxicity demonstrates vasogenic edema in the parietal region bilaterally (*curved arrows*), consistent with PRES. *B*, Axial technetiumTc-99m-HMPAO SPECT study performed the following day demonstrates reduced radiopharmaceutical uptake bilaterally in the parietal region (*curved arrows*), consistent with hypoperfusion.

ane, decreased nitric oxide and prostacycline), increased sympathetic activation, and coagulation effects.[37,45-47,84,88] Immune challenge from the transplant (transplant rejection, GVHD), effects of chemotherapy (preconditioning), and the risks of infection in the immunosuppressed state may further contribute to toxicity. Clearly, a balance exists between adequate immunosuppression and infection risk.

Hypertension. PRES is commonly seen in the setting of hypertension. The upper limits of autoregulation are not typically reached, but moderate-to-severe hypertension is seen in approximately 75% of patients with PRES. Often termed "hypertensive encephalopathy," the reported imaging patterns can vary.[6-8,35,89-93] Areas of deep white matter abnormality have been noted, which may overlap with lacunar disease and may relate to the known histologic findings in hypertension.[8,93,94] Hemispheric PRES patterns have been reported as well as isolated reversible brain stem and cerebellar edema, occasionally resulting in obstructive hydrocephalus.[35]

Recurrent PRES

Recurrent PRES has been anecdotally reported in severe hypertension and after allo-BMT.[66,80] In a recent reported series, recurrent PRES was noted in 3 (3.8%) of 78 patients and was associated with sickle-cell disease with infection, allo-BMT with infection, or atypical autoimmune disease and possible viral infection.[95] Recurrent eclampsia is well recognized with a reported incidence of ~2% of live births.[96]

Histopathology in PRES

Histologic evaluation of PRES is uncommon and often obtained late in the course of complex systemic disease. Biopsy/autopsy obtained during acute toxicity demonstrates vasogenic edema, paralleling observations on DWI.[17,76,97-99] Activated/reactive astrocytes, scattered macrophages, and lymphocytes have been often noted without inflammation, ischemia, or neuronal damage. Late autopsy studies have generally demonstrated evidence of demyelination and myelin pallor along with evidence of ischemia, neuronal anoxic damage, laminar necrosis, or older hemorrhage in the white matter and cortex.[11,13,17,100]

Evidence of acute and chronic vessel injury has been described in late autopsy studies with identification of intimal thickening, segmental vessel narrowing, intimal dissection, and organized thrombi.[11,101] Acute vasculopathy has also been described in a patient with a liver transplant with vessel inflammation and adjacent deep basal ganglia and periventricular infarction.[102]

Advanced Imaging in PRES

Cerebral Blood Vessels in PRES

At catheter angiography (CA), diffuse vasoconstriction, focal vasoconstriction, vasodilation, and even a string-of-beads appearance have been noted in PRES, consistent with what is typically described as vasospasm or arteritis (Fig 1*C*, -*D*).[2,4,14,51,54,103,104] Reported blood pressure in most of these patients demonstrated moderate but not severe hypertension (mean arterial pressure <130 mm Hg). CA in PRES is typically performed in eclampsia, delayed eclampsia, and after cancer chemotherapy, usually in the setting of a clinical presentation in which aneurysm is suspected.

At MRA using a 3D time of flight (TOF) technique, patterns resembling vasculopathy have been noted, with vessel irregularity consistent with focal vasoconstriction/vasodilation and diffuse vasoconstriction (Fig 1*E*).[17,36,60,95,103,105-108] When performed, repeat MRA often demonstrates reversal of the vasculopathy. In normotensive patients, vessels may appear normal or demonstrate pruning of distal intracranial branches, in particular the PCAs.[36]

Abnormal internal carotid or vertebral arteries have, on occasion, been noted in PRES, with intimal irregularity resembling fibromuscular disease demonstrated by CA in delayed eclampsia and dissection noted in PRES on MRA.[51,109] These CA/MRA features reflect previously described vessel histologic observations. MR venography has tended to be normal in PRES.[107]

Cerebral Blood Flow in PRES

The state of brain blood flow in PRES remains controversial (Review, Part 2). Vasoconstriction seen by CA in early studies prompted the authors to postulate that reduced brain perfusion led to the imaging features. In contrast, animal studies suggested that experimentally induced hypertension above the autoregulatory limit (mean arterial pressure >150–160 mm Hg) led to hyperperfusion, breakdown of the blood-brain barrier, and hemispheric edema.

Hyperperfusion was suggested in a single patient with PRES and Wegener's in an early study using technetium Tc99m-hexamethylpropyleneamine oxime (Tc99m-HMPAO) single-photon emission CT (SPECT), with a second patient (eclamptic) demonstrating variable radiotracer distribution.[18] In a later study, increased Tc99m-HMPAO SPECT activity suggesting hyperperfusion was reported in a single patient with a molar pregnancy and eclampsia.[110] In patients

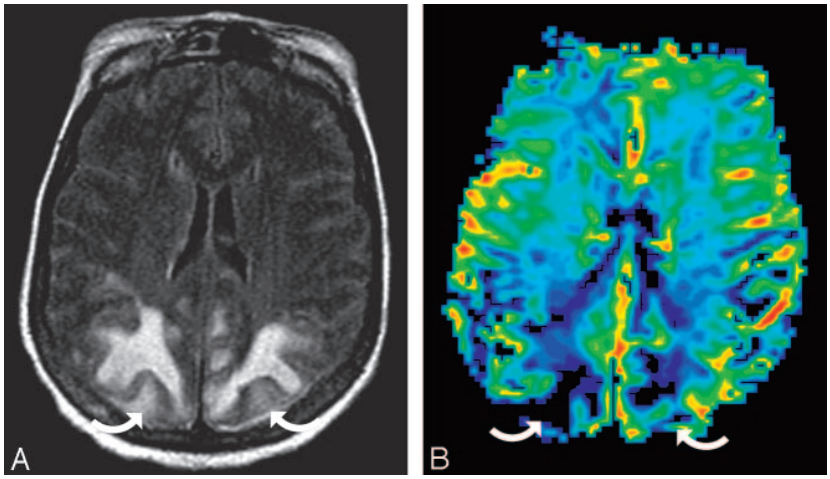

Fig 3. The patient is a 56-year-old woman with a thigh abscess (*Klebsiella* and *Enterococcus* species), baseline blood pressure of 156/68 mm Hg, and multiple organ failure (coagulopathy, acute respiratory distress syndrome, hepatic dysfunction with shock liver, and renal failure). She developed altered mentation and a seizure with toxicity blood pressure 164/75 mm Hg. *A,* Axial MR image (fluid-attenuated inversion recovery sequence) demonstrates extensive PRES vasogenic edema in the parietal region bilaterally (*curved arrows*). *B,* rCBV color map demonstrates severe flow reduction in the parietal region bilaterally (*curved arrows*), consistent with the regions of PRES imaging abnormality. PRES cortex rCBV relative to the reference cortex is 31% in the right parietal and 33% in the left parietal region.

with aneurysmal subarachnoid hemorrhage and vasospasm, Tc99m-HMPAO studies demonstrated patterns of variable perfusion.[111] Increased radiopharmaceutical activity in Tc99m-HMPAO brain studies has been noted in many circumstances associated with stroke but remains controversial.[112]

In contrast, watershed hypoperfusion has been demonstrated by using Tc99m-HMPAO SPECT in a large series of women with eclampsia, with focal hypoperfusion also noted after chemotherapy and in autoimmune disease (Fig 2).[63,113] Reduced perfusion has also been demonstrated using MR perfusion (MRP) in PRES (Fig 3).[103,114,115] Cortex and white matter relative cerebral blood volume (rCBV) has been shown to be reduced moderately in areas of PRES (average, 65%), when compared with normal uninvolved regions in 2 studies.[103,115] Comparing anterior-to-posterior hemispheric flow, Brubaker et al[114] found that MRP has also demonstrated significant posterior brain hypoperfusion with increased mean transit time, reduced CBV, and reduced cerebral blood flow.[114] Critical cortex hypoperfusion (12.2 mL/100 g brain per minute) has been demonstrated by stable xenon CT after blood pressure reduction in a child with hypertensive encephalopathy and PRES, which partially reversed with re-established moderate hypertension (mean arterial pressure, 114 mm Hg).[116]

Proton MR Spectroscopy in PRES

Reduced *N*-acetylaspartate:choline and *N*-acetylaspartate:creatinine ratios have been described by MR spectroscopy in regions of PRES vasogenic edema as well as in unaffected regions.[107,117,118] Quantitative metabolite assessment in 2 patients demonstrated an absolute reduction of metabolite concentration (considered a dilution effect from vasogenic edema), which corrected in 1 patient on follow-up MR spectroscopy.[117] Abnormal metabolite ratios may persist.[107] Lactate has been reported in PRES, and when accompanied by vasoconstriction, a contribution from ischemia has been suggested.[42,107]

The Controversy over the Mechanism of PRES

The cause of PRES is not yet understood. Hypertension with failed autoregulation and hyperperfusion remains a popular consideration for the developing brain edema.[18,92,119,120] Alternatively, endothelial dysfunction/injury, hypoperfusion, and vasoconstriction may lead to altered integrity of the blood-brain barrier.[4,121,122]

Although commonly cited, several problems exist with the hypertension/hyperperfusion theory. PRES is seen in the absence of hypertension in 20%–40% of patients.[17,27,36,39] In the remainder, though some degree of hypertension is present, reported blood pressure does not typically reach the limit of autoregulation (mean arterial pressure >150–160 mm Hg).[123] Also, several recent studies have noted less vasogenic edema in severely hypertensive patients when compared with normotensive patients, contrary to the expected result if severe hypertension with failed autoregulation was the mechanism behind PRES.[36,103] The biologic observations (strengths/weaknesses) related to both theories will be reviewed in detail in Part 2.

Conclusion

PRES develops in patients with complex systemic conditions such as eclampsia, after transplantation, in infection/sepsis/shock and autoimmune disease, and after cancer chemotherapy. Hypertension is absent in ~25% of patients and, when present, does not typically reach the level of failed autoregulation. The imaging appearance typically demonstrates symmetric vasogenic edema with several characteristic patterns, generally representing a distribution between lateral and medial cerebral arterial branches (ie, a watershed distribution). Vasculopathy is commonly identified by CA or MRA, and most studies have demonstrated reduced brain perfusion in regions of PRES. The mechanism responsible for the imaging appearance remains unclear and controversial.

References

1. Colosimo C Jr, Fileni A, Moschini M, et al. **CT findings in eclampsia.** *Neuroradiology* 1985;27:313–17
2. Lewis LK, Hinshaw DB Jr, Will AD, et al. **CT and angiographic correlation of severe neurological disease in toxemia of pregnancy.** *Neuroradiology* 1988;30:59–64
3. Naheedy MH, Biller J, Schiffer M, et al. **Toxemia of pregnancy: cerebral CT findings.** *J Comput Assist Tomogr* 1985;9:497–501
4. Trommer BL, Homer D, Mikhael MA. **Cerebral vasospasm and eclampsia.** *Stroke* 1988;19:326–29
5. Waldron RL 2nd, Abbott DC, Vellody D, et al. **Computed tomography in preeclampsia-eclampsia syndrome.** *AJNR Am J Neuroradiol* 1985;6:442–43
6. Fisher M, Maister B, Jacobs R. **Hypertensive encephalopathy: diffuse reversible white matter CT abnormalities.** *Ann Neurol* 1985;18:268–70
7. Rail DL, Perkin GD. **Computerized tomographic appearance of hypertensive encephalopathy.** *Arch Neurol* 1980;37:310–11
8. Weingarten K, Barbut D, Filippi C, et al. **Acute hypertensive encephalopathy: findings on spin-echo and gradient-echo MR imaging.** *AJR Am J Roentgenol* 1994;162:665–70
9. de Groen PC, Aksamit AJ, Rakela J, et al. **Central nervous system toxicity after**

liver transplantation: the role of cyclosporine and cholesterol. *N Engl J Med* 1987;317:861–66
10. Ghalie R, Fitzsimmons WE, Bennett D, et al. **Cortical blindness: a rare complication of cyclosporine therapy.** *Bone Marrow Transplant* 1990;6:147–49
11. Reece DE, Frei-Lahr DA, Shepherd JD, et al. **Neurologic complications in allogeneic bone marrow transplant patients receiving cyclosporin.** *Bone Marrow Transplant* 1991;8:393–401
12. Truwit CL, Denaro CP, Lake JR, et al. **MR imaging of reversible cyclosporin A-induced neurotoxicity.** *AJNR Am J Neuroradiol* 1991;12:651–59
13. Wilson SE, de Groen PC, Aksamit AJ, et al. **Cyclosporin A-induced reversible cortical blindness.** *J Clin Neuroophthalmol* 1988;8:215–20
14. Will AD, Lewis KL, Hinshaw DB, et al. **Cerebral vasoconstriction in toxemia.** *Neurology* 1987;37:1555–57
15. Hinchey J, Chaves C, Appignani B, et al. **A reversible posterior leukoencephalopathy syndrome.** *N Engl J Med* 1996;334:494–500
16. Bartynski WS, Grabb BC, Zeigler Z, et al. **Watershed imaging features and clinical vascular injury in cyclosporin A neurotoxicity.** *J Comput Assist Tomogr* 1997;21:872–80
17. Bartynski WS, Zeigler Z, Spearman MP, et al. **Etiology of cortical and white matter lesions in cyclosporin-A and FK-506 neurotoxicity.** *AJNR Am J Neuroradiol* 2001;22:1901–14
18. Schwartz RB, Bravo SM, Klufas RA, et al. **Cyclosporine neurotoxicity and its relationship to hypertensive encephalopathy: CT and MR findings in 16 cases.** *AJR Am J Roentgenol* 1995;165:627–31
19. Ay H, Buonanno FS, Schaefer PW, et al. **Posterior leukoencephalopathy without severe hypertension: utility of diffusion-weighted MRI.** *Neurology* 1998;51:1369–76
20. Covarrubias DJ, Luetmer PH, Campeau NG. **Posterior reversible encephalopathy syndrome: prognostic utility of quantitative diffusion-weighted MR images.** *AJNR Am J Neuroradiol* 2002;23:1038–48
21. Koch S, Rabinstein A, Falcone S, et al. **Diffusion-weighted imaging shows cytotoxic and vasogenic edema in eclampsia.** *AJNR Am J Neuroradiol* 2001;22:1068–70
22. Mukherjee P, McKinstry RC. **Reversible posterior leukoencephalopathy syndrome: evaluation with diffusion-tensor MR imaging.** *Radiology* 2001;219:756–65
23. Provenzale JM, Petrella JR, Cruz LC Jr, et al. **Quantitative assessment of diffusion abnormalities in posterior reversible encephalopathy syndrome.** *AJNR Am J Neuroradiol* 2001;22:1455–61
24. Schaefer PW, Buonanno FS, Gonzalez RG, et al. **Diffusion-weighted imaging discriminates between cytotoxic and vasogenic edema in a patient with eclampsia.** *Stroke* 1997;28:1082–85
25. Dahmus MA, Barton JR, Sibai BM. **Cerebral imaging in eclampsia: magnetic resonance imaging versus computed tomography.** *Am J Obstet Gynecol* 1992;167:935–41
26. Raroque HG Jr, Orrison WW, Rosenberg GA. **Neurologic involvement in toxemia of pregnancy: reversible MRI lesions.** *Neurology* 1990;40:167–69
27. Bartynski WS, Boardman JF. **Distinct imaging patterns and lesion distribution in posterior reversible encephalopathy syndrome.** *AJNR Am J Neuroradiol* 2007;28:1320–27
28. Oliverio PJ, Restrepo L, Mitchell SA, et al. **Reversible tacrolimus-induced neurotoxicity isolated to the brain stem.** *AJNR Am J Neuroradiol* 2000;21:1251–54
29. Casey SO, Truwit CL. **Pontine reversible edema: a newly recognized imaging variant of hypertensive encephalopathy?** *AJNR Am J Neuroradiol* 2000;21:243–45
30. de Seze J, Mastain B, Stojkovic T, et al. **Unusual MR findings of the brain stem in arterial hypertension.** *AJNR Am J Neuroradiol* 2000;21:391–94
31. Keswani SC, Wityk R. **Don't throw in the towel! A case of reversible coma.** *J Neurol Neurosurg Psychiatry* 2002;73:83–84
32. McKinney AM, Short J, Truwit CL, et al. **Posterior reversible encephalopathy syndrome: incidence of atypical regions of involvement and imaging findings.** *AJR Am J Roentgenol* 2007;189:904–12
33. Keyserling HF, Provenzale JM. **Atypical imaging findings in a near-fatal case of posterior reversible encephalopathy syndrome in a child.** *AJR Am J Roentgenol* 2007;188:219–21
34. Nussbaum ES, Maxwell RE, Bitterman PB, et al. **Cyclosporine A toxicity presenting with acute cerebellar edema and brainstem compression: case report.** *J Neurosurg* 1995;82:1068–70
35. Lin KL, Hsu WC, Wang HS, et al. **Hypertension-induced cerebellar encephalopathy and hydrocephalus in a male.** *Pediatr Neurol* 2006;34:72–75
36. Bartynski WS, Boardman JF, Zeigler ZR, et al. **Posterior reversible encephalopathy syndrome in infection, sepsis, and shock.** *AJNR Am J Neuroradiol* 2006;27:2179–90
37. Gijtenbeek JM, van den Bent MJ, Vecht CJ. **Cyclosporine neurotoxicity: a review.** *J Neurol* 1999;246:339–46
38. Garg RK. **Posterior leukoencephalopathy syndrome.** *Postgrad Med J* 2001;77:24–28
39. Sibai BM. **Eclampsia. VI. Maternal-perinatal outcome in 254 consecutive cases.** *Am J Obstet Gynecol* 1990;163:1049–54, discussion 1054–55
40. Furukawa M, Terae S, Chu BC, et al. **MRI in seven cases of tacrolimus (FK-506) encephalopathy: utility of FLAIR and diffusion-weighted imaging.** *Neuroradiology* 2001;43:615–21
41. Ishikura K, Ikeda M, Hamasaki Y, et al. **Posterior reversible encephalopathy syndrome in children: its high prevalence and more extensive imaging findings.** *Am J Kidney Dis* 2006;48:231–38
42. Kwon S, Koo J, Lee S. **Clinical spectrum of reversible posterior leukoencephalopathy syndrome.** *Pediatr Neurol* 2001;24:361–64
43. **Hypertensive disorders of pregnancy.** In: Cunningham FG, Gant NF, Leveno KJ, eds. *Williams Obstetrics.* 21st ed. New York: McGraw Hill; 2001:567–618
44. Dekker GA, Sibai BM. **Etiology and pathogenesis of preeclampsia: current concepts.** *Am J Obstet Gynecol* 1998;179:1359–75
45. Holler E, Kolb HJ, Hiller E, et al. **Microangiopathy in patients on cyclosporine prophylaxis who developed acute graft-versus-host disease after HLA-identical bone marrow transplantation.** *Blood* 1989;73:2018–24
46. Zoja C, Furci L, Ghilardi F, et al. **Cyclosporin-induced endothelial cell injury.** *Lab Invest* 1986;55:455–62
47. Zeigler ZR, Shadduck RK, Nemunaitis J, et al. **Bone marrow transplant-associated thrombotic microangiopathy: a case series.** *Bone Marrow Transplant* 1995;15:247–53
48. Haire WD. **The multiple organ dysfunction syndrome in cancer patients undergoing hematopoietic stem cell transplantation.** *Semin Thromb Hemost* 1999;25:223–37
49. Sanders TG, Clayman DA, Sanchez-Ramos L, et al. **Brain in eclampsia: MR imaging with clinical correlation.** *Radiology* 1991;180:475–78
50. Schwartz RB, Feske SK, Polak JF, et al. **Preeclampsia-eclampsia: clinical and neuroradiographic correlates and insights into the pathogenesis of hypertensive encephalopathy.** *Radiology* 2000;217:371–76
51. Bartynski WS, Sanghvi A. **Neuroimaging of delayed eclampsia: report of 3 cases and review of the literature.** *J Comput Assist Tomogr* 2003;27:699–713
52. Delefosse D, Samain E, Helias A, et al. **Late onset of cortical blindness in a patient with severe preeclampsia related to retained placental fragments.** *Anesthesiology* 2003;98:261–63
53. Malow BA, Sandson TA, Schwartz RB. **Reversible MRI lesions in eclampsia with hydatidiform mole.** *Neurology* 1990;40:1471–72
54. Aeby A, David P, Fricx C, et al. **Posterior reversible encephalopathy syndrome revealing acute post-streptococcal glomerulonephritis.** *J Child Neurol* 2006;21:250–51
55. Ozcakar ZB, Ekim M, Fitoz S, et al. **Hypertension induced reversible posterior leukoencephalopathy syndrome: a report of two cases.** *Eur J Pediatr* 2004;163:728–30
56. Yano Y, Kario K, Fukunaga T, et al. **A case of reversible posterior leukoencephalopathy syndrome caused by transient hypercoagulable state induced by infection.** *Hypertens Res* 2005;28:619–23
57. Kur JK, Esdaile JM. **Posterior reversible encephalopathy syndrome: an underrecognized manifestation of systemic lupus erythematosus.** *J Rheumatol* 2006;33:2178–83
58. Magnano MD, Bush TM, Herrera I, et al. **Reversible posterior leukoencephalopathy in patients with systemic lupus erythematosus.** *Semin Arthritis Rheum* 2006;35:396–402
59. Primavera A, Audenino D, Mavilio N, et al. **Reversible posterior leucoencephalopathy syndrome in systemic lupus and vasculitis.** *Ann Rheum Dis* 2001;60:534–37
60. Thaipisuttikul I, Phanthumchinda K. **Recurrent reversible posterior leukoencephalopathy in a patient with systemic lupus erythematosus.** *J Neurol* 2005;252:230–31
61. Cooney MJ, Bradley WG, Symko SC, et al. **Hypertensive encephalopathy: complication in children treated for myeloproliferative disorders—report of three cases.** *Radiology* 2000;214:711–16
62. Morris EB, Laningham FH, Sandlund JT, et al. **Posterior reversible encephalopathy syndrome in children with cancer.** *Pediatr Blood Cancer* 2007;48:152–59
63. Sanchez-Carpintero R, Narbona J, Lopez de Mesa R, et al. **Transient posterior encephalopathy induced by chemotherapy in children.** *Pediatr Neurol* 2001;24:145–48
64. Pihko H, Tyni T, Virkola K, et al. **Transient ischemic cerebral lesions during induction chemotherapy for acute lymphoblastic leukemia.** *J Pediatr* 1993;123:718–24
65. Kishi Y, Miyakoshi S, Kami M, et al. **Early central nervous system complications after reduced-intensity stem cell transplantation.** *Biol Blood Marrow Transplant* 2004;10:561–68
66. Wong R, Beguelin GZ, de Lima M, et al. **Tacrolimus-associated posterior reversible encephalopathy syndrome after allogeneic haematopoietic stem cell transplantation.** *Br J Haematol* 2003;122:128–34
67. Zimmer WE, Hourihane JM, Wang HZ, et al. **The effect of human leukocyte antigen disparity on cyclosporine neurotoxicity after allogeneic bone marrow transplantation.** *AJNR Am J Neuroradiol* 1998;19:601–08, discussion 609–10
68. Kanekiyo T, Hara J, Matsuda-Hashii Y, et al. **Tacrolimus-related encephalopathy following allogeneic stem cell transplantation in children.** *Int J Hematol* 2005;81:264–68
69. Bartynski WS, Zeigler ZR, Shadduck RK, et al. **Pretransplantation condition-**

ing influence on the occurrence of cyclosporine or FK-506 neurotoxicity in allogeneic bone marrow transplantation. *AJNR Am J Neuroradiol* 2004;25:261–69
70. Bartynski WS, Zeigler ZR, Shadduck RK, et al. **Variable incidence of cyclosporine and FK-506 neurotoxicity in hematopoeitic malignancies and marrow conditions after allogeneic bone marrow transplantation.** *Neurocrit Care* 2005;3:33–45
71. Chohan R, Vij R, Adkins D, et al. **Long-term outcomes of allogeneic stem cell transplant recipients after calcineurin inhibitor-induced neurotoxicity.** *Br J Haematol* 2003;123:110–13
72. Provenzale JM, Graham ML. **Reversible leukoencephalopathy associated with graft-versus-host disease: MR findings.** *AJNR Am J Neuroradiol* 1996;17:1290–94
73. Jarosz JM, Howlett DC, Cox TC, et al. **Cyclosporine-related reversible posterior leukoencephalopathy: MRI.** *Neuroradiology* 1997;39:711–15
74. Small SL, Fukui MB, Bramblett GT, et al. **Immunosuppression-induced leukoencephalopathy from tacrolimus (FK506).** *Ann Neurol* 1996;40:575–80
75. Appignani BA, Bhadelia RA, Blacklow SC, et al. **Neuroimaging findings in patients on immunosuppressive therapy: experience with tacrolimus toxicity.** *AJR Am J Roentgenol* 1996;166:683–88
76. Lanzino G, Cloft H, Hemstreet MK, et al. **Reversible posterior leukoencephalopathy following organ transplantation: description of two cases.** *Clin Neurol Neurosurg* 1997;99:222–26
77. Shimono T, Miki Y, Toyoda H, et al. **MR imaging with quantitative diffusion mapping of tacrolimus-induced neurotoxicity in organ transplant patients.** *Eur Radiol* 2003;13:986–93
78. Besenski N, Rumboldt Z, Emovon O, et al. **Brain MR imaging abnormalities in kidney transplant recipients.** *AJNR Am J Neuroradiol* 2005;26:2282–89
79. Parvex P, Pinsk M, Bell LE, et al. **Reversible encephalopathy associated with tacrolimus in pediatric renal transplants.** *Pediatr Nephrol* 2001;16:537–42
80. Reinohs M, Straube T, Baum P, et al. **Recurrent reversible cerebral edema after long-term immunosuppression with tacrolimus.** *J Neurol* 2002;249:780–81
81. Singh N, Bonham A, Fukui M. **Immunosuppressive-associated leukoencephalopathy in organ transplant recipients.** *Transplantation* 2000;69:467–72
82. Wijdicks EF. **Neurotoxicity of immunosuppressive drugs.** *Liver Transpl* 2001;7:937–42
83. Bartynski WS, Tan HP, Boardman JF, et al. **Posterior reversible encephalopathy syndrome after solid organ transplantation.** *AJNR Am J Neuroradiol* 2008;29:924–30
84. Ramanathan V, Helderman JH. **Cyclosporine formulations.** In: Sayegh M, Remuzzi G, eds. *Current and Future Immunosuppressive Therapies Following Transplantation.* The Netherlands: Kluwer Academic; 2001:111–21
85. Shapiro R. **Tacrolimus.** In: Sayegh M, Remuzzi G, eds. *Current and Future Immunosuppressive Therapies Following Transplantation.* The Netherlands: Kluwer Academic; 2001:123–42
86. Wijdicks EFM. **Neurologic manifestations of immunosuppressive agents.** In: Wijdicks EFM, ed. *Neurologic Complications in Organ Transplant Recipients.* Boston: Butterworth-Heinemann; 1999:127–40
87. Furlong T, Storb R, Anasetti C, et al. **Clinical outcome after conversion to FK 506 (tacrolimus) therapy for acute graft-versus-host disease resistant to cyclosporine or for cyclosporine-associated toxicities.** *Bone Marrow Transplant* 2000;26:985–91
88. Kon V, Sugiura M, Inagami T, et al. **Role of endothelin in cyclosporine-induced glomerular dysfunction.** *Kidney Int* 1990;37:1487–91
89. Hauser RA, Lacey DM, Knight MR. **Hypertensive encephalopathy: magnetic resonance imaging demonstration of reversible cortical and white matter lesions.** *Arch Neurol* 1988;45:1078–83
90. Jones BV, Egelhoff JC, Patterson RJ. **Hypertensive encephalopathy in children.** *AJNR Am J Neuroradiol* 1997;18:101–06
91. Kwong YL, Yu YL, Lam KS, et al. **CT appearance in hypertensive encephalopathy.** *Neuroradiology* 1987;29:215
92. Schwartz RB, Jones KM, Kalina P, et al. **Hypertensive encephalopathy: findings on CT, MR imaging, and SPECT imaging in 14 cases.** *AJR Am J Roentgenol* 1992;159:379–83
93. Weingarten KL, Zimmerman RD, Pinto RS, et al. **Computed tomographic changes of hypertensive encephalopathy.** *AJNR Am J Neuroradiol* 1985;6:395–98
94. Chester EM, Agamanolis DP, Banker BQ, et al. **Hypertensive encephalopathy: a clinicopathologic study of 20 cases.** *Neurology* 1978;28:928–39
95. Sweany JM, Bartynski WS, Boardman JF. **"Recurrent" posterior reversible encephalopathy syndrome: report of 3 cases—PRES can strike twice!** *J Comput Assist Tomogr* 2007;31:148–56
96. Sibai BM, Sarinoglu C, Mercer BM. **Eclampsia. VII. Pregnancy outcome after eclampsia and long-term prognosis.** *Am J Obstet Gynecol* 1992;166(6 Pt 1): 1757–61, discussion 1761–63
97. Schiff D, Lopes MB. **Neuropathological correlates of reversible posterior leukoencephalopathy.** *Neurocrit Care* 2005;2:303–05
98. Thyagarajan GK, Cobanoglu A, Johnston W. **FK506-induced fulminant leukoencephalopathy after single-lung transplantation.** *Ann Thorac Surg* 1997;64:1461–64
99. Velu T, Debusscher L, Stryckmans PA. **Cyclosporin-associated fatal convulsions.** *Lancet* 1985;1:219
100. Vaughn DJ, Jarvik JG, Hackney D, et al. **High-dose cytarabine neurotoxicity: MR findings during the acute phase.** *AJNR Am J Neuroradiol* 1993;14:1014–16
101. Koide T, Yamada M, Takahashi T, et al. **Cyclosporine A-associated fatal central nervous system angiopathy in a bone marrow transplant recipient: an autopsy case.** *Acta Neuropathol* 2000;99:680–84
102. Pizzolato GP, Sztajzel R, Burkhardt K, et al. **Cerebral vasculitis during FK 506 treatment in a liver transplant patient.** *Neurology* 1998;50:1154–57
103. Bartynski WS, Boardman JF. **Catheter angiography, MR angiography, and MR perfusion in posterior reversible encephalopathy syndrome.** *AJNR Am J Neuroradiol.* 2008;29:447–55
104. Geraghty JJ, Hoch DB, Robert ME, et al. **Fatal puerperal cerebral vasospasm and stroke in a young woman.** *Neurology* 1991;41:1145–47
105. Ito T, Sakai T, Inagawa S, et al. **MR angiography of cerebral vasospasm in preeclampsia.** *AJNR Am J Neuroradiol* 1995;16:1344–46
106. Lin JT, Wang SJ, Fuh JL, et al. **Prolonged reversible vasospasm in cyclosporin A-induced encephalopathy.** *AJNR Am J Neuroradiol* 2003;24:102–04
107. Sengar AR, Gupta RK, Dhanuka AK, et al. **MR imaging, MR angiography, and MR spectroscopy of the brain in eclampsia.** *AJNR Am J Neuroradiol* 1997;18:1485–90
108. Shbarou RM, Chao NJ, Morgenlander JC. **Cyclosporin A-related cerebral vasculopathy.** *Bone Marrow Transplant* 2000;26:801–04
109. Mellion ML, Rizvi S. **Spontaneous bilateral carotid artery dissection and posterior reversible encephalopathy syndrome.** *Neurology* 2005;65:1990
110. Apollon KM, Robinson JN, Schwartz RB, et al. **Cortical blindness in severe preeclampsia: computed tomography, magnetic resonance imaging, and single-photon-emission computed tomography findings.** *Obstet Gynecol* 2000;95:1017–19
111. Lewis DH, Eskridge JM, Newell DW, et al. **Brain SPECT and the effect of cerebral angioplasty in delayed ischemia due to vasospasm.** *J Nucl Med* 1992;33:1789–96
112. Sugawara Y, Ueda T, Kikuchi T, et al. **Hyperactivity of 99mTc-HMPAO within 6 hours in patients with acute ischemic stroke.** *J Nucl Med* 2001;42:1297–302
113. Naidu K, Moodley J, Corr P, et al. **Single photon emission and cerebral computerised tomographic scan and transcranial Doppler sonographic findings in eclampsia.** *Br J Obstet Gynaecol* 1997;104:1165–72
114. Brubaker LM, Smith JK, Lee YZ, et al. **Hemodynamic and permeability changes in posterior reversible encephalopathy syndrome measured by dynamic susceptibility perfusion-weighted MR imaging.** *AJNR Am J Neuroradiol* 2005;26:825–30
115. Engelter ST, Petrella JR, Alberts MJ, et al. **Assessment of cerebral microcirculation in a patient with hypertensive encephalopathy using MR perfusion imaging.** *AJR Am J Roentgenol* 1999;173:1491–93
116. Casey SO, McKinney A, Teksam M, et al. **CT perfusion imaging in the management of posterior reversible encephalopathy.** *Neuroradiology* 2004;46:272–76
117. Eichler FS, Wang P, Wityk RJ, et al. **Diffuse metabolic abnormalities in reversible posterior leukoencephalopathy syndrome.** *AJNR Am J Neuroradiol* 2002;23:833–37
118. Russell MT, Nassif AS, Cacayorin ED, et al. **Gemcitabine-associated posterior reversible encephalopathy syndrome: MR imaging and MR spectroscopy findings.** *Magn Reson Imaging* 2001;19:129–32
119. Strandgaard S, Olesen J, Skinhoj E, et al. **Autoregulation of brain circulation in severe arterial hypertension.** *BMJ* 1973;1:507–10
120. Dinsdale HB. **Hypertensive encephalopathy.** *Neurol Clin* 1983;1:3–16
121. Coughlin WF, McMurdo SK, Reeves T. **MR imaging of postpartum cortical blindness.** *J Comput Assist Tomogr* 1989;13:572–76
122. Toole JF. **Lacunar syndromes and hypertensive encephalopathy**. In: Toole JF, ed. *Cerebrovascular Disorders.* 5th ed. New York: Raven; 1999:342–55
123. Zwienenberg-Lee M, Muizelaar JP. **Clinical pathophysiology of traumatic brain injury.** In: HR W, ed. *Youmans Neurological Surgery*. 5th ed. Philadelphia: Saunders; 2004:5039–64

A Neuroradiologist's Guide to Operationalizing the Response Assessment in Neuro-Oncology (RANO) Criteria Version 2.0 for Gliomas in Adults

Benjamin M. Ellingson, Francesco Sanvito, Timothy F. Cloughesy, Raymond Y. Huang, Javier E. Villanueva-Meyer, Whitney B. Pope, Daniel P. Barboriak, Lalitha K. Shankar, Marion Smits, Timothy J. Kaufmann, Jerrold L. Boxerman, Michael Weller, Evanthia Galanis, John de Groot, Mark R. Gilbert, Andrew B. Lassman, Mark S. Shiroishi, Ali Nabavizadeh, Minesh Mehta, Roger Stupp, Wolfgang Wick, David A. Reardon, Michael A. Vogelbaum, Martin van den Bent, Susan M. Chang, and Patrick Y. Wen

ABSTRACT

SUMMARY: Radiographic assessment plays a crucial role in the management of patients with central nervous system (CNS) tumors, aiding in treatment planning and evaluation of therapeutic efficacy by quantifying response. Recently, an updated version of the Response Assessment in Neuro-Oncology (RANO) criteria (RANO 2.0) was developed to improve upon prior criteria and provide an updated, standardized framework for assessing treatment response in clinical trials for gliomas in adults. This article provides an overview of significant updates to the criteria including (1) the use of a unified set of criteria for high and low grade gliomas in adults; (2) the use of the post-radiotherapy MRI scan as the baseline for evaluation in newly diagnosed high-grade gliomas; (3) the option for the trial to mandate a confirmation scan to more reliably distinguish pseudoprogression from tumor progression; (4) the option of using volumetric tumor measurements; and (5) the removal of subjective non-enhancing tumor evaluations in predominantly enhancing gliomas (except for specific therapeutic modalities). Step-by-step pragmatic guidance is hereby provided for the neuroradiologist and imaging core lab involved in operationalization and technical execution of RANO 2.0 in clinical trials, including the display of representative cases and in-depth discussion of challenging scenarios.

ABBREVIATIONS: BTIP = Brain Tumor Imaging Protocol; CE = Contrast-Enhancing; CNS = Central Nervous System; CR = Complete Response; ECOG = Eastern Cooperative Oncology Group; HGG = High-Grade Glioma; IDH = Isocitrate Dehydrogenase; IRF = Independent Radiologic Facility; KPS = Karnofsky Performance Status; LGG = Low-Grade Glioma; MR = Minor Response; mRANO = Modified RANO; NANO = Neurological Assessment in Neuro-Oncology; ORR = Objective Response Rate; OS = Overall Survival; PD = Progressive Disease; PFS = Progression-Free Survival; PR = Partial Response; PsP = Pseudoprogression; RANO = Response Assessment in Neuro-Oncology; RECIST = Response Evaluation Criteria In Solid Tumors; RT = Radiation Therapy; SD = Stable Disease; Tx = Treatment

Gliomas are the most common malignant primary brain tumors[1] and have few effective therapies[2,3]. Overall survival (OS) is considered the definitive benchmark for determining treatment efficacy in gliomas, but can be clouded by several confounding factors – particularly in single-arm phase I-II trials – including age, tumor size, molecular status and neurological status, and off-study therapies before or after the treatment of interest[4,5]. To gain a more accurate understanding of the value of a given treatment, earlier radiographic endpoints are desirable, including objective response rate (ORR) and progression-free survival (PFS)[6].

Received May 6, 2024; accepted after revision June 22.

From UCLA Brain Tumor Imaging Laboratory, Department of Radiological Sciences (B.M.E., F.S.), and Department of Radiological Sciences (W.B.P.), and UCLA Brain Tumor Program, Department of Neurology (T.F.C.), David Geffen School of Medicine, University of California Los Angeles, Los Angeles, CA; Department of Radiology, Brigham and Women's Hospital (R.Y.H.), Harvard Medical School, Boston, MA; Departments of Radiology and Neurosurgery (J.E.V.-M.), and Division of Neuro-Oncology, Department of Neurosurgery (J.d.G., S.M.C.), University of California, San Francisco, CA; Department of Radiology (D.P.B.), Duke University Medical Center, Durham, NC; Clinical Trials Branch, Cancer Imaging Program (L.K.S.), and Neuro-Oncology Branch, Center for Cancer Research (M.R.G.), National Cancer Institute, National Institutes of Health, Bethesda, MD; Department of Radiology & Nuclear Medicine (M.S.), Erasmus MC - University Medical Centre Rotterdam, Rotterdam, The Netherlands; Department of Radiology (T.J.K.), and Department of Oncology (E.G.), Mayo Clinic, Rochester, MN; Department of Neurology (M.W.), University Hospital and University of Zurich, Zurich, Switzerland; Department of Diagnostic Imaging (J.L.B.), Rhode Island Hospital and Alpert Medical School of Brown University, Providence, RI; Division of Neuro-Oncology, Department of Neurology, Herbert Irving Comprehensive Cancer Center and Irving Institute for Clinical and Translational Research (A.B.L.), Columbia University Vagelos College of Physicians and Surgeons and New York-Presbyterian Hospital, New York, NY; Department of Radiology (M.S.S.), Keck School of Medicine of the University of Southern California (USC), Los Angeles, CA; Department of Radiology, Perelman School of Medicine (A.N.), University of Pennsylvania, Philadelphia, PA; Miami Cancer Institute (M.M.), Miami, FL; Malnati Brain Tumor Institute, Lurie Comprehensive Cancer Center and Departments of Neurological Surgery, Neurology and Division of Hematology/Oncology (R.S.), Northwestern University, Chicago, IL; Department of Neurology Heidelberg University Hospital & Clinical Cooperation Unit Neurooncology (W.W.), German Cancer Consortium (DKTK), German Cancer Research Center (DKFZ), Heidelberg, Germany; Center For Neuro-Oncology, Dana-Farber Cancer Institute and Harvard Medical School (D.A.R., P.Y.W.), Boston, MA; Department of Neuro-Oncology, (M.A.V.), Moffitt Cancer Center, Tampa, FL; and Department Neuro-Oncology (M.v.d.B.), Erasmus MC Cancer Institute, Rotterdam, The Netherlands.

Benjamin M. Ellingson and Francesco Sanvito contributed equally.

Corresponding Author: Benjamin M. Ellingson, Ph.D. Professor and Director of MRI Research, Director, UCLA Brain Tumor Imaging Laboratory, UCLA Radiology, e-mail: bellingson@mednet.ucla.edu

Indicates article with online supplemental data.

http://dx.doi.org/10.3174/ajnr.A8396

Table 1: Main features of RANO 2.0

RANO 2.0 overview	
Baseline	
Newly diagnosed tumors	Post-RT scan
Recurrent tumors	Pre-Tx scan
Tumor components to evaluate	
CE tissue	In all tumors
Non-CE tissue	- In non-CE tumors - In "mixed" tumors with CE + non-CE components - Optional in CE tumors for trials using agents that affect vascular permeability (e.g., antiangiogenic)
Measurement technique	
Sum of bidimensional products *or* volumetric segmentations	
Thresholds applied to target lesions	
CR	complete disappearance of all lesions
PD	≥ +25% in sum of bidimensional products *or* ≥ +40% in volume
PR	≤ –50% in sum of bidimensional products *or* ≤ –65% in volume
MR[a]	≤ –25% and > –50% in sum of bidimensional products *or* ≤ –40% and > –65% in volume
SD	criteria for CR / PR / MR / PD are not met
Confirmatory scans (performed after >4 weeks)	
For PD	- Mandatory for CE tumors ≤12 weeks from RT - Optional for CE tumors >12 weeks from RT (recommended for agents[b] highly associated with PsP) - Unnecessary for non-CE tumors
For CR/PR	Mandatory for all tumors at all timepoints

Note:—CE indicates contrast-enhancing; CR, complete response; MR, minor response; PD, progressive disease; PsP, pseudoprogression; PR, partial response; RT, radiotherapy; SD, stable disease; Tx, treatment.

[a] MR only applies to non-CE disease.

[b] e.g., immunotherapies.

Starting in 2010, the Response Assessment in Neuro-Oncology (RANO) Working Group developed updated response criteria for high- (RANO-HGG)[7] and low-grade gliomas (RANO-LGG)[8], aiming to enhance the reliability and comparability of response assessments in clinical trials. In 2017, "modified" RANO criteria (mRANO)[9] were introduced after years of data collection and experience with the original RANO. mRANO introduced new concepts that are now integrated into the RANO 2.0 criteria[10], including the use of the post-radiotherapy (post-RT) MRI as baseline scan in newly diagnosed glioblastoma, volumetric equivalent thresholds for response, the removal of non-contrast-enhancing (non-CE) areas evaluation in glioblastoma, and the requirement for confirmation scan to distinguish progression from pseudoprogression (PsP) – the latter being limited to the first 3 months after RT completion in RANO 2.0 or limited to agents at high risk of PsP (e.g., immunotherapies).

Since the 2021 classification of CNS tumors[11], based on combined histological and molecular characteristics, often blurs the traditional distinction between HGGs and LGGs, RANO 2.0 guidelines[10] propose unified criteria for all gliomas, based on recent data from clinical trials[12,13]. This article presents a summary of changes and a guide for how to operationalize RANO 2.0 in clinical trials.

STANDARDIZED BRAIN TUMOR IMAGING PROTOCOL (BTIP) AND RADIOGRAPHIC READ PARADIGMS

RANO 2.0 recommends the use of the standardized glioma BTIP[14,15] for clinical trials (Online Supplemental Data), which features parameter-matched pre- and post-contrast 3D T_1-weighted images with high spatial resolution (≤1.5 mm isotropic), and either 2D (with ≤4 mm slice thickness) or 3D (≤1.5 mm isotropic) T_2-weighted and T_2-weighted FLAIR images[15]. 3D T_2w and T_2w-FLAIR images are encouraged, if available, as they allow better multiplanar reconstruction, tilt adjustment, image registration and volumetric segmentation, which may be preferred in slower growing LGGs as some evidence shows better inter-reader agreement compared to 2D measurements[16]. Although not included in the RANO evaluations, it is encouraged for clinical trials to collect standardized DSC perfusion acquisitions as part of the imaging protocol[15,17].

In addition to the acquisition protocol, the radiographic read paradigm should also be standardized for clinical trials. Later stage clinical trials often require a central review of imaging studies at an independent radiologic facility (IRF) for determination of both eligibility and radiographic response[18]. Eligibility reads in recurrent trials should confirm disease progression before the enrollment[10], while eligibility reads to rule out the presence of contrast-enhancement (CE) in LGG, multifocal disease, or lesions larger than a certain size may also be performed if required by the particular trial. For response, the IRF should adopt a specific read paradigm in collaboration with the sponsor, which will dictate standardized procedures for the reading queue and for the adjudication design, as previously described[18] (Online Supplemental Data). According to different reading queue designs, images can be presented either simultaneously or sequentially, and the corresponding timepoints can be displayed either in chronological or randomized order, either with a "locked" modality or a "hybrid" modality (Online Supplemental Data).

OVERVIEW OF UPDATES IN RANO 2.0

Improvements to RANO (Table 1) were based on consensus recommendations agreed upon by a panel of expert neuroradiologists, neuro-oncologists, neurologists, neurosurgeons, radiation oncologists, and imaging scientists, based on RANO-HGG[7], RANO-LGG[8], and mRANO[9] recommendations, practical considerations, and data gathered from clinical trials[12]. Importantly, RANO 2.0 allow a degree of flexibility, depending on the trial and sponsor needs, and provide standardized language to be incorporated into the protocol document.

Baseline Scan

For newly diagnosed glioblastoma, the first post-RT scan (21-35 days after RT completion) should be used as a reference baseline

for response assessment, *not* the post-surgical or the pre-RT scan. While these scans may be considered in the clinical practice, they should not be evaluated in RANO reads for clinical trials. This recommendation is based on the fact that post-surgical pre-RT scan is typically performed prior to trial enrollment, therefore frequently off study protocol, and is often contaminated by post-surgical changes which can confound the assessment of disease burden. More importantly, subsequent analyses have demonstrated that tumor shrinkage[19] and PFS[12] are better correlated with OS using the first post-RT scan as a reference. Additionally, this scan is often used as a reference in clinical practice due to uncertain radiographic changes during chemoradiation (i.e., possible PsP). Since the radiographic endpoint in the newly-diagnosed setting is typically PFS, the first post-RT scan should also be used as baseline in trials testing RT schemes and/or treatments concomitant with RT to better mitigate issues related to identification of disease progression. The post-surgical MRI acquired within 72 hours after surgery should still be used to evaluate post-surgical complications and extent of resection.

Also in trials for newly diagnosed gliomas that do not involve RT, such as some LGG trials, the MRI acquired up to 72 hours post-surgery is *not* recommended as a baseline for treatment response assessment. Instead, a pre-treatment (pre-Tx) scan should be acquired and used as a baseline, with a standardized timing (defined in the study protocol) with regards both to the day of surgery, to allow sufficient time for post-surgical changes to resolve, and to the day of treatment initiation, to minimize interval tumor growth prior to the start of therapy ($\leq$14 days between the pre-Tx scan and treatment initiation).

For recurrent gliomas, a pre-Tx scan should be used as baseline, with a standardized time interval before the start of treatment. The time interval should be as short as possible to minimize the degree of tumor growth taking place between the pre-Tx scan and the start of the treatment[20], and should always be $\leq$14 days and preferably $\leq$1 week[10]. For trials testing re-irradiation in the recurrent setting, the choice of the baseline scan (pre- or post-re-irradiation) should be selected depending on the radiographic endpoint (ORR or PFS), noting that post-RT changes can complicate response assessment probably even more so in the recurrent setting.

Type of Tumor Components to Evaluate (CE and/or Non-CE)

RANO 2.0 acknowledges three radiographic presentations of gliomas: CE tumors, non-CE tumors, and "tumors with both enhancing and non-enhancing components" ("mixed" gliomas for brevity). Typical glioblastomas presenting as predominantly enhancing lesions are considered CE tumors, whereas tumors that are largely non-enhancing and only present spots/nodules of enhancement should be categorized as "mixed" (e.g., some grade 3 IDH-mutant gliomas). These three radiographic presentations correspond to dedicated RANO 2.0 rules for response assessment. The choice between applying the "CE tumor" rules or the "mixed tumor" rules should be prospectively defined and uniformly applied across all enrolled patients within a trial, depending on the expected radiographic features of the enrolled patients as per the inclusion/exclusion criteria. A clinical trial enrolling patients with tumors that are expected to present as "mixed" may choose to adopt the dedicated criteria and uniformly apply them to all patients, regardless of the case-by-case radiographic appearance. As an example, some recent trials decided to evaluate both CE and non-CE components in recurrent grade 3 astrocytomas (NCT02796261) and in diffuse midline gliomas (NCT05009992).

For all tumors (CE, non-CE, and mixed) the changes in CE components are crucial to establish treatment response, including either the size change of existing CE areas and/or the appearance of new CE lesions. On the other hand, assessing changes in non-CE components is required for non-CE tumors and mixed tumors, but is *not* required for CE tumors such as glioblastoma (although optional for trials testing agents that are expected to significantly reduce vascular permeability – e.g., anti-angiogenic medications). Data suggests that the evaluation of non-CE areas in glioblastoma does not provide much value, adds complexity and costs, and does not improve the association between PFS and OS[12,21].

Measurement Technique

Either bidirectional diameters ("2D measurements") or volumetric assessments ("3D measurements") can be used in RANO 2.0. With 2D measurements, the tumor burden is computed by *adding* the products of the two perpendicular diameters of each target lesion (i.e., sum of bidirectional products). 3D measurements are based on lesion segmentation, whether manual, semi-automated, or fully automated (when available). All segmentations should be formally approved by the human reader. Within a given trial, 2D *or* 3D measurements should be chosen *a priori* and applied consistently.

Thresholds for Response and Progression

The 2D thresholds for response and progression in RANO 2.0 are unchanged from previous RANO, while 3D thresholds are adopted from mRANO. Radiographic progressive disease (PD) or preliminary PD is defined as a 25% (2D measurements) or a 40% (3D measurements) increase in tumor burden. Partial response (PR) or preliminary PR is defined as a 50% (2D measurements) or a 65% (3D measurements) decrease in tumor burden. Finally, a minor response (MR) category is applicable only to non-CE components, if a tumor burden decrease is observed in the range of 25–50% (2D) or 40–65% (3D).

Use of Confirmation Scans for Response and Progression

For response (MR/PR/CR), confirmation scans after $\geq$4 weeks to demonstrate durable response are required, consistent with all previous RANO guidelines. As for PD, confirmation scans were required for mRANO, and optional in the original RANO-HGG in case of uncertainty or borderline progression. RANO 2.0 only requires confirmation of progression $\leq$12 weeks after RT completion. Additionally, confirmation of progression is optional if progression occurs $>$12 weeks after RT completion, but strongly advised in trials testing agents that are expected to be highly associated with PsP (e.g., immunotherapies). In the recurrent setting there can be significant tumor growth between the baseline or screening scans and the start of treatment which can "artificially" trigger a PD categorization at the first follow-up even if the treatment is effective[20]. Ideally, a "*hyperacute*" baseline scan should be

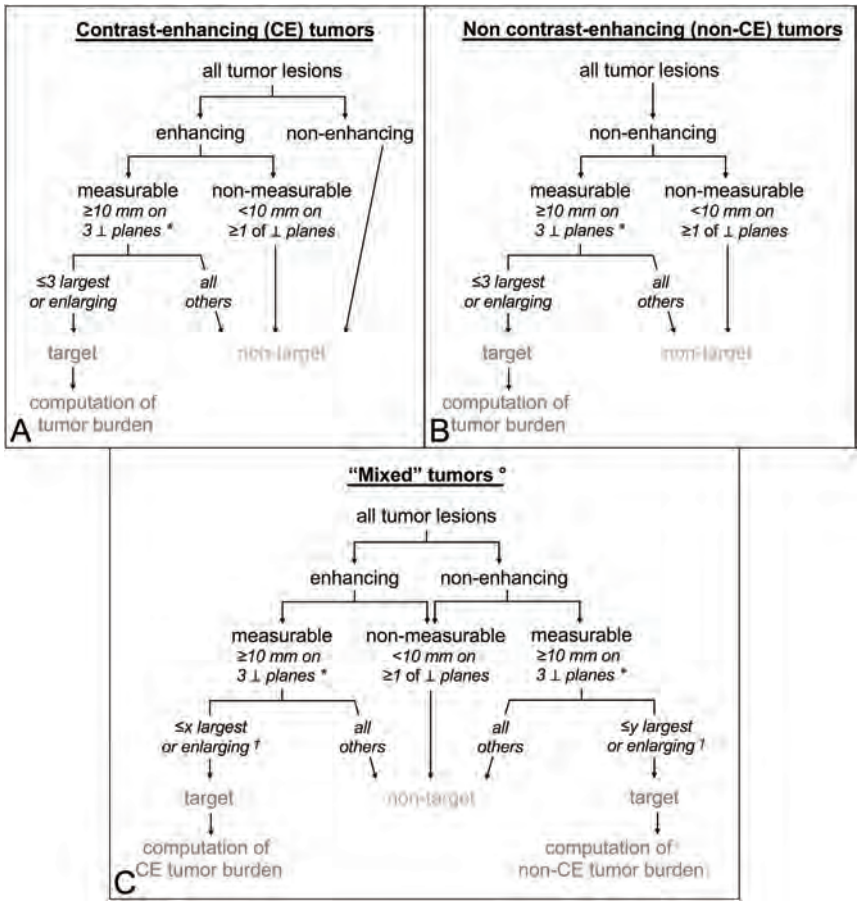

FIG 1. Flow-chart to identify target lesions for CE (*A*), non-CE (*B*), and "mixed" (*C*) tumors. * the size condition for measurable disease is: ≥10 mm on 3 ⊥ planes for 3D images with thin slice (more often applied to CE disease), or ≥ 10 mm on in-plane ⊥ diameters and visible on ≥2 slices for 2D images with thicker slice (more often applied to non-CE disease). Of note, these conditions apply to trials employing bidimensional measurements for treatment response assessment, while for trials employing volumetric segmentations various strategies can be applied for the identification of target lesions (please refer to the dedicated paragraph in the main text). ° "mixed" tumors is short for "tumors with both CE and non-CE components". † in mixed tumors, up to a total of 4 target lesions is allowed (i.e., x + y ≤ 4).

acquired 1-2 days before treatment initiation to negate the influence of this interval growth[20]. However, if this is not possible, an alternative approach would be to consider confirmation of progression for lesions showing progressive disease at the first follow-up scan. The conditions for when and if to use confirmation scans for progression should be dictated by the sponsor and articulated in the study protocol and imaging charter. Of note, after PD confirmation, the date of PD should be backdated, as explained in the following paragraphs.

DEFINITIONS OF MEASURABLE, NON-MEASURABLE, AND TARGET LESIONS (FIGURE 1)

Measurable disease is defined as one or more lesions with clear margins *and* meeting a minimal size threshold. On 3D images, a measurable lesion should have ≥10 mm diameters in all three perpendicular planes. On 2D images, the size threshold is met if both in-plane diameters are ≥10 mm on ≥2 consecutive slices. These criteria apply to both CE and non-CE disease, although in CE tumors only CE lesions can be considered as "target" lesions.

Non-measurable disease includes all lesions not meeting the criteria for measurable disease, either because they are smaller or because their margins are ill-defined. Of note, measurements should never include cystic or necrotic portions, nor the resection cavity. For instance, the rim enhancement surrounding the surgical cavity or surrounding cystic components should be categorized as non-measurable, unless presenting an enhancing nodule that meets the criteria for measurable disease.

Target lesions are measurable lesions selected to be used for the longitudinal quantification of tumor burden. If the baseline scan shows multiple measurable lesions, ≥3 lesions (≥4 for "mixed" tumors) can be selected as target lesions and their size is *combined* to quantify the overall tumor burden. Identifying multiple *components* as target lesions may also be acceptable in cases where a single lesion features two or more separated measurable components connected by non-measurable components (e.g., two clear distinct CE nodules located along a pericavitary rim enhancement, or two well-demarcated non-CE nodules connected by infiltrative components with unclear boundaries). In case of >3 measurable lesions, larger lesions are preferred as targets, or preferably lesions that showed a size increase on the eligibility read (for recurrent tumors). If a simultaneous presentation or a "hybrid" reading queue is used, the choice of target lesions can also be informed by their on-study growth.

Non-target lesions should be evaluated or monitored, but their size is not incorporated in the assessment of the overall tumor burden. If previously non-measurable lesions grow and become measurable, they can become target lesions, and their size is then incorporated into the overall tumor burden.

METHODOLOGY FOR 2D MEASUREMENTS (FIGURE 2)

Measurement Protocol

When 2D measurements are used, the overall tumor burden should be calculated as the *sum* of all bidimensional products of target lesions. Target lesions should be measured on the plane and the slice where they display the largest area (the "main" plane and slice), and the reader should measure the lesion in additional planes (with 3D imaging) or slices (with 2D imaging) to confirm that the conditions for "measurable" disease are met (Figure 2A).

CE Tumors

Only CE regions should be included in the measurements of target lesions. Voxels representing the surgical cavity or cystic

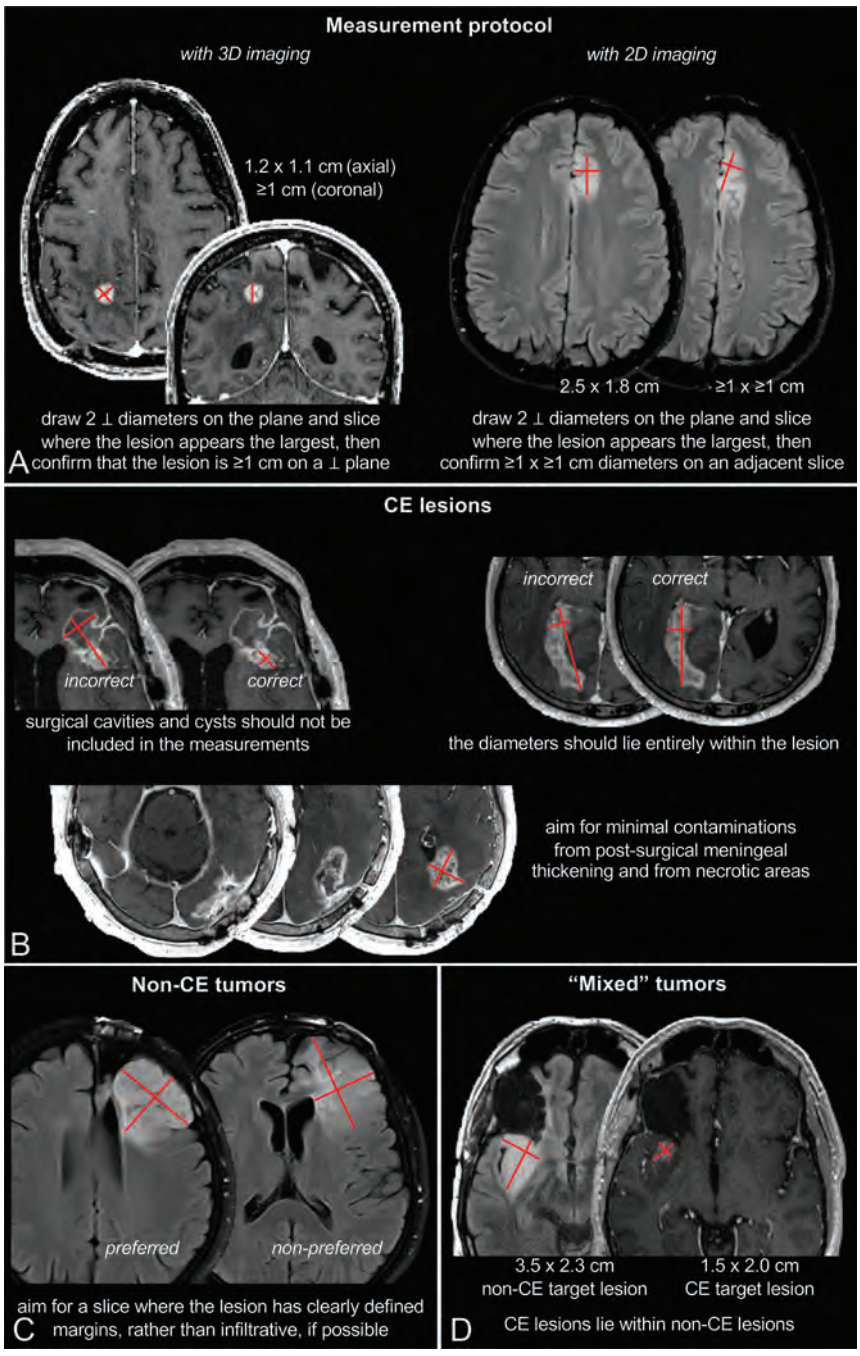

FIG 2. Guidelines and tips for bidirectional "2D" measurements. The measurement protocol for target lesions with 3D images and 2D imaging (*A*) is used both to verify that the lesion meets the criteria for "measurable disease" and to obtain measurements to calculate the tumor burden. Measurements in CE tumors (*B*) should not include the surgical cavity or cystic areas, and should avoid areas where the lesion shows necrotic features or is not distinguishable from post-surgical meningeal thickening. In non-CE tumors (*C*), the presence of infiltrative disease with unclear boundaries can pose a serious challenge when performing measurements. If possible, slices where the tumor shows more defined margins should be preferred for target lesion measurements. In "mixed" tumors (*D*), the CE lesions lie within the boundaries of non-CE lesions. CE and non-CE target lesions should be measured separately and not necessarily on the same plane/slice. Then, longitudinal changes in CE- and non-CE tumor burden are tracked in parallel to define the response category.

components should be excluded from the diameters (Figure 2B), as well as areas with T_1-hyperintensity on pre-contrast images. T_1-weighted digital subtraction maps may be helpful to avoid including areas of inherent T_1-shortening in the CE-measurements[9]. Additionally, readers should avoid measuring tumor size on slices that contain excessive necrotic components or where the boundaries between neoplastic CE tissue and post-surgical meningeal thickening/scarring are not clear (Figure 2B). As discussed, non-CE disease is not included in the tumor burden computation for CE tumors.

Non-CE Tumors

Areas of non-CE disease should be identified on T_2w and T_2w-FLAIR images, and can be used as target lesions as long as they meet the criteria for "measurable disease" in non-CE and mixed tumors. Non-CE components should be measured on the sequence where they appear the largest (T_2w or T_2w-FLAIR), as long as consistency across timepoints is observed. As mentioned, in order to meet criteria for "measurable disease", lesions should not only display a certain size, but also present clearly defined margins. Since non-CE disease can show infiltrative growth patterns with poor demarcation, slices where the non-CE lesion shows more clearly defined borders should be preferred for the 2D measurements (Figure 2C). However, when tumors present with predominantly infiltrative components, it is reasonable to select target lesions with margins that are, to some extent, indistinct, rather than classifying the whole lesion as "non-measurable".

"Mixed" Tumors

For mixed tumors with primarily non-CE disease and some measurable CE-components, both CE and non-CE areas should be evaluated separately, with separate target lesions. While CE disease is always localized within T_2-hyperintense regions of the tumor and changes will frequently evolve consistently with any changes in non-CE tumor, both total CE- and non-CE tumor burden should be computed separately when evaluating radiographic response for each timepoint (Figure 2D).

Consistency Across Timepoints

When selecting and measuring target lesions, the reader may encounter challenging scenarios (e.g., Figure 2), and be forced to perform measurements that are, to some extent, arbitrary. This might include 2D measurements of

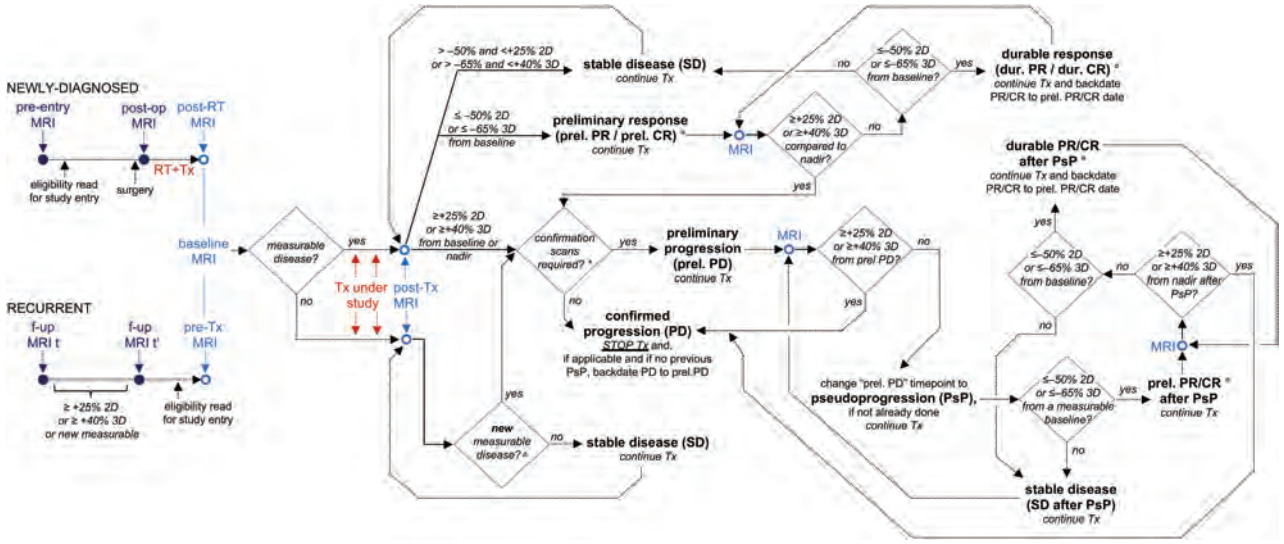

FIG. 3 Schema for determining radiographic treatment response assessment as per RANO 2.0. To assess MR/PR, the change in tumor burden should be compared to the baseline MRI, while for PD it should be compared to the nadir. In clinical trials applying the "mixed" tumor criteria, the whole evaluation should be performed in parallel for *both* the CE and the non-CE tumor burden at each timepoint in order to assign the response category (e.g., PD, SD, PR, . . .), then the *overall* response category is assigned based on both CE and non-CE categories: PD+SD/MR/PR/CR=PD; MR/PR+SD=MR/PR; CR+SD/MR/PR=SD/MR/PR; SD+SD=SD (see text for details). ° the additional categories preliminary and durable "minor response" (MR: > –50% and < –25% 2D *or* > –65% and < –40% 3D) should be taken into consideration, only for non-CE disease. * confirmation scans obtained after ≥4 weeks to confirm PD can be waived in the following scenarios: in CE tumors ≥3 months after RT completion and if the treatment does not include agents highly associated with PsP; in the evaluation of non-CE progression in non-CE tumors or mixed tumors (as PsP is typically contrast-enhancing). Confirmation scans after ≥4 weeks to confirm durable MR/PR/CR are always required. If a patient is lost to follow-up (censored) before obtaining a confirmation scan (when required), the last timepoint showing preliminary CR/PR/MR/PD is classified as SD.

an irregular lesion or 3D measurement of an infiltrating or partly necrotic lesion with boundaries that are not clearly defined. While standardization of MRI acquisitions helps with consistency, this issue is still quite common and the reader should attempt to maintain maximal consistency across timepoints in the selection of slices, also employing coregistration tools if available. Consistency may be further maximized by "simultaneous" or "hybrid" reading queue designs[18] that allow the reader to adjust the measurements at different timepoints. Readers should clearly describe in the patient source document which images and slices were used for the measurements.

STEP-BY-STEP GUIDE TO RANO 2.0 RADIOGRAPHIC READS

No Measurable Disease at Baseline

If the baseline scan shows no measurable disease, the best possible response on subsequent imaging is SD (Figure 3). No objective responses (MR/PR/CR) can be obtained without a measurable target lesion at baseline. The lesion maintains SD if no new *measurable* disease is observed at follow-up time points. If the lesion develops new *measurable* disease, or if a non-measurable component (only CE components, in case of CE tumors) existed in the previous scan and grows sufficiently in comparison to the initial lesion size (i.e., ≥5 × ≥5 mm), the time point response is PD and the treatment is stopped if confirmation is not required for trial operation (Figure 4A) (i.e., if not explicitly required, then only after 12 weeks after RT completion or for non-CE disease). If a confirmation scan is required, the first scan showing progression is annotated as "preliminary PD", and an additional MRI should be obtained after ≥4 weeks for glioblastoma or at the next scheduled follow-up as indicated in the trial design. Confirmed PD is assigned only if the confirmation scan shows an *additional* size increase of the measurable disease (≥25% with product of bidimensional 2D measurements or ≥40% with 3D volumetric segmentation compared to preliminary PD), in which case the treatment is stopped, and the day of PD is backdated to the day of preliminary PD. If the tumor does not continue to grow, the preliminary PD time point is considered a confirmed PsP (i.e., SD), the confirmation scan timepoint is annotated as SD, and the treatment is continued until additional evidence of PD compared to the date of confirmed PsP or the nadir *after* confirmed PsP.

Measurable Disease at Baseline followed by Progressive Disease

If the disease burden is "measurable" at baseline, any timepoint showing size increase ≥25% (2D) or ≥40% (3D) *compared to nadir or baseline* is labeled as either preliminary PD (if confirmation scans are required) or PD (if there is no need for confirmation scans) (Figure 3; Table 2). In case a new measurable lesion is observed, this does not automatically determine PD. The scan is categorized as preliminary PD/PD only if the overall disease burden (including the measurements of the new lesion) exceeds ≥25% (2D) or ≥40% (3D) compared to nadir or baseline. The treatment is stopped only if confirmation scans are not required or if a confirmation scan (after ≥4 weeks) shows additional PD relative to the date of preliminary PD (Figure 4B). If the confirmation scan shows additional progression, PD is backdated to the day of preliminary PD. If the

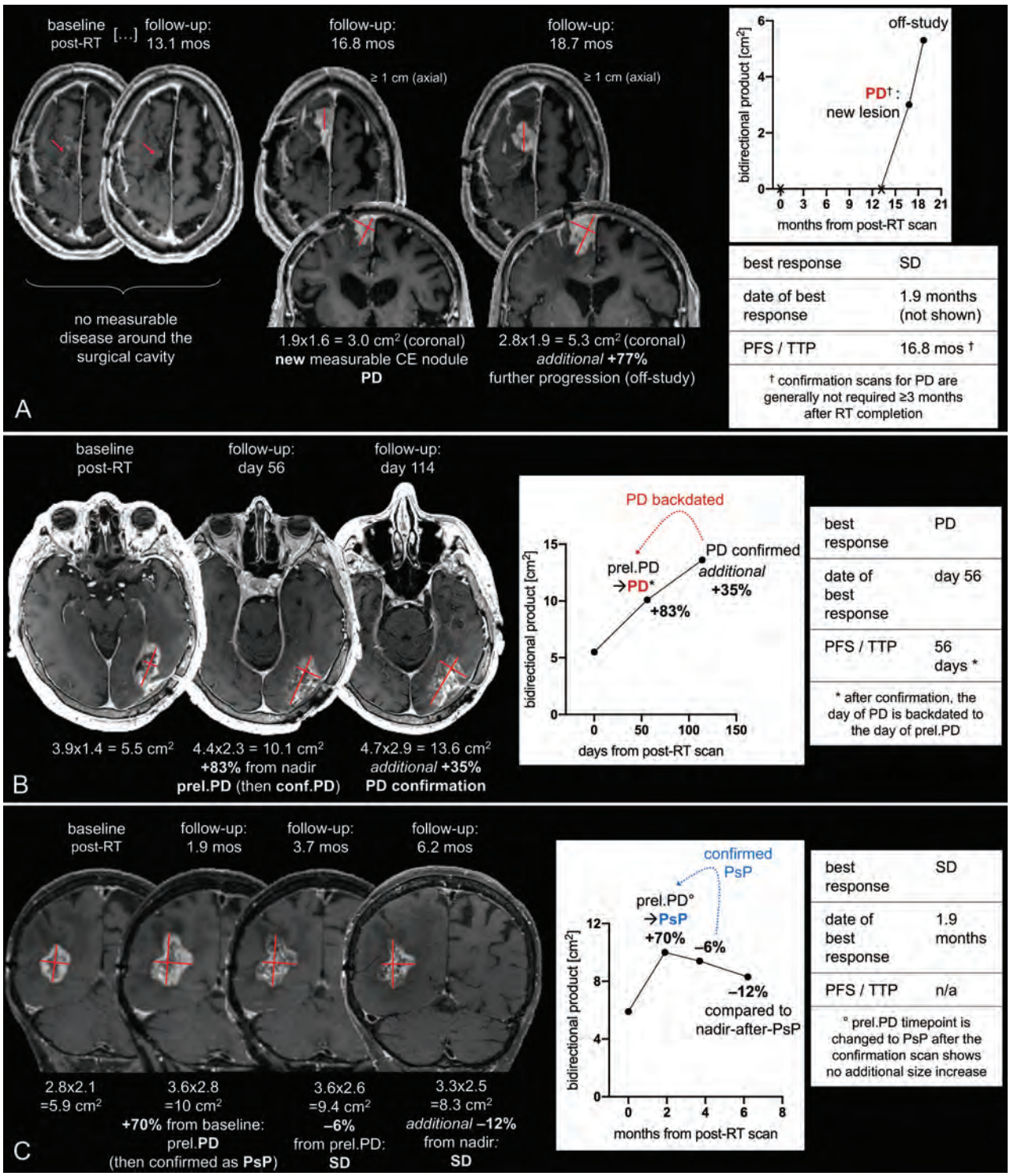

FIG 4. RANO 2.0 evaluations in example cases of newly-diagnosed CE glioblastoma. In case *A*, radiographic findings are stable (stable disease, SD) for 13.1 months from baseline, in the absence of measurable disease around the resection cavity. The appearance of a new measurable CE nodule after ≥12 weeks after RT completion (at 16.8 months in this case) classifies PD generally without the need of a confirmatory scan (unless clearly required by the trial), and the study treatment is stopped. In case *B*, the first follow-up scan shows early progressive disease (PD) <12 weeks after RT completion, "preliminary PD" (prel. PD) is annotated, the patient is kept on treatment, and a confirmation scan is obtained after ≥4 weeks. After confirmation of PD, the treatment is stopped and the confirmed PD (conf. PD) event is backdated to the day of preliminary PD. The time interval between the post-RT baseline scan and the date of confirmed PD corresponds to the time of progression (TTP). In case *C*, the first follow-up scan shows early PD <12 weeks after RT completion, annotated as preliminary PD. The confirmation scan after >4 weeks shows substantially stable findings, with no further size increase of the target lesion, therefore the preliminary PD timepoint is reclassified as pseudoprogression (PsP), and the patient is kept on treatment.

Table 2: Summary of RANO 2.0 criteria

RANO 2.0 categories
Complete Response (CR) – *compare to baseline*
disappearance of target and non-target lesions sustained for ≥4 weeks[a]
and no new lesions[b]
and clinical status is stable or improved
and off corticosteroids (or on physiologic replacement dose)
Partial Response (PR) – *compare to baseline*
at least 50% decrease in tumor burden with 2D measurements, or 65% with 3D measurements, sustained for ≥4 weeks[a,e]
and no newly-measurable lesions[b,c,d]
and clinical status is stable or improved
and corticosteroid dose is stable compared to baseline (or on physiologic replacement dose)
Minor Response (MR, only applicable to non-CE disease) – *compare to baseline*
25% to 50% decrease in tumor burden with 2D measurements, or 40% to 65% with 3D measurements, sustained for ≥4 weeks[a]
and no newly-measurable lesions[b,c,d]
and clinical status is stable or improved
and corticosteroid dose is stable compared to baseline (or on physiologic replacement)
Progressive Disease (PD)[f] – *compare to nadir*
at least 25% increase in tumor burden with 2D measurements, or 40% with 3D measurements, with or without confirmation scan after ≥4 weeks[g]
or appearance of newly-measurable lesions[b,c,d]
or appearance of leptomeningeal disease
or clinical deterioration not ascribable to steroid dose reduction or other causes apart from the tumor
or failure to return for evaluation as a result of death or clinical deterioration
Stable Disease (SD)
all scenarios that do not meet criteria for CR, PR, MR, or PD.
e.g., stable radiographic findings without clinical deterioration.

Note:—CE indicates contrast-enhancing; CR, complete response; MR, minor response; PD, progressive disease; PsP, pseudoprogression; PR, partial response; SD, stable disease.

[a] Confirmation scans after ≥4 weeks to confirm durable MR/PR/CR are always required. If confirmed, MR/PR/CR is backdated to the date of preliminary MR/PR/CR. If a patient is lost to follow-up (censored) before confirmation, preliminary CR/PR/MR is considered SD.

[b] Disregard new non-CE lesions unequivocally ascribable to post-RT.

[c] Either new measurable lesions or previously non-measurable lesions that became measurable and grew ≥5x≥5 mm.

[d] For CE-tumors, only CE lesions should be considered.

[e] In mixed tumors, the assessment should be performed in-parallel for both CE and non-CE components, then combined.

[f] Corticosteroid dose increase *alone* does *not* define PD.

[g] Confirmation scans for PD can be waived: in CE tumors >3 months after RT completion not treated with agents highly associated with PsP; in the evaluation of non-CE progression in non-CE tumors or mixed tumors.

confirmation scan shows stable or improved findings, the timepoint exhibiting preliminary PD is labeled as "confirmed PsP" (Figure 4C; see *No Measurable Disease at Baseline*), and treatment is continued until further evidence of progression.

Measurable Disease at Baseline followed by Radiographic Response

Preliminary MR/PR/CR is assigned when a scan demonstrates a size reduction of tumor burden (computed from target lesions) below the corresponding threshold (PR: 50% 2D or 65% 3D; MR: 25% 2D or 40% 3D; CR: disappearance of all lesions) *compared to baseline*, *and* no new measurable lesions are observed (Figure 3; Table 2). A confirmed MR/PR/CR is then assigned only if the following scan (after ≥4 weeks) verifies the tumor has maintained shrinkage below the specific thresholds for MR/PR/CR compared to baseline. Unlike PD, MR/PR/CR *always* require confirmation scans to confirm response. The duration of response is determined from the time of initial response to disease progression. In case the nadir scan has no measurable disease, further PD will be assigned according to the same rules as in case of "No Measurable Disease at Baseline" (see above).

Measurable Disease at Baseline followed by Stable Disease

All scenarios that do not meet criteria for PD or MR/PR/CR are labeled as SD and treatment is continued. SD is also assigned in case the patient is lost to follow-up (censored) after unconfirmed MR/PR/CR or after unconfirmed preliminary PD (if confirmation of PD is required).

Follow-up after Confirmed Pseudoprogression

In case of previously confirmed PsP, any follow-up scans showing a ≥25% (2D) or ≥40% (3D) increase in tumor burden compared to *either* PsP or nadir after PsP should be labeled as confirmed PD. In this case, the treatment is stopped and no additional confirmation scans required, and the date of PD is *not* backdated (i.e., the date of the 2nd progressive disease event is the date of progression). A *response* after PsP ("PR/CR after PsP") is possible only if the tumor burden meets the thresholds for response compared to *baseline*, *not* compared to the PsP timepoint where progressive enhancement was noted, similar to iRECIST recommendations[22].

ADDITIONAL NOTES ON THE EVALUATION OF CE AND NON-CE DISEASE

Assessment of CE Disease

In CE tumors, CE tumor burden is quantified only with target lesions and then the response category is defined following the recommended thresholds. In non-CE tumors, the appearance of a new *measurable* CE lesion should define preliminary PD or PD (depending on whether a confirmation scan is required, which should be prespecified in the study protocol).

Assessment of Non-CE Disease

In non-CE tumors, non-CE tumor burden is quantified with target lesions and then the response category is defined following the recommended thresholds. New areas of non-CE signal alterations should only be categorized as PD if they are not ascribable to obvious RT-induced changes. As this distinction is often very challenging and potentially arbitrary, we advise to only ascribe to RT those T_2w/FLAIR signal alterations that can be unequivocally attributed to well-established radiographic patterns, such as findings typical of radiation leukoencephalopathy, which acknowledges "capping" of the ventricular horns and confluent homogeneous white matter hyperintensity without mass effect[23].

In CE tumors, as mentioned, non-CE disease should *not* be assessed, apart from trials testing agents that significantly reduce blood-brain barrier permeability (e.g., anti-angiogenic agents), in

which CE may not accurately reflect the actual tumor burden. In this case, no strict methodology is required for the evaluation of non-CE tissue in CE tumors. Two possible approaches may be adopted to evaluate non-CE components: diameters/segmentations as proposed for mixed tumors (see below), or a qualitative assessment ("worsened" vs "stable/improved") similar to 2010 RANO-HGG[7]. Since CE tumors typically present extensive T_2w/FLAIR hyperintese alterations with contamination from vasogenic edema, a qualitative approach may be preferred in these cases. The methodology should ultimately be agreed upon by the sponsor and the contract research organization[18] and clearly stated in the imaging charter prior to the initiation of the trial.

Mixed Tumors

In "mixed" tumors, CE and non-CE tumor burden should be tracked separately, with dedicated target lesions, and *both* should be compared to the proposed thresholds at *each* timepoint. Then, if either one demonstrates PD, the overall response category is PD. If either one shows MR/PR/CR and the other one shows SD, the overall response category is MR/PR. CR is the overall response category only if *both* CE and non-CE disease show CR. Similarly, SD is the overall response category only if *both* CE and non-CE disease show SD. Importantly, the assessment of non-CE components in mixed tumors should not include vasogenic edema. While in typical mixed tumors (i.e., largely non-CE tumors with some CE foci) the vasogenic component of the T_2w/FLAIR hyperintense signal is minimal, in cases with more pronounced blood-brain barrier breakdown the distinction between vasogenic edema and non-CE tumor tissue is not trivial and potentially arbitrary.

Leptomeningeal Disease

The appearance of new and clear leptomeningeal involvement is sufficient to determine PD, and can be evaluated on post-contrast T_1w images and/or post-contrast T_2w-FLAIR images (if acquired as a BTIP variation)[15]. Given the impact of this scenario, which would cause the treatment to be stopped and the patient to be put off-study, it is recommended to only indicate unequivocal and extensive leptomeningeal spread during radiographic reads.

CORRESPONDENCE BETWEEN 2D AND 3D MEASUREMENTS

The sum of bidirectional products (2D measurements) or the volume quantification following segmentation (3D measurements) are both valid approaches for the quantification of tumor burden in RANO 2.0. However, while the rules to operationalize 2D measurements are precisely stated and have been used in trials for decades, instructions to convert such rules to 3D measurements are not strictly dictated.

Measurable Disease

As previously discussed, 2D measurements dictate that measurable disease is defined as a lesion with either: three ≥10 mm perpendicular diameters (if 3D imaging is used), or two ≥10 mm in-plane perpendicular diameters on two adjacent slices (if 2D imaging is used). However, RANO 2.0 criteria do not clearly describe how to extrapolate these criteria to 3D. Indeed, volumetric lesion segmentation potentially allows measurement of lesions that would be classically considered non-measurable by 2D assessments. A clear example is the rim of enhancement surrounding a surgical cavity or surrounding a necrotic/cystic area where there is no nodule to define a clear target lesion in 2D. As such, there should be some guidance on best practices for when and how to use 3D measurements for the purposes of radiographic response assessment.

For multicenter clinical trials with a central read evaluation, it is advisable to confirm presence of measurable disease using 2D criteria, especially during eligibility reads at the local sites, followed by use of volumetric measurements *centrally* of *all* appropriate signal alterations (e.g., all CE tissue for HGG or all tumoral non-CE alterations in LGG) without distinction of measurable and non-measurable *components* (Figure 5A). Conversely, if baseline images do not exhibit a measurable lesion using 2D criteria, regardless of the volume on 3D segmentation, the scan should be considered to show *no* measurable disease (Figure 5B). This approach both preserves the historic definitions of measurable disease and is the most pragmatic solution, as editing 3D segmentations to precisely match 2D criteria would require additional, time-consuming and relatively arbitrary steps for the radiologist.

Target Lesions

In cases of multifocal lesions, up to 3 measurable lesions can be selected as target lesions for 2D measurements. When this is translated to 3D volumetric measurements, one could decide to include only 2D-defined target lesions, target lesions and non-target lesions, or all disease that is thought to be present irrespective of lesion designation. In agreement with the previously proposed solution, it may be favorable to include *all* signal alterations in the segmentations as this would result in a more accurate overall estimate of tumor burden, would arguably result in a better inter-reader agreement, and would avoid partial segmentations that only include some of the lesions[24].

Mixed Tumors

In mixed tumors with CE and non-CE components, CE lesions lie within non-CE lesions. Therefore, with 2D measurements, the diameters of non-CE lesions also include CE lesions, inevitably. Tumor segmentations allow to separately classify voxels as belonging to the CE area or the non-CE area. When 3D assessments are employed, it is advisable to obtain one segmentation for CE areas, and a separate segmentation for the whole T_2-hyperintense lesion, which encompasses both CE and non-CE areas, for consistency with the 2D method.

General Recommendations

Overall, it is recommended that multicenter studies using an IRF for central review, or single center studies, utilize 3D measurements with the same software package for all patients to ensure consistency within the trial. Additionally, 3D measurements should preferably be applied to volumetrically acquired images to further limit the contributions of partial volume effects.

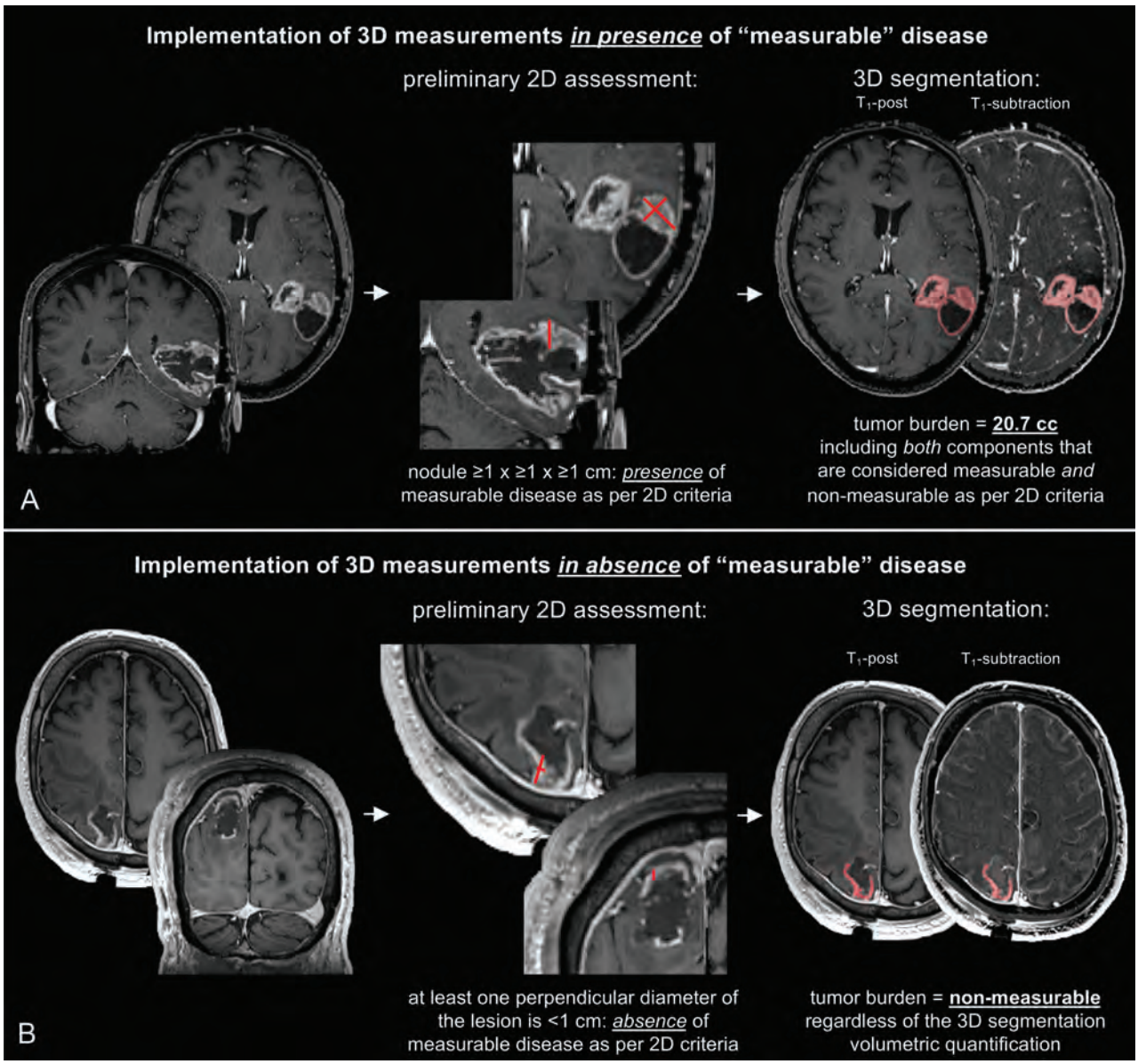

FIG 5. Proposed implementation of volumetric (3D) assessments. A preliminary evaluation should be performed to confirm the presence of measurable disease according to the classic bidimensional criteria. If 2D-defined measurable disease is present, the volumetric tumor burden may be computed by including the whole segmentation of the appropriate tissue (e.g., only CE tissue for CE tumors) which comprises both 2D-defined measurable components and 2D-defined non-measurable components (A). A quality check should always be performed by the reader to correct errors in the segmentation, for instance to exclude vascular structures or healthy meningeal tissue. If 2D-defined measurable disease is absent, the volumetric tumor burden should be set to "non-measurable", regardless of the 3D segmentation (B). In the cases shown, T_1-subtraction maps were used to only include in the segmentation voxels that showed increased T_1-weighted signal when comparing post- to pre-contrast T_1-weighted normalized images.

CLINICAL DETERIORATION AND CORTICOSTEROID USE

The assessment of clinical or neurological status and the change in corticosteroid dose are also required for the response assessment. Clinical deterioration not ascribable to steroid dose reduction or other causes apart from the tumor is *sufficient* to define PD, independently from radiographic findings and without the need for confirmation scans. This may be defined a number of ways, including KPS, ECOG, NANO, or simply "better", "stable", or "worse", and should be clearly defined in the trial protocol and imaging charter.

Changes in corticosteroid dose are known to alter the degree of contrast enhancement[25] and extent of cerebral edema[26] and therefore should also be considered when evaluating radiographic response[9,10]. If a patient exhibits a response (CR/PR/MR) and corticosteroids are *increased* beyond 2 mg per day dexamethasone or equivalent compared to baseline, the response is downgraded to SD because steroids could explain the observed tumor shrinkage. Additionally, to qualify for CR, patients must be either off steroids or on physiological replacement dose, otherwise the response is downgraded to MR/PR if the corticosteroid dose is stable compared to baseline. Conversely, if a patient exhibits radiographic evidence of disease progression (PD) but steroid dose has been *decreased* relative to the nadir,

the response should be changed to SD and the patient should continue treatment. Importantly, an increase in corticosteroid dose alone, without clinical or radiographic progression at the time of evaluation, does *not* dictate disease progression.

CONCLUSIONS

The RANO 2.0 criteria provide unified and improved rules for the standardized determination of radiographic response in adult gliomas on clinical trials. Neuroradiologists and imaging core labs should be aware of the aforementioned suggestions and operational recommendations to maximize the accuracy and reliability of identifying potential therapeutic effects in patients with adult gliomas.

Disclosure forms provided by the authors are available with the full text and PDF of this article at www.ajnr.org.

REFERENCES

1. Ostrom QT, Price M, Neff C, et al. **CBTRUS Statistical Report: Primary Brain and Other Central Nervous System Tumors Diagnosed in the United States in 2016–2020**. *Neuro Oncol* 2023;25:iv1–99 CrossRef Medline
2. Weller M, van den Bent M, Preusser M, et al. **EANO guidelines on the diagnosis and treatment of diffuse gliomas of adulthood.** *Nat Rev Clin Oncol* 2021;18:170–86 CrossRef Medline
3. Wen PY, Weller M, Lee EQ, et al. **Glioblastoma in adults: a Society for Neuro-Oncology (SNO) and European Society of Neuro-Oncology (EANO) consensus review on current management and future directions.** *Neuro Oncol* 2020;22:1073–113 CrossRef Medline
4. Ellingson BM, Wen PY, van den Bent MJ, et al. **Pros and cons of current brain tumor imaging.** *Neuro Oncol* 2014;16 Suppl 7:vii2–11 CrossRef Medline
5. Wen PY, Cloughesy TF, Ellingson BM, et al. **Report of the Jumpstarting Brain Tumor Drug Development Coalition and FDA clinical trials neuroimaging endpoint workshop (January 30, 2014, Bethesda MD).** *Neuro Oncol* 2014;16 Suppl 7:vii36–47 CrossRef Medline
6. Lamborn KR, Yung WKA, Chang SM, et al. **Progression-free survival: an important end point in evaluating therapy for recurrent high-grade gliomas.** *Neuro Oncol* 2008;10:162–70 CrossRef Medline
7. Wen PY, Macdonald DR, Reardon DA, et al. **Updated response assessment criteria for high-grade gliomas: response assessment in neuro-oncology working group.** *J Clin Oncol Off J Am Soc Clin Oncol* 2010;28:1963–72 CrossRef Medline
8. van den Bent MJ, Wefel JS, Schiff D, et al. **Response assessment in neuro-oncology (a report of the RANO group): assessment of outcome in trials of diffuse low-grade gliomas.** *Lancet Oncol* 2011;12:583–93 CrossRef Medline
9. Ellingson BM, Wen PY, Cloughesy TF. **Modified Criteria for Radiographic Response Assessment in Glioblastoma Clinical Trials.** *Neurother J Am Soc Exp Neurother* 2017;14:307–20 CrossRef Medline
10. Wen PY, Van Den Bent MJ, Youssef G, et al. **RANO 2.0: Update to the Response Assessment in Neuro-Oncology criteria for high- and low-grade gliomas in adults.** *J Clin Oncol* 2023;41:5187–99 CrossRef Medline
11. Louis DN, Perry A, Wesseling P, et al. **The 2021 WHO Classification of Tumors of the Central Nervous System: a summary.** *Neuro Oncol* 2021;23:1231–51 CrossRef Medline
12. Youssef G, Rahman R, Bay C, et al. **Evaluation of Standard Response Assessment in Neuro-Oncology, Modified Response Assessment in Neuro-Oncology, and Immunotherapy Response Assessment in Neuro-Oncology in Newly Diagnosed and Recurrent Glioblastoma.** *J Clin Oncol Off J Am Soc Clin Oncol* 2023;41:3160–71 CrossRef Medline
13. Ellingson BM, Sampson J, Achrol AS, et al. **Modified RANO, Immunotherapy RANO, and Standard RANO Response to Convection-Enhanced Delivery of IL4R-Targeted Immunotoxin MDNA55 in Recurrent Glioblastoma.** *Clin cancer Res an Off J Am Assoc Cancer Res* 2021;27:3916–25 CrossRef Medline
14. Ellingson BM, Bendszus M, Boxerman J, et al. **Consensus recommendations for a standardized Brain Tumor Imaging Protocol in clinical trials.** *Neuro Oncol* 2015;17:1188–98 CrossRef Medline
15. Sanvito F, Kaufmann TJ, Cloughesy TF, et al. **Standardized brain tumor imaging protocols for clinical trials: current recommendations and tips for integration.** *Front Radiol* 2023;3. CrossRef Medline
16. Ellingson BM, Kim GHJ, Brown M, et al. **Volumetric measurements are preferred in the evaluation of mutant IDH inhibition in non-enhancing diffuse gliomas: Evidence from a phase I trial of ivosidenib.** *Neuro Oncol* 2022;24:770–8 CrossRef Medline
17. Boxerman JL, Quarles CC, Hu LS, et al. **Consensus recommendations for a dynamic susceptibility contrast MRI protocol for use in high-grade gliomas.** *Neuro Oncol* 2020;22:1262–75 CrossRef Medline
18. Ellingson BM, Brown MS, Boxerman JL, et al. **Radiographic read paradigms and the roles of the central imaging laboratory in neuro-oncology clinical trials.** *Neuro Oncol* 2021;23:189–98 CrossRef Medline
19. Ellingson BM, Abrey LE, Garcia J, et al. **Post-chemoradiation volumetric response predicts survival in newly diagnosed glioblastoma treated with radiation, temozolomide, and bevacizumab or placebo.** *Neuro Oncol* 2018;20:1525–35 CrossRef Medline
20. Ellingson BM, Gerstner ER, Lassman AB, et al. **Hypothetical generalized framework for a new imaging endpoint of therapeutic activity in early phase clinical trials in brain tumors.** *Neuro Oncol* 2022;24:1219–29 CrossRef Medline
21. Huang RY, Rahman R, Ballman K V, et al. **The Impact of T2/FLAIR Evaluation per RANO Criteria on Response Assessment of Recurrent Glioblastoma Patients Treated with Bevacizumab.** *Clin cancer Res an Off J Am Assoc Cancer Res* 2016;22:575–81 CrossRef Medline
22. Seymour L, Bogaerts J, Perrone A, et al. **iRECIST: guidelines for response criteria for use in trials testing immunotherapeutics.** *Lancet Oncol* 2017;18:e143–52 CrossRef Medline
23. Carr CM, Benson JC, DeLone DR, et al. **Intracranial long-term complications of radiation therapy: an image-based review.** *Neuroradiology* 2021;63:471–82 CrossRef Medline
24. Kickingereder P, Isensee F, Tursunova I, et al. **Automated quantitative tumour response assessment of MRI in neuro-oncology with artificial neural networks: a multicentre, retrospective study.** *Lancet Oncol* 2019;20:728–40 CrossRef Medline
25. Watling CJ, Lee DH, Macdonald DR, et al. **Corticosteroid-induced magnetic resonance imaging changes in patients with recurrent malignant glioma.** *J Clin Oncol Off J Am Soc Clin Oncol* 1994;12:1886–9 CrossRef Medline
26. Dietrich J, Rao K, Pastorino S, et al. **Corticosteroids in brain cancer patients: benefits and pitfalls.** *Expert Rev Clin Pharmacol* 2011;4:233–42 CrossRef Medline

Comprehensive Review of External and Middle Ear Anatomy on Photon-Counting CT

Dinesh Rao, John V. Murray, Amit K. Agarwal, Sukhwinder Johnny Sandhu, and Pat A. Rhyner

ABSTRACT

SUMMARY: Photon-counting CT (PCT) allows for improved spatial and contrast resolution compared with traditional energy-integrating detector CT. PCT offers markedly improved visualization of previously described structures, as well as those that were previously beyond the resolution of imaging. Although the anatomic details of the external ear and middle ear structures have been described previously, the rich detail of these structures has not been comprehensively reviewed in the radiology literature. The microarchitecture of the middle ear ossicles and bony protuberances are particularly well visualized on PCT. This review updates the existing literature with a detailed anatomic review of the external ear and the middle ear on temporal bone CT.

ABBREVIATIONS: EAC = external auditory canal; EID = energy-integrating detector; PCT = photon-counting CT; TMJ = temporomandibular joint

Recent developments in photon-counting CT (PCT) have improved spatial and contrast resolution as compared with traditional energy-integrating detector (EID) CT scanners. PCT is particularly useful in imaging of the temporal bone because the anatomic structures are very small and complex. Though temporal bone anatomy has been described previously, PCT allows improved resolution and visualization of structures that are beyond the resolution of conventional EID scanners. This review serves as an update to the existing literature by illustrating the external and middle ear anatomy with PCT images.

REVIEW OF PCT PHYSICS

The superiority of PCT to EID CT is based on differences in the way each system converts x-ray photons into electrical signal. Conventional EID CT systems use a scintillator to convert x-rays into visible light, which are then converted into electrical signal by a photodiode. EID CT must use reflective septa in between the detector elements to reduce optical cross-talk, however these result in decreased dose efficiency, limiting spatial resolution. With EID CT, electrical signal from a single detector is proportional to the sum of the energy of all the photons that contact the scintillator. The energy level from all the x-rays that reach the detector are integrated to create an image. Greater weight is given to photons with higher energy levels, which is not ideal given the K-edge of iodine is 33.2 keV and optimal soft contrast is obtained with lower-energy photons.[1]

In comparison, PCT uses a semiconductor material that converts the energy from each x-ray photon directly into electronic signal. The signal created by a photon is proportional to the energy of the photon. Very low-energy signal from electronic noise is rejected in PCT, thus increasing SNR in comparison to EID, which includes electronic noise.[2] Equal energy contribution from low- and high-energy photons leads to improved soft tissue contrast and increased signal from iodinated contrast. The ability to measure the energy of each photon contacting the detector allows for spectral imaging, similar to dual-energy CT. This can be used to produce virtual monochromatic reconstructions over a wide range of energies, material decomposition, iodine maps, and virtual noncontrast reconstructions. This allows for improved resolution of iodine-based contrast agents and decreased artifacts from beam hardening related to metal or attenuated bone. The technical details and advantages of PCT versus EID have been described previously.[1] Ultra-high-resolution imaging afforded by PCT allows for greater detail of many submillimeter structures routinely encountered in temporal bone imaging.[3,4] There is superior in-plane resolution and thinner section thickness with PCT in comparison with EID CT. The improved resolution allows for "crisper" images that routinely demonstrate fine detail. In particular, the microarchitecture of the ossicles, ossicular ligaments, tendons, and bony protuberances important for proper interpretation are all better visualized on PCT. All images contained in this review were acquired on a NAEOTOM Alpha PCT scanner (Siemens) at 0.2 mm section thickness.

Received April 26, 2024; accepted after revision May 24.

From the Department of Radiology, Mayo Clinic, Jacksonville, Florida.

Please address correspondence to Dinesh Rao, 6500 San Pablo Blvd, Jacksonville, FL 32224; e-mail: Rao.dinesh@mayo.edu

http://dx.doi.org/10.3174/ajnr.A8359

IMAGE REVIEW OF ANATOMY

External Ear

The external ear structure is composed of elastic cartilage and is covered by skin. The helix is the convex outer border of the external ear curving posterior and superiorly. The helix is partially folded inward toward the inner surface of the external ear. Along the posterior helix a small cartilaginous projection can be variably present called "Darwin's tubercle."[5] The antihelix is anterior to the helix, also convex and curves in the same direction as the helix but with a smaller arc. Superiorly, it divides into the superior and inferior crura. Between these 2 crura is the triangular fossa. In between the helix and the antihelix is the scaphoid fossa. The concha, or concha bowl, is the concave depression that directs sound waves toward the external auditory meatus. The external auditory meatus is the anterior most part of the concha and serves as the opening of the external auditory canal (EAC). The tragus is a posteriorly directed cartilaginous structure attached to the anterior margin of the concha. Inferior to the tragus lies the lobule, or earlobe. The antitragus lies posterior to the tragus (Fig 1).

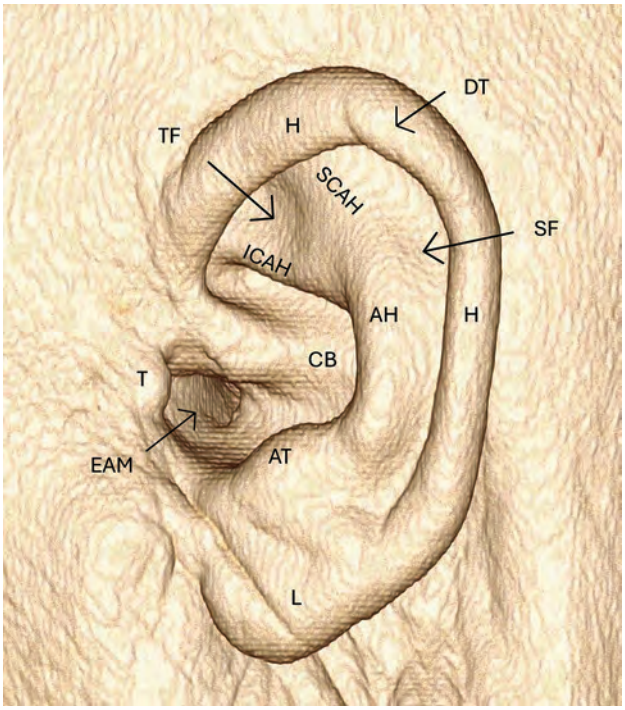

FIG 1. 3D VRT demonstrating the external ear anatomy. AH indicates antihelix; AT, antitragus; CB, concha bowl; DT, Darwin's tubercle; EAM, external auditory meatus; H, helix; ICAH, inferior crus antihelix; L, lobule; SCAH, superior crus antihelix; SF, scaphoid fossa; T, tragus; TF, triangular fossa; VRT, volume-rendered technique.

The temporal bones are at the sides and base of the skull and consist of 5 individual bones: squamous, mastoid, petrous, tympanic, and styloid (Fig 2*A*).[6] The squamous bone forms the anterolateral and superior part of the temporal bone. Superiorly, the bone articulates with the parietal bone at the squamosal suture and anteriorly with the sphenoid bone at the sphenosquamosal suture. It serves as the lateral aspect of the middle cranial fossa and roof of the EAC. It also forms the glenoid fossa of the temporomandibular joint (TMJ).[7] The squamous bone articulates anteriorly with the zygomatic bone at the zygomaticotemporal suture.

The petrous bone is the most complex of all the bones forming the temporal bone superstructure (Fig 2*B*). It has a pyramidal shape with a wide lateral base and anteromedial apex. Anterolaterally, it articulates with the squamous bone at the petrosquamosal fissure. Anteriorly, it articulates with the sphenoid bone at the sphenopetrosal suture. Medially, the petrous bone articulates with the occipital bone at the petro-occipital suture. It forms the boundary of the middle and posterior cranial fossa.[8] The petrous bone contains many structures discussed later herein, including the cochlea and vestibular systems, internal auditory canal, multiple fissures for perforating nerve branches, the tegmen tympani, and others.

The tympanic bone forms the posterior aspect of the TMJ glenoid fossa and the anterior wall, floor, and posteroinferior aspect

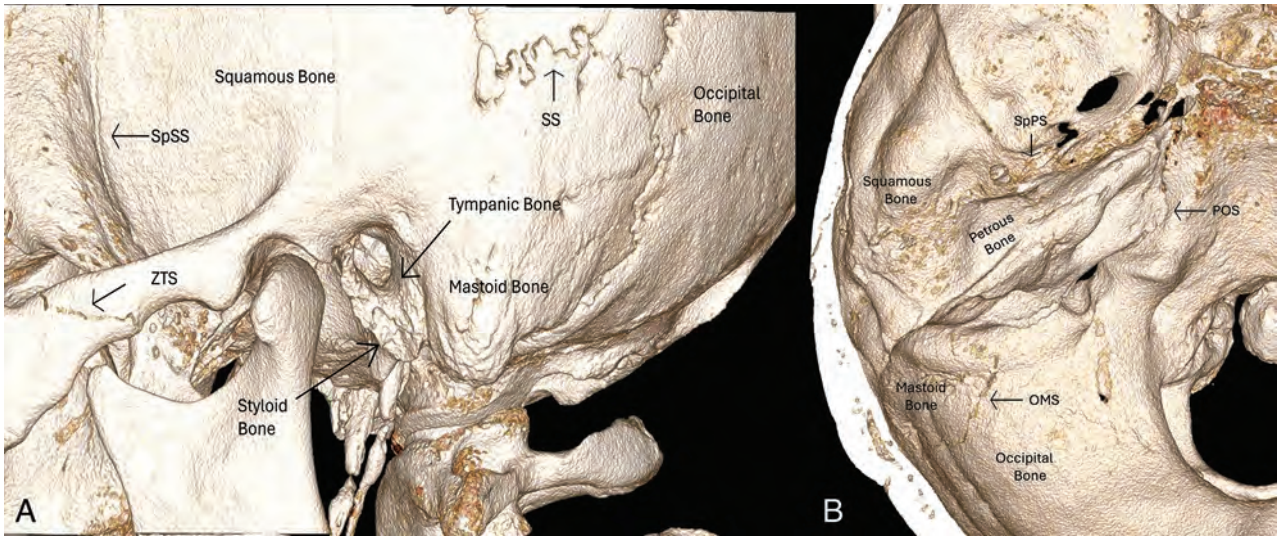

FIG 2. 3D VRT image in lateral (*A*) and superior (*B*) projection. OMS indicates occipital mastoid suture; POS, petro-occipital suture; SpPS, sphenopetrosal suture; SpSS, sphenosquamosal suture; SS, squamosal suture; VRT, volume-rendered technique; ZTS, zygomaticotemporal suture.

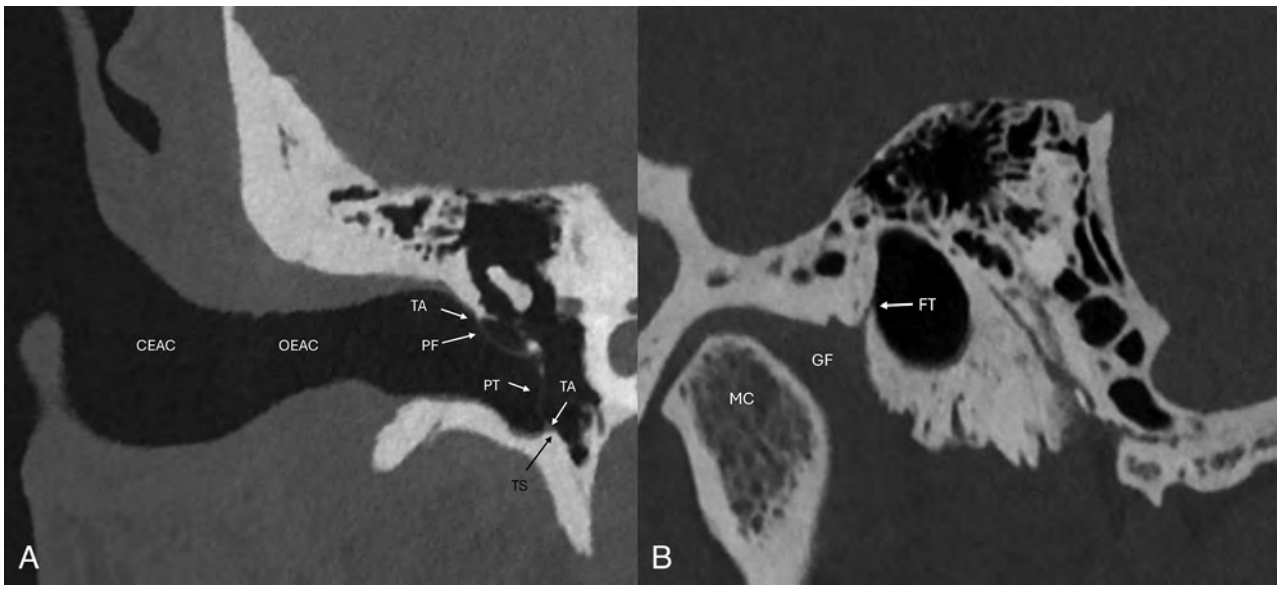

FIG 3. Coronal (*A*) and sagittal (*B*) images of the EAC. CEAC indicates cartilaginous external auditory canal; GF, glenoid fossa; FT, foramen tympanicum; MC, mandibular condyle; OEAC, osseous external auditory canal; PF, pars flaccida; PT, pars tensa; TA, tympanic annulus; TS, tympanic sulcus.

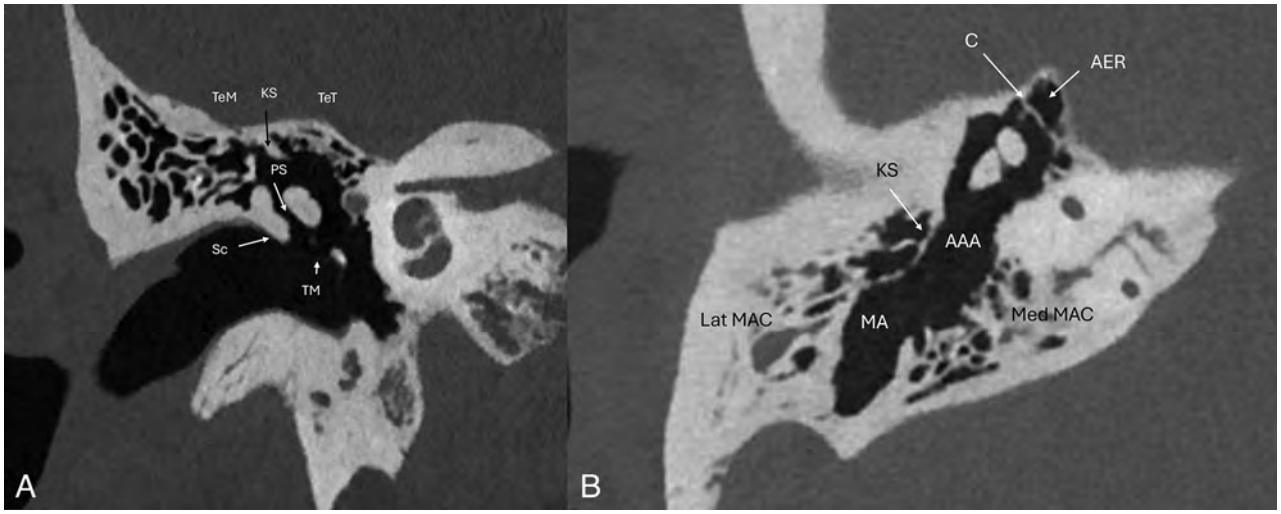

FIG 4. Coronal (*A*) and axial (*B*) PCT images demonstrating the anatomy of the epitympanum: AAA indicates aditus ad antrum; AER, anterior epitympanic recess; C, cog; KS, Koerner septum; Lat MAC, lateral mastoid air cells; MA, mastoid antrum; Med MAC, medial mastoid air cells; PS, Prussak space; Sc, scutum; TeM, tegmen mastoideum; TeT, tegmen tympani; TM, tympanic membrane.

of the bony EAC (Fig 2*A*). The petrotympanic fissure runs from the TMJ to the tympanic cavity and serves as the opening of the chorda tympani to exit the skull base anteriorly before joining the lingual nerve to provide gustatory sensation to the anterior two-thirds of the tongue. The tympanic sulcus serves as the attachment of the tympanic membrane. The mastoid bone is posterior and inferior to the squamous bone and immediately posterior to the tympanic bone. It articulates with the occipital bone posteriorly at the occipitomastoid suture. The styloid process projects downward and forward from the styloid bone. The stylohyoid ligament and stylohyoid, stylopharyngeus, and styloglossus muscles attach to the styloid process.[9]

The EAC consists of a hollow tube extending from the external auditory meatus to the tympanic membrane (Fig 3). The meatus serves as the opening to the canal. The canal is directed medially, anteriorly, and inferiorly relative to the meatus. The lateral one-third is cartilaginous, and the medial two-thirds is osseous and both parts are covered with squamous epithelial skin. The anterior wall, floor, and inferior portion of the posterior wall are formed by the tympanic bone, and the rest of the posterior wall and roof are formed by the squamous temporal bone.[10] The fissures of Santorini are microscopic defects along the anterior portion of the cartilaginous EAC allowing for spread of tumor and/or infection between the anterior EAC at the preauricular soft tissues including the parotid gland.[11] The foramen tympanicum, also known as the foramen of Huschke, is a small defect in the anterior wall of the osseous EAC that allows spread of tumor or infection into the posterior TMJ

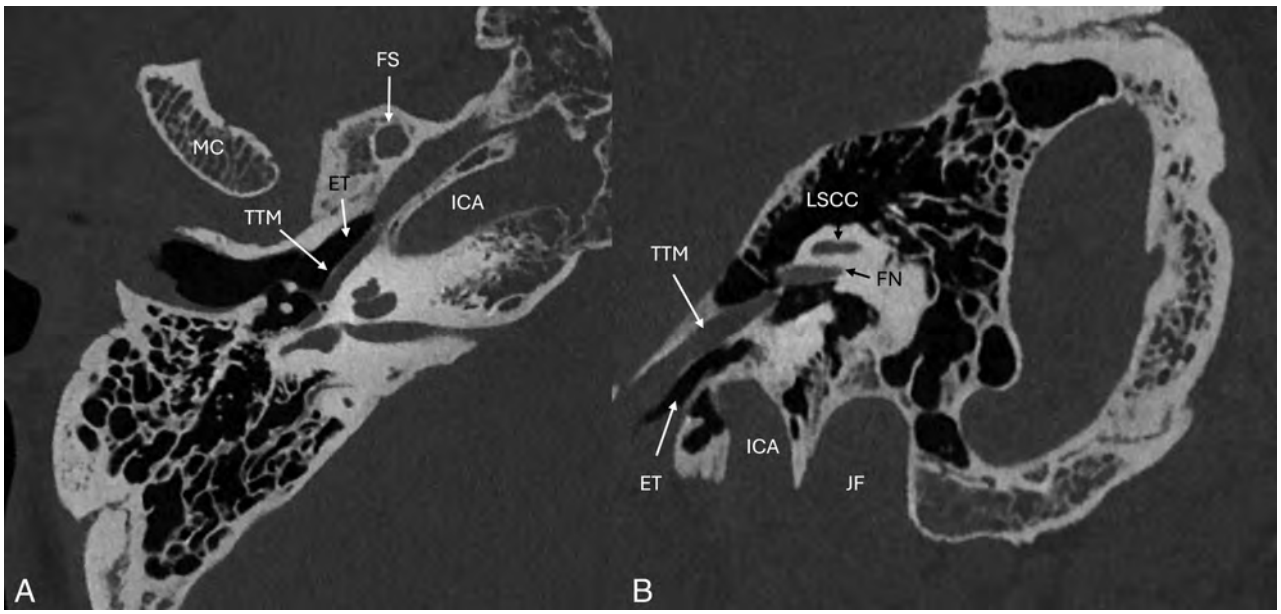

FIG 5. Axial (*A*) and oblique (*B*) PCT images of the hypotympanum. ET indicates Eustachian tube; FS, foramen spinosum; ICA, internal carotid artery; MC, mandibular condyle; TTM, tensor tympani muscle.

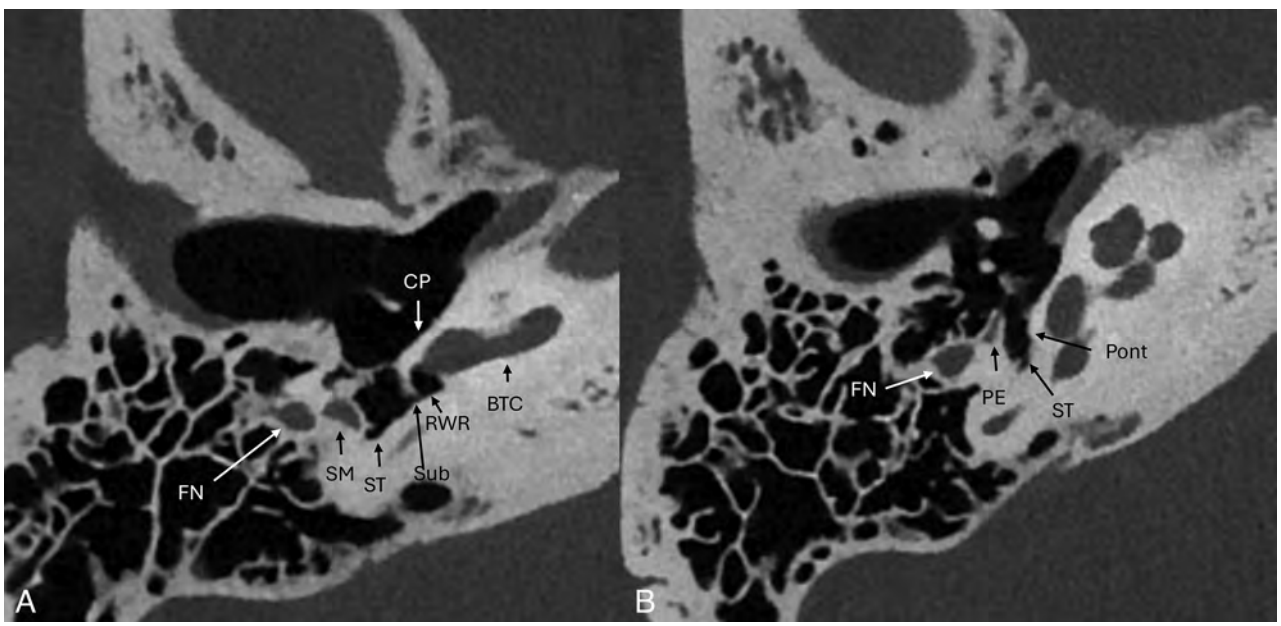

FIG 6. Axial PCT images (*A* and *B*) of the mesotympanum and retrotympanic structures. BTC indicates basal turn cochlea; CP, cochlear promontory; FN, facial nerve mastoid segment; RWR, round window recess; SM, stapedius muscle; ST, sinus tympani; Sub, subiculum; PE, pyramidal eminence; Pont, ponticulus.

(Fig 3*B*). A potential pitfall is confusing this structure for a fracture or an erosion.

The tympanic membrane, the medial boundary of the EAC, is composed of thin fibrocartilaginous tissue. The thin pars flaccida is located superior to the thicker parts tensa. The tympanic annulus is the thickened ring of the membrane periphery that attaches to the tympanic sulcus in the bone. The fibrocartilaginous ring is incomplete superiorly and anteriorly, as is the osseous ring, forming a small gap called the notch of Rivinus. This makes the pars flaccida susceptible to perforation and spread of cholesteatoma.[9]

Middle Ear

The middle ear cavity is an air-filled space between the EAC and the inner ear. The lateral extent is the tympanic membrane. The superior border is the tegmen tympani. The inferior border is the jugular wall, which separates the middle ear from the jugular fossa. The anterior border is made of the carotid wall and the posterior border is the mastoid wall. The medial wall is the otic capsule. The tympanic cavity is further divided into the epitympanum, which is the part of the middle ear cavity above the superior border of the tympanic membrane,

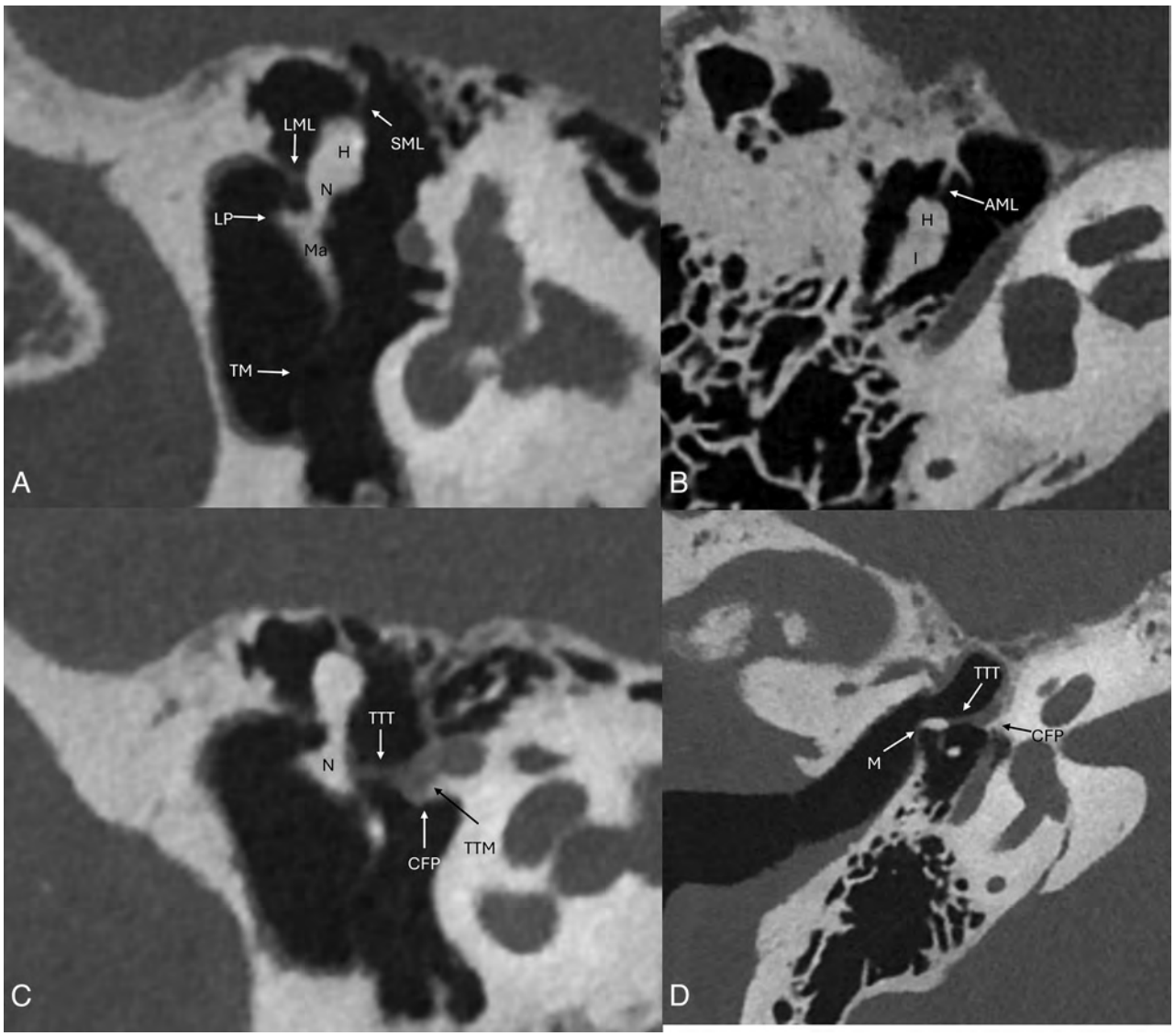

FIG 7. Coronal oblique (*A* and *C*) and axial oblique (*B* and *D*) images of the malleus. AML indicates anterior malleal ligament; CFP, cochleariform process; H, head of malleus; I, incus; LML, lateral malleal ligament; LP, lateral process; M, manubrium attaching to the tympanic membrane; Ma, manubrium; N, neck of malleus; SML, superior malleal ligament; TTM, tensor tympani muscle; TTT, tensor tympani tendon.

mesotympanum, which is at the level of the tympanic membrane; and the hypotympanum, which is below the inferior border of the tympanic membrane. The middle ear cavity can be further subdivided into the protympanic and retrotympanic compartments that are anterior and posterior to the tympanic membrane, respectively.[12]

The tegmen tympani, the superior border of the epitympanum, is part of the petrous bone (Fig 4*A*). It is a thin osseous structure that separates the temporal bone from the middle cranial fossa. Laterally, it continues as the tegmen mastoideum. The lateral margin interdigitates with the squamous bone at the petrosquamous suture. The petrosquamous suture continues into the epitympanum as the Koerner septum and divides the petrous and squamous portion of the mastoid air cells.[13] The Koerner septum is a useful landmark for determining if there is erosive pathology, because it is consistently present while the pneumatization of the mastoid air cells are highly variable.

The anterior aspect of the epitympanum, also known as the anterior epitympanic or supratubal recess, is partitioned from the rest of the epitympanum by a thin bony septation called the "cog" (Fig 4*B*). The lateral epitympanic space is divided into the lateral epitympanic recess located superiorly and the Prusak space inferiorly. Laterally, the Prusak space is bordered by the scutum and pars flaccida of the tympanic membrane, medially by the malleus neck, superiorly by the lateral malleal ligament and inferiorly by the lateral process of the malleus.[8] Superiorly, the epitympanum communicates with the mastoid air cells via the aditus ad antrum. The epitympanum also contains the incudal fossa, which contains the short process of the incus and the posterior incudal ligament. The hypotympanum is the smallest and most inferior part of the middle ear cavity, located below the mesotympanum (Fig 5). The middle ear floor is formed by the jugular plate, also called the fundus tympani. The floor contains the opening to the Eustachian tube and is bordered medially by the internal carotid artery.

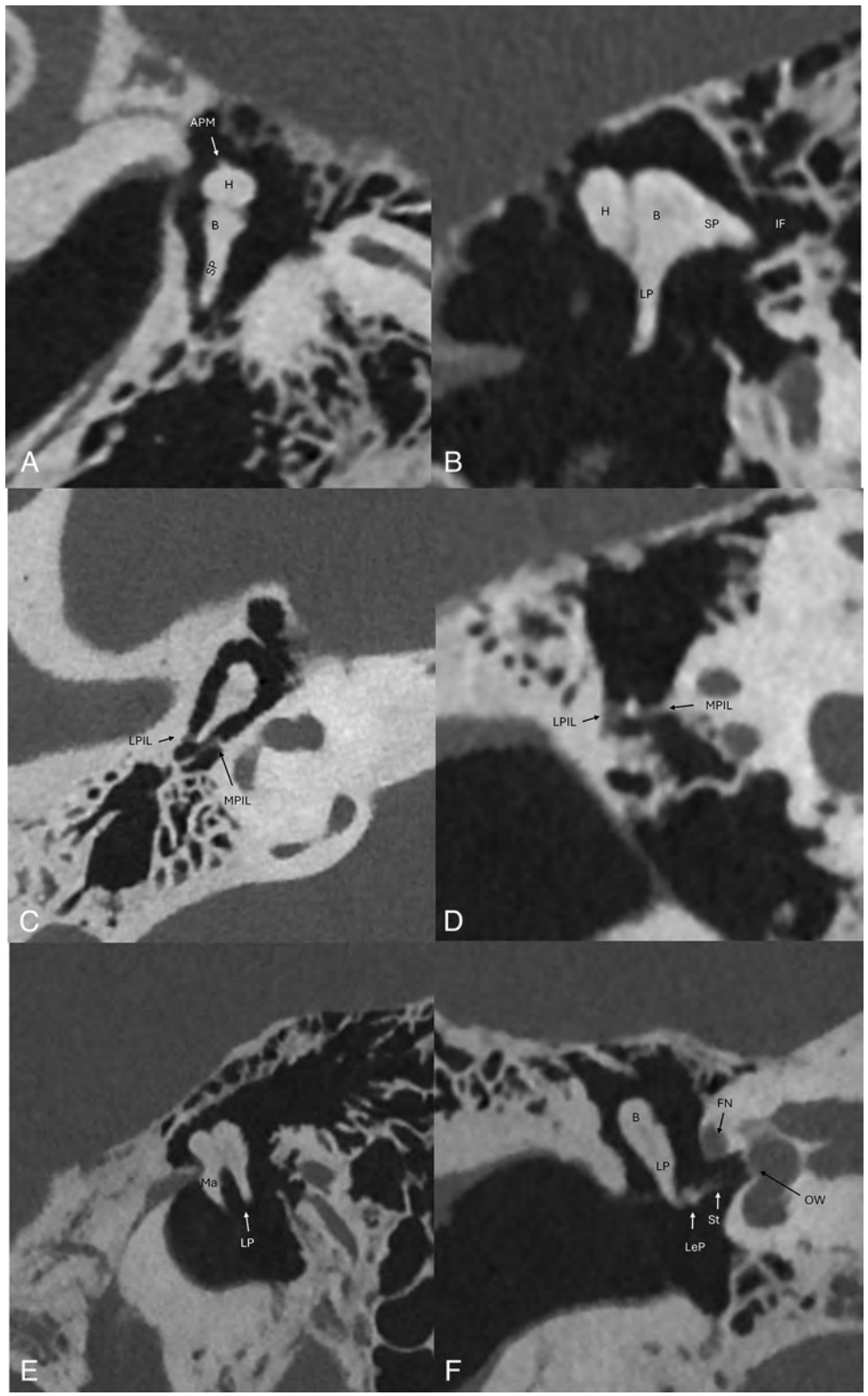

FIG 8. Axial oblique (*A*), sagittal oblique (*B* and *E*), axial (*C*), and coronal oblique (*D* and *F*) PCT images of the middle ear cavity with anatomic details of the ossicular chain. Sagittal oblique image (*E*) depicts the "molar tooth" configuration of the malleus manubrium and long process of the incus in parallel. Axial oblique and axial images of the incudomalleolar joint depicts the classic "ice cream cone" configuration. APM indicates anterior process of malleus; B, body of incus; FN, facial nerve tympanic segment; H, head of malleus; IF, incudal fossa; LeP, lenticular process of incus; LP, long process of incus; LPIL, lateral band of posterior incudal ligament; MPIL, medial band of posterior incudal ligament; OW, oval window; SP, short process of incus; St, stapes.

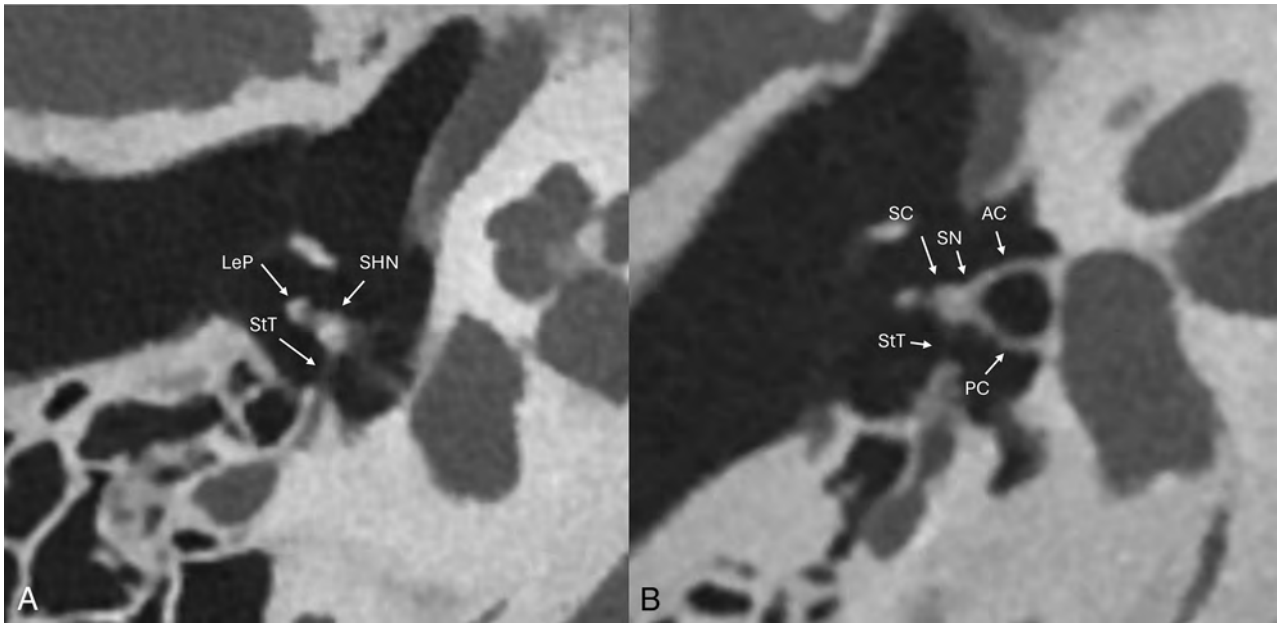

FIG 9. Axial and axial oblique PCT images of the stapes. *A*, LeP indicates lenticular process of incus; SHN, stapes head and neck; StT, stapedius tendon. *B*, AC, anterior crus of stapes; PC, posterior crus of stapes; SC, stapes capitulum (head); SN, stapes neck; StT, stapedius tendon.

The mesotympanum (Fig 6) contains several important osseous protuberances and recesses. The cochlear promontory makes up most of the anteromedial wall of the tympanic cavity. The round window recess or niche is posterior and inferior to the promontory. Small ridges of bone project along the posterior medial wall of the mesotympanum superiorly (ponticulus) and inferiorly (subiculum) and form an osseous bridge between the sinus tympani and round window niche.[14] The pyramidal eminence projects anteriorly from the posterior wall and contains the stapedius muscle within it. The sinus tympani is located medial to the pyramidal eminence. The facial nerve canal and facial recess are lateral to the pyramidal eminence. The oval window niche is a small depression posterior and superior to the cochlear promontory.

The mesotympanum and epitympanum contain most of the ossicular chain, which are composed of the malleus, incus, and stapes. The ossicular chain transmits sound from the tympanic membrane medially to the oval window. The malleus is made up of the head, neck, manubrium, anterior, and lateral processes (Fig 7). The manubrium, also known as the handle, is the longest process and attaches to the tympanic membrane. The tensor tympani muscle tendon, which dampens vibration, attaches to a small medially directed process on the manubrium.[15] The lateral process attaches to the tympanic membrane just below the pars flaccida.[16] The incus (Fig 8) is divided into 4 parts: the body, short process, long process, and lenticular process. The body of the incus articulates with the head of the malleus within the epitympanum at the incudomalleal joint forming the "ice cream cone" appearance on axial images. The short process of the incus projects posteriorly into the incudal fossa. The long process projects posteroinferiorly and parallel to the manubrium of the malleus creating the "molar tooth" appearance (Fig 8*E*).[17] The long process curves medially into the rounded lenticular process, which articulates with the head of the stapes. The long process is often the earliest ossicle to erode in the setting of a pars flaccida cholesteatoma. The stapes (Fig 9) resembles a stirrup, consisting of the head or capitulum, the neck, 2 crura, and the base or footplate. The stapedius muscle tendon, which dampens vibration, attaches to the posterior aspect of the stapes neck.

The ossicular chain is supported by the tensor tympani and stapedius muscles and ligaments specific to each ossicle (Figs 7 and 8). The tensor tympani muscle originates at the superior aspect of the Eustachian tube within the semicanal. The semicanal and the Eustachian tube run parallel to each other and are partially separated by the cochleariform process, which is a small bar of bone that extends laterally from the cochlear promontory. The tensor tympani tendon attaches to the posterior end of the cochleariform process and attaches to the neck of the malleus. The stapedius muscle is contained within a cavity within the pyramidal eminence. The tendon arises from a small hole in the apex of the pyramidal eminence and inserts to the neck of the stapes.

Each middle ear ossicle is supported by suspensory ligaments that provide passive support to aid in the conduction of sound through the middle ear to the oval window.[18] There are 3 ligaments that support the malleus. The anterior ligament attaches to the malleal neck just above the anterior process and to the carotid wall next to the petrotympanic fissure. The superior ligament extends from the head of the malleus to the roof of the epitympanic recess. The lateral ligament extends from the malleal head to the posterior part of the notch of Rivinus. The incus is supported by the posterior incudal ligament, which has medial and lateral bands, and attaches to the posterior part of the short process to the posterior wall of the incudal fossa (Fig 8*C*, *-D*). The annular ligament of the stapes is a fibrous ring that attaches the footplate of the stapes to the margin of the oval window.

CONCLUSIONS

In this review, we highlight the technical differences between traditional EID CT and PCT scanners. Although many structures have been described by using traditional CT scanners, the ultra-high resolution afforded by PCT scanners allows for greater spatial resolution of these structures and visualization of structures that were once beyond the limits of EID CT. Future research should include evaluation of pathology by using this new technology.

ACKNOWLEDGMENTS

The authors would like to thank Dr. Richard D. Beegle for reviewing the manuscript and images.

Disclosure forms provided by the authors are available with the full text and PDF of this article at www.ajnr.org.

REFERENCES

1. Leng S, Bruesewitz M, Tao S, et al. **Photon-counting detector CT: system design and clinical applications of an emerging technology.** *Radiographics* 2019;39:729–43 CrossRef Medline
2. Ferda J, Vendiš T, Flohr T, et al. **Computed tomography with a full FOV photon-counting detector in a clinical setting, the first experience**. *Eur J Radiology* 2021;137:109614 CrossRef Medline
3. Zhou W, Lane JI, Carlson ML, et al. **Comparison of a photon-counting-detector CT with an energy-integrating-detector CT for temporal bone imaging: a cadaveric study.** *AJNR Am J Neuroradiol* 2018;39:1733–38 CrossRef Medline
4. Benson JC, Rajendran K, Lane JI, et al. **A new frontier in temporal bone imaging: photon-counting detector CT demonstrates superior visualization of critical anatomic structures at reduced radiation dose.** *AJNR Am J Neuroradiol* 2022;43:579–84 CrossRef Medline
5. Loh TY, Cohen PR. **Darwin's tubercle: review of a unique congenital anomaly**. *Dermatol Ther (Heidelb)* 2016;6:143–49 CrossRef Medline
6. Som PM, Curtin HD. *Head and Neck Imaging*. 5th ed. Elsevier-OHCE; 2013:1059
7. Gunlock MG, Gentry LR. **Anatomy of the temporal bone.** *Neuroimaging Clin N Am* 1998;8:195–209
8. Benson JC, Lane JI. **Temporal bone anatomy.** *Neuroimaging Clin N Am* 2022;32:763–75 CrossRef Medline
9. Som PM, Curtin HD. *Head and Neck Imaging*. 5th ed. Elsevier-OHCE; 2013:1063
10. Hollinshead W. *Anatomy for Surgeons*. Harper & Row; 1968.
11. Isaacson B. **Anatomy and surgical approach of the ear and temporal bone.** *Head Neck Pathol* 2018;12:321–27 CrossRef Medline
12. Mansour S, Magnan J, Haidar H, et al. **Middle ear compartments**. In: *Comprehensive and Clinical Anatomy of the Middle Ear*. Springer-Verlag; 2013:122–127 CrossRef
13. Wojciechowski T, Skadorwa T, Drożdż A, et al. **The radioanatomical assessment of the Körner's septum**. *Surg Radiology Anat* 2019;41:669–73 CrossRef Medline
14. Virapongse C, Rothman SL, Kier EL, et al. **Computed tomographic anatomy of the temporal bone.** *AJR Am J Roentgenol* 1982;139:739–49 CrossRef Medline
15. Juliano AF. **Cross sectional imaging of the ear and temporal bone.** *Head Neck Pathol* 2018;12:302–20 CrossRef Medline
16. Som PM, Curtin HD. *Head and Neck Imaging*. 5th ed. Elsevier-OHCE; 2013:1067
17. Potter GD. **The lateral projection in tomography of the petrous pyramid.** *Am J Roentgenol Radium Ther Nucl Med* 1968;104:194–200 CrossRef Medline
18. Lemmerling MM, Stambuk HE, Mancuso AA, et al. **CT of the normal suspensory ligaments of the ossicles in the middle ear.** *AJNR Am J Neuroradiol* 1997;18:471–77 Medline

Atypical Parkinsonian Syndromes: Structural, Functional, and Molecular Imaging Features

Graham Keir, Michelle Roytman, Faizullah Mashriqi, Shaya Shahsavarani, and Ana M. Franceschi

ABSTRACT

SUMMARY: Atypical parkinsonian syndromes, also known as Parkinson-plus syndromes, are a heterogeneous group of movement disorders, including dementia with Lewy bodies (DLB), progressive supranuclear palsy (PSP), multisystem atrophy (MSA), and corticobasal degeneration (CBD). This review highlights the characteristic structural, functional, and molecular imaging features of these complex disorders. DLB typically demonstrates parieto-occipital hypometabolism with involvement of the cuneus on FDG-PET, whereas dopaminergic imaging, such as [^{123}I]-FP-CIT SPECT (DaTscan) or fluorodopa (FDOPA)-PET, can be utilized as an adjunct for diagnosis. PSP typically shows midbrain atrophy on structural imaging, whereas FDG-PET may be useful to depict frontal lobe hypometabolism and tau-PET confirms underlying tauopathy. MSA typically demonstrates putaminal or cerebellar atrophy, whereas FDG-PET highlights characteristic nigrostriatal or olivopontocerebellar hypometabolism, respectively. Finally, CBD typically shows asymmetric atrophy in the superior parietal lobules and corpus callosum, whereas FDG and tau-PET demonstrate asymmetric hemispheric and subcortical involvement contralateral to the side of clinical deficits. Additional advanced neuroimaging modalities and techniques described may assist in the diagnostic work-up or are promising areas of emerging research.

ABBREVIATIONS: 3D-SSP = 3D stereotactic surface projection; AD = Alzheimer disease; ASL = arterial spin-labeling; APS = atypical parkinsonian syndrome; CBD = corticobasal degeneration; CBS = corticobasal syndrome; CIS = cingulate island sign; DaT = dopamine transporter; DaTscan = [^{123}I]-FP-CIT SPECT; DIP = drug-induced parkinsonism; DLB = dementia with Lewy bodies; FA = fractional anisotropy; FDOPA = fluorodopa; MCP = middle cerebellar peduncle; MSA = multisystem atrophy; MSA-C = multisystem atrophy–cerebellar; MSA-P = multisystem atrophy–parkinsonian; PA = posterior atrophy; PD = Parkinson disease; PSP = progressive supranuclear palsy; rCBF = regional cerebral blood flow; rs-fMRI = resting-state functional MR imaging; RSN = resting-state network; SCP = superior cerebellar peduncle; SMA = supplementary motor area; VaP = vascular parkinsonism

Atypical parkinsonian syndromes (APSs), also known as Parkinson-plus syndromes, are a heterogeneous group of movement disorders presenting with early dementia, ataxia, dysautonomia, frequent falls, and ocular dysmotility in addition to parkinsonism. Patients with these syndromes, which include dementia with Lewy bodies (DLB), progressive supranuclear palsy (PSP), multisystem atrophy (MSA), and corticobasal degeneration (CBD), are often unresponsive to traditional Parkinson disease (PD) treatments and may even experience harm from such treatments. For example, dopaminergic treatment in DLB has been associated with worsening hallucinations or psychosis in up to one-third of patients.[1] Therefore, accurate diagnosis is critical for the appropriate management of these patients. Though these syndromes are discussed individually, it is important to recognize that neuropathology has demonstrated that multiple neurodegenerative disease processes may occur in the same patient.[2] In addition, protein abnormalities may be present before the onset of defining clinical features.[3] This may at least partially explain the heterogeneity that is seen in the presentation of APS. Key structural and molecular imaging features of Parkinson disease and APS are highlighted in the Table.

Received January 15, 2024; accepted after revision April 16.

From the Neuroradiology Division (G.K., M.R.), Department of Radiology, Weill Cornell Medical College, NY-Presbyterian Hospital, New York, New York; and Neuroradiology Division (F.M., S.S., A.M.F.), Department of Radiology, Donald and Barbara Zucker School of Medicine at Hofstra/Northwell, Lenox Hill Hospital, New York, New York.

Please address correspondence to Ana M. Franceschi, MD, PhD, Department of Radiology, Lenox Hill Hospital, 100 East 77th St, 3rd Floor, New York, NY 10075; e-mail: afranceschi@northwell.edu; @AFrances_MDPhD

Indicates article with online supplemental data.

http://dx.doi.org/10.3174/ajnr.A8313

DEMENTIA WITH LEWY BODIES

DLB is thought to be due to mutations in the alpha-synuclein gene that codes for the SYN protein. This protein is misfolded, forming Lewy bodies and Lewy neurites within the central nervous system, the same pathologic hallmark seen in PD. As such, both PD and DLB are often referred to as the spectrum of Lewy body disorders, along with Parkinson disease mild cognitive impairment and Parkinson disease dementia.[4]

The diagnosis of possible or probable DLB requires several central features, including progressive cognitive decline interfering with normal function, progressive memory impairment, as

Key structural and molecular imaging features in PD and APS

	Disease Entity				
	PD	DLB	PSP	MSA	CBD
Imaging technique					
MRI	Atrophy in the parietotemporal (including hippocampi) and to a lesser degree occipital regions	Atrophy in parieto-occipital regions with widening of the calcarine fissure and parietooccipital sulcus	Selective midbrain atrophy, "hummingbird," "morning glory," and "Mickey Mouse" signs	Prominent cerebellar atrophy, "hot cross bun" sign (MSA-C), and putaminal atrophy, "putaminal rim" sign (MSA-P)	Asymmetric hemispheric atrophy, particularly in superior parietal lobule, plus ipsilateral BG and thalamus
FDOPA-PET	↓ uptake striatum (greater in posterior putamen)	↓ uptake striatum (greater in posterior putamen)	↓ uptake striatum (anterior and posterior putamen)	↓ uptake striatum (greater reduction in MSA-P than MSA-C)	↓ uptake striatum contralateral to clinically affected side
FDG-PET	↓ parietotemporal and lateral occipital uptake, preserved binding in precuneus and posterior cingulate; no BG hypometabolism	↓ parieto-occipital and temporal uptake including in the cuneus and primary visual cortex, "cingulate island" sign	↓ dorsal and paramedian frontal lobe including anterior cingulate, premotor cortex, and SMA; decreased uptake in midbrain and basal ganglia	↓ putaminal (MSA-P) or ↓ cerebellar (MSA-C) uptake	↓ asymmetric hemispheric hypometabolism plus ipsilateral sensorimotor cortex, BG, and thalamus; crossed cerebellar diaschisis
Amyloid PET	+/−	+/−	Normal	Normal	+/−
Tau PET	Normal	Normal	+ (4R tau)	Normal	+ (4R tau)

Note:—BG indicates basal ganglia.

well as deficits in attention, executive function, or visuospatial ability (Online Supplemental Data).[5] Core features of DLB include fluctuating cognition, recurrent well-formed visual hallucinations, rapid eye movement sleep behavior disorder, and extrapyramidal symptoms (ie, bradykinesia, resting tremor, and rigidity). Confirmation of possible or probable DLB requires pathologic confirmation at autopsy. Of note, if cognitive symptoms occur more than 1 year following the onset of motor symptoms, the diagnosis of Parkinson disease dementia should be recommended rather than DLB.[5]

Structural Imaging

Structural imaging findings of DLB are generally nonspecific with varying patterns of atrophy. Therefore, the primary role for CT/MR imaging is to rule out alternate pathologies.[6] Visual scales have been used with varying degrees of success. One such scale is the posterior atrophy (PA) scale by Koedam and colleagues.[7] They described parieto-occipital sulcus widening as a cardinal feature of DLB. However, Oppedal et al[8] studied 333 patients with DLB and 352 patients with Alzheimer disease (AD) and found no statistically significant difference between AD and DLB on the PA scale. They found that mesial temporal atrophy was significantly higher for patients with AD in comparison to DLB and that patients with DLB exhibited atrophy that spared the hippocampi. Per their conclusions, a normal mesial temporal atrophy score in conjunction with abnormal PA and abnormal global cortical atrophy scale-frontal is quite specific for DLB, allowing for possible differentiation from AD. Note, the global cortical atrophy scale-frontal scale scores the degree of frontal atrophy from 0 to 3 (none, mild, moderate, and severe) as determined by enlargement of the posterior cingulate and parieto-occipital sulci and loss of volume involving the precuneus and parietal cortex. Quantification studies utilizing voxel-based morphometry have demonstrated decreased gray matter attenuation in DLB involving the greater mesial temporal and dorsal brainstem regions.[9]

Functional Imaging

There have been several interesting applications of functional imaging in the evaluation of DLB. Schumacher and colleagues[10] used resting-state functional MR imaging (rs-fMRI) to demonstrate decreased within-network connectivity in patients with DLB compared with controls in 9 resting-state networks (lateral sensorimotor, medial sensorimotor, temporal, basal ganglia, right motor, thalamic, insular 1, anterior cingulate, and temporal pole). Of note, there was no significant difference in within-network connectivity of patients with DLB on dopaminergic medications and those who were not medicated. Patients with DLB tended to have lower connectivity between the left frontoparietal and occipital pole networks compared with AD.

Watson and colleagues[11] demonstrated the potential utility of DTI to distinguish DLB from AD. They found reduced fractional anisotropy (FA) in patients with DLB compared with healthy controls, primarily involving the parieto-occipital white matter tracts as well as the pons and left thalamus. Meanwhile, patients with AD exhibited more diffuse changes.

Arterial spin-labeling (ASL) has also been evaluated in patients with DLB. Roquet et al[12] demonstrated greater deficits in CBF in the frontal, insular, and temporal cortices in DLB compared with AD and healthy controls. Meanwhile, AD demonstrated greater CBF reductions in the parietal and parietotemporal cortices. They also found that prodromal DLB could be successfully distinguished by using this technique, though not as accurately classified as mild DLB.

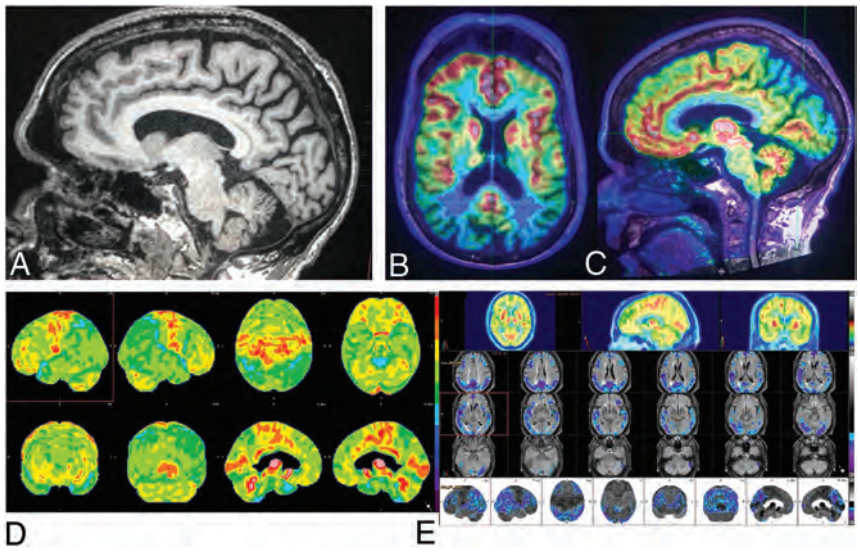

FIG 1. ^{18}F-FDG brain PET/MR imaging in DLB. *A*, 3D T1-MPRAGE sagittal image demonstrates posterior dominant (parieto-occipital) atrophy with widening of the parieto-occipital sulcus and to a lesser degree the calcarine fissure. *B*, Fused axial and (*C*) sagittal 3D T1-MPRAGE MR imaging-PET demonstrate preserved normal uptake in the posterior cingulate gyrus with hypometabolism in the precuneus consistent with cingulate island sign, typically seen in patients with dementia with Lewy bodies. *D*, 3D stereotactic surface projection (3D-SSP) PET cortical surface metabolic maps demonstrate abnormal FDG distribution pattern with moderate-to-severe hypometabolism in the parietotemporal regions, including in the mesial occipital lobe involving the primary visual cortex and cuneus. There is accompanying decreased tracer uptake in the bilateral precuneus with preserved normal binding in the posterior cingulate gyri consistent with cingulate island sign, which has been described in the setting of dementia with Lewy bodies. *E*, *Z* score statistical maps superimposed on FLAIR axials and 3D-SSP PET demonstrate significantly decreased values in bilateral occipital lobes, including in the cuneus, superior, and middle occipital gyri, and also in temporal and parietal regions, including in the precuneus and superior parietal lobules bilaterally.

Molecular Imaging

FDG-PET is a mainstay in the clinical assessment of patients with suspected DLB. FDG-PET demonstrates generalized hypometabolism, more profoundly affecting the parieto-occipital regions, including the medial occipital lobes (Fig 1). Compared with patients with posterior cortical atrophy, patients with DLB exhibit greater hypometabolism in the frontal lobes, anterior temporal lobes, and basal ganglia and tend to maintain greater hemispheric symmetry.[13] The cingulate island sign (CIS) has been highlighted as a specific imaging biomarker in DLB, representing sparing of the posterior cingulate gyrus compared with the precuneus and cuneus on FDG-PET or SPECT. Interestingly, CIS may be most prominent when the Mini-Mental State Examination is near the score of 22. Less clear evidence of CIS at lower Mini-Mental State Examination scores is likely due to the progression of neurodegenerative disease.[14] Statistical Parametric Mapping by using FDG-PET may be a helpful adjunct in the diagnosis of DLB. In a study by Caminiti et al,[15] early SMP-t-maps of regions of interest had nearly 89% agreement with the clinical diagnosis of DLB at final follow-up compared with the initial clinical classification, which was only 46% accurate. They found that medial and lateral occipital cortex hypometabolism with involvement of temporoparietal and frontal cortices denoted DLB-like metabolic patterns, whereas bilateral temporoparietal and/or precuneus/posterior cingulate cortex hypometabolism denoted AD-like metabolic patterns.[15]

Amyloid PET can be particularly helpful for identifying DLB in some patients. There is cortical uptake of amyloid tracers in 50%–70% of patients with DLB, which is not seen in PD and other forms of APS.[16] In addition, amyloid imaging may also help to distinguish DLB from AD. In a postmortem assessment of 39 patients who were scanned antemortem, the amyloid tracer Parkinson disease dementia was able to distinguish solitary DLB from AD with or without DLB copathology with an accuracy of 93%. Patients with AD demonstrated higher Pittsburgh compound B standardized uptake value ratios than solitary patients with DLB.[17]

Dopaminergic imaging can be helpful in distinguishing DLB from AD. Presynaptic ligands targeting the dopamine transporter (DaT) have been particularly effective, warranting their place in the diagnostic criteria. In a study of 10 patients with autopsy-confirmed DLB, [^{123}I]-FP-CIT SPECT (DaTscan; GE Healthcare) was able to predict 100% of DLB subjects by demonstrating reduced binding in the striatum. Furthermore, DaTscan was normal in all patients with clinically suspected DLB but negative autopsy, except 1 who had autopsy-confirmed AD.[18] Similarly,^{18}F-FP-CIT PET is highly sensitive for discriminating AD from DLB. By using a DaT availability cutoff of 2.48 for the whole striatum and a cutoff of 3.05 in the posterior putamen, Chung and colleagues[19] were able to obtain a sensitivity of 100% and a specificity of 78.1%. The presynaptic tracer [^{18}F]-FDOPA has demonstrated similar results in a case series by Khamis et al.[20] This is particularly exciting given the advantages of FDOPA-PET over DaTscan, including superior spatial resolution, lower radiation burden, and shorter examination times (Fig 2). Postsynaptic D2 receptors, which are up-regulated in DLB, have been less frequently utilized. However, Walker and colleagues[21] demonstrated the potential for [^{123}I]-iodobenzamide SPECT to discriminate DLB from AD. They found a significantly lower caudate to putamen ratio of [^{123}I]-iodobenzamide uptake in the left hemisphere compared with AD.[21] Though the presynaptic and postsynaptic dopaminergic tracers are particularly effective at distinguishing DLB from AD, they cannot distinguish DLB from PD or other forms of APS.

Though not entirely intuitive, [^{123}I] metaiodobenzylguanidine cardiac scintigraphy is remarkably effective for supporting the diagnosis of possible or probable DLB, given that patients with DLB typically demonstrate postganglionic cardiac sympathetic denervation. In a study of 85 patients with possible DLB, with 19 patients with DLB confirmed at autopsy, Slaets et al[22] found that all patients with autopsy-confirmed DLB had a heart-to-mediastinum-uptake ratio less than 1.68. The specificity

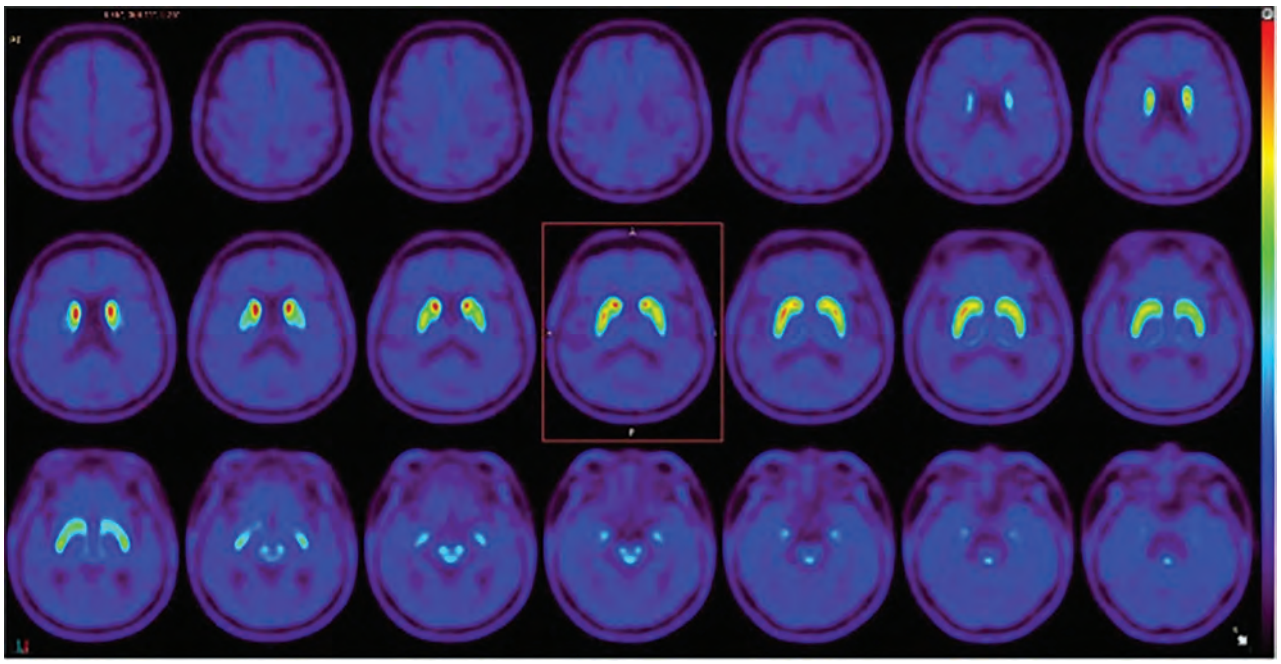

FIG 2. Abnormal ^{18}F-FDOPA-PET in dementia with Lewy bodies demonstrates decreased dopaminergic tracer uptake in the bilateral putamina and to a lesser degree in the caudate nuclei, also known as "loss of comma-tail" sign; findings are more pronounced on the left side.

was not as high, however, with 1 of 3 patients with AD having heart-to-mediastinum-uptake ratio below this threshold.

PROGRESSIVE SUPRANUCLEAR PALSY

PSP is a tauopathy characterized by parkinsonism with postural instability, bradykinesia, pseudobulbar syndrome with dysarthria and dysphagia, supranuclear palsy, and dementia. Given the varied clinical presentations of the different PSP phenotypes, the International Parkinson and Movement Disorder Society published criteria in 2017 that may be used to delineate among the varying PSP phenotypes (Online Supplemental Data).[23] The National Institute of Neurological Disorders and Stroke and the Society for PSP also established criteria that are frequently used in clinical practice.[24] Though the criterion standard remains diagnosis via pathology, imaging may accurately pinpoint afflicted areas of the brain and properly characterize the disease process, thereby improving patient management.

Structural Imaging

There are several well-described structural imaging findings that are classic for PSP. The "hummingbird" or "penguin" sign refers to flattening of the upwardly convex superior margin of the midbrain seen on the midsagittal view (Fig 3). The "Mickey Mouse" sign describes rounding of the cerebral peduncles on the axial view at the level of the superior colliculi. The "morning glory" sign represents loss of the lateral convex margin of tegmentum. Additional findings include enlargement of the third ventricle and atrophy of the superior cerebellar peduncles (SCPs) with associated increased T2 signal.[25] The visual assessment of SCP atrophy had sensitivity of 74% and specificity of 94% for identifying PSP in a study by Paviour et al.[26] Kataoka et al[25] found that patients with PSP with increased T2-weighted-FLAIR signal in the SCPs had significantly longer duration of symptoms compared with T2/FLAIR-negative patients with PSP. A widely utilized measurement is the midbrain anteroposterior diameter, because measurement of less than 12 mm has been associated with PSP. Though Righini et al[27] demonstrated this threshold had a low sensitivity for detecting PSP, they also noted that the discrepancy may have been due to differences in technical factors, such as section thickness compared with prior research. Other measurements include by using a midbrain to pons ratio of less than 0.52 and midbrain measurement of $<$9.35 mm on midsagittal T1-weighted MR imaging. These thresholds yielded 100% specificity for discriminating PSP from MSA and healthy controls in a study by Massey et al.[28]

Functional Imaging

DTI has demonstrated some efficacy in differentiating PSP from other forms of APS. Whitwell et al[29] found that, in contrast to corticobasal syndrome (CBS) and healthy controls, patients with PSP demonstrated reduced FA and increased mean diffusivity in infratentorial regions, primarily the SCPs and midbrain. Bharti et al[30] demonstrated the potential of blood oxygen level–dependent rs-fMRI in the evaluation of PSP. Patients with PSP exhibited significantly higher within-network resting-state functional connectivity than controls in the default mode and cerebellum resting-state networks (RSNs). Patients with PSP also had significantly lower between-network resting-state functional connectivity between lateral visual and auditory RSNs as well as between the cerebellum and insula RSNs.

Molecular Imaging

FDG-PET remains the clinical mainstay in the assessment of patients with PSP. Patients typically exhibit dorsal and paramedian frontal hypometabolism, including in the premotor cortex, supplementary motor area (SMA), and anterior cingulate, and

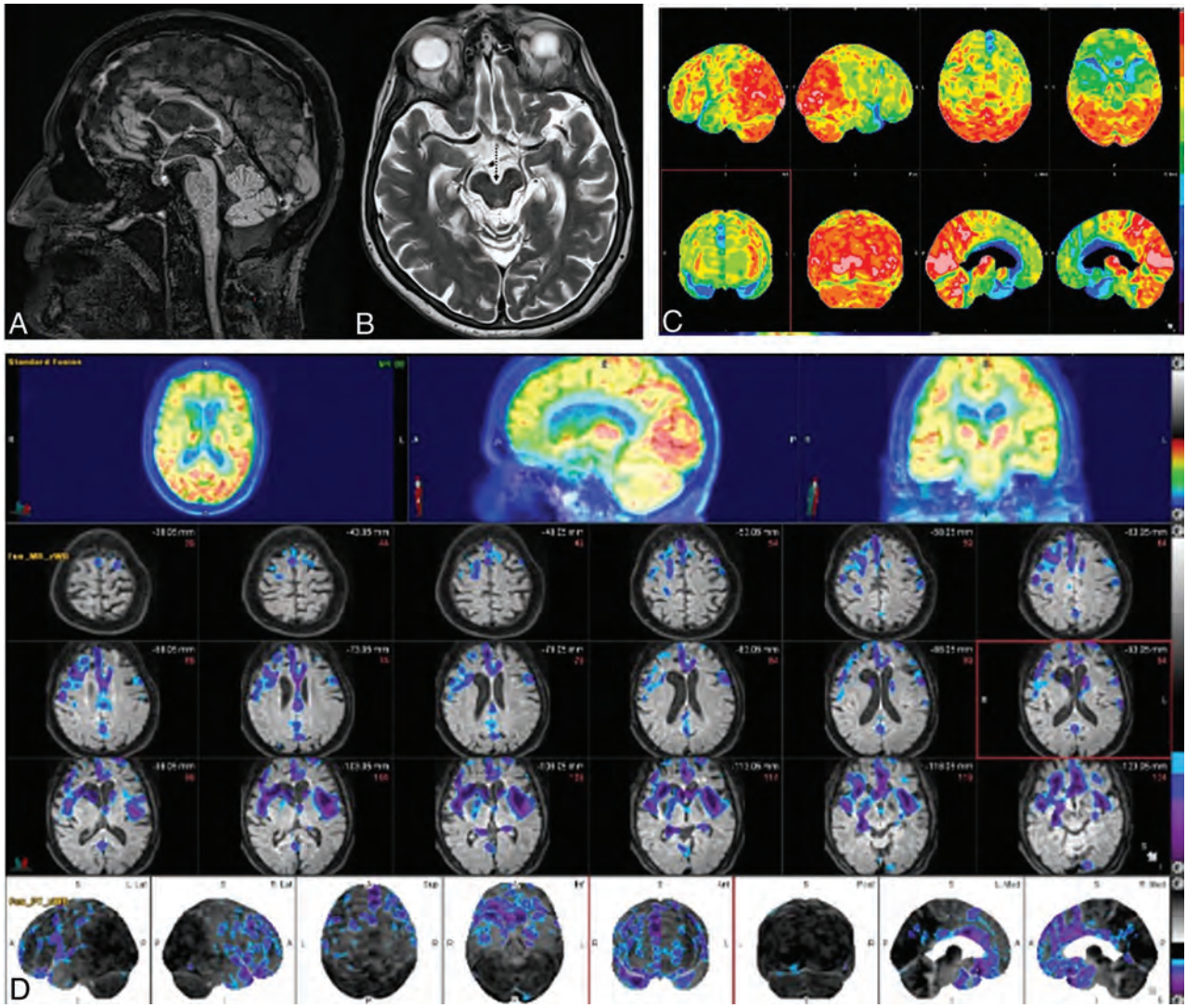

FIG 3. *A*, Sagittal 3D-FLAIR in patient with PSP demonstrates selective midbrain atrophy with prominent atrophy of the tegmentum without pontine atrophy and associated widening of the interpeduncular cistern, resembling the head and body of a hummingbird ("hummingbird sign"). *B*, Axial T2 demonstrates widening of the interpeduncular cistern (*arrow*) with rounded cerebral peduncles ("Mickey Mouse" sign) and increased lateral concavity of the midbrain tegmentum ("morning glory" sign). Note reduced midbrain AP diameter, with <12 mm from the interpeduncular fossa to the intercollicular groove considered abnormal. *C*, 3D stereotactic surface projection (3D-SSP) PET cortical surface metabolic maps demonstrate abnormal FDG distribution pattern with moderate-to-severe hypometabolism in the paramedian and dorsolateral frontal lobes, including in the premotor cortex, supplementary motor area, and anterior cingulate gyri bilaterally. *D*, *Z* score statistical maps superimposed on FLAIR axials and 3D-SSP PET demonstrate corresponding significantly decreased values in the bilateral frontal lobes, including in the middle and inferior frontal gyri, supplementary motor area, anterior cingulate gyri, and caudate nuclei.

may have decreased uptake in the midbrain and basal ganglia (Fig 3).[31] Regional hypometabolism in the insular cortices has also been described.[32] Regional differences in FDG-PET hypoperfusion have been observed in different clinical phenotypes of PSP. For example, hypometabolism in the anterior cingulate cortex correlates with vertical gaze palsy, thalamic hypometabolism with repeated unprovoked falls, decreased uptake in the midbrain with gait freezing, and left medial and dorsolateral frontal hypometabolism with nonfluent aphasia.[33,34]

On FDOPA-PET, PSP typically exhibits decreased FDOPA uptake in the caudate and anterior putamen to the same degree as in the posterior putamen. Furthermore, patients with PSP demonstrate more prominent and earlier loss of dopaminergic function when compared with PD.[33] Yoo et al[35] demonstrated the potential for DaTscan to differentiate PSP from frontotemporal dementia early in the disease course. By using a nonspecific binding ratio of 1.25 of the striatum to the remaining whole brain, they found 100% sensitivity and 84.6% specificity in discriminating between PSP and frontotemporal dementia.

The first-generation tau-PET tracer [^{18}F]-flortaucipir has demonstrated efficacy in differentiating among PSP variants. Whitwell et al[36] found that patients with the most common phenotype, Richardson syndrome, showed elevated uptake in the pallidum, putamen, thalamus, subthalamic nucleus, and red nucleus. Predominant speech/language disorder PSP cases demonstrated increased uptake in the pallidum, putamen, thalamus,

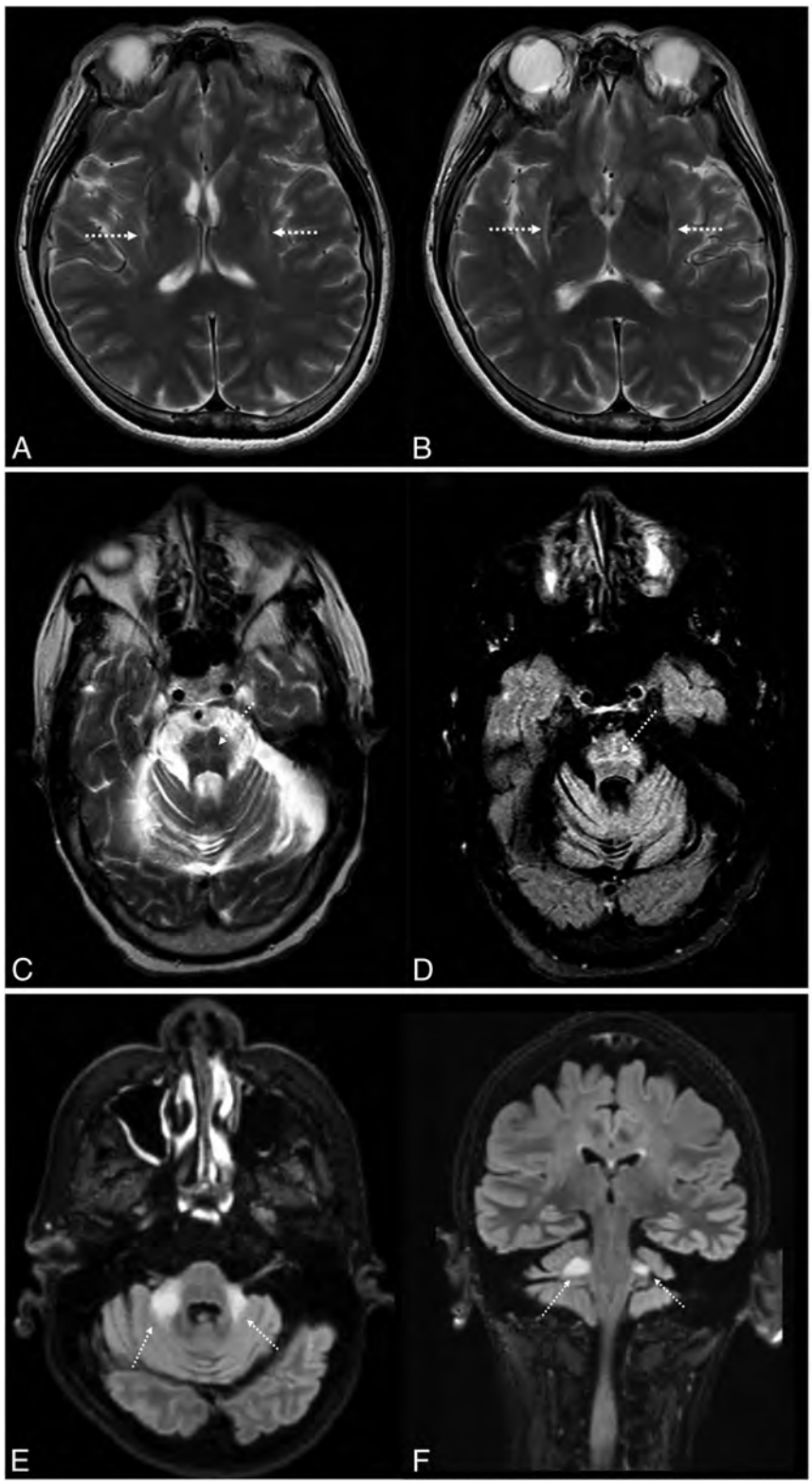

FIG 4. Axial T2 at the level of the basal ganglia (*A* and *B*) in patient with MSA-P demonstrates putaminal atrophy and hyperintense linear rim surrounding the putamen, "putaminal rim" sign, typically described at 1.5T (*arrows*). Axial T2 (*C*) and FLAIR (*D*) images in patient with MSA-C demonstrate marked atrophy of the cerebellum and brainstem with accompanying cruciform hyperintensity in the pons ("hot cross bun" sign) (*arrows*). In another patient with MSA-C, axial (*E*) and coronal FLAIR (*F*) at the level of the middle cerebellar peduncles demonstrate volume loss with prominent hyperintense signal abnormality ("MCP" sign) (*arrows*).

and frontal lobe (left greater than right). The second-generation selective tau tracer [^{18}F]-PI-2620 has demonstrated promise in the evaluation of PSP. By using postmortem autoradiography, Brendel et al[37] found increased [^{18}F]-PI-2620 binding in the basal ganglia and frontal cortex in patients with PSP, which co-localized with AT8-positive aggregated tau on immunohistochemistry. In vivo, [^{18}F]-PI-2620 PET demonstrated increased uptake in the putamen and substantia nigra in PSP-Richardson syndrome, key regions involved in the pathophysiology of PSP, successfully differentiating PSP from AD, healthy controls, and disease controls (MSA). Another tau tracer, MK-6240, has not been as successful in the evaluation of PSP due to poor binding capability. This is possibly due to its high specificity for the 3R + 4R isoform of tau tangles unique to AD.[38]

MULTIPLE SYSTEM ATROPHY

MSA encompasses a variety of neurodegenerative disorders with varying degrees of parkinsonism, cerebellar ataxia, and autonomic dysfunction. Patients are generally classified as having parkinsonian (MSA-P) or cerebellar (MSA-C) subtypes based on the predominating symptoms. Diagnostic criteria were developed by a consensus conference on MSA in 1998 and most recently revised in 2022 (Online Supplemental Data).[39]

Structural Imaging

There are a few characteristic imaging features that are unique to MSA-P and MSA-C. MSA-P generally affects the putamen. The "putaminal rim" or "putaminal slit" sign describes T2/FLAIR hyperintensity along the lateral margin of the putamen (Fig 4). However, this appearance has also been noted in healthy patients, particularly at 3T MR imaging.[40] MSA-P also typically demonstrates prominent T2*/SWI hypointensity in the putamen from iron deposition. Though this finding can be present in healthy controls, iron deposition is predominately dorsolateral in MSA-P, whereas in healthy patients,

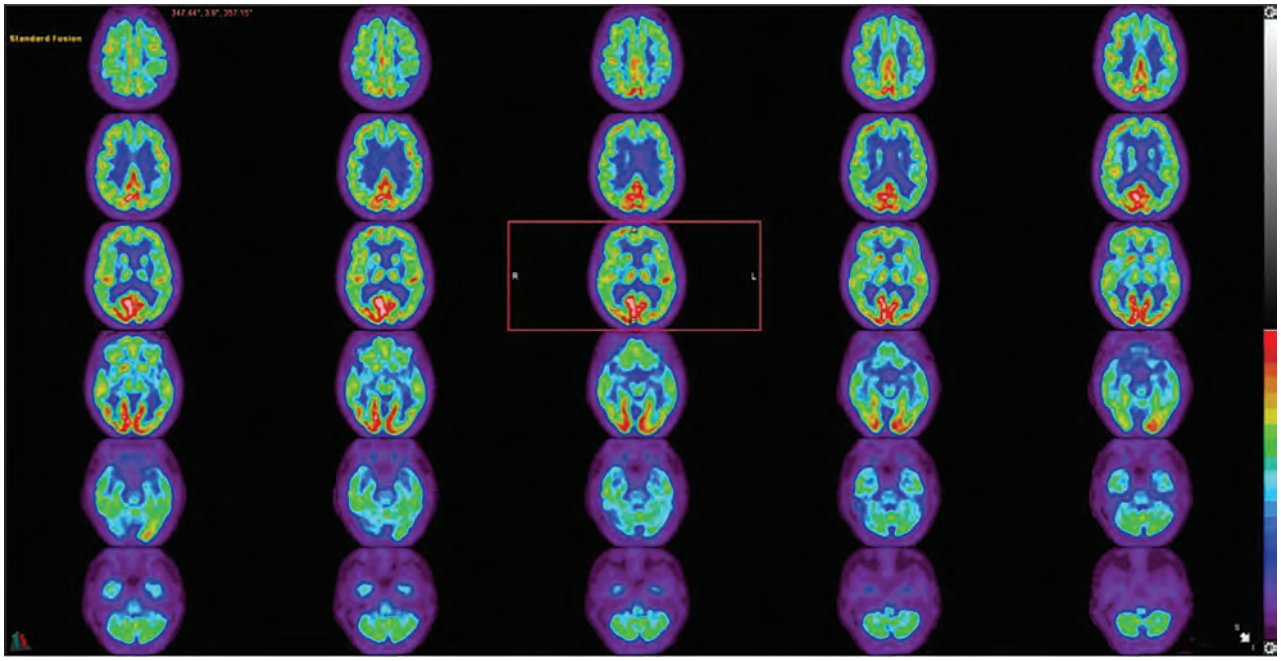

FIG 5. ^{18}F-FDG brain PET/MR imaging in MSA-P. Fused FLAIR MR imaging-PET transaxial views (3-mm slices) scaled to highlight FDG-PET findings demonstrate abnormal FDG distribution pattern with markedly decreased tracer uptake in the bilateral putamina (L > R).

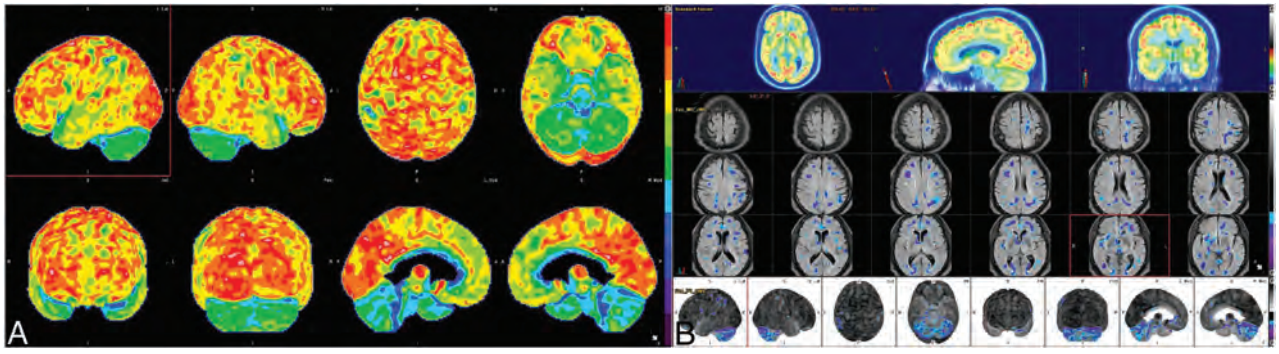

FIG 6. ^{18}F-FDG brain PET/MR imaging in MSA-C. *A*, 3D stereotactic surface projection (3D-SSP) PET cortical surface metabolic maps demonstrate abnormal FDG distribution pattern with moderate-to-severe hypometabolism in the cerebellum and brainstem. *B*, *Z* score statistical maps superimposed on FLAIR axial images and 3D-SSP PET demonstrate corresponding significantly decreased values in the cerebellum, including in the cerebellar vermis, cerebellar hemispheres, and middle cerebellar peduncles, and also in the brainstem, pons, and pontine tegmentum.

iron deposition initiates laterally and progresses medially.[41,42] Putaminal T2 hypointensity has been described,[41,43] though this may also be seen in other neurodegenerative diseases or acquired conditions.[44] Associated putaminal volume loss may help to differentiate MSA from PD and related pathologies.[45]

In contrast to MSA-P, MSA-C tends to affect the infratentorial structures. The "hot cross bun" sign is a classic finding of MSA-C, representing cruciform hyperintensity in the pons on T2/FLAIR due to degeneration of pontocerebellar fibers (Fig 4). Though this sign is noted in up to 80% of patients, it is not specific for MSA-C, as it may also be seen in spinocerebellar ataxia.[46] The middle cerebellar peduncle (MCP) sign is characterized by atrophy and T2/FLAIR signal hyperintensity of the middle cerebellar peduncles (Fig 4).[47,48] Additional areas of atrophy in MSA-C include the cerebellar hemispheres, medulla, and basis pontis, with compensatory dilation of the 4th ventricle.

Functional Imaging

MR spectroscopy has been employed in the evaluation of MSA with variable and at times conflicting results. Multiple studies have shown a decreased NAA:Cr ratio in the lentiform nucleus compared with controls.[49,50] However, this finding is not specific, as similar reductions have been found in PSP. MR spectroscopy abnormalities have also been reported in the pons, cerebellum, medulla, and frontal cortex.[50] DTI has demonstrated decreased FA in the MCP, inferior cerebellar peduncle, basis pontis, and internal capsule. Decreased FA values in the MCP have been shown to correlate with clinical symptoms[51] and occur early in the disease course of MSA-C.[52] rs-fMRI demonstrates differing patterns of functional connectivity modifications in MSA-C and MSA-P compared with healthy controls. MSA-P demonstrates a reduced connectivity of the default mode network whereas MSA-C demonstrates

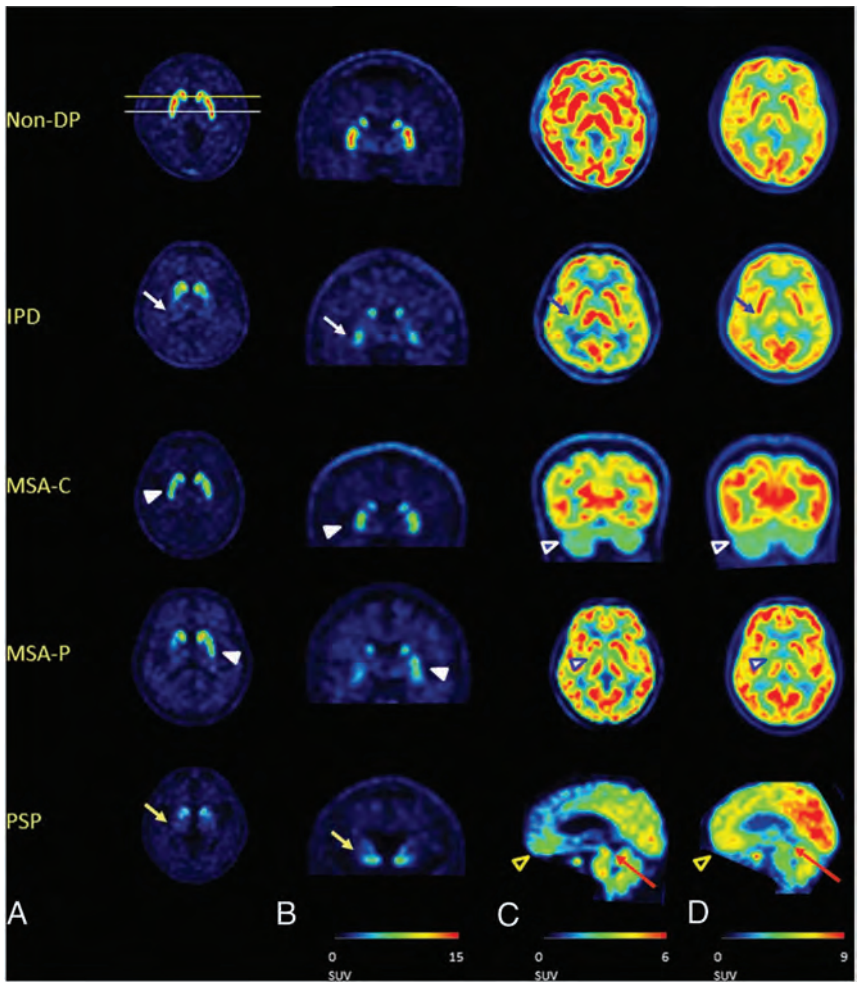

FIG 7. Examples of axial (*A*) and coronal section (*B*) of delayed-phase ^{18}F-FP-CIT PET, early-phase ^{18}F-FP-CIT PET (*C*), and ^{18}F-FDG-PET (*D*) of patients with nondegenerative parkinsonism (*1st row*), idiopathic Parkinson disease (IPD) (*2nd row*), MSA-C (*3rd row*), MSA-P (*4th row*), and PSP (*5th row*). The patient with IPD (*2nd row*) has decreased DaT binding of the bilateral dorsal posterior putamen, with relative sparing of the ventral putamen (*white arrow*) on delayed-phase ^{18}F-FP-CIT PET and normal striatal metabolism or hypermetabolism in the bilateral dorsolateral putamen on early-phase ^{18}F-FP-CIT PET and ^{18}F-FDG-PET (*blue arrow*). The patients with MSA-C and MSA-P (*3rd and 4th rows*), have DaT loss not only in the posterior putamen but also in the ventral putamen (*white arrowhead*) on delayed-phase ^{18}F-FP-CIT PET. On early-phase ^{18}F-FP-CIT PET and ^{18}F-FDG-PET, MSA showed hypometabolism in the cerebellar cortex (*blue arrowhead with white outline*) and/or hypometabolism in the basal ganglia (*blue arrowhead with white outline*). The patient with PSP has extensive DaT loss in both the putamen and caudate nuclei on delayed-phase ^{18}F-FP-CIT PET (*yellow arrow*), which was characterized by hypometabolism in the medial frontal cortices (*black arrowhead with yellow outline*) and midbrain (*red arrow*) on early-phase ^{18}F-FP-CIT PET and ^{18}F-FDG-PET. Non-DP = nondegenerative parkinsonism. *Reproduced with permission from Oh M, Lee N, Kim C, et al. Diagnostic accuracy of dual-phase 18F-FP-CIT PET imaging for detection and differential diagnosis of Parkinsonism. Sci Rep 2021;11:14992.*

Molecular Imaging

FDG-PET generally demonstrates regional hypometabolism corresponding to areas of atrophy and signal abnormality observed on structural imaging. Hypometabolism in MSA-P is often in a nigrostriatal distribution, particularly in the putamen (Fig 5), whereas hypometabolism in MSA-C is in an olivopontocerebellar distribution, with profound deficits in the brainstem and cerebellum (Fig 6).[41,55] The degree of hypometabolism in the striatum and cerebellum correlates with severity of parkinsonism and ataxia, respectively.

FDOPA-PET, a biomarker of nigrostriatal dysfunction, demonstrates decreased uptake in the caudate and putamen in MSA, as seen in other types of APS.[41,45,49] DaTscan demonstrates reduced dopamine transporter availability in the striatum, with a more rapid decline in the caudate and anterior putamen,[45] whereas [^{18}F]-FP-CIT PET highlights decreased uptake in the dorsal striatum with preserved caudate uptake.[56] Oh et al[57] found that dual-phase [^{18}F]-FP-CIT PET in conjunction with FDG-PET had greater than 90% accuracy for the differentiation of PD, MSA, PSP, and nondegenerative parkinsonism (Fig 7). ^{11}C-raclopride, a selective D2 receptor antagonist, has shown promise in distinguishing MSA-P from PD in a study by Van Laere et al.[58]

MSA is an alpha-synucleinopathy, and therefore, cortical binding is not seen on amyloid or tau-PET. There is, however, some evidence that tau accumulation may play a role in the pathogenesis of MSA. [^{18}F]-flortaucipir demonstrates increased binding in the putamen of patients with MSA.[59] On the other hand, [^{18}F]-PI-2620 demonstrated no uptake in patients with MSA, who served as disease controls in a study assessing this tracer as a PSP biomarker.[37]

higher connectivity in the pontocerebellar network, which may play a role in disturbances of eye movement control.[53] ASL may be a useful adjunct for identifying patients with MSA-C. Compared with controls, patients with MSA-C have demonstrated distinct disruption of regional cerebral blood flow (rCBF) in the cerebellum. The rCBF of the vermis demonstrated sensitivity of 95.8% and specificity of 100% in differentiating patients with MSA-C from controls.[54]

CORTICOBASAL DEGENERATION

CBD is a 4R-tauopathy that results in asymmetric degeneration of the basal ganglia and cortical dysfunction. Typical basal ganglia manifestations include asymmetric rigidity, apraxia, limb dystonia, and alien limb phenomenon, which are unresponsive to levodopa therapy. Cognitive symptoms include nonfluent aphasia, sensory loss, behavior changes, and executive dysfunction.[60-62] Accurate diagnosis of CBD is difficult for the clinician

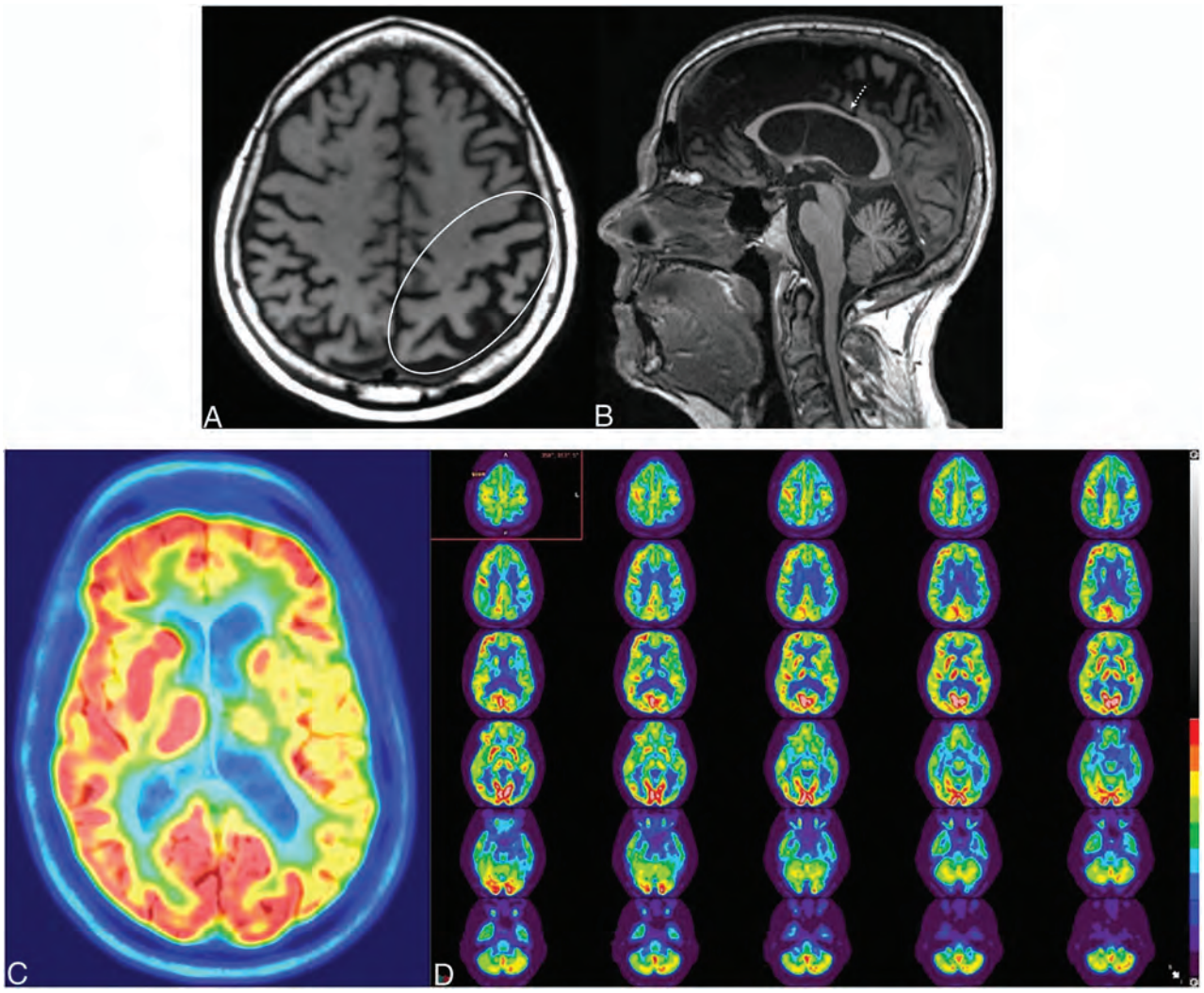

FIG 8. Corticobasal degeneration. *A*, Axial 3D TI-MPRAGE demonstrates asymmetric atrophy in the left cerebral hemisphere that is particularly pronounced in the left sensorimotor cortex and superior parietal lobule (*ellipse*). *B*, Sagittal 3D TI-MPRAGE in the same patient demonstrates marked atrophy of the corpus callosum, which is more pronounced posteriorly (*arrow*). *C*, ^{18}F-FDG brain PET/MR imaging axial view at the level of the basal ganglia demonstrates marked asymmetric hypometabolism involving the left cerebral hemisphere, basal ganglia, and thalamus. *D*, Fused FLAIR MR imaging-PET transaxial views (3-mm slices) scaled to highlight FDG-PET findings also demonstrate hypometabolism in the left sensorimotor cortex and accompanying right-sided crossed cerebellar diaschisis.

given the highly variable spectrum of presentations (Online Supplemental Data).[63]

Structural Imaging

Patients with CBD typically demonstrate asymmetric frontoparietal atrophy, particularly in the perirolandic region and superior parietal lobule (Fig 8), typically contralateral to the side of motor symptoms.[60] However, asymmetric atrophy is not specific to CBD, with the differential including other subtypes of frontotemporal lobar degeneration and atypical Alzheimer disease. CBD may demonstrate accompanying T2/FLAIR hyperintensity in the ipsilateral frontoparietal white matter. Atrophy of the corpus collosum has also been described.[64] A minority of patients have demonstrated ipsilateral basal ganglia atrophy.

Functional Imaging

DTI in CBD demonstrates decreased FA in the corticospinal tract, frontal/prefrontal white matter, and the corpus callosum of the affected hemisphere.[29] Blood oxygen level–dependent fMRI features decreased activation of the sensorimotor, parietal cortices, and SMA contralateral to the affected hand on thumb opposition tasks.[64] Multiple studies by using MR spectroscopy have demonstrated decreased NAA:Cr in the basal ganglia and frontal cortex.[65,66] The marked asymmetry of the changes is most useful in differentiating CBD from other APS entities.[64] Furthermore, ASL has demonstrated rCBF asymmetry in similar regions as structural atrophy, such as the perirolandic and parietal cortex, though possibly with higher sensitivity.[67]

Molecular Imaging

FDG-PET findings typically parallel patterns of atrophy on structural imaging, featuring asymmetric hypometabolism in the frontoparietal cortices, sensorimotor cortex, basal ganglia, and thalamus contralateral to the clinically affected side (Fig 8). Crossed cerebellar diaschisis has also been observed.[34,60,68] Patterns of hypometabolism

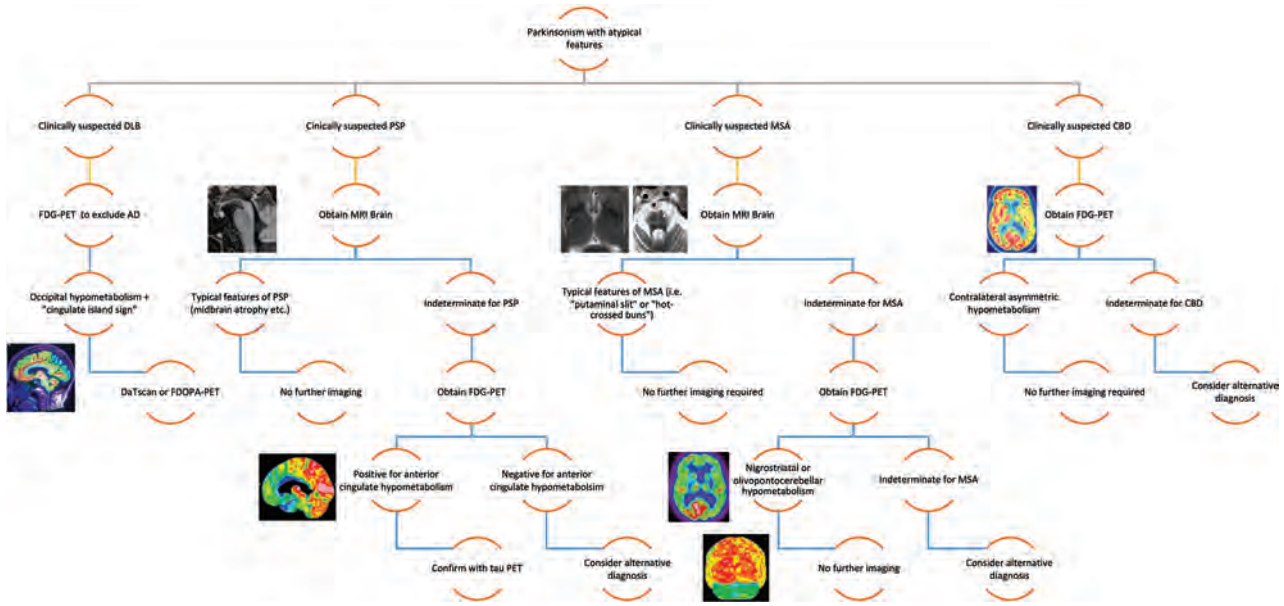

FIG 9. Imaging algorithm for the diagnosis of atypical parkinsonian syndromes.

in CBD typically parallel clinical presentation; for example, the superior and middle frontal gyri as well as the SMA are implicated in patients with apraxia, whereas the left anterior insula and frontal operculum are hypometabolic in patients with language deficits.[69] FDOPA-PET demonstrates decreased binding in the striatum predominately contralateral to the clinically affected side. However, some patients may show a more symmetric decreased radiotracer uptake pattern, though not as extensive as in PD.[64] Presynaptic dopaminergic SPECT ligands including [^{123}I]-β-CIT and [^{123}I]-FP-CIT[70] may demonstrate higher baseline striatal binding in APS relative to Parkinson disease; however, the rate of striatal binding decreases faster in APS. In fact, CBD may have normal DaTscan at presentation, likely related to delayed neuronal loss compared with MSA and PSP.[60,71]

Tau imaging by using [^{18}F]-flortaucipir and [^{18}F]-THK-5351 demonstrates increased uptake in the frontoparietal cortices, basal ganglia, and thalamus contralateral to the clinically affected side.[70,72] By using the second-generation ligand [^{18}F]-PI-2620, Palleis et al[73] demonstrated increased radiotracer uptake in the basal ganglia and dorsolateral prefrontal cortex in both patients with beta-amyloid positive and negative CBS. However, [^{18}F]-PI-2620 uptake was higher in beta-amyloid-positive CBS.[73,74]

NONDEGENERATIVE PARKINSONIAN SYNDROMES

Nondegenerative or "secondary parkinsonism" can result from vascular events, medications, or other insults, such as infection or trauma. Vascular parkinsonism (VaP) is difficult to diagnose due to its clinical heterogeneity and overlapping features with other forms of parkinsonism. Notably, parkinsonism with prominent white matter hyperintensities on MR imaging does not necessarily imply the diagnosis of VaP.[75] The only definite causes of VaP are ischemic or hemorrhagic lesions involving the substantia nigra or nigrostriatal pathway.[76] Presynaptic dopaminergic imaging, such as ^{123}FP-CIT SPECT (DaTscan), is essential in these patients, typically demonstrating preserved or mildly decreased striatal uptake. In acute cases, a reduction in uptake has been observed ipsilateral to the side of infarct.[77] Presynaptic imaging may help predict response to levodopa therapy, which can have a negative effect on these patients.[78]

There are many medications known to cause drug-induced parkinsonism (DIP), with neuroleptics being the most common. If DIP is suspected, discontinuation of the offending medication will typically improve symptoms. A systematic review reported complete recovery at 6 months in 94.85% of patients with DIP following the discontinuation of cinnarizine and flunarizine.[79] When medications cannot be discontinued, dopamine transporter imaging (DaTscan or FDOPA) can be useful. These studies typically demonstrate normal uptake in DIP,[80-82] in contrast to the decreased striatal uptake in neurodegenerative parkinsonism.

DIAGNOSTIC ALGORITHM

A proposed algorithm for APS imaging assessment is shown in Fig 9, demonstrating an approach that may be helpful in the evaluation of APS, depending on the clinical features and suspected etiologies. For example, following a neurologic examination and cognitive assessment, the patient may have fluctuating cognition and visual hallucinations with extrapyramidal symptoms, suspicious for DLB. In this case, an FDG-PET can be obtained to exclude AD and DaTscan or FDOPA-PET may be obtained to evaluate for dopaminergic degeneration. Alternatively, if the patient demonstrates a primary movement disorder, the imaging should be tailored to the specific symptoms. For patients with specific clinical features, such as cerebellar signs (suggesting MSA-C) or vertical gaze palsy (suggesting PSP), the imaging evaluation should be optimized to detect these disorders. For example, in PSP, MR imaging can be utilized to assess for midbrain volume loss, and if detected, then further imaging may not be required. Otherwise, FDG-PET may be considered, which typically demonstrates frontal lobe hypometabolism in PSP. This

may then be confirmed with tau-PET. DaTscan or FDOPA-PET would not be useful in this case, as it would demonstrate decreased striatal binding and not help to differentiate among the APS subtypes. Though many of the discussed advanced neuroimaging techniques are not represented in this algorithm, these remain active areas of investigation that may someday find their way into mainstream clinical practice or perhaps aid in very specific diagnostic dilemmas.

CONCLUSIONS

APS encompasses a heterogeneous group of movement disorders, for which neuroimaging plays a critical role in diagnosis. With an abundance of emerging techniques and radiotracers available to evaluate these conditions, it is essential for neuroradiologists to be aware of the strengths and limitations of each technique so that they can appropriately advise the referring physician, thereby contributing to timely diagnosis and treatment.

Disclosure forms provided by the authors are available with the full text and PDF of this article at www.ajnr.org.

REFERENCES

1. Goldman JG, Goetz CG, Brandabur M, et al. **Effects of dopaminergic medications on psychosis and motor function in dementia with Lewy bodies.** *Mov Disord* 2008;23:2248–50 CrossRef Medline
2. Dugger BN, Adler CH, Shill HA, et al; Arizona Parkinson's Disease Consortium. **Concomitant pathologies among a spectrum of parkinsonian disorders**. *Parkinsonism Relat Disord* 2014;20:525–29 CrossRef Medline
3. Dugger BN, Dickson DW. **Pathology of neurodegenerative diseases.** *Cold Spring Harb Perspect Biol* 2017;9:a028035 CrossRef Medline
4. Irwin DJ, Hurtig HI. **The contribution of tau, amyloid-beta and alpha-synuclein pathology to dementia in Lewy body disorders.** *J Alzheimer's Dis Park* 2018;8:444
5. McKeith IG, Boeve BF, Dickson DW, et al. **Diagnosis and management of dementia with Lewy bodies: fourth consensus report of the DLB Consortium.** *Neurology* 2017;89:88–100 CrossRef Medline
6. Broski SM, Hunt CH, Johnson GB, et al. **Structural and functional imaging in parkinsonian syndromes.** *Radiographics* 2014;34:1273–92 CrossRef Medline
7. Koedam EL, Lehmann M, van der Flier WM, et al. **Visual assessment of posterior atrophy development of a MRI rating scale.** *Eur Radiology* 2011;21:2618–25 CrossRef Medline
8. Oppedal K, Ferreira D, Cavallin L, et al; Alzheimer's Disease Neuroimaging Initiative. **A signature pattern of cortical atrophy in dementia with Lewy bodies: a study on 333 patients from the European DLB consortium**. *Alzheimers Dement* 2019;15:400–09 CrossRef Medline
9. Nakatsuka T, Imabayashi E, Matsuda H, et al. **Discrimination of dementia with Lewy bodies from Alzheimer's disease using voxel-based morphometry of white matter by statistical parametric mapping 8 plus diffeomorphic anatomic registration through exponentiated lie algebra**. *Neuroradiology* 2013;55:559–66 CrossRef Medline
10. Schumacher J, Peraza LR, Firbank M, et al. **Functional connectivity in dementia with Lewy bodies: a within- and between-network analysis.** *Hum Brain Mapp* 2018;39:1118–29 CrossRef Medline
11. Watson R, Blamire AM, Colloby SJ, et al. **Characterizing dementia with Lewy bodies by means of diffusion tensor imaging.** *Neurology* 2012;79:906–14 CrossRef Medline
12. Roquet D, Sourty M, Botzung A, et al. **Brain perfusion in dementia with Lewy bodies and Alzheimer's disease: an arterial spin labeling MRI study on prodromal and mild dementia stages**. *Alzheimer's Res Ther* 2016;8:1–13
13. Whitwell JL, Graff-Radford J, Singh TD, et al. **^{18}F-FDG PET in posterior cortical atrophy and dementia with Lewy bodies.** *J Nucl Med* 2017;58:632–38 CrossRef Medline
14. Iizuka T, Iizuka R, Kameyama M. **Cingulate island sign temporally changes in dementia with Lewy bodies.** *Sci Rep* 2017;7:14745 CrossRef Medline
15. Caminiti SP, Sala A, Iaccarino L, et al. **Brain glucose metabolism in Lewy body dementia: implications for diagnostic criteria.** *Alzheimer's Res Ther* 2019;11:1–14
16. Rowe CC, Villemagne VL. **Brain amyloid imaging.** *J Nucl Med Technol* 2013;41:11–18 CrossRef Medline
17. Kantarci K, Lowe VJ, Chen Q, et al. **β-amyloid PET and neuropathology in dementia with Lewy bodies**. *Neurology* 2020;94:e282–91 CrossRef Medline
18. Walker RWH, Walker Z. **Dopamine transporter single photon emission computerized tomography in the diagnosis of dementia with Lewy bodies.** *Mov Disord* 2009;24 Suppl 2:S754–59 CrossRef Medline
19. Chung SJ, Lee YH, Yoo HS, et al. **Distinct FP-CIT PET patterns of Alzheimer's disease with parkinsonism and dementia with Lewy bodies**. *Eur J Nucl Med Mol Imaging* 2019;46:1652–60 CrossRef Medline
20. Khamis K, Giladi N, Levine C, et al. **The added value of ^{18}F-FDOPA PET/CT in the work-up of patients with movement disorders.** *Neurograph* 2019;9:344–48 CrossRef
21. Walker Z, Costa DC, Janssen AG, et al. **Dementia with Lewy bodies: a study of post-synaptic dopaminergic receptors with iodine-123 iodobenzamide single-photon emission tomography.** *Eur J Nucl Med* 1997;24:609–14 CrossRef Medline
22. Slaets S, Van Acker F, Versijpt J, et al. **Diagnostic value of MIBG cardiac scintigraphy for differential dementia diagnosis.** *Int J Geriatr Psychiatry* 2015;30:864–69 CrossRef Medline
23. Höglinger GU, Respondek G, Stamelou M, et al; Movement Disorder Society-Endorsed PSP Study Group. **Clinical diagnosis of progressive supranuclear palsy: the Movement Disorder Society criteria**. *Mov Disord* 2017;32:853–64 CrossRef Medline
24. Hauw JJ, Daniel SE, Dickson D, et al. **Preliminary NINDS neuropathologic criteria for Steele-Richardson-Olszewski syndrome (progressive supranuclear palsy).** *Neurology* 1994;44:2015–19 CrossRef Medline
25. Kataoka H, Tonomura Y, Taoka T, et al. **Signal changes of superior cerebellar peduncle on fluid-attenuated inversion recovery in progressive supranuclear palsy.** *Parkinsonism Relat Disord* 2008;14:63–65 CrossRef Medline
26. Paviour DC, Price SL, Stevens JM, et al. **Quantitative MRI measurement of superior cerebellar peduncle in progressive supranuclear palsy.** *Neurology* 2005;64:675–79 CrossRef Medline
27. Righini A, Antonini A, De Notaris R, et al. **MR imaging of the superior profile of the midbrain: differential diagnosis between progressive supranuclear palsy and Parkinson disease.** *AJNR Am J Neuroradiol* 2004;25:927–32
28. Massey LA, Micallef C, Paviour DC, et al. **Conventional magnetic resonance imaging in confirmed progressive supranuclear palsy and multiple system atrophy.** *Mov Disord* 2012;27:1754–62 CrossRef Medline
29. Whitwell JL, Schwarz CG, Reid RI, et al. **Diffusion tensor imaging comparison of progressive supranuclear palsy and corticobasal syndromes.** *Parkinsonism Relat Disord* 2014;20:493–98 CrossRef Medline
30. Bharti K, Bologna M, Upadhyay N, et al. **Abnormal resting-state functional connectivity in progressive supranuclear palsy and corticobasal syndrome.** *Front Neurol* 2017;8:248 CrossRef Medline
31. Zhao P, Zhang B, Gao S. **18F-FDG PET study on the idiopathic Parkinson's disease from several parkinsonian-plus syndromes**. *Parkinsonism Relat Disord* 2012;18 Suppl 1:S60–62 CrossRef Medline
32. Tripathi M, Dhawan V, Peng S, et al. **Differential diagnosis of parkinsonian syndromes using F-18 fluorodeoxyglucose positron emission tomography.** *Neuroradiology* 2013;55:483–92 CrossRef Medline

33. Niccolini F, Politis M. **A systematic review of lessons learned from PET molecular imaging research in atypical parkinsonism.** *Eur J Nucl Med Mol Imaging* 2016;43:2244–54 CrossRef Medline
34. Eckert T, Barnes A, Dhawan V, et al. **FDG PET in the differential diagnosis of parkinsonian disorders.** *Neuroimage* 2005;26:912–21 CrossRef Medline
35. Yoo HS, Chung SJ, Kim SJ, et al. **The role of 18F-FP-CIT PET in differentiation of progressive supranuclear palsy and frontotemporal dementia in the early stage.** *Eur J Nucl Med Mol Imaging* 2018;45:1585–95 CrossRef Medline
36. Whitwell JL, Tosakulwong N, Botha H, et al. **Brain volume and flortaucipir analysis of progressive supranuclear palsy clinical variants.** *NeuroImage Clin* 2020;25:102152
37. Brendel M, Barthel H, van Eimeren T, et al. **Assessment of 18F-PI-2620 as a biomarker in progressive supranuclear palsy.** *JAMA Neurol* 2020;77:1408–19 CrossRef Medline
38. Aguero C, Dhaynaut M, Normandin MD, et al. **Autoradiography validation of novel tau PET tracer [F-18]-MK-6240 on human postmortem brain tissue.** *Acta Neuropathol Commun* 2019;7:37 CrossRef Medline
39. Wenning GK, Stankovic I, Vignatelli L, et al. **The Movement Disorder Society criteria for the diagnosis of multiple system atrophy.** *Mov Disord* 2022;37:1131–48 CrossRef Medline
40. Lee WH, Lee CC, Shyu WC, et al. **Hyperintense putaminal rim sign is not a hallmark of multiple system atrophy at 3T.** *AJNR Am J Neuroradiol* 2005;26:2238–42 Medline
41. Zamora C, Muhleman M, Castillo M. **Multiple system atrophy**. In: Franceschi AM, Franceschi D, eds. *Hybrid PET/MR Neuroimaging: A Comprehensive Approach*. Springer-Verlag; 2022:361–82
42. Aquino D, Bizzi A, Grisoli M, et al. **Age-related iron deposition in the basal ganglia: quantitative analysis in healthy subjects.** *Radiology* 2009;252:165–72 CrossRef Medline
43. Tha KK, Terae S, Tsukahara A, et al. **Hyperintense putaminal rim at 1. 5 T: prevalence in normal subjects and distinguishing features from multiple system atrophy.** *BMC Neurol* 2012;12:39 CrossRef Medline
44. Mascalchi M, Vella A, Ceravolo R. **Movement disorders: role of imaging in diagnosis.** *J Magn Reson Imaging* 2012;35:239–56 CrossRef Medline
45. Brooks DJ, Seppi K; Neuroimaging Working Group on MSA. **Proposed neuroimaging criteria for the diagnosis of multiple system atrophy.** *Mov Disord* 2009;24:949–64 CrossRef Medline
46. Lee YC, Liu CS, Wu HM, et al. **The 'hot cross bun' sign in the patients with spinocerebellar ataxia**. *Eur J Neurol* 2009;16:513–16 CrossRef Medline
47. Bhattacharya K, Saadia D, Eisenkraft B, et al. **Brain magnetic resonance imaging in multiple-system atrophy and Parkinson disease: a diagnostic algorithm.** *Arch Neurol* 2002;59:835–42 CrossRef Medline
48. Cicilet S, Furruqh F, Biswas A, et al. **Hot cross bun and bright middle cerebellar peduncle signs in cerebellar type multiple system atrophy.** *BMJ Case Rep* 2017:bcr-2017-220576 CrossRef
49. Chandran V, Stoessl AJ. **Imaging in multiple system atrophy.** *Neurology & Clinical Neurosc* 2014;2:178–87 CrossRef
50. Kim H-J, Jeon B, Fung VSC. **Role of magnetic resonance imaging in the diagnosis of multiple system atrophy.** *Mov Disord Clin Pract* 2016;4:12–20 CrossRef Medline
51. Shiga K, Yamada K, Yoshikawa K, et al. **Local tissue anisotropy decreases in cerebellopetal fibers and pyramidal tract in multiple system atrophy.** *J Neurol* 2005;252:589–96 CrossRef Medline
52. Oishi K, Konishi J, Mori S, et al. **Reduced fractional anisotropy in early-stage cerebellar variant of multiple system atrophy.** *J Neuroimaging* 2009;19:127–31 CrossRef Medline
53. Filippi M, Sarasso E, Agosta F. **Resting-state functional MRI in parkinsonian syndromes.** *Mov Disord Clin Pract* 2019;6:104–17 CrossRef Medline
54. Zheng W, Ren S, Zhang H, et al. **Spatial patterns of decreased cerebral blood flow and functional connectivity in multiple system atrophy (cerebellar-type): a combined arterial spin labeling perfusion and resting state functional magnetic resonance imaging study.** *Front Neurosci* 2019;13:777 CrossRef Medline
55. Meyer PT, Frings L, Rücker G, et al. **^{18}F-FDG PET in parkinsonism: differential diagnosis and evaluation of cognitive impairment**. *J Nucl Med* 2017;58:1888–98 CrossRef Medline
56. Hong C-M, Ryu H-S, Ahn B-C. **Early perfusion and dopamine transporter imaging using ^{18}F-FP-CIT PET/CT in patients with parkinsonism.** *Am J Nucl Med Mol Imaging* 2018;8:360–72 Medline
57. Oh M, Lee N, Kim C, et al. **Diagnostic accuracy of dual-phase ^{18}F-FP-CIT PET imaging for detection and differential diagnosis of Parkinsonism.** *Sci Rep* 2021;11:14992 CrossRef Medline
58. Van Laere K, Clerinx K, D'Hondt E, et al. **Combined striatal binding and cerebral influx analysis of dynamic 11C-raclopride PET improves early differentiation between multiple-system atrophy and Parkinson disease**. *J Nucl Med* 2010;51:588–95 CrossRef Medline
59. Cho H, Choi JY, Lee SH, et al. **^{18}F-AV-1451 binds to putamen in multiple system atrophy.** *Mov Disord* 2017;32:171–73 CrossRef Medline
60. Niethammer M. **Corticobasal degeneration**. In: Franceschi AM, Franceschi D, eds. *Hybrid PET/MR Neuroimaging: A Comprehensive Approach*. Springer-Verlag; 2022:373–86
61. Mahapatra RK, Edwards MJ, Schott JM, et al. **Corticobasal degeneration.** *Lancet Neurol* 2004;3:736–43 CrossRef Medline
62. Boeve BF. **The multiple phenotypes of corticobasal syndrome and corticobasal degeneration: implications for further study.** *J Mol Neurosci* 2011;45:350–53 CrossRef Medline
63. Armstrong MJ, Litvan I, Lang AE, et al. **Criteria for the diagnosis of corticobasal degeneration.** *Neurology* 2013;80:496–503 CrossRef Medline
64. Seritan AL, Mendez MF, Silverman DHS, et al. **Functional imaging as a window to dementia: corticobasal degeneration.** *J Neuropsychiatry Clin Neurosci* 2004;16:393–99 CrossRef Medline
65. Abe K, Terakawa H, Takanashi M, et al. **Proton magnetic resonance spectroscopy of patients with parkinsonism.** *Brain Res Bull* 2000;52:589–95 CrossRef Medline
66. Tedeschi G, Litvan I, Bonavita S, et al. **Proton magnetic resonance spectroscopic imaging in progressive supranuclear palsy, Parkinson's disease and corticobasal degeneration**. *Brain* 1997;120 (Pt 9):1541–52 CrossRef Medline
67. Yamaguchi T, Ikawa M, Enomoto S, et al. **Arterial spin labeling imaging for the detection of cerebral blood flow asymmetry in patients with corticobasal syndrome.** *Neuroradiology* 2022;64:1829–37 CrossRef Medline
68. Blin J, Vidailhet M, Pillon B, et al. **Corticobasal degeneration: decreased and asymmetrical glucose consumption as studied with PET.** *Mov Disord* 1992;7:348–54 CrossRef Medline
69. Pardini M, Huey ED, Spina S, et al. **FDG-PET patterns associated with underlying pathology in corticobasal syndrome.** *Neurology* 2019;92:e1121–35 CrossRef Medline
70. Cho H, Baek MS, Choi JY, et al. **^{18}F-AV-1451 binds to motor-related subcortical gray and white matter in corticobasal syndrome.** *Neurology* 2017;89:1170–78 CrossRef Medline
71. Pirker W, Djamshidian S, Asenbaum S, et al. **Progression of dopaminergic degeneration in Parkinson's disease and atypical parkinsonism: a longitudinal beta-CIT SPECT study**. *Mov Disord* 2002;17:45–53 CrossRef Medline
72. Kikuchi A, Okamura N, Hasegawa T, et al. **In vivo visualization of tau deposits in corticobasal syndrome by 18F-THK5351 PET.** *Neurology* 2016;87:2309–16 CrossRef Medline
73. Palleis C, Brendel M, Finze A, et al; German Imaging Initiative for Tauopathies (GII4T). **Cortical [^{18}F]PI-2620 binding differentiates corticobasal syndrome subtypes.** *Mov Disord* 2021;36:2104–15 CrossRef Medline
74. Tezuka T, Takahata K, Seki M, et al. **Evaluation of [18 F] PI-2620, a second-generation selective tau tracer, for assessing four-repeat tauopathies.** *Brain Commun* 2021;3:1–13
75. Wardlaw JM, Smith EE, Biessels GJ, et al; STandards for ReportIng Vascular changes on nEuroimaging (STRIVE v1). **Neuroimaging standards for research into small vessel disease and its contribution**

to ageing and neurodegeneration. *Lancet Neurol* 2013;12:822–38 CrossRef Medline
76. Vizcarra JA, Lang AE, Sethi KD, et al. **Vascular parkinsonism: deconstructing a syndrome.** *Mov Disord* 2015;30:886–94 CrossRef Medline
77. Ma KKY, Lin S, Mok VCT. **Neuroimaging in vascular parkinsonism.** *Curr Neurol Neurosci Rep* 2019;19:102 CrossRef Medline
78. Antonini A, Vitale C, Barone P, et al. **The relationship between cerebral vascular disease and parkinsonism: the VADO study.** *Parkinsonism Relat Disord* 2012;18:775–80 CrossRef Medline
79. Rissardo JP, Caprara ALF. **Cinnarizine- and flunarizine-associated movement disorder: a literature review.** *Egyp J Neurol Psych Neurosurg* 2020;56:61
80. Pitton Rissardo J, Caprara ALF. **Neuroimaging techniques in differentiating Parkinson's disease from drug-induced parkinsonism: a comprehensive review**. *Clin Pract* 2023;13:1427–48 CrossRef Medline
81. Laruelle M, Abi-Dargham A, van Dyck CH, et al. **Single photon emission computerized tomography imaging of amphetamine-induced dopamine release in drug-free schizophrenic subjects.** *Proc Natl Acad Sci U S A* 1996;93:9235–40 CrossRef Medline
82. Burn DJ, Brooks DJ. **Nigral dysfunction in drug-induced parkinsonism: an 18F-dopa PET study.** *Neurology* 1993;43:552–56 CrossRef Medline

Dural Arteriovenous Fistulas: Baseline Cognitive Changes and Changes following Treatment: A Prospective Longitudinal Study

Zeev Itsekson-Hayosh, Federico Carpani, Pascal J. Mosimann, Ronit Agid, Eef J. Hendriks, Ivan Radovanovic, Hugo Andrade Barazarte, Joanna D. Schaafsma, Karel Terbrugge, Timo Krings, Mary Pat McAndrews, and Patrick Nicholson

ABSTRACT

BACKGROUND AND PURPOSE: Dural arteriovenous fistulas (DAVFs) exhibit varied clinical manifestations, and high-grade cases are associated with both a risk of hemorrhage and (in certain cases) dementia. Less known, however, is the association between DAVF and more subtle cognitive changes, which might not be clinically apparent without formal neurocognitive testing. This study prospectively assesses baseline cognitive changes in patients with unruptured DAVFs and looks at the effects of treatment on any such changes.

MATERIALS AND METHODS: A longitudinal prospective study was conducted to formally evaluate the neurocognitive status of patients with unruptured DAVFs undergoing embolization. Pre- and posttreatment assessments included neurologic examinations and cognitive tests (Repeatable Battery for the Assessment of Neuropsychological Status and Trail-Making Test [TMT]).

RESULTS: A total of 23 patients were treated, with 78% demonstrating cortical venous reflux at baseline. At baseline, 50% of patients demonstrated cognitive impairment in at least 1 cognitive domain, and this was significantly associated with cortical venous reflux ($P < .05$). Following treatment, significant improvements were observed in several cognitive domains. The mean change in Immediate Memory was an increase of 10.5 points (95% CI, 6.2–14.8, $P < .001$). Visuospatial/Constructional abilities showed a mean increase of 3.8 points (95% CI, 1.1–6.5, $P = .008$), while Language improved by a mean of 4.2 points (95% CI, 0.9–7.5, $P = .015$). Attention scores increased by a mean of 6.1 points (95% CI, 2.7–9.5, $P < .001$). Delayed Memory demonstrated a mean improvement of 7.4 points (95% CI, 3.5–11.3, $P < .001$), and the Total Repeatable Battery for the Assessment of Neuropsychological Status Score increased by a mean of 8.6 points (95% CI, 5.0–12.2, $P < .001$). For the TMT, the mean change in TMT-A was a decrease of 9.2 seconds (95% CI, 5.6–12.8, $P < .001$), indicating faster completion times. TMT-B scores decreased by a mean of 12.7 seconds (95% CI, 8.4–17.0, $P < .001$). The TMT B-A difference decreased by a mean of 3.5 seconds (95% CI, 0.5–6.5, $P = .023$), and the TMT B/A ratio showed a mean decrease of 0.18 (95% CI, 0.10–0.26, $P = .002$). Overall, among the patients with baseline cognitive impairment, 70% showed significant cognitive improvement following endovascular treatment, particularly in memory domains.

CONCLUSIONS: In our study, 50% of patients with DAVFs had cognitive impairment when assessed with formal neurocognitive testing, with a significant link to cortical venous reflux. This cognitive impairment improved in 70% of those patients following treatment. These findings expand our understanding of how DAVF affects the brain, highlighting cognitive impairment as a critical factor. Consequently, the treatment of DAVFs should perhaps not only focus on hemorrhagic risk but also consider cognitive outcomes as a potential indicator for intervention.

ABBREVIATIONS: CVR = cortical venous reflux; DAVF = dural arteriovenous fistula; RBANS = Repeatable Battery for the Assessment of Neuropsychological Status; TMT = Trail-Making Test

Dural arteriovenous fistulas (DAVFs) present with a spectrum of clinical manifestations, often correlating with their angiographic grade. The prevailing literature emphasizes the association of "high-grade" DAVFs with an increased risk of intracranial hemorrhage. However, venous hypertension, a hallmark of DAVF, has also been implicated in neurodegenerative presentations, including cognitive decline, dementia, and parkinsonism.[1-2] High-grade

Received May 20, 2024; accepted after revision July 21.

From the Division of Neuroradiology (Z.I.-H., P.J.M., R.A., E.J.H., K.T., T.K., P.N.), University Medical Imaging and Joint Department of Medical Imaging, Department of Neurology, (F.C., J.D.S.), and Department of Neurosurgery (P.J.M., E.J.H., I.R., H.A.B., T.K), Toronto Western Hospital, University Health Network and University of Toronto, Toronto, Ontario, Canada; Department of Psychology (M.P.M.), University of Toronto, Krembil Research Institute, University Health Network, Toronto, Ontario, Canada; Department of Neuroradiology (P.N.), Beaumont Hospital, Dublin, Ireland; and Department of Radiology (P.N.), Royal College of Surgeons of Ireland, Dublin, Ireland.

Please address correspondence to Zeev Itsekson-Hayosh, MD, Division of Neuroradiology, 399 Bathurst Str, Toronto, Ontario, Canada, M5T 2S8; e-mail: zeevits@gmail.com

Indicates open access to non-subscribers at www.ajnr.org

Indicates article with online supplemental data.

http://dx.doi.org/10.3174/ajnr.A8449

DAVFs (ie, those with significant cortical venous reflux [CVR]) are often associated with significant cognitive and neurologic deficits and can necessitate treatment due to the concomitant risk of intracranial hemorrhage.[3-10]

Conversely, treatment of low-grade DAVFs is more variable and can be indicated in some cases by disabling tinnitus, and, rarely, headaches. Relatively little attention has been paid in the literature to cognitive changes in these patients, specifically in those who do not exhibit frank cognitive impairment or dementia. Could there be a significant and largely unrecognized burden of "subclinical" cognitive impairment in these patients? It appears so, and recent research has shown that surgical or endovascular treatment can halt and potentially reverse the trajectory of neurologic and cognitive deterioration in these patients, with a substantial proportion achieving complete clinical recovery.[11,12]

Nevertheless, the specific nature of cognitive impairment at baseline in patients with DAVFs, particularly in distinct domains, requires further exploration. Additionally, while cognitive improvements posttreatment may be demonstrable via psychometric evaluations, there are nuances to these evaluations and the influence of practice effects must be carefully considered. (Practice effects refer to the phenomenon in which repeat testing leads to improved scores due to familiarity with the test material rather than genuine cognitive improvements, presenting a potential confound in longitudinal assessments of neuropsychological function.[13-15]) This article presents findings from a prospective longitudinal study of a cohort of patients who presented with unruptured DAVFs and underwent treatment. We aimed to further investigate the incidence of cognitive impairment in patients with unruptured DAVFs and assess the effects of treatment on these changes. By using reliable change indices within a standardized neuropsychological battery, we aimed to meticulously assess treatment impacts, delineating the cognitive and neurologic statuses of patients with unruptured DAVFs both pre- and postintervention.

MATERIALS AND METHODS

Study Design

This study was conducted following the guidelines provided by the Strengthening the Reporting of Observational Studies in Epidemiology (STROBE) checklist, which is included as Online Supplemental Data. A longitudinal prospective study was designed to assess the baseline and posttreatment neurocognitive statuses of patients with DAVFs. Detailed methodology regarding neurocognitive testing is outlined in the Online Supplemental Data.

Participants

Inclusion criteria for the study:

- Patients older than 18 years of age
- Diagnosed and treated for nonacute DAVF by endovascular embolization
- Baseline mRS of ≤3
- Signed informed consent provided by the participant or the next of kin (depending on baseline cognitive status).

Exclusion criteria:

- A significant language barrier impairing reliable cognitive evaluation
- Active neuroleptic or psychoactive treatment (eg, antipsychotic or antiepileptic medications affecting cognitive status)
- Baseline mRS of 4 or 5, indicating severe baseline cognitive impairment
- Severe complications postprocedure leading to long-term cognitive impairment (eg, ischemic stroke or intracerebral hemorrhage).

Detailed inclusion and exclusion criteria are provided in the Online Supplemental Data.

Cognitive and Neurologic Assessment

Pretreatment and posttreatment assessments included complete neurologic examinations and validated neurocognitive testing using the Repeatable Battery for the Assessment of Neuropsychological Status (RBANS) and the Trail-Making Test (TMT). Both were assessed by a fellowship-trained neurologist. The neurocognitive testing strategy was designed by an experienced clinical neuropsychologist and cognitive neuroscientist. Different forms of RBANS were used for pre- and posttreatment assessments to minimize practice effects. Standard scores for the global index and each of the 5 domain scales (Immediate Memory, Delayed Memory, Attention, Language, and Visuospatial Function) were calculated using age-specific normalization tables.

Imaging and Classification

Pre- and posttreatment imaging included classification of fistula location and DAVF grading (using both the Borden and Cognard classifications). The presence or absence of CVR on a cerebral angiogram was also documented.

Statistical Analysis

Descriptive statistics were used to characterize baseline demographics, cognitive status, and clinical characteristics of the treated patients. The Pearson correlation analysis was performed to quantify correlations between RBANS scores and continuous variables such as patient age and the duration of symptoms. Paired *t* tests were used to identify statistically significant changes in test scores from pre- to posttreatment, with a threshold for statistical significance set at $P < .05$.[16-20]

RESULTS

We prospectively enrolled 23 patients, each presenting with an unruptured brain DAVF. These patients underwent endovascular embolization aimed at curing the DAVF. Posttreatment cognitive function was assessed in 21 patients. Two patients were excluded from the posttreatment evaluation due to significant treatment-related complications: one with a large ischemic stroke and the other with a substantial intracerebral hemorrhage, both of whom required extended rehabilitation. Notably, 1 patient who experienced a mild-to-moderate venous infarct postprocedure was included in the posttreatment cognitive assessment.

Baseline Characteristics

Patient demographics and baseline clinical characteristics are detailed in the Online Supplemental Data. The cohort's mean age

Cognitive performance of patients with DAVF, before and after endovascular embolization, stratified according to presence of CVR[a]

	Patients with CVR			Patients without CVR		
	Baseline (mean) (SD)% Impaired	Posttreatment (mean) (SD)% Impaired	Reliable Change% above Cutoff	Baseline (mean) (SD)% Impaired	Posttreatment (mean) (SD)% Impaired	Reliable Change% above Cutoff
RBANS total	87.7	95.5		86.8	103.3	
	14.98	13.46		14.89	10.50	
	28%	23%	24%	20%	0%	25%
RBANS Immediate Memory	82.9	94.6		79.0	103.5	
	18.72	15.03		15.60	11.79	
	39%	23%	35%	40%	0%	75%
RBANS Delayed Memory	87.3	95.8		86.0	101.8	
	22.49	16.14		24.46	14.17	
	33%	18%	24%	20%	0%	0%
RBANS Visuo spatial	94.3	91.6		93.8	100.8	
	11.58	18.04		18.05	3.77	
	22%	41%	0%	40%	0%	0%
RBANS Language	91.1	98.2		95.8	100.5	
	9.63	14.75		13.92	16.60	
	22%	6%	12%	20%	25%	0%
RBANS Attention	97.4	102.5		97.6	106.8	
	21.26	14.05		6.84	8.26	
	28%	6%	18%	0%	0%	25%
TMT A (raw/*z* score)	52.7/−1.5	50.6/−1.1	NA	52.4/−1.6	43.8/−1.2	NA
	29.52/3.16	28.75/2.10		24.31/1.38	14.75/1.83	
	44%	35%		60%	50%	
TMT B (raw/*z* score)	164.2/−3.1	157.5/−2.7	NA	132.2/−2.6	146.8/−3.0	NA
	113.89/4.39	114.04/4.43		95.93/2.09	105.16/2.19	
	50%	53%		60%	75%	
TMT B-A (raw/*z* score)	111.6/−2.6	106.9/−2.5	NA	79.8/−1.8	103.0/−2.4	NA
	96.64/4.23	95.58/4.49		74.50/2.08	111.41/3.12	
	50%	41%		60%	50%	

Note:—NA indicates not applicable.

[a] RBANS data are presented as scaled scores, which have a mean of 100 (SD, 15). Higher scores indicate better cognitive performance. The RBANS assesses 5 cognitive domains: Immediate Memory, Visuospatial/Constructional Abilities, Language, Attention, and Delayed Memory. TMT A and B scores and their contrasts (B-A, B/a) are presented as raw scores in seconds, which measure the time taken to complete the test. Lower scores indicate faster performance and better cognitive function. These raw scores are also converted into *z* scores, which have a mean of 0 (SD, 1). *Z* scores allow comparison across different tests and populations, with higher *z* scores indicating better performance relative to the normative sample. Sample interpretation: RBANS Immediate Memory: a scaled score of 85 would indicate performance below the average (mean of 100) for the general population, suggesting some impairment in this cognitive domain. TMT: a raw score: 35 seconds would be converted to a *z* score for comparison. If this *z* score is −1.5, it indicates that the performance is 1.5 SDs below the mean, suggesting slower processing speed compared with the normative sample.

was 60.5 (SD, 11.7) years. Men represented 52.1% of the study participants. Nearly all patients exhibited minimal disability, having a baseline mRS score of 0 or 1, except for 1 individual who had an mRS score of 3, attributed to a prior and unrelated ischemic stroke. Two patients presented with previous cerebral venous thrombosis affecting a major dural sinus. Symptomatic DAVF presentations were confirmed in 18 patients, manifesting as tinnitus, headaches, and cognitive decline. Three patients were asymptomatic and were incidentally diagnosed with high-grade DAVFs. The average symptom duration before intervention was 6.6 (SD 10) months.

Fistula Details

The anatomic distribution of DAVFs was diverse among the cohort, spanning the full spectrum of venous shunts as cataloged in the accompanying Table and in more detail in the Online Supplemental Data. Notably, this included 2 instances of indirect carotid cavernous fistulas and a singular case of direct shunting into the deep venous system. Bilateral shunts were observed in 3 patients, while 10 and 9 patients had right- and left-sided shunts, respectively.

In terms of classification, 15% of patients had Borden type I, 5% had Borden type II, and 65% had Borden type III DAVFs. By means of the Cognard classification, 5% were type I, 20% were type 2IIa, 15% were type IIa+b, 15% were type III, and 40% were type IV (Online Supplemental Data).

Notably, 78% of the cohort (18 patients) demonstrated CVR. Of those, nearly one-half (44%) had multiple cerebral lobes impacted by venous reflux. Baseline MRI was performed on 18 patients, revealing signs of cerebral venous congestion in 13 of them, which, intriguingly, included 2 patients classified as having benign Borden type DAVFs (ie, Borden types I and II).

Four patients overall (17% of the cohort) had either a Borden type I or II fistula, without CVR. Three patients had symptomatic carotid cavernous fistulas, 2 of whom had CVR. Another patient presented with a complex DAVF of the right petrous ridge, which was secondary to prior radiation therapy leading to chronic venous occlusion and venous congestion on MRI, yet without CVR. None of the patients had bithalamic edema.

Of the 18 patients with CVR, all except one underwent post-procedural neurocognitive reassessment. The remaining patient

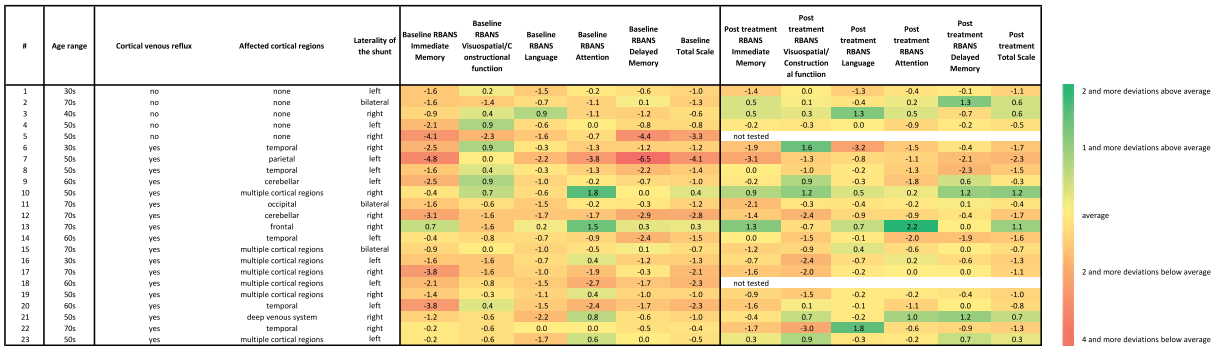

#	Age range	Cortical venous reflux	Affected cortical regions	Laterality of the shunt	Baseline RBANS Immediate Memory	Baseline RBANS Visuospatial/Constructional function	Baseline RBANS Language	Baseline RBANS Attention	Baseline RBANS Delayed Memory	Baseline Total Scale	Post treatment RBANS Immediate Memory	Post treatment RBANS Visuospatial/ Construction al function	Post treatment RBANS Language	Post treatment RBANS Attention	Post treatment RBANS Delayed Memory	Post treatment Total Scale
1	30s	no	none	left	-1.6	0.2	-1.5	-0.2	-0.6	-1.0	-1.4	0.0	-1.3	-0.4	-0.1	-1.1
2	70s	no	none	bilateral	-1.6	-1.4	-0.7	-1.1	0.1	-1.3	0.5	0.1	-0.4	0.2	1.3	0.6
3	40s	no	none	right	-0.9	0.4	0.9	-1.1	-1.2	-0.6	0.5	0.3	1.3	0.5	-0.7	0.6
4	50s	no	none	left	-2.1	0.9	-0.6	0.0	-0.8	-0.8	-0.2	-0.3	0.0	-0.9	-0.2	-0.5
5	50s	no	none	right	-4.1	-2.3	-1.6	-0.7	-4.4	-3.3	not tested					
6	30s	yes	temporal	right	-2.5	0.9	-0.3	-1.3	-1.2	-1.2	-1.9	1.6	-3.2	-1.5	-0.4	-1.7
7	50s	yes	parietal	left	-4.8	0.0	-2.2	-3.8	-6.5	-4.1	-3.1	-1.3	-0.8	-1.1	-2.1	-2.3
8	50s	yes	temporal	left	-1.6	0.4	-0.3	-1.3	-2.2	-1.4	0.0	-1.0	-0.2	-1.3	-2.3	-1.5
9	60s	yes	cerebellar	left	-2.5	0.9	-1.0	-0.2	-0.7	-1.0	-0.2	0.9	-0.3	-1.8	0.6	-0.3
10	50s	yes	multiple cortical regions	right	-0.4	0.7	-0.6	1.8	0.0	0.4	0.9	1.2	0.5	0.2	1.2	1.2
11	70s	yes	occipital	bilateral	-1.6	-0.6	-1.5	-0.2	-0.3	-1.2	-2.1	-0.3	-0.4	-0.2	0.1	-0.4
12	70s	yes	cerebellar	right	-3.1	-1.6	-1.7	-1.7	-2.9	-2.8	-1.4	-2.4	-0.9	-0.9	-0.4	-1.7
13	70s	yes	frontal	right	0.7	-1.6	0.2	1.5	0.3	0.3	1.3	-0.7	0.7	2.2	0.0	1.1
14	60s	yes	temporal	left	-0.4	-0.8	-0.7	-0.9	-2.4	-1.5	0.0	-1.5	-0.1	-2.0	-1.9	-1.6
15	70s	yes	multiple cortical regions	bilateral	-0.9	0.0	-1.0	-0.5	0.1	-0.7	-1.2	-0.9	0.4	-0.6	0.0	-0.7
16	30s	yes	multiple cortical regions	left	-1.6	-1.6	-0.7	0.4	-1.2	-1.3	-0.7	-2.4	-0.7	0.2	-0.6	-1.3
17	70s	yes	multiple cortical regions	right	-3.8	-1.6	-1.0	-1.9	-0.3	-2.1	-1.6	-2.0	-0.2	0.0	0.0	-1.1
18	60s	yes	multiple cortical regions	left	-2.1	-0.8	-1.5	-2.7	-1.7	-2.3	not tested					
19	50s	yes	multiple cortical regions	right	-1.4	-0.3	-1.1	0.4	-1.0	-1.0	-0.9	-1.5	-0.2	-0.2	-0.4	-1.0
20	60s	yes	temporal	left	-3.8	0.4	-1.5	-2.4	-1.7	-2.3	-1.6	0.1	-0.1	-1.1	0.0	-0.8
21	50s	yes	deep venous system	right	-1.2	-0.6	-2.2	0.8	-0.6	-1.0	-0.4	0.7	-0.2	1.0	1.2	0.7
22	70s	yes	temporal	right	-0.2	-0.6	0.0	0.0	-0.5	-0.4	-1.7	-3.0	1.8	-0.6	-0.9	-1.3
23	50s	yes	multiple cortical regions	left	-0.2	-0.6	-1.7	0.6	0.0	-0.5	0.3	0.9	-0.3	-0.2	0.7	0.3

FIG 1. The heat map shows individual patient cognitive performance pre- and posttreatment across various RBANS domains. *Green shades* indicate improvement, while *red shades* indicate declines. Darker colors represent more significant changes. The numeric values reflect deviations from average standardized scores, with positive values indicating above-average performance and negative values indicating below-average performance. These provide a visual representation for baseline values and outcomes for each patient pre- and posttreatment, as well as for the entire cohort.

had a disabling periprocedural ischemic stroke and was thus unable to attend the postprocedural evaluation.

Treatment Details

Transarterial embolization was performed in 9 patients (39.1%); a transvenous approach, in 11 patients (47.8%); and a combined transvenous and transarterial approach, in 3 patients (13.0%). Treatment involved a combination of liquid embolic agents and coils for 10 patients (43.5%), coil embolization exclusively for another 10 patients (43.5%), Onyx (Medtronic) embolization exclusively in 2 patients (8.7%), and a combination of Onyx and glue in 1 patient (4.3%).

On follow-up control cerebral angiography, a residual shunt was identified in 4 patients (17.4%), with a single patient (4.3%) having a high-grade residual shunt.

Neurocognitive Evaluation: Baseline and Posttreatment

Neurocognitive outcomes are detailed in the Table, which compares patients presenting with CVR ($n = 18$) with those without CVR ($n = 5$).

The RBANS is a standardized battery that evaluates multiple cognitive domains, including Immediate Memory, Delayed Memory, Attention, Language, and Visuospatial/Constructional abilities. Improvements in these domains posttreatment suggest a positive effect of DAVF intervention on cognitive function. The TMT, divided into TMT-A and TMT-B, measures processing speed and cognitive flexibility and executive function, respectively. To mitigate learning effects, we used alternate forms of the RBANS and the Reliable Change Index to ensure that observed changes were beyond what could be attributed to practice effects alone.

At baseline, across the entire cohort ($n = 23$), 26.1% (6 patients) displayed cognitive impairment on the RBANS Total Scale, indicating a decrease of >1 SD from age-adjusted norms. Within this subset, 1 patient with a benign DAVF without CVR had a compromised total scale performance.

Subdomain analysis of RBANS revealed additional baseline deficits: 39.1% (9 patients) in Immediate Memory (2 with benign DAVFs without CVR); 26.1% (6 patients) in Visuospatial/Constructional functions (2 with benign DAVFs without CVR); 21.7% (5 patients) in Language (1 with benign DAVF without CVR); 21.7% (5 patients) in Attention (all with CVR); and 30.4% (7 patients) in Delayed Memory (1 with benign DAVF without CVR).

Following treatment, significant improvements were observed in several cognitive domains as measured by the RBANS. The mean change in Immediate Memory was an increase of 10.5 points (95% CI, 6.2–14.8, $P < .001$). Visuospatial/Constructional abilities showed a mean increase of 3.8 points (95% CI, 1.1–6.5, $P = .008$), while Language improved by a mean of 4.2 points (95% CI, 0.9–7.5, $P = .015$). Attention scores increased by a mean of 6.1 points (95% CI, 2.7–9.5, $P < .001$). Delayed Memory demonstrated a mean improvement of 7.4 points (95% CI, 3.5–11.3, $P < .001$), and the Total RBANS Score increased by a mean of 8.6 points (95% CI, 5.0–12.2, $P < .001$).

For the TMT, the mean change in TMT-A was a decrease of 9.2 seconds (95% CI, 5.6–12.8, $P < .001$), indicating faster completion times. TMT-B scores decreased by a mean of 12.7 seconds (95% CI, 8.4–17.0, $P < .001$). The TMT B-A difference decreased by a mean of 3.5 seconds (95% CI, 0.5–6.5, $P = .023$), and the TMT B/A ratio showed a mean decrease of 0.18 (95% CI, 0.10–0.26, $P = .002$).

These results indicate that endovascular treatment of DAVFs leads to significant improvement in cognitive function, particularly in memory, attention, and processing speed.

To account for test-retest reliability, we used the Reliable Change Index, revealing that 5 patients exhibited improvement in total scale performance; 9, in Immediate Memory; 2, in Language; 3, in Attention; and 4, in Delayed Memory. There were 2 instances of a tendency toward postprocedural decline, one associated with a periprocedural venous infarct.

Figure 1 depicts a "heat map" of cognitive performance of the individual patients of the cohort before and after treatment. The heat map uses color coding to represent changes in cognitive performance across various domains assessed by the RBANS. Green shades indicate improvement in cognitive function, with darker greens representing more significant improvement. Red shades indicate declines in cognitive function, with darker reds representing more significant declines. Numeric values reflect deviations from average standardized scores, with positive

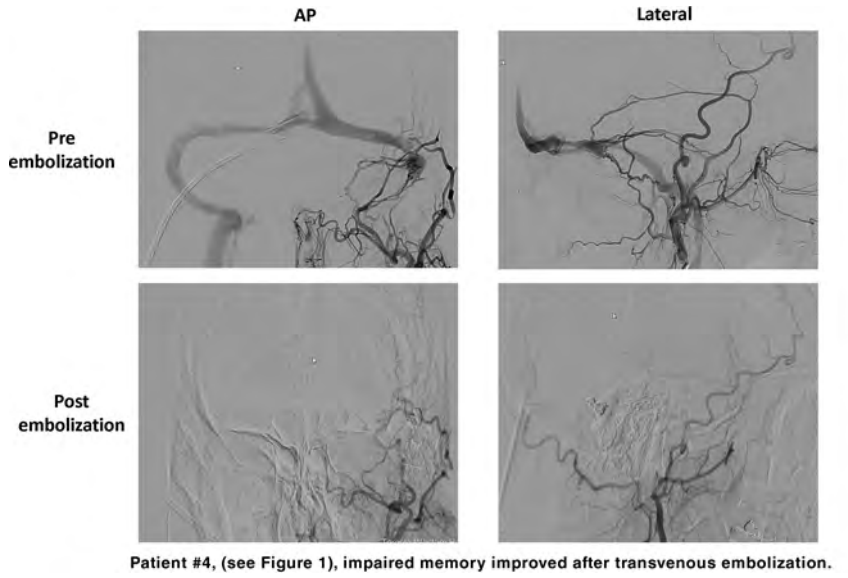

FIG 2. Diagnostic cerebral angiographies (left external carotid artery selective injections) showing a representative patient who presented with a low-grade DAVF (ie, no cortical venous reflux) and cognitive impairment, which improved following endovascular disconnection of the shunt. AP indicates anterior-posterior.

values indicating above-average performance and negative values indicating below-average performance. This visualization allows an at-a-glance understanding of the individual cognitive trajectories of patients before and after treatment, highlighting areas of improvement or decline. Figure 2 demonstrates representative imaging of a patient with a successfully embolized low-grade DAVF, who also exhibited cognitive improvement following the treatment.

The Pearson correlation analysis did not show significant associations between cognitive impairment and patient age, symptom duration, treatment technique, or extent of CVR involvement. (The more detailed results of the Pearson correlation analysis are presented in the Online Supplemental Data).

DISCUSSION

The present study looks into cognitive impairment associated with unruptured cranial DAVFs yields significant insights that warrant a reconsideration of current treatment paradigms. Our cohort comprised 23 patients, of whom 21 were subjected to cognitive assessment post-endovascular treatment. This revealed a high prevalence of pretreatment cognitive dysfunction, with 50% of individuals demonstrating deficits in at least 1 cognitive domain. This finding alone suggests that cognitive impairment is a much more common presentation in cases of unruptured brain DAVFs than was previously documented. This finding is also supported by other recent studies.

Following treatment, 70% of patients who had baseline cognitive impairment exhibited improvement in memory functions in particular. This improvement in cognitive faculties posttreatment is particularly compelling because it challenges the prevailing guidelines, which do not consider cognitive impairment as an isolated criterion for intervention in unruptured DAVFs. Our study highlights the necessity of integrating cognitive function into the clinical evaluation of these patients, potentially expanding the indications for treatment beyond the traditional benchmarks of hemorrhage risk and symptomatic presentation.

Most interesting, the study demonstrated no statistical correlation between the extent of cognitive impairment and other variables such as the location of the DAVF, the age of the patients, or the Borden/Cognard classifications. This observation underscores the complexity of cognitive outcomes in patients with cranial DAVFs and suggests that other as yet unidentified factors may contribute to cognitive dysfunction. Most interesting, none of the patients in our study had bithalamic edema, a recognized pattern associated with neuropsychological changes in DAVFs.[20,21] This finding corresponds with none of the patients having frank dementia or severe cognitive impairment. It also indicates that we should consider assessment for cognitive impairment in all patients with DAVFs, and not merely those with high-grade lesions.

Our findings align with the Neuropshchology in Dural Arterial Fistula (NAIF) study,[12] a multicenter prospective cohort investigation, which demonstrated significant cognitive improvement, particularly in attention, executive functions, memory, and language, following endovascular embolization of DAVFs. The use of a complete neuropsychological battery in the NAIF study parallels our approach, reinforcing the importance of comprehensive cognitive evaluation. While the NAIF study reported substantial improvement using specific cognitive tests, the broader assessment (using RBANS and TMT) of our study allows a more nuanced understanding of cognitive changes across multiple domains, providing robust evidence for the cognitive benefits of treating DAVFs. Moreover, the NAIF study found that cognitive improvement was independent of the risk of hemorrhage, suggesting that even patients with less severe fistulas can experience cognitive benefits from treatment. Our findings support this observation and emphasize the need for routine cognitive assessments in all patients with DAVFs.

Another recent study by the CONDOR Consortium (https://condorprogram.com/consortium) looked at patients who presented with frank cognitive impairment.[22] Unlike our study, this study did not use a standardized neuropsychological battery, which may limit the comparability and generalizability of their findings. By including all patients, regardless of symptomatic presentation, our study demonstrates that cognitive impairment is prevalent even among those not initially presenting with cognitive symptoms. This broader inclusion criterion underscores the need for routine cognitive assessment in all patients with DAVFs, because subclinical cognitive deficits can significantly impact quality of life and may clearly go undetected without a thorough evaluation. The CONDOR study was also retrospective, another significant limitation.

Previous publications on this topic revealed some discrepancies in the reported rates of cognitive impairment, potentially attributable to differences in assessment methodologies.[12-15] The use of a Reliable Change Index in our study minimizes the impact of so-called practice effects associated with repeat cognitive testing, thereby lending credence to the modest improvement effect we observed posttreatment.

In this study, we have focused only on endovascular treatment, which, in our center, is generally a first-line treatment approach for many DAVFs. However, we must also consider other treatment modalities, including both surgery and radiosurgery, and their potential impact on cognitive outcomes. For example, compared with radiosurgery, surgery may offer quicker resolution of venous hypertension (and therefore potentially faster resolution of any cognitive impairment), but this must be balanced against the potentially negative effects of a craniotomy and surgery on any cognitive issues. We simply do not yet know the answers to these questions, and more research is needed in this area.

Our study has several important limitations. First, the relatively small sample size and its single-center design may limit the generalizability of the findings and introduce biases specific to the treatment protocols or patient-selection criteria of the center. Additionally, the absence of a control group—comprising untreated patients or those receiving alternative therapeutic interventions—makes it challenging to definitively attribute observed cognitive and neurologic improvements to the endovascular treatment alone, without considering the natural disease progression or regression toward the mean. Moreover, the follow-up duration might not be sufficiently long to assess the long-term stability of the treatment-induced cognitive improvements or to detect late complications or recurrence of symptoms. However, we can state that our patient recruitment was consecutive, and all treatment decisions were recommended by a multidisciplinary team, emphasizing our methodic and unbiased approach.

The number of patients without CVR in our cohort was only 5. This small sample size warrants cautious interpretation of the findings related to this subgroup. The limited number of patients without CVR may not provide a fully representative view of cognitive outcomes in this population. Thus, further studies with larger cohorts are necessary to validate these observations and better understand the implications of CVR absence on cognitive function. Our study did not account for other potential confounding causes of cognitive dysfunction, such as microvascular disease or Alzheimer disease, which are particularly relevant given the mean age of 60 and the prevalence of hypertension among our patients. Our MRI work-up for DAVF includes relatively standard sequences in addition to MRA (ie, we do not acquire volumetric imaging to assess brain atrophy, nor do we perform perfusion studies). This limitation should be considered when interpreting our findings, and future studies should include a more comprehensive analysis of these factors to better isolate the impact of DAVF on cognitive function.

Last, we chose to exclude patients with severe posttreatment complications, such as large ischemic strokes or significant intracerebral hemorrhages, from the cognitive outcome analysis. This choice was because these outcomes independently affect cognitive function and including them could skew our results. This exclusion is a limitation, and larger studies should consider evaluating these subgroups separately to provide a more complete picture of treatment outcomes.

CONCLUSIONS

Our study shows that cognitive impairment, and in particular memory issues, are much more common in patients with DAVFs than was previously recognized. Indeed, looking at only those patients who present clinically with dementia or frank cognitive impairment almost certainly underestimates the burden of disease. This more subtle cognitive impairment can, however, be picked up through comprehensive neurocognitive assessment, and perhaps we are approaching the stage in which all such patients should be referred for neurocognitive assessment by a qualified specialist in this area. Treatment of cranial DAVFs can lead to cognitive improvements, and the presence of cognitive dysfunction, even in low-grade lesions, may warrant consideration of treatment in these patients.

It is time for a more nuanced approach to the management of DAVFs, one that prioritizes cognitive outcomes and recognizes the potential for cognitive recovery following appropriate intervention, irrespective of the angiographic grade of the DAVF. Treatment considerations for DAVFs should, therefore, be about more than just hemorrhage risk. Our findings indicate the need to reassess current management strategies for DAVFs, with further multicenter studies required to confirm these results.

Disclosure forms provided by the authors are available with the full text and PDF of this article at www.ajnr.org.

REFERENCES

1. Brito A, Tsang AC, Hilditch C, et al. **Intracranial dural arteriovenous fistula as a reversible cause of dementia: case series and literature review.** *World Neurosurg* 2019:121:e543–53 CrossRef Medline
2. Velz J, Kulcsar Z, Büchele F, et al. **The challenging clinical management of patients with cranial dural arteriovenous fistula and secondary Parkinson's syndrome: pathophysiology and treatment options**. *Cerebrovasc Dis Extra* 2020;10:124–38 CrossRef Medline
3. Holekamp TF, Mollman ME, Murphy RK, et al. **Dural arteriovenous fistula-induced thalamic dementia: report of 4 cases.** *J Neurosurg* 2016;124:1752–65 CrossRef Medline
4. Luo Y, Qi J, Cen Z, et al. **Two cases of dural arteriovenous fistula presenting with parkinsonism and progressive cognitive dysfunction.** *J Neurol Sci* 2014;343:211–14 CrossRef Medline
5. Alexandratou A, Mah Y, Ramsey D, et al. **Dural arteriovenous fistula causing reversible cognitive impairment.** *Pract Neurol* 2022;23:82–84 CrossRef Medline
6. Netravathi M, Pal PK, Bharath RD, et al. **Intracranial dural arteriovenous fistula presenting as parkinsonism and cognitive dysfunction.** *J Clin Neurosci* 2011;18:138–40 CrossRef Medline
7. Han Z, Yang H, Du Y, et al. **Progressive cognitive decline with bithalamic and basal ganglia lesions caused by dural arteriovenous fistula.** *Neurology* 2021;97:738–39 CrossRef Medline
8. Xie J, Zhang T, Zhang Y, et al. **Dural arteriovenous fistula with progressive dementia and parkinsonism: two case reports and a literature review.** *Medicine (Baltimore)* 2023;102:E35782 CrossRef Medline
9. Racine CA, Lawton MT, Hetts SW, et al. **Neuropyschological profile of reversible cognitive impairment in a patient with a**

dural arteriovenous fistula. *Neurocase* 2008;14:231–38 CrossRef Medline
10. Wilson M, Doran M, Enevoldson TP, et al. **Cognitive profiles associated with intracranial dural arteriovenous fistula.** *Age Ageing* 2010;39:389–92 CrossRef Medline
11. Sekar S, Kannath SK, Ramachandran S, et al. **Alterations in resting-state functional MRI connectivity related to cognitive changes in intracranial dural arteriovenous fistulas before and after embolization treatment.** *J Magn Reson Imaging* 2022;55:1183–99 CrossRef Medline
12. Gramegna LL, Ortega G, Dinia L, et al. **Cognitive improvement following endovascular embolization in patients with intracranial dural arteriovenous fistula: the Neuropsychology in dural ArterIal Fistula (NAIF) Study.** *J Neurointerv Surg* 2023 Dec 7. [Epub ahead of print] CrossRef Medline
13. Anokhin AP, Luciana M, Banich M, et al. **Age-related changes and longitudinal stability of individual differences in ABCD neurocognition measures.** *Dev Cogn Neurosci* 2022;54:101078 CrossRef Medline
14. Tröster AI, Woods SP, Morgan EE. **Assessing cognitive change in Parkinson's disease: development of practice effect-corrected reliable change indices**. *Arch Clin Neuropsychol* 2007;22:711–18 CrossRef Medline
15. Slade PD, Townes BD, Rosenbaum G, et al. **The serial use of child neurocognitive tests: development versus practice effects.** *Psychol Assess* 2008;20:361–69 CrossRef Medline
16. Shura RD, Brearly TW, Rowland JA, et al. **RBANS validity indices: a systematic review and meta-analysis.** *Neuropsychol Rev* 2018;28:269–84 CrossRef Medline
17. Novitski J, Steele S, Karantzoulis S, et al. **The repeatable battery for the assessment of neuropsychological status effort scale.** *Arch Clin Neuropsychol* 2012;27:190–95 CrossRef Medline
18. Speer DC. **Clinically significant change: Jacobson and Truax (1991) revisited.** *J Consult Clin Psychol* 1992;60:402–08 CrossRef Medline
19. Sherman E, Hrabok M. *A Compendium of Neuropsychological Tests*. New York: Oxford University Press; 2006
20. Tombaugh TN. **Trail Making Test A and B: normative data stratified by age and education.** *Arch Clin Neuropsychol* 2004;19:203–14 CrossRef Medline
21. Chen PM, Olson SE, Handwerker J. **Bithalamic lesions: cranial dural arteriovenous fistula manifesting as thalamic dementia.** *Stroke* 2020;51:E355–58 CrossRef Medline
22. Sanchez S, Wendt L, Hayakawa M, et al. **Dural arteriovenous fistulas with cognitive impairment: angiographic characteristics and treatment outcomes.** *Neurosurgery* 2023 Dec 14. [Epub ahead of print] CrossRef

Automated Segmentation of MRI White Matter Hyperintensities in 8421 Patients with Acute Ischemic Stroke

Hosung Kim, Wi-Sun Ryu, Dawid Schellingerhout, Jonghyeok Park, Jinyong Chung, Sang-Wuk Jeong, Dong-Seok Gwak, Beom Joon Kim, Joon-Tae Kim, Keun-Sik Hong, Kyung Bok Lee, Tai Hwan Park, Jong-Moo Park, Kyusik Kang, Yong-Jin Cho, Byung-Chul Lee, Kyung-Ho Yu, Mi Sun Oh, Soo Joo Lee, Jae-Kwan Cha, Dae-Hyun Kim, Jun Lee, Man Seok Park, Hee-Joon Bae, and Dong-Eog Kim

ABSTRACT

BACKGROUND AND PURPOSE: To date, only a few small studies have attempted deep learning–based automatic segmentation of white matter hyperintensity (WMH) lesions in patients with cerebral infarction; this issue is complicated because stroke-related lesions can obscure WMH borders. We developed and validated deep learning algorithms to segment WMH lesions accurately in patients with cerebral infarction using multisite data sets involving 8421 patients with acute ischemic stroke.

MATERIALS AND METHODS: We included 8421 patients with stroke from 9 centers in Korea. 2D UNet and squeeze-and-excitation (SE)-UNet models were trained using 2408 FLAIR MRIs from 3 hospitals and validated using 6013 FLAIR MRIs from 6 hospitals. WMH segmentation performance was assessed by calculating the Dice similarity coefficient (DSC), the correlation coefficient, and the concordance correlation coefficient compared with a human-segmented criterion standard. In addition, we obtained an uncertainty index that represents overall ambiguity in the voxel classification for WMH segmentation in each patient based on the Kullback-Leibler divergence.

RESULTS: In the training data set, the mean age was 67.4 (SD, 13.0) years, and 60.4% were men. The mean (95% CI) DSCs for UNet in internal testing and external validation were, respectively, 0.659 (0.649−0.669) and 0.710 (0.707−0.714), which were slightly lower than the reliability between humans (DSC = 0.744; 95% CI, 0.738−0.751; $P = .031$). Compared with the UNet, the SE-UNet demonstrated better performance, achieving a mean DSC of 0.675 (95% CI, 0.666–0.685; $P < .001$) in the internal testing and 0.722 (95% CI, 0.719−0.726; $P < .001$) in the external validation; moreover, it achieved high DSC values (ranging from 0.672 to 0.744) across multiple validation data sets. We observed a significant correlation between WMH volumes that were segmented automatically and manually for the UNet ($r = 0.917$, $P < .001$), and it was even stronger for the SE-UNet ($r = 0.933$, $P < .001$). The SE-UNet also attained a high concordance correlation coefficient (ranging from 0.841 to 0.956) in the external test data sets. In addition, the uncertainty indices in most patients (86%) in the external data sets were <0.35, with an average DSC of 0.744 in these patients.

CONCLUSIONS: We developed and validated deep learning algorithms to segment WMH in patients with acute cerebral infarction using the largest-ever MRI data sets. In addition, we showed that the uncertainty index can be used to identify cases in which automatic WMH segmentation is less accurate and requires human review.

ABBREVIATIONS: C_b = bias correction factor; DSC = Dice similarity coefficient; HD = Hausdorff distance; KL = Kullback-Leibler; ReLU = rectified linear unit; SE = squeeze-and-excitation; WMH = white matter hyperintensity

White matter hyperintensities (WMHs), characterized by high signal intensity on T2-weighted MRI and FLAIR MRI, is commonly observed among the elderly.[1] WMHs are associated with an increased risk of stroke,[2] adverse stroke outcomes,[3] dementia,[4] and depression.[5] Manual segmentation of WMH lesions by humans is considered the criterion standard for

Received February 28, 2024; accepted after revision July 9.

From the USC Stevens Neuroimaging and Informatics Institute (H.K.), Keck School of Medicine of USC, University of Southern California, Los Angeles, California; Artificial Intelligence Research Center (W.-S.R, J.P.), JLK Inc, Seoul, Republic of Korea; National Priority Research Center for Stroke and Department of Neurology (W.-S.R, J.C., S.-W.J., D.-S.G., D.-E.K.), Dongguk University Ilsan Hospital, Goyang, Republic of Korea; Department of Neuroradiology and Imaging Physics (D.S.), The University of Texas M.D. Anderson Cancer Center, Houston, Texas; Bioimaging Data Curation Center (J.C., D.-S.G., D.-E.K.), KOREA-BioData Station, Daejeon, Republic of Korea; Department of Neurology (B.J.K., H.-J.B.), Seoul National University Bundang Hospital, Seongnam, Republic of Korea; Department of Neurology (J.-T.K., M.S.P.,), Chonnam National University Hospital, Gwangju, Republic of Korea; Department of Neurology (K.-S.H., Y,-J.C.), Inje University Ilsan Paik Hospital, Goyang, Republic of Korea; Department of Neurology (K.B.L.), Soonchunhyang University Hospital, Seoul, Republic of Korea; Department of Neurology (T.H.P.), Seoul Medical Center, Seoul, Republic of Korea; Department of Neurology (J.-M.P.), Uijeongbu Eulji Medical Center, Uijeongbu, Republic of Korea; Department of Neurology (K.K.), Nowon Eulji Medical Center, Eulji University School of Medicine, Seoul, Republic of Korea; Department of Neurology (B.-C.L., K.-H.Y., M.S.O.), Hallym University Sacred Heart Hospital, Anyang, Republic of Korea; Department of Neurology (S.J.L.), Eulji University Hospital, Daejeon, Republic of Korea; Department of Neurology (J.-K.C., D.-H.K.), Dong-A University Hospital, Busan, Republic of Korea; and Department of Neurology (J.L.), Yeungnam University Hospital, Daegu, Republic of Korea.

H. Kim and W.-S. Ryu equally contributed to this work.

This study was supported by the Multiministry Grant for Medical Device Development (KMDF_PR_20200901_0098), the National Priority Research Center Program Grant

SUMMARY

PREVIOUS LITERATURE: WMH on FLAIR MRI is a quantifiable risk factor for stroke and dementia. Manual WMH segmentation is laborious, supporting automated segmentation methods, but these face difficulties in implementation. Specifically, cerebral infarcts (acute) can obscure the boundaries of WMH lesions (chronic), degrading performance. The few published studies in the current literature did not have sufficient data to undergo full external validation, limiting their ability to address the well-known "domain shift problem": ie, an algorithm that performs well in its source domain but poorly when applied in the target domain.

KEY FINDINGS: We developed deep learning algorithms to segment WMH in patients with ischemic stroke using the largest-ever data set ($n = 8421$ patients), with full validation. Our SE-UNet algorithm achieved high segmentation performance, with DSC values from 0.672 to 0.744 across multiple validation data sets (compared with expert criterion standards), with low (<0.35) uncertainty indices in 86% of patients.

KNOWLEDGE ADVANCEMENT: Deep learning algorithms developed and using large MRI data sets from multicenter patients with stroke can accurately segment WMH lesions, distinguishing FLAIR lesions from DWI-positive infarcts without relying on DWIs. The uncertainty index can be used to identify those WMH segmentation cases that require human inspection.

volumetric assessment of WMHs.[6] However, given the high prevalence of variously-sized scattered WMHs, such a manual procedure is laborious, time-consuming, and prone to rater-dependent bias and errors,[7] particularly in large multicenter studies.

Approximately 40% of stroke survivors eventually have cognitive impairment.[8] The extent and expansion of WMHs are intimately correlated with vascular cognitive impairment.[4,9,10] Nevertheless, there is little evidence available to indicate that attenuating WMH progression can prevent functional decline, partly due to inconsistent volumetric measurement of WMHs.[11] Hence, to further advance our understanding of WMH in patients with ischemic stroke, precise and consistent WMH segmentation is required. Recent advances in deep learning approaches have markedly improved the automatic segmentation of brain lesions.[12-14] Several studies on healthy elderly brains yielded promising results for fully automated WMH segmentation.[12,15,16] However, patients with cerebrovascular lesions, such as acute or chronic infarcts, complicate these analyses because focal stroke-related lesions can obscure WMH borders.[17] This area is understudied, representing a gap in our clinical armamentarium, which requires improved methods. Automated segmentation of WMH versus infarcts will contribute to more accurate quantification of acute-versus-chronic ischemia–related MR lesions. This contribution will help better predict poststroke outcomes such as WMH-related clinical worsening, neurologic recovery, and functional outcomes.[3] It will also support research on WMH in stroke and dementia.

Only a few studies have attempted automatic segmentation of WMH lesions in patients with ischemic stroke.[18,19] One study ($n = 250$) using convolutional neural networks achieved a Dice similarity coefficient (DSC) of near 70% in the test data set.[18] A more recent study ($n = 429$) used the state-of-the-art UNet and UNet with squeeze-and-excitation (SE) blocks (SE-UNet), achieving a higher DSC value of 74%–76%.[19] These single-center studies with small sample sizes cannot address the notorious "domain shift problem," in which an algorithm that performs well in the source domain proceeds to perform poorly in the target domain.[20] Moreover, because the acute and chronic infarcts obscure the boundaries of WMHs, the interrater and intrarater reliability of the manual segmentation of WMHs is reduced. This less reliable voxelwise labeling of WMHs reduces the quality of the training data and compounds the problem. The impact of this factor on the segmentation performance of deep learning algorithms has not yet been systematically investigated.

In this study, we first trained UNet and SE-UNet to segment MWH lesions using 3 different stroke center data sets involving 2408 patients with ischemic stroke and subsequently validated the deep learning algorithms using 6 separate stroke center data sets involving 6013 patients. Next, we used an uncertainty measure[21] (based on the Kullback-Leibler divergence[22]) from the UNet to investigate the possibility of predicting the accuracy of WMH segmentation. We also assessed lesion information that could affect the segmentation accuracy, such as WMH burden and infarct location and volume.

MATERIALS AND METHODS

Data Sets

The Korean Nationwide Image-Based Stroke Database project is a prospective multicenter study in Korea.[2,3,17,23] From May 2011 to November 2013, we consecutively enrolled 10,423 patients with ischemic stroke who were admitted to the 9 participating centers within 7 days of symptom onset. We excluded the following patients: those with a contraindication to MRI ($n = 315$), poor quality or unavailability of FLAIR MRI or DWI ($n = 1632$), and MRI registration error ($n = 55$), leaving 8421 evaluable patients. The institutional review boards of all the participating centers approved the study. All patients or their legally authorized representatives provided a written informed consent for study participation. Brain MRI was performed on 1.5T ($n = 6583$) or 3T ($n = 1803$) MRI systems. FLAIR image protocols were TE = 76–187 ms, TR = 6000–11568 ms, voxel size = 1 × 1 × 3–7 mm^3, spacing = 0.3–1.0 mm, slice thickness = 3–7 mm, FOV = 175–280 mm, and matrix size (row) = 256–768.

(NRF-2021R1A6A1A03038865), and the Basic Science Research Program Grant (NRF-2020R1A2C3008295) of National Research Foundation, funded by the Korean government.

Please address correspondence to Dong-Eog Kim, MD, PhD, Department of Neurology, Dongguk University Ilsan Hospital, 27, Dongguk-ro, Ilsandong-gu, Goyang, South Korea; e-mail: kdongeog@duih.org

Indicates open access to non-subscribers at www.ajnr.org

Indicates article with online supplemental data.

http://dx.doi.org/10.3174/ajnr.A8418

All scans were transferred to the Korean Brain MRI Data Center for central data storage and quantitative analysis. As previously reported,[2,3,17,24-26] each patient's high signal intensity WM lesions on FLAIR images were manually segmented from scratch by 1 of 5 research assistants with at least 5 years' experience in WMH segmentation under careful supervision by an experienced vascular neurologist (W.-S. Ryu; Online Supplemental Data). When chronic WM lesions on FLAIR and acute infarct lesions on DWI overlapped or were adjacent, we determined the extent and distribution of FLAIR WMH on the basis of lesions in the hemisphere contralateral to the acute infarct location, because WMH symmetry of morphology and distribution is quite often observed between hemispheres. In preliminary investigations, we found that the performance of deep learning models reached a plateau at about 2000 patients' FLAIR MRIs. Additionally, we sought to test the robustness of our algorithms across various external data sets. Hence, a total of 2408 patients' FLAIR MRIs from 3 hospitals were designated as a training data set, and the remaining 6013 patients' FLAIR MRIs from 6 hospitals were designated as 6 external validation data sets. A training data set was divided into 6:2:2 ratios by random subsetting as training, validation, and internal test data sets.

Data Preprocessing

We applied 2D B-spline interpolation to resize the FLAIR slices to a dimension of 256 × 256 pixels. Next, we performed slicewise intensity normalization in a uint8 format, ensuring that pixel intensities on each slice ranged from 0 to 255. We subsequently performed casewise intensity equalization to ensure comparability in the imaging data across different MRI vendors using a histogram of 32 bins and shifting the highest peak of the histogram value to 150. Then, we generated a binary brain mask by including all voxels with signal intensities greater than a threshold value of 30 in the histogram domain. We filled tiny holes in this brain mask using binary_fill_holes (SciPy.ndimage).[27] Last, we performed the Gaussian normalization process to yield pixel intensities with a mean of zero and an SD of 1 for the brain area under the brain mask, thereby producing optimal arrays for training a deep learning model.

Deep Learning Algorithms: UNet versus SE-UNet Ensemble Network Architecture

We used the 2 neural network architectures from the literature,[28,29] the 2D UNet and the 2D SE-UNet (Online Supplemental Data). The 2D UNet has an encoder path and a decoder path, each with 3 resolution steps. In the encoder path, each layer has three 3 × 3 convolutions and batch normalization, which is followed by a rectified linear unit (ReLU) activation function, and a 2 × 2 max pooling layer for downsampling. In the decoder path, each layer uses a deconvolution with a kernel size of 2 × 2, followed by three 3 × 3 convolutions and batch normalization with ReLU. The network has shortcut connections from the layers in the encoder path to the corresponding layers with the same resolution in the decoder path. Finally, a fully connected layer with a 32-channel input was added to the end of the decoder path and activated using a sigmoid function, with random initial nonuniform weights. We used the Dice loss function. For the learning and optimization step, we used the Adam optimizer with a 1e-3 learning rate and 1e-3/300 decay rate, 50 epochs. For the training, we did not use data augmentation techniques.

The 2D SE-UNet has a architecture similar to that of the 2D-UNet but with an additional SE-block and global average pooling applied after the convolution layer in the downsampling path. The SE block assigns weights to the network channel. Squeeze involves the portion of the layer that conducts global pooling, which embeds global information. Excitation recalibrates adaptively through ReLU and sigmoid activations.[28] The 2D-UNet and 2D SE-UNet models were trained using the same training data set. Each model was initialized with different random weights to ensure variety. We arbitrarily set the threshold of 0.5 to designate voxels with WMHs. The scripts for training deep learning models are available at GitHub (https://github.com/jlk-jhpark/Whitematter-hyper-intensity-segmentation.git).

The Uncertainty Index That Represents Overall Ambiguity in the Voxel Classification of WMH Segmentation in Each Patient

To calculate uncertainty, we used a deep ensemble of 5 different models. We used soft voting to combine the models. The individual networks share the same architecture but were trained on different 90% subsets of the training data set, each with different random initializations to ensure variability.[30,31] The voxel-level Kullback-Leibler (KL) divergence values were calculated using the SciPy.stats.entropy module.[30] In the formula, the average of the predicted probabilities from the 5 models was used as input data, along with a prior probability of 0.5. This prior probability indicates that each voxel has an equal chance of being predicted as WMH. Because we assigned a prior probability of 0.5, the large KL divergence indicated low uncertainty. Next, we calculated the proportion of voxels with a substantial divergence value (<0.5) of all predicted voxels in each patient. Thus, the following patient-level uncertainty was calculated as

$$\text{Uncertainty index} = \frac{\Sigma\ \textit{predicted WMH pixels with divergence value} < 0.5}{\Sigma\ \textit{predicted WMH pixels}}.$$

Segmentation Performance Evaluation Metrics

The following metrics were used to evaluate the automated WMH segmentation methods compared with manual WMH segmentation.

- DSC = 2× (true-positive WMH voxels) / (true WMH voxels + predicted WMH voxels)
- Hausdorff distance (HD) between 2 sets of points, representing segmented regions (true-positive WMH X and predicted WMH Y), is defined as follows: HD (X, Y) = max[HD(X, Y), HD(Y, X)], where the one-sided HD from X to Y is defined as $hd(X, Y) = \max_{x \in X} \min_{y \in Y} \|x\text{-}y\|$.

$$\text{Correlation coefficient (R)} = \frac{n \times \sum xy - \sum x \sum y}{\sqrt{\left[n\sum x^2 - \left(\sum x\right)^2\right]\left[n\sum y^2 - \left(\sum y\right)^2\right]}},$$

Where n indicates number of samples; *x*, automated WMH volume; *y*, manual WMH volume.

Experiment and Analysis

We implemented the networks in Python 3.6.10 using Keras 2.4.3. The baseline network (UNet, SE-UNet) for training was trained on a GeForce GTX 1080 Ti GPU with 11.0 CUDA Version, taking 13 minutes per epoch for 41,854, 14,303, 14,039 slices with the training/validation/test split of 60%, 20%, 20%. We empirically chose a batch size of 8.

To evaluate the interrater reliability of WMH segmentation, we computed the mean DSC and mean correlation coefficient among 5 research assistants using 135 randomly-sampled FLAIR images.

We validated deep learning models in 6 external data sets using DSC. A relationship between automated WMH volume and manual WMH volume was assessed using a correlation coefficient. After training on 100, 200, 500, 1000, 1500, and 2408 patients' FLAIR MRIs, the mean (SD) DSC in the combined external data set was calculated to evaluate the WMH segmentation performance as the amount of training data increases. In addition, we assessed the model performance after stratifying patients by infarction volume, infarction location, uncertainty, and WMH subregion. The infarction volume was categorized with cutoff points of 1.7 and 14 mL.[15] WMH volumes were categorized into tertiles of the combined external validation data sets. The infarction location was categorized as the cortex, corona radiata, basal ganglia and internal capsule, thalamus, midbrain, pons, medulla, and cerebellum. Infarct location information was retrieved from a prospective stroke registry. In addition, the external validation data set was divided according to uncertainty levels of 0.2, 0.4, 0.6, and 0.8. To differentiate WMH subregions (periventricular versus deep), we trained a deep learning algorithm that automatically segments the ventricles in FLAIR images. A total of 145 patients' FLAIR images were used for the ventricle-segmentation learning using UNet, and the model showed a validation DSC of 0.9034. Then, a distance transform based on the OpenCV algorithm[32] was used to define the periventricular region within 10 and 7.5 mm from the ventricular surface. WMH volumes observed in this region were classified as periventricular WMH, whereas WMH volumes observed outside this region were classified as deep WMH. In addition, we calculated the mean and 95% CI of the uncertainty index for the external validation data sets after stratification by DSCs (with the cutoff values of 0.60, 0.65, 0.70, 0.75, and 0.80) and predicted WMH volume (in quartiles).

Statistical Analysis

To compare subjects' characteristics between training and test data sets, we used the ANOVA or the Kruskal-Wallis test for the analysis of continuous variables and the χ^2 test for categoric variables as appropriate. Mean DSC and Hounsfield unit values were compared between the UNet and the SE-UNet using paired *t* tests. We compared the segmentation performance between automated methods that were applied to the test data set using ANOVA and Bonferroni post hoc analyses. We then compared the segmentation performance between test data subgroups stratified by infarct location, tertiles of WMH volume, uncertainty, and WMH subregion. To evaluate the agreement between automated WMH segmentation volume by SE-UNet and manual segmentation volume, we used the concordance correlation coefficient, which is commonly used to assess agreement between 2 raters or 2 methods to measure a response when the data are measured on a continuous scale.[33] A concordance correlation coefficient of >0.8 has been suggested as an excellent level of agreement.[34] In addition, we measured a bias correction factor (C_b), which measures how far the best-fit line deviates from the 45° line (measure of accuracy).[33] When there is no deviation from the 45° line, the C_b is 1. The Pearson correlation coefficient ρ measures how far each observation deviates from the best-fit line (measure of precision).[33] Data were analyzed using Stata (StataCorp), and a 2-sided *P* value < .05 considered statistically significant.

RESULTS

Baseline Characteristics

Compared with the subjects in the combined data set for training and validation and internal testing (mean age, 67.4 [SD, 13.0] years; 60.4% men), those in the 6 data sets for external testing had significantly different clinical characteristics in terms of age, last-known-well time to admission, stroke subtype, and the frequencies of previous stroke history, coronary artery disease, and other cardiovascular risk factors (Table). Moreover, MRI vendors, magnetic field strength, and imaging parameters were variable across the data sets (Online Supplemental Data). Within the data sets for external testing, subjects' mean age and the prevalence of risk factors also varied across the data sets. These results show that we used distinct training and validation data sets, which should make the deep learning models more robust and effective on new, previously unseen data.

Algorithm Performance for Automatic Segmentation of WMH Lesions

Overall, the mean DSC values for the UNet segmentation on the internal test and external validation data sets were, respectively, 0.659 (95% CI, 0.649 − 0.669) and 0.710 (95% CI, 0.707 − 0.714), which were slightly lower than the reliability between human raters (mean, 0.744; 95% CI, 0.738 − 0.751; $P = .031$; Online Supplemental Data). The mean HD values for the UNet on the internal test and external validation data sets were 10.44 (95% CI, 9.75–11.14) and 10.44 (95% CI, 10.22–10.65), respectively. The mean values for the SE-UNet segmentation on the internal test and external validation data sets were, respectively, 0.675 (95% CI, 0.666–0.685) and 0.722 (95% CI, 0.719–0.726), exhibiting overall superior performance over the UNet (both $P < .001$). The mean HD for the SE-UNet on the internal test and external validation data sets were, respectively, 9.09 (95% CI, 8.43–9.74) and 8.98 (95% CI, 8.77–9.18), again demonstrating superior performance over the UNet (both $P < .001$). The mean (SD) processing times for the UNet and the SE-UNet on the overall external data sets were 67.0 (9.6) ms and 74.0 (6.6) ms, respectively ($P < .001$).

In addition, deep learning algorithms showed similarly high DSCs across multiple external validation data sets with the values

Baseline characteristics of the training, internal validation, and external validation data sets[a]

	Training, Validation, and Internal Test (n = 2408)	External Validation 1 (n = 1105)	External Validation 2 (n = 838)	External Validation 3 (n = 2654)	External Validation 4 (n = 428)	External Validation 5 (n = 571)	External Validation 6 (n = 417)	P
Age (yr)	67.4 (13.0)	68.2 (12.8)	67.5 (13.3)	68.1 (12.5)	70.0 (11.7)	67.9 (13.1)	69.7 (12.7)	<.01
Sex, male	1419 (60.4)	568 (54.3)	491 (60.8)	1497 (57.7)	222 (52.7)	346 (63.0)	235 (58.6)	
LKW to admission (hr)	12.0 (3.5–37.2)	13.1 (3.5–32.0)	13.9 (3.2–39.0)	6.8 (2.6–24.0)	11.4 (3.1–34.8)	13.5 (3.3–39.4)	17.7 (5.7–51)	<.001[a]
Prestroke mRS score >2	285 (12.1)	171 (16.4)	107 (13.2)	426 (16.4)	55 (13.1)	94 (17.1)	115 (28.7)	<.001
Admission NIHSS score	4 (2–8)	4 (2–7)	3 (1–8)	4 (2–9)	4 (2–10)	3 (2–8)	4 (2–8)	.11[a]
Subtype								<.001
LAA	814 (35.4)	331 (32.3)	296 (38.0)	1030 (40.1)	179 (43.0)	197 (36.1)	162 (40.6)	
SVO	469 (20.4)	222 (21.6)	216 (27.7)	221 (8.6)	52 (12.5)	123 (22.5)	98 (24.6)	
CE	525 (22.8)	160 (15.6)	159 (20.4)	625 (24.3)	63 (15.1)	112 (20.5)	65 (16.3)	
Undetermined	435 (18.9)	289 (28.2)	93 (11.9)	654 (25.4)	120 (28.9)	103 (18.9)	64 (16.0)	
Other-determined	59 (2.6)	24 (2.3)	15 (1.9)	42 (1.6)	2 (0.5)	11 (2.0)	10 (2.5)	
Previous stroke	483 (20.5)	250 (23.9)	188 (23.3)	392 (15.1)	112 (26.6)	115 (21.0)	111 (27.7)	<.001
Coronary artery disease	391 (16.6)	95 (9.1)	95 (11.8)	88 (3.4)	37 (8.8)	66 (12.0)	33 (8.2)	<.001
Hypertension	1594 (67.8)	726 (69.4)	559 (69.2)	1585 (61.1)	322 (76.5)	409 (74.5)	311 (77.6)	<.001
Diabetes	791 (33.7)	338 (32.3)	280 (34.7)	730 (28.1)	164 (39.0)	199 (36.3)	158 (39.4)	<.001
Hyperlipidemia	1084 (46.1)	193 (18.5)	324 (40.1)	362 (14.0)	133 (31.6)	268 (48.8)	195 (48.6)	<.001
Smoking, current or quit ≤5 yr	950 (40.4)	391 (37.4)	330 (40.8)	989 (38.1)	162 (38.5)	259 (47.2)	166 (41.1)	<.001
Atrial fibrillation	496 (21.1)	180 (17.2)	158 (20.0)	621 (23.9)	86 (20.4)	114 (20.8)	66 (16.5)	.003
Revascularization	404 (17.2)	147 (14.1)	82 (10.2)	587 (22.6)	73 (17.3)	114 (20.8)	45 (11.2)	<.001
Infarct volume (mL)	1.7 (0.4–9.8)	1.1 (0.3–6.6)	2.0 (0.4–12.2)	3.6 (0.6–17.9)	1.2 (0.3–8.7)	2.2 (0.5–15.4)	1.4 (0.5–9.5)	
WMH volume (mL)	11.4 (5.4–24.7)	14.6 (6.6–30.0)	10.8 (4.2–25.1)	12.7 (6.9–24.3)	14.3 (7.0–28.7)	13.0 (6.7–25.5)	17.7 (8.9–40.0)	<.001[a]

Note:—CE indicates cardioembolism; LAA, large-artery atherosclerosis; LKW, last known well; mRS, modified Rankin Scale; SVO, small-vessel occlusion.
Data are presented as mean ± SD, median (interquartile range), number (percentage).
[a] Kruskal-Wallis test was used.

ranging from 0.672 to 0.744. In line with these findings, WMH volumes that were segmented automatically and manually showed a strong correlation for the UNet ($r = 0.917$, $P < .001$) and the SE-UNet ($r = 0.933$, $P < .001$) in the external validation data sets. Because the SE-UNet outperformed the UNet, the subsequent analyses were performed using the SE-UNet. The mean DSC for the external data sets increased from 0.659 to 0.699 when the training data set size was increased from 100 to 500 (Online Supplemental Data). However, with a larger sample size beyond 500 up to 2048, there was little but statistically significant improvement in DSC (from 0.699 to 0.722; $P < .001$), suggesting a saturation effect.

Impact of Volume and Location of Acute Infarct and WMH on the Accuracy of Automatic Lesion Segmentation

As shown in Fig 1*A*, the mean DSC (for the external data sets) was significantly lower in the large infarct group (>14 mL, DSC = 0.695; 95% CI, 0.688–0.703) and the moderate infarct group (1.7–14 mL, DSC = 0.721; 95% CI, 0.715–0.727), compared with the small infarct group (<1.7 mL, DSC = 0.737; 95% CI, 0.732–0.742; both $P < .001$). After stratification by infarct location (Online Supplemental Data), mean DSCs were comparable across the groups, except for the medulla infarct group with its DSC being <0.7.

The mean DSC for the highest tertile of WMH volume was significantly greater than that for the lowest tertile (DSC = 0.617 versus 0.813, $P < .001$; Fig 1*B*). In addition, the segmentation accuracy for periventricular WMH was significantly higher than that for subcortical WMH (Online Supplemental Data), regardless of the definition of the periventricular region by the distance from the ventricular surface: 10 mm (DSC = 0.751 versus 0.617; $P < .001$) and 7.5-mm cutoff (DSC = 0.751 versus 0.628; $P < .001$).

Predictors of the Accuracy of Automatic WMH Segmentation: Uncertainty Index, Infarct Volume/Location, and WMH Volume

The mean patient-level uncertainty index for the external test data sets was 0.2214 (SD, 0.1184) (see Fig 2 for representative cases with low or high uncertainty indices). The uncertainty index was inversely correlated with the DSC in the combined external data set ($r = -0.753$, $P < .001$; Fig 3*A*). Regardless of the infarct size, the DSC was similar for subjects in the lowest uncertainty group (0–0.2). In higher uncertainty groups (0.4–1.0), however, large infarcts (>14 mL) were associated with a lower segmentation accuracy than small or moderate-sized infarcts (Fig 1*C*). Regardless of the infarct locations, the DSC decreased as the uncertainty index increased (Online Supplemental Data). For both automatic and manual WMH segmentations, the uncertainty index decreased as the WMH volume increased (Online Supplemental Data). In the combined external validation data sets, 86% of patients had an uncertainty index of <0.35 (Fig 3*B*). In these subjects, the mean DSC (0.746) was similar to the interrater reliability of manual segmentations (0.75). When patients were stratified by WMH quartiles and DSCs, we again observed an inverse relationship between the uncertainty index and WMH volume (Fig 1*E*). Of note, within each WMH volume stratum, there was an inverse relationship between the uncertainty index and the DSC. However, when WMH volumes were higher than ~10 mL, the uncertainty indices were lower than ~0.2, regardless of their DSC values. In contrast, when WMH volumes were lower than ~4 mL, the uncertainty indexes were higher than ~0.3, regardless of their DSC values.

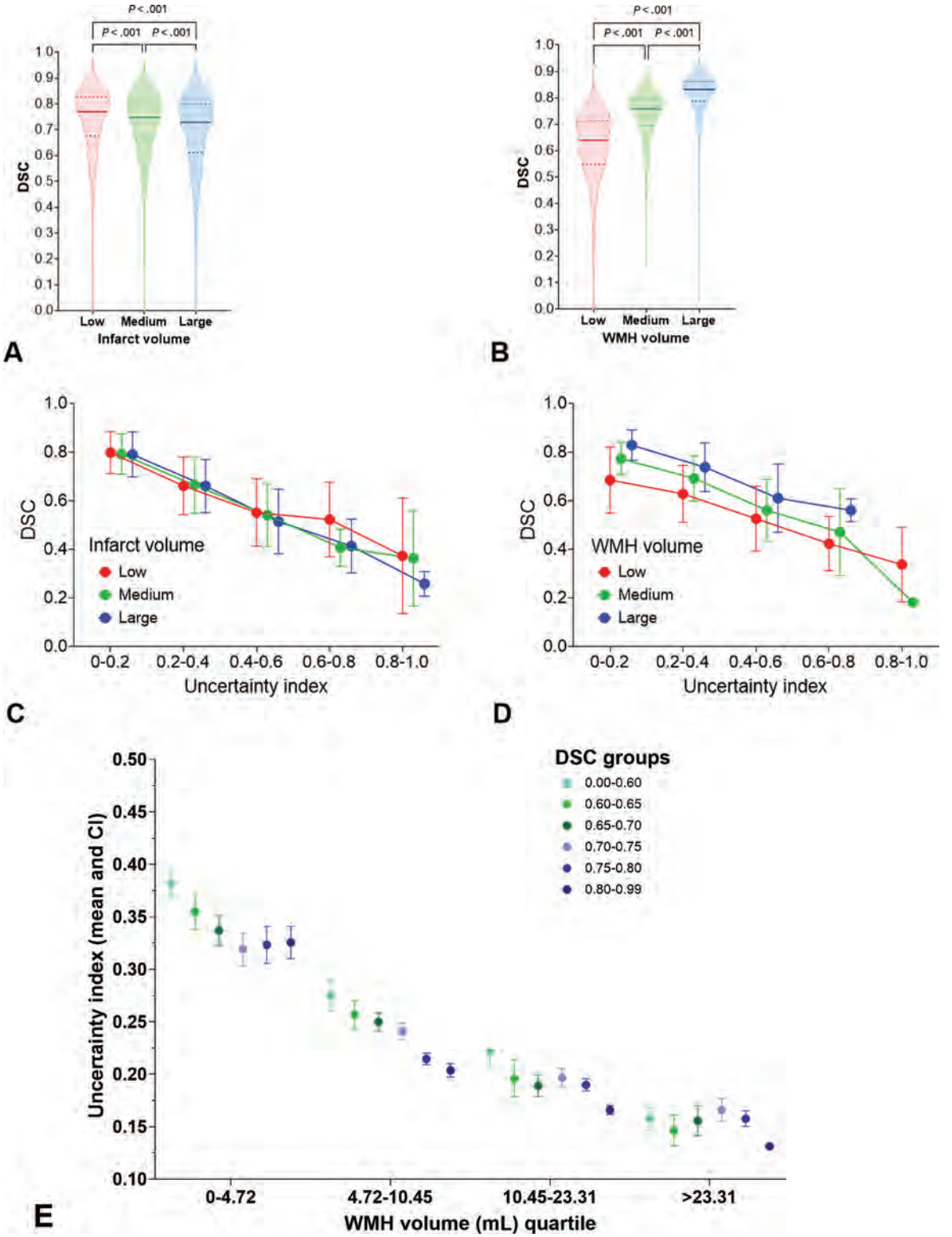

FIG 1. Segmentation performance of the SE-UNet, with stratification by infarct volume, white matter hyperintensity volume, and the uncertainty index in external test data sets. *A*, *Violin plot* for the performance of WMH segmentation, with stratification by infarct volume (low, <1.7 mL, $n = 2792$; medium, 1.7–14 mL, $n = 1785$; and large, >14 mL, $n = 1436$). *B*, *Violin plot* for the segmentation performance, with stratification by WMH volume (low ,<7.6 mL, $n = 1984$; medium, 7.6–19.6 mL, $n = 1984$; and large, >19.7 mL, $n = 2045$). *C*, Segmentation performance stratified by the infarct volume and the uncertainty index. *D*, Segmentation performance, stratified by the WMH volume and the uncertainty index. Due to the association between the volume of WMHs and the uncertainty index, none of the patients in the large-volume group had an uncertainty index exceeding 0.8. *E*, The mean and 95% CI of the uncertainty index after stratification of DSCs and WMH volume (in quartiles). In the *violin plots*, *lines* and *dotted lines* indicate median and interquartile range, respectively. In the *line graphs*, *dots* and *error bars* indicate mean (SD), respectively.

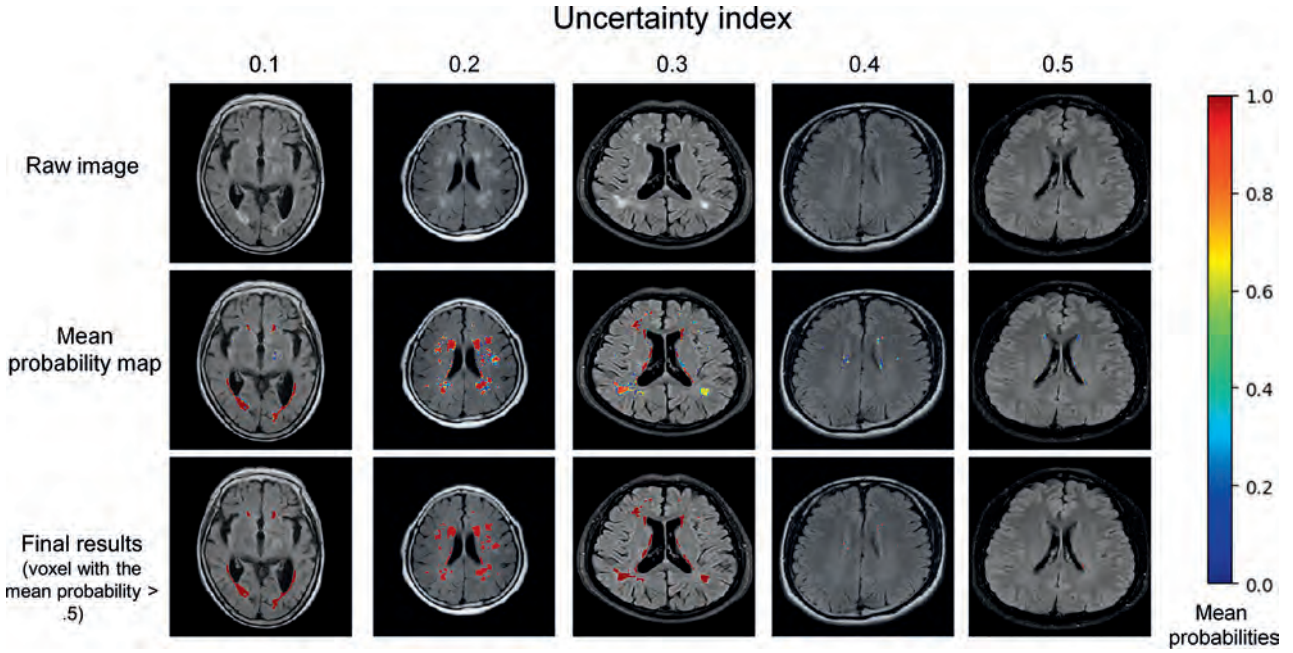

FIG 2. Representative cases of automatic white matter hyperintensity segmentation and their uncertainty indices. *Upper row*: raw images. *Middle row*: red and blue areas, respectively, show areas of agreement and disagreement between human segmentation and deep learning algorithm-based segmentation. *Lower row*: adjudicated final results, with uncertainties resolved.

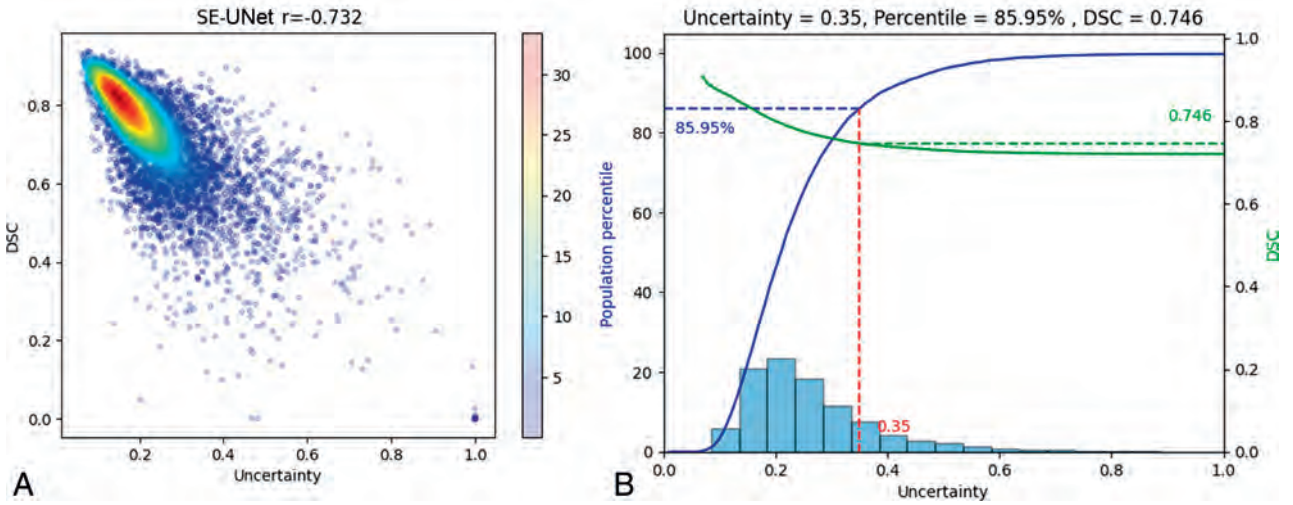

FIG 3. Relationship between the uncertainty index and the DSC. *A*, *Density plot* between the uncertainty index and the DSC. As expected, there is a negative correlation between the 2 values. *B*, Mean DSC, distribution of subjects, and the uncertainty index. The *blue line* represents the cumulative percentile of patients, while the *green line* indicates the mean DSC of cumulative patients. The *blue dotted line* represents the cumulative percentage of patients when the uncertainty index reaches 0.35 from 0 (*red dotted line*). The *green dotted line* shows interhuman DSC. At an uncertainty index of 0.35, accumulated patients comprise approximately 86% of the total population, with a mean DSC of 0.75.

Correlation between Volumes of WMH Segmented Automatically versus Manually

In the combined data set for external testing (6013 patients' MR images from 6 stroke centers), the median WMH volume estimated by the SE-UNet segmentation algorithm was 12.39 mL (interquartile range, 6.02–25.38 mL). There was an excellent correlation between volumes of WMH segmented automatically using the SE-UNet versus manual segmentation by experienced researchers (Fig 4), with the concordance correlation coefficient and the C_b being 0.931 (95% CI, 0.928–0.934) and 0.990, respectively. When each external data set was assessed separately, the concordance correlation coefficient and C_b ranged from 0.841 to 0.956 and 0.973 to 0.994, respectively (Online Supplemental Data). In the combined external data set, 6 outlier cases that appeared to be far off the diagonal line were identified (Online Supplemental Data). In every case, we found that manual segmentation had erroneously designated acute or chronic infarcts as WMHs.

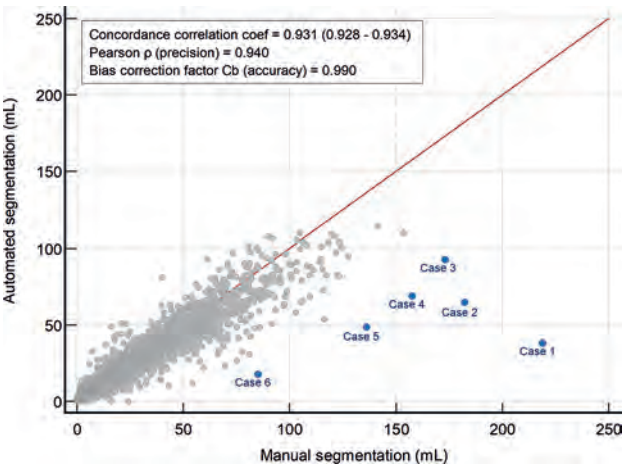

FIG 4. Scatterplot showing a strong correlation between the volumes of WMHs segmented automatically by SE-UNet and manually in external validation. *Gray dots* indicate each subject. The *red line* indicates a 45° line of identity. Outlier subjects (*blue dots*) are reviewed in the Online Supplemental Data. The given equation is $y = 2.1693 + 0.8311x$, where y represents the automatically segmented WMH volume and x represents the manually segmented WMH volume. After eliminating 6 outlier cases from the scatterplot, the slope showed a modest increase, resulting in the equation $y = 2.0671 + 0.8376$ x. Coef indicates coefficient.

DISCUSSION

In the present study using multicenter data sets (MR images with voxelwise lesion [ground truth] annotation and prospectively collected clinical data) from a total of 8421 patients with ischemic stroke, we developed and validated deep learning algorithms for automatic WMH segmentation. This, to the best of our knowledge, is the largest-ever data set used for stroke research of this nature (Fig 5). The SE-UNet algorithm had a very high level of segmentation accuracy, with the concordance correlation coefficient and the C_b being, respectively, 0.919 and 0.987, compared with the ground-truth WMH volumes. As previously reported,[7] however, even among the highly experienced raters, the level of voxelwise agreement was moderate (DSC-based interrater reliability of ~0.77). We found a close correlation between a high uncertainty index and a low DSC, suggesting that researchers can use the index to identify those cases that require human inspection following artificial intelligence–based automatic segmentation of WMH. The sample results and demonstration are available at the Web site https://stroke.medihub.ai/login/JBS_WMH_sample (Online Supplemental Data).

Because manual segmentation of WMH is labor-intensive and time-consuming, visual rating scales have been widely used in WMH research using large or multicenter data sets. However,

Previous studies vs. Current study

Year	Authors	Source of images used for deep learning training	Stroke population	Number of patients in the training and validation datasets	Model	DSC for internal validation	DSC for external validation	Source of images used for external validation	Number of patients in the external datasets
2018	Guerrero et al.[18]	1 scanner at 1 hospital, UK	Yes[a]	167	uResNet	0.695	N/A	N/A	N/A
2020	Lee et al.[19]	5 scanners (from 3 vendors) at 3 hospitals, Netherlands and Singapore (MICCAI 2017)	No	170	SEU-net	0.769	N/A	N/A	N/A
2021	Park et al.[12]	5 scanners (from 3 vendors) at 3 hospitals, the Netherlands and Singapore (MICCAI 2017)	No	170	2D Ensemble U-net	0.81	N/A	N/A	N/A
2021	Sundaresan et al.[16]	1 scanner, a Neurodegenerative cohort (NDGEN), UK	No	21	TrUE-Net	0.89	N/A	N/A	N/A
		1 scanner, Oxford vascular study (OXVASC), UK	Yes[b]	18		0.95			
		5 scanners (from 3 vendors) at 3 hospitals, Netherlands and Singapore (MICCAI 2017)	No	60		N/A			
2022	Li et al.[15]	5 scanners (from 3 vendors) at 3 hospitals, Netherlands and Singapore (MICCAI 2017)	No	60	2D Ensemble SEU-net	0.833	0.783	2 different vendor scanners at 2 hospitals	60
		5 scanners (from 3 vendors) at 5 hospitals, Australia	No	40					
2024	Kim et al.: Current study	6 scanners[c] (from 3 vendors) at 3 hospitals, Korea	Yes	1927	SEU-net	0.675	0.722	7 scanners[c] (from 3 vendors) at 6 hospitals	6013

[a]non-disabling lacunar or mild cortical ischemic stroke; [b]minor non-disabling stroke or transient ischemic attack; [c]Scanners used for >5% of the study population were counted.

Automatic segmentation of WMHs by our deep learning algorithm, distinguishing the FLAIR lesions from DWI-positive infarcts without relying on DWIs

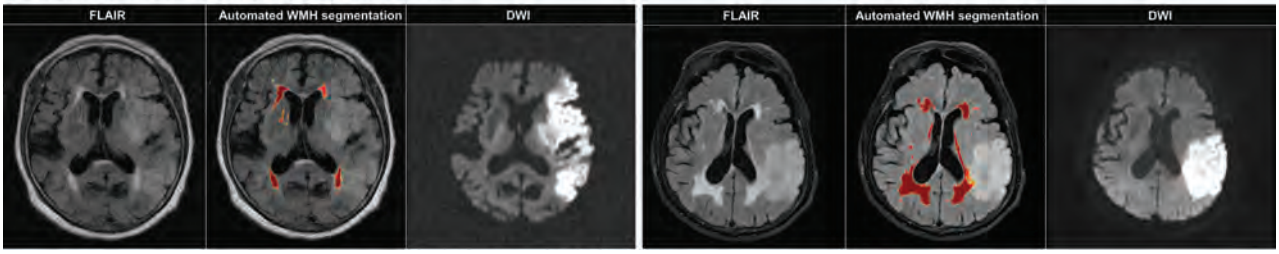

FIG 5. Comparison of previous studies and the current study on automated WMH segmentation using deep learning algorithms, along with representative cases demonstrating the performance of our algorithm. NA indicates not applicable.

visual rating systems showed limited correlation with quantitative assessments of WMH.[35] In addition, when examining longitudinal changes in white matter, volumetric measures of WMH provided a more reliable, sensitive, and objective substitute than visual rating scales.[36] Moreover, according to a recent study, expert agreement in manually segmenting WMH was low, with DSCs ranging from 0.56 to 0.62.[11] In our study, 5 experienced research assistants who have been segmenting WMH for >5 years under careful supervision (including regular audits and consensus discussions) of a vascular neurologist accomplished a DSC of ~0.77. Taken together, these findings raise concerns about the accuracy and consistency of WMH quantifications in large multicenter investigations involving multiple raters, emphasizing the need for a verified automatic WMH segmentation method to serve as a labor saving-yet-accurate reference method. In the present study, multicenter validations demonstrated consistently high performance of the artificial intelligence algorithm, achieving a high DSC across various MRI vendors and parameters.

Because deep learning algorithms can have overfitting,[37] extensive external validation is necessary before they can be used in clinical practice. Unlike previous deep learning studies that have demonstrated similar[18] or superior[16] performance of WMH segmentation, our study rigorously validated our algorithms on 6 external data sets with various MRI vendors, acquisition protocols, and clinical features. This extensive validation underscores the robustness of our approach. As shown in our study, even among the highly experienced raters, the level of voxelwise agreement was moderate (DSC-based interrater reliability of ~0.77). Moreover, the performance of deep learning models reached a plateau at about 2000 FLAIR MRIs. Thus, even with a larger data set for supervised learning, it might be difficult to outperform experts in rigorous internal and external testing.

Prior studies on automatic WMH segmentation using deep learning did not include patients with acute ischemic stroke.[12,15,16,18,19] These studies are difficult to apply to research in patients with stroke because it is challenging to distinguish between acute infarcts and WMH on FLAIR images. We demonstrated that our deep learning algorithm reliably differentiates WMHs from acute infarcts and quantifies WMH volume with excellent agreement with manual segmentation (Fig 5), thereby facilitating WMH research in patients with stroke with a large sample size. Future studies could validate our deep learning algorithms in outpatients with cognitive decline as well, expanding their clinical relevance. The general methodology we established in patients with stroke also should be applicable to many other populations.

Our study shows that manually or via deep learning approaches, segmenting WMHs may have an inherent element of ambiguity when the extent of WMH is small in the periventricular area and there are spatial overlaps between infarcts and WMHs. The uncertainty index that represents a patient-level ambiguity in voxel classification for WMH segmentation was negatively correlated with total WMH volume and DSC. Thus, the uncertainty index could be a useful stratification/triage tool to identify cases that require human inspection in research or clinical practice using WMH segmentation, enabling investigators to evaluate their own models and compare different study results.

Deep learning models typically perform worse on data that were not used for training.[38] In our study however, both the UNet and SE-UNet demonstrated higher DSCs in the external test data sets than in the internal test data set. This finding may be attributed to higher WMH volumes in the external validation data sets (ranging from 10.8 to 17.7 mL) compared with the internal data set (median 11.4 mL). As shown in Fig 1*B*, DSC values were higher when WMH volumes were higher.

Of note, while acknowledging the potential benefits of 3D models, we deliberately opted to use 2D UNets for several reasons: First, in typical clinical settings for screening patients with stroke, MR images mostly have high in-plane resolution (eg, 1 - × 1 mm) but a relatively large slice thickness (3–7 mm), aligning well with the capabilities of 2D UNets. Preliminary investigations with 3D UNet[39] and nnUNet, a semantic segmentation method that automatically adapts to a given dataset,[40] yielded suboptimal segmentation performance compared with 2D methods (Online Supplemental Data). Furthermore, computational constraints, particularly with our large data sets, limited the feasibility of deploying and adjusting 3D approaches without sacrificing efficiency. Using 2D UNets, we achieved a balance between computational efficiency and model performance, ensuring that our experiments could be conducted within reasonable time and resource constraints.

Our study has limitations. First, T1-weighted images were unavailable because MRI was performed in the setting of acute stroke. The performance of deep learning algorithms was reported to improve when trained with both FLAIR and T1-weighted images, compared with the exclusive use of FLAIR images.[12] Second, given that most study participants were of Asian descent, the generalizability of the findings to other ethnic populations might be somewhat restricted. While a recent study found that racial differences in WMH burden are largely influenced by underlying vascular risk factors,[41] further work with multinational cohorts is needed. Third, incorporating FLAIR and DWI into the algorithm may improve the differentiation of WMH from acute infarct. However, this step may limit the utility of the algorithm due to the requirements of both types of images. Finally, our algorithm was trained using FLAIR images acquired >10 years ago (from 2011 to 2013). However, when the algorithm was validated using a recent MRI data set from 30 patients with acute ischemic stroke (Online Supplemental Data), the validation showed a comparable level of DSC: 0.674 (95% CI, 0.619–0.729).

CONCLUSIONS

We developed and validated deep learning algorithms to segment WMH in patients with acute cerebral infarction using the largest-ever MRI data sets. In addition, we showed how the uncertainty index could assist researchers and physicians in identifying challenging cases that may necessitate human review after automatic WMH segmentation.

ACKNOWLEDGMENTS

We are grateful to Dr Sue Young Ha for her assistance with this research.

Disclosure forms provided by the authors are available with the full text and PDF of this article at www.ajnr.org.

REFERENCES

1. Debette S, Markus HS. **The clinical importance of white matter hyperintensities on brain magnetic resonance imaging: systematic review and meta-analysis.** *BMJ* 2010;341:c3666 CrossRef Medline
2. Ryu WS, Schellingerhout D, Hong KS, et al. **White matter hyperintensity load on stroke recurrence and mortality at 1 year after ischemic stroke.** *Neurology* 2019;93:e578–89 CrossRef Medline
3. Ryu WS, Woo SH, Schellingerhout D, et al. **Stroke outcomes are worse with larger leukoaraiosis volumes.** *Brain* 2017;140:158–70 CrossRef Medline
4. Prins ND, Scheltens P. **White matter hyperintensities, cognitive impairment and dementia: an update.** *Nat Rev Neurol* 2015;11:157–65 CrossRef Medline
5. Herrmann LL, Le Masurier M, Ebmeier KP. **White matter hyperintensities in late life depression: a systematic review.** *J Neurol Neurosurg Psychiatry* 2007;79:619–24 CrossRef
6. Wardlaw JM, Smith EE, Biessels GJ, et al. Neuroimaging; STandards for ReportIng Vascular changes on nEuroimaging (STRIVE v1). **standards for research into small vessel disease and its contribution to ageing and neurodegeneration.** *Lancet Neurol* 2013;12:822–38 CrossRef Medline
7. Xiong Y, Yang J, Wong A, et al. **Operational definitions improve reliability of the age-related white matter changes scale.** *Eur J Neurol* 2011;18:744–49 CrossRef Medline
8. Rost NS, Brodtmann A, Pase MP, et al. **Post-stroke cognitive impairment and dementia.** *Circ Res* 2022;130:1252–71 CrossRef Medline
9. Alber J, Alladi S, Bae HJ, et al. **White matter hyperintensities in vascular contributions to cognitive impairment and dementia (VCID): knowledge gaps and opportunities.** *Alzheimers Dement (N Y)* 2019;5:107–17 CrossRef Medline
10. Black S, Gao F, Bilbao J. **Understanding white matter disease: imaging-pathological correlations in vascular cognitive impairment.** *Stroke* 2009;40:S48–52 CrossRef Medline
11. Carass A, Roy S, Gherman A, et al. **Evaluating white matter lesion segmentations with refined Sorensen-Dice analysis.** *Sci Rep* 2020;10:8242 CrossRef Medline
12. Park G, Hong J, Duffy BA, et al. **White matter hyperintensities segmentation using the ensemble U-Net with multi-scale highlighting foregrounds.** *Neuroimage* 2021;237:118140 CrossRef Medline
13. Ryu WS, Kang YR, Noh YG, et al. **Acute infarct segmentation on diffusion-weighted imaging using deep learning algorithm and RAPID MRI.** *J Stroke* 2023;25:425–29 CrossRef Medline
14. Noh YG, Ryu WS, Schellingerhout D, et al. **Deep learning algorithms for automatic segmentation of acute cerebral infarcts on diffusion-weighted images: effects of training data sample size, transfer learning, and data features.** 2023. *medRxiv* https://www.medrxiv.org/content/medrxiv/early/2023/07/09/2023.07.02.23292150.full.pdf. Accessed July 2, 2023
15. Li X, Zhao Y, Jiang J, et al. **White matter hyperintensities segmentation using an ensemble of neural networks.** *Hum Brain Mapp* 2022;43:929–39 CrossRef Medline
16. Sundaresan V, Zamboni G, Rothwell PM, et al. **Triplanar ensemble U-Net model for white matter hyperintensities segmentation on MR images.** *Med Image Anal* 2021;73:102184 CrossRef Medline
17. Ryu WS, Woo SH, Schellingerhout D, et al. **Grading and interpretation of white matter hyperintensities using statistical maps.** *Stroke* 2014;45:3567–75 CrossRef Medline
18. Guerrero R, Qin C, Oktay O, et al. **White matter hyperintensity and stroke lesion segmentation and differentiation using convolutional neural networks.** *Neuroimage Clin* 2018;17:918–34 CrossRef Medline
19. Lee AR, Woo I, Kang DW, et al. **Fully automated segmentation on brain ischemic and white matter hyperintensities lesions using semantic segmentation networks with squeeze-and-excitation blocks in MRI.** *Informatics in Medicine Unlocked* 2020;21:100440 CrossRef
20. Zhou K, Liu Z, Qiao Y, et al. **Domain generalization: a survey.** *IEEE Trans Pattern Anal Mach Intell* 2022;45:4396–415 CrossRef Medline
21. Mehrtash A, Wells WM, Tempany CM, et al. **Confidence calibration and predictive uncertainty estimation for deep medical image segmentation.** *IEEE Trans Med Imaging* 2020;39:3868–78 CrossRef Medline
22. van Erven T, Harremoes P. **Rényi divergence and Kullback-Leibler divergence**. *IEEE Trans Inform Theory* 2014;60:3797–820 CrossRef
23. Ryu WS, Schellingerhout D, Hong KS, et al. **Relation of pre-stroke aspirin use with cerebral infarct volume and functional outcomes.** *Ann Neurol* 2021;90:763–76 CrossRef Medline
24. Kim DE, Park JH, Schellingerhout D, et al. **Mapping the supratentorial cerebral arterial territories using 1160 large artery infarcts.** *JAMA Neurol* 2019;76:72–80 CrossRef Medline
25. Kim DE, Ryu WS, Schellingerhout D, et al. **Estimation of acute infarct volume with reference maps: a simple visual tool for decision making in thrombectomy cases.** *J Stroke* 2019;21:69–77 CrossRef Medline
26. Ryu WS, Schellingerhout D, Ahn HS, et al. **Hemispheric asymmetry of white matter hyperintensity in association with lacunar infarction.** *J Am Heart Assoc* 2018;7:e010653 CrossRef Medline
27. Chityala R, Pudipeddi S. *Image Processing and Acquisition using Python*. CRC Press; 2020; 89–107
28. Hu J, Shen L, Sun G. **Squeeze-and-excitation networks.** In: *Proceedings of the IEEE Conference on Computer Vision and Pattern Recognition.* 2018:7132–41
29. Huang H, Lin L, Tong R, et al. **Unet 3+: a full-scale connected unet for medical image segmentation**. In: *Proceedings of the 2020-2020 IEEE International Conference on Acoustics, Speech and Signal Processing (ICASSP)*. May 4–8, 2020. Barcelona, Spain; 10555–59
30. Lakshminarayanan B, Pritzel A, Blundell C. **Simple and scalable predictive uncertainty estimation using deep ensembles.** In: *Proceedings of the Annual Conference Neural Information Processing Systems.* December 4–8, 2017. Long Beach, California
31. Jungo A, Reyes M. **Assessing reliability and challenges of uncertainty estimations for medical image segmentation.** *Medical Image Computing and Computer Assisted Intervention–MICCAI 2019*. Springer-Verlag; 2019:48–56
32. Tuohy S, O'Cualain D, Jones E, et al. **Distance determination for an automobile environment using inverse perspective mapping in OpenCV**. In: *Proceedings of the IET Irish Signals and Systems Conference.* June14, 2010. Belfast, Northern Ireland
33. Lin LI. **A concordance correlation coefficient to evaluate reproducibility.** *Biometrics* 1989;45:255–68 CrossRef
34. Altman D. *Practical Statistics for Medical Research*. Chapman & Hall/CRC Texts in Statistical Science. 1991; 396–439
35. Kapeller P, Barber R, Vermeulen RJ, et al; European Task Force of Age-Related White Matter Changes.**Visual rating of age-related white matter changes on magnetic resonance imaging: scale comparison, interrater agreement, and correlations with quantitative measurements.** *Stroke* 2003;34:441–45 CrossRef Medline
36. van den Heuvel DM, ten Dam VH, de Craen AJ, et al; PROSPER Study Group. **Measuring longitudinal white matter changes: comparison of a visual rating scale with a volumetric measurement.** *AJNR Am J Neuroradiol* 2006;27:875–78 Medline
37. Seo H, Badiei Khuzani M, Vasudevan V, et al. **Machine learning techniques for biomedical image segmentation: an overview of technical aspects and introduction to state-of-art applications.** *Med Phys* 2020;47:e148–67 CrossRef Medline
38. Zhang L, Wang X, Yang D, et al. **Generalizing deep learning for medical image segmentation to unseen domains via deep stacked transformation.** *IEEE Trans Med Imaging* 2020;39:2531–40 CrossRef Medline
39. Çiçek Ö, Abdulkadir A, Lienkamp SS, et al. *3D U-Net: Learning Dense Volumetric Segmentation from Sparse Annotation*. Springer-Verlag International Publishing; 2016:424–32
40. Isensee F, Jaeger PF, Kohl SAA, et al. **nnU-Net: a self-configuring method for deep learning-based biomedical image segmentation.** *Nat Methods* 2021;18:203–11 CrossRef Medline
41. Morrison C, Dadar M, Manera AL, et al. **Racial differences in white matter hyperintensity burden in older adults.** *Neurobiol Aging* 2023;122:112–19 CrossRef Medline

Clinical and Radiologic Findings in Children with Anomalous Pontine Cranial Nerves

Karen K. Moeller, Brandon H. Tran, Thierry A.G.M. Huisman, Nilesh K. Desai, Marcia K. Kukreja, Rajan P. Patel, Uma S. Ramaswamy, Carol Liu, and Stephen F. Kralik

ABSTRACT

SUMMARY: We retrospectively reviewed the clinical and radiologic findings in 17 children with an aberrant cisternal cranial nerve 7 (CN7), and found that these patients had additional anomalies involving other pontine cranial nerves (CNs). The hallmark imaging feature identified in all patients was an aberrant cisternal segment of an enlarged-appearing CN7. The abnormal nerve coursed anteriorly toward the Gasserian ganglion, where it fanned out toward the internal auditory canal, Meckel cave, or both. This finding was accompanied by a small cisternal CN5, which often had a lateral bowed appearance. CN5 and CN7 were abnormally close to each other. Meckel's cave appeared widened posteriorly and often was close to or merged with the internal auditory canal. Other abnormalities in the pontine CNs included CN8 deficiency in most children and variable CN6 deficiency. This constellation of findings was most often discovered in children having an MR evaluation for sensorineural hearing loss, and most patients had preserved facial nerve function. In patients with available genetic testing, no pathogenic variants were observed. Interestingly, in 13 children with an available birth history, 9 were notable for maternal or gestational diabetes (69%), suggesting a possible early intrauterine insult to the developing nerves.

ABBREVIATIONS: CN = cranial nerve; IAC = internal auditory canal; OAVS = oculo-auriculo-vertebral spectrum; PTCD = pontine tegmental cap dysplasia; SNHL = sensorineural hearing loss

The 4 pontine cranial nerves (CN 5, 6, 7, and 8) are well-depicted on 3D heavily T2-weighted sequences, often acquired in children being evaluated for hearing loss or other CN symptoms. These nerves have a predictable course and appearance in healthy children. Many abnormalities of these nerves are well-known. For example, children with Duane syndrome, Möbius syndrome, and sensorineural hearing loss (SNHL) can have deficiencies in CNs 6, 7, or 8, respectively. Children with external and middle ear malformations including congenital aural dysplasia, oval window atresia, and Oculo Auriculo Vertebral Spectrum (OAVS) often have an anomalous path of CN7 as it courses through the temporal bone.[1-4] Less well-known is an aberrant course of these nerves in the cisternal segments, previously described in only a few patients.[5-7]

In this series, we describe the clinical and radiologic features in a cohort of children with an unusual pattern of CN dysplasia in which the root entry/exit zone and/or cisternal portions of the pontine CNs appeared aberrant or hypoplastic. This pattern was encountered occasionally in our practice and was believed to have potential clinical and surgical relevance, prompting this clinical report. The anomaly included an aberrant appearance of CN7 and, to a lesser extent, CN5, in the pontocerebellar angle cistern. A deficiency of CN8 was observed in nearly all patients, and CN6 deficiency was variably seen. Additional imaging findings in the inner ear and temporal bone were found in many patients and are also described. Imaging of the brain was assessed for intracranial malformations and to quantitatively compare the size of the pons with that in age-matched controls. The medical record was reviewed for clinical factors including CN symptoms, other morbidities or syndromes, birth history, and genetic testing results.

CASE SERIES

Following institutional review board approval, a retrospective radiology PACS database search was performed from 2005 to 2024. Search keywords included aberrancy or anomaly of CN7. The search was expanded to include OAVS, Goldenhar syndrome (within the OAVS spectrum), and pontine tegmental cap dysplasia (PTCD), following a literature review. Patients without 3D T2-weighted images through the brainstem or without an aberrant cisternal CN7 were excluded. MRIs of the brain and internal auditory canals (IACs) in 17 patients with the aberrant CN7 finding were included, 11 of whom also had CT imaging of the temporal bone.

Received May 14, 2024; accepted after revision July 8.

From the Edward B. Singleton Department of Radiology (K.K.M., B.H.T., T.A.G.M.H., N.K.D., M.K.K., R.P.P., S.F.K.), and Department of Pediatric Otolaryngology (U.S.R., C.L.), Texas Children's Hospital, Baylor College of Medicine, Houston, Texas.

Please address correspondence to Karen K. Moeller, 1850 Old Main St, 2703, Houston TX 77030; e-mail: kkmoelle@texaschildrens.org; @pedsneurorad

http://dx.doi.org/10.3174/ajnr.A8414

Table 1: Demographic and clinical findings in children with anomalous pontine cranial nerves

Clinical Finding	
Age (mean) (range)	4 years; 3 weeks to 17 years
Sex (M/F ratio)	1:16
SNHL	16/17 (94%)
CN6 palsy	2/17 (12%)
CN7 palsy	
Ipsilateral to aberrant CN7	2/23 ears (9%)
Contralateral to aberrant CN7	1/23 ears (4%)
Oculo Auriculo Vertebral Spectrum	2/17 (12%)

Table 2: Radiologic findings in children with anomalous pontine cranial nerves

Finding	
Aberrant cisternal CN7	17 patients
Unilateral	11 patients (65%)
Bilateral	6 patients (35%)
Small CN5 ipsilateral to the aberrant CN7	23/23 ears
CN6 deficiency	7/17 (41%)
Contralateral CN7 deficiency	1/17 (5%)
Cochlear nerve deficiency	16/17 (94%)
Narrow IAC	10/17 (59%)

The electronic medical records were reviewed for clinical signs and symptoms, including CN dysfunction, hearing loss, craniofacial malformations, syndromes, and additional diagnoses. The electronic medical record was also interrogated for birth history and the presence of and/or results of genetic testing.

We evaluated 17 patients (Table 1). The aberrant CN7 finding was bilateral in 6 patients and involved 23 ears in total. The male/female ratio was 1:16. The mean age at diagnosis was 4 years (range, 3 weeks to 17 years). Clinical concern prompting MR imaging was hearing loss in 16 patients (94%) and abducens nerve palsy in 1 patient. Two patients had the diagnosis of OAVS. Evaluation by an otolaryngologist was available in all patients with facial paresis and in 13 (81%) patients with hearing loss. The facial motor function ipsilateral to the aberrant CN7 was intact in 21/23 ears (91%). One patient had a contralateral facial nerve palsy. In all children with hearing loss, profound SNHL in at least 1 ear was recorded at audiology examination. Thirteen patients (76%) had an evaluation by an ophthalmologist, and CN6 palsy was recorded in 2 of these.

Genetic testing, available in the 2 patients with OAVS and in 1 additional patient, was negative for pathogenic variants. In 13 patients with available birth history, findings in 9 (69%) were notable for maternal or gestational diabetes. One of these patients also had caudal regression syndrome.

Imaging

MRIs of the brain with high-resolution imaging through the temporal bone were reviewed by 2 pediatric neuroradiologists. The patients had standard brain and IAC MRI on 1.5T or 3T scanner which included a 3D T2 space sequence. The images were evaluated for the course and appearance of the pontine CNs, along with any additional malformations of the inner ear and brain. The pons was measured in the anterior-posterior, TR, and SI planes and was compared with age-matched controls.[8] The dimension of the mid-IAC was measured in the anterior-posterior plane and designated small if < 3 mm.[9,10] CT imaging, when available, was assessed for the location of the facial nerve canal as well as other abnormalities of the external, middle, and inner ear.

Table 2 summarizes the imaging characteristics. The hallmark imaging pattern was an enlarged-appearing CN7, which had an aberrant anterior course in the pontocerebellar angle cistern, coursing toward the Gasserian ganglion, where it fanned out in the direction of the Meckel cave, the temporal bone, or both (Fig 1*B*, *-D*; Fig 2*A*, *-B*). The anomalous facial nerve exited the anterolateral pons, more rostral than typical and close to CN5. CN5 had a caudally positioned root entry zone, close to CN7 (Fig 3A). CN5 was small or bowed laterally in all patients (Fig 1*A*, *-B*). The finding was bilateral in 6 patients (35%). An additional finding was a widened posterolateral Meckel cave, which was caudally positioned, often close to or merged with the IAC (Figs 1 and 2). The IAC was narrowed on the affected side in 10 patients (59%) (Fig 3*C*). In 2 patients, a narrow, separate canal for CN7 was identified, rostral to a narrow IAC.

Cochlear nerve deficiency was noted in 16/17 patients (94%), ipsilateral to the aberrant nerve in 17 ears and contralateral to the aberrant nerve in 6 ears. Contralateral deficiency of CN5 was discovered in both patients with OAVS. Abducens nerve deficiency was found in 7/17 patients (41%), ipsilateral to the aberrant CN7 in 6 of these (Fig 3*B*). A deficiency of the contralateral CN7 was found in 1 patient.

Malformation of the lateral semicircular canal, characterized by a small or absent bone island, was present in 11 ears, ipsilateral to the aberrant nerve in 8/17 patients (47%). Cochlear hypoplasia was observed in both children with OAVS.

No brain malformations were noted in our series. Measurements of the pons were within the range of normal compared to age-matched controls.

In 11 patients with available CT studies, the images were scrutinized for the facial nerve course and other temporal bone findings. In 6 ears ipsilateral to the nerve aberrancy, the labyrinthine segment of the nerve exited the anterior aspect of the IAC far medial compared to normal. In 5 ears, a parallel canal anterior to the IAC containing CN7 or a portion of the nerve ending in the labyrinthine segment was identified. This did not extend laterally to the cerebellopontine angle cistern, distinguishing it from a duplicated IAC (Fig 4). In 3 ears, the tympanic segment of the facial nerve was contiguous with the greater superficial petrosal nerve, and the nerve proximal to the geniculate ganglion was not identified in the petrous temporal bone. In 1 ear, there was a narrow separate canal for CN7, matching the finding on MRI. Other temporal bone findings included aberrant tympanic and mastoid segments in 7 ears and in both ears of the patient with OAVS who had temporal bone imaging. One child had unilateral external auditory canal atresia along with oval window atresia and ossicular malformations involving both ears. Oval window atresia and malformed ossicles were found in 3 other ears, ipsilateral to the aberrant nerve finding.

DISCUSSION

The CNs develop from cranial neural crest cells and ectodermal placode cells. Cellular interactions between these cell groups are

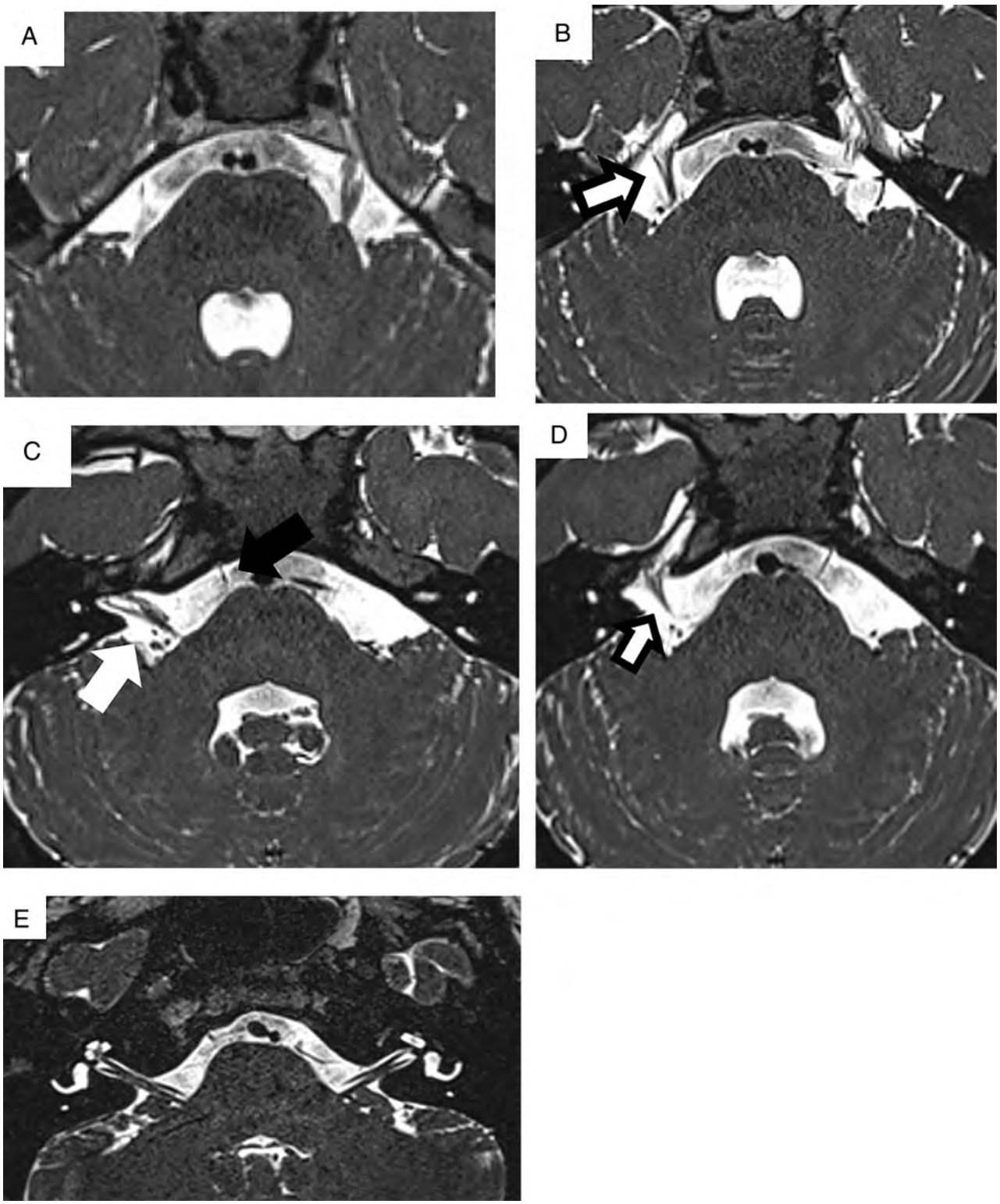

FIG 1. Patient 10 with right anomaly. Axial T2-weighted images of pontine CNs. *A*, normal left CN5. *B*, The right trigeminal nerve (*arrow*) is small compared with the left. It is bowed laterally and has a more caudal root entry zone. *C*, Just inferior to CN 5, a prominent right CN7 (*white arrow*) exits the brainstem at the same level as CN6 (*black arrow*). *D*, There is merging of the Meckel cave with the IAC porus acusticus (*arrow*), and the aberrant nerve fans out toward both compartments. *E*, Normal patient for comparison. Axial image of CN7 and CN8 in cerebellopontine angle cisterns.

important for CN patterning and organization. The pontine cranial nerves, arising from metencephalon, are well-developed and reach their target end organ by 8 weeks' gestation.[11]

CN6 is the simplest of these nerves, functioning as a purely motor nerve. The trigeminal nerve, the first pharyngeal arch nerve, has motor and sensory functions with 3 divisions, each

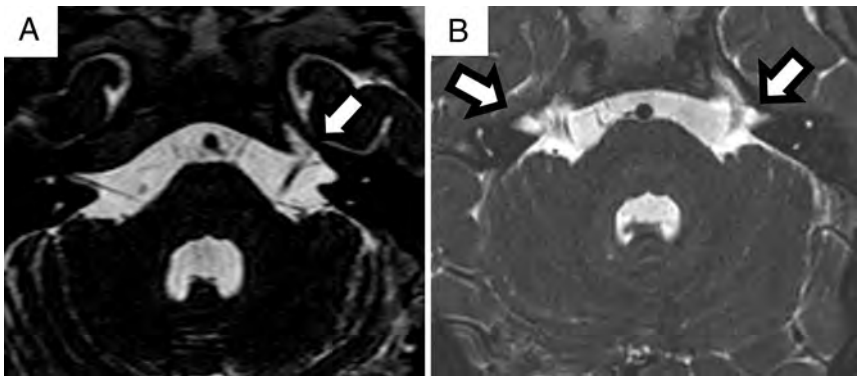

FIG 2. Two different patients with a dysplastic fanned appearance of an aberrant CN7 as it approaches the Meckel cave and IAC (*arrows*). *A*, On the left in patient 3. *B*, Bilateral in patient 9.

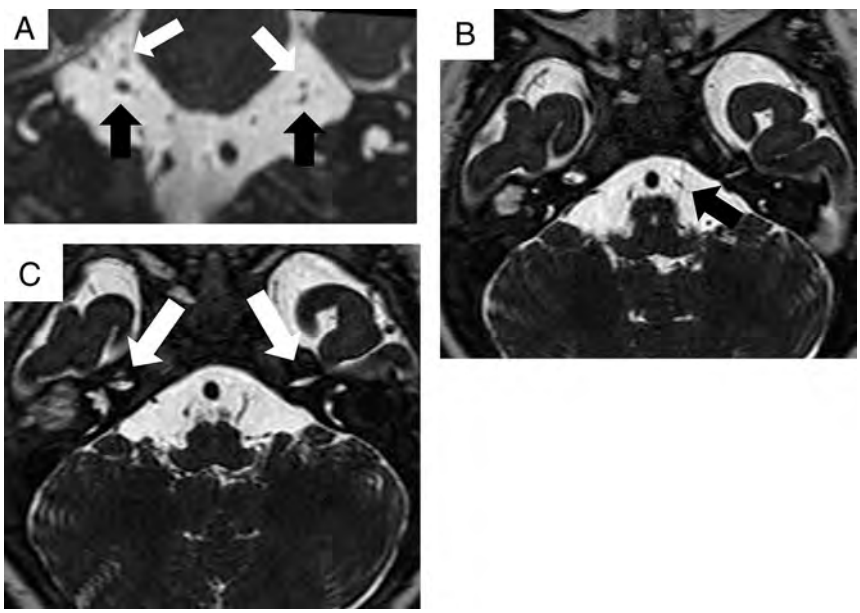

FIG 3. Patient 7 with bilateral findings. *A*, Coronal T2-weighted image. The cisternal trigeminal nerve (*white arrows*) is small compared with CN7 (*black arrows*). These nerves are abnormally close to each other on left. *B*, Axial T2-weighted images. There was a deficiency of CN6 on right (normal on left, *arrow*). C. This patient also has a narrow IAC on both sides, more pronounced on the left (*arrows*).

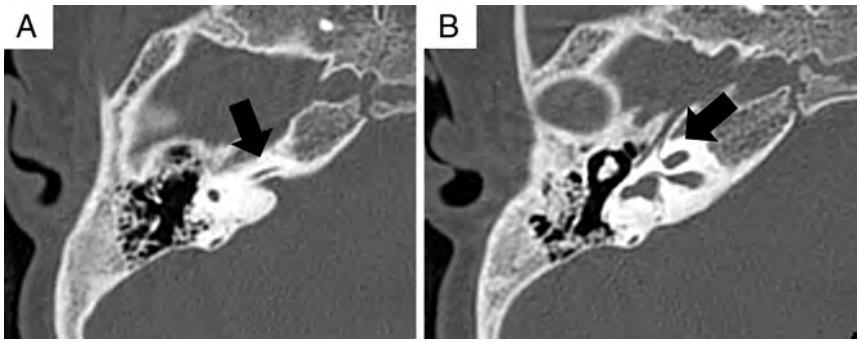

FIG 4. Patient 4. Axial temporal bone CT of the right ear. The aberrant facial nerve canal courses through the petrous bone anterior to IAC to join an anteriorly displaced labyrinthine portion (*arrows*). There was no medial extension to the cerebellopontine angle cistern distinguishing it from a duplicated IAC. The tympanic and mastoid segments had a normal course (not shown).

with intricate branching arising from the Gasserian ganglia. Embryologically, CN7 and CN8 are closely associated with each other and arise from the facioacoustic primordium, which is attached to the metencephalon near the otic vesicle.[12,13] The seventh cranial nerve, the second pharyngeal arch nerve, has motor, sensory, and parasympathetic functions. Its branches have a complicated but predictable course, exiting the lateral pons, traversing the IAC and temporal bone to eventually arrive at their end organ. CN8 has 2 major components and provides special sensory afferents for hearing and balance. Its terminal branches are the latest to develop of all the CNs.[11]

Despite the complex course of the pontine CNs more peripherally, the cisternal course, the segment of the nerve between the brainstem and skull base, is relatively simple and straightforward.

Various congenital abnormalities of pontine CNs are well-described. For example, children with SNHL can have a deficiency of the cochlear nerve, and patients with Duane syndrome may have abducens nerve deficiency. Patients with Möbius syndrome have a deficiency of CN6 and CN7.

An anomalous course of the facial nerve is a well-described congenital abnormality, and its diagnosis affects surgical planning. It typically involves the facial nerve within the temporal bone, lateral to the IAC. It can be encountered as an isolated anomaly in the segment distal to the geniculate ganglion.[3] This finding is also encountered in children with congenital aural dysplasia in which the tympanic and mastoid segments are displaced anteriorly.[2] The tympanic segment can be malpositioned in patients with oval window atresia.[1] An altered course of the canalicular, labyrinthine, and tympanic segments has also been described in patients with inner ear malformations and in children undergoing evaluation for hearing loss.[14-16]

In our series, the hallmark feature was an aberrant appearance of the cisternal segment of CN7. Additionally, CN5 was small, abnormally close to CN7, and often bowed laterally. These findings were accompanied by varying deficiencies in CN6 or CN8 in all patients.

Aberrancy of CN7 in the cisternal segment is less well-known, previously identified in only a few patients.[5-7,13] Giesemann et al[5] showed a pattern similar to that in to our cohort in 6 patients with IAC atresia. This pattern was also illustrated by Manara et al.[6] They described CN anomalies in 29 patients with OAVS, 11 of whom had abnormalities of CN5 or CN7. One of their illustrated cases demonstrates a pattern comparable with ours, which they described as a common origin of CN 5, 7, and 8 from the middle cerebellar peduncle. Wang et al[7] illustrated a case in a 6-year-old child with a duplicated IAC. Finally, a dissimilar pattern of cisternal CN7 aberrancy in patients with Pontine Tegmental Cap Dysplasia (PTCD) was described by Desai et al[13] in association with a duplicated IAC.

In our cohort, 10/17 patients (59%) had IAC narrowing and 2 met the criteria for OAVS. Two patients had a separate facial nerve canal. None of our patients had PTCD.

To our knowledge, our report has the largest cohort describing this anomaly and also captures several patients without IAC atresia, duplicated IAC, or OAVS. We surmise that this anomaly is more prevalent than previously known and is possibly underdiagnosed. We also propose a possible aberrant intertwining of the CN5 and CN7 fascicles early in development. The facial nerve function ipsilateral to the aberrant facial nerve was intact in most patients (91%). Most of our patients had hearing loss, and all but one had a cochlear nerve deficiency. A strong female predominance was seen in this cohort (94%). This is of uncertain significance and may be related to our small sample size. There was no female predilection in the other reported cases with a similar CN anomaly.[5,6,14] Interestingly, maternal or gestational diabetes was found in 69% of patients with an available birth history. The pontine CNs have reached their target end organ by 8 weeks' gestation and are likely vulnerable to teratogenic affects before this. Although gestational diabetes has a recently published association with infant hearing loss, it is otherwise not known to be implicated in CN abnormalities.[17,18]

The strengths of this study include the largest cohort yet described for this specific anomaly. The availability of CT in some of our patients enhanced our understanding of the facial nerve course. Our study also had thorough clinical evaluations, including evaluation by an otolaryngologist and ophthalmologist in most children.

A weakness is the retrospective design of the study. Furthermore, there are no postmortem or surgical findings to confidently distinguish CN5 and CN7 bundles from each other, and assumptions were made on the basis of the expected root entry/exit zone and the rostral/caudal relationship of these nerves with each other. Finally, genetic testing was available in only 3 patients.

Despite these limitations, this clinical report will assist radiologists and other physicians who may encounter a patient with this constellation of findings. It could provide information for further understanding of the patient's clinical symptoms. In addition, this knowledge will arm otolaryngologists with important anatomic aberrations that will aid in treatment and surgical planning.

Genetic evaluation, not available for most of our patients, could be an area for further research. In this regard, Kurosaka et al[19] described a *PTCH1* mutation leading to increased *SHH* signaling and disorganized CN5 and CN7 in a mouse model. An association with maternal or gestational diabetes in a larger cohort could also be an area of further exploration. Other potential areas for study include evaluation of CN nuclei or brainstem pathways with higher Tesla imaging or diffusion tensor imaging.

CONCLUSIONS

In this study, we describe a unique aberrancy in the course of the cisternal segment of CN7, which was accompanied by aberrancies or deficiencies in other ipsilateral or contralateral pontine cranial nerves. In almost all cases, facial nerve function was preserved, and the finding was incidentally discovered in children being imaged for SNHL. Given the unexpected prevalence of maternal or gestational diabetes and the lack of a known pathogenic variant in our series, we hypothesize that this abnormality is related to an early intrauterine insult to the developing nerves.

Disclosure forms provided by the authors are available with the full text and PDF of this article at www.ajnr.org.

REFERENCES

1. Booth TN, Vezina LG, Dubovsky EC, et al. **Imaging and clinical evaluation of isolated atresia of the oval window.** *AJNR Am J Neuroradiol* 2000;21:171–74 Medline
2. Ho ML, Juliano A, Moonis G, et al. **Anatomy and pathology of the facial nerve.** *AJR Am J Roentgenol* 2015;204:W612–19 CrossRef Medline
3. Raghavan P, Mukherjee S, Phillips CD. **Imaging of the facial nerve.** *Neuroimaging Clin N Am* 2009;19:407–25 CrossRef Medline
4. Yu Z, Han D, Gong S, et al. **Facial nerve course in congenital aural atresia–identified by preoperative CT scanning and surgical findings**. *Acta Otolaryngol* 2008;128:1375–80 CrossRef Medline
5. Giesemann AM, Neuburger J, Lanfermann H, et al. **Aberrant course of the intracranial facial nerve in cases of atresia of the internal auditory canal (IAC).** *Neuroradiology* 2011;53:681–87 CrossRef Medline
6. Manara R, Brotto D, Ghiselli S, et al. **Cranial nerve abnormalities in oculo-auriculo-vertebral spectrum.** *AJNR Am J Neuroradiol* 2015;36:1375–80 CrossRef Medline
7. Wang L, Zhang L, Li X, et al. **Duplicated internal auditory canal: high-resolution CT and MRI findings.** *Korean J Radiol* 2019;20:823–29 CrossRef Medline
8. Metwally MI, Basha MA, AbdelHamid GA, et al. **Neuroanatomical MRI study: reference values for the measurements of brainstem, cerebellar vermis, and peduncles.** *Br J Radiol* 2021;94:20201353 CrossRef Medline
9. Erkoç MF, Imamoglu H, Dogan M, et al. **Normative size evaluation of internal auditory canal with magnetic resonance imaging: review of 3786 patients**. *Folia Morphol (Warsz)* 2012;71:217–20 Medline
10. Adunka OF, Roush PA, Teagle HF, et al. **Internal auditory canal morphology in children with cochlear nerve deficiency.** *Otol Neurotol* 2006;27:793–801 CrossRef Medline
11. Smit JA, Jacobs K, Bais B, et al. **A three-dimensional analysis of the development of cranial nerves in human embryos.** *Clin Anat* 2022;35:666–72 CrossRef Medline
12. Jahrsdoerfer RA. **Embryology of the facial nerve.** *Am J Otol* 1988;9:423–26 Medline
13. Desai NK, Young L, Kutz Booth TN, et al. **Pontine tegmental cap dysplasia: the neurotologic perspective.** *Otolaryngol Head Neck Surg* 2011;145:992–98 CrossRef Medline
14. Sennaroğlu L, Tahir E. **A novel classification: anomalous routes of the facial nerve in relation to inner ear malformations**. *Laryngoscope* 2020;130:E696–703 CrossRef Medline
15. Palabiyik FB, Hacikurt K, Yazici Z. **Facial nerve anomalies in paediatric cochlear implant candidates: radiologic evaluation.** *J Laryngol Otol* 2017;131:26–31 CrossRef Medline

16. Glastonbury CM, Fischbein NJ, Harnsberger HR, etal. **Congenital bifurcation of the intratemporal facial nerve.** *AJNR Am J Neuroradiol* 2003;24:1334–37 Medline
17. Gulen Yıldız E, Doluoglu S, Ustun Y, et al. **Comparison of hearing screening outcomes in newborns of gestational diabetic and non-diabetic mothers: a prospective, controlled study**. *J Matern Fetal Neonatal Med* 2022;35:10152–57 CrossRef Medline
18. Wu Y, Liu B, Sun Y, et al. **Association of maternal prepregnancy diabetes and gestational diabetes mellitus with congenital anomalies of the newborn.** *Diabetes Care* 2020;43:2983–90 CrossRef Medline
19. Kurosaka H, Trainor PA, Iulianella A, et al. **Cranial nerve development: cranial nerve development requires co-ordinated Shh and canonical Wnt signaling.** *PLoS One* 2015;10:e0120821 CrossRef Medline

Imaging Transcriptomics of Brain Functional Alterations in MS and Neuromyelitis Optica Spectrum Disorder

Yuna Li, Jun Sun, Zhizheng Zhuo, Min Guo, Yunyun Duan, Xiaolu Xu, Decai Tian, Kuncheng Li, Fuqing Zhou, Haiqing Li, Ningnannan Zhang, Xuemei Han, Fudong Shi, Yongmei Li, Xinghu Zhang, and Yaou Liu

ABSTRACT

BACKGROUND AND PURPOSE: The underlying transcriptomic signatures driving brain functional alterations in MS and neuromyelitis optica spectrum disorder (NMOSD) are still unclear.

MATERIALS AND METHODS: Regional fractional amplitude of low-frequency fluctuation (fALFF) values were obtained and compared among 209 patients with MS, 90 patients with antiaquaporin-4 antibody (AQP4)+ NMOSD, 49 with AQP4− NMOSD, and 228 healthy controls from a discovery cohort. We used partial least squares (PLS) regression to identify the gene transcriptomic signatures associated with disease-related fALFF alterations. The biologic process and cell type–specific signature of the identified PLS genes were explored by enrichment analysis. The correlation between PLS genes and clinical variables was explored. A prospective independent cohort was used to validate the brain fALFF alterations and the repeatability of identified genes.

RESULTS: MS, AQP4+ NMOSD, and AQP4− NMOSD showed decreased fALFF in cognition-related regions and deep gray matter, while NMOSD (both AQP4+ and AQP4−) additionally demonstrated lower fALFF in the visual region. The overlapping PLS1− genes (indicating that the genes were overexpressed as regional fALFF decreased) were enriched in response to regulation of the immune response in all diseases, and the PLS1− genes were specifically enriched in the epigenetics profile in MS, membrane disruption and cell adhesion in AQP4+ NMOSD, and leukocyte activation in AQP4− NMOSD. For the cell type transcriptional signature, microglia and astrocytes accounted for the decreased fALFF. The fALFF-associated PLS1− genes directly correlated with Expanded Disability Status Scale of MS and disease duration across disorders.

CONCLUSIONS: We revealed the functional activity alterations and their underlying shared and specific gene transcriptional signatures in MS, AQP4+ NMOSD, and AQP4− NMOSD.

ABBREVIATIONS: AHBA = Allen Human Brain Atlas; AQP4 = antiaquaporin-4 antibody; EDSS = Expanded Disability Status Scale; fALFF = fractional amplitude of low-frequency fluctuation; FDR = false discovery rate; GO = gene ontology; HC = healthy controls; KEGG = Kyoto Encyclopedia of Genes and Genomes; NMOSD = neuromyelitis optica spectrum disorder; PASTA = Paramedic Acute Stroke Treatment Assessment; pFDR = *P* value with false discovery rate corrected; PLS = partial least squares; rsfMRI = resting-state fMRI

MS and neuromyelitis optica spectrum disorder (NMOSD, including antiaquaporin-4 antibody-positive [AQP4+] and antiaquaporin-4 antibody-negative [AQP4−] subtypes) are recognized as inflammatory demyelination disorders of the CNS,[1,2] with overlapping clinical symptoms but distinct genetic and neuropathophysiological features.[3-5] Brain functional deficits in MS and

Received February 14, 2024; accepted after revision July 17.

From the Department of Radiology (Yuna Li, J.S., Z.Z., M.G., Y.D., X.X., Yaou Liu) and Center for Neurology (D.T., X.Z.), Beijing Tiantan Hospital, Capital Medical University, Beijing, China; Department of Radiology (K.L.), Xuanwu Hospital, Capital Medical University, Beijing, China; Department of Radiology (F.Z.), The First Affiliated Hospital, Nanchang University, Nanchang, Jiangxi Province, China; Department of Radiology (H.L.), Huashan Hospital, Fudan University, Shanghai, China; Department of Radiology and Tianjin Key Laboratory of Functional Imaging (N.Z.) and Department of Neurology (F.S.), Tianjin Neurological Institute, Tianjin Medical University General Hospital, Tianjin, China; Department of Neurology (X.H.), China-Japan Union Hospital of Jilin University, Changchun, China; China National Clinical Research Center for Neurological Diseases (F.S.), Beijing, China; and Department of Radiology (Yongmei Li), The First Affiliated Hospital of Chongqing Medical University, Chongqing, China.

Yuna Li and J. Sun contributed equally to the article.

Yuna Li and Jun Sun are first authors and contributed equally to this work.

Yongmei Li, Huxing Zhang and Yaou Liu are senior authors and contributed equally to this work.

This work was supported by the Ministry of Science and Technology of China-National Key Research Project (NO.2022YFC2009904), National Science Foundation of China (NO.82330057), Beijing Hospital Management Center-Climb Plan (No. DFL20220503), Capital Medical University Young Scholars (Y.L), Capital Medical Science Innovation Center Scientific Research Pioneering Project (NO.CX23YQ06), National Science Foundation of China (NO. 822020840), Young Scientists Program of Beijing Tiantan Hospital, Capital Medical University (NO.YSP202205), and Youth Project of Beijing Natural Science Foundation (NO.7244328).

Please address correspondence to Yaou Liu, MD, PhD, Department of Radiology, Beijing Tiantan Hospital, Capital Medical University, No.119, the West Southern 4th Ring Rd, Fengtai District, Beijing, 100070, China; e-mail: liuyaou@bjtth.org

Indicates article with online supplemental data.

http://dx.doi.org/10.3174/ajnr.A8480

Demographic and clinical characteristics

	HC (n = 228)	MS (n = 209)	AQP4+ NMOSD (n = 90)	AQP4- NMOSD (n = 49)
Age (year), No.	228	209	90	49
Median [IQR]	37 [27–48]	36 [28–45]	46 [35–57] [a,b]	41 [30–53]
Sex, No.	228	209	90	49
Female/male	124/104	135/74[a]	83/7[b]	37/12
Education (year), No.	162	158	44	34
Median [IQR]	16 [15–19]	14 [11–15]	12 [9–14]	14 [11–15]
Disease duration (month), No.	NA	218	86	48
Median [IQR]		19 [5–19]	48 [15–84][b]	12 [8–60]
EDSS, No.	NA	194	84	40
Median [IQR]		2.0 [1.0–3.0]	3.5 [2.5–6.0][b]	3.5 [2.5–6.0]
PASAT, No.	152	65	44	30
Median [IQR]	51.5 [43–57]	42 [35–48][a]	39 [32–46][a]	42 [36.5–53.5][a]
No. of relapses, No.	NA	66	59	35
Median [IQR]		3 [2–4]	3 [2–5]	2 [1–4]

Note:—PASAT indicates Paced Auditory Serial Addition Test; NA, not applicable.
[a] A statistical significance compared with HC.
[b] Statistical significance compared with MS.
[c] Statistical significance compared with AQP4+ NMOSD.
[d] Statistical significance compared with AQP4− NMOSD.

NMOSD are crucial for diagnosis and for predicting physical disability and cognitive impairment.[6,7]

Fractional amplitude of low-frequency fluctuations (fALFF) is a commonly used resting-state fMRI (rsfMRI) metric, which reflects neural activity strength on a voxel-by-voxel basis.[8] Previous studies have demonstrated that both MS and NMOSD showed fALFF alterations in sensorimotor, visual, and cognitive networks, but more decreased fALFF in visual networks was observed in patients with NMOSD.[9-11] These functional alterations have been reported to correspond to varying levels of physical disability and cognitive impairment.[11-13] However, the underlying physiologic substrates of these disease-related fALFF alterations remain unclear.

Imaging transcriptomics analysis provides a promising approach that allows brain-wide spatial analysis of microscopic transcriptome data combined with macroscopic neuroimaging phenotypes.[14,15] Recently, established resources, such as the Allen Human Brain Atlas (AHBA; http://human.brain-map.org), can be used to spatially associate macroscale imaging data with the expression patterns of thousands of genes. Shen et al[16] identified genes related to leukocyte activation and ribose phosphate anabolism in microglia as possible mechanisms underlying functional regional homogeneity abnormalities in patients with MS using the AHBA. However, the genetic mechanisms related to the functional alterations in NMOSD are unknown. An enhanced understanding of these genetic mechanisms in MS and NMOSD would provide insights into the potential drivers of fALFF alterations, elucidate clinical disabilities, and guide targeted therapy.

Therefore, in this study, we first explored the potential genetic mechanisms by spatially correlating brain-wide gene expression with functional alterations in MS and NMOSD. Furthermore, we investigated the associations between brain-wide gene expression and functional alterations across different clinical phenotypes to assess the clinical relevance of fALFF-associated genes.

MATERIALS AND METHODS

Participants

The discovery cohort was retrospectively enrolled from 7 centers, including 209 patients with relapsing-remitting MS, 90 with AQP4+ NMOSD, 49 with AQP4− NMOSD, and 228 healthy controls (HCs). The patients recruited fulfilled the inclusion criteria: 1) 2017 revised McDonald criteria for MS[17] and 2015 International Panel for NMOSD Diagnosis;[18] 2) being in remission, defined as relapse-free for at least 4 weeks and steroid-free within 4 weeks before MRI scans;[19] and 3) AQP4 antibody tested at least twice using a cell-based array with quantitative flow cytometry. Only patients who were seronegative with excluded myelin oligodendrocyte glycoprotein antibody in all tests were considered AQP4− NMOSD. The subjects were excluded on the basis of the following criteria: 1) incomplete clinical information; 2) poor image quality; and 3) a history of other neurologic or neuropsychological diseases. Clinical variables including sex, age, disease duration, Expanded Disability Status Scale (EDSS) scores, Paced Auditory Serial Addition Test scores, and the number of relapses were recorded. The Table lists the demographic and clinical characteristics of the patients and HCs.

The replication cohort prospectively collected in 2 centers included individuals with MS (n = 171), AQP4+ NMOSD (n = 149), and AQP4− NMOSD (n = 32). All participants provided informed consent. This study was approved by the local institutional review board.

MRI Preprocessing and Individual-Level fALFF Calculation

MRI scans were performed on a 3T MR scanner, including T2WI, FLAIR, high-resolution 3D T1WI, and rsfMRI. The MRI scan parameters for each center are summarized in the Online Supplemental Data. All rsfMRI data were processed using the Data Processing Assistant for Resting-State fMRI (DPABI, 4.3, Advanced edition software; http://rfmri.org/dpabi)[20] based on Matlab 2019b (MathWorks). The fALFF in 142 cortical regions defined by the Destrieux cortical atlas (aparc.a2009s.annot in FreeSurfer; http://surfer.nmr.mgh.harvard.edu) was extracted

in MS, AQP4+ NMOSD, and AQP4− NMOSD (Online Supplemental Data).

Brain Gene Expression Data Processing

The human microarray-based gene expression data from AHBA were processed with a toolbox (abagen toolbox, Version 0.1.3; https://github.com/rmarkello/abagen).[21] We used a recently published pipeline to estimate regional gene expression levels across the cortex samples[22] (Online Supplemental Data). After preprocessing and excluding tissue samples from the cerebellum and right hemisphere, we finally obtained the normalized regional expression data for 15,633 genes across 68 regions of the left hemisphere, compiled to form a $68 \times 15{,}633$ regional transcription matrix.

Donor-Level Partial Least Squares Regression Analyses

Partial least squares (PLS) was used to explore genes significantly associated with regional fALFF alterations. The first component of the PLS (PLS1) was the linear combination of gene expression values, which were most strongly correlated with regional fALFF alterations. The statistical significance of the variance explained by PLS1 was tested by permuting the response variables 10,000 times. Bootstrapping was used to estimate the variability of the positive or negative weight of each gene on PLS1 ($|Z|$ scores of >5 and false discovery rate [FDR] adjusted P of .001, either negative, PLS1−, or positive, PLS1+) and rank its contribution to PLS1. Validation analysis is provided in the Online Supplemental Data.

Enrichment Analysis of Brain fALFF Alteration–Associated Genes

The shared and specific PLS1+ and PLS1− gene lists were input into the Metascape Web site (https://www.metascape.org), and Gene Ontology (GO), Kyoto Encyclopedia of Genes and Genomes (KEGG), and Hallmark Gene Sets enrichment analyses were performed to obtain the biologic pathways ($P < .05$, corrected by FDR). Expression-weighted cell-type (including microglia, endothelial cells, oligodendrocytes, astrocytes, excitatory and inhibitory neurons, and oligodendrocyte precursors) enrichment analysis was performed to determine whether the fALFF-related genes had higher expression within a particular cell type than expected by chance.[23] The P value of the number of overlapping genes in each cell type was obtained by a hypergeometric distribution model and corrected by FDR with $P < .05$.

Links of PLS1 Genes and Clinical Indicators

We investigated whether brain fALFF alteration–related genes have an effect on disease clinical variables. The patients with MS, AQP4+ NMOSD, and AQP4− NMOSD were divided into 2 subgroups (subgroups 1 and 2) based on clinical variable values, such as EDSS–associated (EDSS ≤3 versus >3),[24,25] disease duration–associated (disease duration ≤3 years versus >3 years), or relapse number–associated (relapse number = 1 versus >1). An fALFF t map (subgroup 1 versus subgroup 2) was obtained, and the correlation between the fALFF -t value and the normalized Z score of the identified PLS1− and PLS1+ genes was analyzed.

RESULTS

Group Differences in Brain Regional fALFF

MS showed decreased fALFF in the left medial frontal cortex ($t = -3.75$, $P = .0015$), hippocampus ($t = -3.77$, $P = .01$), and thalamus proper ($t = -3.92$, $P = .0087$). Patients with AQP4+ NMOSD showed significantly decreased fALFF in the left thalamus proper ($t = -3.51$, $P = .046$) and occipital pole ($t = -3.55$, $P = .012$). AQP4− NMOSD showed specifically decreased fALFF in extensive associative regions, including the left medial frontal cortex ($t = -4.07$, $P = .0003$), hippocampus ($t = -3.96$, $P = .01$), gyrus rectus ($t = -3.54$, $P = .0095$), medial orbital gyrus ($t = -3.74$, $P = .0003$), inferior temporal gyrus ($t = -3.24$, $P = .045$), and anterior cingulate gyrus ($t = -3.03$, $P = .01$). Decreased fALFF was also involved in visual regions, such as the left fusiform gyrus ($t = -3.69$, $P = .007$) and deep gray matter, such as the left pallidum ($t = -3.69$, $P = .0037$) in patients with AQP4− NMOSD (Fig 1*A* and Online Supplemental Data). The correlation between fALFF alteration and clinical variables, including Paramedic Acute Stroke Treatment Assessment (PASTA, https://www.hra.nhs.uk/planning-and-improving-research/application-summaries/research-summaries/paramedic-acute-stroke-treatment-assessment-pasta/) and EDSS score is presented in the Online Supplemental Data.

Genes Related to fALFF Alteration

The PLS1 component explained a large variance in gene expression across case-control regional fALFF alterations (33.7% for MS, $P_{[\text{permutation}]\ =\ 5000} = .0014$; 28.0% for AQP4+ NMOSD, $P_{(\text{permutation})\ =\ 5000)} = .0076$; 34.3% for AQP4− NMOSD, $P_{(\text{permutation})\ =\ 5000} = .0002$ using a spatial permutation test) (Fig 1*B*).

The PLS1 loading was spatially correlated with the fALFF alteration of MS (Pearson $r = 0.58$, $P_{[\text{permutation}]\ =100{,}000)} < .0001$), AQP4+ NMOSD (Pearson $r = 0.53$, $P_{[\text{permutation}]\ =\ 100{,}000]} < .0001$), and AQP4− NMOSD (Pearson $r = 0.59$, $P_{[\text{permutation}]\ =\ 100{,}000)} < .0001$) (Fig 1*C*). fALFF-PLS1− and fALFF-PLS1+ genes were further defined according to the normalized PLS1 weightings ($Z < -5$ and $Z > 5$, pFDR $_{[\text{bootstrap}\ =\ 100{,}000]} < .0001$). Finally, 1016 fALFF-PLS1− genes and 1419 fALFF-PLS1+ for MS; 694 fALFF-PLS1− genes and 645 fALFF-PLS1+ for AQP4+ NMOSD; 977 fALFF-PLS1− genes and 1114 fALFF-PLS1+ for AQP4− NMOSD were overexpressed (or underexpressed) as regional changes in fALFF increased (or decreased), respectively. The leading PLS1− and PLS1+ genes associated with fALFF are provided in Fig 2*A*. Validation results are present in the Online Supplemental Data.

There were 444 overlapping fALFF-PLS1− genes and 418 overlapping fALFF-PLS1+ genes across MS, AQP4+ NMOSD, and AQP4− NMOSD. The specific fALFF-PLS1+ and fALFF-PLS1− genes of MS, AQP4+ NMOSD, and AQP4− NMOSD are further provided in Fig 2*B*.

Enrichment Pathway Associated with fALFF Alteration

MS, AQP4+ NMOSD, and AQP4− NMOSD showed extensive decreased fALFF; we further emphasized the shared or specific biologic process of the identified fALFF-PLS1− genes (in the discussion section, we will also focus on the underlying mechanism of fALFF-PLS1− genes).

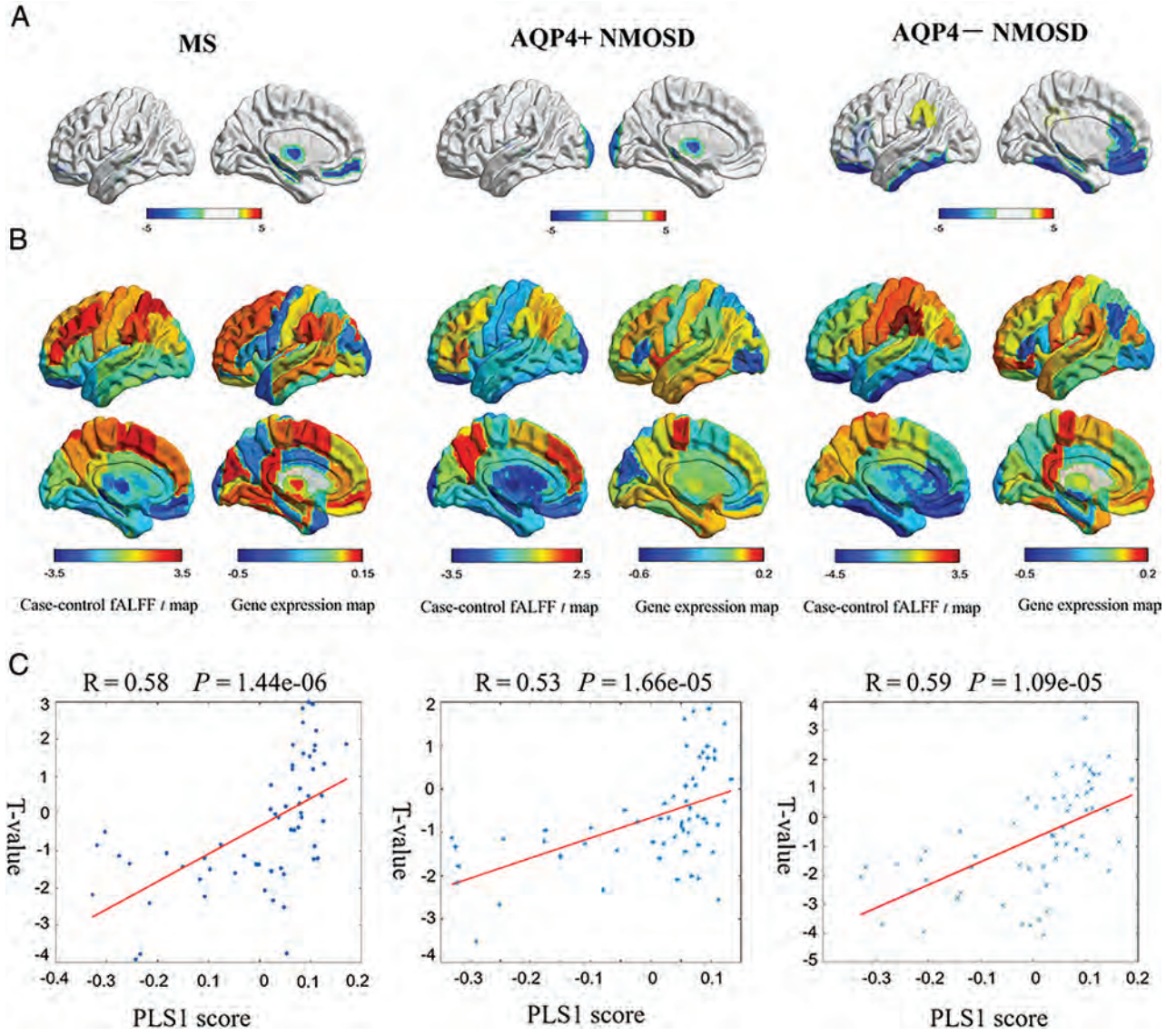

FIG 1. Gene-expression profiles related to fALFF alterations. *A*, Cortical regions show statistically significant fALFF alterations in the MS, AQP4+NMOSD, and AQP4− NMOSD groups compared with the HC group (pFDR < .05). *B*, Regional case–control fALFF *t* map and corresponding weighted gene-expression map of regional PLS1 scores in the left hemisphere of MS (*left*), AQP4+NMOSD (*middle*), and AQP4− NMOSD (*right*). *C*, Scatterplots of regional PLS1 scores and regional changes in fALFF in MS (*left*), AQP4+NMOSD (*middle*), and AQP4− NMOSD (*right*).

The shared fALFF-PLS1− genes across MS, AQP4+ NMOSD, and AQP4− NMOSD were enriched for GO terms, including "regulation of response to biotic stimulus," "pattern recognition receptor signaling pathway," and "regulation of type I infection production," and KEGG pathway of "Notch signaling pathway" and Hallmark genes set of "HALLMARK INTERFERON GAMMA RESPONSE" (Fig 3*A*).

The specific MS-PLS1− genes enriched for GO terms included "chromatin binding," "ATP-dependent chromatin remodeller activity," and "promoter-specific chromatin binding" (Fig 3*B*). The specific AQP4+ NMOSD-PLS1− genes enriched for GO terms included "mitotic nuclear membrane reassembly," "positive regulation of cell adhesion," and "endothelial cell migration" (Fig 3*C*). The specific AQP4− NMOSD-PLS1− genes were enriched for GO terms, including "cell activation," "leukocyte activation," and "regulation of B-cell proliferation" (Fig 3*D*). The enrichment analysis of shared and specific fALFF-PLS1+ genes across MS, AQP4+ NMOSD, and AQP4-NMOSD is provided in the Online Supplemental Data.

Canonical Cell Type Associated with fALFF Alteration

Most of fALFF-PLS1− genes across MS, AQP4+ NMOSD, and AQP4− NMOSD were enriched in astrocytes and microglia (all pFDR < .05 using the hypergeometric test, Fig 4*A*), while fALFF-PLS1+ genes were enriched in both excitatory and inhibitory neurons (all pFDR < .05 using the hypergeometric test, Fig 4*B* and Online Supplemental Data). Furthermore, enrichment analyses of identified fALFF-associated genes for each canonical cell type revealed similar biologic pathways across disorders. Specifically, fALFF-PLS1− genes enriched in microglia are relevant to the immune response, while the genes enriched in astrocytes are relevant to metabolic regulation. fALFF-PLS1+ genes enriched in neurons are relevant to the process of synaptic transmission (Online Supplemental Data).

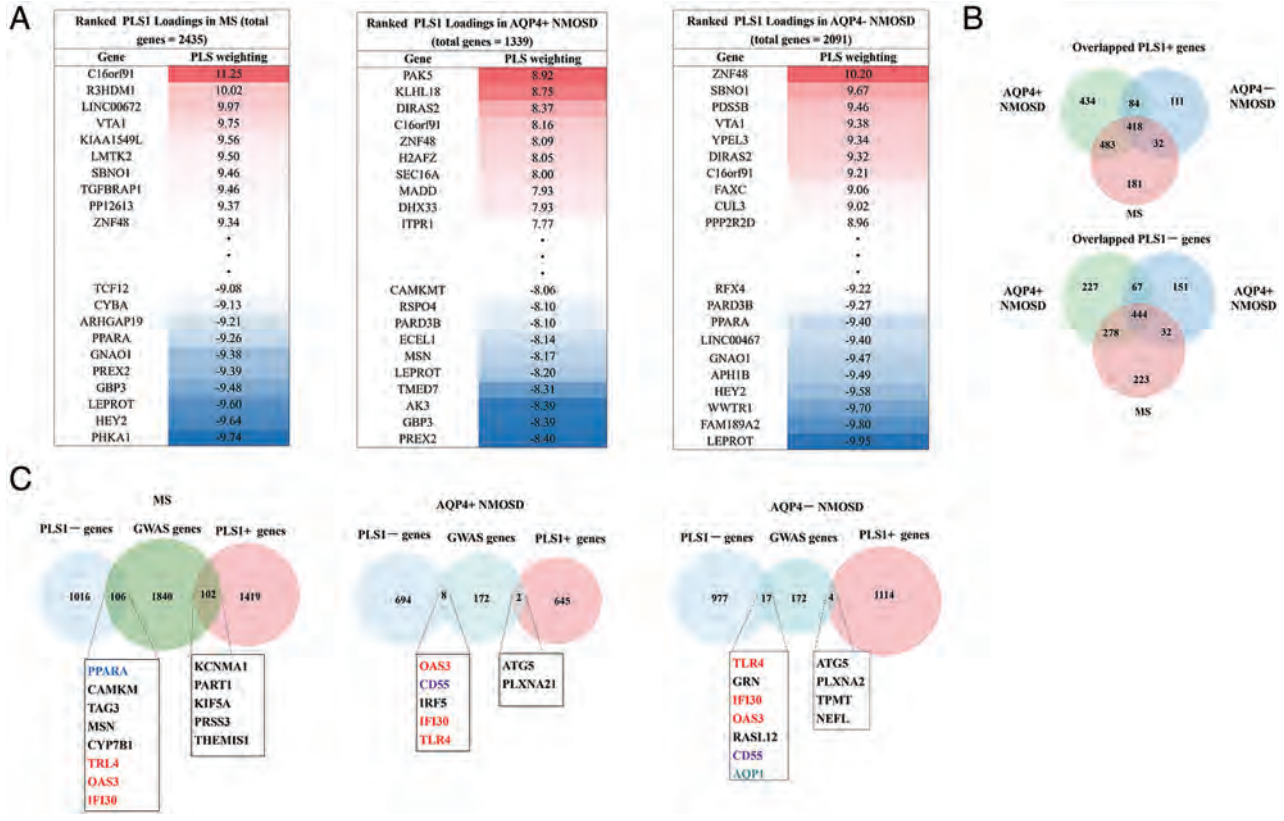

FIG 2. Ranked PLS1 loading and overlapping genes. *A*, Identified leading fALFF-PLS1 gene (both PLS1+ genes, $Z \leq 5$ and PLS−genes, $Z > 5$) listed using PLS regression for MS, AQP4+NMOSD, and AQP4− NMOSD. *B*, The number of overlapping PLS1+ and PLS1− genes among MS, AQP4+NMOSD, and AQP4− NMOSD genes. *C*, Overlapping genes of identified fALFF-PLS1 genes of MS, AQP4+NMOSD, and AQP4− NMOSD with the disease genome-wide association studies gene database. GWAS indicates genome-wide association study.

Links of fALFF-Associated PLS1 Weighted Genes and Clinical Variables

In MS, PLS1− and PLS1+ genes were negatively and positively correlated with the EDSS (mean value = −0.18 for PLS1− genes, 0.18 for PLS+ genes) and disease duration (mean value = −0.17, 0.20) and had no obvious correlation with the number of relapses (mean value = −0.020, −0.0053). In AQP4+ NMOSD, PLS1− and PLS1+ genes were positively and negatively correlated with disease duration (mean value = −0.19, 0.21) and had no obvious correlation with EDSS (mean value = 0.041, 0.028) and the number of relapses (mean value = −0.035, 0.053). In AQP4− NMOSD, PLS− and PLS+ genes positively and negatively correlated with disease duration (mean value = −0.077, 0.15) and had no obvious correlation with the EDSS (mean value = −0.040, −0.041) and number of relapses (mean value= −0.067, 0.045) (Fig 5).

DISCUSSION

MS, AQP4+ NMOSD, and AQP4− NMOSD showed decreased fALFF in the associative cortex and deep gray matter, while NMOSD (both AQP4+ and AQP4−) additionally demonstrated lower fALFF in the visual region. Gene transcriptional signatures associated with fALFF alterations were explored by combining AHBA. We observed that MS, AQP4+ NMOSD, and AQP4− NMOSD fALFF-related PLS− genes: 1) shared a biologic process response to regulation of immune response but were specifically enriched in epigenetics profile in MS, membrane disruption and cell adhesion in AQP4+ NMOSD, and leukocyte activation in AQP4− NMOSD; 2) were associated with a glial immune response and astrocytic metabolic regulation; and 3) were directly associated with EDSS of MS and disease duration across disorders. These results illuminated the microscopic genetic molecular mechanisms underlying the macroscopic fALFF alterations in MS and NMOSD, enhancing our understanding of the pathologic similarities and differences among these neuroinflammatory diseases. Furthermore, the fALFF-associated genes might serve as potential regulatory targets for improving clinical manifestations.

Regional fALFF Alterations in MS, AQP4+NMOSD, and AQP4- NMOSD

Decreased fALFF in patients with MS involved the left hippocampus and thalamus proper, as consistently reported in previous studies.[6,26] MS and AQP4+ NMOSD both showed significantly decreased fALFF in the thalamus proper, suggesting that the thalamus may be collectively highlighted in the pathogenesis of both MS and AQP4+ NMOSD. Notably, fALFF shows a positive correlation with PASTA in patients with MS, but a negative correlation with PASTA in patients with AQP4+ NMOSD. This finding suggests that decreased fALFF in the thalamus may impair cognitive ability in MS, while there may be a harmful compensatory activation in the thalamus for the cognitive ability of patients with AQP4+ NMOSD. The differential involvement of the

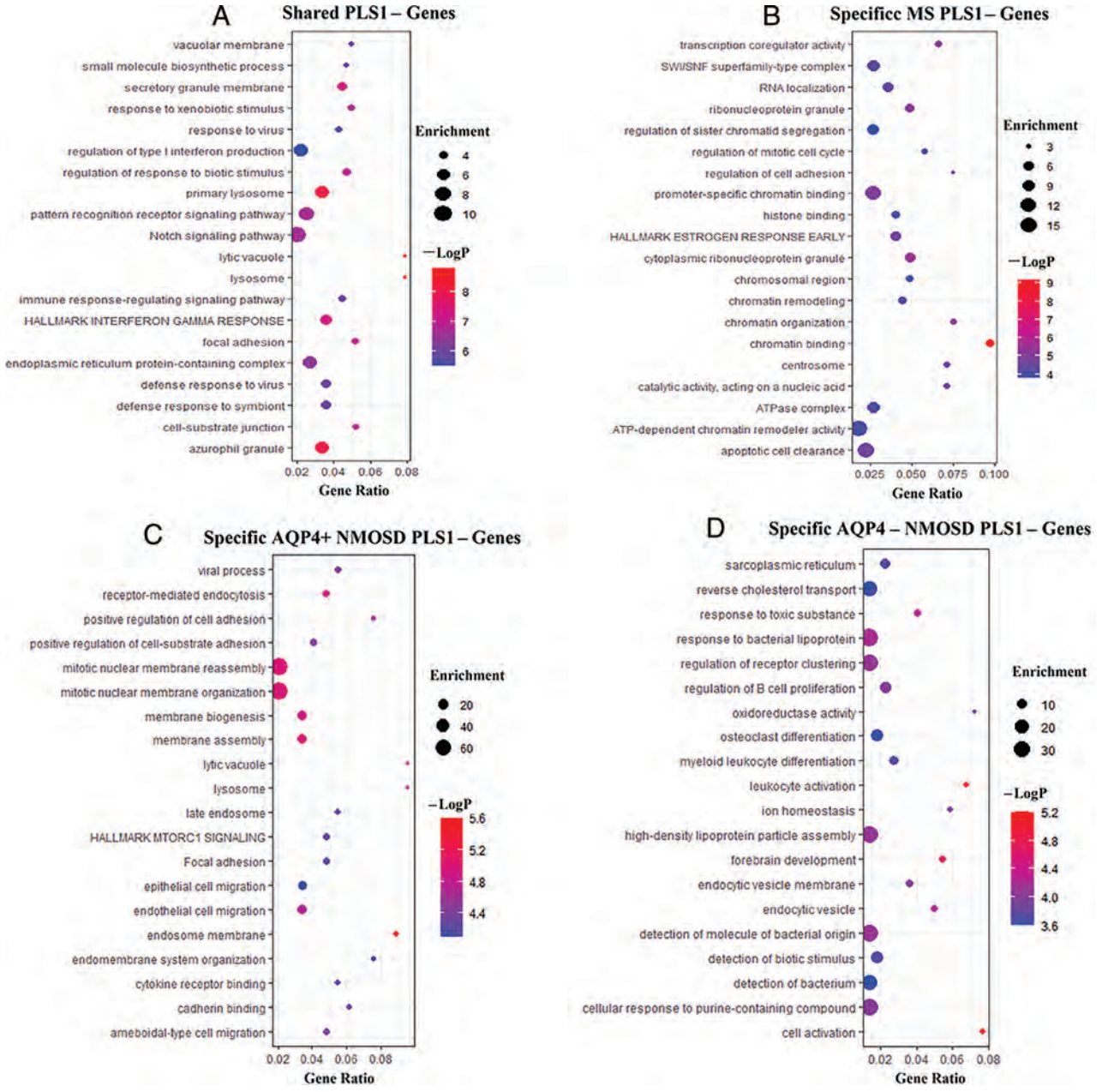

FIG 3. GO/KEGG/hallmark gene set enrichment analysis of fALFF-PLS1− genes. *A*, GO/KEGG/hallmark gene set enrichment analysis of shared fALFF-PLS1− genes across MS, AQP4+NMOSD, and AQP4-NMOSD. *B*, GO/KEGG/hallmark gene set enrichment analysis of specific fALFF-PLS1− genes of MS. *C*, Same as *B*, but specific fALFF-PLS1− genes for AQP4+NMOSD. *D*, Same as *B*, but specific fALFF-PLS1− genes for AQP4− NMOSD. −logP Indicates the logarithm of the *P* value.

thalamus between MS and AQP4+ NMOSD has been reported in a multimodal study of the thalamus.[6] One intriguing aspect of our results is that the thalamus was little affected in AQP4− NMOSD. A disease-specific pattern in the thalamus may indicate a disassociation between AQP4− NMOSD and AQP4+ NMOSD. We speculate that the different injury mechanisms for the 2 subtypes of NMOSD may be attributed to the expression of different isoforms of AQP. AQP4 has been found diffusely in the dorsal thalamus, and AQP4- immunoglobulin G may significantly accelerate neurotoxicity by destroying the BBB of the thalamic region.[27] Additionally, decreased fALFF of the visual region was observed in participants with AQP4+ NMOSD and AQP4− NMOSD, supporting the more severe visual impairment in patients with NMOSD than in those with MS.[11]

The Shared Biologic Process across MS, AQP4 + NMOSD, and AQP4− NMOSD

MS, AQP4+ NMOSD, and AQP4− NMOSD shared biologic processes that respond to immune regulation. Interferon gamma is proinflammatory and produced by T-helper 1 cells, particularly the most potent stimuli for initiating inflammatory mediators.[28] Interferon gamma–secreting cells appear in the CNS shortly before the onset of clinical signs in the experimental autoimmune encephalomyelitis (EAE) model.[29] The Notch signaling pathway

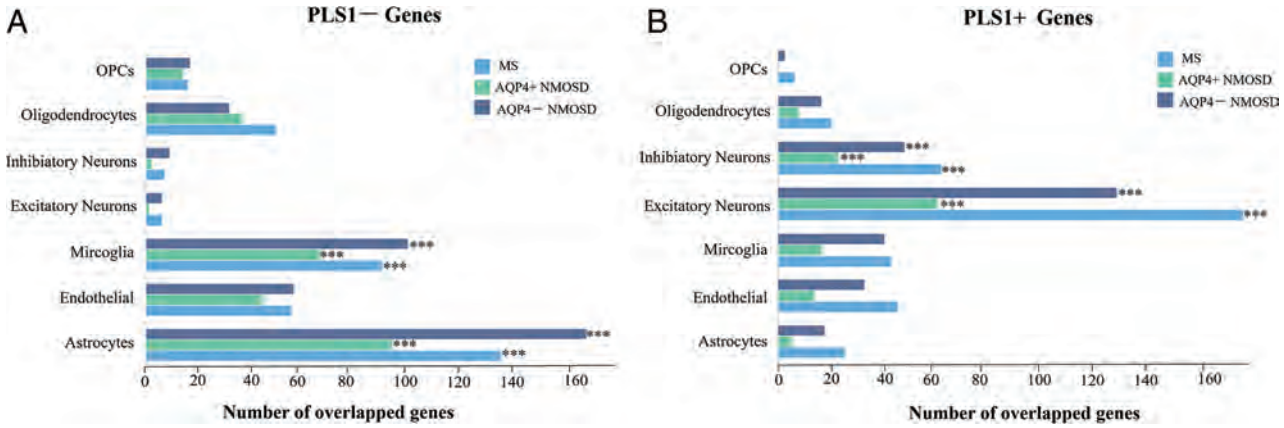

FIG 4. Cell type–specific expression of fALFF alteration–associated genes. *A*, Overlapping genes between the PLS1− gene list and each cell type–specific gene in MS, AQP4+NMOSD, and AQP4−NMOSD. *B*, Same as *A*, but for the PLS1+ gene list in MS, AQP4+NMOSD, and AQP4−NMOSD. OPCs indicate oligodendrocyte precursors.

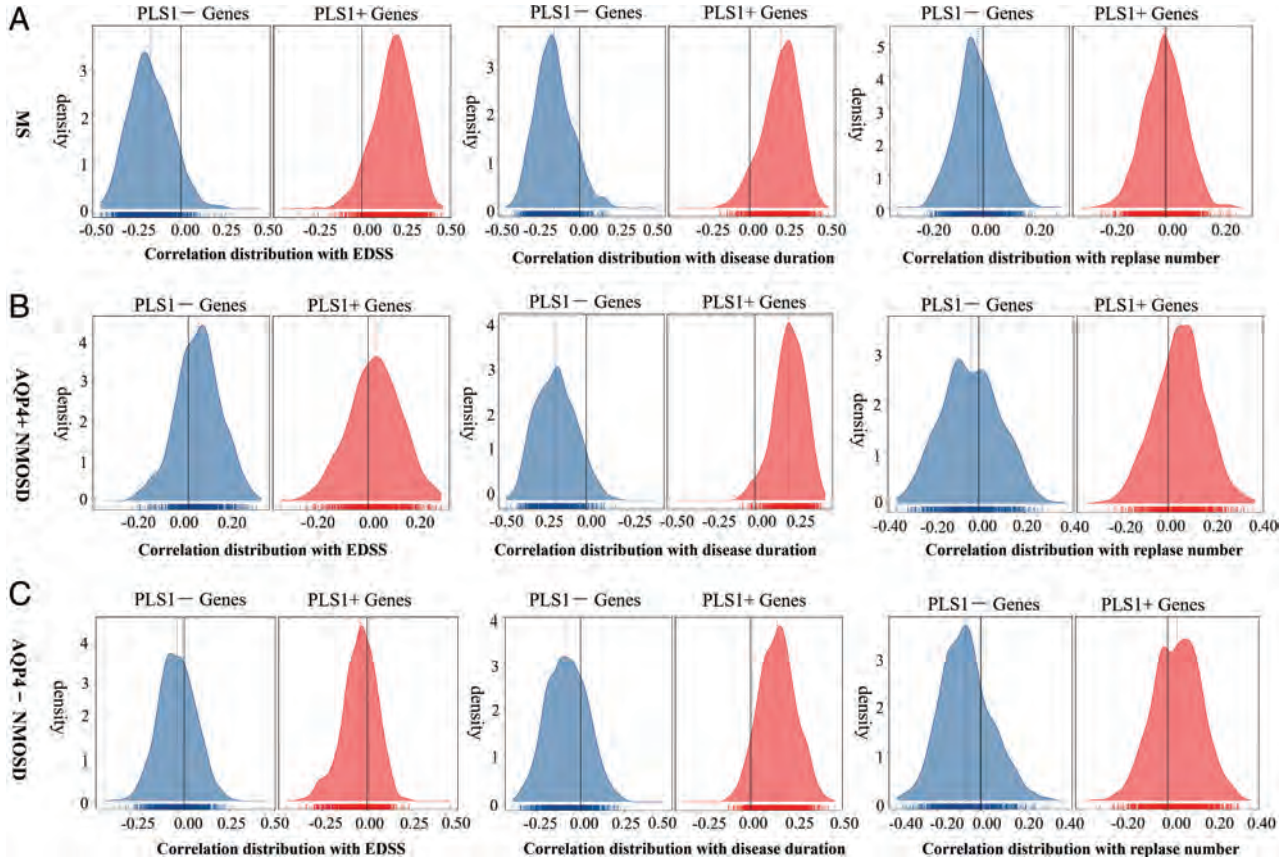

FIG 5. The correlation between fALFF alteration–related genes and clinical variables. The correlation distributions between PLS1− (blue) and PLS1+ genes (red) and clinical indicators, such as EDSS (≤3 versus >3), disease duration (−3 years versus >3 years), and number of relapses (= 1 versus >1) in MS (*A*), AQP4+NMOSD (*B*), and AQP4−NMOSD (*C*).

has been shown to regulate the development and function of both T-helper cells and oligodendrocytes in MS.[30,31] We inferred that the involved immune response and the proinflammatory might cause neurologic dysfunction, as reflected by regionally decreased fALFF in patients with MS and NMOSD. Minter et al[32] inhibited Notch signaling in an experimental EAE model, resulting in a notable decrease in clinical disease and a reduction in T-helper 1–associated cytokines.[32] Our results are complementary to previous studies.[32] The shared Notch signaling pathway may suggest potential therapeutic implications not only in MS but also in both AQP4+ and AQP4− NMOSD.

The Specific Biologic Processes of MS, AQP4+ NMOSD, and AQP4− NMOSD

The different PLS− genes underlying fALFF alterations provided insight into the high heterogeneity across MS, AQP4+ NMOSD,

and AQP4− NMOSD. The identified specific MS-PLS1− genes were significantly enriched for the epigenetics (chromatin modification) profile. Studies have implied that epigenetic modifiers coordinate with transcriptional regulators or signaling pathways, which expand the regulatory network of myelination.[33] The thalamus is typically more densely myelinated and serves as a key brain hub with extensive afferent and efferent connections in subcortical and cortical areas.[34] Under physiologic conditions, myelin functions in axonal ensheathment and supports axonal integrity.[35] Studies have shown that apoptotic neurons and transected neurites are significantly increased in demyelinated compared with myelinated cortex.[36] The observed decreased fALFF in the thalamus in MS may due to local inflammatory demyelination and changes secondary to axonal transection.

The unique AQP4+ NMOSD-PLS1− genes were significantly enriched in membrane disruption and cell adhesion. AQP4+ NMOSD exhibits serious BBB disruption because AQP4-immunoglobulin G plays a direct role in damaging astrocytes.[27] The destruction of the BBB may trigger neurotoxicity, suggesting that the reduction in fALFF within the thalamus is primarily due to pathogenic factors in the CSF affecting neurons as a result of BBB damage in AQP4+ NMOSD. Generally, the neuropathological features of decreased fALFF in the thalamus in NMOSD differ from those in MS. Pathological studies have shown that certain features, such as lymphocyte infiltration, complement deposition, and BBB disruption, are usually absent in chronic postmortem MS samples.[37] These findings provide reasonable evidence supporting our results.

The unique AQP4− NMOSD-PLS1− genes, which code for leukocyte activation and regulation of B-cell proliferation, indicate that AQP4− NMOSD is primarily a B-cell-driven disease.[38] We inferred that the inflammatory brain state caused by widespread immune activation could lead to decreased neural activity in extensive associative and visual regions. Additionally, although specific autoantibodies have still not been confirmed in AQP4− NMOSD, the specific fALFF-PLS− gene *AQP1* may provide a clue.

Cellular Characterization of MS-, AQP4+ NMOSD-, and AQP4− NMOSD–Related Genes

Astrocytes and microglia were the most significant proportion in fALFF-PLS− cell-type genes in MS and NMOSD (both AQP4+ NMOSD and AQP4− NMOSD), suggesting that they have central roles in the disease process. The activated microglial immune response plays a crucial role in the disease process of MS and NMOSD by initiating inflammation and aggravating neuronal damage.[39] Additionally, synaptic stripping has been classically linked to microglial function, and the overactivation of microglia might result in severe synapse loss, as we observed in MS and NMOSD.[35] It is well-known that brain function primarily depends on synaptic function.

Astrocytic metabolic regulation disorder suggests the increased susceptibility of astrocytes to damage. Neural activity depends on the structure and function of the neuro-glio-vascular unit, and astrocytes can signal to endothelial cells to increase local blood flow to adapt to energy demand.[40] The regulatory mechanism of CBF is the crucial neural basis for available detected fALFF signals. The demyelinated core of MS lesions consists of reactive astrogliosis, which builds sclerotic tissue thought to damage the neuro-glio-vascular unit and inhibit neural activity.[41] In NMOSD, astrocyte lysis and fibrous gliosis also interfere with the function of the neuro-glio-vascular unit.[42] These findings link fALFF-related putative genetic molecular perturbations with cell vulnerability and highlight the important role of microglia and astrocytes.

The Correlation between fALFF Alteration–Related Genes and Clinical Variables

In the current study, we observed that fALFF alteration–associated PLS1− genes were negatively correlated with EDSS-associated fALFF alterations in MS, indicating that the underlying genes responsible for decreased fALFF in MS may further clinically translate into more severe physical disability. However, this correlation was not observed in AQP4+ NMOSD and AQP4− NMOSD. These findings indicate that targeting the genes underlying decreased fALFF in MS might improve physical ability in patients, though such modulation may be less effective in NMOSD.

Regional fALFF alteration–associated PLS1− genes have a significantly negative correlation with disease duration but not relapse number–associated fALFF alterations across MS, AQP4+ NMOSD, and AQP4− NMOSD. Although NMOSD has a rapid onset and MS is a chronic demyelinating disease,[43] irreversible damage to neural activity occurs with prolonged disease duration. This outcome suggests that therapeutic strategies targeting these underlying genetic factors may be effective in the early stages of the diseases.

Limitations

The current study should be interpreted in light of several limitations. First, because fALFF is an indirect reflection of neural activity, the significant contribution from vascular signals should be considered carefully. Second, only one-half of the fALFF-associated genes had good repeatability in the retrospective and prospective cohorts. We inferred that balancing the sample size of different multicenters is warranted to validate our findings. Third, we observed that correlation between genes and fALFF alterations does not directly reveal causal mechanisms, because the AHBA gene data were derived from postmortem measurements of a small sample.[44] Further biologic validations of the identified genes are needed to confirm our current results. Finally, the regional gene expression may be influenced by MS and the use of disease-modifying treatments. However, due to the evaluation of an atlas-based distribution of gene expression obtained from HC, these influences cannot be explored exactly.

CONCLUSIONS

Collectively, we clarified the genetic molecular mechanisms underlying the macroscopic fALFF alterations in MS and NMOSD. The underlying shared and specific gene transcriptional signatures driving the brain functional alterations in MS, AQP4+, and AQP4− NMOSD enhanced our understanding of the pathologic similarity and differences of these neuroinflammatory diseases. Genes associated with fALFF alterations were further clinically relevant and may serve as potential regulatory targets for improving clinical manifestations.

Disclosure forms provided by the authors are available with the full text and PDF of this article at www.ajnr.org.

REFERENCES

1. Wingerchuk DM, Lennon VA, Lucchinetti CF, et al. **The spectrum of neuromyelitis optica.** *Lancet Neurol* 2007;6:805–15 CrossRef Medline
2. Katz Sand I. **Classification, diagnosis, and differential diagnosis of multiple sclerosis.** *Curr Opin Neurol* 2015;28:193–205 CrossRef Medline
3. Patsopoulos NA, Baranzini SE, Santaniello A, et al; International Multiple Sclerosis Genetics Consortium. **Multiple sclerosis genomic map implicates peripheral immune cells and microglia in susceptibility.** *Science* 2019;365:eaav7188 CrossRef
4. Satoh J, Obayashi S, Misawa T, et al. **Neuromyelitis optica/Devic's disease: gene expression profiling of brain lesions**. *Neuropathology* 2008;28:561–76 CrossRef Medline
5. Estrada K, Whelan CW, Zhao F, et al. **A whole-genome sequence study identifies genetic risk factors for neuromyelitis optica.** *Nat Commun* 2018;9:1929 CrossRef Medline
6. Liu Y, Duan Y, Huang J, et al. **Multimodal quantitative MR imaging of the thalamus in multiple sclerosis and neuromyelitis optica.** *Radiology* 2015;277:784–92 CrossRef Medline
7. Rocca MA, Agosta F, Mezzapesa DM, et al. **A functional MRI study of movement-associated cortical changes in patients with Devic's neuromyelitis optica**. *Neuroimage* 2004;21:1061–68 CrossRef Medline
8. Zou QH, Zhu CZ, Yang Y, et al. **An improved approach to detection of amplitude of low-frequency fluctuation (ALFF) for resting-state fMRI: fractional ALFF.** *J Neurosci Methods* 2008;172:137–41 CrossRef Medline
9. Du XF, Liu J, Hua QF, et al. **Relapsing-remitting multiple sclerosis is associated with regional brain activity deficits in motor- and cognitive-related brain areas.** *Front Neurol* 2019;10:1136 CrossRef Medline
10. Liang P, Liu Y, Jia X, et al. **Regional homogeneity changes in patients with neuromyelitis optica revealed by resting-state functional MRI.** *Clin Neurophysiol* 2011;122:121–27 CrossRef Medline
11. Finke C, Zimmermann H, Pache F, et al. **Association of visual impairment in neuromyelitis optica spectrum disorder with visual network reorganization.** *JAMA Neurol* 2018;75:296–303 CrossRef Medline
12. Liu Y, Liang P, Duan Y, et al. **Brain plasticity in relapsing-remitting multiple sclerosis: evidence from resting-state fMRI.** *J Neurol Sci* 2011;304:127–31 CrossRef Medline
13. Dobryakova E, Hafiz R, Iosipchuk O, et al. **ALFF response interaction with learning during feedback in individuals with multiple sclerosis.** *Mult Scler Relat Disord* 2023;70:104510 CrossRef Medline
14. Fornito A, Arnatkevičiūtė A, Fulcher BD. **Bridging the gap between connectome and transcriptome**. *Trends Cogn Sci* 2019;23:34–50 CrossRef Medline
15. Richiardi J, Altmann A, Milazzo AC, et al; IMAGEN Consortium. **BRAIN NETWORKS: correlated gene expression supports synchronous activity in brain networks.** *Science* 2015;348:1241–44 CrossRef Medline
16. Shen J, Yang B, Xie Z, et al. **Cell-type-specific gene modules related to the regional homogeneity of spontaneous brain activity and their associations with common brain disorders.** *Front Neurosci* 2021;15:639527 CrossRef Medline
17. Thompson AJ, Banwell BL, Barkhof F, et al. **Diagnosis of multiple sclerosis: 2017 revisions of the McDonald criteria.** *Lancet Neurol* 2018;17:162–73 CrossRef Medline
18. Wingerchuk DM, Banwell B, Bennett JL, et al; International Panel for NMO Diagnosis. **International consensus diagnostic criteria for neuromyelitis optica spectrum disorders.** *Neurology* 2015;85:177–89 CrossRef Medline
19. Duan Y, Zhuo Z, Li H, et al. **Brain structural alterations in MOG antibody diseases: a comparative study with AQP4 seropositive NMOSD and MS.** *J Neurol Neurosurg Psychiatry* 2021;92:709–16 CrossRef Medline
20. Yan CG, Wang XD, Zuo XN, et al. **DPABI: data processing and analysis for (resting-state) brain imaging.** *Neuroinformatics* 2016;14:339–51 CrossRef Medline
21. Hawrylycz MJ, Lein ES, Guillozet-Bongaarts AL, et al. **An anatomically comprehensive atlas of the adult human brain transcriptome.** *Nature* 2012;489:391–99 CrossRef Medline
22. van der Poel M, Ulas T, Mizee MR, et al. **Transcriptional profiling of human microglia reveals grey-white matter heterogeneity and multiple sclerosis-associated changes.** *Nat Commun* 2019;10:1139 CrossRef Medline
23. Martins D, Dipasquale O, Davies K, et al. **Transcriptomic and cellular decoding of functional brain connectivity changes reveal regional brain vulnerability to pro- and anti-inflammatory therapies.** *Brain Behav Immun* 2022;102:312–23 CrossRef Medline
24. Kister I, Chamot E, Cutter G, et al; MSBase Investigators. **Increasing age at disability milestones among MS patients in the MSBase Registry.** *J Neurol Sci* 2012;318:94–99 CrossRef Medline
25. Kurtzke JF. **Rating neurologic impairment in multiple sclerosis: an expanded disability status scale (EDSS).** *Neurology* 1983;33:1444–52 CrossRef Medline
26. Di Filippo M, Portaccio E, Mancini A, et al. **Multiple sclerosis and cognition: synaptic failure and network dysfunction.** *Nat Rev Neurosci* 2018;19:599–609 CrossRef Medline
27. Dasdelen D, Mogulkoc R, Baltaci AK. **Aquaporins and roles in brain health and brain injury.** *Mini Rev Med Chem* 2020;20:498–512 CrossRef Medline
28. Jansen M, Reinhard JF Jr. **Interferon response heterogeneity: activation of a pro-inflammatory response by interferon alpha and beta: a possible basis for diverse responses to interferon beta in MS.** *J Leukoc Biol* 1999;65:439–43 CrossRef Medline
29. Olsson T. **Cytokines in neuroinflammatory disease: role of myelin autoreactive T cell production of interferon-gamma.** *J Neuroimmunol* 1992;40:211–18 CrossRef Medline
30. Bassil R, Orent W, Elyaman W. **Notch signaling and T-helper cells in EAE/MS.** *Clin Dev Immunol* 2013;2013:570731 CrossRef Medline
31. Shang Y, Smith S, Hu X. **Role of Notch signaling in regulating innate immunity and inflammation in health and disease.** *Protein Cell* 2016;7:159–74 CrossRef Medline
32. Minter LM, Turley DM, Das P, et al. **Inhibitors of gamma-secretase block in vivo and in vitro T helper type 1 polarization by preventing Notch upregulation of Tbx21.** *Nat Immunol* 2005;6(7):680–8 Medline
33. Castro K, Casaccia P. **Epigenetic modifications in brain and immune cells of multiple sclerosis patients.** *Mult Scler* 2018;24:69–74 CrossRef Medline
34. Kipp M, Wagenknecht N, Beyer C, et al. **Thalamus pathology in multiple sclerosis: from biology to clinical application.** *Cell Mol Life Sci* 2015;72:1127–47 CrossRef Medline
35. Friese MA, Schattling B, Fugger L. **Mechanisms of neurodegeneration and axonal dysfunction in multiple sclerosis.** *Nat Rev Neurol* 2014;10:225–38 CrossRef Medline
36. Peterson JW, Bo L, Mork S, et al. **Transected neurites, apoptotic neurons, and reduced inflammation in cortical multiple sclerosis lesions.** *Ann Neurol* 2001;50:389–400 CrossRef Medline
37. Minagar A, Barnett MH, Benedict RH, et al. **The thalamus and multiple sclerosis: modern views on pathologic, imaging, and clinical aspects.** *Neurology* 2013;80:210–19 CrossRef Medline
38. Kinzel S, Weber MS. **The role of peripheral CNS-directed antibodies in promoting inflammatory CNS demyelination.** *Brain Sci* 2017;7:70 CrossRef Medline
39. Schirmer L, Schafer DP, Bartels T, et al. **Diversity and function of glial cell types in multiple sclerosis.** *Trends Immunol* 2021;42:228–47 CrossRef Medline
40. Wardlaw JM, Smith C, Dichgans M. **Small vessel disease: mechanisms and clinical implications.** *Lancet Neurol* 2019;18:684–96 CrossRef Medline
41. Thompson AJ, Baranzini SE, Geurts J, et al. **Multiple sclerosis.** *Lancet* 2018;391:1622–36 CrossRef Medline
42. Tradtrantip L, Jin BJ, Yao X, et al. **Aquaporin-targeted therapeutics: state-of-the-field.** *Adv Exp Med Biol* 2017;969:239–50 CrossRef Medline
43. Fujihara K. **Neuromyelitis optica spectrum disorders: still evolving and broadening.** *Curr Opin Neurol* 2019;32:385–94 CrossRef Medline
44. Arnatkeviciute A, Markello RD, Fulcher BD, et al. **Toward best practices for imaging transcriptomics of the human brain.** *Biol Psychiatry* 2023;93:391–404 CrossRef Medline

Macro- and Microstructural White Matter Differences in Neurologic Postacute Sequelae of SARS-CoV-2 Infection

Erin E. O'Connor, Rosangela Salerno-Goncalves, Nikita Rednam, Rory O'Brien, Peter Rock, Andrea R. Levine, and Thomas A. Zeffiro

ABSTRACT

BACKGROUND AND PURPOSE: Neuropsychiatric complications of SARS-CoV-2 infection, also known as neurologic postacute sequelae of SARS-CoV-2 infection (NeuroPASC), affect 10%–60% of infected individuals. There is growing evidence that NeuroPASC is a multi system immune dysregulation disease affecting the brain. The behavioral manifestations of NeuroPASC, such as impaired processing speed, executive function, memory retrieval, and sustained attention, suggest widespread WM involvement. Although previous work has documented WM damage following acute SARS-CoV-2 infection, its involvement in NeuroPASC is less clear. We hypothesized that macrostructural and microstructural WM differences in NeuroPASC participants would accompany cognitive and immune system differences.

MATERIALS AND METHODS: In a cross-sectional study, we screened a total of 159 potential participants and enrolled 72 participants, with 41 asymptomatic controls (NoCOVID) and 31 NeuroPASC participants matched for age, sex, and education. Exclusion criteria included neurologic disorders unrelated to SARS-CoV-2 infection. Assessments included clinical symptom questionnaires, psychometric tests, brain MRI measures, and peripheral cytokine levels. Statistical modeling included separate multivariable regression analyses of GM/WM/CSF volume, WM microstructure, cognitive, and cytokine concentration between-group differences.

RESULTS: NeuroPASC participants had larger cerebral WM volume than NoCOVID controls (β = 0.229; 95% CI: 0.017–0.441; t = 2.16; P = .035). The most pronounced effects were in the prefrontal and anterior temporal WM. NeuroPASC participants also exhibited higher WM mean kurtosis, consistent with ongoing neuroinflammation. NeuroPASC participants had more self-reported symptoms, including headache, and lower performance on measures of attention, concentration, verbal learning, and processing speed. A multivariate profile analysis of the cytokine panel showed different group cytokine profiles (Wald-type-statistic = 44.6, P = .046), with interferon (IFN)-λ1 and IFN-λ2/3 levels higher in the NeuroPASC group.

CONCLUSIONS: NeuroPASC participants reported symptoms of lower concentration, higher fatigue, and impaired cognition compatible with WM syndrome. Psychometric testing confirmed these findings. NeuroPASC participants exhibited larger cerebral WM volume and higher WM mean kurtosis than NoCOVID controls. These findings suggest that immune dysregulation could influence WM properties to produce WM volume increases and consequent cognitive effects and headaches. Further work will be needed to establish mechanistic links among these variables.

ABBREVIATIONS: COVID = SARS-CoV-2 infection; DKI = diffusional kurtosis imaging; dMRI = diffusion MRI; FA = fractional anisotropy; FWE = family-wise error; IL = interleukin; IFN = interferon; NeuroPASC = neurologic postacute sequelae of SARS-CoV-2 infection; NeuroQOL = neuro-quality of life; PASC = postacute sequelae of SARS-CoV-2 infection; SD = standard deviation; TFCE = threshold-free cluster enhancement; WTS = Wald-type statistic

Neuropsychiatric complications of SARS-CoV-2 infection, also known as neurologic postacute sequelae of SARS-CoV-2 infection (NeuroPASC), affect 10%–60% of infected individuals.[1,2] These sequelae include fatigue, memory problems, attention deficits, sleep disorders, headaches, anosmia/hyposmia, depression, and anxiety, constituting a syndrome that can last for months or even years after infection.[3,4] While the signs and symptoms of NeuroPASC are well-documented, its biologic basis is poorly understood.

Received May 11, 2024; accepted after revision July 11.

From the Departments of Diagnostic Radiology & Nuclear Medicine (E.E.O., N.R., T.A.Z.), Pediatrics (R.S.-G.), Anesthesiology (P.R.), Medicine (A.R.L.), Division of Pulmonary and Critical Care Medicine, University of Maryland School of Medicine, Baltimore, Maryland; and Lantern Lab (R.O.), Fulton, Maryland.

Erin E. O'Connor and Thomas A. Zeffiro contributed equally to this work.

This work was supported by K23MH118070l University of Maryland Baltimore, Institute for Clinical & Translational Research, and the National Center for Advancing Translational Sciences (NCATS) CTSA grant number 1UL1TR003098.

Please address correspondence to Erin O'Connor, MD, University of Maryland School of Medicine, Department of Diagnostic Radiology & Nuclear Medicine, 22 S Greene St, Baltimore, MD 21201; e-mail: erin.oconnor@umm.edu

Indicates article with online supplemental data.

http://dx.doi.org/10.3174/ajnr.A8481

The behavioral manifestations of NeuroPASC, such as impairments in processing speed, executive function, memory retrieval, and sustained attention, suggest the type of widespread WM injury associated with "white matter syndromes."[5–7] The psychometric profile characterizing WM syndromes includes cognitive slowing, executive dysfunction, memory retrieval deficits, sustained attention problems, visuospatial impairment, and emotional dysregulation.[5,8] The behavioral importance of WM function is underscored by associations among WM injury, cognitive impairment, and depression in other diseases, including vascular dementia, major depressive disorder, multiple sclerosis, traumatic brain injury, and following chemotherapy.[7,9–12] Deficits in executive function, processing speed, attention, and memory are common in these studies. Nevertheless, as distributed neuronal dysfunction could mimic many of these signs, we cannot exclude that possibility. Because the behavioral problems seen in NeuroPASC are consistent with WM syndrome, we focused on WM macrostructural and microstructural measures.

WM tracts comprise approximately one-half of total brain volume, connecting cortical and subcortical GM regions into functional neural networks. The wide distribution of these tracts lends itself to variation as to which neural networks can be impaired.[13] As SARS-CoV-2 does not appear to have high specificity for any particular WM tract, high behavioral variability can be expected in the NeuroPASC phenotype.

In acute SARS-CoV-2 infection, cross-sectional studies find WM hyperintensities by using conventional FLAIR MRI.[14–16] Although acute imaging studies can be confounded by infection severity and mechanical ventilation effects, WM injury has also been found following mild and moderate acute infection.[17] By contrast, visual examination of clinical structural MRI frequently fails to detect abnormalities in NeuroPASC, even in the presence of neurologic symptoms and signs.

To examine the contribution of WM dysfunction to cognitive impairment in NeuroPASC, we used quantitative analysis of high-resolution MRI to examine WM macrostructure and diffusion MRI (dMRI) to examine WM microstructure. For clinical characterization, we used postacute sequelae of SARS-CoV-2 infection (PASC) scores, a symptom framework used for clinical case identification that heavily weights NeuroPASC symptoms. Because there is growing evidence that persisting symptoms after SARS-CoV-2 infection may be related to immune dysregulation, we measured chemokine/cytokine concentrations to determine if cytokine differences accompanied the WM, cognitive performance, and clinical manifestations. Our central hypothesis is that self-reported clinical symptoms summarized by using the PASC score and associated psychometric deficits consistent with WM syndromes would be accompanied by WM structural effects. These effects will scale with NeuroPASC clinical severity.

We used a STROBE reporting checklist to guide this work.

MATERIALS AND METHODS

Ethics Statement

Study procedures were approved by our Institutional Review Board. We conducted procedures in accordance with principles outlined in the 1964 Declaration of Helsinki and the International Conference on Harmonization Good Clinical Practice guidelines. Before enrollment, we informed participants of research objectives and procedures. Written informed consent was obtained.

Participants

We recruited participants through medical center referrals, advertisements, and the university COVID-19 biorepository. Inclusion criteria included 1) men or women of any ethnicity, ages 18–70 years, 2) fluency in English, and 3) adequate visual and auditory acuity for testing. Recruitment took place between September 2021 and February 2023. SARS-CoV-2 infected participants were asked about the presence of "cognitive fog" or mental fatigue beginning after SARS-CoV-2 infection.

To increase generalizability, alcohol, marijuana, and nicotine use were permitted. Marijuana use was not permitted on the day of, or day before, participation. Participants were excluded if substance use or substance use disorder was reported in the past 180 days. We administered urine drug screens on the testing day.

Other exclusion criteria included 1) pregnancy, 2) claustrophobia, 3) MRI contraindications, 4) neurologic disorders unrelated to SARS-CoV-2 infection including seizure disorders, closed head injuries with loss of consciousness greater than 15 minutes, CNS neoplasm, multiple sclerosis, neurodegenerative disease or stroke, 5) unstable cardiac or pulmonary disease, and 6) chronic fatigue. All participants had a negative rapid antigen test to screen for acute SARS-CoV-2 infection.

To determine if cognitive fog or mental fatigue were present, participants were asked during initial screening if they experienced problems with remembering events, concentrating, sustaining mental effort, thinking and focus, slowed conversational responses, or timely word selection and word retrieval. All participants assigned to the NeuroPASC group responded yes to 1 or more of these questions.

After the initial screening, SARS-CoV-2 participants completed structured questionnaires to better characterize their self-reported neurologic and systemic symptoms. We administered the neuroquality of life questions from the NIH Toolbox (NeuroQOL).[18] It included self-reported measures of anxiety, depression, apathy, fatigue, sleep, executive function, and cognition. A separate headache questionnaire identified the presence of persistent headaches beginning after the acute SARS-CoV-2 infection. Another questionnaire probed the history of drug use. Participants also answered 8 items regarding any dates of acute infection, hospitalization for SARS-CoV-2 infection (COVID-19), treatments, and vaccination status. Depression was assessed by using the Center for Epidemiological Studies Depression Scale (CES-D).[19]

Using the questionnaires and NeuroQoL answers, we computed a composite, weighted symptom score that classified participants as having PASC on the basis of 12 pertinent symptoms, of which at least 6 reflected neurologic effects[2] (Online Supplemental Data). The PASC score was developed by using a sample of over 5000 patients.[2] The score was used as a continuous estimate of clinical severity to probe associations with WM volume and psychometric performance, as described below. Other studies characterizing patients with persistent symptoms after SARS-CoV-2 infection have had less stringent inclusion criteria.[20–22] All our participants with persistent symptoms after SARS-CoV-2 infection had at least 1 neurologic symptom and met World Health Organization criteria for post-COVID syndrome.[23]

We confirmed prior SARS-CoV-2 infection with polymerase chain reaction and/or antibodies to SARS-CoV-2 nucleocapsid protein, which has sensitivity for at least 15 months after infection.[24] Infected participants were enrolled at least 12 weeks after their initial date of infection. Uninfected control participants (NoCOVID) had no known history of SARS-CoV-2 infection, no neurologic complaints, and no detectable antibodies to SARS-CoV-2 nucleocapsid protein.

Psychometric Assessments

As patients' self-reported symptoms can sometimes be at variance with objective testing results in neurologic disease, we further assessed cognitive signs by using psychometric tests that evaluated domains known to be abnormal in WM syndrome.

The d2 Test of Attention measured attention, concentration, and processing speed by requesting participants to differentiate visually similar stimuli by using a pencil to mark target characters ("d" with a total of 2 dashes placed above and/or below) occurring among nontarget characters ("d" with more or less than 2 dashes, and "p" characters with any number of dashes) in 14 consecutive 20-second trials. The Auditory Verbal Learning Test from the NIH Toolbox measured immediate memory by presenting 15 unrelated words, followed by attempted recall.

Image Acquisition

Using a 3T Prisma Scanner (Siemens) we collected 1) high-resolution (1 mm^3) T1-weighted MPRAGE structural scans to derive global and regional estimates of GM/WM/CSF volume, 2) multishell dMRI (1.7 mm^3, fractional anisotropy [FA] = 90, TE = 89, TR = 4200, multiband = 3, with 96 directions and b = 0, 500, 1000, 2000, and 3000) to assess WM microstructure, and 3) high-resolution (1 mm^3) FLAIR images to assess WM hyperintensities. Processing of T1-weighted structural images with CAT12[25] included spatial normalization, tissue segmentation, and smoothing (8 mm full width at half maximum), followed by computation of regional maps of GM, WM, and CSF volume.[26] CAT12 provides voxelwise estimates as well as total estimates of GM, WM, CSF and total intracranial volume based on the tissue segmentations. Processing of multi shell dMRI images with PyDesigner included tools from FSL and MRtrix3 for DICOM conversion, denoising, Gibbs ringing correction, eddy current motion correction, brain masking, image smoothing, and Rician bias correction.[27]

Plasma Cytokine/Chemokines

Because there is growing evidence that persisting symptoms after SARS-CoV-2 infection may be related to immune dysregulation, we investigated a select panel of chemokines/cytokines. Blood was collected and centrifuged at the study visit. Plasma was stored at −80°C. Using the LEGENDplex Human Anti-Virus Response Panel, a bead-based multiplex flow cytometric assay (Biolegend), we measured 13 cytokines/chemokines, including interleukin (IL)-1β, IL-6, IL-8, IL-10, IL-12p70, interferon (IFN)-α2, IFN-β, IFN-λ1, IFN-λ2/3, IFN-γ, TNF-α, interferon-inducible protein-10, and GM-CSF.[20] Beads were acquired by flow cytometry on an LSR-II instrument (BD Biosciences). Samples were run in duplicate, and 4000 beads per analyte were acquired per sample. Data were analyzed by using Qognit LEGENDplex software (BioLegend).

Statistical Analysis

Univariate and multivariate statistical analysis was done by using R 4.4.1 and included separate analyses of Fazekas scores, brain global GM/WM volumes, psychometric test results, and cytokine concentration differences. Voxelwise analysis of regional GM/WM was done by using SPM12/CAT12. Voxelwise analysis of dMRI mean kurtosis measures was done by using PyDesigner. Models were adjusted for age and sex.

Between-group differences in psychometric test results were investigated by using multivariable regression and reported as standardized parameter estimates and 95% confidence intervals.

To assure that differences in the WM segmentations were not influenced by WM hyperintensities, the study neuroradiologist quantified WM lesions from the FLAIR images by using the Fazekas score, a widely used ordinal scale ranging from 0–3 to visually rate the severity of hyperintense WM signal abnormalities in MRI data.[28,29] Group differences in the Fazekas score were examined by using multivariable regression.

To examine brain macrostructural effects, tissue volumes were examined for 1) total cerebral WM/GM/CSF volume differences by using multivariable regression and 2) regional cerebral WM/GM volume differences by using voxelwise multivariable regression adjusted for age and sex, in which the critical thresholds for the voxelwise statistics were corrected for multiple tests by using Gaussian random field theory (family-wise error [FWE], $P < .05$).

After processing of dMRI, voxelwise FA was estimated from the tensor fit and nonlinearly registered with FSL tools to an FA template in MNI-152 space.[30] Diffusional kurtosis imaging (DKI) analysis used the same multi shell diffusion images, allowing estimates of voxelwise mean kurtosis.[31,32] Tract-based spatial statistics (TBSS; https://fsl.fmrib.ox.ac.uk/fsl/fslwiki/TBSS) identifies WM voxels with high FA by registering all participants to a common reference, then creating an FA skeleton by erosion for voxelwise statistical modeling. The dMRI parameter maps were modeled as outcomes and group as a predictor, adjusting for age and sex. Critical thresholds were corrected for multiple tests by using Gaussian random field theory (FWE, $P < .05$).

A multivariate repeated measures cytokine profile analysis with 1 within-subject factor (cytokine) and 3 between-subject factors (group, age, and sex) was used to examine group cytokine effects, by using a Wald-type statistic (WTS; with critical threshold of $P < .05$.

RESULTS

Participants

We screened a total of 159 potential participants and enrolled 72 participants, including 41 asymptomatic controls (NoCOVID) and 31 NeuroPASC participants, with groups balanced for age, sex, and education (Table). No participant reported more than 1 SARS-CoV-2 infection. Participant substance use, demographic, and clinical characteristics are shown in Online Supplemental Data, and Tables 2–4).

Quality of Life Self-Report

In the NeuroPASC group, NeuroQoL symptoms in all domains were significantly higher compared with NoCOVID participants, with higher scores reflecting more impairment (Fig 1).

Participant characteristics

	NoCOVID	NeuroPASC	SMD
n	41	31	
PASC score[2]	1.6 (3.1)	13.0 (10.8)	1.43
Age in years (mean [SD])	46.8 (15.6)	45.0 (13.5)	0.12
Sex = F (%)	19 (46.3)	14 (45.2)	0.024
Education years (SD)	16.7 (3.1)	16.7 (3.9)	0.009
CES-D score (mean [SD])	6.4 (5.4)	14.3 (11.0)	0.913
Headache	6 (14.6)	17 (54.8)	0.931
Vaccination = Yes (%)	40 (100.0)	29 (93.5)	–
Hospitalization = Yes (%)	–	9 (29.0)	–
Supplemental oxygen = Yes (%)	–	7 (23.3)	–
Mechanical ventilation = Yes (%)	–	3 (10.0)	–
Days from infection (mean [SD])	–	322.13 (179.52)	–

Note:—SD indicates standard deviation; SMD, standardized mean difference.

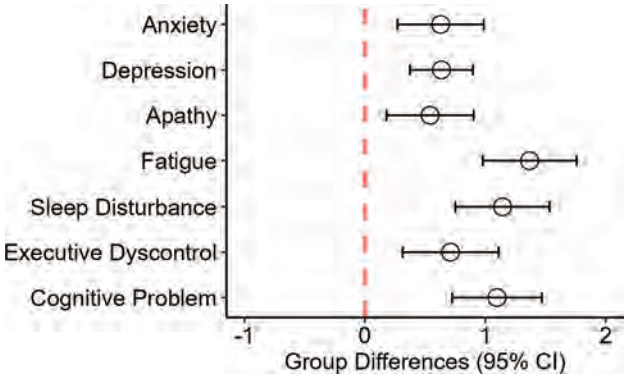

FIG 1. In NeuroPASC compared with NoCOVID participants, NeuroQoL symptoms were higher in all domains, reflecting greater disability. Group differences are shown as a forest plot by using θ scores, with values of 1 representing 1 standard deviation (SD) of difference.

Psychometric Tests

In the d2 Test of Attention, NeuroPASC participants had significantly lower processing speed ($t = -2.66$), concentration ($t = -2.28$), and accuracy ($t = -2.55$) (Fig 2). The NeuroPASC group also exhibited significantly fewer correct items in Auditory Verbal Learning test performance ($\beta = -0.51$; 95% CI: −0.94–−0.07; $t = -2.32$).

WM Hyperintensities

Using a linear model adjusted for age and sex, we did not find evidence for group differences in WM hyperintensities. FLAIR image Fazekas scores ($\beta = 0.22$; 95% CI: −0.14–0.57; $t = 1.21$) showed that clinically apparent WM changes were not associated with the observed WM macrostructural effects. WM hyperintensity scores increased with age ($\beta = 0.69$; 95% CI: 0.51–0.86; $t = 7.81$) and were lower in women ($\beta = -0.51$; 95% CI: −0.86–−0.17; $t = -2.95$) (Online Supplemental Data).

Total Tissue Volumes

CAT12 provides ROI estimates of total GM, WM, CSF, and total intracranial volume. Adjusting for age, sex, and total intracranial volume, total cerebral WM volume was 18.1 mL higher in the NeuroPASC compared with the NoCOVID group (95% CI: 1.34–34.85; $t = 2.16$). Total GM volume was 11.4 mL higher (95% CI: −12.627–34.911; $t = 0.94$). CSF volume was 29.2 mL lower (95% CI: −62.592–4.121; $t = -1.75$) (Fig 3, *left*). As expected, we observed no between-group differences in total intracranial volume.

WM Regional Cerebral Volume

A related voxelwise analysis of WM volume revealed predominantly frontal higher regional WM volume in the NeuroPASC group by using threshold-free cluster enhancement (TFCE) FWE-corrected, $P < .005$ (Fig 3, *right*).

GM Regional Cerebral Volume

GM voxelwise analysis revealed clusters of higher GM volume in the NeuroPASC group, including orbitofrontal cortex and the anterior cingulate (TFCE FWE-corrected, $P < .05$) (Fig 4).

WM Regional Microstructure

To investigate possible WM microstructural effects consistent with neuroinflammation, we used TBSS voxelwise analysis, finding that WM mean kurtosis was higher in the NeuroPASC group. Areas of higher mean kurtosis (*red-yellow*) superimposed on the DTI fractional anisotropy skeleton (*blue*) represent areas of higher WM mean kurtosis in NeuroPASC compared with NoCOVID group (TFCE FWE-corrected, $P < .05$) (Fig 5, *axial view—left, coronal view—right*).

We also investigated the relationship between psychometric attention measures and self-reported clinical severity in both groups. Higher PASC scores were negatively associated with psychometric measures, including significantly lower processing speed, lower concentration, and fewer correct responses (Fig 6).

Plasma Cytokine/Chemokine Profiles

Previous studies have demonstrated different cytokine/chemokine profiles in PASC, also known as long-COVID.[20,33] Nevertheless, it remains unclear whether these cytokine/chemokine profile differences are seen in NeuroPASC. To investigate this, we measured a panel of plasma cytokines. A multivariate repeated measures profile analysis with 1 within-subject factor (cytokine) and 3 between-subject factors (group, age, and sex) revealed a main effect of cytokine (WTS = 542.09, $P < .001$) and a group x cytokine interaction (WTS = 44.6, $P = .046$). To facilitate visualization of the group profile differences, normalized concentration values are shown in Fig 7. These results show higher IFN-λ 1 and IFN-λ 2/3 in NeuroPASC.

DISCUSSION

Summary of Results

In a sample of NeuroPASC and NoCOVID participants, we investigated SARS-CoV-2 effects on GM/WM/CSF volume, WM microstructure, cognitive performance, and peripheral cytokine concentrations. We have 4 main findings. First, our NeuroPASC group had larger global and regional (voxelwise) cerebral WM volume compared with the NoCOVID group. Second, the observed GM differences were of lesser magnitude. Third,

the NeuroPASC participants exhibited more self-reported PASC symptoms, more headaches, and lower psychometric performance on measures of attention, concentration, verbal learning, and processing speed. The WM volume differences were largest in the frontal lobe, consistent with the cognitive findings. Fourth, the NeuroPASC group showed widespread higher mean diffusional kurtosis in WM, indicating an increase in microstructural complexity possibly related to neuroinflammatory effects of SARS-CoV-2 infection. Five cytokine concentration profiles differed between the groups, suggesting that immune dysregulation following SARS-CoV-2 infection might result in cerebral WM macrostructural and microstructural injury causing NeuroPASC clinical signs and symptoms. NeuroPASC participants were seen a mean of 322 days after infection, demonstrating the persistent nature of these effects.

Total Cerebral WM Volume Differences

Our NeuroPASC group had larger total WM and GM volumes that were accompanied by smaller CSF volumes. The observed larger total WM volume and the higher mean kurtosis in NeuroPASC may reflect greater cellularity in the setting of chronic neuroinflammation, with mildly higher WM/GM volume compensated for by mildly lower CSF volume.[34]

Regional Cerebral WM Volume Differences

Our NeuroPASC group had a pattern of larger regional WM volume in frontal cortex, including WM in orbitofrontal and primary olfactory cortices. The regional specificity of effects in these areas might be explained by entry of SARS-CoV-2 via the olfactory bulb with subsequent local axonal spread to neighboring cortex.[35]

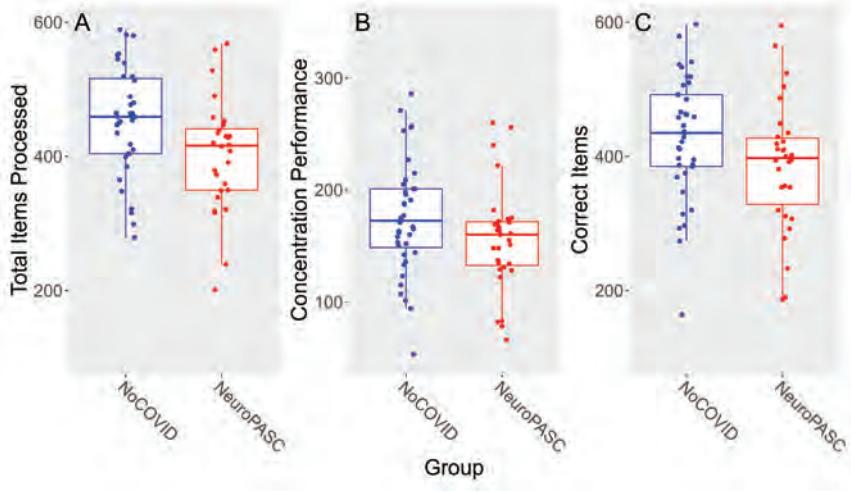

FIG 2. On the d2 Test of Attention between-group comparisons, NeuroPASC participants showed significantly: (*A*) lower processing speed ($\beta = -0.30$; 95% CI: −0.51–−0.09; $t = -2.80$), (*B*) concentration ($\beta = -0.22$; 95% CI: −0.43–−0.01; $t = -2.09$), and (*C*) accuracy ($\beta = -0.27$; 95% CI: −0.48–−0.06; $t = -2.60$).

Regional Cerebral GM Volume Differences

Larger GM volume and higher cortical thickness in the frontotemporal lobes have been reported in NeuroPASC. Like previous reports in long-COVID,[36,37] we also observed larger GM volumes in the NeuroPASC group. Although other studies have reported lower GM volume in acute SARS-CoV-2 infection, these studies did not focus on patients with persistent symptoms after SARS-CoV-2 infection.[38,39]

WM Microstructure

Using diffusional kurtosis methods, we found widespread higher kurtosis in the WM, indicating greater microstructural

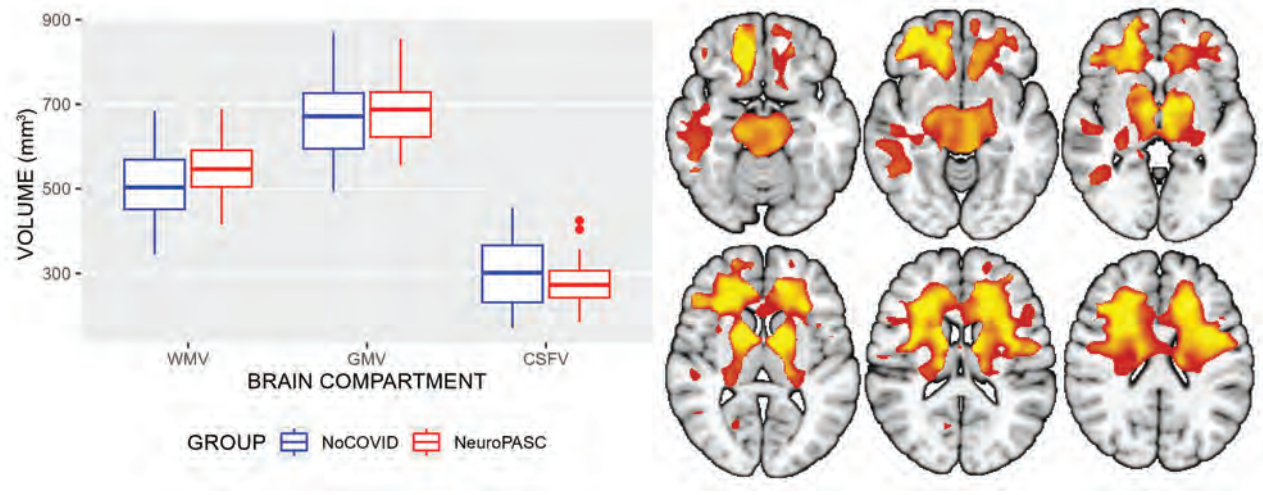

FIG 3. The total intracranial tissue compartments show interrelated changes consistent with maintenance of constant intracranial volume for each participant. In NeuroPASC participants, cerebral global WM volume is significantly higher, GM is higher, and CSF is lower (*left*). A voxelwise map of WM volume revealed widespread, predominantly frontal and subcortical, higher regional WM volume in the NeuroPASC group (*red-yellow*; $P = .005$, by using TFCE FWE-correction (*right*).

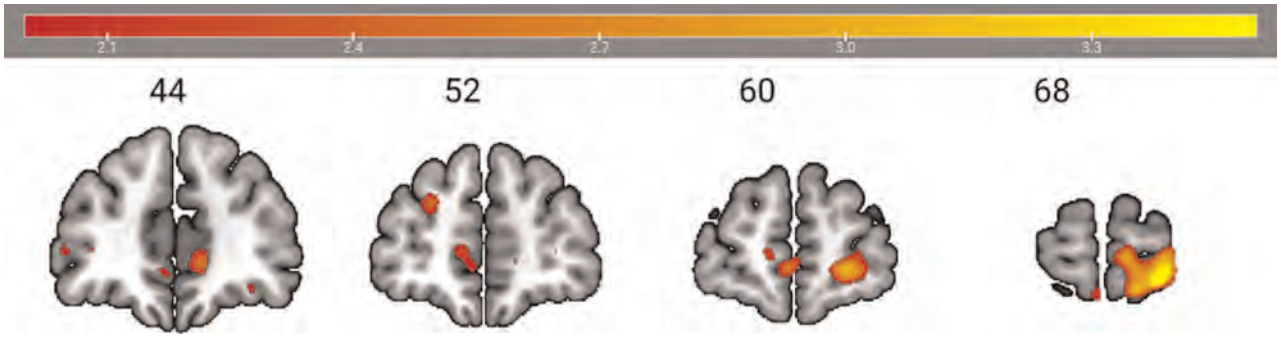

FIG 4. In NeuroPASC participants, regional GM volume was higher in the prefrontal cortex. Voxelwise analysis of group differences in GM volume (*red-yellow*) are superimposed on the group mean T1-weighted structural images. Suprathreshold voxels that represent areas of higher GM volume in NeuroPASC compared with NoCOVID ($P = .005$, TFCE FWE-corrected) are shown in coronal slices with MNI coordinates and participant left on viewer left. The color bar shows T statistic values.

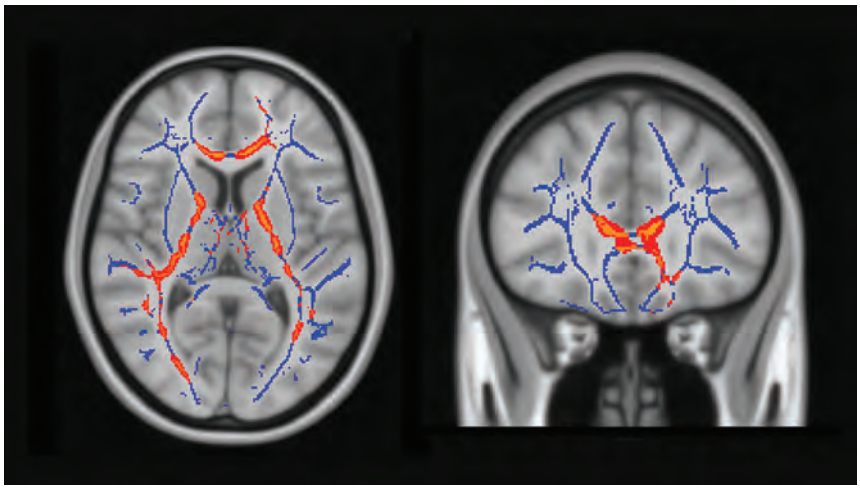

FIG 5. In NeuroPASC participants, WM mean kurtosis is significantly higher. A voxelwise analysis demonstrates group differences. Areas of higher mean kurtosis (*red-yellow*) superimposed on the DTI fractional anisotropy skeleton (*blue*) represent areas of higher WM mean kurtosis in NeuroPASC compared with NoCOVID (*left*) axial view, and (*right*) coronal view. The critical threshold was ($P = .05$, TFCE FWE-corrected).

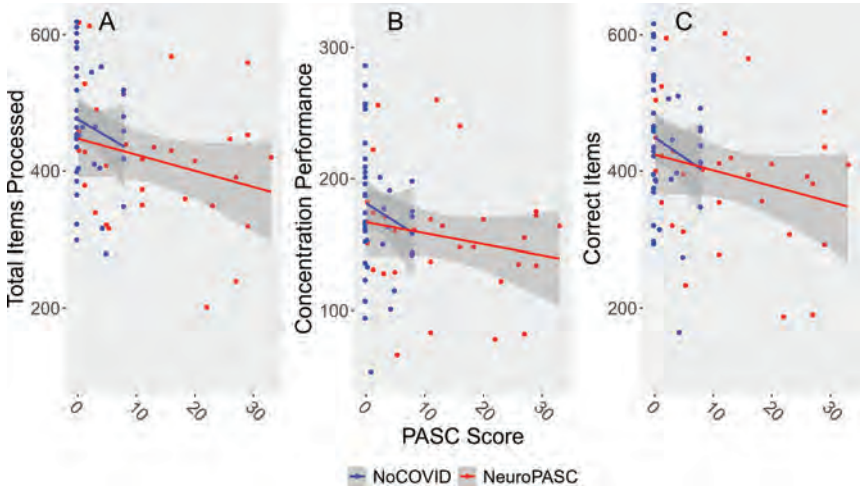

FIG 6. Higher clinical PASC scores were associated with significantly lower processing speed (*A*: $\beta = -0.30$; 95% CI: −0.51–−0.09; $t = -2.80$), lower concentration (*B*: $\beta = -0.22$; 95% CI: −0.43–−0.01; $t = -2.09$), and fewer correct responses (*C*: $\beta = -0.27$; 95% CI: −0.48–−0.06; $t = -2.60$).

complexity. Higher kurtosis has also been reported in the basal ganglia and substantia nigra in Parkinson disease, in various WM regions after concussion or repetitive sub-concussive impacts, following acute ischemia, and in higher grade gliomas.[40–45] Potential physiologic mechanisms underlying higher kurtosis include increased cellularity, neurite beading, and cellular swelling.[46,47] Greater microstructural complexity has been reported with microglial and astrocytic proliferation occurring after brain injury.[48,49] Astrocytic and microglial activation has been found on postmortem examination of patients with COVID-19, albeit not specifically in patients with NeuroPASC.[50,51]

DKI is sensitive to microstructural changes associated with reactive astrogliosis, which may be missed by standard DTI measures.[49] Microglia, the brain's resident immune cells, have shown pronounced sensitivity to the systemic immune changes in SARS-CoV-2 infection, particularly in the WM. Preclinical evidence includes WM selective microglial reactivity seen 7 weeks after mild SARS-CoV-2 infection in mice.[52] Postmortem human brain specimens reveal elevated subcortical and hippocampal WM microglial activity following mild/moderate SARS-CoV-2 infection.[52] In vivo evidence includes WM microstructure alterations detected with diffusion MRI in the subacute to chronic phase after SARS-CoV-2 infection, even in mild/moderate acute infection.[37,38,53,54] Notably, WM injury has been linked to depression, cognitive decline, and fatigue in other neuropsychiatric conditions.[9–12,55,56]

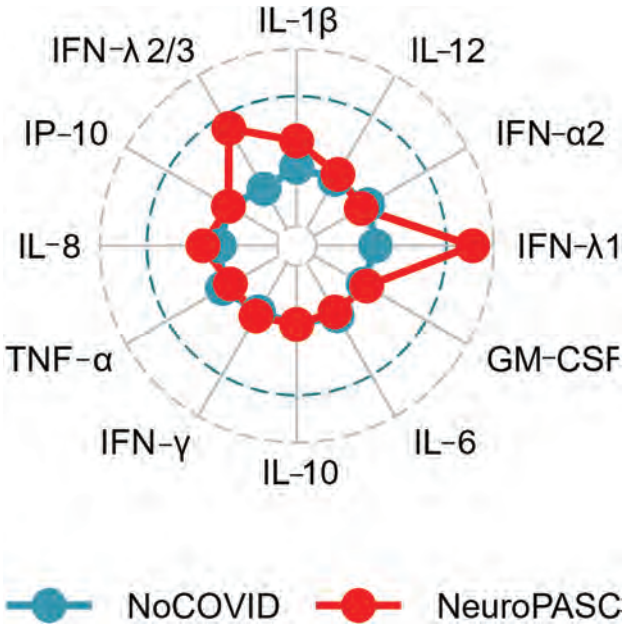

FIG 7. Normalized cytokine profiles differ between the NeuroPASC and NoCOVID groups ($P < .05$). IFN-λ 1, IFN-λ 2/3, and IL-1β concentrations were higher in the NeuroPASC group.

Our findings agree with other studies that found evidence of fluid shifts in patients with persistent neuropsychiatric symptoms following SARS-CoV-2 infection. Using diffusion MRI, Rau et al[22] found widespread fluid shifts from the intra- and extra-axonal space into the free water fraction in the supratentorial WM in patients with NeuroPASC. These WM fluid shifts accompanied cognitive impairment.

Peripheral Cytokines

There is growing evidence that persisting signs and symptoms after SARS-CoV-2 infection may be related to immune dysregulation, with cytokine profile differences reported up to 8 months after infection.[20,21,52] Cytokine concentration differences, including IFN-λ 1 and IFN-λ 2/3, have been reported in long-COVID/post-acute sequelae of COVID-19.[20,21] ILs and INFs are mainly secreted by monocytes, macrophages, and helper T-cells following inflammation. These proteins then activate processes critical for controlling viral infections, including antigen presentation, NK cell activity, and T-cell expansion, differentiation, and function.[57] The elevated cytokine concentrations observed in acute SARS-CoV-2 infection are more pronounced compared with other viral infections.[20]

Treatment Implications

Identifying WM effects of SARS-CoV-2 infection suggests potential biologic mechanisms contributing to the NeuroPASC syndrome. If the WM microstructural concomitants of NeuroPASC can be isolated, their nature may suggest underlying cellular mechanisms. If so, experimental treatments could be directed toward specific neuropathophysiologic mechanisms. For example, recovery of WM is far more likely when axons are preserved.[58] Targeted treatments have improved damaged WM macro- and microstructure in diseases such as multiple sclerosis, systemic lupus erythematosus, AIDS dementia complex, vitamin B12 deficiency, traumatic brain injury, and hypertension.[59–62] Remediating the effects of WM damage has potential ramifications for treatment and prevention of cognitive dysfunction.

Limitations

Our study has some limitations. First, some participants were referred from a post-COVID clinic with clinically diagnosed long-COVID. This may have led to higher observed clinical severity in our sample. Second, our limited sample size may have led to type II errors in detecting associations with some of the tested cytokines. Third, although we found associations among WM volume, microstructure, and PASC clinical severity, stronger evidence for causal effects of infection must await future longitudinal study. Fourth, we did not collect an asymptomatic infected control group for comparison. Finally, cytokine concentrations were likely affected by unaccounted interplay among environmental factors and genetic variation. These limitations and the generalizability of the main results can best be addressed with a larger, longitudinal sample.

CONCLUSIONS

NeuroPASC participants have larger WM volumes than NoCOVID controls and these larger WM volumes are associated with higher PASC scores and greater psychometric deficits. The WM effects may be related to neuroinflammation, with attendant inflammatory microstructural changes and extracellular fluid shifts, a conjecture that can be confirmed with further studies employing free water measures obtained by using multi shell diffusion and myelin water imaging.

ACKNOWLEDGMENTS

The authors thank the participants for their time and effort.

The authors would like to acknowledge the support of University of Maryland Medicine (UMM) Biorepository, Baltimore, Maryland, in conducting this study.

Disclosure forms provided by the authors are available with the full text and PDF of this article at www.ajnr.org.

REFERENCES

1. Taquet M, Geddes JR, Husain M, et al. **6-month neurological and psychiatric outcomes in 236 379 survivors of COVID-19: a retrospective cohort study using electronic health records**. *Lancet Psychiatry* 2021;8:416–27 CrossRef Medline
2. Thaweethai T, Jolley SE, Karlson EW; RECOVER Consortium, et al. **Development of a definition of postacute sequelae of SARS-CoV-2 infection.** *JAMA* 2023;329:1934–46 CrossRef Medline
3. Schou TM, Joca S, Wegener G, et al. **Psychiatric and neuropsychiatric sequelae of COVID-19—a systematic review**. *Brain Behav Immun* 2021;97:328–48 CrossRef Medline
4. Taquet M, Sillett R, Zhu L, et al. **Neurological and psychiatric risk trajectories after SARS-CoV-2 infection: an analysis of 2-year retrospective cohort studies including 1284437 patients**. *Lancet Psychiatry* 2022;9:815–27 CrossRef Medline
5. Filley CM. **White matter dementia.** *Ther Adv Neurol Disord* 2012; 5:267–77CrossRef Medline
6. Filley CM. **The behavioral neurology of cerebral white matter.** *Neurology* 1998;50:1535–40 CrossRef Medline

7. Gibson EM, Nagaraja S, Ocampo A, et al. **Methotrexate chemotherapy induces persistent tri-glial dysregulation that underlies chemotherapy-related cognitive impairment.** *Cell* 2019;176:43–55.e13 CrossRef Medline
8. Schmahmann JD, Smith EE, Eichler FS, et al. **Cerebral white matter: neuroanatomy, clinical neurology, and neurobehavioral correlates.** *Ann N Y Acad Sci* 2008;1142:266–309 CrossRef Medline
9. Kinnunen KM, Greenwood R, Powell JH, et al. **White matter damage and cognitive impairment after traumatic brain injury.** *Brain* 2011;134:449–63 CrossRef Medline
10. Ungvari Z, Toth P, Tarantini S, et al. **Hypertension-induced cognitive impairment: from pathophysiology to public health.** *Nat Rev Nephrol* 2021;17:639–54 CrossRef Medline
11. van Velzen LS, Kelly S, Isaev D, et al. **White matter disturbances in major depressive disorder: a coordinated analysis across 20 international cohorts in the ENIGMA MDD working group.** *Mol Psychiatry* 2020;25:1511–25 CrossRef Medline
12. Hickie I, Scott E, Wilhelm K, et al. **Subcortical hyperintensities on magnetic resonance imaging in patients with severe depression–a longitudinal evaluation**. *Biol Psychiatry* 1997;42:367–74 CrossRef Medline
13. Catani M, Ffytche DH. **The rises and falls of disconnection syndromes.** *Brain* 2005;128:2224–39 CrossRef Medline
14. Radmanesh A, Derman A, Lui YW, et al. **COVID-19-associated diffuse leukoencephalopathy and microhemorrhages.** *Radiology* 2020; 297:e223–27 CrossRef Medline
15. Wang Y, Wang Y, Huo L, et al. **SARS-CoV-2-associated acute disseminated encephalomyelitis: a systematic review of the literature.** *J Neurol* 2022;269:1071–92 CrossRef Medline
16. Klironomos S, Tzortzakakis A, Kits A, et al. **Nervous system involvement in coronavirus disease 2019: results from a retrospective consecutive neuroimaging cohort.** *Radiology* 2020;297:e324–34 CrossRef Medline
17. Marcic L, Marcic M, Kojundzic SL, et al. **Personalized approach to patient with MRI brain changes after SARS-CoV-2 infection.** *J Pers Med* 2021;11:442 CrossRef
18. Gershon RC, Lai JS, Bode R, et al. **Neuro-QOL: quality of life item banks for adults with neurological disorders: item development and calibrations based upon clinical and general population testing.** *Qual Life Res* 2012;21:475–86 CrossRef Medline
19. Radloff LS. **The CES-D scale: a self-report depression scale for research in the general population.** *App Psychol Meas* 1977;1:385–401 CrossRef
20. Phetsouphanh C, Darley DR, Wilson DB, et al. **Immunological dysfunction persists for 8 months following initial mild-to-moderate SARS-CoV-2 infection.** *Nat Immunol* 2022;23:210–16 CrossRef Medline
21. Schultheiß C, Willscher E, Paschold L, et al. **The IL-1β, IL-6, and TNF cytokine triad is associated with post-acute sequelae of COVID-19**. *Cell Rep Med* 2022;3:100663 CrossRef Medline
22. Rau A, Schroeter N, Blazhenets G, et al. **Widespread white matter oedema in subacute COVID-19 patients with neurological symptoms.** *Brain* 2022;145:3203–13 CrossRef Medline
23. Soriano JB, Murthy S, Marshall JC, WHO Clinical Case Definition Working Group on Post-COVID-19 Condition, et al. **A clinical case definition of post-COVID-19 condition by a Delphi consensus.** *Lancet Infect Dis* 2022;22:e102–07 CrossRef Medline
24. Swartz MD, DeSantis SM, Yaseen A, et al. **Antibody duration after infection from SARS-CoV-2 in the Texas coronavirus antibody response survey.** *J Infect Dis* 2023;227:193–201 CrossRef Medline
25. Gaser C, Dahnke R, Thompson PM, et al. **CAT–a computational anatomy toolbox for the analysis of structural MRI data**. *Gigascience* 2024;13:giae049
26. O'Connor EE, Zeffiro TA, Lopez OL, et al. **Differential effects of an AIDS defining illness and chronic HIV infection on gray matter volume**. *Clin Infect Dis* 2021;73:e2303–107 CrossRef Medline
27. Dhiman S, Hickey RE, Thorn KE, et al. **PyDesigner v1.0: a pythonic implementation of the DESIGNER pipeline for diffusion magnetic resonance imaging.** *J Vis Exp* 2024;207. CrossRef
28. Fazekas F, Chawluk JB, Alavi A, et al. **MR signal abnormalities at 1.5 T in Alzheimer's dementia and normal aging**. *AJR Am J Roentgenol* 1987;149:351–56 CrossRef Medline
29. Ding T, Cohen AD, O'Connor EE, et al. **An improved algorithm of white matter hyperintensity detection in elderly adults**. *Neuroimage Clin* 2020;25:102151 CrossRef Medline
30. Mori S, Oishi K, Jiang H, et al. **Stereotaxic white matter atlas based on diffusion tensor imaging in an ICBM template.** *NeuroImage* 2008;40:570–82 CrossRef Medline
31. Jensen JH, Helpern JA, Ramani A, et al. **Diffusional kurtosis imaging: the quantification of non-Gaussian water diffusion by means of magnetic resonance imaging.** *Magn Reson Med* 2005;53:1432–40 CrossRef Medline
32. Jensen JH, Helpern JA. **MRI quantification of non-Gaussian water diffusion by kurtosis analysis.** *NMR Biomed* 2010;23:698–710 CrossRef Medline
33. Low RN, Low RJ, Akrami A. **A review of cytokine-based pathophysiology of long COVID symptoms.** *Front Med (Lausanne)* 2023;10: 1011936 CrossRef Medline
34. Ho ML, Rojas R, Eisenberg RL. **Cerebral edema.** *AJR Am J Roentgenol* 2012;199:W258–73 CrossRef Medline
35. de Melo GD, Perraud V, Alvarez F, et al. **Neuroinvasion and anosmia are independent phenomena upon infection with SARS-CoV-2 and its variants.** *Nat Commun* 2023;14:4485 CrossRef Medline
36. Besteher B, Machnik M, Troll M, et al. **Larger gray matter volumes in neuropsychiatric long-COVID syndrome.** *Psychiatry Res* 2022; 317:114836 CrossRef Medline
37. Lu Y, Li X, Geng D, et al. **Cerebral micro-structural changes in COVID-19 patients - an MRI-based 3-month follow-up study.** *EClinicalMedicine* 2020;25:100484 CrossRef Medline
38. Qin Y, Wu J, Chen T, et al. **Long-term microstructure and cerebral blood flow changes in patients recovered from COVID-19 without neurological manifestations.** *J Clin Invest* 2021;131:e147329 CrossRef
39. Douaud G, Lee S, Alfaro-Almagro F, et al. **SARS-CoV-2 is associated with changes in brain structure in UK Biobank.** *Nature* 2022;604: 697–707 CrossRef Medline
40. Davenport EM, Apkarian K, Whitlow CT, et al. **Abnormalities in diffusional kurtosis metrics related to head impact exposure in a season of high school varsity football.** *J Neurotrauma* 2016;33:2133–46 CrossRef Medline
41. Chung S, Chen J, Li T, et al. **Investigating brain white matter in football players with and without concussion using a biophysical model from multishell diffusion MRI.** *AJNR Am J Neuroradiol* 2022;43:823–28 CrossRef Medline
42. Alves R, Henriques RN, Kerkelä L, et al. **Correlation tensor MRI deciphers underlying kurtosis sources in stroke**. *Neuroimage* 2022;247:118833 CrossRef Medline
43. Wang JJ, Lin WY, Lu CS, et al. **Parkinson disease: diagnostic utility of diffusion kurtosis imaging.** *Radiology* 2011;261:210–17 CrossRef Medline
44. Rong Y, Xu Z, Zhu Y, et al. **Combination of quantitative susceptibility mapping and diffusion kurtosis imaging provides potential biomarkers for early-stage Parkinson's disease**. *ACS Chem Neurosci* 2022;13:2699–708 CrossRef Medline
45. Shi W, Qu C, Wang X, et al. **Diffusion kurtosis imaging combined with dynamic susceptibility contrast-enhanced MRI in differentiating high-grade glioma recurrence from pseudoprogression.** *Eur J Radiology* 2021;144:109941 CrossRef Medline
46. Budde MD, Frank JA. **Neurite beading is sufficient to decrease the apparent diffusion coefficient after ischemic stroke.** *Proc Natl Acad Sci U S A* 2010;107:14472–77 CrossRef Medline
47. Raab P, Hattingen E, Franz K, et al. **Cerebral gliomas: diffusional kurtosis imaging analysis of microstructural differences.** *Radiology* 2010;254:876–81 CrossRef Medline

48. Steven AJ, Zhuo J, Melhem ER. **Diffusion kurtosis imaging: an emerging technique for evaluating the microstructural environment of the brain.** *AJR Am J Roentgenol* 2014;202:W26–33 CrossRef Medline
49. Zhuo J, Xu S, Proctor JL, et al. **Diffusion kurtosis as an in vivo imaging marker for reactive astrogliosis in traumatic brain injury.** *NeuroImage* 2012;59:467–77 CrossRef Medline
50. Thakur KT, Miller EH, Glendinning MD, et al. **COVID-19 neuropathology at Columbia University Irving Medical Center/New York Presbyterian Hospital.** *Brain* 2021;144:2696–708 CrossRef Medline
51. Matschke J, Lütgehetmann M, Hagel C, et al. **Neuropathology of patients with COVID-19 in Germany: a post-mortem case series**. *Lancet Neurol* 2020;19:919–29 CrossRef Medline
52. Fernández-Castañeda A, Lu P, Geraghty AC, et al. **Mild respiratory COVID can cause multi-lineage neural cell and myelin dysregulation**. *Cell* 2022;185:2452–2468.e16 CrossRef Medline
53. Benedetti F, Palladini M, Paolini M, et al. **Brain correlates of depression, post-traumatic distress, and inflammatory biomarkers in COVID-19 survivors: a multimodal magnetic resonance imaging study.** *Brain Behav Immun Health* 2021;18: 100387 CrossRef Medline
54. Petersen M, Nägele FL, Mayer C, et al. **Brain imaging and neuropsychological assessment of individuals recovered from a mild to moderate SARS-CoV-2 infection**. *Proc Natl Acad Sci U S A* 2023; 120:e2217232120 CrossRef Medline
55. Shan ZY, Kwiatek R, Burnet R, et al. **Progressive brain changes in patients with chronic fatigue syndrome: a longitudinal MRI study.** *J Magn Reson Imaging* 2016;44:1301–11 CrossRef Medline
56. Papadopoulou A, Müller-Lenke N, Naegelin Y, et al. **Contribution of cortical and white matter lesions to cognitive impairment in multiple sclerosis**. *Mult Scler* 2013;19:1290–96 CrossRef Medline
57. Dowling JW, Forero A. **Beyond good and evil: molecular mechanisms of type I and III IFN functions.** *J Immunol* 2022;208:247–56 CrossRef Medline
58. Medana IM, Esiri MM. **Axonal damage: a key predictor of outcome in human CNS diseases.** *Brain* 2003;126:515–30 CrossRef Medline
59. Mulero P, Midaglia L, Montalban X. **Ocrelizumab: a new milestone in multiple sclerosis therapy.** *Ther Adv Neurol Disord* 2018;11: 1756286418773025 CrossRef Medline
60. Xu J, Cheng Y, Chai P, et al. **White-matter volume reduction and the protective effect of immunosuppressive therapy in systemic lupus erythematosus patients with normal appearance by conventional magnetic resonance imaging.** *J Rheumatol* 2010;37:974–86 CrossRef Medline
61. Blasko I, Hinterberger M, Kemmler G, et al. **Conversion from mild cognitive impairment to dementia: influence of folic acid and vitamin B12 use in the VITA cohort.** *J Nutr Health Aging* 2012;16:687–94 CrossRef Medline
62. Mayer AR, Ling J, Mannell MV, et al. **A prospective diffusion tensor imaging study in mild traumatic brain injury.** *Neurology* 2010;74: 643–50 CrossRef Medline

Evidence for a Link of COVID-19-Associated Long-Term Neurologic Symptoms and Altered Brain Integrity?

A substantial number of individuals who have contracted coronavirus disease 2019 (COVID-19) experience prolonged symptoms. In total, it is estimated that between 6% and 10% of patients will develop a "post-Covid condition" (PCC) or "postacute sequelae of Severe Acute Respiratory Syndrome (SARS)-CoV-2" (PASC).[1-3] Among the most prevalent symptoms are fatigue and neurocognitive deficits, which can markedly contribute to the overall disease burden.[4] At present, there is no definitive pathophysiologic explanation for this condition. However, the brain is a region of interest that may warrant further investigation.[5] In light of the debilitating nature of this condition and its substantial socioeconomic implications,[6] the identification of cerebral changes associated with PCC/PASC represents an important contribution to the understanding of this pathology.

Several recent studies have identified an association between PCC and altered cerebral integrity. These findings include gray matter atrophy,[7-9] altered functional connectivity,[8,10] and altered microstructural integrity.[7,8,10,11]

In a recent study conducted by the University of Maryland School of Medicine in Baltimore,[12] O'Connor et al identified alterations in both macro- and microstructure of the brain in a total of 31 patients diagnosed with neuro-postacute sequelae of SARS-CoV-2 infection (NeuroPASC). In this study, the researchers conducted an analysis of MRI data from patients with NeuroPASC approximately 1 year after the infection compared with a group of 41 matched healthy controls. The authors reported an increase in white matter volume in the prefrontal and anterior temporal regions of patients with NeuroPASC, along with alterations in cerebral microstructure indicating a reduction in integrity. A voxel-based analysis revealed an increase in gray matter volume in the prefrontal cortex. Neurocognitive testing demonstrated a reduction in attention, concentration, processing speed, and verbal learning abilities in patients with NeuroPASC. A cytokine panel revealed elevated interferon λ1 and λ2/3 levels in the NeuroPASC group.

The most noteworthy finding of the study of O'Connor et al[12] is the substantial alteration in white matter, particularly evident in the frontal regions and encompassing the brainstem. The observation of altered diffusivity in these areas is consistent with patterns reported in previous studies by Díez-Cirarda et al[8] and Paolini et al.[10] Specifically, O'Connor et al[12] observed a higher mean kurtosis in NeuroPASC, indicating a more complex microstructure or increased tissue heterogeneity. This finding aligns with the previously observed reduction in mean diffusivity.[8] However, the increase in gray matter volume in the prefrontal cortex observed by O'Connor et al[12] contradicts existing data, which report volume or cortical thickness reduction in the frontal and limbic regions[8,9] or widespread gray matter microstructural alterations.[11]

In larger cohorts, associations between altered microstructure and clinical symptoms have been established. For instance, reduced microstructural integrity has been linked to cognitive dysfunction,[8,10,11] fatigue,[7,11] and diminished olfactory performance.[11] In addition to their imaging findings, O'Connor et al[12] present data from comprehensive neurocognitive assessments and elevated levels of type III interferon subtypes. Type III interferon receptors are expressed on epithelial cells and selected immune cells, mediating their antiviral effects primarily in barrier tissues. Given these characteristics, their potential involvement in the pathogenesis of virus-mediated autoimmune disorders is gaining increasing attention.[13] In the present study, no association between clinical and serologic data was reported, but this may be the subject of future work.

Beyond PCC/NeuroPACS, the effects of COVID-19 infection per se on the brain are not yet fully understood. There is evidence of altered cerebral integrity in otherwise healthy individuals following COVID-19.[11,14] Further research is needed to distinguish the specific patterns of brain changes associated with COVID-19 itself from those associated with PCC or NeuroPACS.

In conclusion, the findings of O'Connor et al[12] complement existing literature and indicate that patients with PCC/NeuroPASC exhibit macro and microstructural alterations in the brain. Further research is required to demonstrate the temporal kinetics of these changes in a longitudinal study and to integrate serologic and immunologic markers in a multimodal approach to gain a comprehensive understanding.

REFERENCES

1. Thaweethai T, Jolley SE, Karlson EW, et al; RECOVER Consortium. **Development of a definition of postacute sequelae of SARS-CoV-2 infection.** *JAMA* 2023;329:1934–46 CrossRef Medline

2. Adjaye-Gbewonyo D, Vahratian A, Perrine CG, et al. **Long COVID in adults: United States, 2022.** *NCHS Data Brief* 2023;1–8 Medline
3. Augustin M, Schommers P, Stecher M, et al. **Post-COVID syndrome in non-hospitalised patients with COVID-19: a longitudinal prospective cohort study.** *Lancet Reg Health Eur* 2021;6:100122 CrossRef Medline
4. Peter RS, Nieters A, Kräusslich HG, et al; EPILOC Phase 1 Study Group. **Post-acute sequelae of COVID-19 six to 12 months after infection: population-based study**. *BMJ* 2022;379:e071050 CrossRef Medline
5. Davis HE, McCorkell L, Vogel JM, et al. **Long COVID: major findings, mechanisms and recommendations.** *Nat Rev Microbiol* 2023;21:133–46 CrossRef Medline
6. Kerksieck P, Ballouz T, Haile SR, et al. **Post COVID-19 condition, work ability and occupational changes in a population-based cohort.** *Lancet Reg Health Eur* 2023;31:100671 CrossRef Medline
7. Heine J, Schwichtenberg K, Hartung TJ, et al. **Structural brain changes in patients with post-COVID fatigue: a prospective observational study.** *eClinicalMedicine* 2023;58:101874 CrossRef Medline
8. Díez-Cirarda M, Yus M, Gómez-Ruiz N, et al. **Multimodal neuroimaging in post-COVID syndrome and correlation with cognition**. *Brain* 2023;146:2142–52 CrossRef Medline
9. Dacosta-Aguayo R, Puig J, Lamonja-Vicente N, et al; Aliança ProHEpiC-19 Cognitiu (The APC Collaborative Group). **Reduced cortical thickness correlates of cognitive dysfunction in post-COVID-19 condition: insights from a long-term follow-up**. *AJNR Am J Neuroradiol* 2024;45:647–54 CrossRef Medline
10. Paolini M, Palladini M, Mazza MG, et al. **Brain correlates of subjective cognitive complaints in COVID-19 survivors: a multimodal magnetic resonance imaging study.** *Eur Neuropsychopharmacol* 2023;68:1–10 CrossRef Medline
11. Hosp JA, Reisert M, Dressing A, et al. **Cerebral microstructural alterations in post-COVID-condition are related to cognitive impairment, olfactory dysfunction and fatigue.** *Nat Commun* 2024;15:4256 CrossRef Medline
12. O'Connor EE, Salerno-Goncalves R, Rednam N, et al. **Macro and microstructural white matter differences in neurologic postacute sequelae of SARS-CoV-2 infection**. *AJNR Am J Neuroradiol* 2024 [Epub ahead of print] CrossRef
13. Manivasagam S, Klein RS. **Type III interferons: emerging roles in autoimmunity.** *Front Immunol* 2021;12:764062 CrossRef Medline
14. Douaud G, Lee S, Alfaro-Almagro F, et al. **SARS-CoV-2 is associated with changes in brain structure in UK Biobank.** *Nature* 2022;604:697–707 CrossRef Medline

Alexander Rau
Horst Urbach
Department of Neuroradiology
University of Freiburg
Freiburg, Germany

Jonas A. Hosp
Department of Neurology and Clinical Neuroscience
Medical Center
Faculty of Medicine
University of Freiburg
Freiburg, Germany

http://dx.doi.org/10.3174/ajnr.A8433

Spontaneous Intracranial Hypotension in Children: A Multi-Institutional Review of Spinal CSF Leaks Localized on Advanced Myelography

Ajay A. Madhavan, Peter G. Kranz, Lalani Carlton Jones, Edward S. Ahn, Timothy J. Amrhein, Waleed Brinjikji, Andrew Callen, Jeremy K. Cutsforth-Gregory, Mark D. Mamlouk, V. Michelle Silvera, and Julie B. Guerin

ABSTRACT

SUMMARY: Spontaneous intracranial hypotension is an increasingly recognized syndrome caused by a spinal CSF leak, with most reported cases occurring in adults. The use of specialized or advanced myelography to localize spinal CSF leaks has evolved substantially in recent years, particularly since the initial description of CSF-venous fistulas in 2014. To our knowledge, no prior series have evaluated the use of specialized myelographic techniques to localize CSF leaks in children with spontaneous intracranial hypotension, likely because the disease is rare in this patient population. This issue may be compounded by a hesitation to perform invasive procedures in children. In this clinical report, we conducted a multi-institutional review of pediatric patients with spontaneous spinal CSF leaks localized using advanced myelographic techniques, such as prone and decubitus digital subtraction and CT myelography, as well as dynamic CT myelography. We report the clinical features of these patients, as well as imaging findings, types of leaks discovered, and method of treatment. We found that the primary types of spontaneous spinal CSF leaks that occur in adults, including dural tears and CSF fistulas, can be seen in children, too. Furthermore, we show that specialized myelographic techniques can successfully localize these leaks and facilitate effective targeted treatment.

ABBREVIATIONS: CTM = CT myelography; CVF = CSF-venous fistula; DSM = digital subtraction myelography; ICHD = International Classification of Headache Disorders; SIH = spontaneous intracranial hypotension

Spontaneous intracranial hypotension (SIH) is a clinical syndrome that is almost always caused by a spinal CSF leak. In recent years, knowledge regarding the types of CSF leaks that cause SIH has evolved substantially. One commonly used classification system divides spinal CSF leaks into ventral dural tears (type 1a), posterior/lateral dural tears (type 1b), leaking meningeal diverticula (type 2), and CSF-venous fistulas (CVFs, type 3).[1] Although the diagnosis of SIH can be made on the basis of symptoms and brain MRI findings, advanced myelographic techniques such as digital subtraction myelography (DSM), dynamic CT myelography (CTM), or decubitus CTM without a dynamic component are typically needed to determine the exact type and location of the underlying spinal CSF leak.[2,3] These types of specialized or advanced myelography differ from conventional CTM insofar as images are typically obtained more quickly after contrast injection and patient positioning is maintained after injection to prevent dilution of contrast throughout the subarachnoid space. Because all leak types usually have similar clinical presentations related to the common pathway of unregulated CSF volume loss and spinal MRI and conventional CTM can only rarely localize spinal CSF leaks, advanced myelography with a proper technique and patient positioning is typically necessary for accurate diagnosis and localization.

Most cases of SIH occur in adults. However, SIH can occur in children as well. The largest series of pediatric patients with SIH was described by Schievink et al[4] in 2013. This was a comprehensive study illustrating clinical presentations, as well as brain MRI, spinal MRI, and conventional CTM findings in 24 children. Since that time, the various specialized myelographic techniques to localize CSF leaks more precisely have been developed. To our knowledge, examples of pediatric spinal CSF leaks localized using modern myelographic techniques have been limited to individual case reports. This is likely because SIH in children is quite rare, and leaks that have been localized on myelography are rarer still. We conducted a retrospective, multi-institutional review of cases of SIH in children whose leaks were precisely diagnosed and localized on advanced myelography, such as prone/decubitus

Received June 10, 2024; accepted after revision July 8.

From the Division of Neuroradiology (A.A.M., W.B., V.M.S., J.B.G.), Department of Neurosurgery (E.S.A.), and Department of Neurology (J.K.C.-G.), Mayo Clinic, Rochester, Minnesota; Department of Radiology (L.C.J.), Guys and St Thomas's and Kings College Hospitals NHS Foundation Trusts, London, UK; Division of Neuroradiology (P.G.K., T.J.A.), Department of Radiology, Duke Health, Durham, North Carolina; Department of Radiology (A.C.), University of Colorado Hospital, Aurora, Colorado; and Department of Radiology (M.D.M.), Permanente Medical Group, Kaiser Permanente Medical Center Santa Clara, Santa Clara, California.

Please address correspondence to Ajay Madhavan, MD, Division of Neuroradiology, Department of Radiology, Mayo Clinic, 200 First St SW, Rochester, MN 55905; e-mail: madhavan.ajay@mayo.edu

Indicates article with online supplemental data.

http://dx.doi.org/10.3174/ajnr.A8430

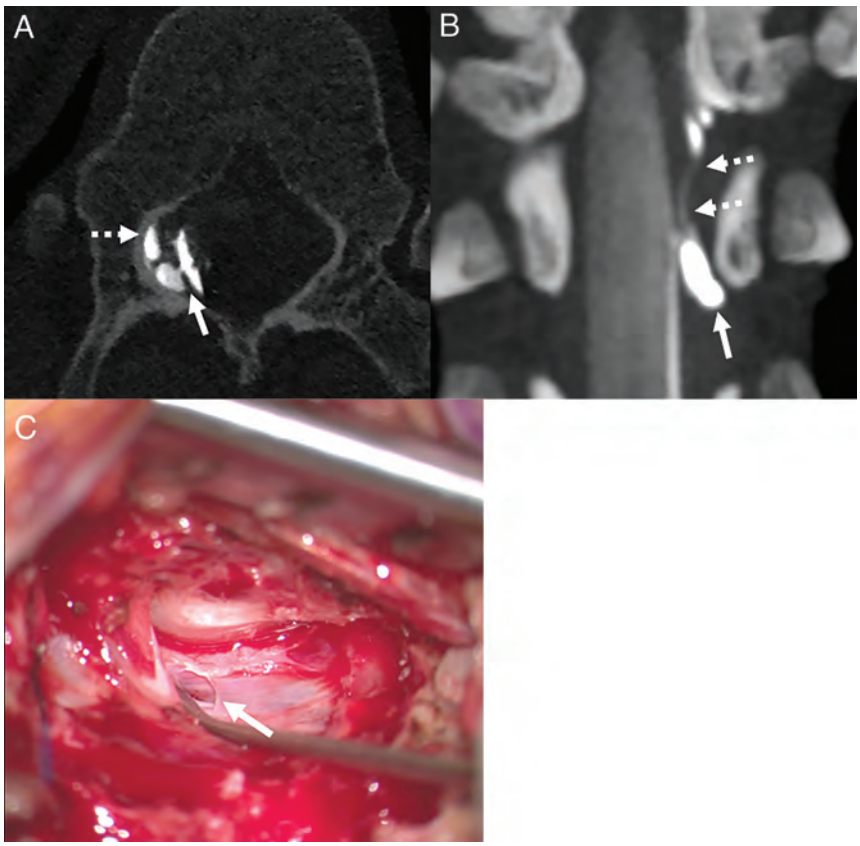

FIG 1. Right T11 (*A*) and left T4 (*B* and *C*) lateral dural tears in a 17-year-old girl and a 12-year-old girl, respectively. In the first patient, a right decubitus photon-counting CT myelogram demonstrates a right T11 lateral dural tear (*A*, *solid arrow*) with an arachnoid diverticulum herniating through the dural defect and adjacent epidural contrast (*A*, *dashed arrow*). In the second patient, coronal MIP image from a left decubitus CT myelogram shows a left T4 lateral dural tear. An arachnoid diverticulum herniates through the dural defect (*B*, *solid arrow*) with epidural contrast accumulating in the lateral epidural space (*B*, *dashed arrows*). Intraoperative photograph shows the left T4 lateral dural tear (*C*, *arrow*), which was subsequently repaired.

DSM, decubitus CTM, and prone/decubitus dynamic CTM. Our goal was to describe the various etiologies of SIH present in children and elucidate the potential benefits of advanced myelography in establishing a diagnosis and permitting targeted treatment.

CASE SERIES

Materials and Methods

The study was deemed exempt by Mayo Clinic institutional review board. The radiologic databases from 5 different institutions specializing in the diagnosis and treatment of SIH were queried. The date range for inclusion spanned 8 years (January 2016 through May 2024), with the starting date corresponding to the establishment of modern myelographic techniques at participating institutions. Inclusion criteria were the following: 1) diagnosis of SIH using the International Classification of Headache Disorders (ICHD-3) criteria, 2) age younger than 18 years at the time of symptom onset, and 3) CSF leak precisely localized by using advanced myelography, including decubitus CTM, prone/decubitus DSM, or prone/decubitus dynamic CTM.[5] We excluded any patients with nonspontaneous (ie, iatrogenic or posttraumatic) CSF leaks.

Clinical information for each patient was obtained from the medical record, including presenting symptoms, pertinent history, and details of any known genetic or other syndromes. Brain MRI and spine MRI findings were reviewed by 1 radiologist from each institution. Note that the SIH Bern score was not recorded, because this system was initially validated in an adult-only cohort.[6] Instead, we assessed the presence of subjective brain sagging, pachymeningeal enhancement/thickening, and/or venous sinus distention.

Myelographic images were reviewed by the performing radiologist at each institution to confirm the site, level, and type of leak. An additional radiologist reviewed each study independently to confirm the findings. All reviewing physicians were board-certified, practicing neuroradiologists. Each radiologist reviewing the studies had subspecialty expertise in performing and interpreting advanced myelography for patients with spinal CSF leaks. Clinical information from each patient was obtained, including a history of any connective tissue disorder or specific heritable syndrome, presenting symptoms, the presence of any major inciting factor before symptom onset, details of leak treatment, and posttreatment follow-up information.

Results

Among the 5 participating institutions, we identified 12 pediatric patients with SIH who had myelographically localized spinal CSF leaks. No patients were excluded. The mean patient age at the time of symptom onset was 13.5 years (range, 9–17 years). Nine of 12 patients were female. Eleven of 12 patients had an orthostatic headache as their chief symptom, and 1 patient presented with myelopathy with orthostatic headaches as a secondary symptom. No patients had any major trauma preceding their symptoms. Patient characteristics are summarized in the Online Supplemental Data.

Specific protocols for brain and spine MR imaging varied across institutions. However, all centers generally included similar key sequences for SIH evaluation, including sagittal T1-weighted pre- and postcontrast imaging of the brain, as well as high-resolution 3D imaging of the spine (such as T2 sampling perfection with application-optimized contrasts by using different flip angle evolution [SPACE sequence; Siemens] or CISS/FIESTA sequences). Ten of 12 patients underwent contrast-enhanced brain MRI, demonstrating dural enhancement, brain sagging, and/or venous distention in all 11 patients. One patient underwent a noncontrast MRI of the brain, showing dural thickening and effacement of the suprasellar cistern. Eleven of 12 patients

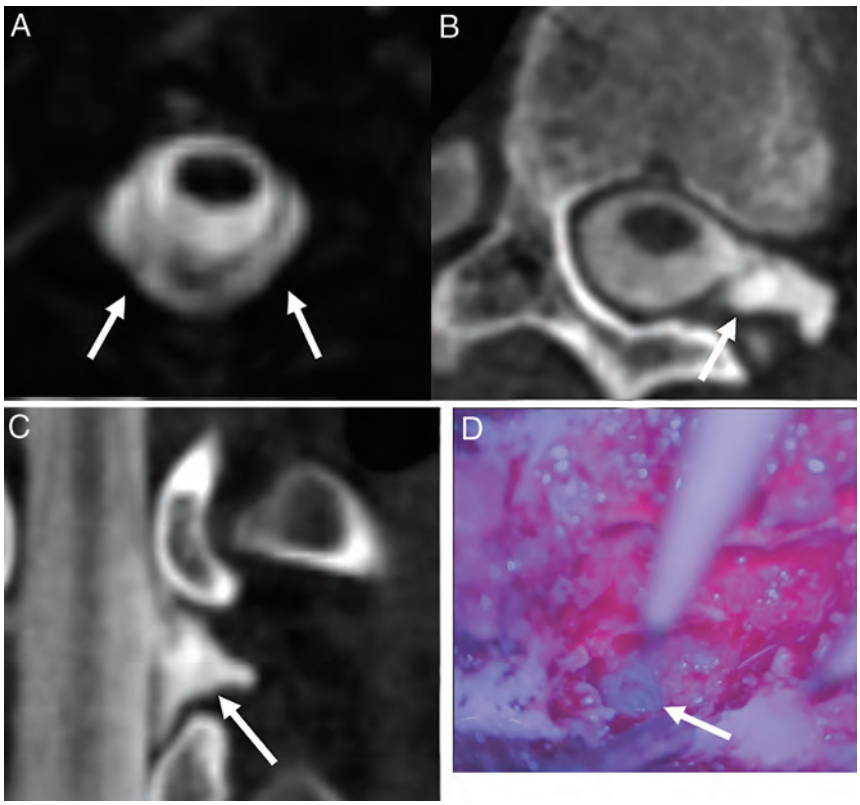

FIG 2. Left T10 lateral dural tear in a 12-year-old girl. Axial 3D T2-weighted image shows a dorsal epidural fluid collection (*A*, *arrows*). A left decubitus CT myelogram (*B* and *C*) shows a left T10 lateral dural tear with an arachnoid diverticulum herniating through the dural defect (*B* and *C*, *arrows*). Intraoperative photograph shows the lateral dural tear (*D*, *arrow*), which was subsequently repaired.

underwent noncontrast MRI of the spine, demonstrating longitudinally extensive (>4 spinal levels) extradural CSF in 7/11 patients (Online Supplemental Data). Five of 7 patients with extradural CSF had a predominantly dorsal CSF collection, 1 of 7 had a diffuse extradural collection (ventral and dorsal), and 1 of 7 had a predominantly ventral collection. Note that the 1 patient who did not have a brain MRI did have a spinal MRI demonstrating extradural CSF, which satisfies the ICHD-3 criteria for a diagnosis of SIH.

All patients underwent some form of advanced myelography, which included prone dynamic CTM ($n = 1$), decubitus CTM with or without a dynamic component ($n = 10$), or decubitus DSM with concurrent cone-beam CTM ($n = 1$).[7] Leak types observed included lateral dural tears ($n = 7$, Figs 1 and 2), CSF fistulas ($n = 4$, including 3 CVFs and 1 direct CSF-lymphatic fistula, Figs 3–5), and ventral dural tears ($n = 1$, Fig 6). Five of 7 patients with lateral dural tears had herniating/billowing arachnoid diverticula associated with the dural tear.[8] Two of 4 patients with CSF fistulas had a paraspinal venous or lymphatic malformation draining the fistula. The 2 radiologists reviewing the cases concurred on these findings for all patients.

All patients eventually underwent targeted treatment of their CSF leak, which entailed a targeted blood patch followed by surgical repair ($n = 5$), targeted blood and fibrin glue injection ($n = 1$), targeted blood patch alone ($n = 2$), targeted fibrin glue injection alone ($n = 1$), transvenous Onyx (Medtronic) embolization ($n = 1$), or surgical repair alone ($n = 2$). Eleven of 12 patients had near-complete or complete symptomatic resolution at the last clinical follow-up, with the mean timing of follow-up being 10.5 months (range, 1–24 months). One patient has not yet had clinical follow-up after the targeted intervention.

Four of 12 patients had underlying genetic or phenotypic disorders (including but not limited to connective tissue disorders) that were thought to be related to SIH, including Marfan syndrome, autosomal dominant lymphedema-distichiasis syndrome (heterozygous FOXC2 mutation), kaposiform lymphangiomatosis, and Klippel-Trenaunay syndrome (Online Supplemental Data).

DISCUSSION

We have described a multi-institutional series of 12 pediatric patients with SIH. In each case, advanced myelography was performed to localize and determine the specific type of leak present. This permitted targeted treatment in all 12 patients, leading to symptom improvement or resolution in 11/12 patients, with 1 patient awaiting clinical follow-up. To our knowledge, this is the first series describing the use of advanced myelography in pediatric patients with SIH. This contributes to the current literature, because myelographic techniques for CSF leak localization have been refined substantially in recent years, particularly since the initial description of CVFs in 2014.[9] Despite these advances, most studies on this continuously evolving topic have focused on adults.

Our study allows several insights into SIH in children. First, we found that the typical diagnostic algorithm used for adults with SIH can be successfully applied to children.[3] In adults, this entails brain and spine MRI followed by advanced myelography, with positioning for myelography being dictated by the presence or absence of extradural CSF, as well as the distribution of extradural CSF in the axial plane (ventral versus dorsal/lateral).[10] Brain MRI findings were abnormal in all 11 patients who underwent the test, and spine MRI reliably helped predict the type of leak present (dural tear in those with extradural CSF, and CVF or CSF-lymphatic fistula in those without extradural CSF).[3] Notably, patients with or without extradural CSF can theoretically also have leaks from meningeal diverticula, but these were not observed in our cohort.[1,8] For any type of leak, either DSM or CTM (with or without a dynamic component) would be a reasonable option, and this depended on institutional preference in this study. Patients were positioned prone when a ventral dural tear was suspected and positioned

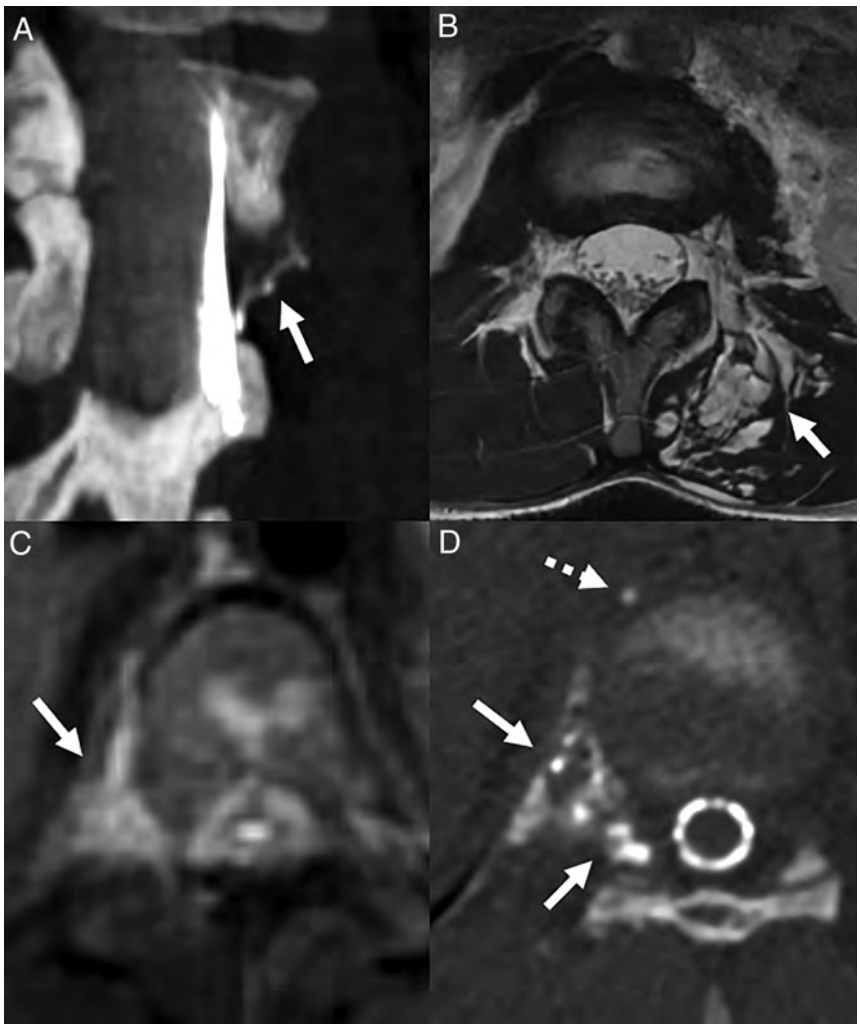

FIG 3. CSF fistulas associated with paraspinal venous and lymphatic malformations in 2 children. In the first patient, a 17-year-old girl with known Klippel-Trenaunay syndrome, a coronal oblique image from a left decubitus cone-beam CTM (*A*) performed during DSM shows a left L1 CVF (*A*, *solid arrow*). The fistula was only very subtly present on the DSM (not shown) and was draining into a lumbar paraspinal venous malformation best seen on T2-weighted MRI (*B*, *arrow*). In the second patient, a 9-year-old girl who had a history of kaposiform lymphangiomatosis, axial T2-weighted MRI shows a T2 hyperintense lymphatic malformation (*C*, *arrow*). A dynamic CT myelogram shows a right T10 CSF-lymphatic fistula, which drained to a paraspinal lymphatic malformation (*D*, *solid arrows*) and the thoracic duct (*D*, *dashed arrow*).

decubitus when a lateral dural tear, CVF, or other CSF fistula was anticipated.[10,11]

Second, we observed that lateral dural tears were the most common type of leak (seen in 7/12 patients), followed by CSF fistulas (4/12). Ventral dural tears were the least common (1/12). Although the use of a multi-institutional, retrospective format limits conclusions about the exact prevalence of different leak types, it is interesting that our findings differ from those in studies on adults, in which ventral dural tears account for a higher proportion of leaks.[1,12] Given the association of ventral dural tears with degenerative etiologies such as calcified microspurs, it is probable that the lower prevalence of ventral leaks in the pediatric population reflects the absence of spinal degenerative disease in this age group.[13] If this supposition is true, lateral dural tears and CVFs would be expected to be relatively more common in children, and this finding was observed in our cohort.

Third, our study suggests that while connective tissue disorders and/or specific genetic mutations may be present in children with SIH (as seen in 4/12 of our patients), many do not have any identifiable heritable or phenotypic abnormality known to be associated with SIH. In a prior study by Schievink et al,[4] connective tissue disorders were more common, present in 13/24 patients. The lower prevalence of these and other disorders in our cohort could be secondary to underdiagnosis or selection bias. Nonetheless, both studies suggest that heritable disorders are not universally present in children with SIH, and the diagnosis should be considered even in patients without these syndromes.

Fourth, it is interesting that 2/4 patients with CSF fistulas (CVFs or CSF-lymphatic fistulas) had paraspinal venous or lymphatic malformations. Several prior studies have shown that CVFs can be associated with such vascular lesions, and this finding was particularly common in our pediatric cohort.[14-17] These lesions may be especially important in children with SIH, and we encourage close scrutiny of premyelographic MRI or other imaging to search for such paraspinal abnormalities.

When advanced myelography is pursued to localize CSF leaks in children, care should be taken to minimize the radiation dose. DSM generally has a lower radiation dose than CTM, though availability and experience with DSM vary across institutions.[18] While DSM has better spatial and temporal resolution, only CTM provides cross-sectional detail, which is helpful and sometimes necessary to localize leaks. CTM also provides better contrast resolution, which may be helpful in detecting particularly subtle leaks.[19] The dose for CTM (especially dynamic CTM) can be mitigated by reducing the number of scans performed and limiting the scan range to the area of interest, which are the main factors that can cause dynamic CTM or other techniques to have a higher dose than conventional CTM.[20,21] Examples of applying this type of dose reduction would include scanning only levels where extradural CSF is present or focusing the search for a CVF to levels with paraspinal venous malformations. Photon-counting detector CT generally has a lower radiation dose than energy-integrating detector scanners, representing another way to reduce the dose in these patients.[22,23] Intrathecal gadolinium MR myelography was not used in any of our patients,

largely because it is generally considered to have a low diagnostic yield. Nonetheless, this would be a theoretic option to avoid ionizing radiation altogether.[24,25]

Regarding procedural techniques, needle size and type and contrast dose are important considerations for any type of myelography. Many radiologists advocate the use of small (22–25 ga) atraumatic needles to reduce the risk of post-lumbar puncture CSF leaks.[26] These may be particularly important in children with connective tissue disorders, whose dura may take longer to heal. The intrathecal contrast dose is another important consideration, and specific guidelines and evidence for pediatric patients are lacking. Ultimately, there remains substantial variability among institutions in this regard, and further study of this topic is needed. In our practices, patient and proceduralist preference usually dictates the type of needle used. Many factors such as the patient's weight, the presence or absence of meningeal diverticula, and the type of myelography being performed dictate the total contrast dose and concentration used.

Our study has limitations, one of which is its relatively small sample size. Despite reviewing databases from 5 institutions during a several-year period, we identified only 12 children with SIH who underwent advanced myelography. SIH has an overall incidence of approximately 4–5 per 100,000 per year in population-based studies.[27,28] The incidence in children is likely lower, and because only a subset of children with SIH undergoes advanced myelography, relatively few patients met our stringent inclusion criteria. Additionally, we recognize that not all institutions routinely perform advanced myelography in patients with SIH, in part because some can be cured with nontargeted blood patching or conservative measures. This approach is reasonable for some patients, and ultimately many factors such as patient and provider preference and institutional resources must be weighed to guide work-up and treatment strategies. Many types of treatment, including Onyx embolization, targeted fibrin injection, and surgery necessitate leak localization.[29,30]

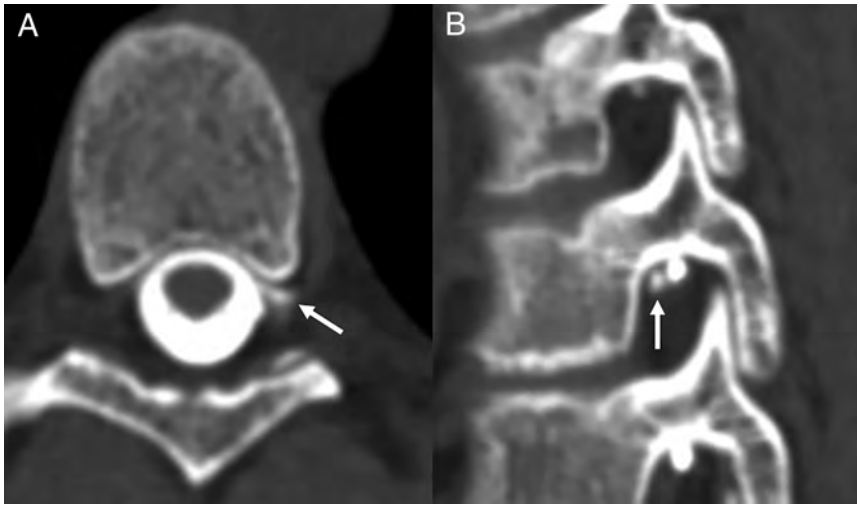

FIG 4. A left T6 CVF in a 12-year-old boy with orthostatic headaches. Axial (*A*) and sagittal (*B*) reconstructions from a left decubitus CT myelogram demonstrate a CVF (*A* and *B*, *arrows*) draining into the ventral internal epidural venous plexus and left T6 foraminal vein.

CONCLUSIONS

DSM and specialized variations of CTM to localize dural tears and CSF fistulas can be successfully applied to children with SIH. Many interesting differences in leak types and frequency compared with adults were apparent in our pediatric cohort, and future studies

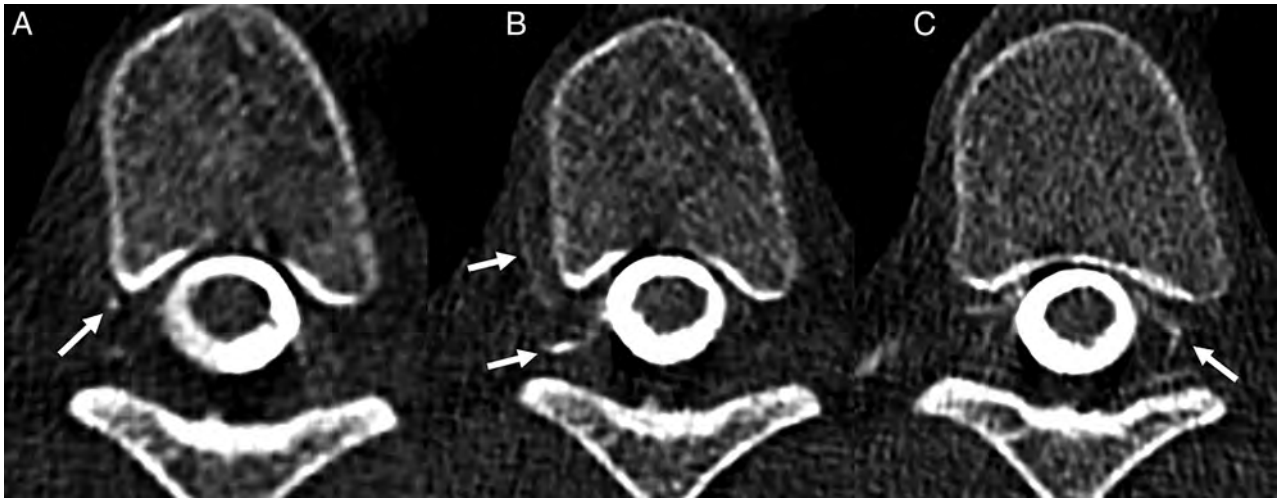

FIG 5. Complex bilateral CVF in a 13-year-old girl with an elevated BMI, presenting with new orthostatic headaches. Selected images from a same-day left (*A*) and right (*B* and *C*) decubitus CT myelograms demonstrate a CVF involving the right T7 foraminal vein (*A*, *arrow*), as well as the right T7 internal epidural venous plexus and paraspinal segmental vein (*B*, *arrows*). Most interesting, involvement of the left-sided internal epidural venous plexus was also evident on the right decubitus examination (*C*, *arrow*). Because it was uncertain from which side the fistula originated, bilateral fibrin glue injection was chosen as the treatment strategy, with follow-up pending.

FIG 6. Ventral dural tear with spinal cord herniation in a 15-year-old girl. Axial (*A*) and sagittal (*B*) images from a prone dynamic CT myelogram at the time of presentation show a ventral extradural CSF collection (*A* and *B*, *dashed arrows*). Although the ventral leak was not discreetly seen on these images (which were too delayed to see the ventral leak), the leak site was inferred from a small focus of ventral cord herniation through a dural defect at T5–T6 (*A* and *B*, *solid arrows*). The patient underwent targeted epidural blood patching. Axial (*C*) and sagittal (*D*) images from a delayed CT myelogram after treatment demonstrate resolution of the extradural CSF collection, with a small amount of ventral cord adhesion at the prior leak site (*C* and *D*, *arrows*).

will be needed to determine whether this finding represents selection bias versus true variation between children and adults.

Disclosure forms provided by the authors are available with the full text and PDF of this article at www.ajnr.org.

REFERENCES

1. Schievink WI, Maya MM, Jean-Pierre S, et al. **A classification system of spontaneous spinal CSF leaks.** *Neurology* 2016;87:673–79 CrossRef Medline
2. Carlton Jones L, Butteriss D, Scoffings D. **Spontaneous intracranial hypotension: the role of radiology in diagnosis and management.** *Clin Radiol* 2022;77:e181–94 CrossRef Medline
3. Callen AL, Timpone VM, Schwertner A, et al. **Algorithmic multimodality approach to diagnosis and treatment of spinal CSF leak and venous fistula in patients with spontaneous intracranial hypotension.** *AJR Am J Roentgenol* 2022;219:292–301 CrossRef Medline
4. Schievink WI, Maya MM, Louy C, et al. **Spontaneous intracranial hypotension in childhood and adolescence.** *J Pediatr* 2013;163:504–10 CrossRef Medline
5. **Headache Classification Committee of the International Headache Society (IHS). The International Classification of Headache Disorders, 3rd edition.** *Cephalalgia* 2018;38:1–211 CrossRef Medline
6. Dobrocky T, Grunder L, Breiding PS, et al. **Assessing spinal cerebrospinal fluid leaks in spontaneous intracranial hypotension with a scoring system based on brain magnetic resonance imaging findings.** *JAMA Neurol* 2019;76:580–87 CrossRef Medline
7. Madhavan AA, Cutsforth-Gregory JK, Benson JC, et al. **Conebeam CT as an adjunct to digital subtraction myelography for detection of CSF-venous fistulas.** *AJNR Am J Neuroradiol* 2023;44:347–50 CrossRef Medline
8. Madhavan AA, Farb RI, Brinjikji W, et al. **Expounding on the distinction between lateral dural tears and leaking meningeal diverticula in spontaneous intracranial hypotension.** *AJNR Am J Neuroradiol* 2024 Jan 27. [Epub ahead of print] CrossRef Medline
9. Schievink WI, Moser FG, Maya MM. **CSF-venous fistula in spontaneous intracranial hypotension.** *Neurology* 2014;83:472–73 CrossRef Medline
10. Madhavan AA, Verdoorn JT, Shlapak DP, et al. **Lateral decubitus dynamic CT myelography for fast cerebrospinal fluid leak localization.** *Neuroradiology* 2022;64:1897–903 CrossRef Medline
11. Kranz PG, Gray L, Amrhein TJ. **Decubitus CT myelography for detecting subtle CSF leaks in spontaneous intracranial hypotension.** *AJNR Am J Neuroradiol* 2019;40:754–56 CrossRef Medline
12. Kranz PG, Luetmer PH, Diehn FE, et al. **Myelographic techniques for the detection of spinal CSF leaks in spontaneous intracranial hypotension.** *AJR Am J Roentgenol* 2016;206:8–19 CrossRef Medline
13. Thielen KR, Sillery JC, Morris JM, et al. **Ultrafast dynamic computed tomography myelography for the precise identification of high-flow cerebrospinal fluid leaks caused by spiculated spinal osteophytes.** *J Neurosurg Spine* 2015;22:324–31 CrossRef Medline
14. Schievink WI, Maya MM, Moser FG, et al. **Spontaneous spinal CSF-venous fistulas associated with venous/venolymphatic vascular malformations: report of 3 cases.** *J Neurosurg Spine* 2019;32:305–10 CrossRef Medline
15. Madhavan AA, Kim DK, Brinjikji W, et al. **Diagnosis of a cerebrospinal fluid-venous fistula associated with a venous malformation using digital subtraction and computed tomography myelography.** *World Neurosurg* 2020;135:262–66 CrossRef Medline
16. Soderlund KA, Mamlouk MD, Shah VN, et al. **Cerebrospinal fluid-lymphatic fistula causing spontaneous intracranial hypotension in a child with kaposiform lymphangiomatosis.** *Pediatr Radiol* 2021;51:2093–97 CrossRef Medline
17. Madhavan AA, Kim DK, Carr CM, et al. **Association between Klippel-Trenaunay syndrome and spontaneous intracranial hypotension: a report of 4 patients.** *World Neurosurg* 2020;138:398–403 CrossRef Medline
18. Nicholson PJ, Guest WC, van Prooijen M, et al. **Digital subtraction myelography is associated with less radiation dose than CT-based techniques.** *Clin Neuroradiol* 2021;31:627–31 CrossRef Medline

19. Kranz PG, Gray L, Malinzak MD, et al. **CSF-venous fistulas: anatomy and diagnostic imaging.** *AJR Am J Roentgenol* 2021;217:1418–29 CrossRef Medline
20. Mamlouk MD, Shen PY, Dahlin BC. **Modified dynamic CT myelography for type 1 and 2 CSF leaks: a procedural approach.** *AJNR Am J Neuroradiol* 2023;44:341–46 CrossRef Medline
21. Mamlouk MD, Ochi RP, Jun P, et al. **Decubitus CT myelography for CSF-venous fistulas: a procedural approach.** *AJNR Am J Neuroradiol* 2021;42:32–36 CrossRef Medline
22. Marth AA, Marcus RP, Feuerriegel GC, et al. **Photon-counting detector CT versus energy-integrating detector CT of the lumbar spine: comparison of radiation dose and image quality.** *AJR Am J Roentgenol* 2024;222:e2329950 CrossRef Medline
23. Madhavan AA, Yu L, Brinjikji W, et al. **Utility of photon-counting detector CT myelography for the detection of CSF-venous fistulas.** *AJNR Am J Neuroradiol* 2023;44:740–44 CrossRef Medline
24. Madhavan AA, Carr CM, Benson JC, et al. **Diagnostic yield of intrathecal gadolinium MR myelography for CSF leak localization.** *Clin Neuroradiol* 2022;32:537–45 CrossRef Medline
25. Chazen JL, Robbins MS, Strauss SB, et al. **MR myelography for the detection of CSF-venous fistulas.** *AJNR Am J Neuroradiol* 2020;41:938–40 CrossRef Medline
26. Rochwerg B, Almenawer SA, Siemieniuk RAC, et al. **Atraumatic (pencil-point) versus conventional needles for lumbar puncture: a clinical practice guideline.** *BMJ* 2018;361:k1920 CrossRef Medline
27. Pradeep A, Madhavan AA, Brinjikji W, et al. **Incidence of spontaneous intracranial hypotension in Olmsted County, Minnesota: 2019-2021.** *Interv Neuroradiol* 2023 Mar 22 [Epub ahead of print] CrossRef Medline
28. Schievink WI, Maya MM, Moser FG, et al. **Incidence of spontaneous intracranial hypotension in a community: Beverly Hills, California, 2006-2020.** *Cephalalgia* 2022;42:312–16 CrossRef Medline
29. Brinjikji W, Madhavan A, Garza I, et al. **Clinical and imaging outcomes of 100 patients with cerebrospinal fluid-venous fistulas treated by transvenous embolization.** *J Neurointerv Surg* 2024 Jun 27 [Epub ahead of print] CrossRef Medline
30. Callen AL, Jones LC, Timpone VM, et al. **Factors predictive of treatment success in CT-guided fibrin occlusion of CSF-venous fistulas: a multicenter retrospective cross-sectional study.** *AJNR Am J Neuroradiol* 2023;44:1332–38 CrossRef Medline